

AD-A216 143

1

ANNUAL REPORT
University Research Initiative
Contract No.: N00014-86-K-0753
September 15, 1988-September 14, 1989



The Processing and Mechanical Properties of High Temperature/High Performance Composites

by

A. G. Evans & R. Mehrabian
University of California,
Santa Barbara

Arizona State University
Cambridge University
Harvard University
Stanford University
Washington State University
University of Wisconsin-Madison

DISTRIBUTION STATEMENT A
Approved for public release
Distribution Unlimited

Sponsored by: The Defense Advanced Research Projects Agency
Monitored by: Office of Naval Research

Book 3 of 6
Section 2: STRENGTH and FRACTURE RESISTANCE
Part 2 of 2

8 0 1 1 0 1 4

SUMMARY

of

TABLE OF CONTENTS

EXECUTIVE SUMMARY

SECTION 1: COATINGS AND INTERFACES Book 1

SECTION 2: STRENGTH AND FRACTURE RESISTANCE

Part 1 Book 2

Part 2 Book 3

SECTION 3: FLOW AND CREEP STRENGTH Book 4

SECTION 4: PROCESSING: Matrices and Composites

Part 1 Book 5

Part 2 Book 6

Accession For	
NTIS CR-61	J
DTIC TAG	()
Unpublished	()
Justification	
By <i>pe, CS</i>	
Distribution	
Applied by codes	
Dist	Added for Special
A-1	

BOOK 3

SECTION 2: STRENGTH AND FRACTURE RESISTANCE ~

Part 2 of 2

Ductile Reinforcement; (con't.)

- | | | |
|-----|--|--|
| 38. | A Test Procedure for Characterizing the Toughening of Brittle Intermetallics by Ductile Reinforcements | H.C. Cao
B.J. Dalgleish
H.E. Deve
C.K. Elliott
A.G. Evans
R. Mehrabian
G.R. Odette |
| 39. | Method for Processing Metal Reinforced Ceramic Composites | F.F. Lange
B.V. Velamakanni
A.G. Evans |
| 40. | High Toughness Ceramics and Ceramic Composites | M. Rühle
A.G. Evans |
| 41. | Whisker Toughening: A Comparison Between Al_2O_3 and Si_3N_4 Toughened with SiC | G.H. Campbell
M. Rühle
B.J. Dalgleish
A.G. Evans |
| 42. | High Toughness Ceramics | A.G. Evans |
| 43. | Some Recent Developments in Numerical Modelling of Fracture Toughness in Brittle Matrix Composites | C.L. Hom
P.A. Mataga
R.M. McMeeking |
| 44. | Numerical Results for Transformation Toughening in Ceramics | C.L. Hom
R.M. McMeeking |
| 45. | Crack Growth Resistance in Transformation-Toughened and Ductile-Particle Reinforced Ceramic | D.M. Stump |

9 and 1 Matrix Toughening. Keywords: Toughness, Ceramic Composites, Brittle Matrix Composites, Whisker Composites, Cracks. (AG)

- | | | |
|-----|---|---------------------|
| 46. | A First Order Perturbation Analysis on
Crack Trapping by Arrays of Obstacles | H. Gao
J.R. Rice |
| 47. | Crack Fronts Trapped by Arrays of Obstacles:
Numerical Solutions Based on Surface
Integral Representation | N. Fares |
| 48. | On the Engineering Properties of Materials | M.F. Ashby |
| 49. | Materials Selection in Conceptual Design | M.F. Ashby |

EXECUTIVE SUMMARY

The third annual report of the University Research Initiative project at UCSB on High-Temperature, High-Performance Composites consists of sections compiled in a total of six books. The first section in Book 1 is concerned with the properties and structure of bimaterial *interfaces* and the related problem of *coating* decohesion and cracking. The second section describes research on the *strengths and fracture resistance* of brittle matrix composites manufactured with fibers, whiskers and ductile phases. This information is presented in Books 2 and 3. The third section addresses the *flow and creep strength* of reinforced systems, with emphasis on effects of aspect ratio and the incidence of damage, and is offered in Book 4. The fourth section, Books 5 and 6, describes work on processing of intermetallic and ceramic matrices and composites, as well as numerical modelling of the melt-spinning process.

This is Book 3, Section 2 of the Series. Contents of this Section: Introduction to

SECTION 2: STRENGTH AND FRACTURE RESISTANCE

FIBER REINFORCEMENT

The axial tensile properties of a range of fiber reinforced ceramics have been rigorously evaluated and shown to be consistent with models previously developed in the program. In particular, the matrix cracking stresses and the ultimate strength have been predicted through the models based on independent measurements of the elastic properties, the interface sliding stress, the interface debond energy, the residual strain and the *in situ* strengths of the fibers. The basic models applicable to tensile properties, as well as the methods for measuring the important microstructural properties, are thus concluded to capture the essential features of composite behavior.

Mode I resistance curve measurements have been made on composites heat treated to produce fiber interfaces having sufficient sliding resistance that delamination cracking is suppressed (Sbaizero). The materials and test specimens lead to large scale bridging and the measured data require correction for this, as elaborated below. The crack growth behavior has also been numerically simulated (Hom and McMeeking) based on bridging and sliding traction laws derived in previous research within the program. Good agreement between the simulation and experimental data is demonstrated for an interface sliding stress consistent with the measured fiber pull-out lengths. The results also reveal that frictional dissipation during pull-out provides the main contribution to the toughness ($K_{IC} = 20 \text{ MPa}\sqrt{\text{m}}$ at steady-state) and that large scale bridging effects lead to substantial overestimates of actual toughness levels when conventional linear elastic fracture mechanics formulae are used.

Delamination cracking has been investigated in a laminated composite (Sbaizero et al.) and the data have been interpreted based on solutions for mixed mode cracking in anisotropic media (Suo). Delamination crack growth resistances have been deduced and shown to be governed primarily by the matrix fracture energy, with some contribution from distributed fibers that bridge the crack surfaces. The crack is also found to progress into a steady-state trajectory along a laminate interface; furthermore, the initial crack path rotates toward that interface in a sense governed by the sign of K_{II} .

To further understand these effects, a new method for fabricating ceramic composites has been invented (Folsom et al.). The method involves bonding together thin ceramic sheets and thin layers of fibers to form a multiple sandwich composite comprising of alternate layers of ceramic and fibers. The thin, strong ceramic sheets are formed by a method used to make ceramic substrates for electronic packaging. The fiber layers can be in the form of either aligned fibers or

cloth, which are penetrated with an appropriate bonding agent, e.g., an epoxy resin, metal or ceramic powder. The composite is formed by sandwiching the ceramic sheets with fiber layers and then bonding the ceramic sheets to the fiber layers with an applied pressure at the appropriate temperature. Current work emphasizes composites formed with epoxy resin, carbon fiber prepregs laminated between ceramic sheets comprised of either alumina, transformation toughened zirconia, or glass by hot-pressing. Because processing is simple and carried out at low temperatures, large numbers of composite modifications are being explored.

Fracture resistance caused through bridging by fiber and/or by ductile reinforcements has been addressed in the large scale bridging regime (Zok and Hom), by experiments conducted on metal reinforced ceramics (Velamakanni et al.), on fiber reinforced ceramics (Sbaizero et al.) and on a metal fiber reinforced polymer. The results establish a strong influence of large scale bridging on the apparent fracture resistance, consistent with numerical simulations of crack growth in such materials. An approximate analytical solution has also been developed that correlates well with the data and may be used for interpretation purposes and, furthermore, generates actual material resistances from the experimental results. *Additionally, this work clearly indicates that nominal fracture toughness results can substantially overestimate actual properties and must be used with caution.*

DUCTILE REINFORCEMENT

Following the results of the previous year which highlighted the importance of interface debonding and of the reinforcement ductility (Ashby et al.) on the toughness, a systematic study has been completed on the effects of those variables (Cao et al.; Dève et al.). For this purpose, experiments have been conducted on composite cylinders and on laminated systems consisting of TiAl and Nb/Ti alloys (thickness, 2R), with various thin oxide coatings and/or reaction product layers

between the matrix and reinforcements. The results reveal that Y_2O_3 coatings inhibit reactions and also allow extensive debonding (debond length $d \approx 20R$), consistent with its relatively low fracture energy ($\Gamma_i \approx 25 \text{ Jm}^{-2}$). For high ductility reinforcements, such as high purity Nb, debonding leads to a large work of rupture ($\chi \rightarrow 6-7$). In the absence of a coating, more limited debonding occurs ($d \approx 5-6R$) along a σ -phase reaction product layer, resulting in a smaller work of rupture ($\chi \approx 2.5$). Furthermore, for the latter, χ is found to be similar for composite cylinders, for laminates and for actual composites. High strength, low ductility reinforcements, such as Ti-33% Nb, indicate different characteristics. In this case, extensive debonding (induced by Y_2O_3 coatings) results in abrupt reinforcement rupture and small χ (1-1.5). However, when debonding is suppressed by averting the formation of a brittle reaction products layer, inhomogeneous deformation in the Ti/Nb apparently suppresses necking and allows a moderately large work of rupture ($\chi \approx 2-3$ in laminates and $\chi \approx 4-5$ in composites). The approach needed to achieve optimum toughening thus depends sensitively on the flow and fracture behavior of the reinforcement. An important effect of matrix crack offset on χ has also been found (Ashby) in the sense that χ increases as the offset angle increases. It remains to ascertain how this benefit can be encouraged in actual composites.

An essential, related aspect of this study concerns diffusion-couple annealing experiments which have been used to explore interactions between γ -TiAl matrices and ductile-phase reinforcements based on β -(Ti,Nb) alloys. The nature and rate of evolution of the interfacial layers have been characterized and the interdiffusion coefficients of Nb and Al in the β -(Ti,Nb) phase have been calculated for the 900-1000°C temperature range using a Matano-Boltzmann analysis. While the interdiffusion coefficients are dependent on alloy composition, the activation energies were found to be quite similar in all cases, about $250 \pm 40 \text{ kJ/mole}$ (Jewett et al.).

A process for producing ceramics with an interpenetrating network of a metallic alloy has been invented (Velakammani et al.). In this process, ceramic powder is packed within a pyrolyzable preform, e.g., an organic fiber felt, by pressure filtration. The preform is then pyrolyzed at low temperature to produce a powder compact containing pore channels remnant of the preform. The ceramic powder is densified at higher temperatures without eliminating the pore channels which are infiltrated with a molten metal. A systematic study of the fracture toughness based on the above variables, which can be changed with this new processing method, is in progress. Initial studies have emphasized Al_2O_3 and transformation toughened ZrO_2 matrices containing 20 μm fibers of a Al-Mg alloy with an architecture remnant of a needled felt used to create the channels within the ceramic. Squeeze casting is used to intrude the molten metal into the pore channels. Preliminary fracture mechanics testing to determine crack growth resistance as a function of crack length has shown that the ductile bridging ligaments increase fracture toughness.

Studies of the deformation behavior of the reinforcements have provided additional insight. Deformation of TiNb involves rafted dislocation pile-ups in narrow, coarsely distributed slip bands that extend large distances away from the crack surfaces. Fracture occurs at the intersection of these bands. In the Nb system, twinning and slip occur in the γ matrix around the interface and near the crack plane. Furthermore, debonds along the σ phase reaction product layers appear to initiate at sites where the twins intersect this layer:

MATRIX TOUGHENING

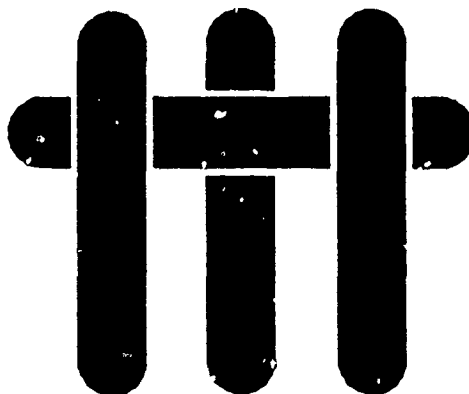
An investigation of ceramics toughened with whiskers (Campbell et al.) has established both the prevalent contributions to toughness, as well as the realistic toughening potential. The two principal toughening contributions derive from the extra surface energy associated with debonding along the amorphous phase at the interface and the energy dissipated as acoustic waves when the whiskers fail in the crack wake. These contributions can lead to toughness of order $K_{Ic} \approx 10 \text{ MPa}\sqrt{\text{m}}$. Much larger toughness could be induced by encouraging frictional dissipation by sliding and pull-out along debonded interfaces. Direct measurements of these effects (Ashby) produce an opportunity to understand how this contribution can be understood and emphasized.

Fracture resistance effects have also been explored for process zone toughening mechanisms (Stump and Budiansky; Hom and McMeeking). These results show that the resistance curves exhibit a peak preceding steady-state and that the peak height is related to the gradient in volume fraction of transformed material in the process zone, $f(y)$, in the sense that uniform transformation in the zone leads to the maximum peak height. A comparison of simulated fracture resistance curves with experimental results (Hom and McMeeking) reveals good agreement when independent measurements of $f(y)$ and of the process zone size and shape are used to set the magnitudes of the parameters used in the simulation.

The overall toughness of a reinforced system may involve multiplicative effects between matrix toughening and reinforcement toughening. Matrix toughening behaviors include the transformation and whisker mechanisms noted above, as well as twin toughening. Multiplicative effects with reinforcement toughening occurs primarily with process zone mechanisms (twinning, transformation, etc.). Analysis of the coupled toughening (Stump and Budiansky, Hom and McMeeking) have demonstrated conditions that provide the extremes of

multiplicative and additive behavior. Also, resistance curves applicable when multiple mechanisms operate have been simulated. These calculations provide the insight needed to select matrix microstructures consistent with that reinforcement scheme of choice.

M A T E R I A L S



A TEST PROCEDURE FOR CHARACTERIZING THE TOUGHENING OF BRITTLE INTERMETALLICS BY DUCTILE REINFORCEMENTS

by

H. C. Cao, B. J. Dalgleish, H. E. Dève, C. K. Elliott
A. G. Evans, R. Mehrabian and G. R. Odette

Materials Department
College of Engineering
University of California
Santa Barbara, California 93106

ABSTRACT

A cylindrical test specimen for evaluating the toughening of brittle intermetallics by ductile reinforcements has been evaluated. A processing procedure capable of producing specimens has been devised, using HIPing, and a method for the tensile testing of the specimen has been established. Results are presented for γ -TiAl reinforced with Nb and a Ti-33at%Nb alloy. The toughening imparted by these materials is interpreted in terms of their strength, ductility and interface reactions, as well as loss of constraint mediated by the extent of debonding along the reaction product layers. Finally, the results are compared with those previously obtained on actual composites.

1. INTRODUCTION

The concept whereby a brittle material can be toughened using ductile reinforcements is now well established. Indeed, this approach has been used to toughen both ceramics¹⁻⁴ and intermetallics,⁵ resulting in increases in the critical stress intensity factor by as much as four hundred percent. The mechanism primarily responsible for the increased toughness has been attributed to the plastic work that occurs in the ductile ligaments as they stretch to failure between the crack surfaces.^{2,6-8} The toughness systematically increases with increase in length of the ductile bridge zone and eventually realizes a steady-state level at a maximum bridge length governed by ligament rupture.⁶ At steady-state the increase in toughness, ΔG_c is given by,^{3,7}

$$\Delta G_c = f \sigma_0 R \chi \quad (1)$$

where f is the area fraction of ductile material on the fracture surface, σ_0 is the uniaxial yield stress, R is a representative cross sectional radius for the reinforcement and χ is a "work of rupture" function which depends on the debond length at the reinforcement matrix interface, d , the plastic displacement at ligament failure, u^* , and the work hardening coefficient, n . The ductile reinforcements may also increase toughness by crack deflection⁵ and by trapping mechanisms. However, the dominance of the plastic work contribution has been verified for several toughened composites,^{5,8} leading to identification of σ_0 , R , d and u^* as critical parameters controlling the toughness. These parameters are interdependent and governed by the combined properties of the reinforcements and the interfaces. In particular, deformation of the ductile phase takes place under evolving conditions of constraint associated with debonding from the elastic matrix, strain hardening

and large geometry changes due to necking, crack propagation or shear band formation. Easy debonding leads to lower deformation stresses and higher ductilities, whereas strong bonding increases the effective deformation stresses but decreases the ductilities. The interactions between these variables are clearly complex. However, it is noteworthy that, for highly ductile reinforcements, such as Nb in TiAl and Pb in glass, the effects on χ appear to be manifest in a single plastic stretch parameter,³ u^*/R (Fig. 1a), with the effects of debonding implicit in the trend with plastic stretch. Conversely, Ti-33at%Nb reinforcements in TiAl give an anomalously high work of rupture.

The properties of the ductile phase and interface are mediated by their respective microstructures. For example, precipitation hardening in the ductile phase increases σ_0 , but may also diminish the ductility. Debonding is expected to be a function of the constitutive properties of the ductile phase, as well as the fracture energy of the interface and/or reaction product layers. The purpose of the present study is to establish a composite cylinder test procedure that allows systematic investigation of the issues outlined above for composites having practical utility.

The test procedure is based both on the concept that toughening can be described in terms of the stress/displacement relationship for a composite cylinder^{2,3,6,7} (Fig. 1b) and on the original success of testing such specimens conducted on the model glass/Pb alloy system.³ This approach is extended in the present study, by developing solid-state processing methods suitable for composite cylinder testing applicable to material combinations having practical importance. Specifically, the procedures are developed for a TiAl matrix reinforced with pure Nb alloys and a Nb alloy. However, the methods have broad applicability to intermetallic and ceramic matrix composites reinforced with high melting temperature ductile alloys.

Ancillary characterization techniques are used to relate the macrostructure and microstructure to the mechanical performance of the composite specimens. Furthermore, the results of the composite specimen tests are compared with actual toughness measurements made on similar alloys fabricated by powder processing procedures.⁵

2. THE TEST SPECIMEN

The basic test specimen consists of a concentric cylinder shown in Fig. 2, with an outer matrix bonded to a central ductile reinforcement.³ The specimen, after processing, is circumferentially notched and precracked up to the reinforcement. A key experimental variable is the notch geometry in the vicinity of the wire. Precracking is facilitated by a deep notch with a low flank angle which terminates close to the wire interface. However, in order to accurately simulate the behavior of the reinforcement in the actual composite, it is also important that the matrix maintain an appropriate degree of elastic constraint. Clearly, this requirement places limits on the notch width and the distance between the notch tip and the wire interface. The appropriate balance between these requirements depends, in turn, on the combined properties of the composite cylinder and the method of precracking. Hence, identifying appropriate notching and precracking techniques was one of the objectives of this preliminary work.

2.1 PROCESSING

Test specimens have been prepared using the following general sequence of operations: casting cylinders of TiAl matrix material; introducing a concentric hole;

inserting the wire with a small clearance into the hole; creeping the cylinder onto the wire to create a pressure-diffusion bond between the matrix and reinforcing alloy. Such matrix cylinders with an outer diameter of 9mm, consisting of Ti-50.5at%Al, were acquired from TiMet. The microstructure of the matrix consisted primarily of single-phase γ -TiAl with a small proportion of α_2 . A 4mm diameter concentric hole was bored into each cylinder using a lathe with a diamond drill. The wires were acquired from Teledyne Wah Chang, extruded to a diameter of slightly less than 2mm, and annealed at 1060°C for 4 hours.

The wires were inserted into the TiAl matrix hole and the composite incorporated into a Ti can. The can was evacuated and sealed by welding. The canned system was inserted into a hot isostatic press (HIP) and exposed to a pressure/heating cycle (182 MPa at 1200°C for either 2 or 4 h) capable of creeping the matrix onto the wire and creating a diffusion bond.

2.2 SPECIMEN PREPARATION

Subsequent to HIPing, tensile test specimens were machined on a precision lathe. First, the outer radius of the canned system was turned to ensure that the reinforcement was centrally located. A concentric circumferential notch was then introduced into the specimen midplane. Three types of notches were employed (Fig. 3), in order to investigate a range of possible procedures. The first procedure, notch type A, used for the Ti-33at%Nb specimens consisted of initial notching with a carbide tool yielding a 2 mm outside width tapering at a low flank angle to within about 100 μ m of the wire interface (Fig. 3a); in this case the tip was further sharpened using a thin diamond blade. A similarly sharpened notch, type B, was used for one Nb specimen, except that the flank angle was zero and the root located about 300 μ m from the wire interface (Fig. 3b). The third procedure, notch C, used for the second

Nb specimen, involved diamond grinding at a flank angle of 90° to within about $400\mu\text{m}$ of the interface (Fig. 3c).

After notching, stainless steel gripping threads were adhesively bonded to each end in an alignment jig in order to maintain concentricity, by using an adhesive that maintains a bond up to the load levels expected upon testing.⁹

Tensile test specimens of the reinforcement wire, annealed at 1060°C for 4h, were also prepared. A 2cm central gauge section was formed on a 7.5 cm long 2mm diameter wire, by abrasive removal of approximately $250\mu\text{m}$ with abrasive paper. Threaded ends were then adhesively attached in an alignment jig.

2.3 TESTING PROCEDURES

Testing of the composite cylinder was performed in uniaxial tension. Load train alignment was achieved by coupling the grips to a universal joint on the top and a Teflon lubricated ball seating fixture on the bottom. The tests were conducted under displacement control at $1\mu\text{m/s}$. Displacements were measured in the gauge section using an axial extensometer attached to the specimen. The tests were also monitored optically, by using a long focal length microscope coupled with a video recorder, capable of magnifications up to 100. The real-time optical observations were found to be useful in characterizing the general features, as well as detailed aspects of crack initiation and reinforcement deformation.

Precracking was carried out as an integral part of the tensile test. Ideally, the precrack should extend from the root of the machined notch, up to the reinforcement wire, at a load below that required to yield the wire. Then, the wire deformation commences from a very sharp crack, and the entire elastic-plastic stress/deformation curve for the reinforcement is monitored. This condition is

difficult to achieve, but is most closely approximated by precracking at a slow rate with a low compliance loading train.

3. MECHANICAL CHARACTERISTICS

3.1 REINFORCING ALLOY WIRES

Tensile tests on the Nb and Ti-33at%Nb alloy wires gave the true stress/strain curves shown in Fig. 4. The properties are summarized in Table I. The Nb wire exhibited an upper yield stress of 140MPa followed by a yield drop (≈ 20 MPa) and a region of Luder's strain (0.001 to 0.01). At higher strains, hardening was rapid with strain hardening exponent $n \approx 0.3$. The uniform engineering strain upon formation of a diffuse neck was about 0.3 and the ultimate tensile stress 200MPa. The total engineering fracture strain was about 0.45 and the reduction of area (RA) 0.98. The Ti-33at%Nb alloy wire exhibited very different behavior. This material had a much higher yield stress of 430MPa, but deformed with negligible strain hardening, following a slight stress drop of ~ 20 MPa. The wire failed by the development of a pronounced local neck at a total engineering strain of only 0.16 and a RA of 0.89. Optical observation revealed the formation of a large number of surface slip bands immediately following yield and, at higher strains, indicated the development of external facets.

3.2 COMPOSITE CYLINDERS

Tensile tests on composite cylinders resulted in stress/displacement curves (Fig. 5) qualitatively similar to those previously reported.³ The test parameters are summarized in Table II, including the ligament "work of rupture" evaluated using

$$\chi = \int_0^{u^*/R} (\sigma/\sigma_0) d(u/R) \quad (2)$$

where σ is the stress and u the crack opening displacement.

The specimens containing *Nb* reinforcements experienced a load drop upon crack formation (Fig. 5), followed by a broad stress maximum at stresses in the range 1.0 to 1.7 σ_0 for displacements u between 0.2 and 1.0 R . Final fracture occurred at a critical stretch, $u^*/R = 2.0$. The "work of rupture" χ was about 1.7 for notch type C and 2.6 for notch type B. The difference between the two specimens is attributed to the large load drop involved in precracking with notch C (Fig. 5). The reinforcement morphology, observed optically, revealed a broad neck accompanied by considerable debonding, followed by final failure after extensive necking. Such deformation and failure can be characterized as low strength, low constraint and relatively high ductility. Consequently, the above result for notch B accords well with the work of rupture, plastic stretch relation applicable to ductile reinforcements (Fig. 1).

Tests on specimens with *Ti-33at%Nb* reinforcements revealed matrix crack extension well below the yield stress of the wire and hence, no load drop. The normalized stress exhibited a maximum of about 1.7 σ_0 , the fracture displacement was about 0.75 R , and the fracture work parameter $\chi = 0.75$. Optical observations revealed the formation of an asymmetric, "crack-like" neck, with the sharper side propagating to final fracture without evident debonding. The associated deformation patterns were similar to those observed in the unconstrained tensile wire test. This deformation and failure behavior can be characterized as high strength, low constraint and relatively low ductility. However, the work of rupture is anomalously low (cf. Fig. 1). The discrepancy is believed to be caused by multiple

fracture of the matrix around the notch because of the proximity of the notch tip to the wire, as discussed below.

4. MICROSTRUCTURAL AND FRACTOGRAPHIC OBSERVATIONS

4.1 INTERFACES

The interfacial regions have been studied using a variety of analytical and electron microscopy techniques on polished cross sections, as well as on foils prepared by mechanical dimpling followed by ion beam thinning. Such studies indicate that a 15 μm reaction layer has formed between the TiAl matrix and the Nb wire (Fig. 6a), although the width of the reaction zone is expected to be a function of time, temperature and pressure, as well as the gap width between the matrix and the wire. The compositions of the different regions in the reaction layer are assessed from line scans (points 1 to 20 in Fig. 6b). The measured compositions, plotted on the 1200°C isotherm of the Ti-Al-Nb ternary phase diagram¹⁰ (Fig. 7) suggest the reaction zones summarized in Table III. These results are in good agreement with the diffusion couple experiments of Hsieh et al.¹¹ Transmission electron microscopy of the reaction layer is currently underway to clarify the nature of the phases present between the α (α_2 below $\sim 1120^\circ\text{C}$) and σ fields. In particular, it would be of interest to see whether T_1 , T_2 or other phases have formed and to determine if solid-state transformations, other than α to α_2 , occurred upon cooling, because the studies of Jewett et al.¹⁰ have shown that the region between α , T_1 , T_2 and γ is sensitive to the cooling rate.

The reaction zone between TiAl and the Ti-33at%Nb was about 100 μm thick (Fig. 8a). The composition was analyzed from points 1 to 12 (Fig. 8b) and plotted on

the phase diagram in Fig. 7. The different zones in the reaction layer are summarized in Table III.

4.2 DEFORMATION, DEBONDING AND FRACTURE

Scanning electron microscopy (SEM) investigations of the fracture surfaces have revealed major differences between the Nb and the Ti-33at%Nb reinforcements. The Nb reinforcement exhibited extensive plastic deformation (i.e., a large reduction in area) and debonding (Fig. 9). Fracture occurred by void nucleation and growth (Fig. 9a). Cross sections indicated debonding to a depth of the order 0.8–1.25R (Fig. 9b). Investigation of the Nb surface in the plastic stretch zone indicated attached brittle fragments cracked in a mudcake pattern (Fig. 9b). This observation suggests that debonding occurred predominantly within the *brittle reaction product layers*, probably the σ phase (see Fig. 6). Also, plastic blunting occurred wherever the debond terminated at the ductile Nb (Fig. 9c).

The Ti-33at%Nb exhibited low ductility and minimal, if any, debonding (Fig. 10), consistent with the absence of a brittle reaction product layer (see Fig. 8). Deformation in the TiNb was characterized by a series of coarse slip steps in the regions of initial necking. The final fracture surface was relatively flat and revealed a mix of facets with areas of ductile rupture. Also, multiple cracking of the matrix and of the reaction product layers is apparent near the notch tip.

5. TOUGHENING

Initially, it is instructive to compare the composite cylinder results with measurements and observations made on powder processed alloys with reinforcing phases in the form of pancake shaped particles⁵, about 20 to 40 μ m thick. Specifically,

the Nb phase in the composite is relatively soft and ductile, forming a knife edge fracture surface, with considerable debonding from the γ -TiAl matrix. Furthermore, the deformation/fracture behavior of the Nb in the alloy is almost identical to that determined for the composite cylinder: $u^*/R = 1.6$, and $\chi = 2.7$ (Fig. 1). Consequently, by using χ values from the composite cylinder tests along with the appropriate values of f , R and σ_0^\dagger for the powder processed alloy, the predicted toughness increment of $13\text{MPa}\sqrt{\text{m}}$ for the composite is in exact agreement with the value measured for the alloy. Moreover, it is noted that composites produced using larger reinforcement radii of, say, 1mm would be predicted (Eqn. 1) to exhibit a steady-state toughness of 68kJm^{-2} at a reinforcement volume fraction of 0.2. This toughness coincides with a critical stress intensity factor of about $115\text{MPa}\sqrt{\text{m}}$. While this toughness is large, it is important to appreciate the associated implications. The "steady-state" toughness is manifest only after appreciable crack growth, estimated to be several cm for bend specimen geometries. Additionally, such large reinforcements may not be practical in many cases.

For the Ti-33at%Nb system, significant differences exist between the results obtained for composite cylinders and for the reinforced alloys.¹² In particular, the plastic work parameter was much larger for the alloy ($\chi = 4.1$) than that obtained for the composite cylinder ($\chi = 0.75$), although u^*/R was similar (0.6). This difference is governed by the lack of constraint in the composite wire specimens, resulting from multiple cracking between the notch tip and wire (Fig. 10).

Finally, it is emphasized that the toughening behavior of the Nb reinforcements in γ TiAl is much less than the optimum measured for Pb

[†] Based on hardness measurements, the Nb in the alloy had a effective strength about a factor of about 1.75 larger than in the Nb in the composite cylinder.

reinforcements in glass⁷ (Fig. 1). The difference is attributed to different debonding characteristics. Further study of such effects is of evident importance.

6. CONCLUDING REMARKS

A composite cylinder test procedure for assessing trends in the ductile reinforcement toughening of brittle intermetallics has been established. The specimens were processed by HIPing a hollow cylinder of TiAl onto Nb and Nb-alloy wires. The composite cylinders were then notched and precracked in tension. The results of the tests are in broad agreement with the behavior of reinforcements in alloys containing similar reinforcing materials and previous tests of constrained deformation of lead wires in glass. However, the constraint was not accurately simulated in the Ti-33at%Nb specimens which experienced multiple fracture of the matrix near the notch tip. This conclusion suggests that larger distances between the notch tip and wire interface are required to maintain appropriate constraint for high strength, low ductility reinforcements.

The tests demonstrate that large differences in deformation and fracture behavior exist for soft, ductile Nb and the stronger but less ductile Nb alloy. These differences are manifest in tensile tests as well as in actual composites and composite cylinders. Consequently, the need for further study of the behavior of Nb alloy reinforcements is demonstrated.

ACKNOWLEDGEMENT

The support of the Defense Advanced Research Projects Agency (DARPA) through the contract URI-N00014-86-K-0753, supervised by Dr. B. Wilcox and monitored by Dr. S. G. Fishman of the Office of Naval Research, is gratefully acknowledged. The authors would like to thank Mr. D. Stave for preparation of the HIP specimens.

TABLE I

Tensile Properties of Wires

Material	Yield Stress (MPa)	UTS (MPa)	Uniform Strain	Fracture Strain	Reduction of Area	n
Nb	140	200	0.30	0.45	0.98	0.3
Ti-33at%Nb	430	—	—	0.16	0.89	~0

TABLE II

Tensile Properties of Composite Cylinders

Reinforcing Material	Maximum Stress σ_m	Plastic Stretch u_p	Work of Rupture χ
Nb (C)	$1.4\sigma_0$	1.75R	1.7
Nb (B)	$1.9\sigma_0$	2.00R	2.6
Ti-33at%Nb	$1.7\sigma_0$	0.75R	0.75

TABLE III

Reaction Product Regions

a) Nb: TiAl					
Region:	1-2	3-4	5-13	15-18	19-20
Phase:	γ	α_2	T_2	σ	β

b) Ti-33at%Nb: TiAl			
Region:	1-2	3-6	6-12
Phase:	γ	α_2	β

REFERENCES

- [1] J. Bowling and G. W. Groves, *Jnl. Mater. Sci.* **14** (1979) 443.
- [2] L. S. Sigl, A. G. Evans, P. Mataga, R. M. McMeeking and B. J. Dalgleish, *Acta Metal.* **36** (1988) 945.
- [3] M. F. Ashby, F. J. Blunt and M. Bannister, *Acta Metall.*, in press.
- [4] A. J. Pysik, I. A. Aksay and M. Sarikaya, *Ceramic Microstructures, Materials Science Research*, Vol. 21 (ed. J. A. Pask and A. G. Evans) 1986, p. 45.
- [5] C. K. Elliott, G. R. Odette, G. E. Lucas and J. W. Sheckard, *High Temperature, High Performance Composites* (ed. Lemkey et al.) *MRS Proceedings*, Vol. 120 (1988) p. 95.
- [6] B. Budiansky, J. C. Amazigo and A. G. Evans, *Jnl. Mech. Phys. Solids* **36** (1988) 167.
- [7] P. Mataga, *Acta Metall.*, in press.
- [8] B. Flinn, M. Rühle and A. G. Evans, *Acta Metall.*, in press.
- [9] H. C. Cao and A. G. Evans, *Mechanics of Mtls.*, in press
- [10] T. J. Jewett, J. C. Lin, N. R. Ronda, L. E. Seitzman, K. C. Hsieh, Y. A. Chang and J. H. Perepezko, *Proc. MRS Fall Meeting* 1988.
- [11] K. C. Hsieh, T. J. Jewett, Y. A. Chang and J. H. Perepezko, *URI Report*, Contract No. N00014-86-K-0753, 1987.
- [12] G. R. Odette, C. K. Elliott, G. E. Lucas and J. W. Sheckhard, to be published.

FIGURE CAPTIONS

- Fig. 1. a) The work of rupture as a function of plastic stretch and
b) calculated stress, stretch curves.
- Fig. 2. The composite cylinder test specimen.
- Fig. 3. The three notch configurations used for tensile testing of the composite cylinder.
- Fig. 4. True stress-strain curves measured for the Nb and Ti-33at%Nb wires in the annealed state.
- Fig. 5. Tensile stress/crack opening curves measured for composite cylinders with Nb and Ti-33at%Nb reinforcements.
- Fig. 6. a) Cross section SEM micrograph of the Nb wire in the TiAl matrix.
b) Magnified view of the reaction layer between TiAl and Nb.
- Fig. 7. Ternary phase diagram at 1200°C. The solid circles show the diffusion path of TiAl/Nb. The arrows show the diffusion path of TiAl/Ti-33at%Nb. [Preliminary phase diagram is from Chang Perepezko.]
- Fig. 8. a) Cross section SEM micrograph of the Ti-33at%Nb wire in the TiAl matrix.
b) Magnified view of the reaction layer between TiAl and Ti-33at%Nb.
- Fig. 9. Scanning electron micrographs of fractured Nb composite cylinder specimen
a) End view of specimen after fracture showing necking of the Nb and interface debonding
b) View of the debond region showing brittle fragments on both the Nb and TiAl debond surfaces
c) A view of the end of the debond region showing brittle crack extension in the reaction product layers and blunting in the Nb.
- Fig. 10. Scanning electron micrographs of the failure process in the Ti-33at%Nb composite cylinder specimen

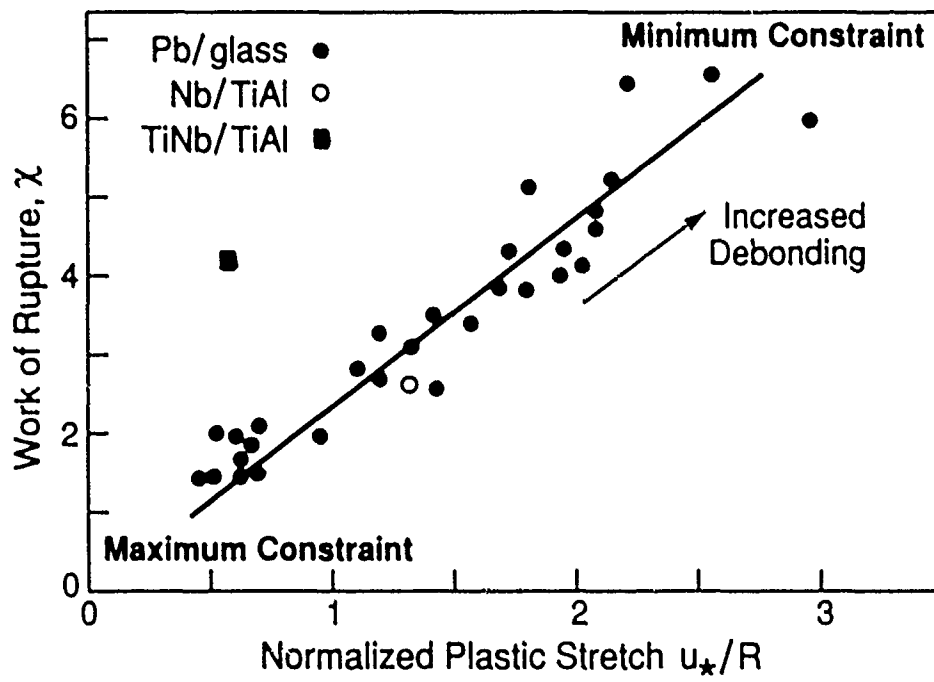


FIG. 1A

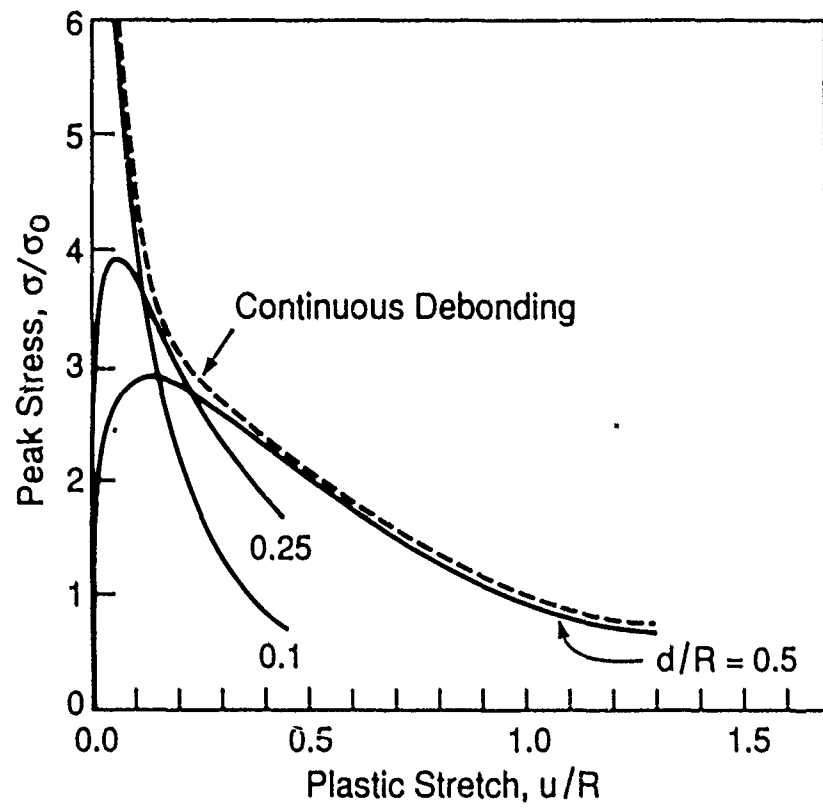


FIG. 1B

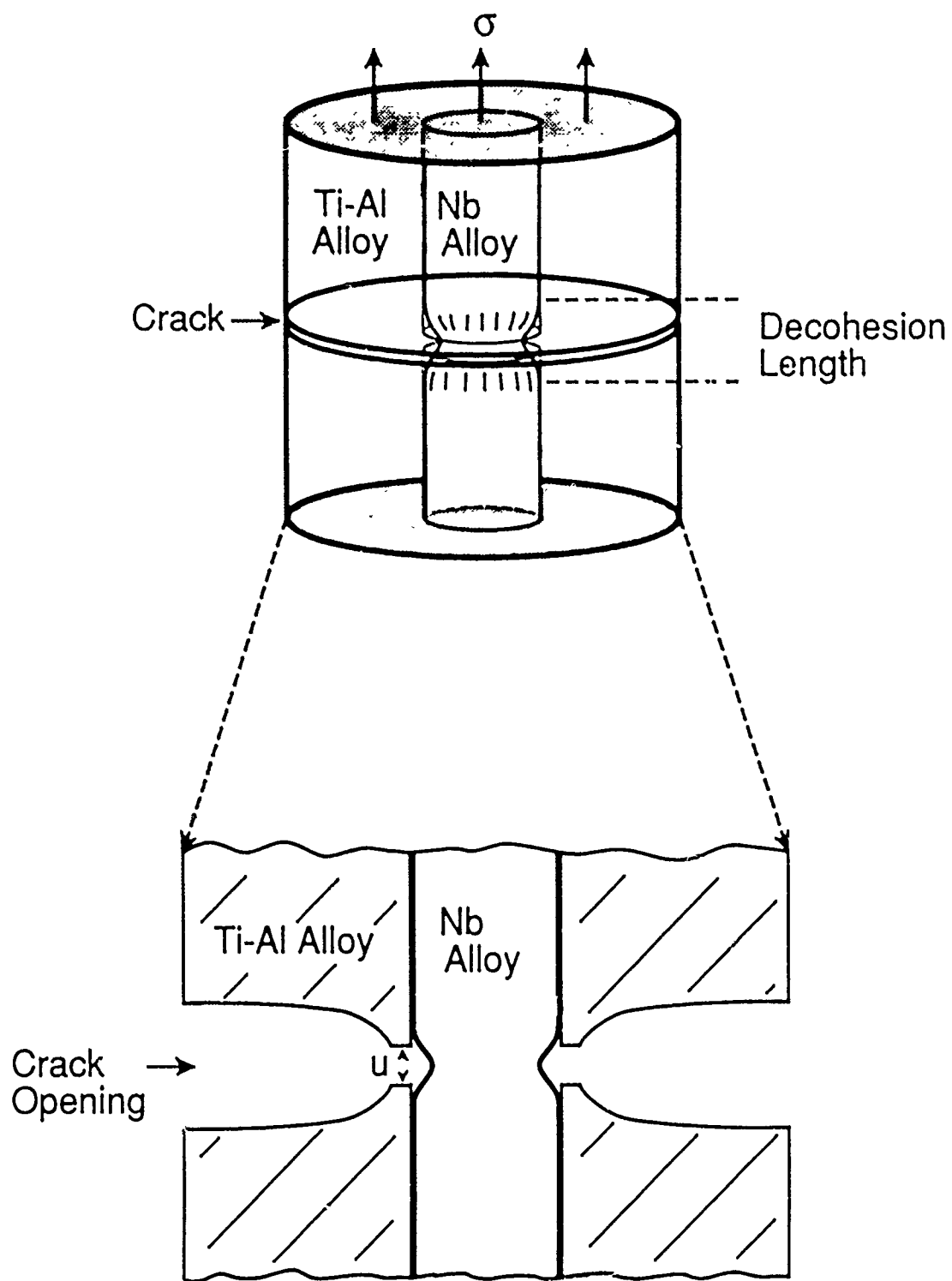
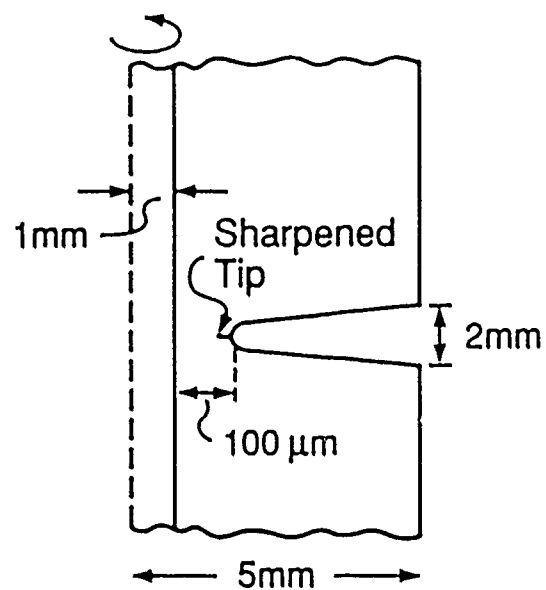
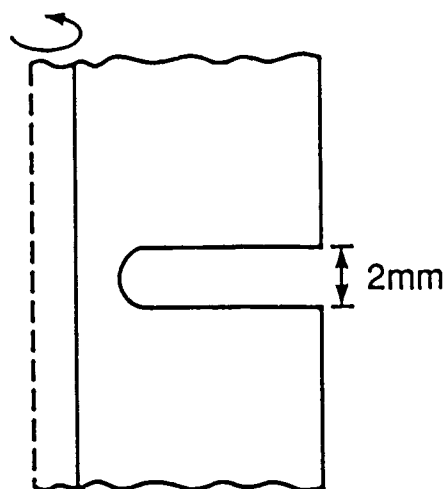


FIG. 2

a) Notch Type A



b) Notch Type B



c) Notch Type C

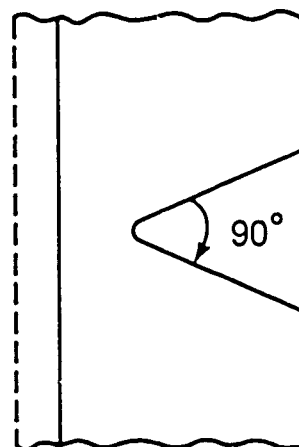


FIG. 3

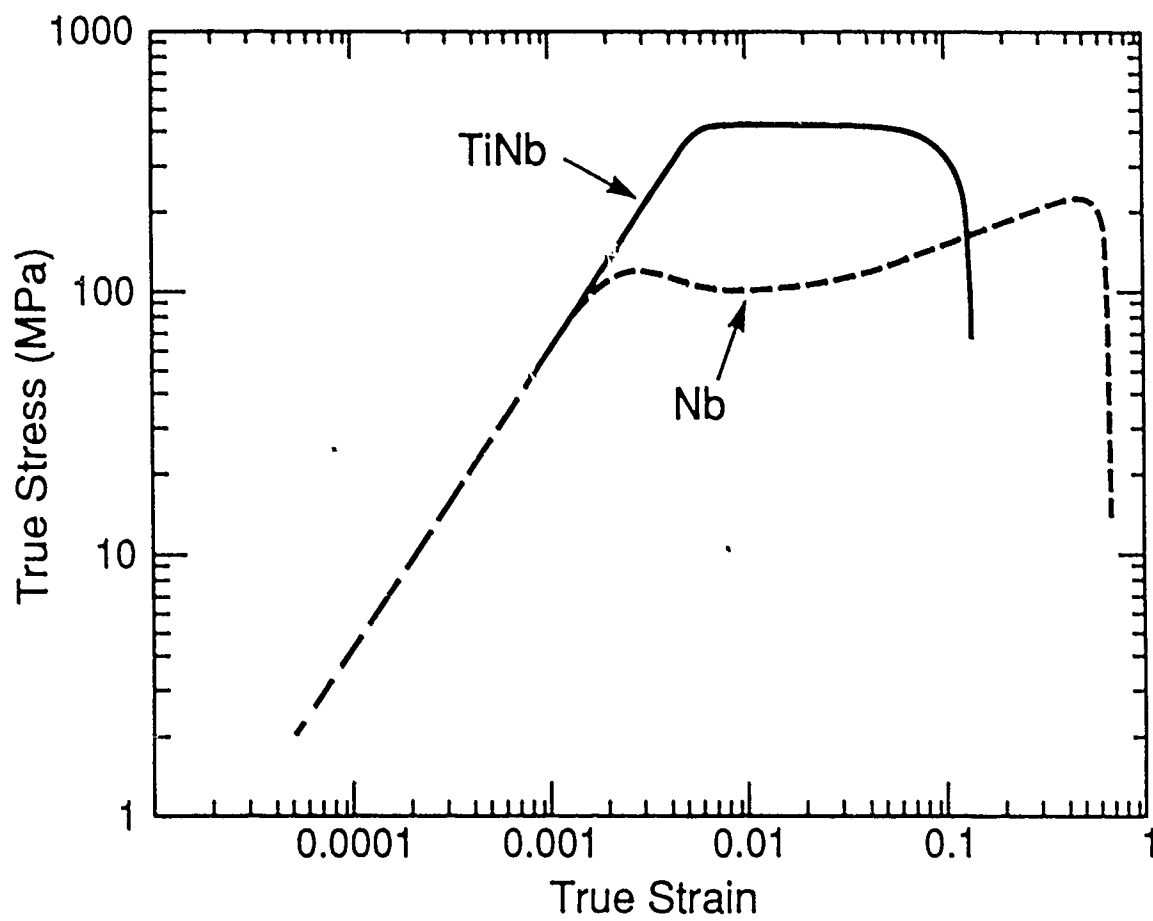


FIG. 4

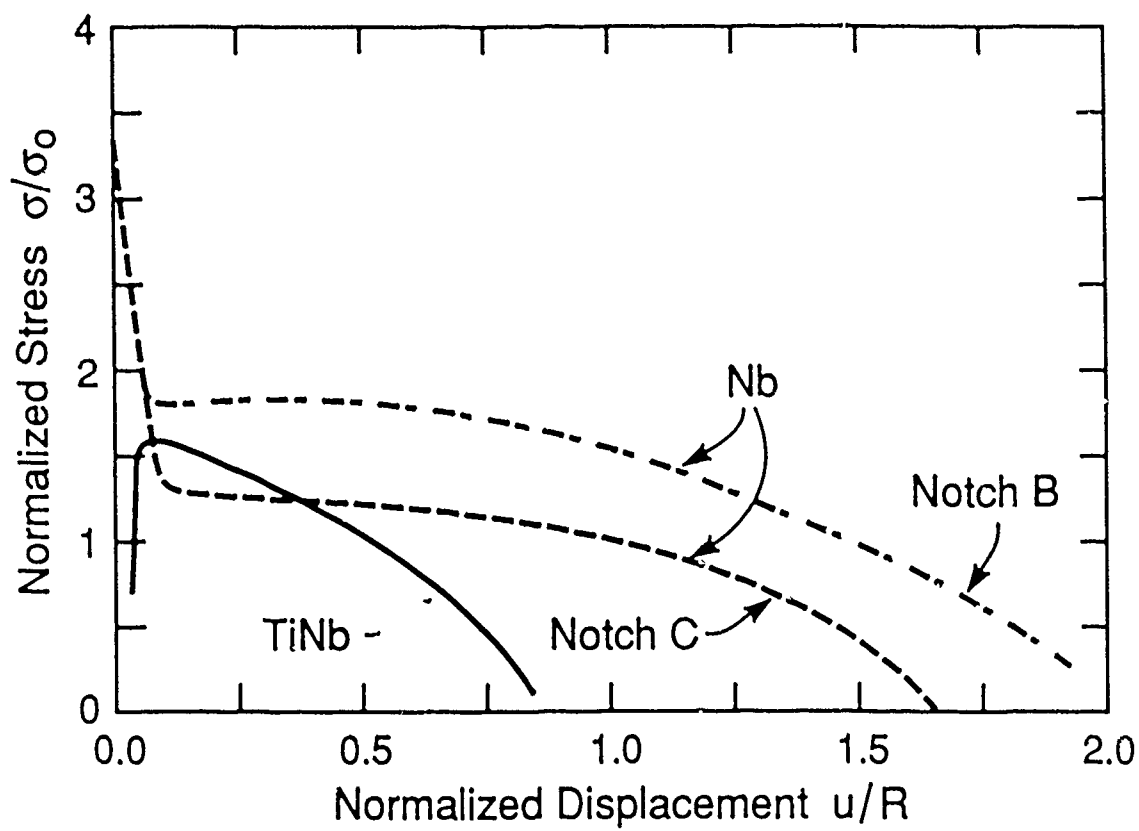
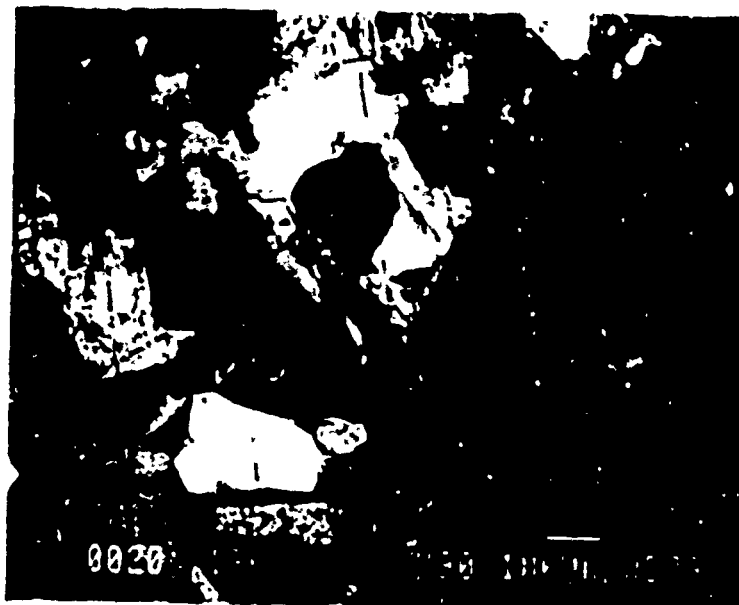
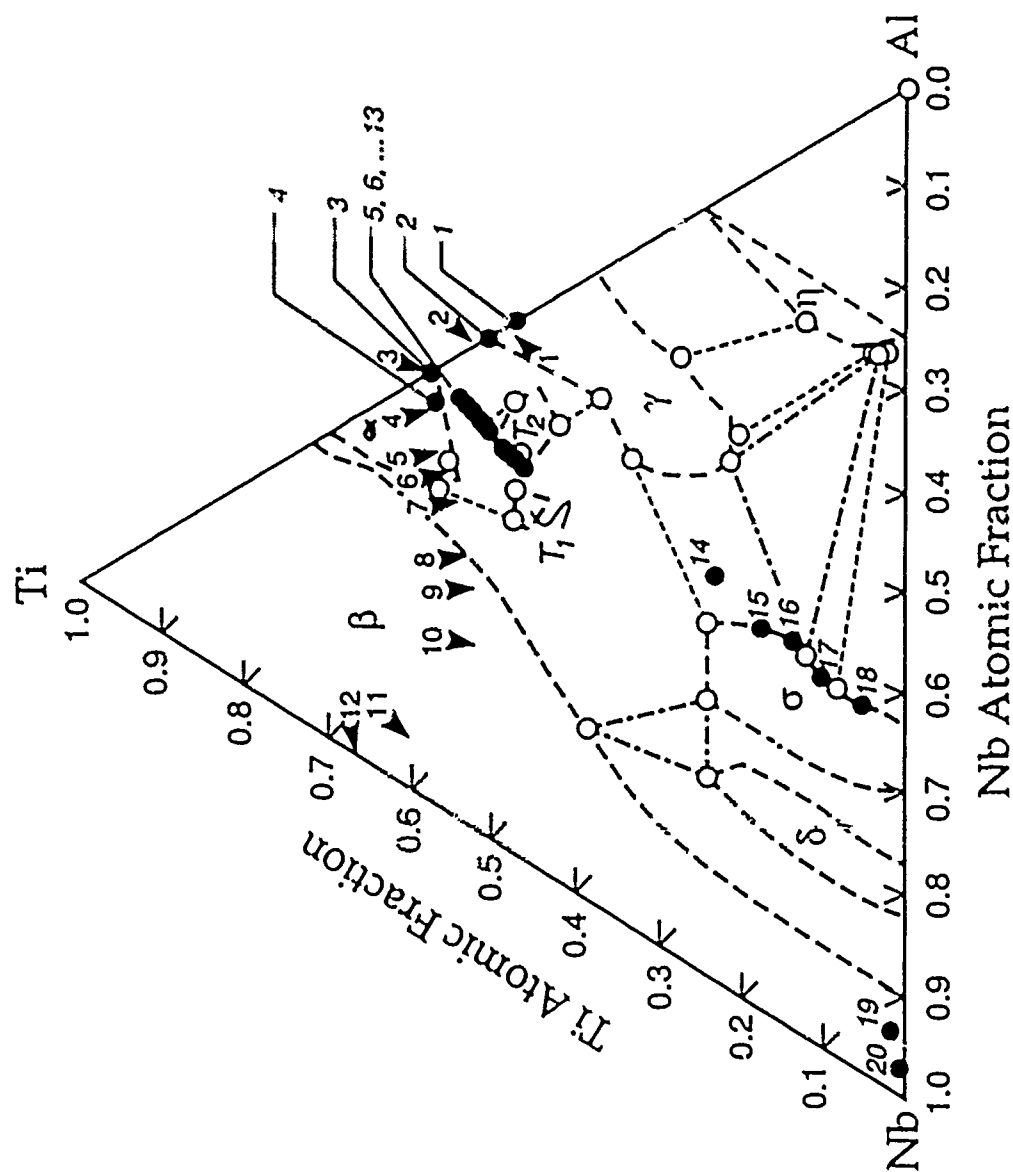


FIG. 5



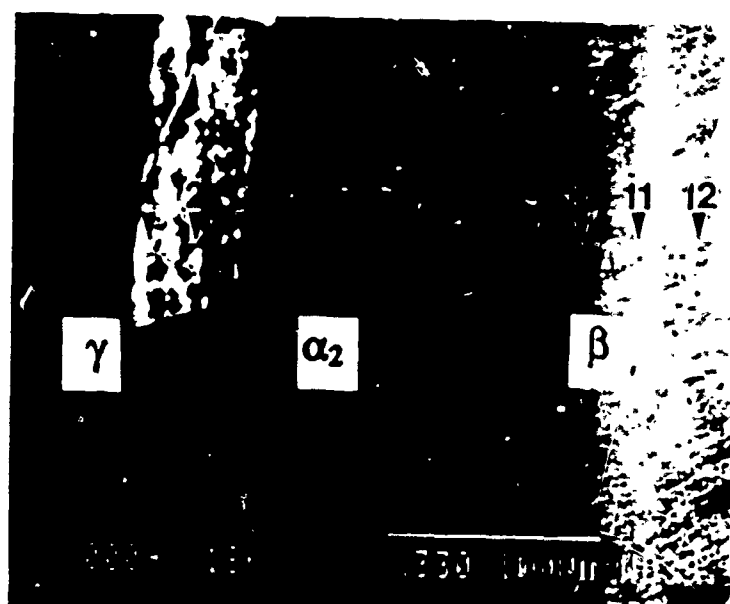
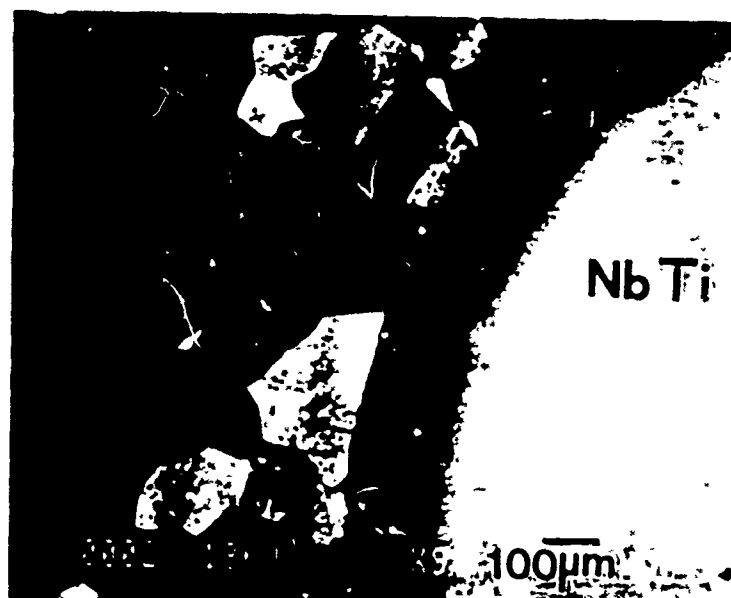
(a) Cross section SEM micrograph of the Nb wire in the TiAl matrix.
 (b) Magnified view of the reaction layer between TiAl and Nb.

Nb-Ti-Al 1200°C



Ternary phase diagram at 1200°C [from Chang and Perepezko et al].
 The solid circles show the diffusion path of TiAl/Nb.
 The arrows show the diffusion path of TiAl/Ti-33at.%Nb.

FIG. 7



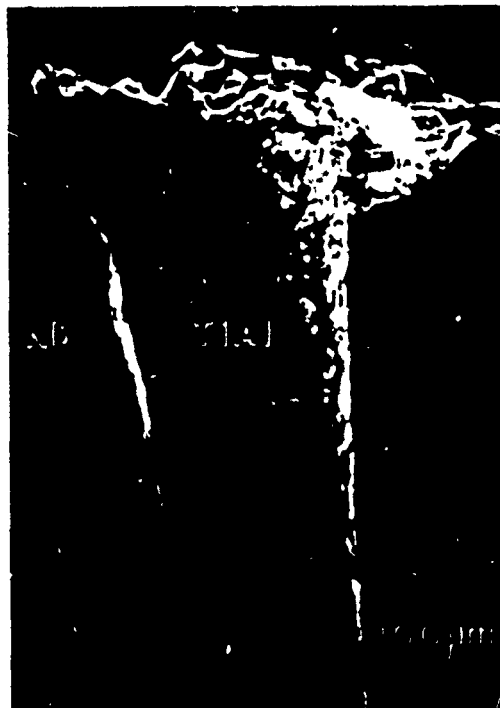
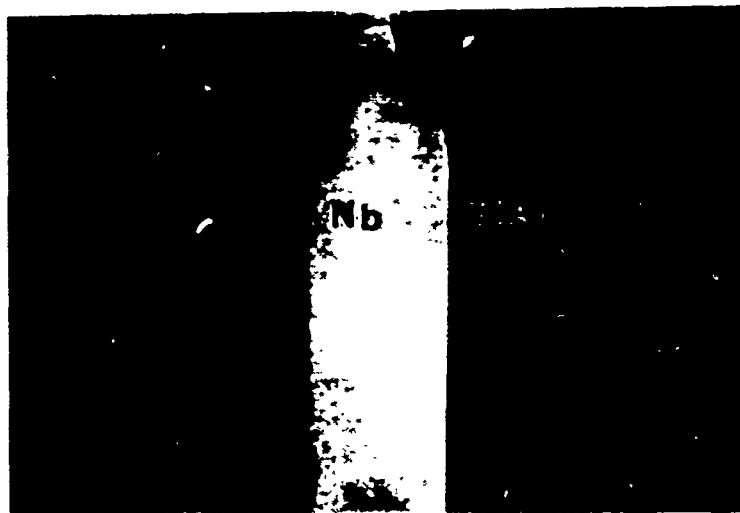
(a) Cross section SEM micrograph of the Ti-33at%Nb wire in the Ti-Al matrix.
 (b) Magnified view of the reaction layer between TiAl and Ti-33at%Nb.

FIG. 8

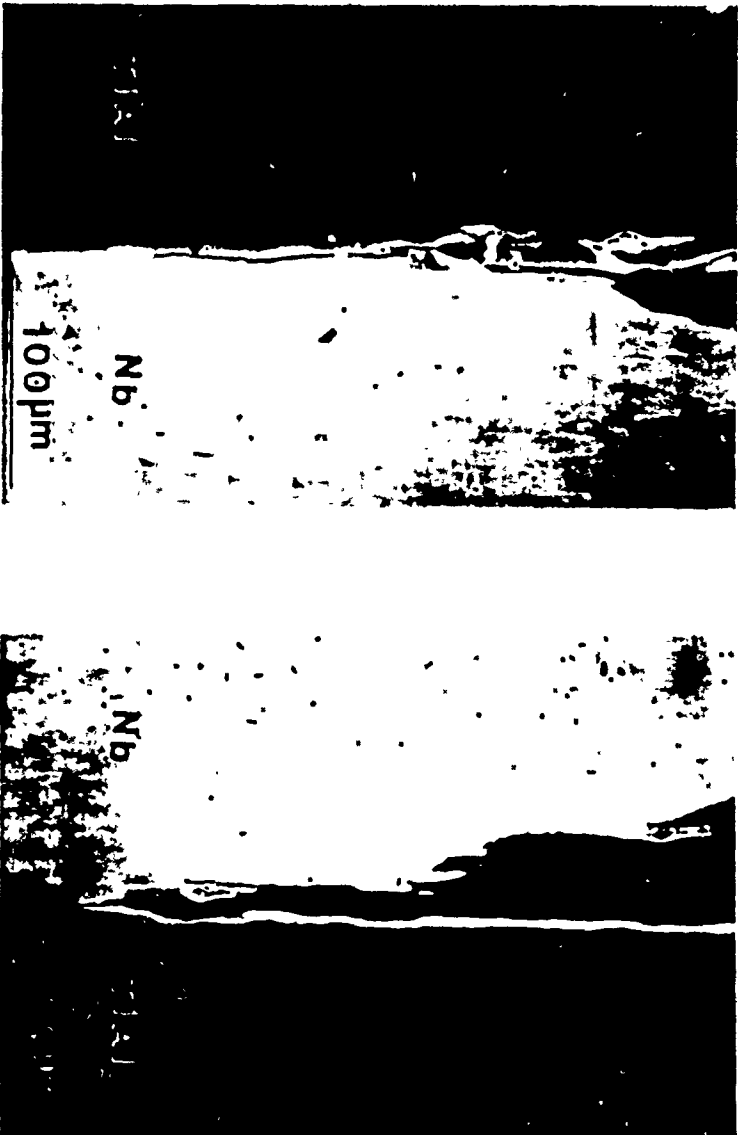


SEM VIEWS showing Ductile Fracture of the Nb wire
and cleavage fracture of the adjacent zone in the TiAl matrix

FIG. 9A



Debond surface in TiAl (matrix)/
Nb (wire) Fractured specimen



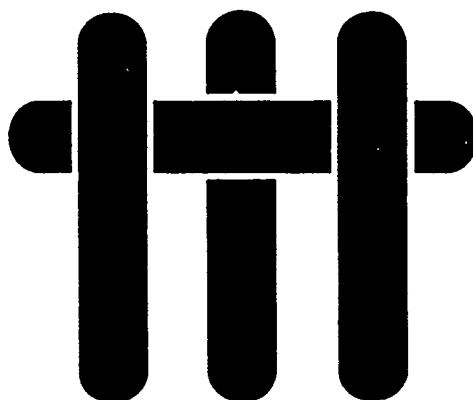
Debonding at the TiAl (matrix)/Nb (wire) interface showing plastic blunting of crack and brittle crack renucleation



SEM Views of Fracture in TiAl/Ti-33at%Nb Specimen.

FIG. 10

M A T E R I A L S



**METHOD FOR PROCESSING
METAL REINFORCED
CERAMIC COMPOSITES**

**F. F. Lange, B. V. Velamakanni
and A G. Evans**

**Materials Department
College of Engineering
University of California, Santa Barbara
Santa Barbara, California 93106**

**Presented at the 41st Pacific Coast Regional Meeting
of the American Ceramic Society
San Francisco, California, October 26, 1988 (#39-B-88P)**

Method for Processing Metal Reinforced Ceramic Composites

Abstract

A new process is developed to form a ceramic containing a three dimensional network of metal reinforcement. The process involves four steps: 1) forming a powder compact containing a continuous network of either organic or carbon material by pressure filtration, 2) pyrolyzing the network to form channels within the powder compact, 3) densifying the powder while retaining the channel network, and 4) intruding metal into the channel network by squeeze casting. Pressure filtration is used to form the powder compact containing the pyrolyzable network either by mixing slurries of powder with chopped fiber or by packing powder within pyrolyzable preforms. When pressure is removed after filtration, the differential strain recovery of the powder matrix relative to the organic material can cause damage. Such damage is prevalent for a powder matrix formed from flocced slurries. However, this problem was avoided by using dispersed slurries which produced consolidated bodies that alleviate stresses arising from differential strain recovery by viscous flow. Metal reinforced ceramic composites with different reinforcement architectures, volume fractions and sizes can be produced with this technique.

Method for Processing Metal Reinforced Ceramic Composites

F. F. Lange*, B. V. Velamakanni* and A. G. Evans*

Department of Materials
College of Engineering
University of California
Santa Barbara, CA 93106

Abstract

A new process is developed to form a ceramic containing a three dimensional network of metal reinforcement. The process involves four steps: 1) forming a powder compact containing a continuous network of either organic or carbon material by pressure filtration, 2) pyrolyzing the network to form channels within the powder compact, 3) densifying the powder while retaining the channel network, and 4) intruding metal into the channel network by squeeze casting. Pressure filtration is used to form the powder compact containing the pyrolyzable network either by mixing slurries of powder with chopped fiber or by packing powder within pyrolyzable preforms. When pressure is removed after filtration, the differential strain recovery of the powder matrix relative to the organic material can cause damage. Such damage is prevalent for a powder matrix formed from flocced slurries. However, this problem was avoided by using dispersed slurries which produced consolidated bodies that alleviate stresses arising from differential strain recovery by viscous flow. Metal reinforced ceramic composites with different reinforcement architectures, volume fractions and sizes can be produced with this technique.

Introduction

Metal reinforcements are incorporated into ceramics in an attempt to increase the fracture toughness of the ceramic matrix and impart R-Curve behavior. To realize these properties, the reinforcements must act as bridges behind an extending crack. Consequently, the extending crack must by-pass the reinforcement and the bridging reinforcement must dissipate energy. Ductile reinforcements can be by-passed because of their much larger fracture toughness relative to the matrix. They dissipate energy through constrained, plastic deformation. The magnitude of the plastic work per reinforcement times the number intercepted governs the incremental increase in fracture toughness. Toughness increases as the crack

* Member American Ceramic Society

extends if the bridging reinforcements do not immediately fail. This increasing resistance to crack extension as the crack grows longer is known as R-Curve behavior and, if significant, can make the strength relatively insensitive to crack length.

Theoretical work ¹ suggests that the improved fracture resistance imparted by a highly ductile phase will increase with increase in its volume fraction, yield strength, and bridge diameter. Recent experimental work ² also shows that some debonding of the metal/ceramic interface will increase the plastic work. It would be advantageous to fabricate composites wherein these fracture related parameters could be changed in order to test theoretical predictions and to produce optimally reinforced microstructures.

One innovative method for forming metal reinforced ceramic composites, is under commercial development.³ This method involves the environmental reaction of a molten metal (e.g., the oxidation of certain aluminum alloys) in which a reaction product (e.g., Al_2O_3) continues to form as metal is wicked through channels within the reaction layer until the molten pool is depleted. This unusual reaction phenomenon can also be used to form the reaction product within powder compacts and inorganic fiber preforms ⁴. After solidification, the metal remaining in the channels is the ductile reinforcement.

All other metal reinforced ceramic composites are formed with powder methods. They include the liquid phase sintering of ceramic powder with a molten metal (e.g., commercial WC/Co composites), the intrusion of a molten metal into a partially sintered powder compact ⁵, the reduction of certain polycrystalline oxides to form a metallic phase at grain junctions ⁶, and the deformation processing (hot-pressing and HIPing) of powder/refractory metal mixtures. ⁷ In the first three of these methods, the metal reinforcement lies at and along grain junctions and the size of bridging ligaments produced during fracture is less than the grain size. Deformation processing can produce larger diameter reinforcements, but the metal must be at least as refractory as the ceramic. Reaction between the ceramic and metal during deformation processing can also be a concern.

The processing method introduced here has the potential to fabricate many different ceramic/metal systems in which the architecture, bridging ligament diameter, and volume fraction of the metal reinforcement can be engineered to optimize fracture behavior. With this method a powder compact containing a pyrolyzable network is formed by pressure filtration. After the network is removed by pyrolysis, the powder matrix is densified. Channels, remnant of the pyrolyzed network, are then infiltrated with a molten metal.

The following sections review pertinent aspects of the pressure filtration method used to incorporate a pyrolyzable network into a powder compact and the procedures used to form a metal reinforced ceramic. Disruptive phenomena produced by differential strain recovery after filtration are then discussed and methods used to avoid this by controlling the rheology of the consolidated body are discussed. Finally, the microstructures of different composites formed by this process are presented.

Pressure Filtration

Pressure filtration is a method for consolidating powders from a slurry. Large quantities of ferrite components are produced by this method.⁸ Furthermore, with the development of moldable, porous plastic die materials⁹, sectors of the ceramic industry are automating plants that consolidate complex shaped, clay-based ceramics by pressure filtration. Pressure filtration is also a desired method for consolidating advanced structural components in which heterogeneities (agglomerates, inclusions, etc.), which lead to strength degrading flaw populations, are removed by colloidal methods.¹⁰

During pressure filtration, particles within a slurry build up a consolidated layer as the liquid flows through the layer and filter. The kinetics of pressure filtration¹¹ are well described for slurries containing either non-interacting or repulsive (dispersed) particles.¹² The function describing the thickness (h) of the consolidated layer as a function of time was derived by solving Darcy's differential equation describing flow through a powder bed. This function includes the viscosity of the fluid (η), the permeability (k) of the consolidated layer, the volume fraction of solids in the slurry (f_s) and consolidated layer (f_c), and the pressure applied to the slurry (P),

$$h = \left[\frac{f_s}{f_c - f_s} \right]^{\frac{1}{2}} \left[\frac{k P t}{2 \eta} \right]^{\frac{1}{2}} \quad (1)$$

In deriving this expression, it is assumed that the permeability is constant during filtration. The permeability is a function of the particle size and particle packing density.

Consolidated powders exhibit non-linear elastic stress-strain behavior similar to that described by Hertz¹³ for two spheres pressed together. The compressive stress (σ)-strain (ϵ) response of a powder can be expressed¹⁴ as $\sigma = A \epsilon^{3/2}$, where A depends on the relative density of the powder compact (average number of contacts per particle) and the elastic properties of the particles. Fig. 1 describes this response for Al_2O_3 powder compacts as determined with strain recovery measurements¹² after pressure filtration of both flocced and dispersed slurries. As illustrated, relatively small stresses produce large strains and the compact becomes stiffer as the stress is increased. Thus, after a powder has been consolidated and the pressure is released, large elastic strains are recovered and the compact expands.

Since the consolidated layer is formed under pressure, it stores elastic strain during filtration. After filtration is complete and the applied pressure is removed, the stored elastic strain is released and the compact grows. Experiments have shown¹² that the recovery of this strain is time dependent and that the rate of strain release depends on the rheology of the saturated, consolidated body. Bodies consolidated from dispersed slurries flow despite their very high particle packing density, because the particles still repulse when pressure is released. The resulting strain occurs

within a relatively short period. Bodies consolidated from flocced slurries appear stiff, exhibit thixotropic rheology and continue to strain for many hours. In these bodies, as the particle network attempts to relax, the surrounding liquid is placed in tension, causing liquid (or air) to flow from the surface to the interior leading to expansion of the network. The time required to dissipate the associated stresses by fluid flow is governed by Darcy's Law. Dispersed bodies, on the other hand, appear to strain by body flow. As addressed below, these strains are of critical importance in the structural integrity of bodies containing either reinforcements or pyrolyzable networks.

Jamet et al.¹⁵ were the first to show that a powder could be packed within a fiber preform using pressure filtration. In this process, schematically shown in Fig. 2, a fiber preform is placed on top of the filter and particles within a slurry flow through the preform channels to build a consolidated layer within the preform during filtration. Before a consolidated layer builds up on the filter, a uniform pressure exists within the slurry and within the liquid filled (or slurry filled) preform. As the consolidation layer builds within the preform, the combined pressure exerted by the consolidated layer and the liquid is identical to the pressure within the slurry. That is, throughout all stages of pressure filtration, the preform is never subjected to non-hydrostatic loads which would produce disruptive effects, such as preform compaction and/or crushing.

Our experience has shown that the success of this processing method depends on three conditions. Firstly, particles must be small enough to flow through the preform channels. The filtration literature¹⁶ suggests that the particles should at least be 7-10 times smaller than the percolation channels to prevent the preform from acting as a filter. However, to produce a compact with a high packing density, the particles must be even smaller. This requirement was made evident in recent experiments in which Lam and Lange¹⁷ showed that the reinforcement did not interfere with the powder packing density if the ratio of the reinforcement to particle diameter was > 50 . Smaller ratios produced lower packing densities. When these results are converted to channel size, they suggest that the particle diameter should be at least 100 times smaller than the average channel diameter. Secondly, the particles can not be attracted either to themselves (should not floc) or to the preform material as they flow through the channels. That is, when attractive surface force conditions prevail, the channels are quickly blocked, the preform itself acts as the filter, and a consolidated layer builds up on top instead of within the preform. The third condition was made evident during the present investigation. As described in the last section, it concerns the differential strain between the network and the powder. This differential strain can disrupt the powder compact.

Experimental Approach

Pyrolyzable Networks

Two types of pyrolyzable networks were used in this study. The first was a three-dimensional preform consisting of interconnected network prior to pressure

filtration and the second, a connective fiber network formed during the pressure filtration of slurries containing chopped fibers.

Three dimensional preforms are commercially available in a variety of architectures (reticulated foams, felts, woven and knitted mats) made from a variety of pyrolyzable materials (natural and synthetic polymers, and carbon). Although different preform architectures and materials have been tested, this paper will emphasize the use of reticulated polyurethane foams. Because of their large channel size, powder can be packed within reticulated foams by pressure filtration using either dispersed or flocced slurries. Two different polyurethane reticulated foams were used in this study: a low density foam^a (~0.03 g/cc) with average cell and strut sizes of 250 μm (40 cells/cm) and 50 μm , respectively, and a high density foam^b (0.18 g/cc) with average cell and strut sizes of 250 μm (120 cells/cm) and 150 μm , respectively. As described below, chopped carbon fibers with an aspect ratio of 8 (mean diameter 11 μm and length 88 μm) were also used to form a pyrolyzable continuous network.

Powder Slurries

Aqueous alumina^c slurries were used in this study. For the case wherein the slurry was used to form a consolidated layer within the polyurethane reticulated foams, the interparticle forces were altered by controlling the pH of the slurry. Zeta potential measurements for this Al_2O_3 as a function of pH showed that it exhibits the highest zeta potential between pH 2 and 4 (-60 mV). Beyond pH 4 the zeta potential decreases gradually, reaching near zero around pH 9. Because of its high zeta potential between pH 2 and 4, the strong electrostatic repulsive force between particles facilitate dispersion of particles in the water. However, around pH 9, van der Waals attractive forces dominate electrostatic repulsive forces, thus causing particles to flocculate/aggregate. A high-shear field, obtained by immersing an ultrasonic horn^d in the slurry (pH = 4), aided in breaking apart soft agglomerates. After this dispersion procedure, the average particle diameter was 0.4 μm ^e. In this study, either dispersed (pH 4) or flocced (pH 8) slurries were used to pack particles, via pressure filtration, within the polyurethane reticulated foams. Separate pressure filtration studies with these alumina slurries in flocced and dispersed slurry states produced consolidated bodies with relative packing densities of 54% and 62% by volume, respectively.

Since pourable alumina suspensions are required for pressure filtration into three-dimensional preforms, it is necessary to vary the solids content as well as the chemistry of the slurry. For example, alumina with an average particle size of 0.4 microns can be loaded to as high as 55 volume percent to formulate a pourable aqueous, dispersed slurry. On the other hand, with the same alumina, a pourable

^a Scott Foam Div., Eddystone, PA.

^b Twin Rivers Engg., East Boothbay, Maine.

^c AKP-50, Sumitomo Corp. of America, New York, NY.

^d Sonic Dismembrator, Model 300, Fisher Scientific Co., Pittsburgh, PA.

^e SediGraph 5000 ET, Micromeritics, Norcross, GA.

flocced slurry can be made with a maximum solids content of only 15 volume percent. In this work, the solids loading of dispersed and flocced alumina slurries were 20% and 15% by volume, respectively.

Pressure Filtration into a Three Dimensional Network

Pressure filtration was used to pack particles within the reticulated foams. Because of their very large channel size, the powder could be consolidated within the foams with either dispersed or flocced slurries. To avoid pressure differentials within the foam during the initial stages of filtration and to eliminate entrapped air, the foam was soaked with the same fluid and surfactant used in making the slurry prior to placing it on top of the filter within the cylindrical die cavity. The slurry was then poured into the cylinder and pressure applied to the slurry with a plunger fitted into the cylinder as shown in Fig. 2. Sufficient slurry is used such that the consolidated layer completely fills the preform. During filtration the plunger displacement is monitored. After a period of 15 minutes in which no plunger displacement is observed, filtration was terminated by releasing the pressure and removing the composite body from the die cavity. A maximum pressure of 14.6 MPa was used for these consolidation experiments.

Pressure Filtration of Chopped Fiber Powder Slurries

As detailed elsewhere¹⁷, alumina powder and chopped carbon fibers (10, 20, and 30 volume percent, based on solid content) were dispersed in water (pH = 8) with 0.1 weight percent (based on solid content) of an ammonia based polyelectrolyte^f. The polyelectrolyte was used in these experiments to facilitate wetting of carbon fiber in water and to codisperse alumina and carbon in water. This mixed slurry was pressure filtered at 14.6 MPa in the manner described above.

Network Pyrolysis and Matrix Densification

After the powder compacts containing the pyrolyzable networks are removed from the die cavity, they are fully saturated with liquid. After drying the composite bodies at 50°C for 24 hours, they were placed in an air furnace and heat treated to first pyrolyze the organic network/carbon fibers (heating rate of 1°C/min to 800°C, 4 hours hold) to produce the desired channel network and then to densify the ceramic powder (heating rate of 5°C/min to 1550°C, 30 min. hold) while retaining the channel network.

Metal Infiltration

The last step is accomplished by intruding molten metal into the channels, remnant of the pyrolyzed network, within the dense ceramic matrix by squeeze casting¹⁸. The advantages of squeeze casting are that infiltration is achieved under

^f Darvon C. R. T. Venderbilt Co., Norwalk, CT.

relatively short times, preventing extensive metal-ceramic reactions, and subsequent solidification takes place under externally applied pressure which results in a fine-grained microstructure free of shrinkage voids. To accomplish this intrusion, the ceramic matrix was preheated to 800°C and then placed in a preheated steel die. A molten aluminum-4 wt.% Mg alloy, held in a separate crucible at 780°C was then poured onto the preheated ceramic. A plunger was then activated by hydraulic pressure⁸ to force the molten metal into the channels at 170 MPa.

Results and Discussion

Differential Strain Recovery and Structural Integrity

The structural integrity of the dense ceramic (prior to metal intrusion) containing the channels remnant of the reticulated foam was observed to depend on whether it was produced from a flocced or a dispersed slurry. In repeated experiments, flocced slurries produced weak materials that granulated into well defined cells under moderate impact loads. Dispersed slurries produced relatively strong materials in which the crack surface traversed the channels remnant of the pyrolyzed, reticulated foam. Examination of fracture surfaces of bodies produced from flocced slurries with the scanning electron microscope revealed the intercellular fracture morphology shown in Fig. 3a. With the exception of the channel walls, the surfaces of the separated cells appeared rough and were first thought to be fracture surfaces. Upon closer observation (Fig. 3b), it was discovered that only the center portion of each cell surface (approximately 15 %) exhibited a surface morphology typical of a fractured, polycrystalline ceramic (trans- and intergranular fractured grains). Grains on the surrounding, rougher surface were not fractured, but had morphologies typical of a sintered surface (smooth grain surfaces and equilibrium boundary grooves). In addition, this portion of each cell surface was very irregular giving an appearance of being torn prior to densification. In contrast, the bodies formed from the dispersed slurry were much stronger, and when fractured, the crack plane traversed the cells as shown in Fig. 4.

Using the discussion concerning pressure filtration, it can be hypothesized that the weakness and granulation of the ceramic formed from the flocced slurry was caused by the differential recovery strain of the polymer relative to the consolidated powder when pressure was released after filtration. As shown in Fig. 2, a typical polyurethane, with a bulk elastic modulus of approximately 1 GPa, will recover more strain than the powder compact after both are subjected to the same pressure. That is, the reticulated foam will expand more than the consolidated powder. For the case of the body formed from the flocced slurry, it appears that the expanding foam separated the consolidated powder into granules, defined by the cells within the foam, when pressure is removed after filtration. This problem did not arise when the body was consolidated from the dispersed slurry.

The difference in disruption between the body consolidated from the flocced slurry and that within the body produced from the dispersed slurry can be explained

⁸ AutoForge, 200 T, North American Rockwell Corp., Reading, PA.

by the effect of body rheology on the stresses generated by differential strain recovery. After the composites formed from the flocced slurry were removed from the die cavity, they appeared stiff, whereas the dispersed slurries produced composites in which the consolidated powder was still fluid and could be squeezed from the reticulated foam with moderate pressure. It can be concluded that the more elastic bodies produced from flocced slurries produce high stress and could only accommodate the differential strain by cracking (or tearing). Conversely, the bodies produced from the dispersed slurry could easily alleviate the stresses caused by the differential strains through a viscous flow process. It can be surmised that the disruption produced by differential stress relaxation after pressure filtration could be prevented by consolidating with a dispersed slurry and by maintaining the particles in a state of repulsion as the consolidation strain is released.

The strain recovery associated with powder consolidation is of great importance to ceramic processing, especially while processing composite systems. Inclusions within the powder which are either stiffer (for example, dense agglomerates, whiskers and fibers) or more compliant (organic inclusions as lint, hair, and polymer fibers) store less or more strain relative to the powder compact, respectively, during consolidation. When stress is removed, an isolated inclusion with a lower elastic modulus will expand relative to the powder matrix, produce radial tensile stresses within the surrounding powder, and cause cracking. On the other hand, an inclusion with a higher modulus will contract relative to the matrix and may separate from the powder matrix. Lange and Miller¹² have shown that (in monolithics) disruptive phenomenon can also be avoided by increasing the strength of the interparticle bonds through additions of certain polymers.

Microstructure of Metal Reinforced Ceramics

Observations of polished sections showed that the only porosity remaining after network pyrolysis and ceramic densification was associated with the channels remnant of the pyrolyzed network. Relative densities > 0.98 were measured for heat treated bodies that did not contain the pyrolyzable material. Linear shrinkage measurements of bodies containing the pyrolyzable networks were identical to those without the network. This observation shows, as expected, that the channel network produced within the powder compact during pyrolysis shrinks, but certainly does not disappear (Fig. 5). The surfaces of these channels produced by the pyrolyzed carbon fibers (Fig. 5b) are typical of a sintered surface: smooth grain surfaces and grain boundary grooves.

Polished sections of metal intruded materials produced with the low and high density reticulated foams (Fig. 6) reveal that the architecture of the metal reinforcement replicates the architecture of the pyrolyzed foams. Metal was observed to intrude into all sharp corners of this structure. Infiltration of molten Al alloy was attempted into alumina preforms containing 10, 20 and 30 volume percent channels. However, an interconnected network of metal was only obtained with the preform containing 30 volume percent channels (Fig. 7).

An investigation of the fracture behavior of these and other metal reinforced composites fabricated by this new method has been initiated. Preliminary fracture

experiments show that the aluminum alloy bridges cracks and undergoes constrained plastic deformation (Fig. 8).

Conclusions

A new and simple process is developed to form a three dimensional network of metal reinforcement in a densified ceramic matrix. This new processing method not only allows the processing of a range of metal/ceramic composite systems, which may not be processed by other methods, but also allows the materials engineer to manipulate the architecture, volume fraction and the size of the metal reinforcement. The key combined features of this discovery are a) powder can be packed either within or around a network of a second material by pressure filtration, b) after powder packing, the network material can be removed to define a continuous network of channels, c) after the network material is removed, the powder compact can be made dense by a high temperature heat treatment, and d) after densification of the ceramic matrix, molten metal is intruded into the network channels to create the desired reinforcement network configuration. Using this approach alumina-aluminum alloy composites with metal architectures similar to that of reticulated foam and of randomly oriented fibers were processed.

It was also demonstrated that the differential strain recovery between the consolidated powder and the reinforcement is a critical issue in processing composites. Damage inflicted by this differential strain can be eliminated by controlling the rheology of the consolidated body through the use of dispersed slurries and maintaining state of interparticle repulsion as strain is relieved. Stresses induced by differential strain in these bodies appear to dissipate by viscous flow. Relations between differential strain recovery, body rheology and stress dissipation are a subject of future research.

Acknowledgements

Authors wish to thank the Defence Advanced Research Projects Agency for financial support under ONR contract N 00014-86-0753. Also, the assistance of Dr. J. Valencia with squeeze casting and of Mr. B. Flinn with fractography is gratefully acknowledged.

References

1. L. S. Sigl, P. A. Mataga, B. J. Dalgleish, R. M. McMeeking and A. G. Evans, "On the Toughness of Brittle Materials Reinforced with a Ductile Phase," *Acta Metall.*, 36 [4] 945-953 (1988).
2. J. Eberhardt and M. F. Ashby, "Flow Characteristics of Highly Constrained Metal Wires," Annual Report, URI Contract No. N00014-86-K-0753, *The Processing and Mechanical Properties of High Temperature/High Performance Composites*, Book 5, Ed. by A. G. Evans and R. Mehrabian (1988).

3. M. S. Newkirk, H. D. Lesher, D. R. White, C. R. Kennedy, A. W. Urquhart, T. D. Claar, "Preparation of Lanxide™ Ceramic Matrix Composites: Matrix Formation by the Direct Oxidation of Molten Metals," *Ceram. Engg. and Sci. Proc.*, 8 [7-8] 879 (1987).
4. P. Barron-Antolin, G. H. Schiroky, C. A. Anderson, "Properties of Fiber-Reinforced Alumina Matrix Composites," presented at the 12th Annual Conf. on Composites and Advanced Ceramic Materials, Cocoa Beach, FL, January 1988.
5. A. J. Pyzik, A. A. Aksay and M. Sarikaya, "Microdesigning of Ceramic-Metal Composites," in *Ceramics Microstructures '86, Role of Interfaces*, pp 45-54, Ed. by J. A. Pask and A. G. Evans, Plenum Press, N.Y. (1987).
6. M. I. Mendelson and M. E. Fine, "Enhancement of Fracture Properties of Wustite by Precipitation," *J. Am. Ceram. Soc.*, 57[4], 154-159 (1974).
7. V. V. Kristic and P. S. Nicholson, "Toughening of Glasses by Metallic Particles," *J. Am. Ceram. Soc.*, 64 [9] 499-504 (1981).
8. S. Strijbos, "Pressure Filtration of Permanent Magnetic Powders," Proc. Conf. Hard Magnetic Materials, Ed. H. Zijlstra, Publ. Bond voor Materialenkennis, Den Haag, Netherlands (1974); C. A. M. Van den Broek and A. L. Stuijts, "Ferroxdure," *Philips Tech. Rev.* 37 [7] 157-75 (1977).
9. Gebruder Netzsch, Maschinenfabric GmbH & Co., Tech. Inform. Bul. GK 012, D-8672 Selb/Bavaria, FRD (1985).
10. F. F. Lange, "Powder Processing Science and Technology for Increased Reliability," *J. Am. Ceram. Soc.* 72 [1], 3-15 (1989).
11. F. M. Tiller and C.-D. Tsai, "Theory of Filtration of Ceramics: I Slip Casting," *J. Am Ceram. Soc.* 69 [12], 882-87 (1986).
12. F. F. Lange and K. T. Miller, "Pressure Filtration: Kinetics and Mechanics," *Bul. Am. Ceram. Soc.* 66 [10], 1498-1504 (1987).
13. S. Timoshenko, *Strength of Materials, Part II, Advanced Theory and Problems*, D. Van Nostrand Co., New York, p 339, 1958.
14. K. Walton, "The Effective Elastic Modulus of a Random Packing of Spheres," *J. Mech. Phys. Solids.* 35 [2], 213-26 (1987).
15. J. Jamet, D. Damange and J. Loubeau, "Nouveaux Matériaux Composites Alumine-Alumine à Rupture Fortement Dissipative et Leur Préparation," French Patent No. 2,526,785, Nov. 18, 1983.

16. C. Tien and A. C. Payatakes, "Advances in Deep Bed Filtration," *AIChE J.*, 25[5], 737-759 (1979).
17. D. C. C. Lam and F. F. Lange, "Packing of Particles in Reinforcements," to be published.
18. R. Mehrabian, "New Pathways to Processing Composites," *Mat. Res. Soc. Symp. Proc.*, Vol. 120, 3-21 (1988).
19. B. Kellett and F. F. Lange, "Thermodynamics of Densification, Part I: Sintering of Simple Particle Arrays, Equilibrium Configurations, Pore Stability, and Shrinkage," *J. Am. Ceram. Soc.* (in press).

Figures

Fig. 1 Strain recovered in alumina powder, pressure filtered as dispersed and flocced slurries. ¹² Elastic behavior of a polymer with a bulk elastic modulus of 1 GPa is also shown for comparison.

Fig. 2 Schematic of pressure filtration into a pyrolyzable preform.

Fig. 3 a) Micrograph of intercellular fracture of alumina preform containing interconnected channels which are remnant of pyrolyzed reticulated foam pressured filtered from a flocced slurry. b) Higher magnification of cell surfaces showing fractured surface (dark region at the center) is surrounded by sintered surface.

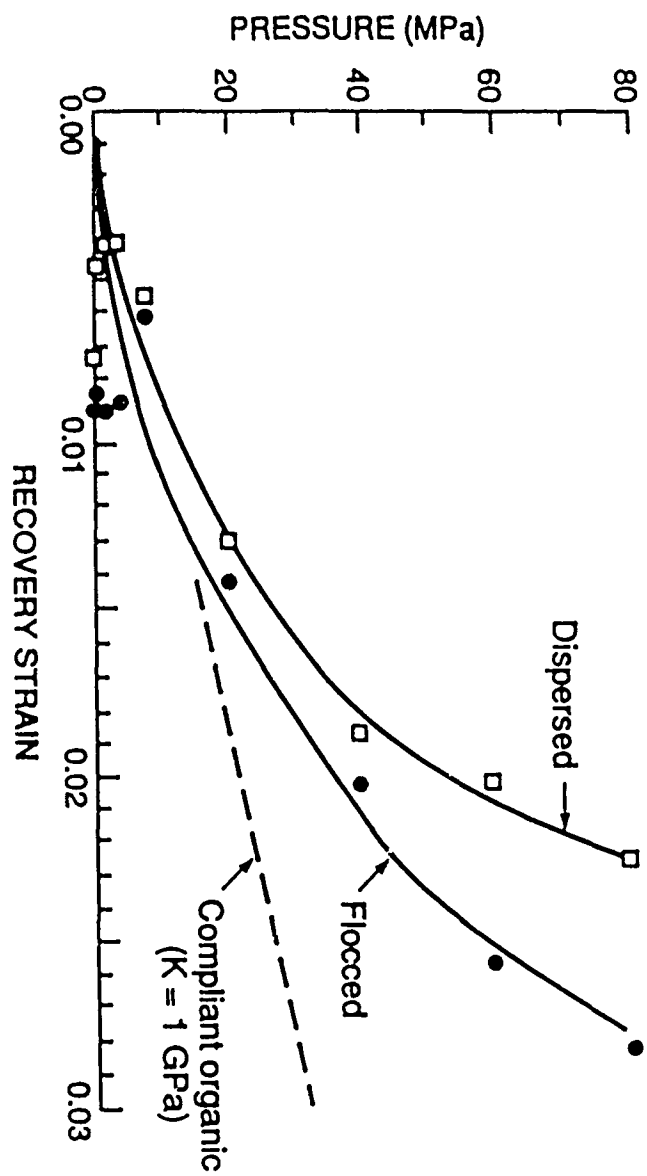
Fig. 4 Micrograph of intercellular fracture of alumina ceramic containing channel network remnant of pyrolyzed reticulated foam pressured filtered from a dispersed slurry.

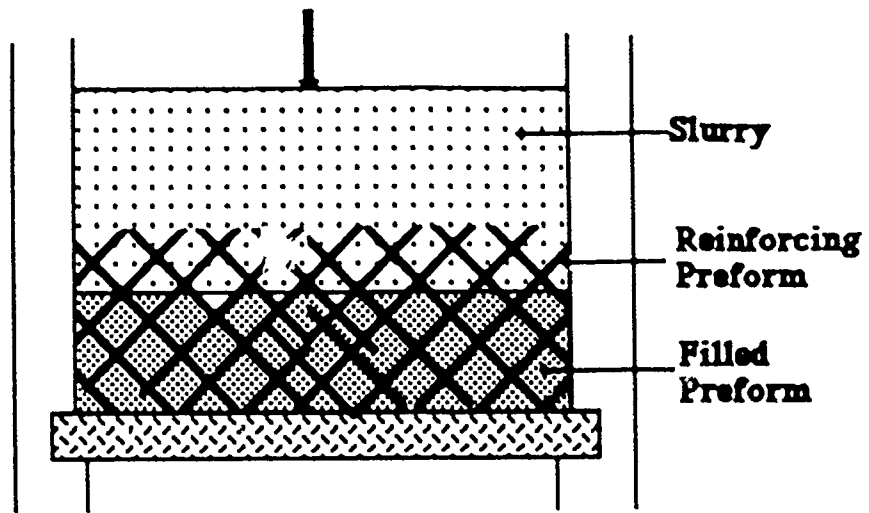
Fig. 5 a) Micrograph of alumina ceramic containing continuous channel network remnant of pyrolyzed carbon fibers. b) Higher magnification showing sintered surface of one channel.

Fig. 6 Micrograph of alumina ceramic containing channel network produced by pyrolysis of low density (a) and high density (b) reticulated foams intruded with aluminum alloy by squeeze casting.

Fig. 7 Polished section of alumina containing approximated 30 volume percent aluminum alloy intruded by squeeze casting into channels remnant of pyrolyzed carbon fibers.

Fig. 8 Interaction of crack with aluminum alloy 'fiber' produced during squeeze casting into channel network of pyrolyzed carbon fibers. Note that metal reinforcement bridges crack and deforms.

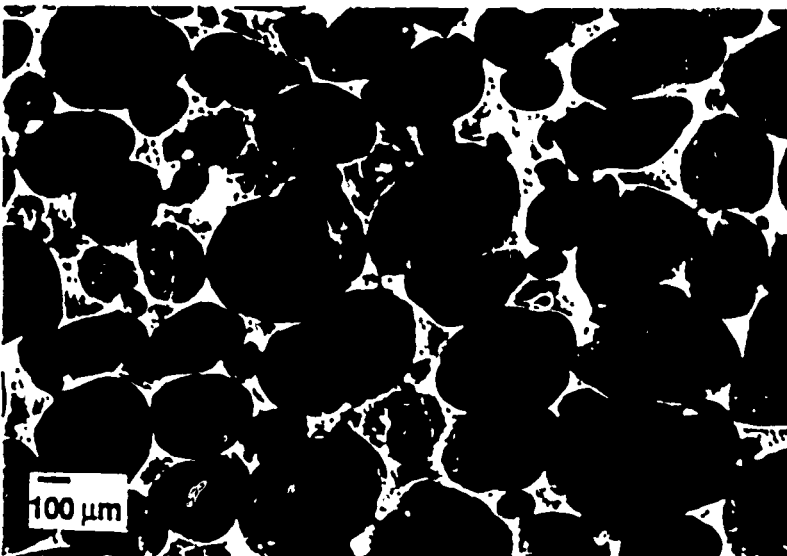


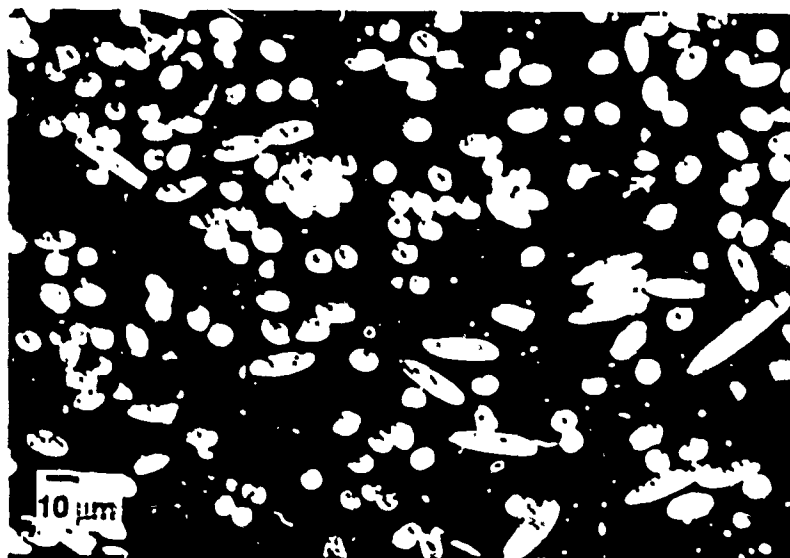


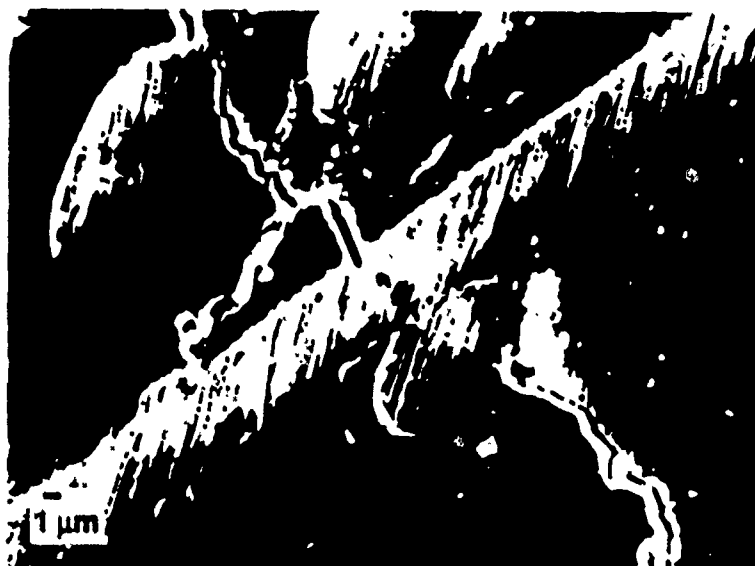




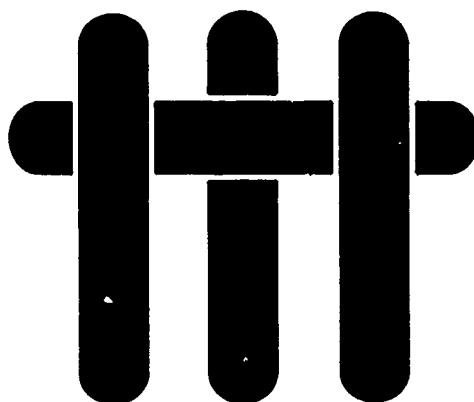








M A T E R I A L S



**HIGH TOUGHNESS CERAMICS AND
CERAMIC COMPOSITES**

M. Rühle* and A. G. Evans

**Materials Department
College of Engineering
University of California, Santa Barbara
Santa Barbara, California 93106**

* Now at Max-Planck-Institut für Metallforschung, Institut für Werkstoffwissenschaft, Seestraße 92, D-7000 Stuttgart 1, FRG

1 High Toughness Ceramics and Ceramic Composites

2 M. Rühle* and A. G. Evans

3 Materials Department, College of Engineering, University of California
Santa Barbara, California 93106

* Now at:

Max-Planck-Institut für Metallforschung, Institut für Werkstoffwissenschaft, D-7000 Stuttgart 1, FRG

4 High Toughness Ceramics and Ceramic Composites

5 Max-Planck-Institut für Metallforschung, Institut für Werkstoffwissenschaft, Seestraße 92, D-7000 Stuttgart 1,
FRG

6 Keywords:

Ceramics, Composites, Toughness, Transformation

ABSTRACT

Relationships that govern trends in the toughness of ceramics and ceramic composites with microstructure are well-developed. The status of present understanding is reviewed. Two principal mechanistic classes are described: process and bridging zone mechanisms. Process zone mechanisms, which include transformation, microcrack and twin toughening are shown to be governed by the size of the zone and by the non-linear strain provided by the mechanism. Bridging zone mechanisms exhibit toughness dictated by a coupled measure of the strength of the reinforcement and a rupture displacement: toughening by fibers, whiskers and ductile networks are mechanisms of this type. Both types of mechanism demonstrate resistance curve behavior, dominated by crack wake effects. Interactions between mechanisms are briefly addressed.

NOTATION

α	linear thermal expansion coefficient
β	monoclinic angle
Γ_i	fracture energy of interface
Γ_m	fracture energy of matrix
Γ_f	fracture energy of fiber
ϵ	microcrack density parameter
ϵ_s	maximum microcrack density parameter
ϵ_{ij}	strain tensor
ϵ^t_{ij}	stress-free strain
δ_{ij}	Kronecker delta
η	microcrack density parameter
Σ	ratio of Young's modulus of fiber to matrix, E_f/E_m
σ_{ij}	stress tensor
σ^*_{ij}	critical stress for transformation
σ_m	steady-state matrix cracking stress in composite
σ_2	equivalent stress
σ_u	ultimate strength of composite
σ	applied stress
$\bar{\sigma}$	mean stress

τ	shear resistance of interface <u>after debonding</u>
θ_T	misfit strain for microcracking
χ	ductile reinforcement toughening parameter
μ	friction coefficient
ν	Poisson's ratio
$\bar{\nu}$	Poisson's ratio for microcracked body
A_0	Reference area 1m^2
B	bulk modulus
\bar{B}	bulk modulus of microcracked body
c	microcrack dimension
d	debond length
E	Young's modulus of composite
E_m	Young's modulus of matrix
E_f	Young's modulus of fiber
F	non-dimensional crack closure force
f	volume fraction
G	shear modulus
\bar{G}	shear modulus of microcracked body
\dot{g}	strain energy release rate
\dot{g}_c	critical strain energy release rate for the composite
$\Delta\dot{g}_c$	increase in toughness of composite above matrix toughness
h	process zone width
h_p	fiber pull-out length
I	I-integral
J	J-integral
K	stress intensity factor
K_{tip}	crack tip stress intensity factor
K_∞	stress intensity factor associated with applied loads
K_c	critical stress intensity factor for composite
K_0	critical stress intensity factor for crack tip extension
ΔK	crack shielding stress intensity factor
ΔK_c	increase in critical stress intensity factor above matrix value
l	slip length
L	bridging zone length
L_g	gauge length
m	shape parameter for fiber strength distribution
n	work hardening rate
p	axial residual axial stress in the <u>matrix</u> in aligned fiber composite
q	residual stress normal to interface in fiber composite
R	reinforcement radius
r	distance from crack front
s	saturation matrix crack spacing
s_{ij}	deviatoric stress
S	fiber strength
S_0	scale parameter for fiber strength distribution

ℓ	stress acting on reinforcement between crack surfaces
U	residual stress work
u	crack opening displacement
u_*	crack opening upon reinforcement rupture
Y	uniaxial yield strength

1. INTRODUCTION

The objective of research concerned with structural ceramics is the generation of materials having high reliability. To achieve this objective, there are two fundamentally different approaches (Fig. 1.1): flaw control and toughening. The first approach accepts the brittleness of the material and attempts to control the large extreme of processing flaws. The second approach attempts to create microstructures that impart sufficient fracture resistance (Fig. 1.2) that the strength becomes insensitive to the size of flaws (Fig. 1.3). The former has been the subject of considerable research that identifies the most detrimental processing flaws, as well as the processing step responsible for those flaws (Lange 1989, Evans 1982, Rice 1977). The toughening approach has emerged more recently, and has the obvious advantage that appreciable processing and post-processing damage can be tolerated without compromising the structural reliability (Evans 1989, Cook et al. 1985).

The resistance of brittle solids to the propagation of cracks can be strongly influenced by microstructure and by the use of various reinforcements. The intent of the present article is to provide a succinct review of the known effects of microstructure and of reinforcements on the fracture resistance. In most cases, toughening results in resistance-curve characteristics (Fig. 1.2), wherein the fracture resistance systematically increases with crack extension. The individual mechanisms include: transformation, microcracking, twinning, ductile reinforcement and fiber/whisker reinforcement.

An underlying principle concerns the essential role of non-linearity in toughening, as manifest in mechanisms of dissipation and energy storage in the material, upon crack propagation. Consequently, the potent toughening mechanisms can be modelled in terms of stress/displacement constitutive laws for representative volume elements (Fig. 1.4). Furthermore, the toughening can be explicitly related to stress/displacement hysteresis (Fig. 1.4), as will be elaborated for each of the important mechanisms. The general philosophy thus adopts the *classical concept of homogenizing* the properties of the material around the crack and then formulating a *constitutive law* that characterizes the material response.* This approach rigorously describes the toughening behavior whenever the length of the non-linear zone is appreciably larger than the spacing between the relevant microstructural entities. *Such conditions invariably exist when the material exhibits high toughness.* The coupling between experiment and theory is another prevalent theme, because toughening is sufficiently complex and involves a sufficiently large number of independent variables that microstructure optimization only becomes practical when each of the important modes has been described by a rigorous model, validated by experiment.

The known mechanisms can be conveniently considered to involve either a *process zone* or a *bridging zone* (Fig. 1.5). The former category exhibits a toughening fundamentally governed by a critical stress for the onset of non-linearity σ_{ij}^* in elements near the crack and by the associated stress-free strain ϵ_{ij}^T (Evans and Cannon 1986, McMeeking and Evans 1982, Budiansky, Hutchinson and Lambropoulos 1983, Marshall, Drory and Evans 1983). The resulting stress-strain hysteresis of those elements within a *process zone* then yields a toughness, given by (Marshall, Drory and Evans 1983),

*Models that discretize microstructural details are typically less rigorous, because three-dimensional interactions along the crack front are not readily described.

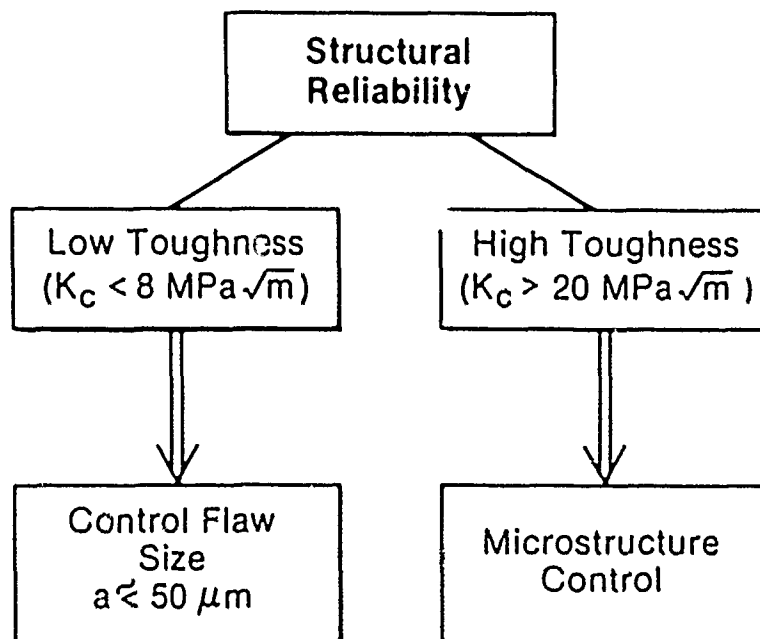


Fig. 1.1 Approaches to achieve high reliability ceramics.

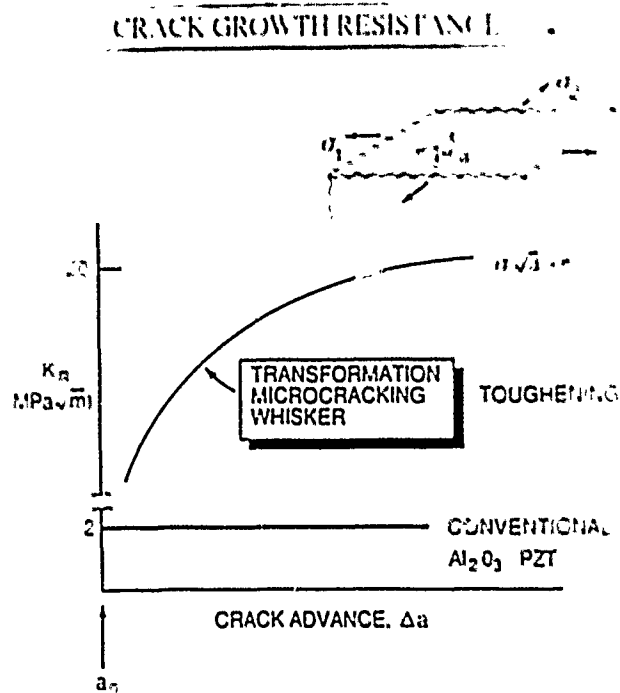


Fig. 1.2 Resistance curve behavior characteristically encountered in tough ceramics. K_R is the fracture resistance and Δa is the crack advance.

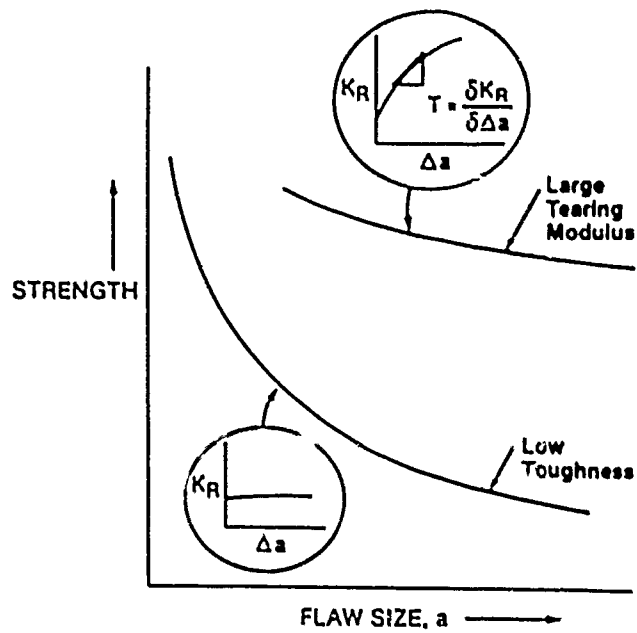


Fig. 1.3 Schematic representation of dependence of strength on flaw size.

NON-LINEAR PHENOMENA

- MARTENSITIC TRANSFORMATION
- MICROCRACKING / DEBONDING
- INTERFACIAL SLIDING
- PLASTIC DEFORMATION

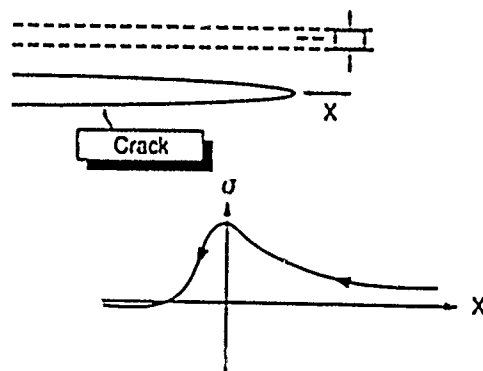
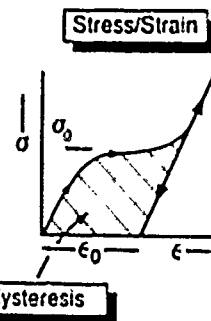


Fig. 1.4 A schematic diagram illustrating non-linear hysteretic elemental response and associations with enhanced toughness.

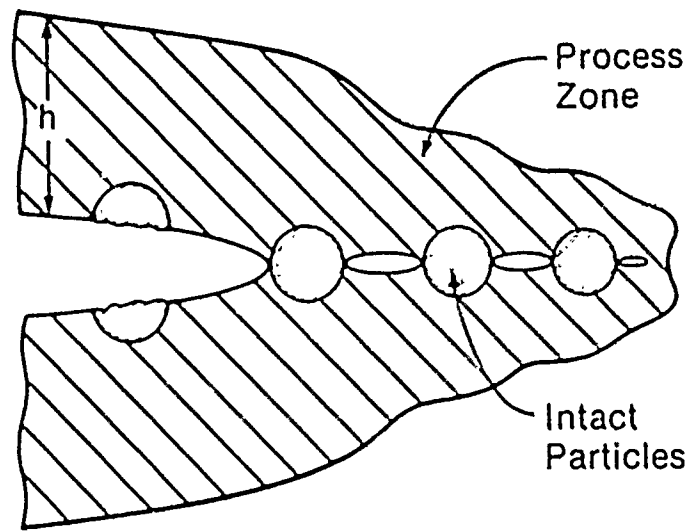


Fig. 1.5 A schematic diagram illustrating both process zone and bridging zone mechanisms of toughening.

$$\Delta \dot{G}_c = 2f \sigma_{ij}^* \epsilon_{ij}^T h \quad (1.1)$$

where $\Delta \dot{G}_c$ is the increase in critical strain energy release rate where the crack is long,** f is the volume fraction of toughening agent and h is the width of the process zone in steady-state (McMeeking and Evans 1982, Stump and Budiansky 1989). Transformation, microcrack and twin toughening are mechanisms of this type.

The bridging category exhibits toughening governed by hysteresis along the crack surface (Evans and McMeeking 1986, Budiansky, Amazigo and Evans 1988) induced by intact material ligaments.

$$\Delta \dot{G}_c = 2f \int_0^{u^*} t(u) du \quad (1.2)$$

where $2u$ is the crack opening, $2u^*$ the opening at the edge of the bridging zone, t the tractions on the crack surfaces exerted by the intact toughening agent (Fig. 1.5) and f is the area fraction of reinforcements along the crack plane. Ductile reinforcements, as well as whiskers and fibers, toughen by means of bridging tractions.

In the "toughest" materials, a steady-state cracking phenomenon occurs (Aveston, Cooper and Kelly 1971, Marshall, Cox and Evans 1985, Budiansky, Hutchinson and Evans 1986, McCartney 1988), wherein the crack extension stress becomes independent of crack length. For such materials, the toughness is usually non-unique and not, therefore, a useful design parameter. Instead, the steady-state cracking stress and the ultimate strength become the more relevant material properties. *Transitions between toughness control and steady state cracking are thus of major significance.*

**Short cracks and cracks without fully developed process zones give smaller changes in toughness, as elaborated in the section on resistance curves.

Some of the materials to be considered in this review along with the associated mechanisms of toughening, coupled with the highest verifiable toughness for each mechanism, are summarized in Table 1.1. This list is impressive when it is appreciated that conventional ceramics have a toughness, $K_{Ic} \approx 1 - 3 \text{ MPa}\sqrt{\text{m}}$. However, some caution is also necessary because the highest levels of toughness cannot always be used to effectively enhance strength and reliability.

Table 1.1 Tough Ceramics

Mechanism	Highest Toughness (MPa $\sqrt{\text{m}}$)	Exemplary Material	Limitation
Transformation	~ 20	$\text{Zr}_2\text{O}_3(\text{MgO})$ HfO_2	$T \geq 900\text{K}$
Microcracking	~ 10	$\text{Al}_2\text{O}_3/\text{ZrO}_2$ $\text{Si}_3\text{N}_4/\text{SiC}$	$T \geq 1300\text{K}$ Strength
Metal Dispersion	~ 25	$\text{Al}_2\text{O}_3/\text{Al}$ ZrB_2/Pr $\text{Al}_2\text{O}_3/\text{Ni}$ WC/IO	$T \geq 1300\text{K}$ Oxidation
Whiskers	~ 15	$\text{Si}_3\text{N}_4/\text{SiC}$ $\text{Si}_3\text{N}_4/\text{Si}_3\text{N}_4$ $\text{Al}_2\text{O}_3/\text{SiC}$	Oxidation Interface $T < 1500\text{K}$
Fibers	≥ 30	LAS/SiC $\text{Al}_2\text{O}_3/\text{SiC}$ SiC/SiC SiC/C	Processing Interfaces Coatings $\lambda > ?$

LAS: Lithium Aluminum Silicate Glass-Ceramic

The article is organized as follows. Chapters 2-4 summarize transformation effects with Chapter 2 concentrating on phase transformations in ZrO_2 . Chapter 3 encompasses *in situ* transmission electron microscopy observations and toughening is covered in Chapter 4. Microcrack toughening is considered in Chapter 5. Chapter 6 summarizes ductile reinforcement toughening. The paper concludes with an assessment of fiber/whisker toughening and strengthening.

2. PHASE TRANSFORMATIONS IN ZrO_2

While a variety of lattice displacive transformations have been identified in different inorganic materials (Kriven 1982, 1988), the martensitic phase transformation that occurs in ZrO_2 is most widely used for toughening. ZrO_2 undergoes several phase transformations upon cooling from the melt (Subbarao, 1981). At least three crystallographic modifications exist, which possess cubic (c), tetragonal (t) and monoclinic (m) symmetry and are stable at high, intermediate and low temperatures:



The high temperature c phase has the fluorite structure (fmm), whereas the other polymorphs (t, $\text{P4}_2/\text{nmc}$, m, $\text{P2}_1/\text{c}$) are distorted versions of this structure (Fig. 2.1). The $t \rightarrow m$ transformation is martensitic in nature (Subbarao 1981, Bansal and Heuer 1972, 1974).

Tough ZrO_2 alloys typically contain fine t- ZrO_2 particles within a ceramic matrix. For such materials, the martensite start, M_s , temperature is suppressed below room temperature. Also, the martensitic transformation within the t- ZrO_2 particles can be induced by stress, especially the stress field associated with propagating cracks. This transformation is the source of toughness in ZrO_2 -containing ceramics (Heuer and Hobbs 1981, Claussen, Rühle and Heuer 1984, Heuer et al. 1986, Sômiya, Yamamoto and Hanagida 1988, Green, Hannink and Swain 1989, Garvie, Hannink and Pascoe 1975, Evans and Cannon 1986).

An important theme will be the difficulty involved in nucleating the martensitic phase, with emphasis on nucleation in small particles. Such nucleation and growth aspects of martensitic transformations, while traditionally of great concern, have been underemphasized in many treatments of transformation-toughening in ceramics. Furthermore, since growth velocities of martensitic interfaces approach the speed of sound, the nucleation step in the $t \rightarrow m$ transformation of ZrO_2 is of primary importance.

Several types of microstructure can be used as a basis for ZrO_2 -toughened ceramics (ZTC). Of particular importance are two different compositions, materials I and II, shown on the phase diagram (Fig. 2.2). Material I may be densified in the t- ZrO_2 phase field and cooled to room temperature (RT). Then, provided that the grain size is less than the critical size required for the transformation, a single-phase t- ZrO_2 material may be produced ("Tetragonal Zirconia Polycrystals," TZP). Composition II (Fig. 2.2) consists of t- ZrO_2 in a cubic matrix. Generally, these materials are sintered in the cubic phase field, but on cooling to the two-phase field, the tetragonal phase forms as precipitates. The size and size distribution of the tetragonal precipitates depends on the thermal treatment in the two-phase field. The t- ZrO_2 precipitates, when small, remain tetragonal upon cooling down to very low temperatures (liquid He). This class of material is referred to as partially stabilized zirconia (PSZ). The shape of the t- ZrO_2 particles depends on the stabilizing agent (Heuer and Hobbs 1979, Claussen, Rühle and Heuer 1984, Green, Hannink and Swain 1989). Conversely, large precipitates transform thermally to m- ZrO_2 . Finally, TZP may be used as one of the components in a composite material. Such materials are referred to as ZrO_2 dispersed ceramics (ZDC). The predominant system is Al_2O_3 - ZrO_2 (zirconia-toughened alumina, ZTA). The size and distribution of the ZrO_2 regions depend on the processing conditions.

The $t \rightarrow m$ phase transformation (Fig. 2.3) involves a set of transformation strains that increase the volume and change the shape of the particle/grain. Isolated grains invariably transform provided that the nucleation conditions are satisfied. However, for grains embedded in a matrix, strain energy changes tend to oppose the transformation. Then,

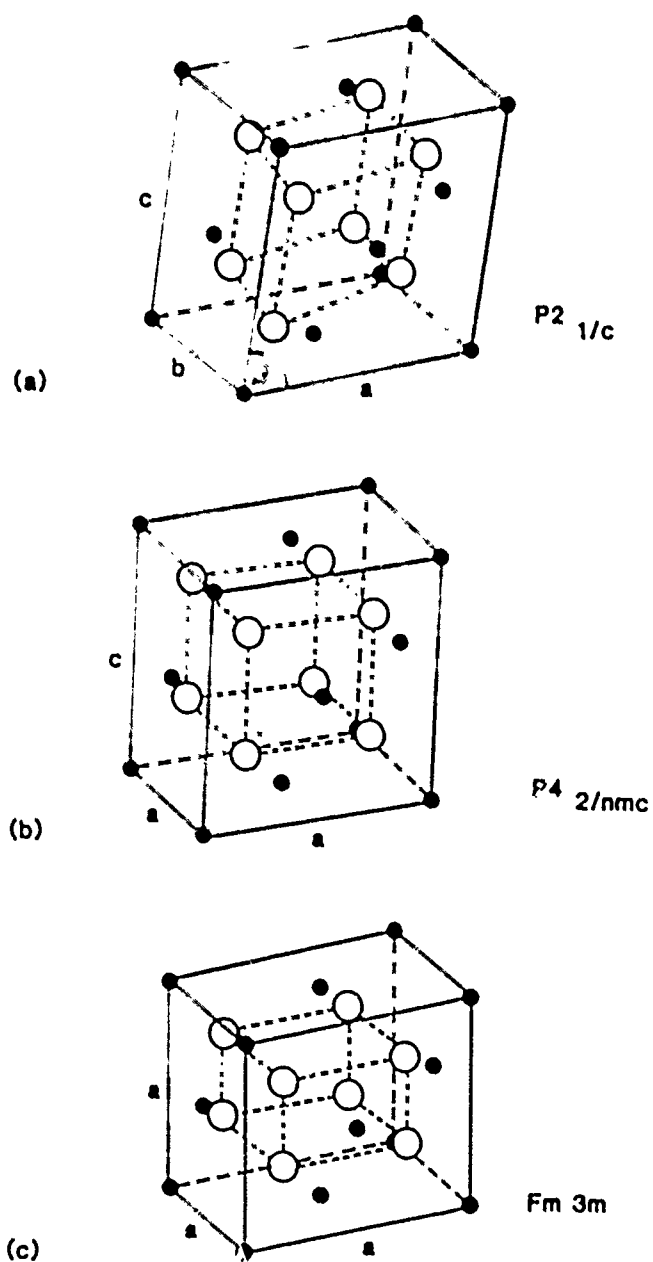


Fig 2.1 Schematic representation of the three zirconia polymorphs: a, cubic; b, tetragonal; c, monoclinic. Their space groups are indicated.

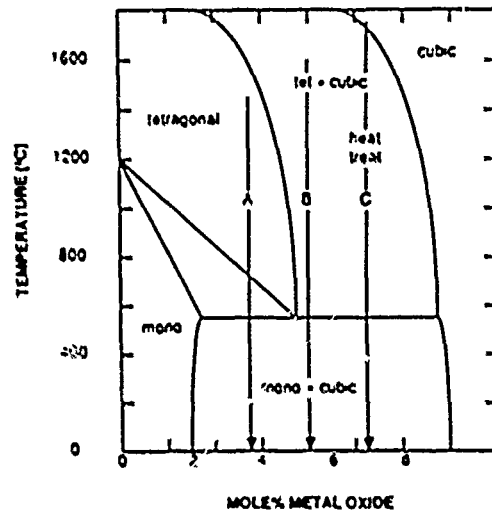


Fig. 2.2 A schematic metal oxide-zirconia phase diagram showing routes for fabricating three different microstructures.

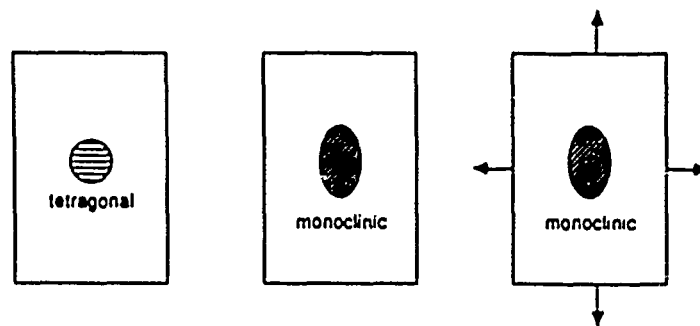


Fig. 2.3 A schematic representation of the zirconia phase transformation. The normal phase transformation to monoclinic is represented by going from A to B and indicated that the zirconia particle undergoes a size and shape change. The material surrounding the particle will oppose the transformation and it is the strain energy that is involved in this constraint that allows the tetragonal phase to be retained. As shown in C, the transformation from A to C can be aided by an applied stress.

for the transformation to proceed, the system has to be "supercooled" to sufficiently increase the chemical driving force. The retention of t-ZrO₂ to room temperature can be controlled by several microstructural and chemical factors, such as grain size and alloy content.

The microstructures of these materials can be characterized by methods which depend on the level of resolution required for the identification of structures and morphologies. Usually, electron optical instruments are needed. For example, scanning electron microscopy has allowed the determination of the grain sizes and of phases in ZrO₂ materials down to dimensions of about 0.1 μm, whereas transmission electron microscopy (TEM) has allowed the identification of phases and defects to the atomic level. Some typical TEM micrographs obtained for Mg-PSZ, ZTA (with intercrystalline and intracrystalline ZrO₂) and Y-TZP particles are depicted in Figs. 2.4–2.6. Major defects in these materials, such as dislocations and precipitates, have also been analyzed by conventional TEM (Hirsch et al. 1977, Ruhle and Wilkens 1982, Reimer 1984), while analytical TEM has allowed the characterization of chemical composition with high spatial resolution of ~4 nm (Hren, Golstein, Joy 1979, Egerton 1986). Finally, high-resolution TEM (HREM) has allowed the determination of the atomistic structure, wherein experimentally obtained images have been compared with results of image simulations using specific models (Spence 1988, Buseck, Cowley and Eyring 1988).

2.1. The Cubic-to-Tetragonal Phase Transformation

Pauling (1960) provided a set of semiempirical "rules" for predicting crystal structures of inorganic materials based on radius ratio ($r_{\text{cation}}/r_{\text{anion}}$) considerations. AX₂ compounds with large cations and radius ratios approaching 1 should have the fluorite structure, whereas those with small cations and radius ratios < 0.4 should have tetrahedral coordination and crystallize with one of the silica structures. Intermediate-sized cations should form AX₂ compounds with the rutile structure. The radius ratio for ZrO₂ in eightfold coordination is 0.59. This radius ratio is much lower than that for other materials with the fluorite structure (CeO₂ 0.68, UO₂ 0.70, ThO₂ 0.75, CaF₂ 0.85, HgF₂ 0.86, CuF₂ 0.88, SrF₂ 0.94, etc.). Consequently, pure c-ZrO₂ is stable only between 2370°C and the melting point at ~2680°C (Smith and Cline 1962). The instability of c-ZrO₂ at lower temperatures does not lead to a rutile form of ZrO₂ because the Zr⁴⁺ ion is large. Instead, t- and m-ZrO₂ form at progressively lower temperatures. Both of these polymorphs are distorted versions of the fluorite structure (Fig. 2.1).

The electronic structure of both c- and t-ZrO₂, calculated using quantum mechanical cluster techniques, yields additional insight into the stability of these polymorphs (Morinaga et al. 1983, Jansen and Gardner 1988, Zandiehnam et al. 1988). Such calculations reveal that t-ZrO₂ is more covalent than the c-polymorph: 28 percent and 22 percent, respectively. The higher covalency of t-ZrO₂ leads to a larger band gap and a lower center of mass energy of the valence band. Consequently, t-ZrO₂ is generally more stable than c-ZrO₂. However, at elevated temperature, c-ZrO₂ is more stable because it has a higher entropic contribution to the free energy.

Virtually all the rare earth ions in solid solution reduce the c → t transformation temperature. Additionally, when ZrO₂ loses oxygen, the c phase in the resulting nonstoichiometric ZrO_{2-x} has a larger stability field (Zandiehnam 1988). Quantum mechanical calculations by Morinaga et al. (1983) and Jansen and Gardner (1988) show that there is a large change in the electronic structure and in the energy of the valence band as anions are displaced from their ideal fluorite positions. Consequently, since the charge compensating defects in both rare earth doped and oxygen deficient ZrO₂ are oxygen vacancies, it is likely that the stabilization of c-ZrO₂ is related to local structural relaxation around the anion vacancies (Morinaga et al. 1983).

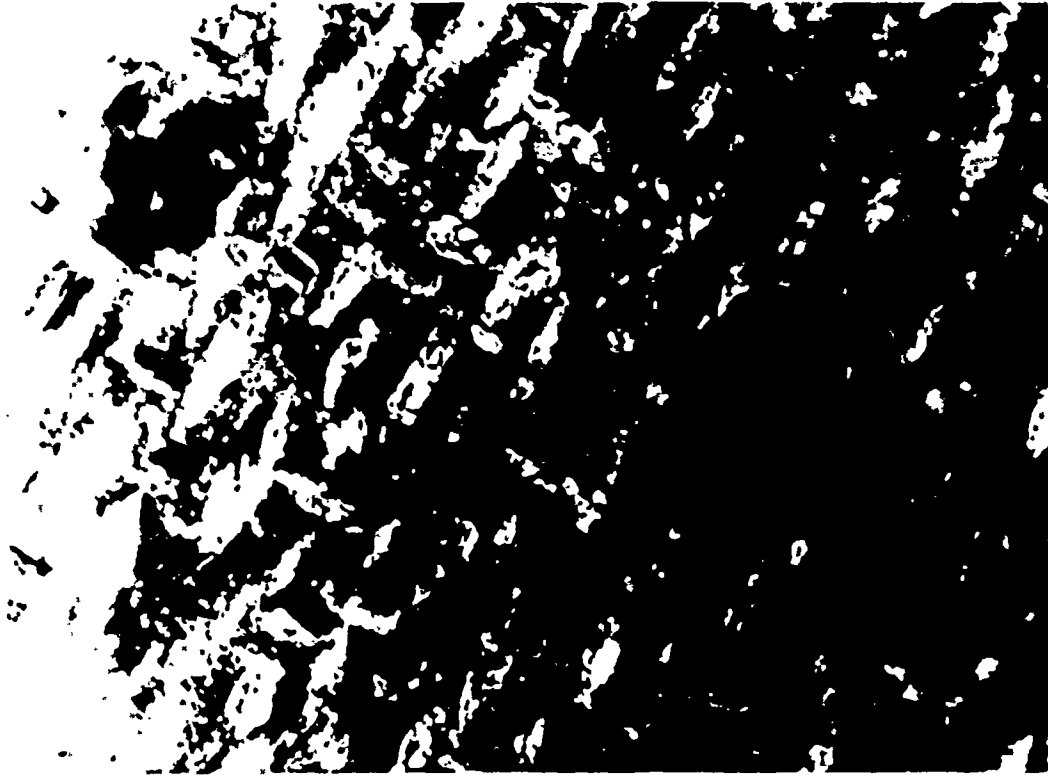


Fig. 2.4 TEM micrograph of a Mg-PSZ ceramic. The grain size of the cubic matrix is $\sim 50\mu\text{m}$. Small precipitates are visible.



2.5 a



2.5 b

Fig. 2.5 TEM micrograph of an Al_2O_3 ceramic containing dispersed ZrO_2 particles
 a) Irregular-shaped, faceted ZrO_2 particles are intercrystalline;
 b) Regular-shaped ZrO_2 particles are intracrystalline; the orientation of the particle is random inside the matrix.



Fig. 2.6 TEM micrograph of a TZP ceramic which is 100% t-ZrO₂. Grain size range \approx 0.8 μ m.

These stabilization effects are manifest in the phase diagrams. Stubican (1988) describes the exact solubility of MgO in m- and t-ZrO₂ with reasonable certainty (Fig. 2.7).² Conversely, the details of phase equilibria in ZrO₂/C³ are elusive. The last major attempt (Stubican 1988) has been the subject of four revisions involving either the composition or temperature of the invariant eutectoid and the stability fields of the intermediate compounds, ϕ_1 -CaZr₂O₆ and ϕ_2 -Ca₂Zr₁₉O₂₄. The most recent diagram shows that ϕ_1 and ϕ_2 are stable below 1233° and 1355°C, respectively, while the eutectoid is at 1140°C and 17 mol% CaO. Morinaga et al. (1983) and Pascual and Duran (1983) pointed out that uncertainty exists in the Y₂O₃-ZrO₂ system. Many of the problems arise from the use of classical techniques with poor spatial resolution. Furthermore, the free energy, composition curves are relatively flat.

Enhanced precision is illustrated by studies of subsolidus equilibria using analytical electron microscopy to determine the compositions of the coexisting t- and c-ZrO₂ with high spatial resolution and with calibrated standards to determine absolute concentrations (Ruhle et al. 1984, Lanteri et al. 1984). The data (Fig. 2.8) obtained using crystals containing 6 or 8 wt% Y₂O₃, grown by skull melting and annealed for long times between 1300°C and 1600°C have an absolute uncertainty \pm 0.2% and represent the best determination to date of subsolidus phase equilibria in a ceramic system in which both coexisting phases show appreciable solid solubility.

² The lens-shaped t-ZrO₂ precipitates found in this alloy are consistent with the geometrical transformation theory of Khachaturyan (1983).

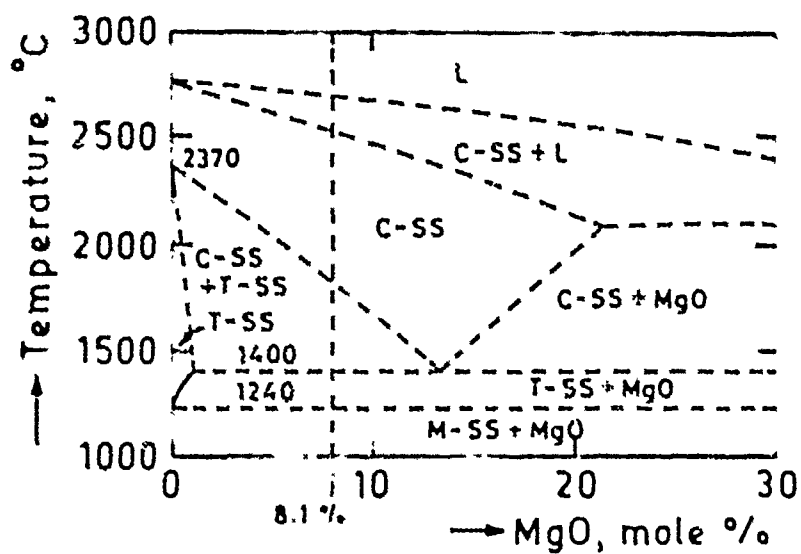


Fig. 2.7 The ZnO rich end of the MgO-ZnO equilibrium phase diagram.

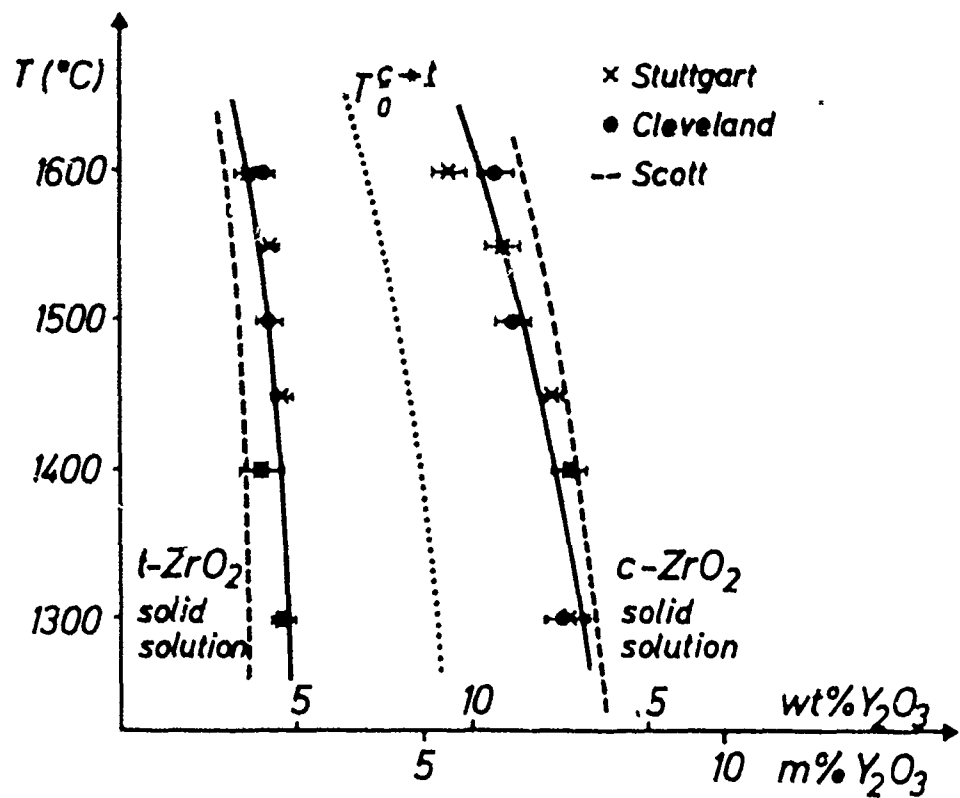


Fig. 2.8 Zirconia rich end of the yttria-zirconia equilibrium diagram. The equilibrium compositions were determined by energy dispersive x-ray spectroscopy.

2.2. The Tetragonal-to-Monoclinic Transformation

2.2.1. Crystallography

The crystallographic aspects of the martensitic $t \rightarrow m$ transformation in ZrO_2 are well established and the basic results are summarized in the Appendix. Experimental studies show that the c axis of the t - ZrO_2 is parallel to the c axis of m - ZrO_2 . The nonvanishing components of the symmetrical unconstrained transformation strain tensor, ϵ^T , defined with respect to the tetragonal lattice, is for pure ZrO_2 (Kriven et al. 1981)

$$\begin{aligned}\epsilon_{11}^T &= (a^m/a^t) \cos \beta - 1 = 0.00149 \\ \epsilon_{22}^T &= (b^m/b^t) - 1 = 0.02442 \\ \epsilon_{33}^T &= (c^m/c^t) - 1 = 0.02386 \\ \epsilon_{13}^T &= \epsilon_{31}^T = 1/2 \tan \beta = 0.08188\end{aligned}\quad (2.1)$$

The shear components have the largest values, while the volume strain at room temperature $(\epsilon_{11}^T + \epsilon_{22}^T + \epsilon_{33}^T)$ is about 4.7%.

2.2.2. Strain Fields

Strain fields that occur in association with ZrO_2 particles are important to the transformation, as elaborated below. Consequently the local strain field in the matrix surrounding a zirconia particle has been examined by HVEM (Rühle and Kriven 1982, 1983). The strain analysis was performed at intracrystalline, regular-shaped, spherical and slightly ellipsoidal t - ZrO_2 particles completely embedded in the Al_2O_3 matrix. Extended contrast fringes are visible around the embedded particles when the matrix is imaged under two-beam dynamical diffraction conditions. By imaging the Al_2O_3 surrounding the particles with different diffraction vectors (Fig. 2.9) and different orientations, it was determined that an anisotropic strain field surrounds the t - ZrO_2 inclusions and that the particle is a center of dilatation. The strain anisotropy is attributed to the anisotropic thermal expansion mismatch.* Preliminary experiments correlating the strain field with the internal orientation of tetragonal phase (Rühle and Kriven 1983) are consistent with the hypothesis that maximum misfit with respect to the alumina matrix occurs along c_t . Computer simulated images from contrast calculations based on the above model match well with the observed tetragonal strain field (Mader and Rühle 1982, Mader 1987). Additionally, approximate contrast calculations conducted using elastic dipoles yield misfit parameters which agree reasonably well with those expected from the misfit strain (Rühle and Kriven 1983, Mader 1987).

Transformed particles are internally twinned, leading to very high displacement fields localized at the particle-matrix interface (Fig. 2.10). A semiquantitative analysis by Rühle and Kriven (1983) and Mader (1987) indicates that the particle is a center of compression due to the volume increase and that the strain field symmetry axis is perpendicular to the internal twin plane. The transformation and deformation twinning mechanism for a transforming ZrO_2 particle in an Al_2O_3 suggested by the observations is summarized in Fig. 2.11 (Kriven 1988).

* The specimens were fabricated in equilibrium at $\sim 1500^\circ C$.

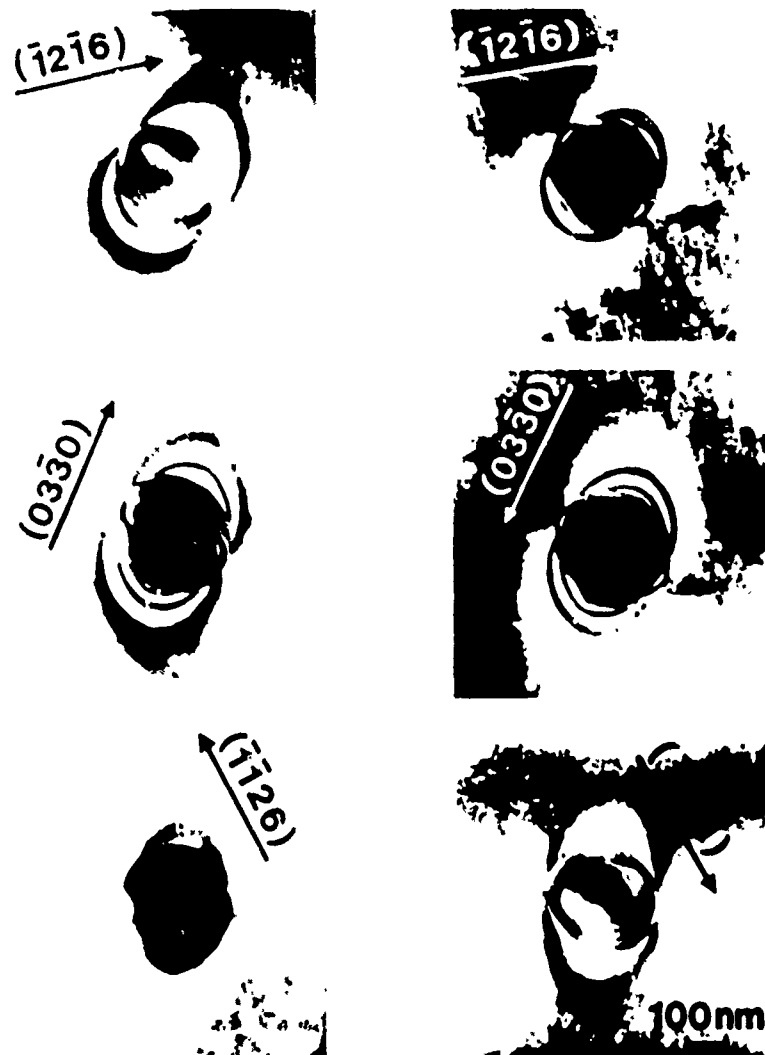


Fig. 2.9 a-f) HVEM analysis of the anisotropic strain field in the alumina matrix surrounding an intragranular t-ZrO₂ particle which formed a center of dilatation at room temperature. The particle was imaged in bright field and dark field modes under two-beam dynamical conditions with the plane normals (diffraction vectors *g*) indicated.

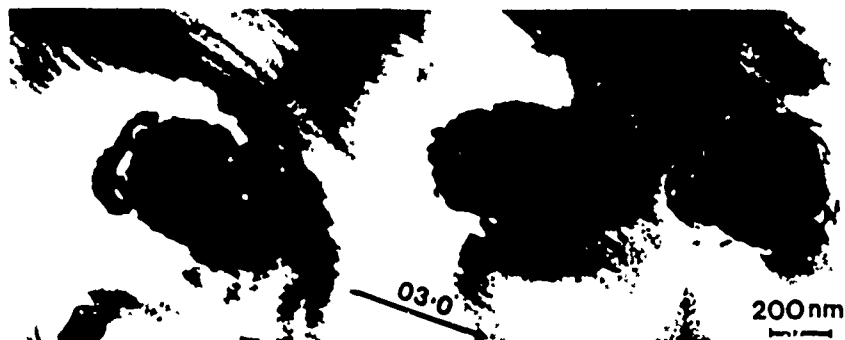


Fig. 2.10 HVEM micrograph of strain fields due to internal monoclinic twins, localized at the particle-matrix interface.

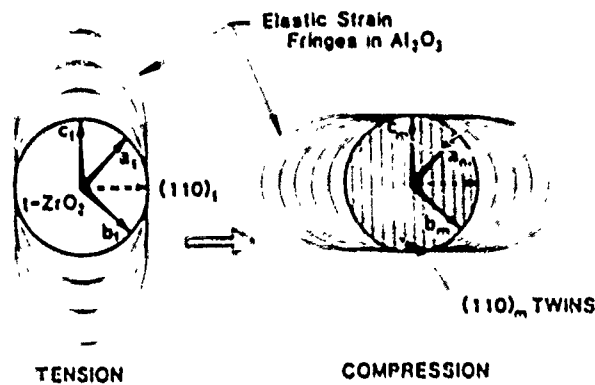


Fig. 2.11 Suggested transformation and deformation twinning mechanism for a transforming ZrO_2 particle in an $\alpha\text{-Al}_2\text{O}_3$ matrix (Kriven 1982, 1988).

2.2.3. Nucleation

The nucleation of martensite can be treated using either a discrete analysis with the structure of the martensite phase or by invoking a gradual, diffuse transition. In the former, classical approach, the interfacial and strain energies associated with martensitic nuclei prevent their forming by conventional statistical fluctuations (*homogeneous* nucleation). Possible sites for *heterogeneous* nucleation ("embryos") are thus inferred (Knapp and Dehlinger 1956, Kaufmann and Cohen 1958). For steels, a dislocation array susceptible to dissociation has been proposed as the embryonic nucleus (Olson and Cohen 1981, 1982). For such a case, the free energy function describing the formation of a martensite nucleus of volume V and interfacial area S can be expressed as

$$g = g^D + (g^I + g^{sr} + g^{ch})V + S\gamma \quad (2.2)$$

where g^D is the change in self-energy of the dislocation embryo, g^I the interaction energy with the nucleus, g^{ch} the chemical-free energy/unit volume accompanying nucleus formation, g^{sr} the strain energy attendant on formation of the nucleus and γ the parent/martensite interfacial energy. g^I can be expressed in the form

$$g^I = \sigma_{ij}^D \epsilon_{ij}^T \quad (2.3)$$

where σ_{ij}^D is the prior stress field associated with the dislocation and ϵ_{ij}^T the unconstrained transformation strain. If ϵ_{ij}^T is an invariant plane strain, as must approximately be true for any martensitic reaction, the nucleus is expected to be a thin plate of radius r and semithickness t , for which

$$g^{sr} = K/t/r \quad (2.4)$$

where

$$K = \left[\frac{\pi(2-\nu)}{8(1-\nu)} \right] \mu \gamma_t^2 + \left[\frac{\pi}{4(1-\nu)} \right] \mu \epsilon_n^2 \quad (2.5)$$

where μ and ν are the isotropic shear modulus and Poisson's ratio, respectively, and γ_t and ϵ_n the deviatoric and dilatational components of ϵ_{ij}^T . If the nucleus is coherent, γ consists of a "chemical" term, whereas if it is

semicoherent, an additional term due to the short-range stress fields of interfacial dislocations must also be taken into account.

A plot of trends in g with n , the number of atoms in a nucleus (Fig. 2.12) illustrates the basic features. For homogeneous nucleation, Δg^* represents the activation energy necessary for a structural fluctuation to achieve a critical embryo size n^* . As already mentioned, Δg^* for homogeneous nucleation is very large, because of the magnitude of the strain and interfacial energy terms in Eqn. (2.2). Chen and Chiao (1983, 1985) verified for the ZrO_2 transformation that such nucleation is essentially impossible. When strain "embryos" are present, a much smaller activation barrier may exist. Furthermore, in principle, the defect interaction can be so large that "barrierless" nucleation is possible. However, as elaborated below, this nucleation mechanism seems unlikely in ZrO_2 .

A *nonclassical* transformation (Fig. 2.13) requires a diffuse interface between parent and transformed lattice as proposed by Cahn and Hilliard (1958). The transformation may be nucleated if lattice anharmonicity leads to instabilities, preferentially activated at lattice defects; this process has been termed "localized soft mode" (LSM) nucleation (Suzuki and Wuttig 1975). Such transformations are likely if one or more elastic constant has a marked temperature dependence as the transformation temperature is approached. *Soft zones* should occur near free surfaces (Clapp 1973), as well as adjacent to grain boundaries and interphase interfaces, and be encouraged by strains arising from coherency, thermal expansion mismatch, etc. (Guénin and Gobin 1981). Nucleus formation occurring at localized soft modes adjacent to $t\text{-ZrO}_2$ interfaces provides the best rationalization of available data, as elaborated below.

i) Tetragonal ZrO_2 Polycrystals (TZP)

In Y_2O_3 -containing $t\text{-ZrO}_2$ polycrystals (Y-TZP), the $t\text{-ZrO}_2$ grains are $\leq 1\mu\text{m}$ in diameter and constitute ≥ 80 percent of the microstructure; in some samples, $c\text{-ZrO}_2$ grains are present. All grains are surrounded with a thin continuous amorphous phase (Rühle et al. 1984). No grain boundary dislocations can therefore be present. Nevertheless, such boundaries are sites of localized residual stresses arising from the thermal expansion anisotropy of $t\text{-ZrO}_2$ $\alpha_1 = 7.1 \cdot 10^{-6}/^\circ\text{C}$ and $\alpha_2 = 11.4 \cdot 10^{-6}/^\circ\text{C}$ (Schubert 1986).

Y_2O_3 is a very effective stabilizing solute and increases the difficulty of martensite nucleation. Among other manifestations of this difficulty, the transformation zone found from *in situ* crack propagation experiments in the HVEM (see Sect. 3)[†] is discontinuous. The relative stability of $t\text{-ZrO}_2$ in this system facilitates study of the nucleation process. Specifically, Rühle et al. (1988) have shown that $t\text{-ZrO}_2$ can often be made to transform during TEM observations, due to stresses induced by electron beam heating (ZrO_2 has one of the lowest thermal conductivities among inorganic crystalline solids). Nucleation is found to occur preferentially at grain boundaries and grain corners and it is possible to photograph various stages of transformation. Typical examples are shown in Figs. 2.14 and 2.15 (Rühle et al. 1988, Heuer and Rühle, 1985). A typical essentially-featureless high-angle grain boundary exists at the beginning of the experiment. After a short interval of electron irradiation, strain contours develop at a specific site along the grain boundary [the arrowed features in Fig. 2.14b]. These strain contours oscillate during the experiment, and sometimes die away. Occasionally, however, a small lath of martensite ($m\text{-ZrO}_2$) forms out of the oscillatory contours and begins to grow across the grain, (Figs. 2.14c and d). It is notable that the strains close to dislocations, small-angle boundaries and stacking faults do not act as preferred embryos. For example, Fig. 2.15 is a bright field/dark field pair showing several martensite lathes (the arrowed features). One of these nucleated at a grain facet and grew completely across the grain. The second had nucleated at an otherwise featureless site at a grain boundary: Note that these

[†] This is quite different from dispersion-toughened and precipitation-toughened materials, for which uniform zones adjacent propagating cracks are the rule (Rühle et al., 1984).

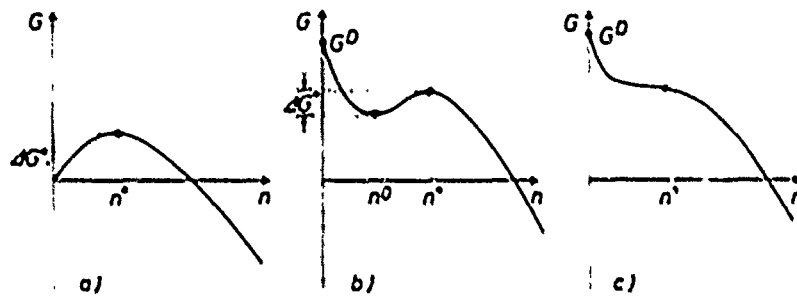


Fig. 2.12 Schematic free energy curves for nucleation via a classical path.
 a) Homogeneous nucleation for which a very high nucleation barrier must be surmounted to form the critical nucleus of site n^* .
 b) Heterogeneous nucleation in the neighborhood of a defect of energy G^D ; only a small thermal activation barrier, ΔG^* , must be surmounted, n^0 denotes a strain "embryo."
 c) Barrier-less heterogeneous nucleation (Guénin and Gobin 1982).

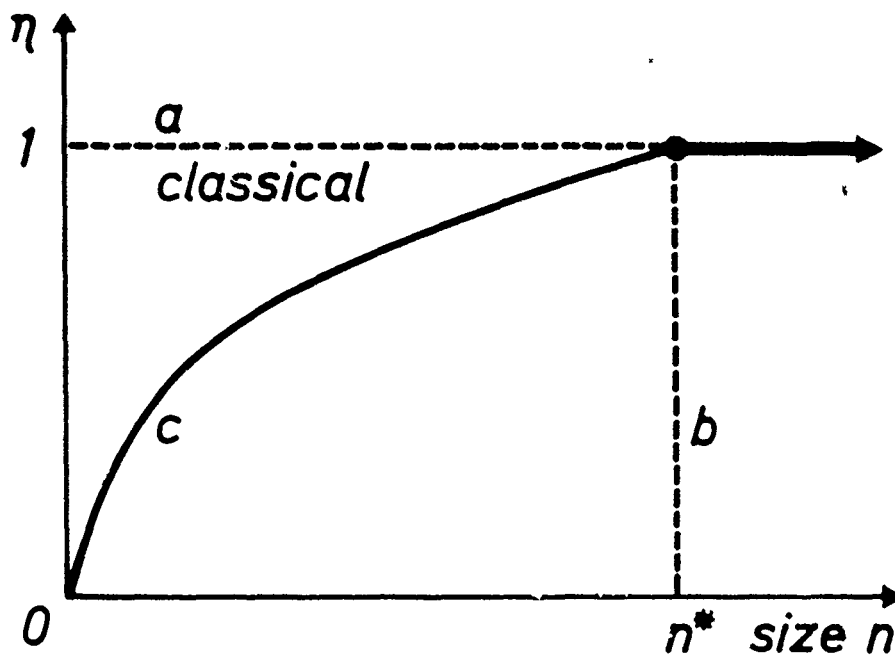


Fig. 2.13 Classical and nonclassical nucleation paths. A nucleus of site n^* of the martensitic phase is characterized by $\eta = 1$.
 a) The classical path.
 b) and c) show two examples of nonclassical paths (Olson and Cohen 1981, 1982).

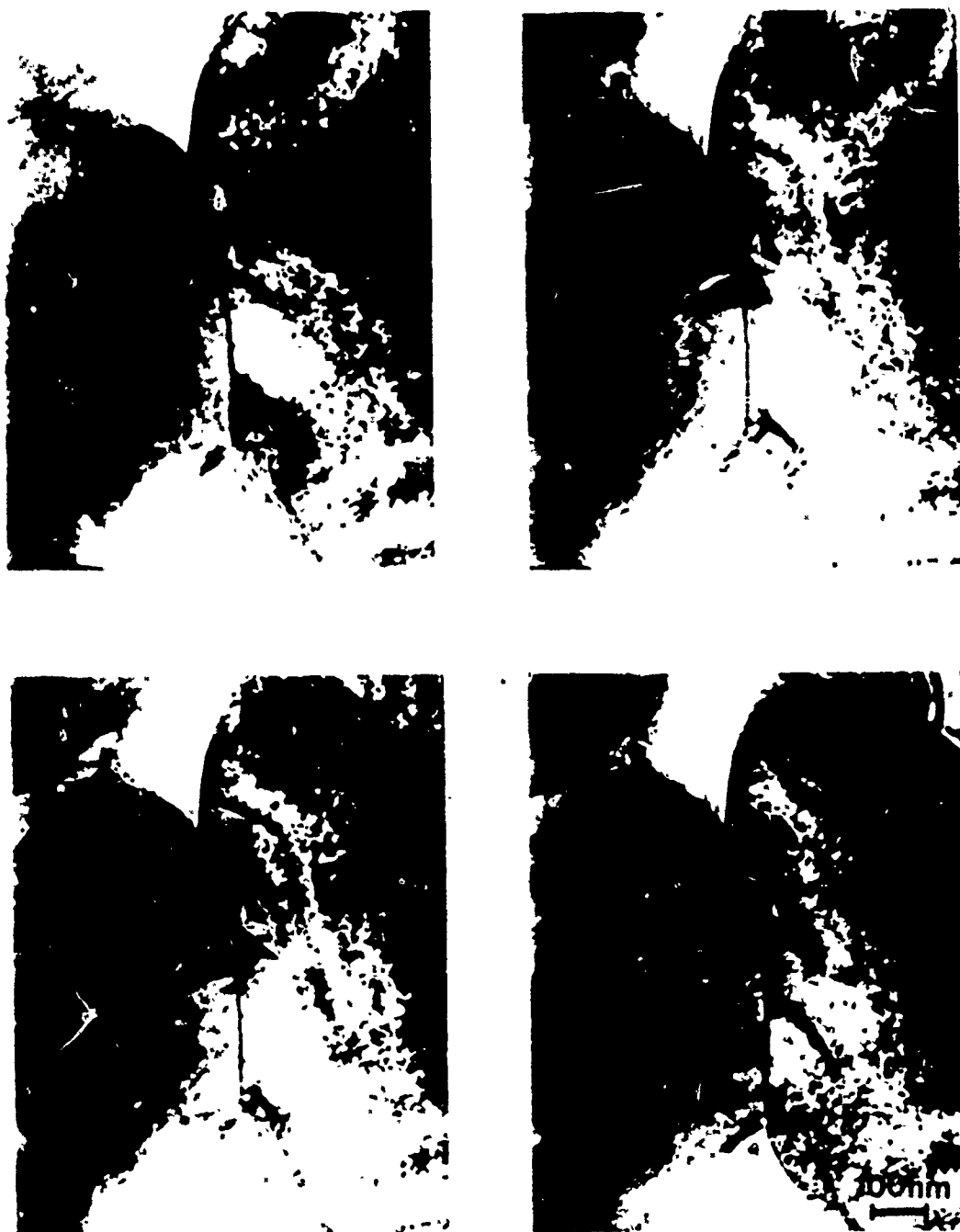


Fig. 2.14 Nucleation in Y-TZP. (a) At the beginning of the experiment, no defects or localized strain contours are visible on the grain boundary, but develop during irradiation, as shown by the arrowed region in (b). On continued irradiation, a martensite lath (a $m\text{-ZrO}_2$ plate) develops [the arrowed feature in (c)] and grows into the grain (d). Bright field electron micrographs.

nucleation events occurred at grain boundaries, despite the presence both a small angle grain boundary (SAGB) and a stacking fault (SF). This mode of transformation may differ from that found in bulk materials due to the lack of constraint afforded by the free surfaces in thin foil experiments. Nevertheless, the oscillatory "premonitory" phenomenon shown in Fig. 2.14 is precisely that expected for the LSM model for the nucleation at a strain concentration.

The expected strain distribution in a cuboidal particle (an adequate model of a grain in TZP) embedded in a solid possessing both elastic and thermal expansion anisotropy (Schmauder et al. 1984) includes logarithmic singularities at edges and corners.[‡] Consequently, the expectation for achieving a critical strain over the nucleus volume increases with increasing grain size, qualitatively consistent with a particle size dependence of M_2 .

ii) Dispersion Toughened Ceramics

In dispersion-toughened ceramics (ZTS, ZTA, ZTM), the difficulty of nucleation is found to be greater for rounded particles embedded in a grain than for faceted particles at grain junctions. Additionally, the nucleation difficulty increases with decreasing particle size and, furthermore, correlates with the thermal expansion mismatch to the matrix phase. Thus, α -ZrO₂ inclusions are particularly stable in spinel (Rühle et al. 1984). Conversely, the average thermal expansion coefficients of Al₂O₃ are less than those of pure α -ZrO₂ and the latter is in residual tension. Consequently, intergranular ZrO₂ particles in ZTA have a well-defined critical particle size (Heuer et al. 1982): M_2 is above room temperature for virtually all particles $\geq 0.6\mu\text{m}$ (Fig. 2.16). The stress concentration at grain facets exerts a critical influence on martensite nucleation in these materials (as the particle-matrix interface is the only "defect" visible in the TEM). However, spherical intragranular particles are extremely stable up to $2\mu\text{m}$ diameter and can exhibit an M_2 temperature less than 20K (Heuer et al. 1982).

iii) Precipitation-Toughened Ceramics

The α -ZrO₂ is present as coherent precipitates in partially-stabilized ZrO₂ (PSZ) and it has been suggested (Heuer and Hobbs 1981, Rühle and Heuer 1984) that the size dependence of M_2 is related to loss of coherency during extended high-temperature aging: the interface dislocations acting as sites for heterogeneous nucleation. Indeed, Chen and Chiao (1983) concluded that a single screw dislocation with [001] Burgers vector should suffice to nucleate the transformation at room temperature. However, virtually all PSZ ceramics studied to date in the TEM have been essentially dislocation-free: dislocations could not be imaged even at precipitate-matrix interfaces. The role of dislocations as nuclei thus appears ambiguous.

Additional aspects of the nucleation emerge from consideration of transformations in Mg-PSZ. The α -ZrO₂ precipitates in this material are lenticular in shape (Fig. 2.17) and the tetragonal c axis (c_t) is parallel to (100) of the matrix. The aspect ratio of the particles is about 4 and can be rationalized on the basis of Khachaturyan's theory (1983) for the morphology of tetragonal particles precipitated coherently from a cubic matrix. Specifically, the tetragonality of α -ZrO₂ in Mg-PSZ is large, 1.021 (Green et al. 1989) and the oblate particle shape minimizes strain along c_t . However, the particle tips are very sharp, as visualized by comparison of the actual particle in Fig. 2.11 with a perfect ellipse of the same aspect ratio. The sharp tips, combined with the aspect ratio, minimize the net coherency strain energy and interfacial energy accompanying precipitation. When coherency is lost, the misfit dislocations must have a significant component along the axis of greatest misfit such that [001] edge-type dislocations on (100) planes should be produced

[‡] The strain levels in faceted particles are not sensitive to the actual grain shape.



Fig. 2.15 Partially transformed tetragonal grain in Y-TZP. Several martensitic laths are arrowed, having formed at a grain facet and grown across the grain or at a grain boundary and are still growing. Nucleation has not occurred at a small angle grain boundary (SAGB) or stacking fault (SF).
a) A bright field electron micrograph.
b) A dark field electron micrograph.

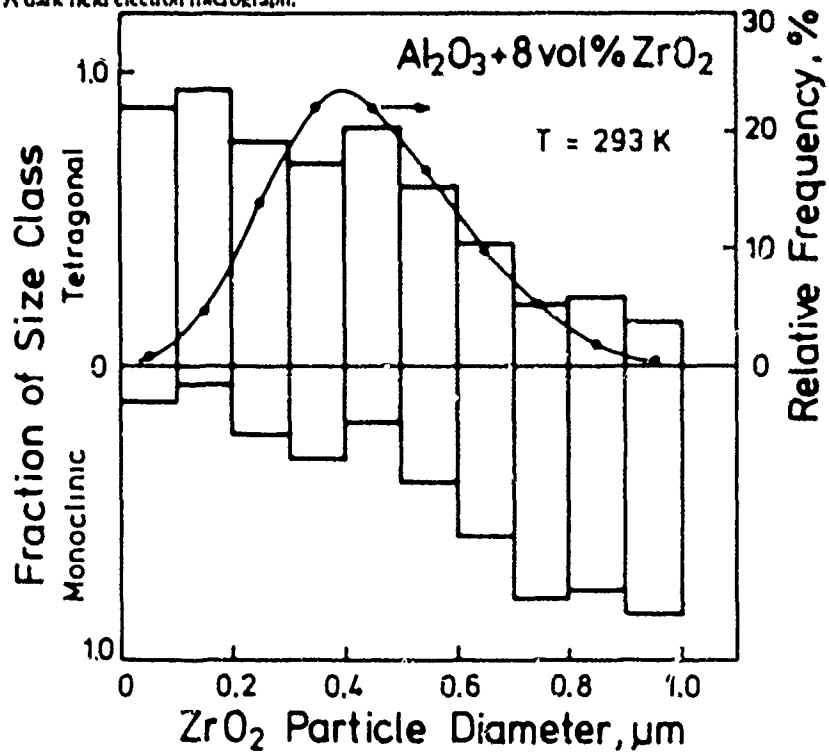


Fig. 2.16 Microstructural characterization of Al_2O_3 -15 vol % ZrO_2 ceramic containing mostly intergranular particles. Size distribution of ZrO_2 particles, which are subdivided for each size group into those with t symmetry and those with m symmetry. The critical particle size is $0.6\mu\text{m}$.



Fig. 2.17 Comparison of $t\text{-ZrO}_2$ precipitate in Mg-PSZ with an oblate ellipsoid having the same principal axes.

(Heuer and Rühle 1984). Such dislocations differ from the array of $[001]$ screw dislocations on a (110) slip plane postulated by Chen and Chiao (1983) as the nucleating defect.

The size dependence of M_s for $t\text{-ZrO}_2$ particles is pronounced in Mg-PSZ. Particles of the type shown in Fig. 2.17 have $M_s < 6\text{K}$ (Heuer et al. 1982). Coarsening during aging causes the particles to elongate and M_s to rapidly increase; M_s for overaged particles can range to $> 100\text{K}$. Furthermore, the aspect ratio correlates with the M_s . Specifically, Mg-PSZ solution annealed at 2073K , cooled rapidly to room temperature, and aged at 1673K for various times revealed that samples aged for four hours or less had M_s below room temperature, while M_s was $\sim 575\text{K}$ for six hours aging and $\sim 725\text{K}$ for an eight-hours aging. These results seem most consistent with the LSM model with nucleation facilitated by residual stress concentrations at sharp particle tips.

The corresponding size dependence for $t\text{-ZrO}_2$ in Ca-PSZ, in which the particles are cuboidal, is similar. This similarity is probably coincidental, because the volume strain on precipitation is smaller in Ca-PSZ than in Mg-PSZ (-0.58% and $+1.95\%$, respectively), due to the marked difference between the ionic radii of Ca^{2+} and Mg^{2+} (Heuer and Rühle 1984). However, these volume strains are modified by the thermal expansion mismatch between c and $t\text{-ZrO}_2$, such that the stress concentration at cuboid facets in Ca-PSZ is less than at the lens tips in Mg-PSZ. The net result is a similar critical particle dimension in the two systems.

The corresponding critical size in Y-PSZ is relatively large, but has not been rigorously determined. Both the tetragonality and the volume strain on precipitation are small, 1.008 and $+0.02\%$, respectively. Also, Y_2O_3 is much more soluble in $t\text{-ZrO}_2$ than either HfO or CaO . Finally, the precipitate morphology is unusual, as the $t\text{-ZrO}_2$ exists as twinned "colonies," the twinning serving to further reduce coherency strains (cf., Khachaturyan 1983, Lanteri et al. 1986).

3. *IN SITU* OBSERVATION OF TRANSFORMATION

In situ straining experiments performed in a high-voltage electron microscope with cracks introduced during the deformation reveal the processes occurring around crack tips (Rühle et al. 1984). TZP, PSZ and ZTA materials have been studied. For studies on ZTA, the $\text{Al}_2\text{O}_3/\text{ZrO}_2$ powders were milled for different times to vary the ZrO_2 particle sizes. The size distributions of the Al_2O_3 and ZrO_2 , as well as the fraction of ZrO_2 particles with *m* symmetry were determined by TEM (Fig. 3.1 and Table 3.1). Specimens were carefully polished to a thickness of 40 to 80 μm . By a special ion thinning technique, two elongated holes with a transparent ridge between them were formed (Figs. 3.2 and 3.3). The transparent area was photographed and the *t*- ZrO_2 particles identified. The specimen was slowly strained inside a high-voltage electron microscope at a constant rate until a crack was initiated, usually at a region of highest stress concentration such as a thinner area in the ridge. The progress of the crack could be stopped by ceasing to apply further strain. The *t*- ZrO_2 particles were observed to transform suddenly (Fig. 3.4) ahead of the crack tip, at a distance dependent on the size of the particle, to form twinned monoclinic particles (Fig. 3.5). After the relief of the applied stress, the reverse transformation could not be observed.

The spatial distribution of zirconia particles which transformed ahead of the crack as it progressed through the material is summarized in Figs. 3.5 and 3.6. The general shape of the transformation zone could be outlined (Fig. 3.6), although its dimensions were dependent on microstructure homogeneity. Clusters of zirconia particles which were susceptible to transformation even at larger distances from the crack, modified the shape of the zone. The expected transformation ahead of a crack tip within a well-defined transformation zone was thus experimentally verified. Furthermore, the zone height could be evaluated by investigation of the *t* \rightarrow *m* transformation in the 100 μm long wake of the crack. The results are summarized in Fig. 3.7.

$\text{Al}_2\text{O}_3 + 15\% \text{ZrO}_2$

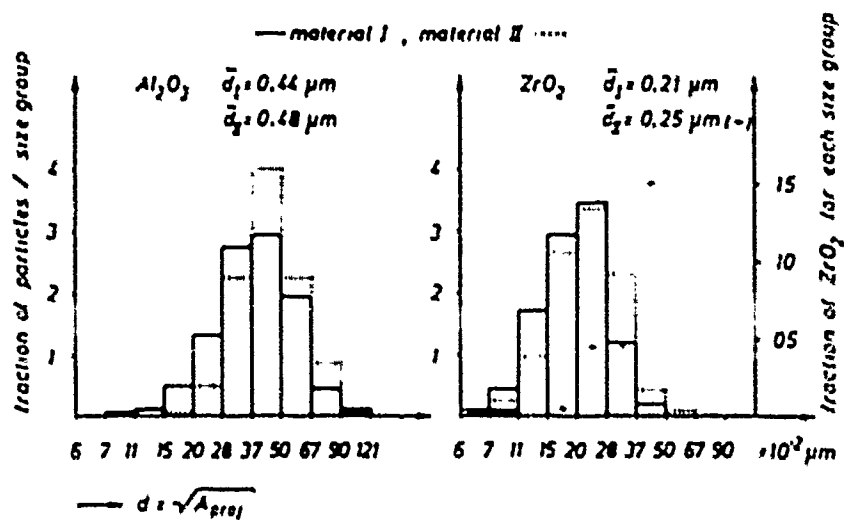
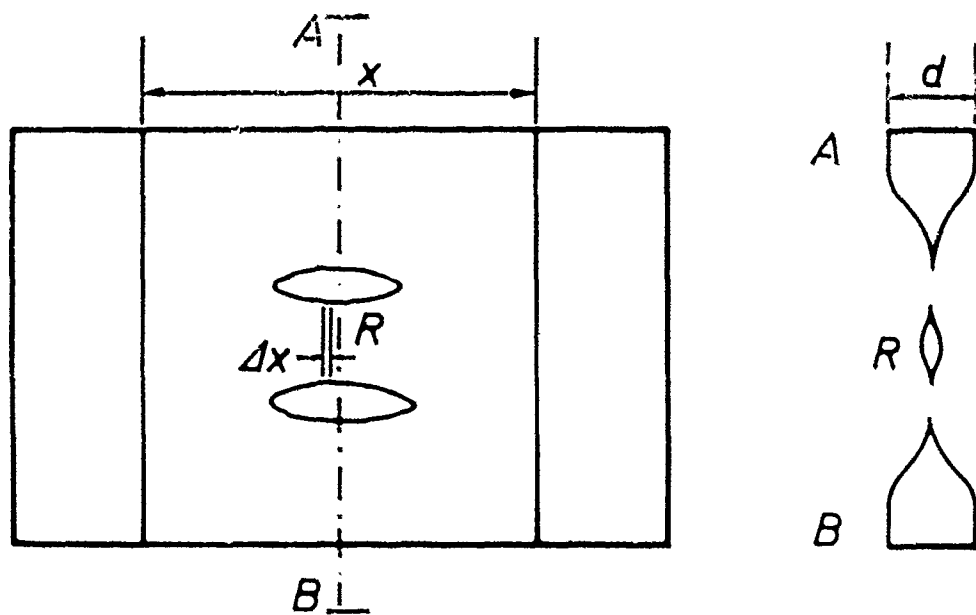


Fig. 3.1 Size distribution of Al_2O_3 and ZrO_2 grains in two $\text{Al}_2\text{O}_3 + 15 \text{ vol } \% \text{ZrO}_2$ ceramics. The fraction of m- ZrO_2 is noted for each size group of the different materials. Material I (16-h milling time); material II (12-h milling time).

Table 3.1 Size range of the different size groups—logarithmic scale

Size group	Lower bound (μm)	Upper bound (μm)
1	0	0.10
2	0.10	0.13
3	0.13	0.18
4	0.18	0.24
5	0.24	0.32
6	0.32	0.44
7	0.44	0.59
8	0.59	0.79
9	0.79	1.06
10	1.06	1.42
11	1.42	1.91
12	1.91	∞



geometry of specimens suitable for

Fig. 3.2(a) Specimen and straining stage for *in situ* straining experiments: Cross section through specimen (original thickness $d \approx 40$ to $70\mu\text{m}$).

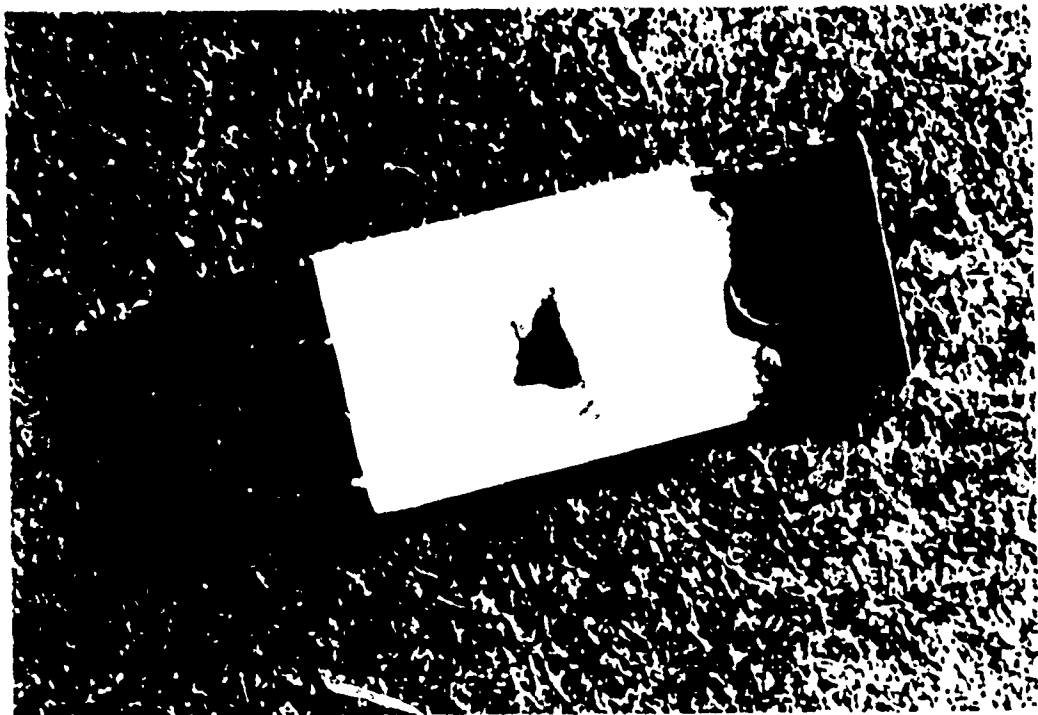


Fig. 3.2(b) Specimen and straining stage for *in situ* straining experiments: Specimen glued on specimen holder.

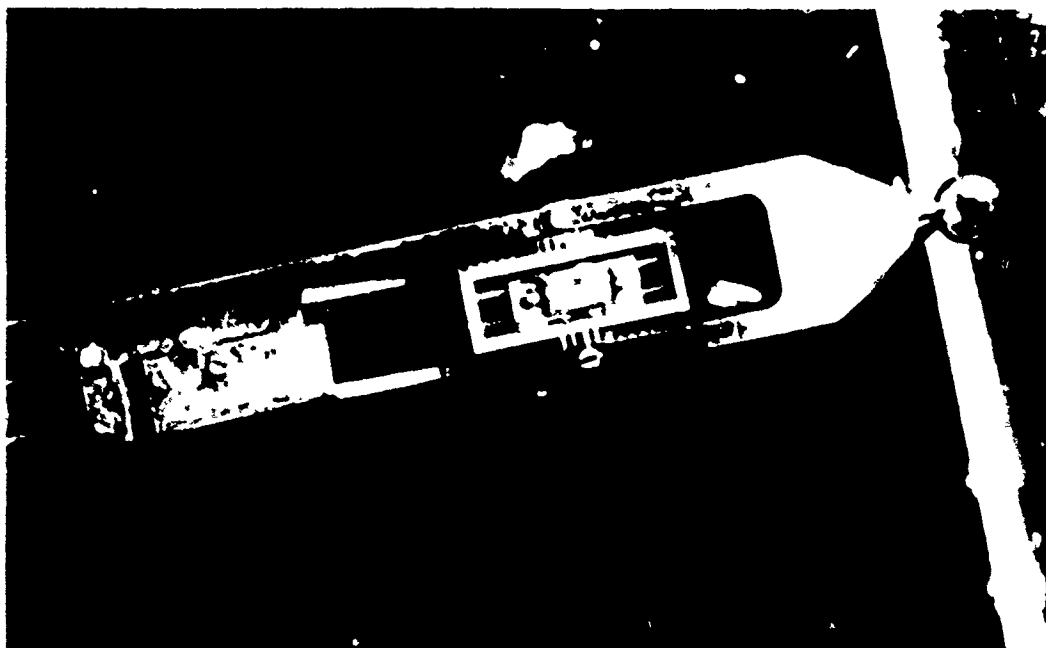


Fig. 3.2(c) Specimen and straining stage for *in situ* straining experiments: Double tilting straining stage.



Fig. 3.3 Specimen for *in situ* straining experiments. The ridge between the two holes is (nearly) transparent to 1 MeV electrons (low magnification TEM).

- a) Unstrained specimen.
- b) Deformed specimen with crack.

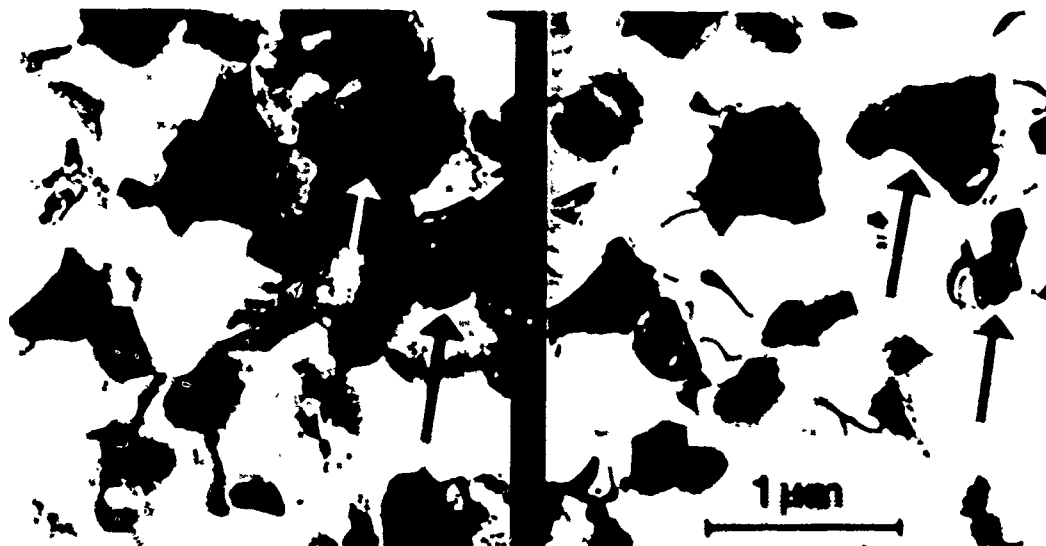


Fig. 3-4 Transformation of t -ZrO₂ grain in front of a crack tip.

a) Micrograph taken prior to straining.

b) Micrograph taken after straining. Marked t -ZrO₂ inclusions transformed to m symmetry. Twins can be observed in the m -ZrO₂.

The results of *in situ* straining experiments for Mg-PSZ and TZP ceramics revealed that those ceramics form a very narrow transformation zone. However, material optimization leads to larger widths as detected either by micro Raman spectroscopy (Clarke and Adair 1982) or by optical techniques (Swain and Rose 1986).

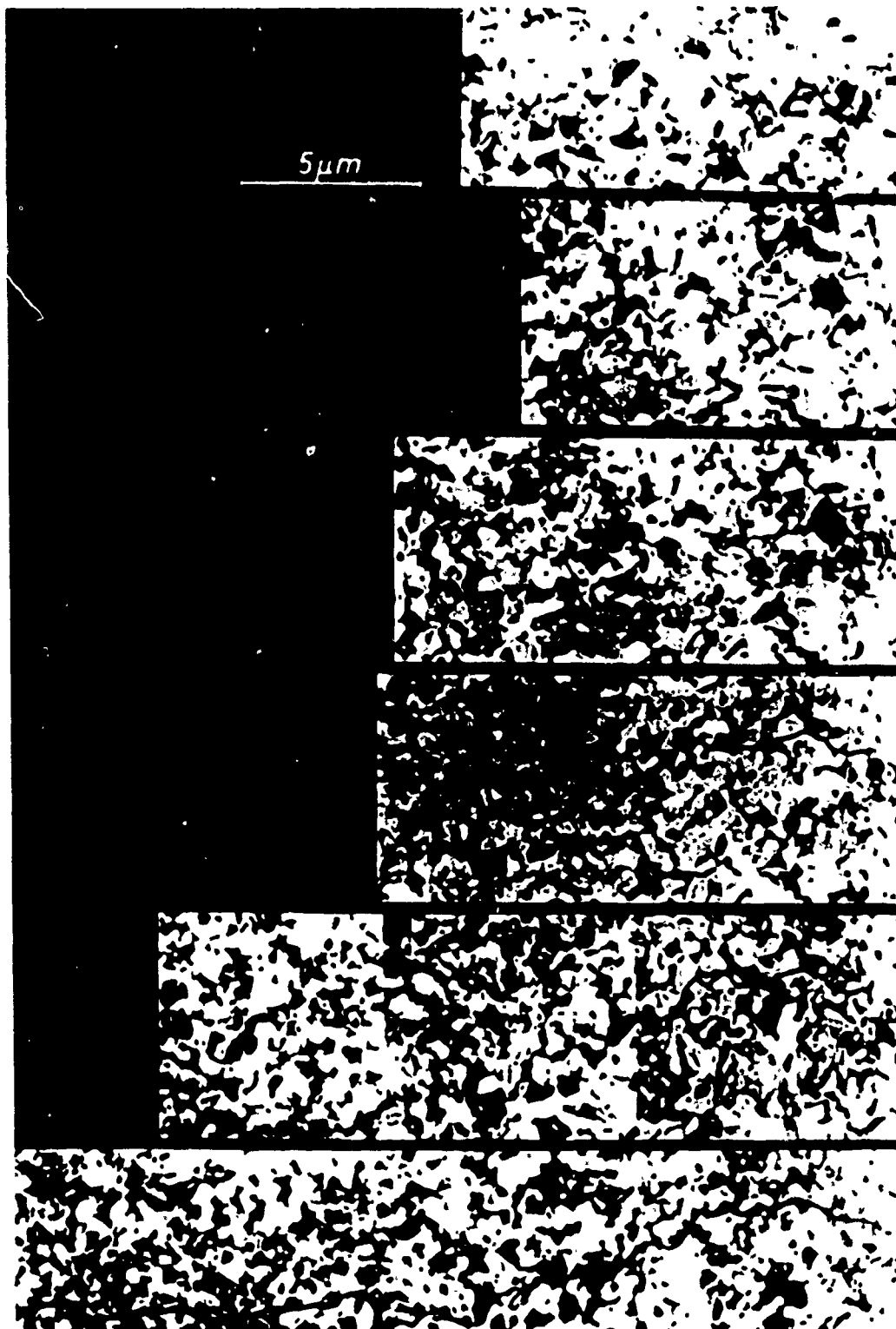


Fig. 3.5 Sequence of straining experiments. (a) TEM micrograph taken prior to straining. No m-ZrO₂ inclusions are present. (b) Crack starts to propagate. The crack is marked on all micrographs. (c) to (f) Straining experiment. Crack propagates by increased loading. t-ZrO₂ inclusion transformed to m symmetry.

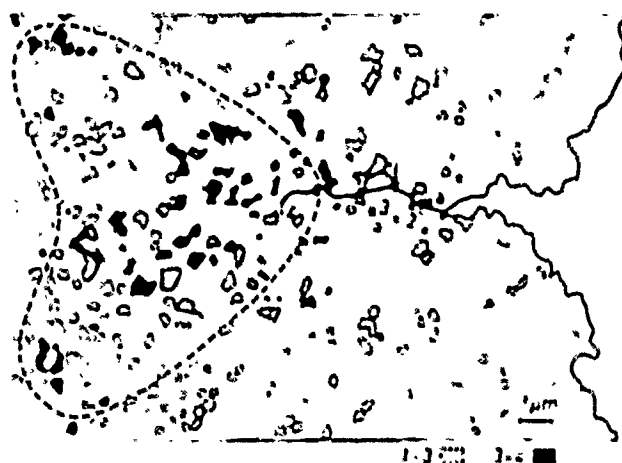


Fig. 3.6 Schematic representation of (partial) evaluation of straining experiment. The specimen was strained so that the crack propagated to different positions (1, 2, 3, 4). All ZrO_2 inclusions are marked on the schematic drawing. Hatched areas: ZrO_2 grains transformed during propagation of crack from hole to position 3. Dark areas: ZrO_2 grains transformed during crack propagation from position 3 to 4. The transformation zone is outlined.

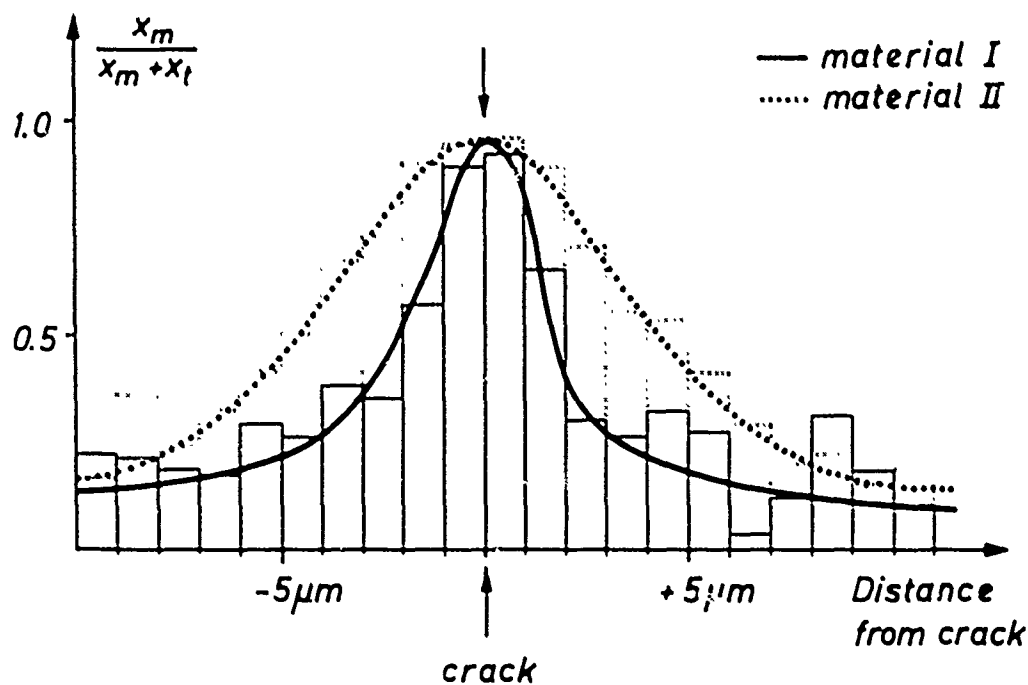


Fig. 3.7 Determination of transformation zone size h (perpendicular to crack). The fraction of transformed ZrO_2 grains is plotted as a function from distance of the crack for materials I and II.

4. TRANSFORMATION TOUGHENING

The stress induced transformations that can cause significant toughening include martensitic (Evans and Heuer 1984) and ferroelastic (Virkar and Matsumoto 1986, 1988) transformations, as well as twinning. The former involves both dilatational and shear components of the transformation strain, while the latter typically have only a shear component.

At the simplest level, transformation toughening can be regarded as a process dominated by a volume increase (dilatational stress-free strain ϵ_{II}^T) (see Fig. 2.2). Then, based on simple concepts, it is apparent that a stress induced frontal process zone must have no effect on the crack tip field and thus, initial crack growth must occur without toughening, Fig. 4.1 (McMeeking and Evans 1982, Budiansky et al. 1983). However, upon crack extension, process zone elements unload in the wake, hysteresis occurs (Fig. 4.2) and toughening develops, given by,

$$\Delta \bar{\gamma}_c = 2 / \bar{\sigma}^c \epsilon_{II}^T \quad (4.1)$$

where $\bar{\sigma}^c$ is the critical mean stress for supercritical^a transformation. This *steady-state* level of toughening is attained after substantial crack extension. A directly equivalent result for the increase in critical stress intensity factor, ΔK_c , can be derived by considering that a residual compressive stress created within the transformation zone. This stress inhibits crack opening, resulting in crack shielding such that,

$$\Delta K_c = 0.22 E \epsilon_{II}^T f \sqrt{h} / (1 - \nu) \quad (4.2)$$

where E is the composite modulus (McMeeking and Evans 1982).

Evans and Cannon (1986) and Green et al. (1989) compared the theoretical predicted values with experimental data based on actual zone size measured in steady-state (Swain and Rose 1986) (Fig. 4.3) and revealed that Eqn. (4.2) consistently underestimates the toughness. It has been surmised that the disparity arises because shear effects have not been incorporated. One hypothesis regarding the shear strain invokes non-associated flow (Evans and Cannon 1986). Specifically, it is presumed that the *shear stress dominates the nucleation* of the transformation, but that the *residual strain is predominantly dilatational*, because of extensive twinning (Evans et al. 1981). This premise results in a zone profile, in plane strain, with diminished transformed material ahead of the crack. The resultant toughening exceeds Eqn. (4.2) and furthermore, agrees quite well with experimental data (Fig. 4.3). However, the necessary zone shapes are not consistent with experiment. Some inconsistency thus remains to be addressed, and other mechanisms, such as twin induced microcracking, may also be involved (see section 5).

The zone size h represents the major *microstructural influence on toughness*. Clearly, h is governed by a martensite nucleation law. However, a fully validated law does not yet exist. Consequently, connections between h and the microstructure still cannot be specified. Nevertheless, certain trends are apparent, based on the free energy of the fully transformed product. Specifically, h invariably decreases with increase in temperature and decrease in particle size. *A temperature and particle size dependent toughness is thus inevitable for this mechanism.*

^aSupercritical refers to the condition wherein all particles within the process zone fully transform.

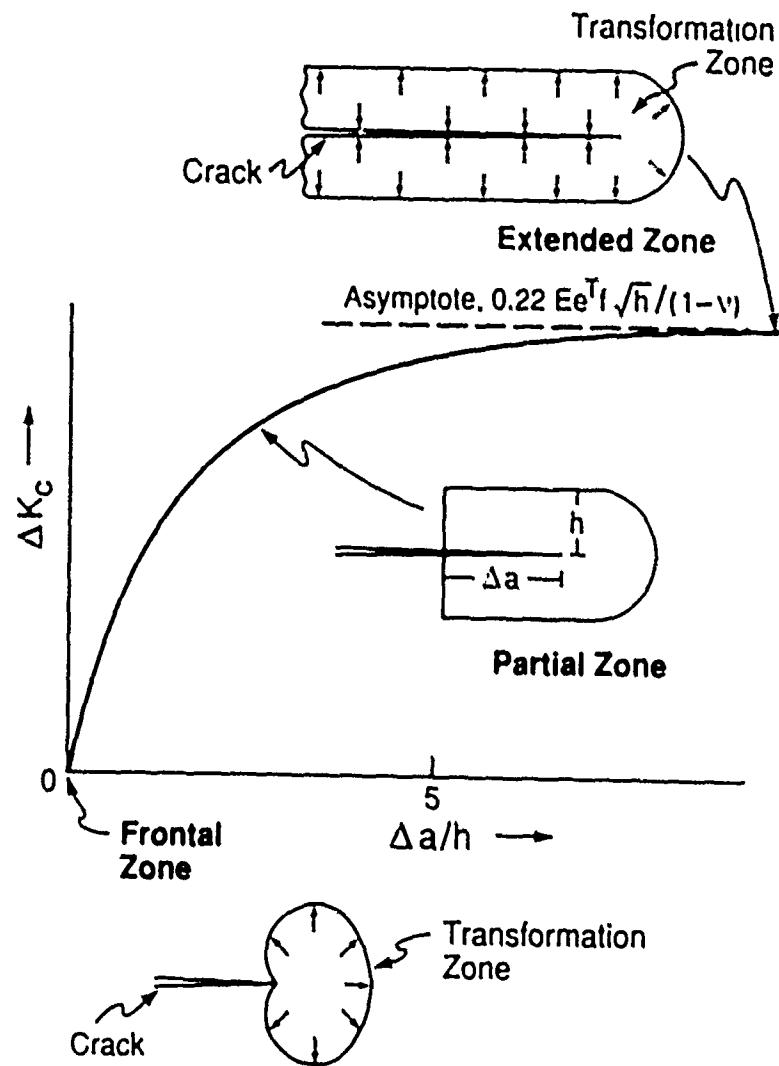


Fig. 4.1 Transformation zones illustrating the dimensions used in describing the transformation toughening process: a frontal zone and a steady-state zone for a dilatational driven transformation. R-curve for zones with intermediate profiles is also shown.

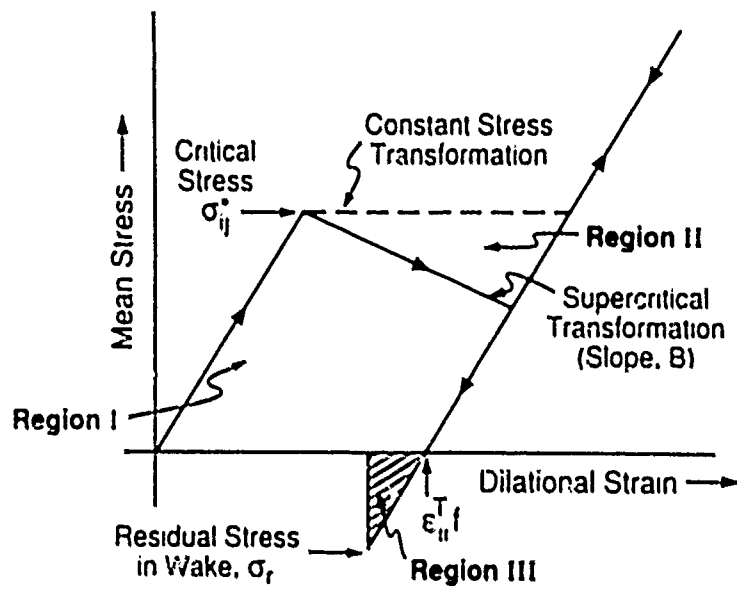


Fig. 4.2 A schematic stress-strain curve for the supercritical martensitic transformation indicating the critical stress and the permanent strain.

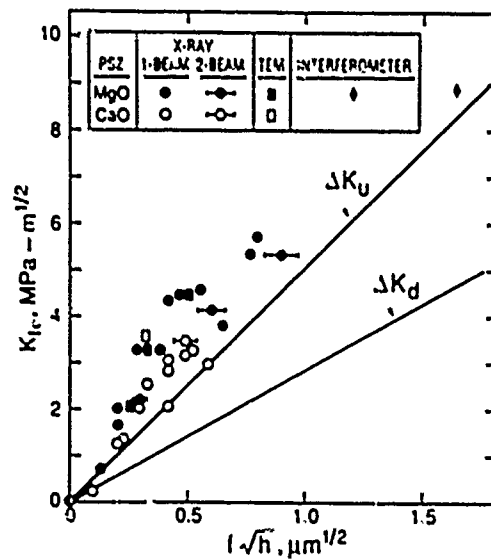


Fig. 4.3 A comparison between theory and experiment for various partially stabilized zirconia materials: ΔK_u refers to a zone shape dictated by the equivalent stress, whereas ΔK_d refers to a zone shape governed by the mean stress.

4.1. Constitutive Laws

Constitutive laws expressly relate the components of the stress and transformation strain tensors in the transforming solid. The stresses are most conveniently expressed in terms of the mean stress, σ , the deviatoric stresses, $s_{ij} = \sigma_{ij} - \delta_{ij} \sigma$, and/or the equivalent stress, $\sigma_e = \sqrt{3s_{ij}s_{ij}/2}$ and their variation during transformation. Such relations are, in fact, the equivalent of the more familiar constitutive laws used to describe plastic deformation and crack tip fields in elastic/plastic solids. A viable constitutive law must account for the effect of particle size and shape upon the incidence of transformation by allowing only a certain fraction, f , of the solid to actually transform at a given imposed stress σ_{ij} . The simplest yield criterion has the form (Chen and Reyes-Morel 1986),

$$\tilde{\sigma}/\Omega + \sigma_e/\tau = 1 \quad (4.3)$$

where Ω and τ are experimentally determined normalizing parameters that depend on f , ϵ^T and particle size. Experiments performed on PSZ and TZP (Chen and Reyes-Morel 1988), are consistent with this transformation condition. However, knowledge of the nucleation is not yet sufficient to allow Ω and τ to be expressed explicitly in terms of these variables.

The preceding constitutive laws provide the basis for determining crack tip fields and hence, for predicting trends in transformation toughening, as discussed below.

4.2. Crack Tip Stress Fields

McMeeking and Evans (1982) pointed out that the general form of the crack tip stress field in the presence of a transformation zone, depicted in Fig. 4.4, is characterized by two stress intensity factors. Outside the zone, for small scale transformation (i.e., a small zone compared with crack length and specimen dimensions), the field is given by the linear elastic solution ($h < r \leq a$)

$$\sigma_{ij} = (K_\infty / \sqrt{2\pi r}) \delta_{ij} \quad (4.4)$$

where K_∞ is the stress intensity determined by the applied loads and r is the distance from the crack tip. Close to the tip, the transformation strain is saturated and hence, the material is again linear and can, consequently, be characterized by another stress intensity factor K_{tip} , such that

$$\sigma_{ij} = (K_{tip} / \sqrt{2\pi r}) \delta_{ij} \quad (4.5)$$

The coefficient, σ_{ij}^T , which depends on polar angle, approaches that for elastic materials when $\tilde{\epsilon}^T E / \sigma_u'$ is small.

The transformation may thus be characterized by a stress intensity change ΔK , defined as

$$\Delta K = K_{tip} - K_\infty \quad (4.6)$$

When $K_{tip} < K_\infty$, the transformation zone shields the tip from the applied loads. The fracture behavior is governed by the values of K_{tip} and K_∞ at the fracture criticality. Knowledge of the stress in the intervening regions is not required for analysis of the toughening (Budiansky et al. 1983). Specifically, the near tip field provides a plausible crack extension criterion

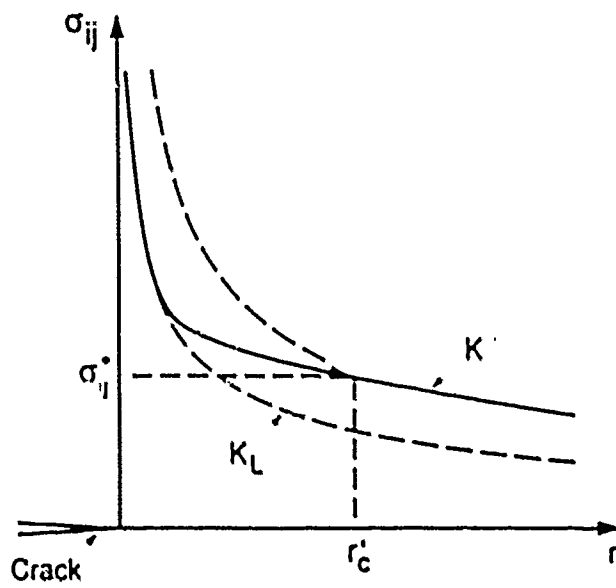


Fig. 4.4 Crack tip stress fields in the presence of a dilatational transformation zone for a supercritical transformation.

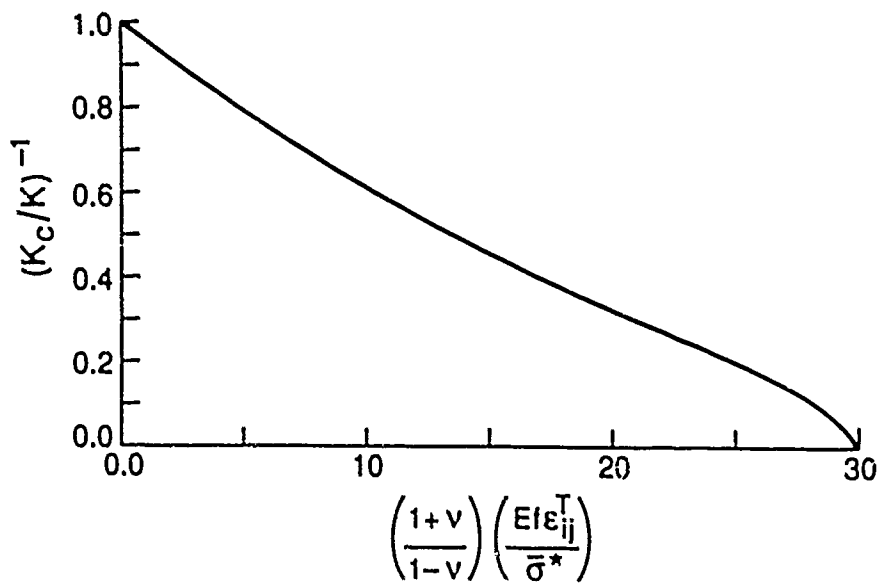


Fig. 4.5 Change in normalized toughness as a function of normalized transformation strain.

$$K_{tip} = K_A \quad (4.7)$$

where K_A is the fracture resistance of the material in the transformation zone immediately ahead of the crack tip; whereupon, the observed toughness is

$$K_c = K_0 + \Delta K_c \quad (4.8)$$

where ΔK_c is the quantity $-\Delta K$, evaluated at the fracture criticality.

4.3. Toughening Models

There are two equivalent analytical methods for determining trends in toughness: one based on stress intensity factors and the other with conservation integrals. Both approaches predict the same behaviors, but have different utility when various aspects of toughening require elucidation. Consequently, both approaches are briefly described.

1) Stress Intensity Factors

The magnitude of ΔK clearly depends on the shape of the zone and on the components of the transformation strain tensor. Initially, it is pertinent to consider a crack in an untransformed parent, such that a frontal zone develops as the load is imposed. Subsequently, a steady-state zone of uniform width over the crack surfaces (Fig. 4.1) is examined. McMeeking and Evans (1982) have shown that the ΔK levels are different for these two zone configurations, resulting in R-curve effects.

Frontal zone. When the long-range strain field of the transformed particles is purely dilatational (i.e., an extensively twinned particle with uniform twins and thereby, no long-range shear strain), the mean stress may dictate the shape of the transformation zone, which then has the shape depicted in Fig. 4.1. For this condition, $\Delta K = 0$. However, zone shape effects may be important when the zone deviates, for some reason, from the simple dilatational shape. Such effects might arise because transformed dilatant regions ahead of the crack $\theta < \pi/3$ provide deleterious, positive ΔK contributions ($K_{tip} > K_\infty$), whereas those regions at $\theta > \pi/3$ provide negative contributions. Consequently, if, for example, the zone profile were determined solely by the deviatoric stresses, $\Delta K < 0$ and appreciable toughening would exist. Such effects might arise when transformation occurs by an autocatalytic process, in the form of shear bands emanating from the crack tip (Lambropoulos 1986).

Steady-state zone. The calculation of ΔK for the steady-state configuration is, again, most straightforward for the purely dilatational transformation. For this case, when the transformation does not reverse in the wake and when all particles within h are transformed, the plane strain zone width for small-scale transformation is

$$h = \frac{\sqrt{3}(1+\nu)^2}{12\pi} \left(\frac{K_\infty}{\sigma_c} \right)^2 \quad (4.9)$$

(McMeeking and Evans 1982, Budiansky et al. 1983). The corresponding extent of crack shielding is given by Eqn. (4.2),

$$\Delta K = -0.22E/\epsilon_u^T \sqrt{h}/(1-\nu). \quad (4.10)$$

The supercritical plane strain toughness can thus be expressed in the following forms

$$\Delta K_c = 0.22E/\epsilon_u^T \sqrt{h}/(1-\nu)$$

or

$$\Delta K_c / K_c = (\sqrt{3}/12\pi)(1+\nu)E/\epsilon_h^T/\delta^c(1-\nu) \quad (4.11)$$

or

$$K_c/K_0 = [1 - (\sqrt{3}/12\pi)(1+\nu)E/\epsilon_h^T/\delta^c(1-\nu)]^{-1} \quad (4.12)$$

If the transformation is not activated by the hydrostatic crack tip field, but instead occurs in shear bands, inclined at $\pm \pi/3$ to the crack plane ($\Omega > \tau$ in Eqn. 4.3), all of the deleterious transformations in front of the crack are excluded. As shown by Evans and Cannon (1986), the supercritical ΔK_c then increases to

$$\Delta K_c = 0.38 E/\epsilon_h^T \sqrt{h}/(1-\nu). \quad (4.13)$$

Zone profile considerations are thus of prime importance in determining the magnitude of the transformation toughening. For conditions of plane stress, the zone width is predicted to be smaller, causing the toughness to diminish.

When the transformation zone is not small, the zone width is affected by the previously transformed material and Eqn. (4.9) does not apply. In this case, a numerical solution has revealed the trend in toughening ratio K_c/K_0 with $E/\epsilon_h^T/\delta^c$ depicted in Fig. 4.5. In particular, it is noted that "lock-up" occurs ($K_c \rightarrow \infty$) when $E/\epsilon_h^T/\delta^c = 30$. This phenomenon, first recognized by Rose (1986) has been elaborated by Amazigo and Budiansky (1989).

ii) Conservation Integrals

For the frontal zone, the volume elements within the zone do not experience unloading. Consequently, the path-independent J-integral applies and the relation

$$J = (1-\nu^2)K^2/E \quad (4.14)$$

pertains for all line contours around the crack tip. Furthermore, since the elastic properties of the transformed and untransformed materials are essentially the same, contours around the tip (giving K_{tip}) and remote from the tip (giving K_∞) yield identical values of K : whereupon $K_{tip} = K_\infty$.

Conversely when a fully developed zone exists (Fig. 4.1), the material within the zone, behind the crack tip, has experienced unloading and a path independent J does not apply. In this case, the appropriate conservation integral, I, has the same form as J at the tip

$$I = (1-\nu^2)K_{tip}^2/E \quad (4.15)$$

but remote from the tip

$$I = (1-\nu^2)K_\infty^2/E - 2 \int_0^h U(y) dy \quad (4.16)$$

where $U(y)$ is the residual energy density in the wake. Equating the magnitude of the conservation integral for the near-tip and remote paths gives

$$K_{II}^2 = K_{IIp}^2 + [2E/(1-\nu^2)] \int_0^y U(y) dy \quad (4.17)$$

or

$$\Delta \mathcal{G}_c = 2 \int_0^y U(y) dy \quad (4.18)$$

The integral in $U(y)$ can be simply related to the elemental stress-strain curve (Fig. 4.2). Specifically, material in the process zone undergoes a complete loading and unloading cycle as the element translates from the front to the rear of the crack tip during crack advance. Hence, each element in the wake is subject to the residual stress work contained by the hysteresis loop (Fig. 4.2). Consequently, by appreciating that the wake is subject to a residual compression the residual energy density can be readily evaluated as (Budiansky et al. 1983),

$$U(y) = \delta^2 \epsilon_H^T / 2 + \frac{B^* (\epsilon_H^T / f)^2}{2(1 - B^*/B)} + \frac{E (\epsilon_H^T / f)^2}{9(1-\nu)} \quad (4.19)$$

where B^* is the slope of the stress-strain curve of the transforming material. The three terms in Eqn. (4.18) derive from the areas I, II and III under the stress-strain curve depicted in Fig. 4.2. The latter two terms cancel when

$$\begin{aligned} B^* &\approx -2E/3(1+\nu) \\ &= -4G/3 \end{aligned} \quad (4.20)$$

and Eqn. (4.18) for the toughening is then identical to Eqn. (4.1). This condition for B^* has been determined to coincide with the supercritical condition (Budiansky et al. 1983).

iii) Sub-critical Transformations

The preceding discussion has referred exclusively to supercritical transformations, wherein all particles within the zone transform. Such behavior is only observed in PSZ. More generally, subcritical transformation occurs, whereupon only a fraction of the phase transforms. Sub-critical transformations are characterized by a transformation slope $B^* > -4G/3$. Some typical results determined numerically for the dilatational transformation are plotted in Fig. 4.6 (Budiansky et al. 1983). In these instances, the overall transformation mechanism is important, in the sense that the shape of the stress-strain curve is dictated by the nucleation, growth and twinning characteristics of the martensite.

Alternatively, sub-critical toughening can be characterized in terms of the distribution of transformed particles $f(y)$ as a function of the distance y from the crack plane. This formulation is particularly useful because $f(y)$ can be determined experimentally (Rühle et al. 1984). The solutions can be straightforwardly evaluated from the supercritical transformation solutions by considering the contribution to ΔK from each part of the distribution (McMeeking and Evans 1982).

iv) Resistance Curves

Resistance curve behavior is inevitable in transformation toughened materials, because initial crack growth is largely unaffected by transformations produced by the stationary crack. The slope of the resistance curve (the tearing modulus) is governed by the current geometry of the zone, which depends on zone evolution (Charalambides and

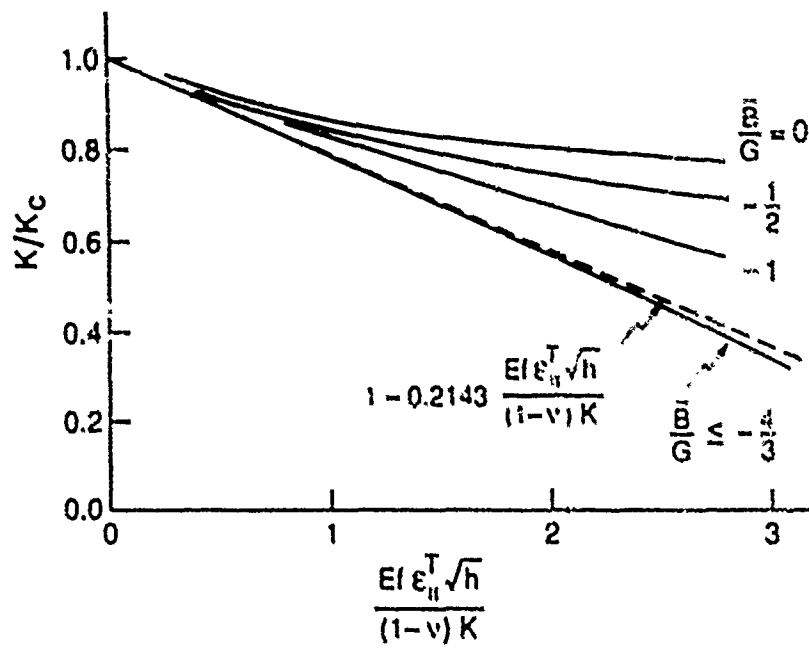


Fig. 4.6 Ratio of near-tip to remote stress intensity factor. The dashed line is the asymptotic result for small ϵ_h^T . The curves for sub-critically transforming materials were calculated with $\nu = 0.3$.

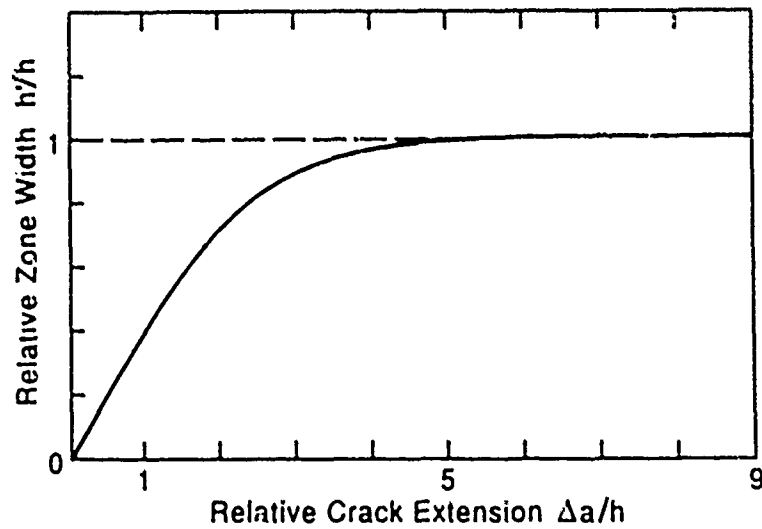


Fig. 4.7 The dependence of relative zone width on relative crack extension.

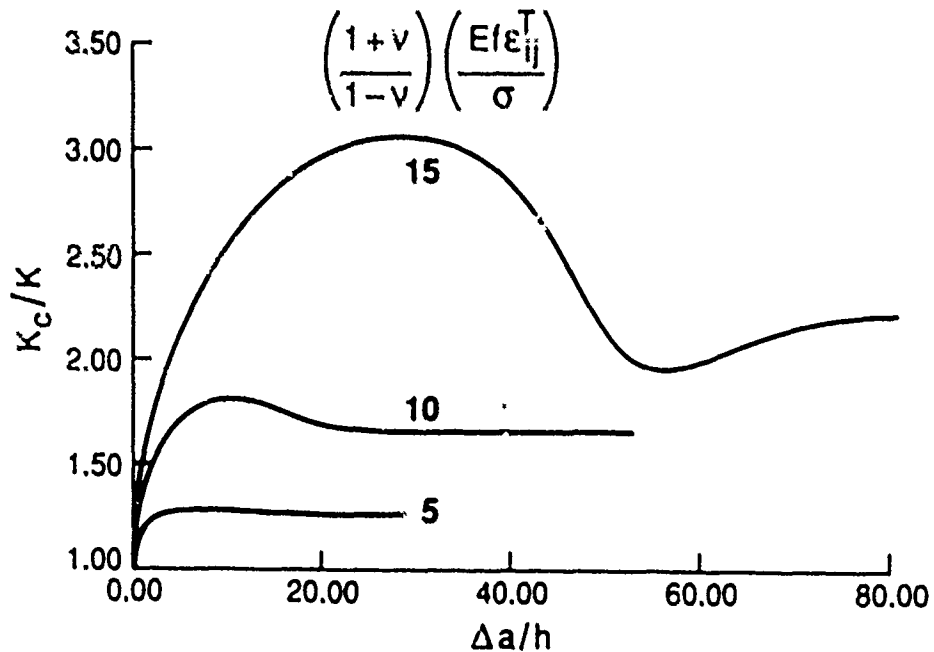


Fig. 4.8 Theoretically predicted ratio of (relative) toughness to crack extension.

McMeeking 1987, Budiansky 1989). Consequently, toughening curves can only be calculated by applying incremental crack growth methods. Such analysis reveals that the zone initially widens as the crack extends and eventually reaches a steady-state crack width (Fig. 4.7). The actual zone morphology and thus, the shape of the resistance curve, depend on the transformation criterion and on the flow rule. Calculations based on a dilatational law indicate a large tearing modulus and a peak prior to steady-state (Fig. 4.8) (Stump and Budiansky 1989). The peak is most pronounced for supercritical condition when the zone height is large. The existence of the peak is not physically obvious but may be rationalized by appreciating that the rising resistance curve and the steady-state resistance have a separate dependence on the frontal zone shape evolution and are thus not uniquely connected. The occurrence of a peak fracture resistance coincides with a peak in zone height. Such zone height peaks have been observed by experiment (Marshall et al. 1989).

The resistance curves are also dependent on the length of the crack, resulting in *short crack effects* which influence trends in strength (Stump and Budiansky 1989). For crack lengths in the range $a \lesssim 5h$, interaction between the zones at the opposite crack tips reduces the zone shielding.

McMeeking 1987, Budiansky 1989). Consequently, toughening curves can only be calculated by applying incremental crack growth methods. Such analysis reveals that the zone initially widens as the crack extends and eventually reaches a steady-state crack width (Fig. 4.7). The actual zone morphology and thus, the shape of the resistance curve, depend on the transformation criterion and on the flow rule. Calculations based on a dilatational law indicate a large tearing modulus and a peak prior to steady-state (Fig. 4.8) (Stump and Budiansky 1989). The peak is most pronounced for supercritical condition when the zone height is large. The existence of the peak is not physically obvious but may be rationalized by appreciating that the rising resistance curve and the steady-state resistance have a separate dependence on the frontal zone shape evolution and are thus not uniquely connected. The occurrence of a peak fracture resistance coincides with a peak in zone height. Such zone height peaks have been observed by experiment (Marshall et al. 1989).

The resistance curves are also dependent on the length of the crack, resulting in *short crack effects* which influence trends in strength (Stump and Budiansky 1989). For crack lengths in the range $a \approx 5h$, interaction between the zones at the opposite crack tips reduces the zone shielding. The corresponding variations in strength are revealed in Fig. 4.9.

5. MICROCRACK TOUGHENING

Buresch (1975), Hoagland et al. (1975) and Evans (1976) postulated the phenomenon of microcrack toughening more than a decade ago and indeed, a range of materials exhibit trends in toughness with particle size, temperature etc., qualitatively consistent with this mechanism. However, as yet there is only one fully validated example of this mechanism: Al_2O_3 toughened with monoclinic ZrO_2 (Rühle et al. 1986, 1987b). This material is discussed in Section 5.3. The fundamental premise concerning the mechanism is depicted in Fig. 5.1. Microcracks occur within regions of local residual tension, caused by thermal expansion mismatch and/or by transformation (Evans and Faber 1984, Hutchinson 1987). The microcracks locally relieve the residual tension and thus cause a dilatation governed by the volume displaced by the microcrack. Furthermore, the microcracks reduce the elastic modulus within the microcrack process zone. Consequently, the elemental stress-strain curve for a microcracking solid has the form depicted in Fig. 5.1. The hysteresis dictated by this curve, when the microcracks are activated by the passage of a macrocrack, contributes to the change in toughness, as elaborated below. However, this contribution is partially counteracted by a degradation of the material ahead of the microcrack. The full extent of the degradation is presently unknown.

The crack shielding can be conveniently separated into dilatational and modulus contributions. The former depends on the process zone size and shape, while the latter depends only on the zone shape. The *dilatational contribution* has essentially the same form as Eqn. (4.2). Hutchinson (1987) showed that for asymptotic supercritical conditions,

$$\Delta K_c = 0.32 E \theta_T \sqrt{h} \quad (5.1)$$

where θ_T is now the misfit strain caused by microcracks (analogous to $f c_u^T$ in Eqn. 4.2). Following Hutchinson (1987) the asymptotic modulus contribution is

$$(1 - \nu) \Delta K_c / K_c = (k_1 - \frac{1}{2})(G/\bar{G} - 1) + (k_2 + \frac{1}{2})(\bar{\nu} G/\bar{G} - \nu) \quad (5.2)$$

where k_1 and k_2 depend on the microcracking criterion. In general, the ΔK_c due to dilatation and modulus effects are not additive: interaction terms are involved.

Comparison between theory and experiment has been made for the $\text{Al}_2\text{O}_3/\text{ZrO}_2$ system (see Sect. 5.4). For this case, the contributions to toughening from the dilatation and the modulus are evaluated as ~ 2.5 and $5 \text{ MPa}\sqrt{\text{m}}$

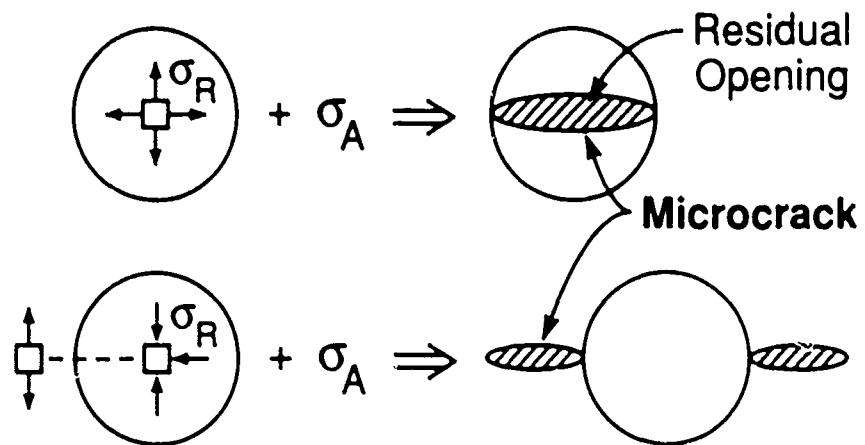
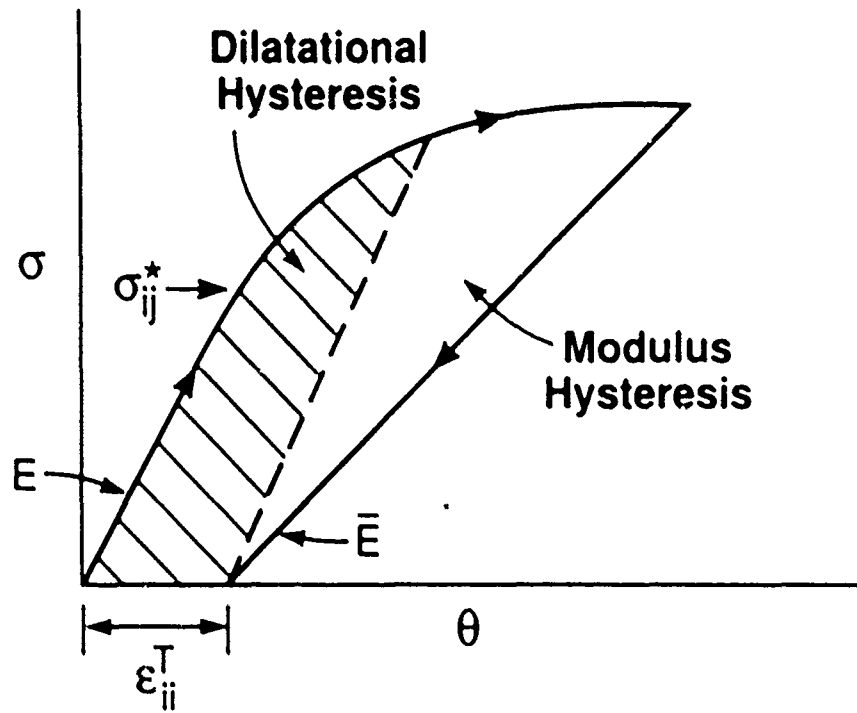


Fig. 5.1 The basic concepts of microcrack toughening.

respectively, compared with a measured composite toughness of $\sim 6 \text{ MPa}\sqrt{\text{m}}$. While this comparison is reasonable and appears to validate microcracking as the prevalent toughening mechanism, it is emphasized that present understanding of microcrack toughening is incomplete. In particular, interaction effects between the modulus and dilatational contribution as well as near-tip degradation effects, require further investigation. Furthermore, because of the experimental difficulty involved in detecting microcracks,* the incidence of microcrack toughening in other ceramic systems is doubted.

One potentially detrimental feature of microcrack toughening is the incidence of thermal microcracks at the largest particles in the distribution (Rühle et al. 1987b). Such cracks can be strength limiting, resulting in material that is relatively tough, but has only moderate strength. Avoidance of such strength limiting cracks requires stringent control of the size distribution of the reinforcing particles, just beneath the critical size for thermal microcracking.

5.1. Constitutive Laws

The reduction in elastic moduli caused by microcracks, as well as the permanent strain governed by release of the residual stress, depend upon microstructure. Characteristic constitutive laws are illustrated for two important cases consisting of spherical particles subject to either residual tension or residual compression. For the former case, the microcracks occur within the particle, while for the latter, the matrix develops microcracks (Fig. 5.1). Results for these cases have been derived for materials having homogeneous elastic properties prior to microcracking. For particles subject to residual tension in which penny-shaped microcracks forms (Fig. 5.1), the volume of each opened microcrack is (Hutchinson 1987)

$$\Delta V = (16R^3/3)(1-\nu^2)\sigma_u^2/E \quad (5.3)$$

(Hutchinson 1987, Evans and Cannon 1986) where

$$\sigma_u^2 = 2E\epsilon_u^T/9(1-\nu) \quad (5.4)$$

R is the particle radius and ϵ_u^T is the misfit strain between particle and matrix. This volume increase dictates the permanent strain, such that the *microcrack misfit strain* becomes

$$\theta_T = (16/3)(1-\nu^2)\eta\sigma_u^2/E \quad (5.5)$$

where $\eta = N(R^3)$ is the number density of microcracked particles, with N being the number of microcracked particles per unit volume. Solutions for the elastic moduli of microcracked bodies establish the modulus effect (Hutchinson 1987),

$$\begin{aligned} G/\bar{G} &= 1 + (32/45)(1-\nu)(5-\nu)\eta/(1-\nu) \\ B/\bar{B} &= 1 + (16/9)(1-\nu^2)\eta/(1-2\nu) \end{aligned} \quad (5.6)$$

where the bar refers to microcracked material. Based on the above characteristics, Hutchinson (1987) showed that the constitutive law has the form

*Typical residual crack openings are $< 2\text{nm}$.

$$\epsilon_{ij} = \frac{1+\bar{\nu}}{E} \sigma_{ij} - \frac{\bar{\nu}}{E} \sigma_{\lambda\lambda} \delta_{ij} + (\theta_T/3) \delta_{ij}, \quad (5.7)$$

For particles in residual compression, the corresponding constitutive law depends sensitively on the response of the interface to the microcrack. For the one material studied thus far ($\text{Al}_2\text{O}_3/\text{ZrO}_2$), some debonding occurs at the interface (Fig. 5.1) and the basic parameters derived for the microcracks are:

$$\theta_T = 3.6(u_R/R) \eta/\xi^2 \quad (5.8)$$

where u_R is the residual microcrack opening of the interface, as affected by the debond length, d and

$$\xi = c/R$$

where c is the microcrack length (Fig. 5.1). The above results may be used in conjunction with Eqn. (5.1) and (5.2) to predict toughening, as discussed below.

5.2. Toughening Models

The crack tip fields and the stress intensity factors for microcracked materials have the same general form described above for transformations. However, for microcracking, it is expedient to separate the contributions to K_{IIp} from the modulus reduction and from the residual strain (Evans and Faber 1984, Hutchinson 1987). These contributions are additive when $\Delta K_{IIp}/K$ is small. Otherwise, interaction effects are involved and specific solutions must be obtained numerically (Charalambides and McMeeking 1987).

The contribution to K_{IIp} from the residual field has precisely taken the same form as that associated with transformations, but with $f \epsilon_{ij}^T$ replaced by θ_T . This contribution thus depends on zone size and shape, as in the case of transformation toughening. For example, when the microcrack nucleation condition involves a critical normal stress, the steady-state shielding is,

$$\Delta K_{IIp} = -0.40E \theta_T \sqrt{h} \quad (5.9a)$$

while for a critical mean stress,

$$\Delta K_{IIp} = -0.32E \theta_T \sqrt{h} \quad (5.9b)$$

(Hutchinson 1987). By contrast, the toughening imparted by the modulus reduction *depends on zone shape, but not on zone size*. The size independence arises because the "inelastic" strain caused by the modulus reduction is itself governed by the distance from the crack tip. Values of $\Delta K_{IIp}/K$ can be obtained by simply inserting G/\bar{G} and $\bar{\nu}$ into Eqn. (5.2). Typical results for the steady-state shielding are, for a critical normal stress and penny-shaped microcracks

$$\Delta K_{IIp}/K = -1.42\eta \quad (5.10)$$

Resistance curves in microcracking materials also have many of the same features as in transformation toughening, with the difference that the modulus contribution has a weak influence on the tearing modulus. Numerical simulations of resistance curves are summarized in Fig. 5.2.

MICROCRACK WAKE - ZONES

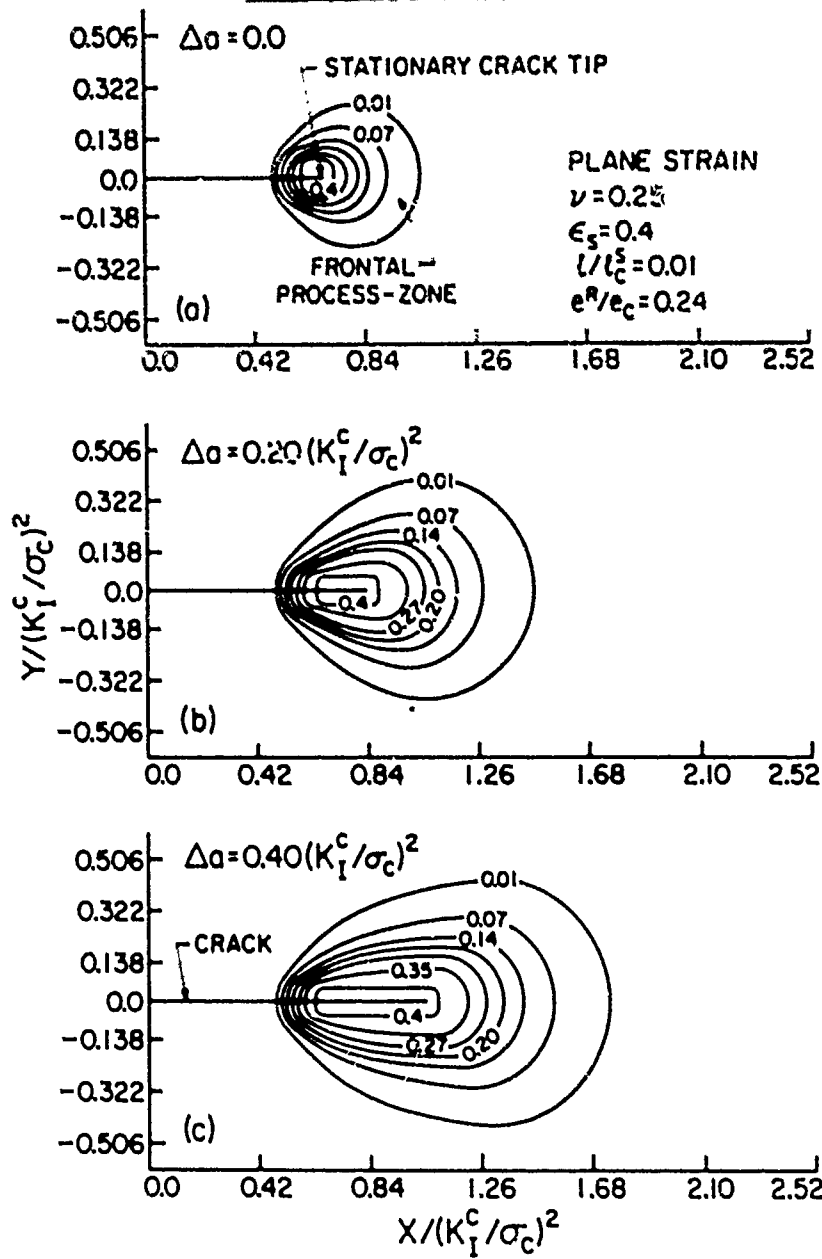


Fig. 5.2 Numerical simulations for resistance curves for microcracked material.

5.3. Experimental Results

Ruhle et al. (1987b) performed microstructural and microcracking studies on various ZTA materials wherein the proportion of ZrO_2 thermally transformed to the monoclinic phase was varied between 14 and 77% (Fig. 5.3). Transmission electron microscopy (TEM) studies revealed that in these materials all ZrO_2 particles and Al_2O_3 grains are faceted, that the ZrO_2 particles are intercrystalline and that grain boundaries and interface boundaries were circumvented by an amorphous layer (Clarke 1979). The size distribution of the grains and particles have been measured in foils up to $0.3\mu\text{m}$ in thickness with the radii separated into different nonlinear size groups using the volume fraction per size group as the ordinate (Fig. 5.4). ZrO_2 particles with radii $b_p > 0.3\mu\text{m}$ were found to be monoclinic and contained twin lamellae.

Small interfacial microcracks were usually observed between monoclinic ZrO_2 particles and the Al_2O_3 matrix grains in those regions where the twin planes of m- ZrO_2 terminated (Fig. 5.5). Occasional, thermally induced microcracks were also detected, remote from the macrocrack (Fig. 5.6). These were invariably associated with larger monoclinic ZrO_2 particles – the largest having a diameter of $\sim 7\mu\text{m}$. These cracks dominate the strength, resulting in strengths less than those apparent in the predominantly tetragonal material (Fig. 5.3).

Matrix microcracking caused by the growth of macrocracks was studied by preparing thin foils at four distances, y , from a macrocrack (0.5, 1.5, 3 and $6\mu\text{m}$). Radial matrix microcracks were observed, as exemplified in Fig. 5.7. All such radial microcracks occurred along grain boundaries in the Al_2O_3 . Usually, the interface between the Al_2O_3 and ZrO_2 was debonded at the origin of the microcrack (Fig. 5.8). The detectability of radial microcracks depended on their inclination with respect to the incoming electron beam. Trends in the visibility of microcracks upon tilting around one axis (Fig. 5.9) indicated that tilting in all directions would be needed to detect each microcrack present in the foil. However, tilting in the TEM is limited to $\pm 45^\circ$ in all directions, so that only 0.3 of the solid angle is covered. Therefore, the fraction of detectable microcracks is limited to ~ 0.3 .

Subject to this detectability limitation, large regions of TEM foils of known thickness have been investigated. One example is shown in Fig. 5.10, wherein all microcracks observable under different tilting conditions are marked. It is noted, on average, that at least two microcracks emanate from each m- ZrO_2 particle. In most cases, the microcracks terminate at the Al_2O_3 grain triple junctions. The associated projected length, l , of each microcrack has been measured and related to the radius, b , of the originating monoclinic ZrO_2 particle (Fig. 5.11). Additionally, the residual opening of the microcracks, δ has been determined at the ZrO_2 particle intersection, where the opening is usually largest (Fig. 5.12).

The utility of microcrack length measurements is facilitated by defining a representative geometry and determining the related microcrack density parameter, introduced by Budiansky and O'Connell (1976):

$$c = N\langle c^3 \rangle \quad (5.10)$$

where N is the number of microcracks per unit volume and c is the relevant microcrack dimension. Evaluation of the microcrack profiles observed by tilting suggests that each ZrO_2 particle is circumvented by a radial microcrack (Fig. 5.13a), consistent with the symmetry of the residual strain field around each particle. The model depicted in Figs. 5.13b and 5.13c has thus been used for further analysis.

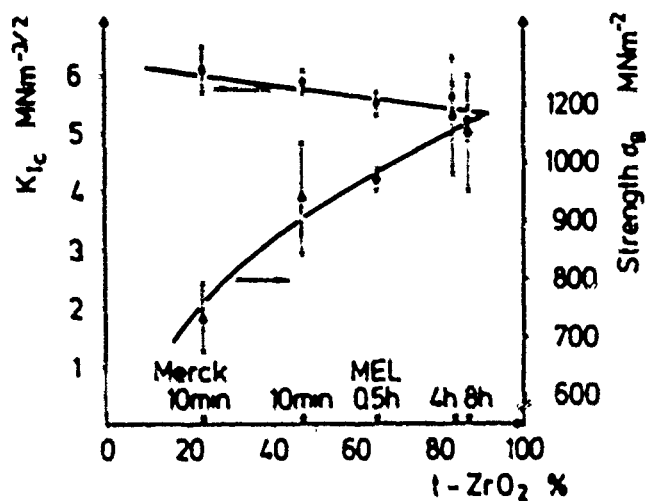


Fig. 5.3 Trends in the strength and toughness of ZTA with relative tetragonal content for a 1.5 volume % ZrO₂ material.

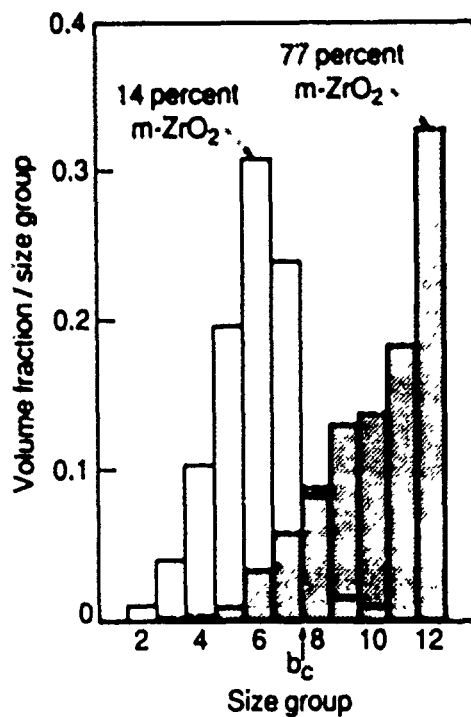


Fig. 5.4 ZrO₂ particle size distribution for the materials having 14% and 77% of the ZrO₂ in the monoclinic form. The size groups are defined in Table 1. All particles larger than b_c are monoclinic.



Fig. 5.5 Three examples of microcracks observed at twin terminations in the $\text{Al}_2\text{O}_3/\text{ZrO}_2$ interface.

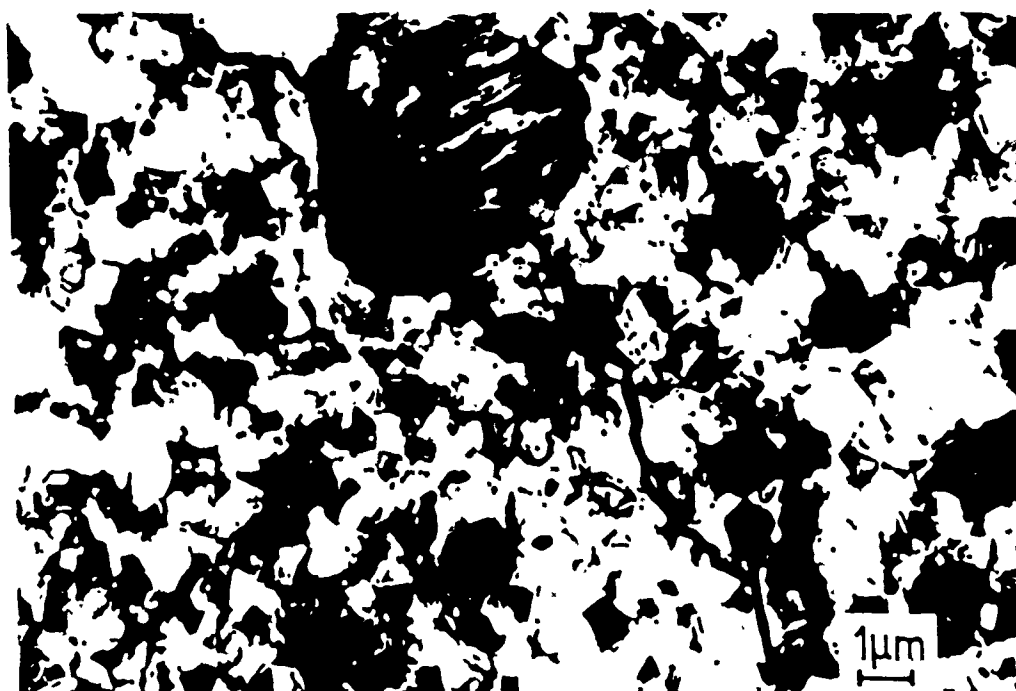


Fig. 5.6 A TEM revealing a thermally induced microcrack at a large thermally transformed monoclinic ZrO_2 particle.



Fig. 5.7 A TEM micrograph revealing a typical microcrack in the process zone.



Fig. 5.8 A TEM micrograph showing the debonding of the interface near a microcrack.

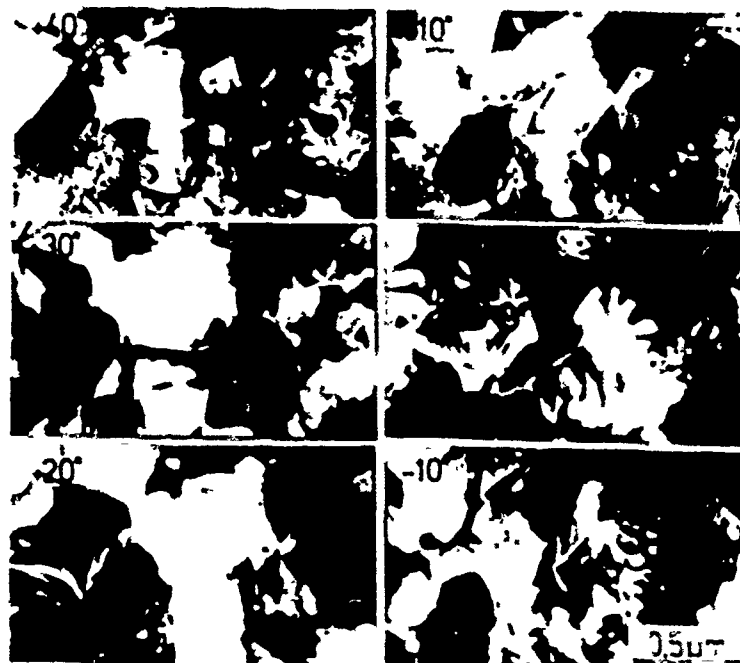


Fig. 5.9 A tilting sequence indicating the technique used to trace microcracks.

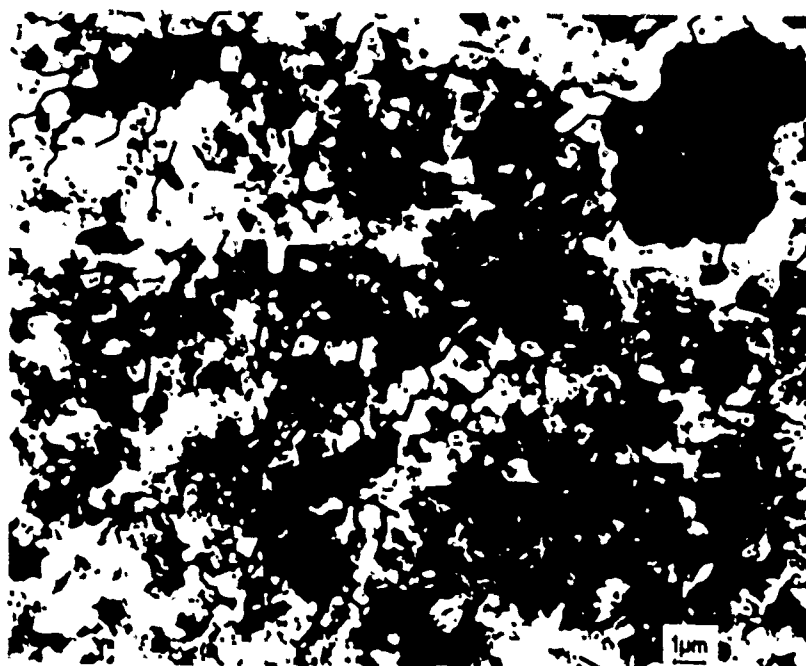


Fig. 5.10 A TEM micrograph with all observable microcracks marked.

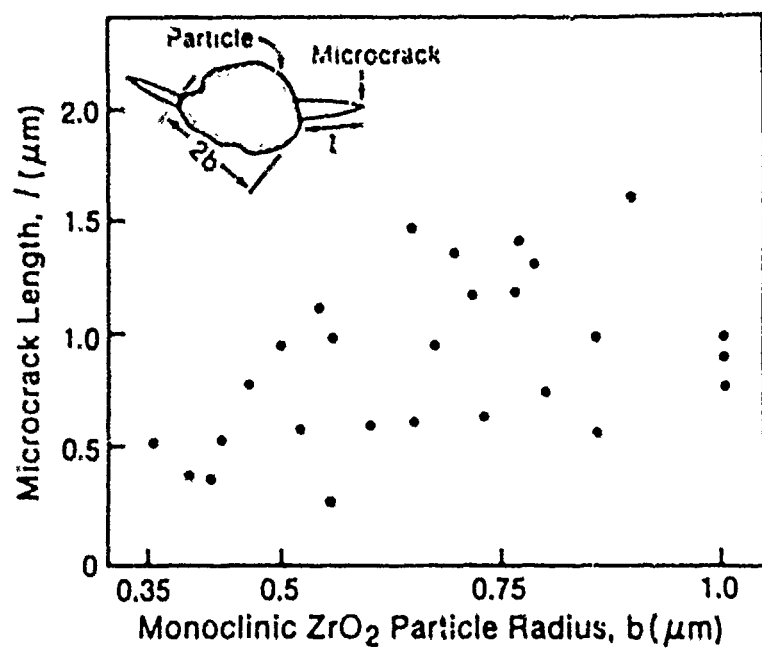


Fig. 5.11 Trends in microcrack length, l , with the effective radius, b , of the associated monoclinic ZrO_2 particles.

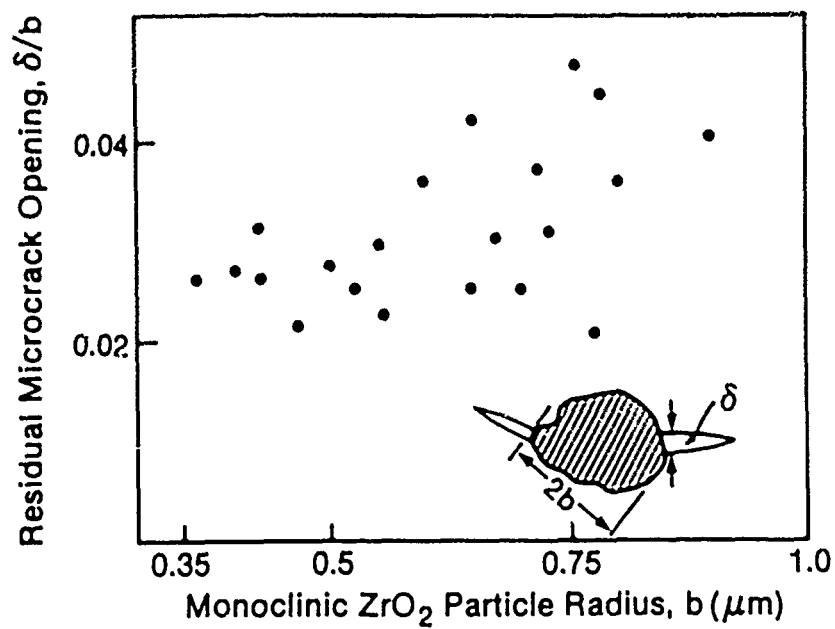
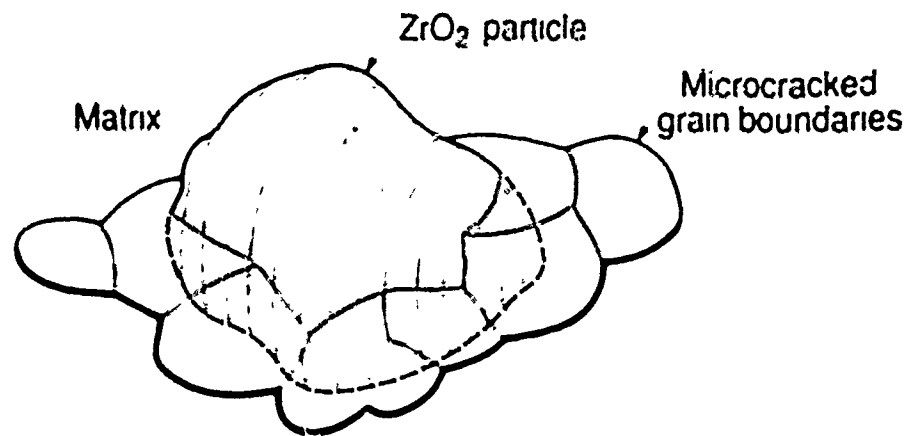
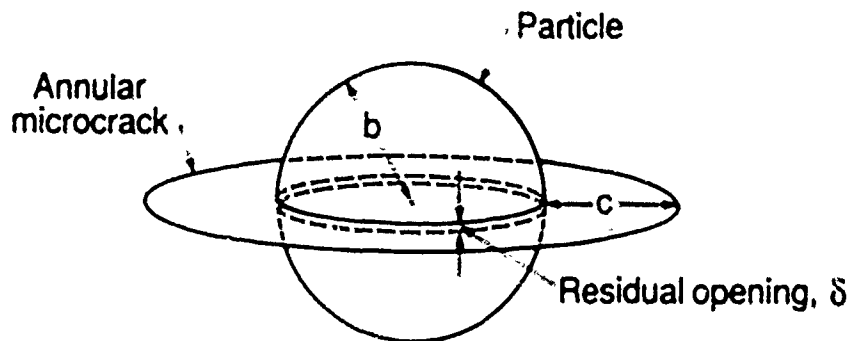


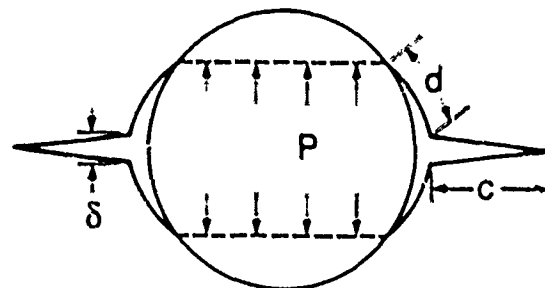
Fig. 5.12 Trends in residual crack opening with particle size.



a. Suggested microcrack configuration



b. Microcrack model



c. Micro mechanics model

Fig. 5.13 The microcrack model used to measure crack densities and to analyze the changes in crack volume and elastic modulus: a) a schematic drawing of a typical configuration b) the microcrack model used for analysis c) the mechanics model.

An example of the frequency distribution, $f(l)dl$, of projected microcrack lengths, measured on a series of TEM foils from the material containing 77% m-ZrO₂ is plotted in Fig. 5.14. The microcrack density may be evaluated from such a frequency distribution by using a procedure devised by Budiansky and O'Connell (1976),

$$\epsilon = (6/\pi) \int_0^\infty l^2 f(l) dl / q \quad (5.11)$$

where q is the fraction of microcracks detected. The results obtained are plotted in Fig. 5.15, recalling that two traces constitute one annular crack (Fig. 5.13).

Several features are evident from Fig. 5.15. The microcrack density diminishes with distance from the crack plane. A maximum density ϵ_s adjacent to the crack surface suggests a saturation value, governed by the total ZrO₂ particle content. The decrease with distance y is approximately linear, such that

$$\epsilon = \epsilon_s (1 - y/h) \quad (5.12)$$

where h is the process zone width.

The residual strain contribution to the shielding is (Rühle et al. 1987b),

$$\Delta K_d = \left[(2/3) \frac{(1+\nu)}{1-\nu} (\delta/b) g(\xi) \right] G \epsilon_s \sqrt{h} \quad (5.13)$$

where $g(\xi) = 3.6\xi^{-2}$. The appropriate values of the parameters in Eqn. (5.13) are: $\xi = 1.4$, $\delta/b = 0.03$, $G = 150\text{GPa}$, $\epsilon_s = 0.15$. Consequently, for the material containing 77% m-ZrO₂ ($h = 7\mu\text{m}$), the residual strain reduced shielding is, $\Delta K_d = 2.5 \pm 1\text{MPa}\sqrt{\text{m}}$. The modulus reduced shielding depends only on K for the composite and on ϵ_s . With $\epsilon_s = 0.15$ and $\xi = 1.4$, G/G_0 is obtained from Eqn. (5.5) as 0.4. Then with $K = K_c = 6\text{MPa}\sqrt{\text{m}}$ (Fig. 5.1), the modulus shielding is obtained from (Eqn. 5.3) as $\Delta K_m = 2.5 \pm 2\text{MPa}\sqrt{\text{m}}$. Simple addition of the dilatational and modulus contributions would indicate toughening $\Delta K_c = 7.5\text{MPa}\sqrt{\text{m}}$, sufficient to account fully for the measured toughness $K_c = 6\text{MPa}\sqrt{\text{m}}$. It should be appreciated, however, that the individual contributions to the shielding are relatively large and additivity is not strictly valid. Interaction effects should be taken into account before more rigorous comparisons between theory and experiment are attempted.

It is of interest to note that, the modulus reduction and dilatational contributions to the shielding are similar in magnitude. This is important because, while the former contribution cannot be readily changed (being governed almost entirely by the saturation microcrack density, ϵ_s), the dilatational contribution may be enhanced by increasing both the process zone size and the microcrack density within the zone. This may be achieved by control of the m-ZrO₂ particle size distribution, through its influence on the nucleation of the microcracks.

A number of substantive problems exist in the analysis of microcrack toughening; both experimental and theoretical. Among the problems are a poor fundamental understanding of the degradation caused by the microcracks directly ahead of the crack front and limited knowledge of the interactions between modulus and dilatational contributions to crack shielding, as well as experimental microcrack detectability limitations in the TEM. These topics require further study before authoritative conclusions can be reached regarding toughening in ZTA and before predictions of toughening trends can be contemplated.

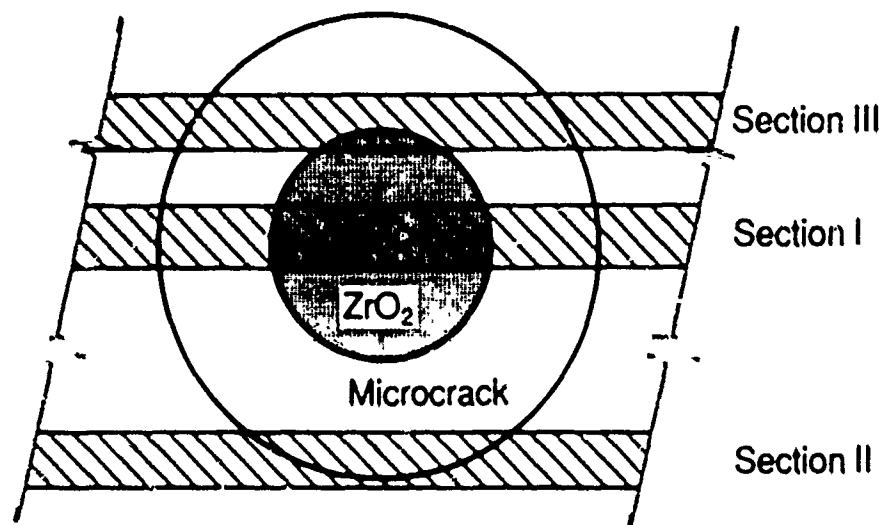


Fig. 5.14 The microcrack length distribution at four distances (0.5, 1.5, 3, and 6 μm) from the crack plane obtained on a material containing 77% initial m- ZrO_2 . Note the position insensitivity.

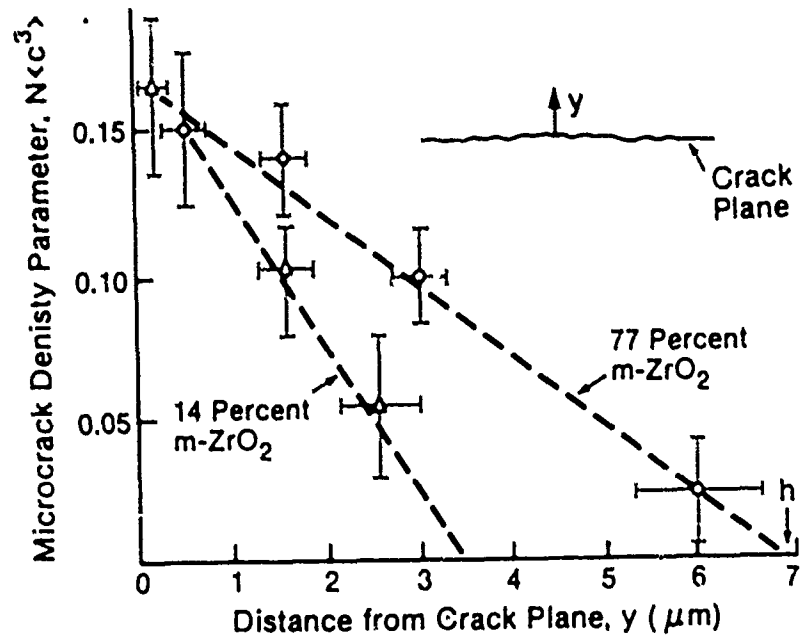


Fig. 5.15 Trends in the microcrack density parameter, $\epsilon = N \langle c^3 \rangle$, with distance y from the crack surface.

6. DUCTILE REINFORCEMENT TOUGHENING

6.1. Synopsis

Ductile reinforcements may profoundly increase the toughness. One contribution to the toughness derives from crack trapping (Rice 1988), another involves crack bridging (Krstic 1983, Sigl et al. 1988, Ashby et al. 1989, Budiansky et al. 1988) and yet another involves crack shielding and plastic dissipation associated within a plastic zone (Marshall et al. 1989). Experience and analysis have indicated that crack bridging is usually the most potent of these mechanisms: a result that can be appreciated by realizing that the only ductile regions which experience extensive plastic strain (much larger than elastic strains) are those segments that stretch between the crack surfaces in the bridging zone. The plastic dissipation in this zone can be relatively large and provide a major increase in toughness.

The material systems that exhibit plasticity induced toughening have three distinct microstructures: isolated ductile reinforcements, interpenetrating networks and a continuous ductile phase. The former is exemplified by ductile fibers (Hill and Groves 1972, Cooper and Kelly 1971, Gerberich 1971) by Nb alloy plates in TiAl (Cao et al. 1989) and, probably, by ferrite in the quasi-cleavage of steels (Hogland et al. 1972, Gerberich and Kurman 1985). An example of an interpenetrating network is Al alloy reinforced Al_2O_3 produced by the Lanxide method (Newkirk et al. 1986). The continuous ductile network case includes most metal matrix composites and, probably, cemented carbides (Sarin 1988). An important difference between the two former microstructures and the latter concern the potential for plastic strain in the composite outside the bridging ligaments. Plastic strain in the former is limited by elastic strains in the elastic network (Sigl et al. 1988) leading to bilinear stress/strain characteristics. Conversely, a composite with a continuous metal network is subject to non-linear power law deformation and can experience substantial plastic strain. Consequently, the potential for appreciable plastic dissipation within a plastic zone is much greater for the latter microstructure. Attendant differences in toughness optimization may thus exist.

The predictive design of microstructures having high toughness is still in the formative stages. Nevertheless, some important indications are unequivocally provided by the bridging models. Most importantly, debonding seems to be exceptionally beneficial. Additionally, small incoherent precipitates that induce hardening while maintaining good ductility are advantageous. Furthermore, large diameter reinforcements are superior. However, in practice, an optimum reinforcement radius is expected, because of the increased probability of having relatively large hard particles that limit ductility, as the radius increases. Limited experience indicates that this optimum size is in the range 10–100 μm , depending upon the ductility of the reinforcement.

6.2. Constitutive Laws

Understanding of the toughness generated by ductile ligaments is contingent upon the law that characterizes the stress/stretch relation, $t(u)$. Insights regarding the parameters that affect this relation can be gained from simplified analytical models. Complementary numerical solutions then allow determination of specific trends. Budiansky et al. (1988) and Rose (1987) analyzed small-scale bridging, in which bridge length is small in relation to crack length, specimen dimensions and distances from the crack to the specimen boundaries. The stress/stretch relation $t(u)$ depends strongly on the mode of failure of the ductile ligaments. A small-scale yielding analysis indicates that t should increase rapidly with *initial* crack opening. A large strain necking analysis then reveals that, without debonding, the stress attains high initial levels because of the elastic constraint of the matrix, but should decrease as the crack opens and furthermore, should depend sensitively on the work hardening rate. These simple results already provide the important insight that a peak stress exists at small crack openings, such that the plastic dissipation is dominated by the large strain (necking) regime (Figs. 6.2, 6.3). The importance of interface debonding thereby becomes apparent, because debonds reduce the constraint, but increase the plastic stretch prior to failure. Numerical solutions obtained with prescribed initial debonds

Fig. 6.1 Nondimensional stress vs. stretch behaviors and associated "work of rupture" χ

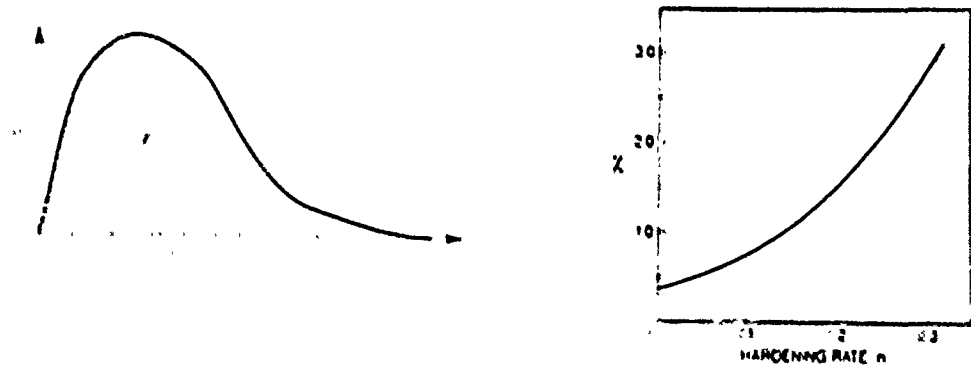


Fig. 6.2 Trend in χ with work hardening rate n without debonding

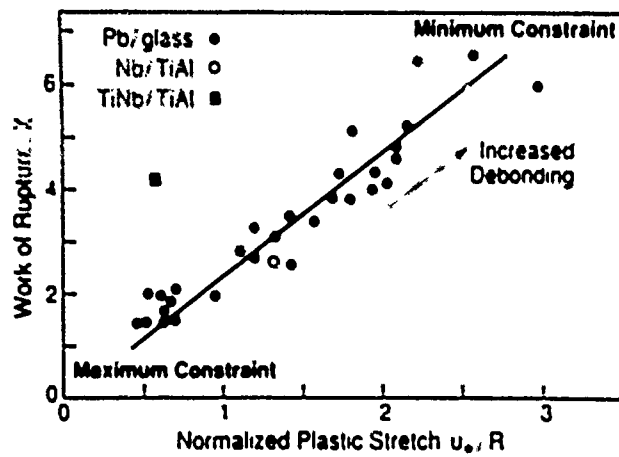


Fig. 6.3 The work of rupture as a function of plastic stretch measured for various ductile reinforcements

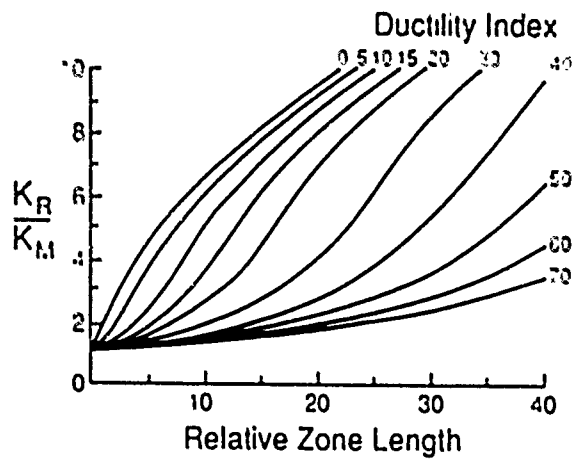


Fig. 6.4 Resistance curves calculated for bridging by non-hardening ductile ligaments

establish the salient trends (Fig. 6.3). Notably, in the important range $0 < d/R < 2$, the plastic dissipation increases systematically as d/R increases. Furthermore, if the debond evolves during crack opening, the dissipation is further enhanced. The above predictions are generally similar to experimental measurements, which confirm large stresses at small u and increased dissipation when debonding occurs.

6.3. Toughening

The toughness attributed to bridging, based on Eqn. (1.2), can be re-expressed in non-dimensional form by noting that the flow stress scales with the uniaxial yield strength, Y , and that the plastic stretch is proportional to the radius of cross section of the reinforcing ligaments, R ; consequently (Sigl et al. 1988, Ashby et al. 1989), the asymptotic toughness is,

$$\Delta \bar{W}_c / f Y R = \chi \quad (6.1)$$

where χ is a "work of rupture" parameter that depends on the critical plastic stretch u_c (or ductility) of the reinforcement and on the extent of interface debonding, d . Values of χ have been obtained both by calculation (Budiansky et al. 1988, Sigl et al. 1988, Mataga 1989) and by experiment (Ashby et al. 1989), based on determinations of the area under the stress/stretch curve for the reinforcing ligaments (Fig. 6.1). For a well-bonded interface ($d = 0$) and for ductile ligaments that fail by necking to a point, the resultant trend in χ with work hardening rate n (Fig. 6.2) indicates that χ is in the range 0.3 to 1. Less ductile ligaments that rupture prematurely by profuse hole nucleation have correspondingly smaller values of χ . Systems subject to debonding exhibit larger χ and approach 6 for debond length d of order $1-2R$. Experimental results have indicated that trends in χ with d are reflected in a plot of χ with relative plastic stretch u_c/R (Fig. 6.3).

The basic non-dimensional solution (Eqn. 6.1) can be used both to rationalize toughness measurements and to develop a predictive capability. For purposes of the former, Y and n can be inferred either from a TEM characterization of the microstructure (Flinn et al. 1989) or from microhardness measurements (Elliott et al. 1988), while f , R , u_c and d can be determined by quantitative SEM of the fracture surface. Estimates of the ductility can also be obtained from SEM measurements of the plastic stretch (Flinn et al. 1989). Such studies performed for composite systems in which ductile failure occurs by necking ($\text{Al}_2\text{O}_3/\text{Al}$ and TiAl/Nb) indicate acceptable agreement between theory and experiment.

The basic characteristics of steady-state toughening by ductile bridging are given by Eqn. (6.1) with the attendant implications for the strength and ductility of the reinforcement and the debonding tendencies of the interface discussed above. However, steady-state is preceded by a resistance curve. Calculations of resistance curves (Budiansky et al. 1988) for a Dugdale zone indicate trends (Fig. 6.4), but the predictions have not been verified. Simple analysis also reveals that the slope of the resistance curve diminishes as the debond length increases.

The contribution to toughness from plastic dissipation within a *plastic zone* is less well understood. Preliminary calculations of plastic dissipation (Sigl et al. 1988, Charalambides and Mataga 1989) establish that it is dominated by a narrow strip near the crack plane in which the plastic strains are large. The consequences are that the dissipation depends sensitively on those microstructural features that establish the cut-off distance. As yet, there is no clear understanding of the appropriate choice for this cut-off. This behavior is very different from transformation toughening, which is governed by the zone height, because the transformation strain is uniform and prescribed.

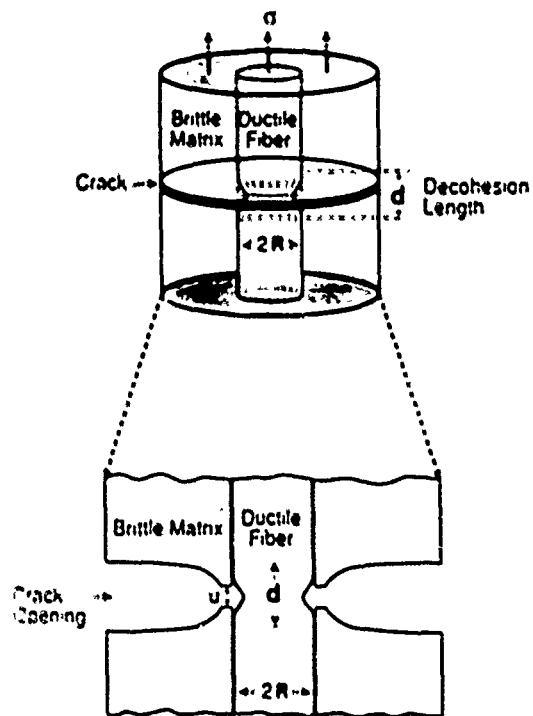


Fig. 6.5 The composite cylinder test specimen

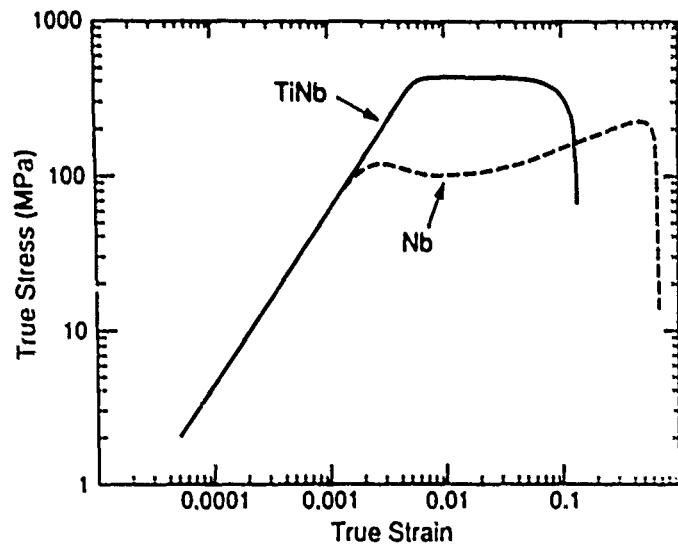


Fig. 6.6 True stress strain curves measured for the Nb and Ti-33at%Nb wires

6.4. Experimental Observations

While many brittle materials are toughened by a plastically deformable component, and while many experiments have been performed in an attempt to gain understanding about the toughening mechanisms (Viswanadham et al. 1983, Almond et al. 1986, Sarin 1988), controlled experiments have only recently been devised. The latter experimental observations, which lead to quantitative insight into mechanisms, are emphasized below.

6.4.1. Composite Cylinder Tests

A composite cylinder test specimen (Fig. 6.5) suitable for simulating toughening (Ashby et al. 1989) consists of a concentric cylinder with an outer brittle matrix bonded to a central ductile reinforcement. The specimen, after processing, is circumferentially notched and precracked up to the reinforcement. Precracking is straightforward for lead within a low toughness glass cylinder (Ashby et al. 1989), but more difficult for the relatively tough TiAl reinforced with Nb (Cao et al. 1989b). A key experimental variable is the notch geometry in the vicinity of the wire. Precracking is facilitated by a deep notch with a low flank angle which terminates close to the wire interface. However, in order to accurately simulate the behavior of the reinforcement in the actual composite, it is also important that the matrix maintain an appropriate degree of elastic constraint, which places limits on the notch width and the distance between the notch tip and the wire interface.

Tensile tests on the composite cylinders resulted in the stress/displacement curves depicted in Fig. 6.6 (Cao et al. 1989b). For TiAl specimens containing Nb reinforcements (Fig. 6.6), the "work of rupture" χ varied between 1.7 and 2.6 for different notch geometries. The difference is attributed to the incidence of a load drop during precracking which invalidates the test. The result without the load drop accords well with the work of rupture, plastic stretch relation ascertained for ductile Pb reinforcements in glass (Fig. 6.3).

The interfacial regions studied using a variety of analytical and electron microscopy techniques revealed no reaction products for glass/Pb. The variation in debonding is related to contamination and to process conditions. In the case of TiAl/Nb, a brittle reaction product forms (σ phase) which controls the debonding behavior at the interface and thereby governs the work of rupture χ .

6.4.2. Composites of Al_2O_3 reinforced with Al

Composites consisting of Al_2O_3 reinforced with an Al alloy network processed using the Lanxide method (Newkirk et al. 1986) investigated by TEM (Flinn et al. 1989), as well as by SEM of the fracture surface, revealed several salient features. Bright field views provided information on two important characteristics: precipitates (Fig. 6.7a) and dislocations (Fig. 6.7b). The precipitates exhibited a bimodal size distribution. The larger precipitates (median diameter ~ 100nm) contribute to void nucleation upon ductile fracture. The smaller precipitates (median diameter ~ 20nm) are potent dislocation pinning sites (Fig. 6.7b). Analytical electron microscopy using X-rays (EDS) has provided information concerning the character of the precipitates. The larger precipitates contain Cu, Si and Fe in addition to Al with trace amounts of Cr. The smaller precipitates are predominantly Cu and Al. The matrix contains some Mg and Si in solution. High resolution images of the interface containing lattice fringes in the Al_2O_3 (Fig. 6.8) show no evidence of an interphase between the Al and Al_2O_3 . This latter characteristic is confirmed by analytical TEM which indicates that the alloying/impurity elements (Cu, Mg, Si, Fe,) have concentrations essentially identical in the interface region and elsewhere within the alloy.

The SEM investigations of the fracture surface have provided quantitative information about the plastic stretch and the extent of debonding (Fig. 6.9a). Also, various modes of ductile failure have been identified, as also observed

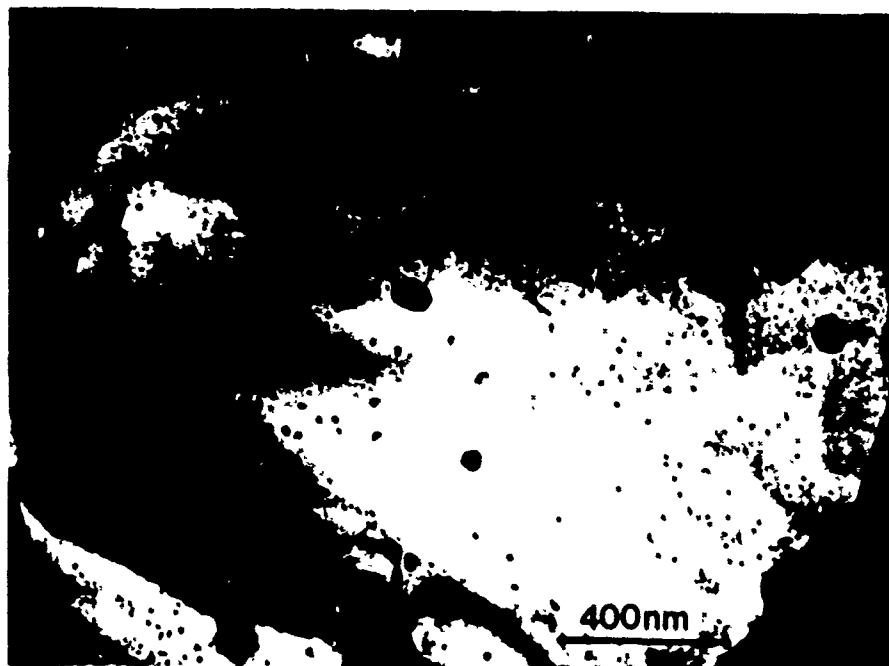


Fig. 6.7 Bright field TEM views of the Al phase
a) Precipitates



Fig. 6.7 Bright field TEM views of the Al phase
b) Dislocations pinned by the precipitates



Fig. 6.8 The AlAl_2O_3 interface: atomic resolution image

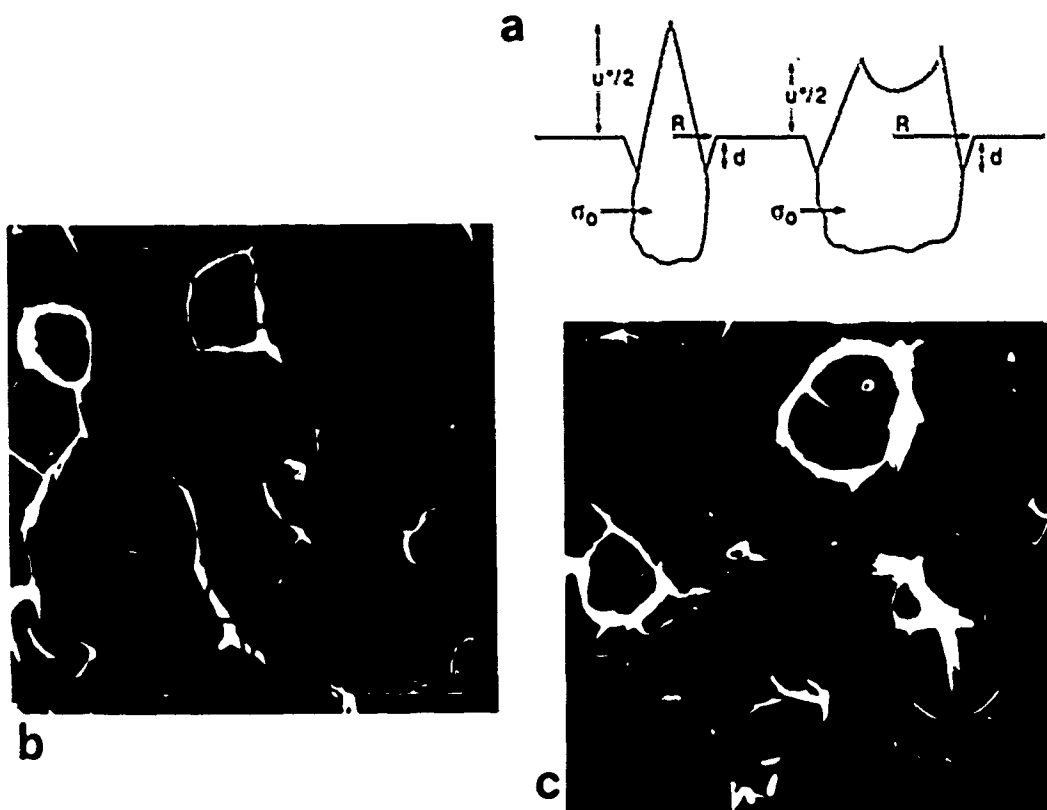


Fig. 6.9 a) A schematic of the ligament cross section after failure
 b) A scanning electron micrograph of a fracture surface with the topology of the ductile ligaments (as evaluated by stereo microscopy) superposed: a typical failure of a ligament having circular cross section indicating final ductile rupture by nucleation of a single hole
 c) SEM of a large precipitate at the base of a hole

on Pb/glass. Specifically, failure of axisymmetric reinforcement zones often involves the nucleation of a single hole at the center of the neck which rapidly expands to failure. In some instances, particles are apparent at the base of the holes (Fig. 6.9b). These particles are $\sim 100\text{nm}$ in diameter and probably coincide with the larger Al/Cu/Fe/Si precipitates identified by TEM.

Stereo measurements used to evaluate the plastic stretch to failure, u^* , and the interface debond length, d , revealed that the normalized plastic stretch, u^*/R varied appreciably between ligaments, ranging from $u^*/R \sim 0.8$ to 2.8 . However, there was no systematic dependence on either the ligament dimension R or the aspect ratio. All ligaments have thus been used to provide a cumulative distribution, such that the mean stretch is $\overline{u^*/R} = 1.6$. The debond length also has appreciable variability and ranges between $d/R \sim 0.1$ to ~ 0.5 , but there is no discernable dependence on aspect ratio. The median value is $\overline{d/R} = 0.2$.

The comparison between theory and experiment is most readily achieved by re-expressing Eqn. (6.1) in the form:

$$\Delta G_c = f \sigma_0 \bar{R} \chi (\overline{u^*/R}) \quad (6.2)$$

To use this result, σ_0 is first obtained, followed by evaluation of χ , using $\overline{u^*/R}$, and ΔG_c is then examined for consistency by comparison with the experimentally determined value of $150\text{--}200 \text{ Jm}^{-2}$ (Sigl et al. 1988). The yield strength can be evaluated by noting that Al-Cu precipitates behave as impenetrable obstacles, as evident from the observed dislocation pinning (Fig. 6.7b). Consequently, their influence on yielding should be represented by Orowan hardening (Dieter 1976):

$$\sigma_0 = Gb/\lambda + \sigma_s \quad (6.3)$$

where σ_0 is the yield strength in tension, b the Burger's vector, λ the spacing between precipitates and σ_s the contribution to the yield strength from solution hardening by the Mg, etc. Using literature values for σ_s ($\sim 70\text{MPa}$) and inserting the precipitate spacing measured from Fig. 6.7a ($\lambda = 100\text{nm}$), the yield strength is predicted to be: $\sigma_0 = 220\text{MPa}$. This value is comparable to typical values quoted for Al alloys precipitation hardened with Cu. The plastic stretch to failure, $\overline{u^*/R} = 1.6$ indicates that χ is in the range 2-3.5. Substituting the above values of σ_0 and χ into Eqn. (6.2) and noting that $f = 0.2$ and $\bar{R} = 2.0\mu\text{m}$, ΔG_c is calculated as $170\text{--}300 \text{ Jm}^{-2}$. Consequently, there is acceptable agreement with the measured value of $150\text{--}200 \text{ Jm}^{-2}$. Such behavior is consistent with the interpenetrating network microstructure which limits plastic dissipation in the plastic zone.

6.4.3. Cemented Carbides

Two toughening mechanisms have been invoked for cemented carbide materials: dissipation in the plastic zone and bridging behind the crack tip. Bridging ligaments have been observed directly in WC/Co (Sigl et al. 1988) and zone sizes measured. For reasonable choices of the flow stress of the Co alloy, the contribution of bridging deduced from these zone sizes is found to be relatively small ($\Delta G_c = 40 \text{ Jm}^{-2}$) compared with the overall toughness ($G_c = 400 \text{ Jm}^{-2}$).

More recently, Marshall et al. (1989) have reported measurements of plastic zone sizes in the range $h = 40\mu\text{m}$. Furthermore, optical interference microscopy has indicated that in-plane residual strain exists in the plastic zone, which is approximately constant over the zone. The relationship between these strains and the plastic dissipation in the plastic zone is not yet apparent. Nevertheless, it is reasonable to suppose that the dissipation is

appreciable and may be the predominant contribution to the toughness of these materials, consistent with the relatively small contribution from bridging.

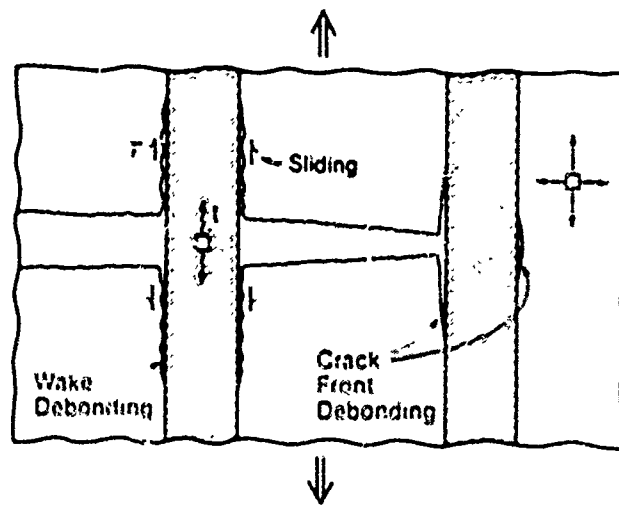


Fig. 7.1 A schematic illustrating the initial debonding of fibers at the crack front, as well as fiber debonding and sliding in the crack wake

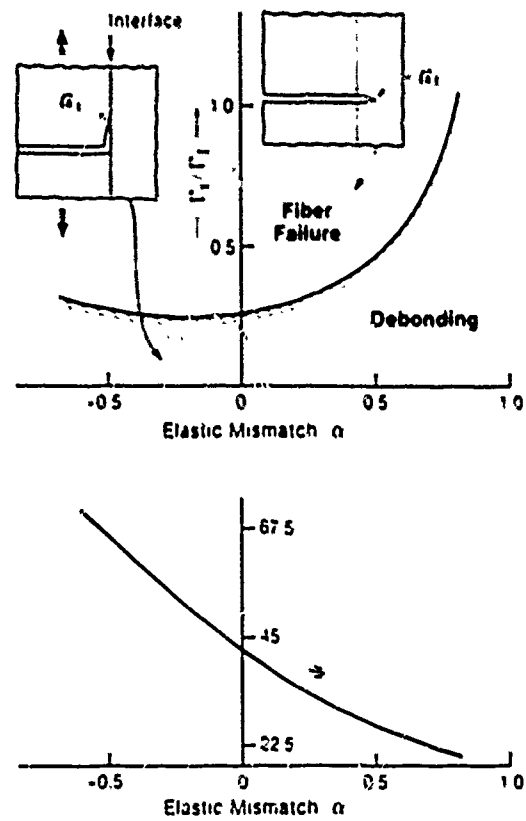


Fig. 7.2 Fracture energy requirements for crack front debonding

7. FIBER/WHISKER REINFORCEMENT

7.1. Synopsis

Practical ceramic matrix composites reinforced with *continuous fibers* exhibit important failure/damage behaviors in mode I, mode II and mixed mode I/II, as well as in compression. The failure sequence depends on whether the reinforcement is uniaxial or multiaxial and whether woven or laminated architectures are used. However, the *underlying failure processes* are illustrated by the behavior of uniaxially reinforced systems. The basic features, sketched in Fig. 7.1, provide some basic rules that govern "toughness." The composite properties are known to be dominated by the interface, and bounds must be placed on the interface debonding and sliding resistance in order to have a composite with attractive mechanical properties. The strong dependence of ceramic matrix composite properties on the mechanical properties of the interface generally demands consideration of fiber coatings and/or reaction product layers. Residual stresses caused by thermal expansion differences are also very important.

The specific microstructural parameters that govern mode I failure are the relative fiber/matrix interface debond toughness, Γ_f/Γ_f , the misfit (thermal expansion) strain between fiber and matrix, ϵ_f^* , the friction coefficient at the debonded interface, μ , the statistical parameters that characterize the fiber strength, S_0 and m , the matrix toughness, Γ_m , and the fiber volume fraction f . The prerequisite for "toughness" is that $\Gamma_f/\Gamma_f \lesssim 1/4$ in order to allow crack front debonding (Fig. 7.2). Subject to this requirement, the misfit strain must be small ($\epsilon_f^* \lesssim 3 \times 10^{-3}$) and preferably negative, such that the interface is in tension. Furthermore, the friction coefficient along the debonded interface should be small. The ideal fiber properties include a high median strength (large S_0) and large variability (small m), as needed to encourage large pull-out lengths. When Γ_f/Γ_f and μ are both small, experience has indicated that the tensile stress/strain behavior illustrated in Fig. 7.3a obtains. Three features of this curve are important: matrix cracking at a stress σ_0 , fiber bundle failure at σ_0 and pull-out. Conversely, larger Γ_f/Γ_f and μ cause the stress-strain curve to become linear (Fig. 7.3b). The ultimate strength then coincides with the propagation of a single dominant crack.

Present understanding of debonding is consistent with the following sequence of events during matrix crack propagation. Initial debonding along the interface at the crack front, requires that Γ_f/Γ_f be small enough to lie within the debond zone depicted in Fig. 7.2 (He and Hutchinson 1989). Furthermore, the extent of debonding is typically small when residual compression exists at the interface, but can be extensive when the interface is in residual tension and the fibers are smooth. Further debonding is usually induced in the crack wake (Charalambides and Evans 1989), (Fig. 7.1). The extent of this debonding is governed largely by the residual field. Residual radial tension results in unstable conditions and encourages the extensive debonding of smooth fibers. Residual compression and/or an irregular fiber morphology cause stable debonding (Sigl and Evans 1989), with extent determined by the friction coefficient and the roughness of the debonded interface. Subsequent fiber fracture involves the statistics of fiber failure (Thouless and Evans 1988), subject to an axial stress governed by the sliding resistance of the debonded interface. The above sequence suggests that, while debonding is a prerequisite for high toughness, the properties of the composite are dominated by the sliding resistance of the debonded interface, which dictate the major contribution to "toughness," caused by pull-out. The locations of fiber failure that govern the pull-out distributions can be determined from the stresses on the fibers, using concepts of weakest link statistics. Analysis of this phenomenon has been performed for composites having debonded interfaces subject to a constant sliding stress τ (Thouless and Evans 1988). The magnitude of τ governs the load transfer from the fiber to the matrix. Large values of τ cause the fiber stress to vary rapidly with distance from the matrix crack and induce fiber failure close to the crack, leading to small pull-out lengths, h_p . Conversely, small τ results in large h_p .

Various observations of crack interactions with fibers are supportive of the above rules. In particular, experiments on glass and glass ceramic matrix composites reinforced with SiC fibers reveal that materials with a C interlayer satisfy debonding requirements (Fig. 7.4) and also have small τ and thus demonstrate extensive pull-out (Marshall and Evans 1985, Prewé and Brennan 1982, Cao et al. 1989a). Conversely, composites having a continuous SiO₂ layer between the matrix and fiber exhibit matrix crack extension *through* the fiber without debonding (Bischoff et al. 1989, Cao et al. 1989a) (Fig. 7.5). Experiments on these composites and on whisker reinforced composites also confirm the strong influence of τ . Notably, systems which debond but do not slide readily because of either a high friction coefficient or morphological irregularity exhibit small pull-out lengths and moderate toughness. Such behavior is exemplified by LAS/SiC composites with oxide interphases and by various whisker reinforced materials, respectively.

Tough composites can be obtained by creating the appropriate interphases between the fiber and matrix, either by coating or, in situ, by segregation/interdiffusion. The most common approach is the use of a dual coating: the inner coating satisfies the debonding and sliding requirements, while the outer coating provides protection against the matrix during processing. However, the principal challenge is to identify an inner coating that has the requisite mechanical properties while also being thermodynamically stable in air at elevated temperatures. Most existing composites have either C or BN as the debond layer. However, both materials are prone to degradation in air at elevated temperatures. More stable alternatives have been proposed (e.g., Nb, Mo, Pt, NiAl) but not evaluated.

7.2. Constitutive Laws

7.2.1. Crack Opening

The mechanical properties of uniaxially reinforced ceramic matrix composites are largely governed by the relationships between the opening of a matrix crack, u , and the stresses, t , exerted on the crack by the intact bridging fibers and the failed fibers as they pull-out. The traction $t(u)$ is well known for composites in which debonding occurs easily (very small Γ/Γ_f) which also slide easily along the debonded interface (small τ). For other cases, reliable $t(u)$ functions have yet to be elucidated. Easy debonding and sliding provides a crack opening function that depends on the sign of the misfit strain, as well as the roughness of the debond interface, through their effect on the sliding resistance. For instance, sliding can be described by a Coulomb friction law

$$\tau = \mu q_n \quad (7.1)$$

where μ is the friction coefficient and q_n the nominal residual compression normal to the interface. At the simplest level, q_n is set by the residual misfit strain and the fiber/coating morphology, such that τ is essentially invariant. In this case, prior to the incidence of fiber failure, t and u are related by (Marshall et al. 1985, Budiansky et al. 1986)

$$t = \frac{2fE}{E_m(1-f)} \left[\frac{\tau E_f}{R} \right]^{1/2} u^{1/2} \quad (7.2)$$

Expression (7.2) has been used to describe the mechanical behaviors that obtain while the fibers are largely intact. At another extreme, when all of the fibers have failed, the traction on any fiber is (Phillips 1972, Thouless and Evans 1988)

$$t_f = 2f\tau(h_f - u)/R \quad (7.3)$$

where h_f is the distance from the matrix crack plane at which that fiber failed.

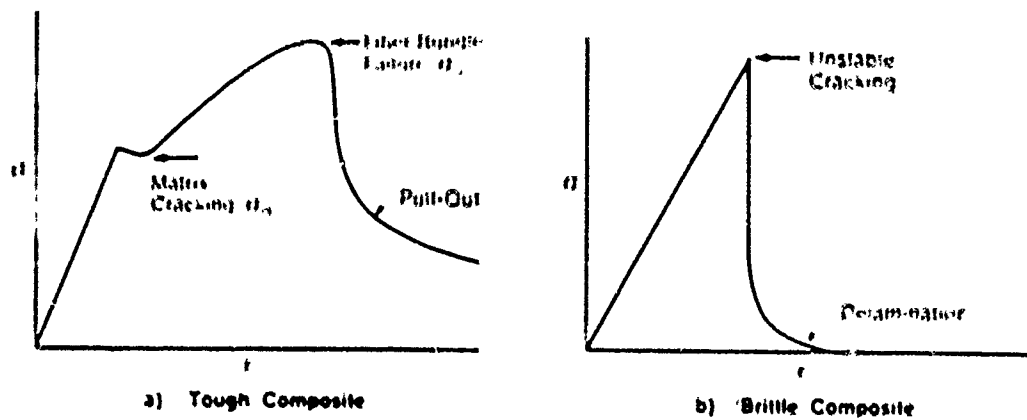


Fig. 7.3 Schematic illustrating the range of stress/strain characteristics exhibited by ceramic matrix composites



Fig. 7.4 Crack front debonding in a fiber reinforced glass matrix composite

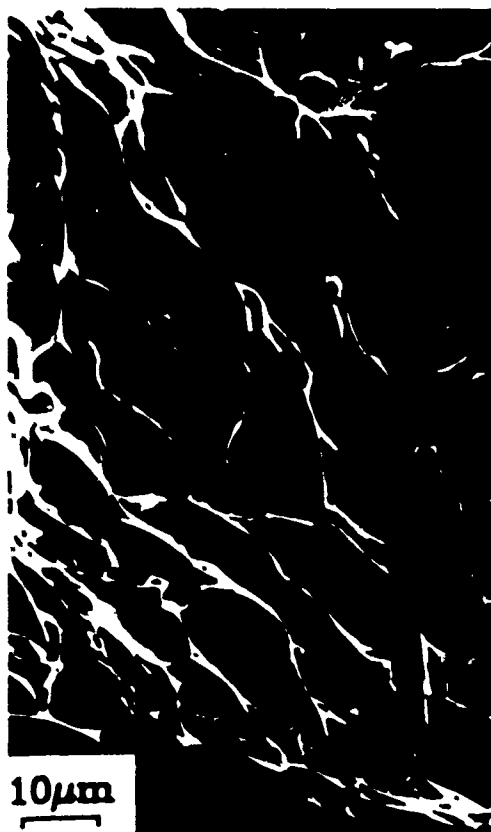


Fig. 7.5 A fracture surface indicating fracture through the fiber in a silica/SiC fiber composite

More difficult problems to address concern the incidence and location of fiber failure. This has been regarded as a problem in weakest link statistics (Oh and Finnie 1970), whereupon the function $t(u)$ depends upon the statistical parameters S_0 and m in addition to the variables contained in Eqn. (7.2). The expressions are unwieldily and are not reproduced here, but can be located in the article by Thouless and Evans (1988). Some trends, expressed in non-dimensional form, are summarized in Fig. 7.6. The small displacement behavior is dominated by the intact bridging fibers, whereas the long tail is governed by the pull-out of failed fibers.

Another level of complexity is involved when the interface stress q_0 varies with the loads t on the fiber. A simplified result obtained using a modified shear lag approach (Sigl and Evans 1989) suggests the following features ($E_f = E_m = E$; $\nu_f = \nu_m = \nu$):

$$t/R = \{1 - \mu\} [1 - (1 - \mu)^2] + \nu [1 - \nu + \nu(1 - \mu)^2] \quad (7.3)$$

where

$$\mu = 1/r_u^T E$$

with ϵ_u^T being the misfit strain which causes the interface to be in residual compression. Expression (7.4) while approximate, has several salient features. In particular, as expected, crack opening is inhibited by large values of the friction coefficient. Furthermore, as $F \rightarrow 1/\nu$, the fiber and matrix surface separate, leading to unrestricted crack opening. Additional complexity is involved when debonding and sliding occur simultaneously. Some preliminary results for such behavior exist, but are not addressed here. It is simply noted that, in such cases, the fracture energy of the coating becomes another parameter of interest.

The preceding constitutive laws are the bases for analyzing the most pertinent mechanical characteristics of fiber and whisker reinforced ceramics. Most notably, derivation of the matrix cracking stress and the crack growth resistance originates with expressions for $t(u)$, as elaborated below.

7.2.2. Pull-Out Lengths

The location of fiber failure vis-a-vis the matrix crack plane is of crucial importance because this location governs the pull-out length h_p . Both theory (Thouless and Evans 1988) and experiment (Thouless et al. 1989) suggest that, for aligned reinforcements, h_p is governed by weakest link statistics. For the simplest case, wherein the sliding stress τ remains constant, an expression for the mean pull-out length has been derived as (Thouless and Evans 1988),

$$(2h_p/R)^{m+1} = [1/2 \pi (m+1)] (A_0/R^2) (S_0/\tau)^m \Gamma[(m+2)/(m+1)] \quad (7.5)$$

where Γ in this expression is the gamma function and A_0 is a reference area for the fibers (usually set equal to $1m^2$). Consequently, for aligned fibers, it is evident that h_p/R is essentially governed by S_0/τ : *high fiber "strength" and low sliding resistance encourage large pull-out lengths*. Corresponding trends for inclined fibers are unknown.

7.3. The Matrix Cracking Stress

The stress σ_0 at which matrix cracking occurs has been the most extensively studied behavior in ceramic matrix composites. For composites in which the residual stress normal to the interface, q_0 , is tensile and the interface

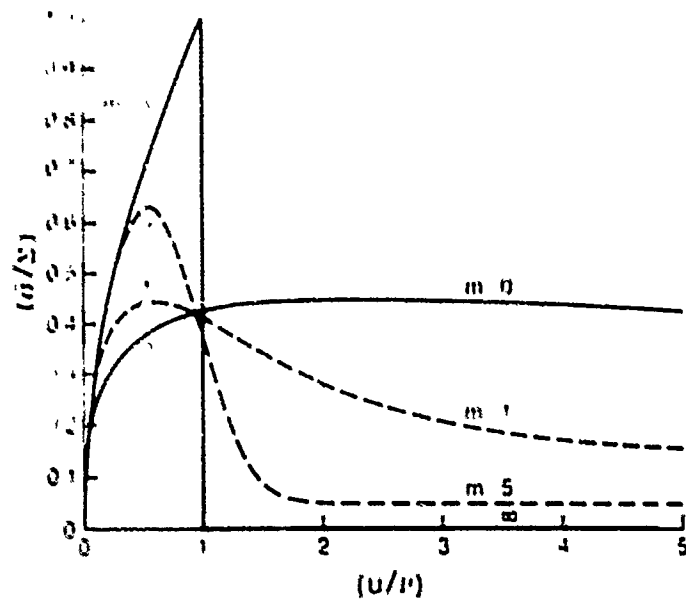


Fig. 7.6 The non-dimensional crack closure stress as a function of crack opening

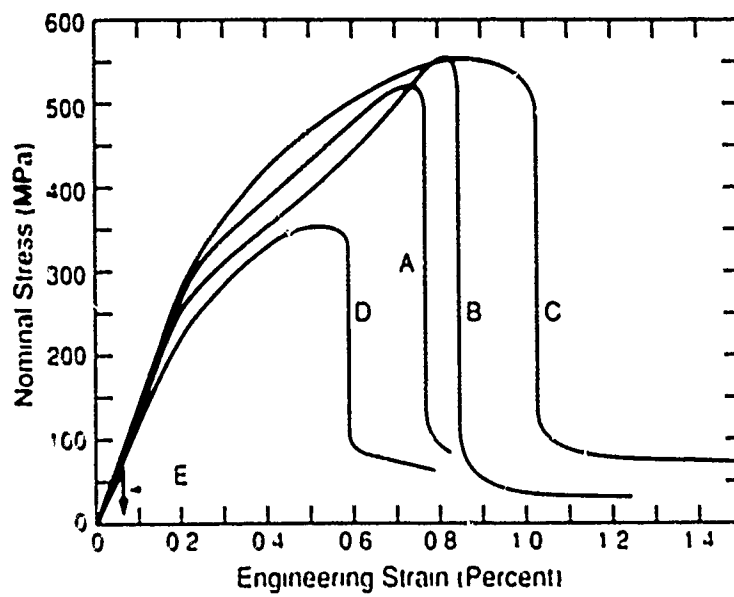


Fig. 7.7 Tensile stress/strain curves for a range of glass and glass ceramic matrix composites reinforced with SiC (Nicalon) fibers

properties can be effectively represented by an unique sliding stress, τ . Eqn. (7.2) may be used to derive the lower bound, steady-state matrix cracking stress (Budiansky et al. 1986),

$$\frac{\sigma_c}{E} = \frac{\sigma^*}{E} - \frac{p}{E_m}$$

where

$$\frac{\sigma_c}{E} = \left(\frac{6f^2 E_f \tau^2 R}{(1-f) E E_m R} \right)^{1/2} \quad (7.6)$$

supporting the axial residual stress in the matrix. This result is independent of the matrix crack length because the crack is "fully" bridged by fibers (Marshall et al. 1985). Measurements performed on many different glass and ceramic matrix composites (Fig. 7.7) have verified that Eqn. (7.6), in fact, provides an adequate representation of matrix cracking provided that $\tau < 30 \text{ MPa}$ (Cao et al. 1989a). Values of τ in this range have been demonstrated for fibers coated with either C and BN, as elaborated below. For these systems, it is recognized that τ depends on the mist strain and consequently, for the simple case wherein τ and q_c are related through a friction coefficient (Eqn. 7.1), the matrix cracking stress exhibits a maximum, σ_o^* , given by (Budiansky et al. 1986),

$$\sigma_o^*/E = (2/3) [2f\mu\Gamma_m/(1+E/E_f)E_m R]^{1/2} \quad (7.7)$$

This result has evident implications for material design.

More detailed diagnosis of matrix cracking confirms that Eqn. (7.6) is a lower bound for the onset of cracking. Further cracking occurs as the stress is raised above σ_o , resulting in a periodic crack array (Fig. 7.8) (Aveston et al. 1971). The crack spacing reaches a saturation value, s , when the stress everywhere in the "matrix blocks" between cracks becomes smaller than that applied stress. The magnitude of the saturation crack spacing is governed by the sliding stress, τ , such that τ and s are related by (Cao et al. 1989a),

$$\tau = 1.34 \left[(1-f)^2 \Gamma_m E_f E_m R^2 / f E s^3 \right]^{1/2} \quad (7.8)$$

Consequently, the matrix cracking stresses can be expressed in terms of the crack spacing as:

$$\sigma_o = 2 \left[f \frac{\Gamma_m E_f E}{E_m s} \right]^{1/2} - q \frac{E}{E_m} \quad (7.9)$$

The crack spacing clearly provides an approach for estimating τ and for establishing a self-consistent description of matrix cracking. However, other methods for measuring τ provide additional insights, as elaborated below.

While the matrix cracking stress appears to be adequately understood, the other failure mechanisms that operate in ceramic composites, as well as transitions between these mechanisms and matrix cracking, are still subject to investigation. These other effects are discussed in the following sections.

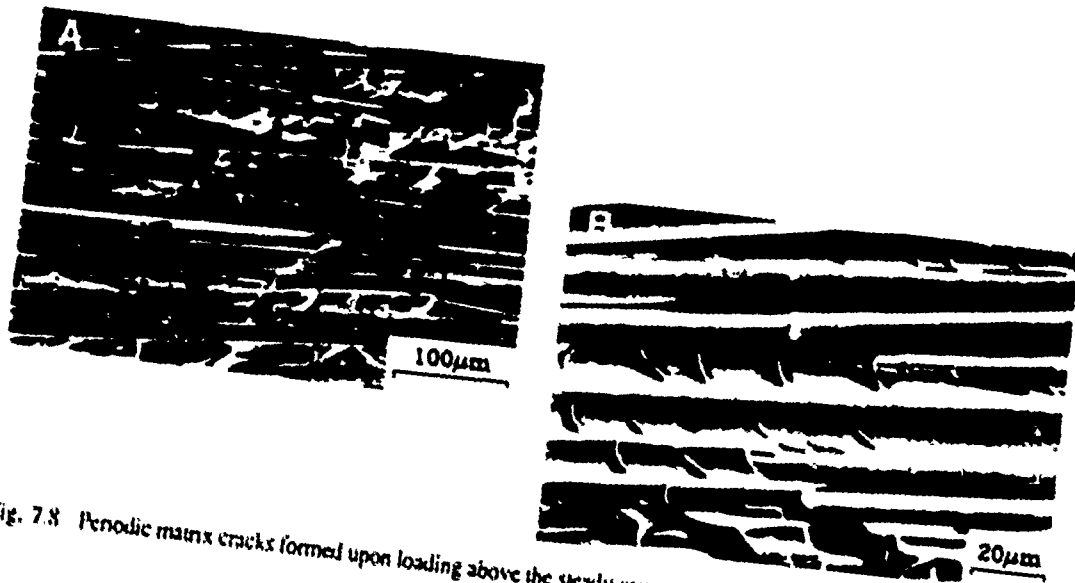


Fig. 7.8 Periodic matrix cracks formed upon loading above the steady-state matrix cracking stress

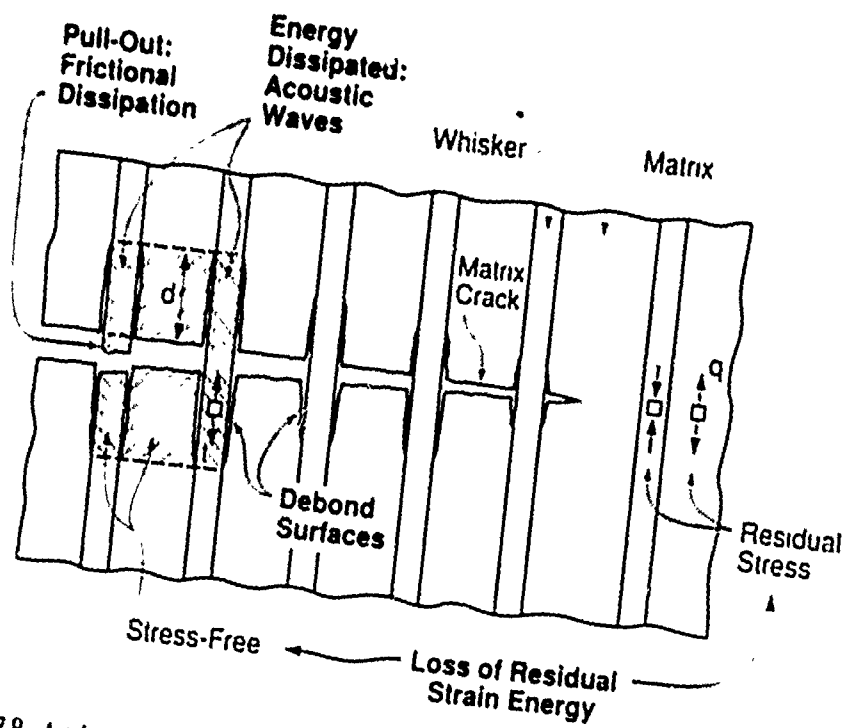


Fig. 7.9 A schematic indicating the various contributions to the steady-state toughness

7.4. Toughness

In certain reinforced ceramics, fracture occurs by the growth of a single dominant flaw in mode I. Material characteristics that lead to this mode of behavior are examined in a later section. Herein, consideration is given to relationships between the toughness and the various constituent properties of the composite. The most basic features of the toughness phenomenon, visualized in Fig. 7.9, recognize that there are *four* effects which influence toughness (Campbell et al., 1989). *Debonding* generates new surface and contributes *positively* to toughness. Frictional dissipation upon *pull-out* results in local heating and again contributes *positively*. *Residual stresses* present in the material are partially relieved by matrix cracking and debonding and thus *detract* from the toughness. Finally, when the fibers fail, some of the *elastic energy* stores in the fiber is dissipated through acoustic waves and appears as a *positive* contribution to toughness.

The above effects are indicative of resistance curve behavior, since each contribution is only fully realized when the fibers fail and pull-out. The full details of the increase in the fracture resistance can be calculated from the crack surface tractions (u) by applying Eqn. (1.2). Results of this type are available (Hom, Shaizero and Evans 1989). However, a useful simplification for further discussion is the peak (or asymptotic) toughness that obtains when each mechanism exerts its maximal contribution. At the simplest, physically relevant level, this toughness is given by (Campbell et al. 1989),

$$\Delta G_c = \{d[S^2/E - E(\epsilon_r^T)^2 + 4\Gamma_i/R(1 - I)] + 2\tau(h_f^2/R) \quad (7.10)$$

The first term is a bridging contribution that derives from the stored strain energy dissipated as acoustic waves, with S being the reinforcement "strength." The second term is the loss of residual strain energy caused by matrix crack extension and debonding. The third term reflects the new "surface area" caused by debonding and the last term is the pull-out contribution, dissipated by frictional sliding of the interfaces.

Experience indicates that the residual strain term is small in systems of practical utility and can often be neglected. The largest potential for toughness resides in the pull-out term, *provided that h_f/R is large*. An extreme range of pull-out behaviors is apparent among the available range of fiber and whisker reinforced ceramics, resulting in wide variations of toughness. Understanding pull-out thus dominates our capability for producing ceramic composites having exceptional toughness. Finally, the elastic and debond energy terms are of intermediate magnitude. They are thus of negligible relevance when h_f/R is large, but may dominate when there is no pull-out.

The dominance of toughness by pull-out provides a focus for specifying those properties of the fibers and fiber coatings that optimize the frictional dissipation. For aligned reinforcements, wherein weakest link statistics govern the pull-out length (Eqn. 7.5), it is apparent that the pull-out contribution to toughness varies as (Thouless and Evans 1988),

$$\Delta G_p = S_0^{2m/(m+1)} / \tau^{(m-1)/(m+1)}$$

An explicit dependence of toughening on fiber "strength" and sliding resistance is thus evident. Physically stated; *high-fiber strength and low sliding resistance combine to maximize the frictional dissipation, by inducing sliding over the largest possible fiber surface area*. The inverse dependence of pull-out toughening on τ emphasizes the need to control and understand sliding. Some of the qualitative features are depicted in Fig. 7.10: illustrating the importance of the fiber morphology, the misfit strain and the friction coefficient.

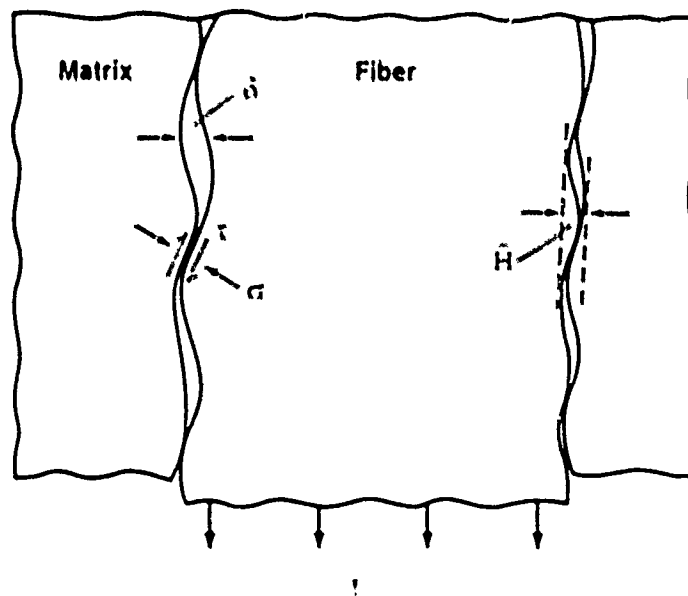


Fig. 7.10 A schematic of the pull-out process for debonded fibers indicating the roles of fiber morphology, misfit strain and friction coefficient

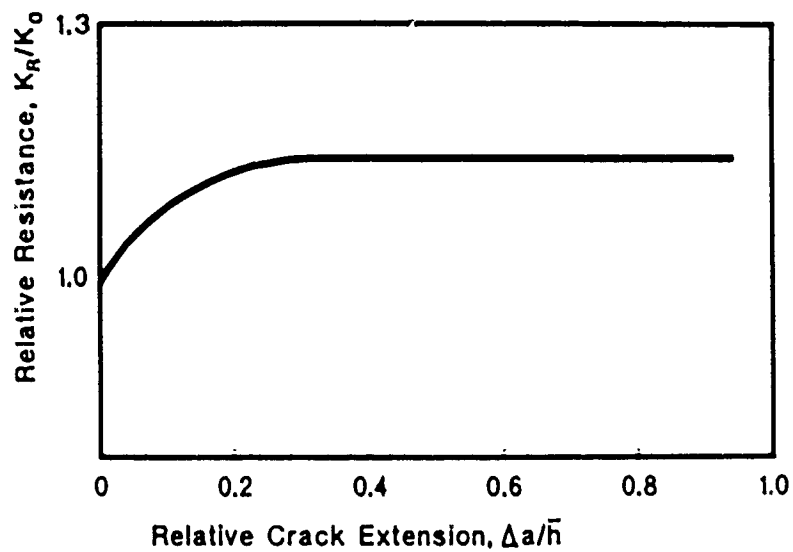


Fig. 7.11 Resistance curve calculated for bridging and debonding only and for pull-out. Note that, for the latter, the crack extension needed to achieve the asymptotic toughness is very large compared with the pull-out length.

Non-aligned fibers and whiskers clearly suppress pull-out by virtue of bending strains in the reinforcements that encourage fracture near the matrix crack plane. Indeed, fibers having low flexural resilience, such as SiC, tend to fail at the matrix crack plane when inclined to the crack (Campbell et al. 1989, Rühle et al. 1987) whereas C fibers may still pull-out over large distances (Prewé 1986). Fiber alignment issues associated with pull-out thus depend on fiber properties.

When fiber pull-out does not contribute to toughness, as in many whisker reinforced ceramics, the elastic energy and debonding energy terms tend to govern the fracture resistance, such that:

$$\Delta G_c \approx f d S^2 / E + 4 \Gamma_i f (d/R) / (1 - f) \quad (7.11)$$

To interpret this expression, it is essential to appreciate that the debond length d depends on the interface fracture energy Γ_i , on the misfit strain ϵ^* , and on the friction coefficient. The associated relationships are unknown, but dimensional analysis suggests that (Charalambides and Evans 1989, Sigl and Evans 1989),

$$d/R = H \left[E_f R (\epsilon_w^*)^2 / \Gamma_i, S/E \epsilon_w^*, 1/\mu \right] \quad (7.12)$$

where H is a function. The important point is that there remains much scope for controlling toughness by manipulating the interface debonding and sliding properties and by maximizing the fiber/whisker strength.

As already noted, resistance curve effects cause the toughness to gradually build up to the asymptotic values. Consequently, the full toughness cannot usually be utilized. The toughening rate (tearing modulus) has not been broadly studied and trends are relatively unknown. However, some numerical results for pull-out dominated toughness (Fig. 7.11) indicate that asymptotic behavior is achieved only after considerable crack extension (Hom et al 1989).

7.4. Ultimate Strength

When matrix cracking precedes ultimate failure, the *ultimate strength* coincides with fiber bundle failure (Thouless et al. 1989). A simple estimate of this strength, based on weakest link statistics that neglect interaction effects between failed fibers and ignores the stress supported by fractured fibers by means of stress transfer from the matrix through interface friction gives:

$$\sigma_u = \hat{S} \exp \left[- \frac{\{1 - (1 - \tau s / R \hat{S})^{m+1}\}}{(m+1) \{1 - (1 - \tau s / R \hat{S})^m\}} \right] \quad (7.13)$$

with

$$(R \hat{S} / \tau s)^{m+1} = (A_0 / 2 \pi R L_g) (R S_0 / \tau s)^m \{1 - (1 - \tau s / R \hat{S})^m\}^{-1}$$

and L_g the specimen gauge length. The effect of the sliding stress on σ_u appears directly, as well as through its effect on the crack spacing s , while the effect of residual stress is present through its effect on τ . The ultimate strength is also expected to be influenced by the residual stress. Specifically, in systems for which the fiber is subject to residual compression, the axial compression should suppress fiber failure and elevate the ultimate strength to a level in excess of that predicted by Eqn. (7.12). This effect may be estimated by regarding the matrix as clamping onto the fiber and thus, simply superposing the residual stress onto \hat{S} .

The above results are clearly simplified and their improvement should be addressed by further research that couples the mechanics of fiber cracking and interface sliding with the statistics of failure.

7.5. Property Transition

Non-linear macroscopic mechanical behavior in tension is most desirable for structural purposes. Analysis of the transition between this regime and the linear regime is thus important, and involves comparison of the basic trends in the steady-state matrix cracking stress, σ_0 and in the asymptotic fracture resistance, ΔG_c . Most significantly, σ_0 increases but ΔG_c decreases as τ increases. These opposing trends with τ suggest the existence of an optimum τ that permit good matrix cracking resistance while still allowing high toughness.

More specifically, a property transition is expected when the matrix cracking stress attains the stress needed for fiber bundle failure. One estimate on the property transition can be obtained by simply allowing σ_0 to exceed the ultimate strength, σ_u , whereupon a non-dimensional parameter β which governs the transition when τ is small is:

$$\beta = \tau E \Gamma_m / S_0^3 R \quad (7.14)$$

Specifically, when β exceeds a critical value, brittle behavior initiates. This estimate has not been tested and furthermore, alternate parameters may be conceived.

7.6. Experimental Results

7.6.1. Stress/Strain Behavior

Uniaxially reinforced ceramic and glass matrix composites with either C or BN interlayer generally satisfy crack front debonding requirements and the materials exhibit axial and transverse mechanical properties that accord well with the above expressions for the matrix crack stress and the ultimate strength (Cao et al. 1989). To achieve these comparisons, each of the parameters in Eqns. (7.6) and (7.12) must be independently ascertained. As already mentioned, τ can be measured using various techniques: the matrix crack spacing (Aveston et al. 1971, Cao et al. 1989), the indentation push-through stress (Marshall and Oliver 1987, Weihs et al. 1988) and the matrix crack opening hysteresis (Marshall and Evans 1985). The misfit strain ϵ_d^T can also be determined using a variety of methods: X-ray or neutron line shifts, offset stresses in the crack opening and residual displacements obtained from nanoindenter tests. Accurate values of the matrix fracture energy Γ_m and of the constituent elastic properties are also needed. Furthermore, it is noted that the comparison between theory and experiment for the matrix cracking stress is contingent upon having accurate values of the above parameters.

Correlations of trends in the ultimate strength are primarily contingent upon knowledge of the *in situ* mechanical properties of the fibers. Appreciation for these properties can be gained by examining and measuring fracture mirrors on the fiber fracture surfaces in the composite. Specifically, the distribution of mirror radii can be used to evaluate the axial stress S on the fiber of the fracture location (Mecholsky and Powell 1982, Jamet et al. 1984, Eckel and Bradt 1989). Some typical results for two materials with different ultimate strength are shown in Fig. 7.12 (Cao et al. 1989). Limited experience has indicated that the ratio of median strengths scales with the ratio of composite ultimate strengths.

When amorphous oxide coatings have been used with SiC fibers and whiskers, debonding requirements are marginal: $\Gamma/\Gamma_f \approx 1/2 - 1/4$ (He and Hutchinson 1989, Evans et al. 1989). Consequently, fibers and whiskers with axis normal to the matrix crack *do not debond* (Fig. 7.5) and thus, do not contribute to "toughness." Acutely inclined whiskers can debond (Fig. 7.13), but cannot pull-out.

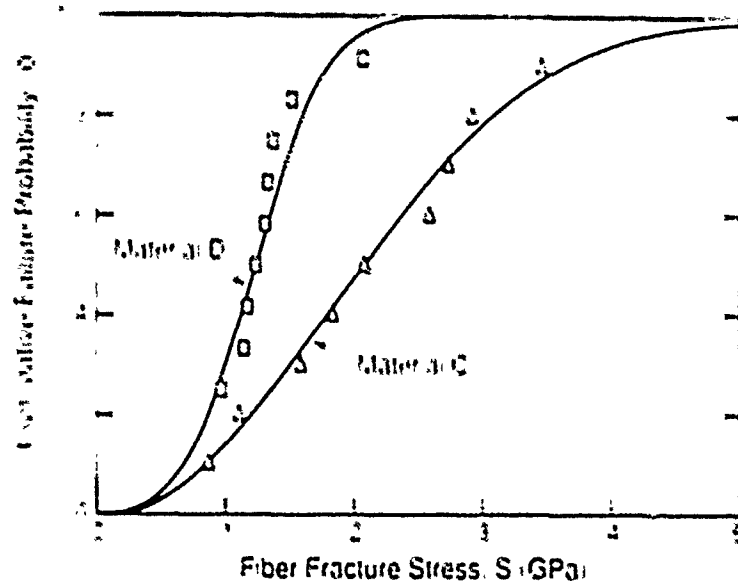


Fig. 7.12 Fiber strength distributions ascertained on two composites (refer to Fig. 7.7 for the corresponding stress/strain curves) using fracture mirror measurements



Fig. 7.13 Debonding of acutely inclined whiskers in a SiC whisker reinforced Al_2O_3

Based on the above experimental features that C and BN coatings are effective in terms of satisfying crack front debonding and also providing a low sliding resistance, whereas amorphous oxides are incapable of debonding, it may be concluded that C and BN are the preferred coatings. However, both of these materials are susceptible to rapid oxidation (Luh and Evans 1987; Bischoff et al. 1989) and mostly incapable of performing their required debonding and sliding functions at elevated temperatures in oxidizing environments. A variety of other coatings are thus under investigation. When such coatings have been developed, some of the more complex crack opening and pull-out constitutive laws presented in Section 7.1 may be needed to describe the mechanical properties of the composite.

7.6.2. Toughness

Various fiber and whisker reinforced materials fail in mode I by the propagation of a predominant crack, with contributions to the toughness from the terms expressed in Eqn. (7.10). Such behavior typically obtains in systems having reinforcements that are either non-aligned or morphologically irregular. It is also observed in aligned composites with high friction coefficient coatings (Hom et al. 1989). Lack of alignment imposes bending moments onto debonded reinforcements and reinforcement failure typically occurs close to the matrix crack plane, whereupon there is a negligible contribution of pull-out to the toughness.[‡] Morphologically irregular whiskers and fibers exhibit mechanical interlocking during pull-out resulting in large τ and again, reinforcement failure close to the matrix crack plane. For such materials, careful measurements of debond lengths using transmission electron microscopy have allowed an evaluation of the principal contributions to toughness (Campbell et al. 1989). Seemingly, there are similar contributions from bridging and interface debonding, such that reasonable agreement exists between theory and experiment. Good insight regarding approaches for further enhancing toughness can thus be gained from Eqn. (7.10).

8. MULTIPLE MECHANISMS

The preceding sections have described microstructural issues concerned with toughness optimization when a single mechanism operates. In practice, more than one mechanism may exist. Consequently, interactions between mechanisms must be considered. In some instances, the interactions may be highly beneficial and produce synergism between mechanisms. Such synergism has been illustrated to exist when both bridging and process zone mechanisms operate simultaneously (Amazigo and Budiansky 1989) (Fig. 1.5). Conversely, some interaction effects can be detrimental and reduce the efficacy of the individual mechanisms.

Synergism is most likely when bridging and process zone mechanisms interact. Multiplicative interactions are evident in this case because the crack surface tractions caused by bridging can expand the process zone width h in the crack wake, causing an additional increase in shielding, proportional to this increase in h . Straightforward logic indicates that multiplicative toughening between bridging and process zone effects should occur when the ratio of the bridging zone size, L , to the process zone width, h , is small, because bridging generates a new effective crack tip toughness, that causes the process zone size to further increase. Calculations of coupled bridging and process zone effects have been performed (Amazigo and Budiansky 1989) in the case that the bridging tractions are constant (Dugdale zone). The results reveal two bounds given by:

$$K_c/K_m = \lambda_p \lambda_b \quad (8.1a)$$

the synergistic limit and

[‡] Chopped C fibers appear to be an exception because their anisotropy provides a high flexural resilience.

$$K_t/K_m = \sqrt{\lambda_p^2 + \lambda_b^2 - 1} \quad (8.16)$$

the lower bound, where λ_p and λ_b are the toughening ratios for the process zone and bridging mechanisms, respectively. Furthermore, and surprisingly, the synergistic limit was found to obtain when $L/h \approx 10$. Rigorous experimental substantiation of synergism has yet to be obtained.

The interactions between either two bridging zone mechanisms or two process zone mechanisms are relatively unexplored. At the simplest level, two bridging mechanisms are additive with each $\Delta\sigma_c$ given by Eqn. (1.2). However, the critical stretch u for one mechanism may be affected by the other, whereupon additivity may not be realized. Interactions between process zone mechanisms are more difficult to express, because the zone sizes and the transformation strains are coupled. Preliminary attempts have been made to examine concurrent transformation and microcrack toughening (Evans and Cannon 1986, Faber 1988) which indicate that the coupling can result in an augmentation of toughness.

APPENDIX

THE CRYSTALLOGRAPHY OF THE $t \rightarrow m$ TRANSFORMATION IN ZrO_2

The crystal structures of t - and m - ZrO_2 are shown in Fig. 1.6. Three lattice correspondences (LCs) may arise between the t and m polymorphs, called for convenience LC A, B or C, depending on which m axis, a , b or c , is parallel to the c axis of t - ZrO_2 .

The martensitic character of the $t \rightarrow m$ transformation in ZrO_2 was first suggested by Wollen (1964). Shortly afterward, Bailey (1964) studied this transformation *in situ* in the electron microscope, using oxidized foils of Zr, and found twinning on $(100)_m$, $(1\bar{1}0)_m$ and $(\bar{1}00)_m$ planes, as well as direct evidence for all three lattice correspondences; however, LC C was strongly pronounced.

Bansal and Heuer (1972, 1974) examined the transformation in ZrO_2 single crystals by transmission electron microscopy and X-ray precession experiments. These authors performed a detailed analysis of the orientation relationship between parent and product and also determined the orientations of the habit planes (the common plane between the t and m phases). The observations were compared to martensitic calculations using the phenomenological theory of Wechsler et al. (1953). After this work, the martensitic nature of the $t \rightarrow m$ transformation was no longer in doubt. Kriven et al. (1981) extended these calculations to different LCs and slip systems and Chowdry and Crocker (1984) further refined the calculations and showed discrepancies with the experimental observations of Bansal and Heuer (1972, 1974), due to different values of the lattice parameters used by the two groups of investigators. Resolution of the discrepancy between these calculations and experimental determination of the habit planes requires more detailed habit-plane determinations and more accurate knowledge of lattice parameters, orientation relationships and lattice-invariant deformation systems.

Little work has been performed to date on the crystallography of ZrO_2 particles transformed while confined within ceramic matrices. Porter and Heuer (1979) showed that large t - ZrO_2 precipitates transformed above room temperature in overaged Mg-PSZ and were invariably twinned. The twinning occurred on at least two systems: "midrib" twins parallel to $(100)_m$ (i.e., parallel to the long axes of the lenticular t - ZrO_2 precipitates) and "cross" twins parallel to $(110)_m$. The factors which govern the type of twins formed on cooling such particles in PSZ have not yet been determined.

Kriven (1981) studied the crystallography of twins formed in transformed ZrO_2 particles in an Al_2O_3 matrix. Small ZrO_2 particles ($< 0.5 \mu\text{m}$) usually contained one set of parallel twins, frequently on $(100)_m$. The situation in larger ($> 1 \mu\text{m}$) particles was more complex, as different areas of the particle contained different martensite variants. More recently, Kriven showed (1983) that a particle transformed *in situ* in the HVEM transformed via LC C and was internally twinned (see Fig. 2.5); however, the twinning was inconsistent with the prediction of the phenomenological martensitic theory (Chowdry and Crocker 1984). It is not known if this is due to a failure of the theory or to twinning occurring after the transformation.

Detailed TEM studies of transformed ZrO_2 inclusions in a mullite ($3 \text{ Al}_2\text{O}_3 \cdot 2 \text{ SiO}_2$) matrix by Bischoff and Ruhle (1983) showed that the twins present in large ZrO_2 particles reduced the transformation-induced stresses at the particle-matrix interface and in the surrounding matrix by forming "domains of closure". However, microcracks were frequently observed within such transformed particles and it is still not established if post-transformation deformation twinning occurs to further reduce the strain energy of a transformed m-ZrO_2 inclusion.

ACKNOWLEDGEMENT

The authors wish to thank the Defense Advanced Research Projects Agency for financial support through the University Research Initiative Program at UCSB under ONR contract N00014-86-K-0753.

REFERENCES

- E. A. Almond, C. A. Brookes and R. Warren (eds.) (1986), Science of Hard Materials, Inst. of Physics Conference Series Number 75, Adam Hilger Ltd., Bristol and Boston.
- J. C. Amazigo and B. Budiansky (1989) Harvard Univ. Report, Mech 112.
- M. F. Ashby, F. J. Blunt and M. Bannister (1989) Acta Metall., in press.
- J. Aveston, G. A. Cooper and A. Kelly (1971) The Properties of Fiber Composites, IPC Science and Technology, NPL, p. 15.
- J. E. Bailey (1964) Proc. R. Soc. (London), Sect. A 279, 359.
- G. K. Bansal and A. H. Heuer (1972) Acta Metall. 20, 1281.
- G. K. Bansal and A. H. Heuer (1974) Acta Metall. 22, 409.
- E. Bischoff and M. Ruhle (1983) J. Am. Ceram. Soc. 66, 123.
- E. Bischoff, O. Sbaizero, M. Ruhle and A. G. Evans (1989) J. Am. Ceram. Soc. 72, 114.
- B. Budiansky and J. C. Amazigo (1989) Int. Mech. Phys. Solids 27, 93.
- B. Budiansky, J. C. Amazigo and A. G. Evans (1988) Int. Mech. Phys. Solids 36, 167-187.
- B. Budiansky, J. W. Hutchinson and A. G. Evans (1986) Int. Mech. Phys. Solids 34, 167.
- B. Budiansky, J. W. Hutchinson and J. C. Lambropoulos (1983) Int. J. Solids Struct. 19, 337.
- B. Budiansky and R. J. O'Connell (1976) Int. J. Solid Struct. 12, 81.
- F. E. Buresch (1975) Fract. Mech. Ceram. 4, 835.
- P. Buseck, J. Cowley and L. Eyring (eds.) (1988) High-Resolution Transmission Electron Microscopy and Associated Techniques, Oxford University Press, New York and Oxford.
- J. W. Cahn and J. E. Hilliard (1958) J. Chem. Phys. 28, 258.
- G. H. Campbell, B. J. Dalgleish, M. Ruhle and A. G. Evans (1989) J. Am. Ceram. Soc., in press.
- H. C. Cao, B. J. Dalgleish, H. E. Dève, C. K. Elliott, A. G. Evans, R. Mehrabian and G. R. Odette (1989a), Acta Metall., in press.
- H. C. Cao, E. Bischoff, M. Ruhle, A. G. Evans, D. B. Marshall and J. J. Brennan (1989b) J. Am. Ceram. Soc., in press.

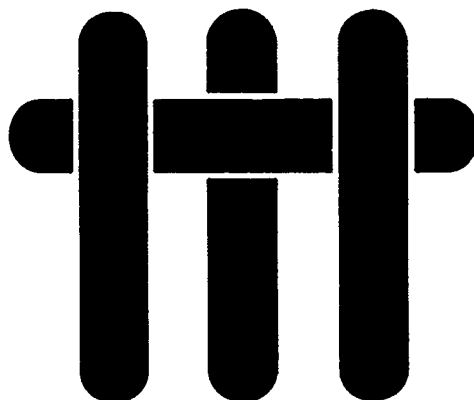
- P. G. Charalambides and A. G. Evans (1989) *J. Am. Ceram. Soc.*, in press.
- P. G. Charalambides and R. M. McMeeking (1987) in: *Constitutive Modelling for Nontraditional Materials* (eds. V. K. Stokes and D. Krajcinovic), ASME-AMD **85** pp. 189-216.
- I. W. Chen and Y.-H. Chiao (1983) *Acta Metall.* **31**, 1627.
- I. W. Chen and Y.-H. Chiao (1985) *Acta Metall.* **33**, 1827.
- M. A. Chaudry and A. G. Crocker in: "Science and Technology of Zirconia. II" (N. Claussen, M. Rühle and A. H. Heuer, eds.) *Adv. in Ceramics* **12** (1984) 46.
- P. C. Clapp (1973) *Phys. Stat. Sol.* **B57**, 561.
- D. R. Clarke (1979) *Ultramicroscopy* **4**, 33.
- D. R. Clarke and F. Adar (1982) *J. Am. Ceram. Soc.* **65**, 254.
- N. Claussen, M. Rühle and A. H. Heuer (eds.) (1984), "Science and Technology of Zirconia II" *Advances in Ceramics* Vol. 12, The American Ceramic Society, Columbus, OH.
- B. I. Cook, H. R. Lawn and C. J. Fairbanks (1985) *J. Am. Ceram. Soc.* **68**, 602.
- G. A. Cooper and A. Kelly (1967) *J. Mech. Phys. Solids* **15**, 279.
- G. I. Dieter, (1976) *Mechanical Metallurgy* McGraw-Hill, New York and London.
- A. J. Eckel and R. C. Bradt (1989) *J. Am. Ceram. Soc.* **72**, 455.
- R. F. Egerton (1986) *Electron Energy Loss Spectroscopy in the Electron Microscope*, Plenum, New York and London.
- C. K. Elliott, G. R. Odette, G. E. Lucas and J. W. Sheppard (1988) *MRS Symposium Proceedings* Vol. **120**, pp. 95-102.
- A. G. Evans (1976) *Scripta Metall.* **10**, 93.
- A. G. Evans (1982), *J. Am. Ceram. Soc.* **65**, 127-137.
- A. G. Evans (1984) *Adv. in Ceramics* **12**, 193.
- A. G. Evans (1989) *Ceramic Transactions* (Ed. Messing et al.) Vol. 1, pp. 989-1010.
- A. G. Evans, N. H. Burlingame, W. M. Kriven and M. D. Drozy (1981) *Acta Metall.* **29**, 447.
- A. G. Evans and R. M. Cannon (1986) *Acta Metall.* **34**, 701-800.
- A. G. Evans and K. T. Faber (1984) *J. Am. Ceram. Soc.* **67**, 255.
- A. G. Evans, M. He, B. J. Dalgleish and J. W. Hutchinson (1989) *J. Am. Ceram. Soc.*, in press.
- A. G. Evans and A. H. Heuer (1980) *J. Am. Ceram. Soc.* **63**, 241.
- A. G. Evans and R. M. McMeeking (1986) *Acta Metall.* **34**, 2635-2441.
- K. T. Faber (1984) *Advances in Ceramics* **12**, 512.
- B. Flinn, M. Rühle and A. G. Evans (1989) *Acta Metall.*, in press.
- R. C. Garvie, R. H. J. Hannink and R. T. Pascoe (1975) *Nature (London)* **258**, 703.
- W. W. Gerberich, (1971) *J. Mech. Phys. Solids* **19**, 71.
- W. W. Gerberich and E. Kurman (1985) *Scripta Met.* **19**, 295.
- D. J. Green, R. H. J. Hannink and M. V. Swain (1989) *Transformation Toughening of Ceramics*, CRC Press Inc., Boca Raton, FL.
- G. Guénin and P. F. Gobin (1982) *Metall. Trans AIME* **13A**, 1127.
- M. He and J. W. Hutchinson (1989) *Int. Appl. Mech.*, in press.
- A. H. Heuer (1987) *J. Am. Ceram. Soc.* **70**, 689.
- A. H. Heuer, N. Claussen, W. M. Kriven and M. Rühle (1982) *J. Am. Ceram. Soc.* **65**, 642.
- A. H. Heuer and L. W. Hobbs (eds.) (1981) "Science and Technology of Zirconia," *Advances in Ceramics* Vol. 3, The American Ceramic Society, Columbus, OH.
- A. H. Heuer, F. F. Lange, M. V. Swain and A. G. Evans (eds.), 1986, *Transformation Toughening*, *J. Am. Ceram. Soc.*, Special issues, Vol. **69**, No. 3 and 9.

- A. H. Heuer and M. Rühle (1985) *Acta Metall.* **33**, 2101.
- P. Hing and G. W. Groves (1972) *J. Mater. Sci.* **1**, 427.
- P. Hirsch, A. Howie, P. B. Nicholson, D. W. Pashley and M. J. Whelan (1977) *Electron Microscopy of Thin Crystals*, Robert E. Krieger, Huntington, NY.
- R. G. Hoagland, A. P. Rosenfield and G. T. Hahn (1972) *Met. Trans.* **3**, 123.
- R. G. Hoagland, J. D. Embury and D. J. Green (1973) *Scripta Metall.* **2**, 907.
- C. L. Hom, O. Sbaizero and A. G. Evans (1989) to be published.
- J. J. Hren, J. I. Goldstein and D. C. Joy (eds.) (1979) *Introduction to Analytical Electron Microscopy*, Plenum, New York and London.
- J. W. Hutchinson (1974) *Harvard Univ. Rep.* 38.
- J. W. Hutchinson (1987) *Acta Metall.* **35**, 1605.
- J. J. Janet, D. Lewis and E. Y. Lu (1984) *Ceramic Eng. Sci. Proc.* **5**, 625.
- H. J. F. Jansen and J. V. Gardner (1985) *Physica* **115**, 10.
- L. Kaufmann and M. Cohen (1955) *Prog. in Metall. Phys.* **2**, 165.
- A. G. Khachaturyan (1983) *Theory of Structural Transformations in Solids*, Wiley, New York.
- H. Knapp and U. Dehlinger (1956) *Acta Metall.* **4**, 289.
- W. M. Kriven (1982) in *Proc. Intern. Conference on Solid-to-Solid Phase Transformations* (H. I. Aaronson, D. E. Laughlin, R. I. Sekerka and C. M. Wayman, eds.) AIME Pittsburgh, PA 1507.
- W. M. Kriven (1988) *J. Am. Ceram. Soc.* **71**, 1021.
- V. D. Krue (1983) *Phil. Mag.* **A48**, 695.
- J. C. Lambropoulos (1986) *J. Am. Ceram. Soc.* **69**, 218.
- F. F. Lange (1983) *J. Am. Ceram. Soc.* **66**, 396.
- F. F. Lange (1989) *J. Am. Ceram. Soc.* **72**, 1.
- V. Lanteri, T. E. Mitchell and A. H. Heuer, *J. Am. Ceram. Soc.* **69** (1986) 564.
- B. R. Lawn (1983) *J. Am. Ceram. Soc.* **66**, 83.
- E. Y. Lu and A. G. Evans (1987) *J. Am. Ceram. Soc.* **70**.
- W. Mader (1987) *Phil. Mag.* **A55**, 59.
- W. Mader and M. Rühle (1982) *Proc. 10th Int. Congr. Electron Microscopy* **2**, 103.
- D. B. Marshall, B. N. Cox and A. G. Evans (1985) *Acta Met.* **33**, 2013.
- D. B. Marshall, M. D. Drory and A. G. Evans (1983) in: *Fracture Mechanics of Ceramics Vol. 5* (Edited by R. C. Bradt, A. G. Evans, F. F. Lange and D. P. H. Hasselman) Plenum, New York pp. 289-307.
- D. B. Marshall and A. G. Evans (1985) *J. Am. Ceram. Soc.* **68**, 225.
- D. B. Marshall, A. G. Evans and M. D. Drory (1983) *Fracture Mechanics of Ceramics*, Vol. 6, pp. 289-307.
- D. B. Marshall, F. Morris and B. N. Cox (1989a), to be published.
- D. B. Marshall and W. Oliver (1987) *J. Am. Ceram. Soc.* **70**, 542.
- D. B. Marshall, M. Shaw, A. H. Heuer, M. Readey, R. O. Ritchie and R. H. Dauskardt (1989b), to be published.
- P. Mataga (1989) *Acta Metall.*, in press.
- L. N. McCartney (1987) *Proc. Roy. Soc.* **A409**, 329-350.
- R. M. McMeeking and A. G. Evans (1982) *J. Am. Ceram. Soc.* **65**, 242-247.
- J. J. Mecholsky and S. R. Powell (1982) *ASTM STP* 827.
- M. Morinaga, H. Adachi and M. Tsukuda (1982) *J. Phys. Chem. Solids* **44**, 301.
- T. Mura (1982) *Micromechanics of Defects*, Martinus Nijhoff, The Hague.
- M. S. Newkirk, A. W. Urquhart and H. R. Zwickler (1986) *J. Mat. Res.* **1**, 81.
- H. L. Oh and I. Finnie (1970) *Int. Jnl. Frac. Mech.* **6**, 287.

- G. B. Olson and M. Cohen (1981) *Ann. Rev. Mater. Sci.*, 11, 1; (b) *J. Physique* 43 (1982) C4-75.
- C. Pascual and P. Duran (1983) *J. Am. Ceram. Soc.* 66, 23.
- L. Pauling (1960) *Nature of Chemical Bond*, 3rd ed., Cornell University Press, Ithaca, NY.
- D. C. Phillips (1972) *Int. Mater. Sci.* 2, 1175.
- D. L. Porter and A. H. Heuer (1979) *J. Am. Ceram. Soc.* 62, 298.
- K. M. Prewé (1986) *Int. Mater. Sci.* 21, 3590.
- K. M. Prewé and J. J. Brennan (1982) *Int. Mat. Sci.* 17, 1201-1206.
- L. Reimer (1984) *Transmission Electron Microscopy*, Springer, Berlin.
- J. R. Rice (1968) in: *Fracture* (H. Liebowitz, ed.) Vol. 2 pp. 191, Academic Press, New York.
- J. R. Rice (1988) Harvard Univ. Report, MECH-116.
- R. W. Rice (1977) *Treatise On Materials Science and Technology II*, 199-381.
- R. W. Rice (1981) *Ceramic Engineering Science* 2, 661-701.
- L. R. F. Rose (1986) *J. Am. Ceram. Soc.* 69, 208.
- L. R. F. Rose (1987) *J. Mech. Phys. Solids* 35, 383.
- L. R. F. Rose and M. V. Swain (1986) *J. Am. Ceram. Soc.* 69, 208.
- M. Rühle, N. Claussen and A. H. Heuer (1986) *J. Am. Ceram. Soc.* 69, 195.
- M. Rühle, B. J. Dalgleish and A. G. Evans (1987a) *Scripta Met.* 21, 681-686.
- M. Rühle, A. G. Evans, R. M. McMeeking, P. G. Charalambides and J. W. Hutchinson (1987b) *Acta Metall.* 35, 2701.
- M. Rühle and W. M. Kriven (1983) *Ber. Bunsenges. Phys. Chem.* 87, 222.
- M. Rühle and W. M. Kriven (1982) in: *Proc. Intern. Conf. on Solid - to - Solid Phase Transformations* (H. I. Aaronson, D. E. Laughlin, R. F. Sekerka and C. M. Wagman, eds.) AIME Pittsburgh, PA 1569.
- M. Rühle, L. T. Ma, W. Wunderlich and A. G. Evans (1988) *Physica B* 150 86.
- M. Rühle, A. Srecker, D. Waidelich and B. Kraus (1984) *Adv. Ceram.* 12, 256.
- M. Rühle and M. Wilkens (1987) *Physical Metallurgy* 3rd ed. (R. W. Cahn and P. Haasen, eds.) North Holland, Amsterdam-Oxford-New York 713.
- V. K. Sarin (ed.) (1988) *Sc' lard Materials-3, Mat. Science and Eng.* A105/106 Elsevier Applied Science, London and New York.
- H. Schubert (1986) *J. Am. Ceram. Soc.* 69, 270.
- R. D. Shannley and C. T. Prewitt (1969) *Acta Cryst.* B25 925.
- L. S. Sigl and E. Exner, *Mat. Trans.* (1987) 18a, 1299.
- L. S. Sigl and A. G. Evans (1989) *Mechanics of Mtls.*, in press.
- L. S. Sigl and H. F. Fitzmeister (1988) *Acta Metall.* 36, 887.
- L. S. Sigl, F. Mataga, B. J. Dalgleish, R. M. McMeeking and A. G. Evans (1988) *Acta Metall.* 36, 945-953.
- D. K. Smith and C. F. Cline (1962) *J. Am. Ceram. Soc.* 45, 249.
- S. So'miya, N. Yamamoto, H. Hanagida (eds.) (1988) "Science and Technology of Zirconia III," *Advances in Ceramics* Vol 24a and 24b, The American Ceramic Society, Columbus, OH.
- J. C. H. Spence (1988) *Experimental High-Resolution Electron Microscopy*, 2nd ed., Oxford University Press, New York and Oxford.
- R. W. Steinbrech and A. H. Heuer (1986) *Mat. Res. Soc. Symp. Proc.* 60, 469.
- D. M. Stump and B. Budiansky (1989) Harvard University Report, MECH-138. (1989) Harvard University Report, MECH-138.
- E. C. Subbarao (1981) *Adv. Ceram.* 3, 1.
- T. Suzuki and M. Wuttig (1975) *Acta Metall.* 23, 1069.
- M. V. Swain (1985) *Acta Metall.* 33, 2083.

- M. V. Swain and L. R. F. Rose (1986) *J. Am. Ceram. Soc.* 69, 511.
- M. D. Thouless and A. G. Evans (1988) *Acta Metall.* 36, 517.
- M. D. Thouless, O. Sbaizero, L. S. Sigl and A. G. Evans (1989) *J. Am. Ceram. Soc.* 72, 525.
- R. K. Viswanadham, D. J. Rowcliffe and J. Gurland (eds.) (1983) *Science of Hard Materials*, Plenum Press, New York and London.
- E. E. Underwood (1970) *Quantitative Stereology*, Addison-Wesley, Reading, Mass..
- A. V. Virkar and R. L. K. Matsumoto (1986) *J. Am. Ceram. Soc.* 69 C-224.
- M. S. Weschsler, D. S. Lieberman and T. A. Read, *Trans.* (1953) *AIIME* 197, 1503.
- T. P. Weiss, C. M. Dick and W. D. Nix (1988) *MRS Symposium Proceeding*, Vol 120 pp. 247-252.
- G. M. Wolten (1964) *J. Am. Ceram. Soc.* 46, 418.
- F. Zandiehnam, R. A. Murray and W. Y. Ching (1988) *Physica* B150 19

M A T E R I A L S



WHISKER TOUGHENING; A COMPARISON BETWEEN Al_2O_3 AND Si_3N_3 TOUGHENED WITH SiC

G. H. Campbell, *M. Rühle, B. J. Dalgleish and A. G. Evans

Materials Department
College of Engineering
University of California, Santa Barbara
Santa Barbara, California 93106

(Presented at the 91st Annual Meeting of the American Ceramic Society,
Indianapolis, Indiana, April 25, 1989, Paper No. 57-SI-89)

* Now at Max-Planck-Institut für Metallforschung, Institut für
Werkstoffwissenschaft, Seestraße 92, D-7000 Stuttgart, FRG

ABSTRACT

Two whisker toughened materials have been subject to study, with the objective of identifying the mechanism that provides the major contribution to toughness. It is concluded that, for composites with randomly oriented whiskers, bending failure of the whiskers obviates pull-out, whereupon the major toughening mechanisms are the fracture energy consumed in creating the debonded interface and the stored strain energy in the whiskers, at failure, which is dissipated as acoustic waves. The toughening potential is thus limited. High toughness requires extensive pull-out and hence, aligned whiskers with low fracture energy interfaces.

KEY WORDS: Ceramic, Composite, Toughness, Model, TEM

1. INTRODUCTION

The toughening of ceramics by whiskers typically includes contributions from debonding, crack bridging, pull-out and crack deflection.¹⁻³ It is important to ascertain the relative roles of these contributions, because each mechanism predicts very different dependencies of toughness upon microstructure. Crack deflection is ostensibly governed only by whisker shape and volume fraction⁴; albeit that the relative elastic moduli and thermal expansion coefficients may have implicit effects on the deflection path. Conversely, the other contributions depend sensitively upon the mechanical properties of the interface, the whisker strength/toughness, the whisker radius and the volume fraction, as elaborated below.

Toughening by bridging is induced by debonding along whisker/matrix interfaces¹ (Fig. 1). The debonding allows the whiskers to remain intact within a small bridging zone behind the crack.¹ The magnitude of the toughening involves considerations of the debond extent and the mode of fiber failure, as well as of residual stress effects.^{1,5} Various attempts have been made to model the toughening and to compare the predictions with experiment. The most comprehensive and recent attempt⁶ established many of the salient features. However, neither residual stress effects nor the contribution to toughness from the energy of the debonded surfaces were included and, furthermore, explicit determination of the debond extent was not used for comparison between experiment and theory. The present article examines these and related issues by further experimental investigation and by presenting a fully inclusive model in a form that provides direct physical insight. For this purpose, crack/microstructure interactions are investigated in two whisker-toughened systems: the $\text{Al}_2\text{O}_3/\text{SiC}$ system which has interfaces subject to residual compression and $\text{Si}_3\text{N}_4/\text{SiC}$ with interfaces in residual tension.

2. SOME RELEVANT MECHANICS

2.1 INTERFACE DEBONDING

Cracks on bimaterial interfaces are characterized by a strain energy release rate, G , and a phase angle of loading, ψ .^{7,8} The latter is a measure of the mode mixity, such that $\psi = 0$ refers to a pure crack opening mode and $\psi = \pi/2$ represents an interface crack subject to crack surface shear. Specifically, debonding along the interface occurs when G reaches the interface fracture energy Γ_i at the relevant phase angle, ψ . For a matrix crack subject to mode I loading, the incidence of *initial debonding*, rather than cracking into the fiber, is found to be governed by the ratio of interface to fiber fracture energies Γ_i/Γ_f and the whisker orientation (Fig. 2).⁸ For the present composites, values of Γ_i/Γ_f needed to debond whiskers normal to the crack plane should be either $< 1/3$ for $\text{Si}_3\text{N}_4/\text{SiC}$ or $< 1/4$ for $\text{Al}_2\text{O}_3/\text{SiC}$. Note that this prediction is *independent* of the residual stress.

Growth of the initial debond along the interface is influenced by additional variables, such as the residual stress and the whisker radius. Debond growth is most prevalent in the crack wake.^{9,10} Analysis of wake debonding for interfaces under *residual tension*⁹ indicates that debond growth in the wake occurs when the stress t on the fiber reaches a critical value t^* , given by,

$$t^* = 2.2E_f e_T \quad (1)$$

where E_f is Young's modulus for the fiber and e_T is the misfit strain. When $t > t^*$, the debond propagates unstably up the interface.

Residual compression results in different behavior. In this case, G is strongly influenced by the friction coefficient μ along the previously debonded interface.¹⁰ The basic debonding features indicate that again, a threshold stress must be exceeded

before debonds can further propagate in the wake. However, for stresses in excess of the threshold, debonding occurs stably to an extent determined by the friction coefficient μ and the residual strain, until $t \rightarrow E_f e_T / v$ (with v being Poisson's ratio for the fiber), whereupon the interface separates and further debonding occurs unstably. The debonding behavior is thus sufficiently complex that prediction of trends with e_T , Γ_i and other material variables is unlikely to be instructive. Instead, the preceding results may be used as the mechanics background needed to facilitate interpretation of observed trends in debonding, as elaborated below.

2.2 TOUGHENING

The steady-state toughening ΔG_c imparted by whiskers can be considered to have four essential contributions, as elaborated in the Appendix. These contributions can be insightfully expressed in the simple form (Fig. 3);

$$\Delta G_c / f d \sim S^2 / E - E e_T^2 + 4(\Gamma_i / R) / (1 - f) + (\tau / d) \sum_i (h_i^2 / R) \quad (2)$$

where d is the debond length, R the fiber radius, f the volume fraction and S the whisker "strength." The first term S^2/E is simply the *strain energy stored* in the whisker *over the debonded length* on both sides of the matrix crack, before the whisker fails ($S^2/2E$ on either side of the crack). This strain energy *dissipates* as acoustic waves and thus contributes *positively* to the toughening. The second term is the *residual strain energy* in each composite element *within the debond length*, as governed by the misfit strain e_T . This strain energy is *lost* from the system when the fiber fails and thus, *detracts* from the toughness, independently of the sign of e_T . The third term is the energy needed to create the *debond fracture surface*, with Γ_i

being the fracture energy per unit area. This term must be *positive*. The last term is the *pull-out contribution*, with h_i being the pull-out length and τ the sliding resistance of the debonded interface. This term is again positive, because heat is generated by the frictional sliding at the interfaces. The above result is all inclusive and has not been specifically presented elsewhere.† Furthermore, it deviates from certain of the other results reported in the literature for each of the individual terms, principally in the magnitude of the constants of proportionality. It is believed that Eqn. (2) is the simplest possible result that is also physically consistent with the mechanisms involved.

Optimization of toughness based on these terms is discussed later. Presently, it is noted that all contributions scale with the debond length d , indicating that large d is desirable. However, it is also recognized that d should have a functional dependence,

$$d/R = F(\Gamma_i, e_T, S) \quad (3)$$

where the function F has yet to be determined.

The present experimental results are examined using Eqn. (2) to assess the various contributions to toughness, based on direct measurements of h , d , R , f . Thereafter, implications for high toughness are discussed.

† The results are strictly applicable to reinforcements *normal to the crack plane*. Whiskers inclined to the crack are more likely to fail by bending and thus, result in smaller pull-out toughening.

3. MATERIALS

Four basic materials have been used for the present investigation: two whisker toughened materials and two reference matrix materials. One whisker toughened material is a commercial product, consisting of Al_2O_3 toughened with 20 vol. % SiC whiskers, prepared by hot pressing*. The other toughened material was a SiC toughened Si_3N_4 ** containing 20 vol. % SiC whiskers, 4 wt-% Y_2O_3 as a sintering aid and was densified by reaction bonding followed by HIPing. Microstructural investigations were performed, not only for the composites, but also for the matrices and those observations were used as reference. The Al_2O_3 matrix material was a hot pressed system containing 1/4 volume percent MgO, heat treated to create the corresponding grain size. The reference Si_3N_4 ** contained 4 wt % Y_2O_3 .

The mode I toughnesses G_c of the four materials, evaluated using a surface flaw technique,¹ are summarized in Table I. A comparison with models requires evaluation of the increase in toughness caused by the whiskers, ΔG_c , which for $\text{Al}_2\text{O}_3/\text{SiC}$ is 40–80 Jm^{-2} and for $\text{Si}_3\text{N}_4/\text{SiC}$ is 25–55 Jm^{-2} (Table I).

4. CHARACTERIZATION

4.1 MICROSTRUCTURE OF WHISKERS

Characterization of two different as-received SiC whiskers*** indicated a broad distribution of length (1 μm ... 25 μm) and diameter (0.1 μm to 1.0 μm). Quite frequently, clusters of whiskers and irregular, serrated-edged whiskers were found.

* Greenleaf, Inc.

** Norton Company

*** ARCC and Tateho whiskers

The average length and diameter were $17.5\mu\text{m}$ and $0.5\mu\text{m}$, respectively, for ARCO whiskers and $11.7\mu\text{m}$ and $0.42\mu\text{m}$ for Tateho whiskers.

The whiskers had a high density of planar faults lying on the close-packed plane (basal plane) perpendicular to the long axis.¹² The faults resulted in a complex arrangement in thin lamellae of different α and β polytypes normal to the whisker axis. Furthermore, the core region of the ARCO whiskers contained a high density of small spherical impurity clusters and/or cavities. Half of the Tateho whisker are hollow. The outer skin of both types of whiskers was covered with a 2nm SiO_2 rich layer as revealed by defocus imaging (Fig. 4a)¹³ and X-ray photoelectron spectroscopy (Fig. 6b).¹⁴

4.2 MICROSTRUCTURE OF THE COMPOSITES

Thin foils of each of the materials suitable for TEM have been prepared by mechanical polishing and dimpling followed by ion beam thinning. Transmission electron microscope (TEM) characterization of the materials has been accomplished using conventional, analytical and high resolution microscopy. From conventional TEM micrographs of the *SiC whisker toughened Al_2O_3 material*, a matrix grain size of $\sim 1\mu\text{m}$ was determined. Dark field studies¹⁵ have indicated the presence of a thin ($< 5\text{nm}$ thickness) amorphous layer at the interface between the whiskers and the matrix, consistent with previous studies. The thickness of the amorphous layer at the whisker/matrix interface depends on the purity of the Al_2O_3 . However, even in Al_2O_3 -SiC composites processed using ultraclean materials,¹⁶ a thin (1nm -thick) SiO_2 layer can be detected by TEM imaging. Specifically, by using a range of defocus conditions^{13,15} (Fig. 5), the expected contrast reversal for different signs of defocusing can be observed. Furthermore, it is apparent that the contrast at the interface is not caused by preferential etching. Notably, the interface between the

whiskers and the Al_2O_3 matrix in Fig. 5 is perpendicular to the edge of the foil and no preferential etching is visible close to the amorphous region near the edge, because the interface contrast disappears gradually in the amorphous part of the specimen.† Occasionally, amorphous pockets also exist at junctions between matrix grain boundaries and the interface (Fig. 5b). However, within the resolution of dark field and high resolution procedures ($\sim 1\text{nm}$), the matrix grain boundaries appear to be devoid of amorphous material.

Occasionally, a whisker is completely embedded in *one* Al_2O_3 grain. In such cases, strain contours become visible under dynamical TEM imaging (Fig. 6). A semi-quantitative evaluation of the strain perpendicular to the whisker diameter is possible by calculating the scattering of modified Bloch waves¹⁷ in the thick foil approximation and evaluating the number and distance of contrast oscillations for different excitation errors. The observations confirm that a homogeneous compressive strain ϵ occurs in the whisker, with $2 \cdot 10^{-3} < \epsilon < 6 \cdot 10^{-3}$: a result consistent with the known thermal expansion characteristics of Al_2O_3 and SiC and a cooling range $\Delta T \approx 1000^\circ\text{C}$.

Studies conducted on the Si_3N_4 reference material have revealed several relevant microstructural features. Dark field and high resolution microscopy have indicated that an intercrystalline phase, presumably amorphous, is present as a thin continuous film of equilibrium thickness (Fig. 7a). Grain pockets are mostly crystalline, except for the thin, intercrystalline outer layer (Fig. 7b). Analytical microscopy and diffraction studies are consistent with $\alpha\text{-Y}_2\text{Si}_2\text{O}_7$ being the predominant crystalline grain boundary phase. The crystalline pockets are typically 50–100nm in diameter. The whisker toughened Si_3N_4 had several different characteristics. The whiskers are typically 100–500nm in diameter. About half of the

† A hole would be visible at the site of the interface for the case of preferential thinning.

whiskers are hollow, in which case they become filled by the sintering-aid phase. This phase, which is also present at grain pockets, remains glassy upon cooling to room temperature. Analytical microscopy indicates a relatively high SiO_2 content in this phase. Presumably, the excess SiO_2 that prevents crystallization of this phase is introduced by the oxide layer that preexists on the SiC whiskers. High resolution microscopy shows that this intercrystalline phase is present as a thin film at *all* Si_3N_4 grain boundaries and, most importantly, at the interface between the Si_3N_4 grains and the SiC whiskers (Fig. 7c).

Finally, in order to clarify ambiguity, it is noted that it has been occasionally reported in the literature that *no* glassy phase can be observed at interfaces between SiC whiskers and the surrounding matrix.¹⁸ A careful inspection of available micrographs¹⁸ suggests that the interface plane in such studies was inclined to the electron beam, whereupon the glassy interphase would not be detected. Specifically, it is evident from Fig. 8 that an amorphous interface layer can only be imaged if the foil thickness t is such that $t \leq \sqrt{aD/2}$, with a being the thickness of the amorphous foil and D the diameter of the whiskers and if the interface is parallel to the electron beam.

4.2 DEBONDING AND BRIDGING

i) Transmission Electron Microscopy

Observations of debonding and of bridging zones have been made in the TEM. The procedure developed for studying these characteristics consists of indenting the material, mechanically dimpling in the region of the indentation crack tips and then ion thinning to a thickness in excess of the whisker diameter. This procedure ensures debonding and bridging representative of plane strain crack propagation in bulk material and avoids the anomalous crack extension and

debonding that can occur upon thinning to less than the whisker diameter. In order to use these foils to investigate near tip phenomena, it is imperative that the specimens be subject to tilting through a large angular range, because the debond and matrix crack opening displacements are small and only detectable when the electron beam is essentially aligned with the crack plane. Some typical views of the bridge zone with schematic drawings used to highlight the salient features.

For $\text{Al}_2\text{O}_3/\text{SiC}$, the matrix cracks are mostly transgranular and conchoidal, while cracks in the whiskers are planar and always parallel to the basal plane of SiC. These distinctive fracture paths facilitate interpretation of the micrographs. The series of micrographs and schematical drawings summarized in Fig. 9 illustrate the salient features. Locations A and B refer to the crack/whisker interaction, which include whiskers having axis either normal or inclined to the crack plane. In both cases, the whiskers are debonded and are fractured. Near the crack tip (location C), a bridging zone with intact whiskers is apparent, with the crack tip located at the arrow. Tilting studies have revealed the extent of debonding at the whisker/matrix interface as illustrated in the accompanying schematic (Fig. 9d). Such observations are typical of whiskers that exist within a bridging zone that usually extends to about 4 to 6 whisker spacings. *The length of the debonds is variable and ranges between about $2R$ and $6R$, R being the whisker radius.*

For $\text{Si}_3\text{N}_4/\text{SiC}$, the same general features noted for Al_2O_3 are again evident, as exemplified by Fig. 10a, wherein the debonds are between the arrows. The lengths of these debonds, which can be measured directly from the micrograph, range from R to $3R$. Usually, the second whisker behind the crack tip is fractured, indicating that the bridging zone is very small. It is also noted that, because elongated Si_3N_4 grains are present, debonding along the grain boundaries with the equiaxed matrix grains is evident (Fig. 10b). Such debonding is exactly analogous to that occurring at whisker interfaces. Consequently, the debonds of the whisker interface are more

difficult to detect than in the Al_2O_3 composite. An interesting sequence of events can be deduced from Fig. 10c, in which the main crack is clearly visible (large white gap). This crack propagated from the upper right to the lower left. It is surmised that, when the crack first interacted with the whisker, the interface debonded (to a length of about 3 whisker radii). The whisker then fractured within the debond length and pulled out by about 20nm (the width of the gap). While being pulled out, the whisker would be subject to bending, resulting in enhanced stresses, as manifest in strain fringes at the corner of the whisker (arrow in Fig. 10c). Consequently, the whisker fractured a second time in the plane of the matrix crack.

It is also of importance to examine whisker failure. In general, whisker fracture can either initiate at the end of the debond by kinking into the whisker,⁵ or the debond cracks could remain at the interface such that the whisker fails by the propagation of a pre-existing flaw within the debonded length. The former mode has been rigorously verified in several cases (Figs. 9 and 10) by extensive tilting to confirm the absence of a debonded region beyond the location of the whisker fracture. The latter is much more difficult to unambiguously identify and cannot be substantiated at this juncture.

ii) Scanning Electron Microscopy

Polished surfaces containing indentation cracks have been examined in the scanning electron microscope. The residual crack opening allows observation of some aspects of bridging and debonding. For the $\text{Al}_2\text{O}_3/\text{SiC}$, a low accelerating voltage provides contrast between the Al_2O_3 and SiC and facilitates observation. Within the spatial resolution of the SEM, *debonds* are only occasionally evident, usually at intact inclined whiskers (Fig. 11a) remote from the crack front. Crack surface interlocking is also evident (Fig. 11b), caused by debonding around the

whisker ends. In some cases, whisker cracks are apparent (Fig. 11a), again at inclined whiskers, with the crack often forming near the end of the debond. Measurements of bridging zones associated with intact whiskers are not possible by direct SEM, because of resolution limitations. However, for $\text{Al}_2\text{O}_3/\text{SiC}$, use of a dilute orthophosphoric acid etch allows dissolution of some of the matrix, preferentially around the crack (Fig. 12). Matrix removal permits both the intact (Fig. 12b) and fractured whiskers (Fig. 12c) to be identified, with reference to the crack front and thus, allows measurement of the bridging zone size, L . For this composite, L is about 3 to 4 whisker spacings.

Inspection of fracture surfaces by SEM provides complementary information regarding *pull-out* as well as debonding (Fig. 13). Studies on both composites reveal that inclined whiskers fracture on a plane normal to the whisker axis, such that the crack-surface is within one whisker radius of the matrix crack plane. *Pull-out* is thus negligible.

5. COMPARISON BETWEEN THEORY AND EXPERIMENT

Initial comparison between theory and experiment can be achieved based on measured values of the debond length and using Eqn. (2) for the toughness. The relative magnitudes of the four contributions to toughness from elastic bridging, residual strain, debond surface energy and pull-out can then be readily assessed, using the material properties listed in Table I and using $d/R = 2-6$ for Al_2O_3 and 1-3 for Si_3N_4 with $f = 0.2$ and $R = 0.25\mu\text{m}$ for both composites. The *pull-out* contribution is negligible since only a small fraction of whiskers exhibit this phenomenon. The reduction in toughness from the *residual strain*, Ee_f^2fd , ranges between 0.3 Jm^{-2} for $\text{Si}_3\text{N}_4/\text{SiC}$ to 2 Jm^{-2} for $\text{Al}_2\text{O}_3/\text{SiC}$ and is thus of negligible

importance (in part, accounting for the similar toughening levels measured for both composites). The toughening contribution from the *elastic strain energy* stored in the whiskers up to failure, $S^2 \ell d / E$, is dominated by the choice of whisker "strength." The appropriate choice for S is unclear because the "gauge length" is small and because the whiskers may be subject to degradation upon composite processing. For initial purposes, it is *assumed* that S is in the range 4–8 GPa,⁶ whereupon this component of toughening is at most 45 Jm⁻² for Al₂O₃/SiC and 25 Jm⁻² for Si₃N₄/SiC. Finally, the *debonding energy* contribution is estimated by noting that amorphous silicates have a fracture energy, $\Gamma_1 = 6-8$ Jm⁻². The toughening caused by debonding is then of order 50 Jm⁻² for Al₂O₃/SiC and 25 Jm⁻² for Si₃N₄/SiC. The energy needed to create the debond surface and the strain energy dissipated from elastic bridging thus appear to provide similar contributions to toughness. Furthermore, the toughness level provided by the combination of both processes is comparable to the measured values (Table I).

6. IMPLICATIONS AND CONCLUSIONS

The preceding experiments and calculations firstly indicate that *non-aligned*, inclined whiskers typically fail by bending and do not provide a pull-out contribution to toughening.* Consequently, composites with *randomly oriented whiskers cannot normally be expected to exhibit high toughness*. Subject to this limitation, useful toughness increases are still possible, as governed by an optimum combination of bridging and debonding. Since residual strain is invariably detrimental, *matched thermal expansions are desirable*. *Enhanced debonding* is also

* An exception may be graphite whiskers which can sustain very high bending strains and have debonded interfaces with a low sliding resistance.

desirable, but then the relative contributions to toughness from bridging and from the debonded surfaces requires further elaboration. The debond length is expected to scale directly with the whisker radius, to increase with increase in S and to depend inversely on Γ_i (Eqn. 3). Consequently, d/R and Γ_i are coupled in such a way that the contribution to ΔG_c from the *energy of the debonded surfaces* is expected to be weakly dependent on Γ_i and *insensitive to whisker radius*, but should increase as the *whisker strength* increases. A corresponding assessment of the *bridging contribution* yields very different conclusions. In this case, the direct dependence on debond length suggests that this contribution should *increase* appreciably as either Γ_i *decreases* or the *whisker radius increases* and should become the dominant contribution to toughness for small Γ_i and large R , provided that the "strength" S is also high. Indeed, it is important to note that careful experiments⁶ indicate a systematic dependence of ΔG_c on R , confirming an important contribution of elastic bridging to toughening. However, the whisker "strength" is not related in simple form to the uniaxial fracture strength of the whiskers. Further research is needed to understand the operative relationships.

The factors which govern the *debond length* merit brief additional consideration. While small Γ_i and large S clearly enhance debonding, such variables as residual strain, surface roughness and friction coefficient could be important. The available calculations (Appendix) indicate that, when the non-dimensional residual strain parameter Q ($= Sv/E_f|e_T|$) is much larger than unity, the Poisson contraction of the whisker is large compared with the misfit displacements. Then, residual strain is unimportant: instead, the amplitude of the roughness on the debond surface dominates debonding. Conversely, when $Q < 1$, residual strain effects dominate debonding in the sense that positive e_T (interface tension) enhances debonding and vice versa. For the present materials, the inverse trend with residual strain (*large* debond lengths for Al_2O_3/SiC in which e_T is

negative) suggests that roughness effects and interface characteristics are more important in debonding than the residual strain. Indeed, consistent with this implication, Q is larger than unity. Whisker roughness effects would thus appear to merit further investigation.

APPENDIX

CRACK BRIDGING AND TOUGHNESS

Several aspects of crack bridging have been addressed by analysis, particularly the stress/crack opening relation $t(u)$. For whiskers *normal* to the crack plane with interfaces subject to *residual tension*, u/t is linear when the debond length is constant and a threshold stress is needed to achieve initial opening of the crack, such that⁹

$$u/R e_T = (t/E_T e_T) (\lambda_1 + \lambda_2 d/R) + \lambda_3 + \lambda_4 d/R \quad (A1)$$

where λ_i ($i = 1-4$) are coefficient tabulated in Table II. When the whiskers fail at a critical axial stress $t = S$, the change in toughness imparted by the whiskers, ΔG_c , when d is fixed, becomes;¹¹

$$\begin{aligned} \Delta G_c &= 2f \int_0^{t=S} t du + 4f \Gamma_1 d/(1-f)R \\ &= \frac{f S^2 R [(\lambda_1 + \lambda_2 d/R)^2 - (E_T e_T/S)^2 (\lambda_3 + \lambda_4 d/R)^2]}{E (\lambda_1 + \lambda_2 d/R)} + 4f \Gamma_1 d/(1-f)R \end{aligned} \quad (A2)$$

The first term is the contribution to toughness from elastic bridging, whereas the second term is the contribution from the debond surface energy. When $d/R \gg 1$ and the material is elastically homogeneous, Eqn. (A2) reduces to

$$\Delta G_c \approx \frac{f S^2 d}{E} [1 - (E e_T/S)^2] + 4f \Gamma_1 d/(1-f)R \quad (A3)$$

revealing that the toughness increases linearly with increase in the debond length and diminishes as the residual strain increases. Indeed, $\Delta G_c \rightarrow 0$ as $E_f |e_T| \rightarrow S$ because then, the whiskers fail upon cooling from the processing temperature.

For composites containing whiskers normal to the crack and with interfaces in residual compression, $t(u)$ is dependent on the friction coefficient as well as the debond length. For fixed d ,¹⁰

$$\frac{u}{e_T R} = (d/R)(1+\nu)/\nu - (1-\nu F)(1-2\nu^2\phi) [\exp(2\mu d\phi/R) - 1]/2\mu\phi\nu \quad (A4)$$

where

$$\phi = \nu(1-f+f\Sigma)/[\Sigma(1+f)+(1-f)(1-2\nu)]$$

and $\Sigma = E_f/E_m$, with E_m being the matrix modulus.

For homogeneous elastic properties, Eqn. (A4) reduces to;

$$\frac{u}{e_T R} = (1+\nu)d/R - (1-\nu F) [\exp(D) - 1]/\mu\nu \quad (A5)$$

where $D = \mu\nu d/R$. The toughness for constant d is thus;¹⁰

$$\Delta G_c = \frac{fS^2R[\exp(D)-1]}{\mu\nu E} \left\{ 1 - \left(\frac{e_T E}{\nu S} \right)^2 \left[\frac{(1+\nu)D}{\exp(D)-1} - 1 \right]^2 \right\} + 4f\Gamma_1 d/(1-f)R \quad (A6)$$

Furthermore, for small μ , the toughness reduces to Eqn. (A3).

The above results for ΔG_c are clearly simplifications because the debonds are expected to extend in the crack wake and the integral should include this behavior.

Subject to this limitation, it is apparent that, for brittle whiskers which fail at a characteristic stress, S , the composite toughness invariably decreases with increase in misfit strain, e_T , whether tensile or compressive in sign, provided that the debond length is independent of e_T . Furthermore, when the friction coefficient is small, the toughness is also essentially independent of the sign of the residual stress.

TABLE I
Properties of Materials and Constituents

Material	$\alpha(\text{C}^{-1} \times 10^6)$	E(GPa)	$G_c(\text{Jm}^{-2})$	$\Delta G_c(\text{Jm}^{-2})$	
				Experiment	Theory
Al_2O_3	7.5	400	25 ± 5		
Si_3N_4	3.5	320	50 ± 10		
SiC	4.5	420	15 ± 5		
Amorphous Silicate Interphase	—	100	7 ± 1		
$\text{Al}_2\text{O}_3/\text{SiC}$		420	85 ± 15	60 ± 20	~ 80
$\text{Si}_3\text{N}_4/\text{SiC}$		350	90 ± 15	40 ± 15	~ 30

TABLE II

The Coefficients $\lambda_i (i = 1, 4)$, used in the expression for the Matrix Crack Opening:
 $\Sigma = E_f/E_m$

$\lambda_1(\Sigma, f)$								
$\Sigma \backslash f$	0.05	0.1	0.2	0.3	0.4	0.5	0.6	0.7
0.4	3.22	3.42	2.04	1.76	1.55	1.40	1.28	1.19
1.0	1.85	1.96	1.30	1.14	1.00	0.87	0.75	0.63
2.5	0.96	1.01	0.72	0.64	0.57	0.49	0.41	0.30

$-\lambda_3(\Sigma, f)$								
$\Sigma \backslash f$	0.05	0.1	0.2	0.3	0.4	0.5	0.6	0.7
0.4	2.59	2.75	1.64	1.42	1.25	1.12	1.03	0.95
1.0	1.73	1.84	1.23	1.07	0.94	0.81	0.70	0.59
2.5	1.05	1.11	0.79	0.71	0.62	0.54	0.44	0.33

Σ	$\lambda_2(\Sigma)$	$-\lambda_4(\Sigma)$
0.4	0.838	1.062
1.0	0.910	1.058
2.5	0.964	1.043

REFERENCES

- [1] M. Rühle, B. J. Dalgleish and A. G. Evans, *Scr. Metall.* 21 (1987) 681.
- [2] P. F. Becher and G. C. Wei, *J. Am. Ceram. Soc.* 67 (1984) C267.
- [3] P. Becher, *Mtls. Sci. Eng.*, in press.
- [4] K. T. Faber and A. G. Evans, *Acta Met.* 31 (1983) 565.
- [5] D. B. Marshall and A. G. Evans, *Materials Forum*, 11 (1988) 304.
- [6] P. F. Becher, C. H. Hsueh, P. Angelini and T. N. Tiegs, *J. Am. Ceram. Soc.* 71 (1988) 1050.
- [7] J. R. Rice, *J. Appl. Mech.* 110 (1988) 98.
- [8] M. He and J. W. Hutchinson, *Jnl. Appl. Mech.*, in press.
- [9] P. G. Charalambides and A. G. Evans, *Jnl. Am. Ceram. Soc.*, in press.
- [10] L. S. Sigl and A. G. Evans, *Mechanics of Materials*, in press.
- [11] P. G. Charalambides, to be published.
- [12] S. R. Nutt, *J. Am. Ceram. Soc.* 67 (1984) 428.
- [13] L. Reimer, *Transmission Electron Microscopy*, Springer Berlin (1986) p. 201.
- [14] V. K. Sarin and M. Rühle, *Composites* 18 (1987) 129.
- [15] D. R. Clarke, *Ultramicroscopy* 4 (1979) 33.
- [16] J. R. Porter, unpublished.
- [17] M. Wilkens and M. Rühle, *phys. stat. sol.(b)* 49 (1972) 749.
- [18] W. Braue, R. W. Carpenter and D. J. Smith, *Proc. 46th EMSA Conference*, San Francisco Press, Inc. (1988) P. 734.

FIGURE CAPTIONS

- Fig. 1. A schematic of a bridging zone in a reinforced composite
- Fig. 2. A debond diagram: the dependency of fracture energy on elastic mismatch and whisker orientation
- Fig. 3. A schematic representation of the four mechanisms that contribute to toughening by whiskers
- Fig. 4. Analysis of outer layer on a Tateho SiC whisker
- a) Through-focus images at the edge of a whisker (i) $\Delta f < 0$, (ii) $\Delta f = 0$, (iii) $\Delta f > 0$. The amorphous layer is clearly visible on the infocus image ($\Delta f = 0$). The defocus images indicate that the density (scattering power) of the outermost layer is less than that of SiC (bright contrast for negative defocusing)
 - b) XPS spectrum (courtesy Sarin and Rühle¹⁴)
- Fig. 5. TEM micrograph of interface between SiC whisker and Al_2O_3 matrix (i) $\Delta f = -96\text{nm}$, (ii) $\Delta f = 0$, (iii) $\Delta f = 96\text{nm}$. The interface is parallel to the electron beam. The contrast of the amorphous grain boundary phase is equivalent to that of the amorphous layer at the edge of the foil.
- Fig. 6. Stress contours around whiskers: dynamical
- a) Bright field and b) Dark field images. A quantitative evaluation the matrix strain can be obtained from the number and positions of contrast oscillations (micrograph taken by E. Bischoff)
- Fig. 7. Transmission electron microscopy study of Si_3N_4 materials
- a) High-resolution image revealing continuous thin amorphous layer in the matrix
 - b) High-resolution image of the interface of the crystalline phase at the matrix grain pockets and a Si_3N_4 grain
 - c) High-resolution image of the amorphous layer between a matrix grain and a SiC whisker
- Fig. 8. Maximum allowed thickness, t , for imaging at amorphous layer of thickness a

Fig. 9. Transmission electron microscopy studies of the crack tip region in thick foils of $\text{Al}_2\text{O}_3/\text{SiC}$. A comprehensive visualization of debonding and cracking can only be achieved by imaging under different orientations by extensive tilting. Consequently, to assist in summarizing the behavior, a schematic drawing is shown in addition to *one* TEM micrograph of each crack/whisker interaction:

- a) Overview of crack tip region
- b) Region A with schematic 3-dimensional drawing
- c) Region B with schematic 3-dimensional drawing
- d) Region C bridging zone with schematic overview. The debonded interface zones between whiskers and matrix are hatched. The whiskers are not fractured.

Fig. 10 a) Transmission electron micrograph of a region close to crack tip in $\text{SiC}/\text{Si}_3\text{N}_4$. On the micrograph, the crack enters from the lower left and ends at the position of the uppermost arrow. Debond cracks are between arrows along the interfaces.

- b) Transmission electron micrograph of $\text{Si}_3\text{N}_4/\text{SiC}$ indicating grain boundary debonding in the matrix between an elongated grain and equiaxed grains
- c) Transmission electron micrograph of a multiply-fractured whisker well into the crack wake

Fig. 11. Scanning electron microscope image of the crack tip region in $\text{Al}_2\text{O}_3/\text{SiC}$

- a) Initiation of a whisker crack from the end of an inclined debond
- b) Debonding around the whisker end resulting in crack surface interlocking

Fig. 12. SEM investigation of a crack in $\text{Al}_2\text{O}_3/\text{SiC}$ after etching in orthophosphoric acid

- a) Overview
- b) Crack tip region showing intact whiskers

Fig. 13. Scanning electron microscope image of fracture surface of $\text{Si}_3\text{N}_4/\text{SiC}$

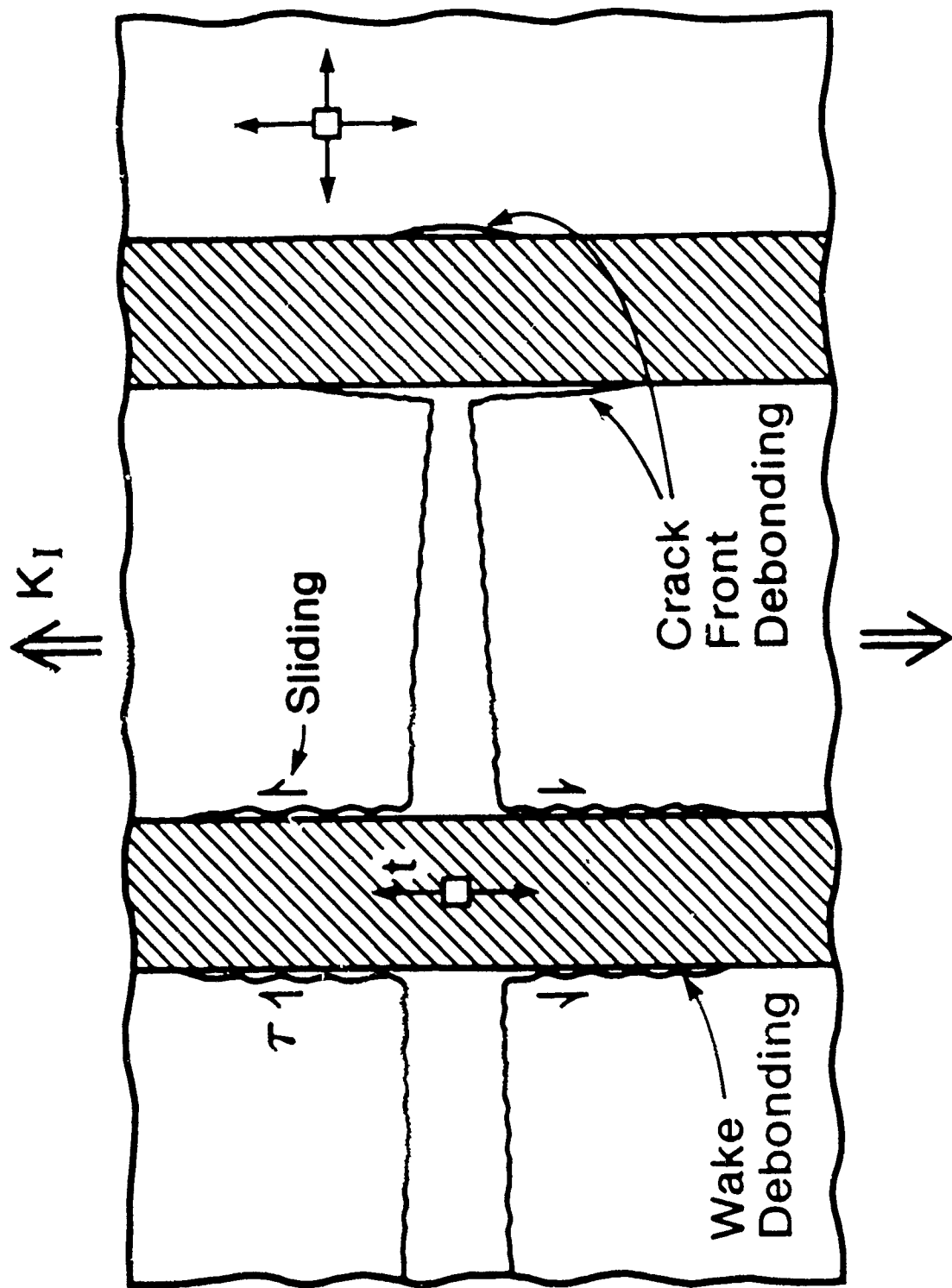


Figure 1

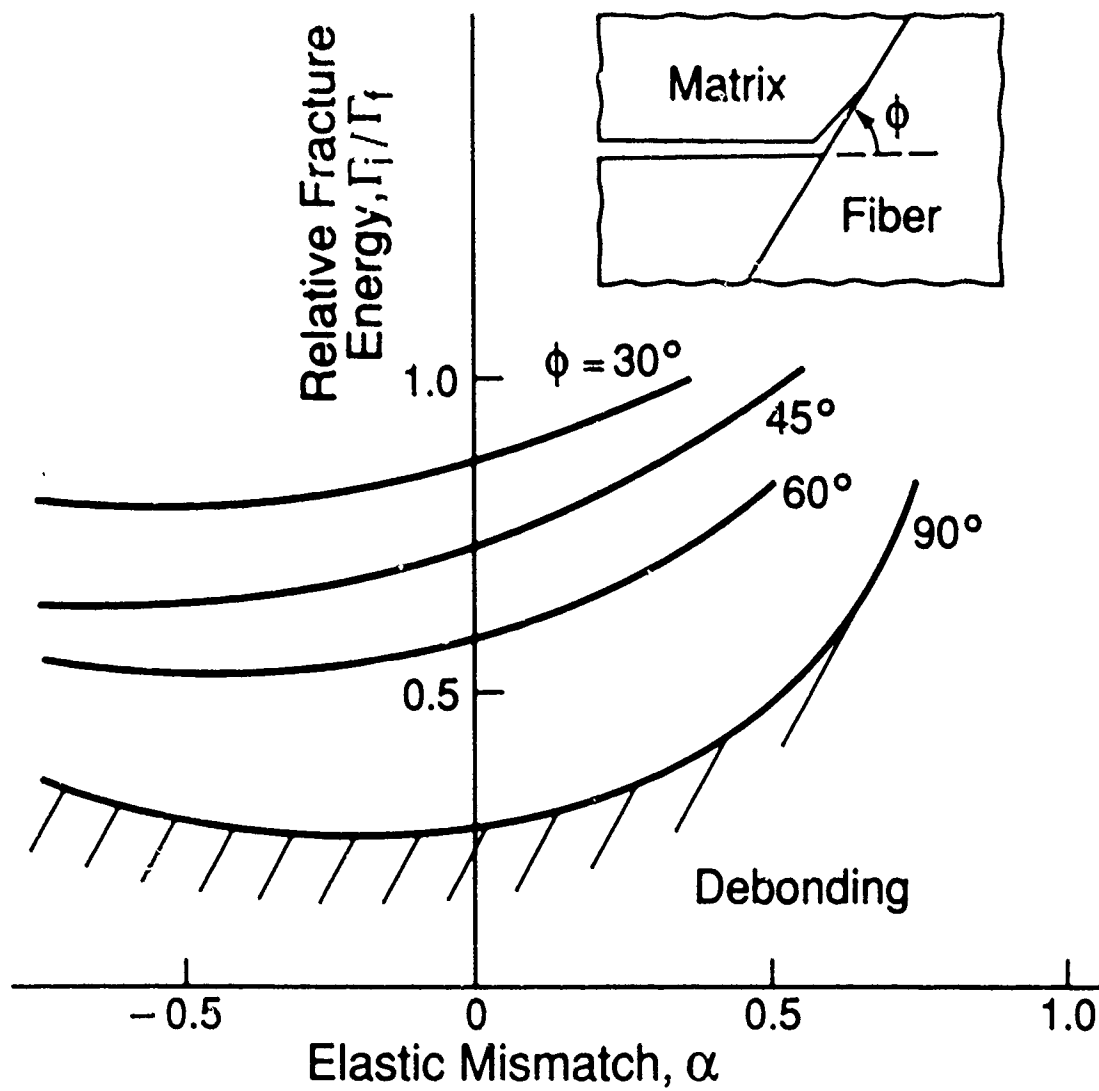


Figure 2

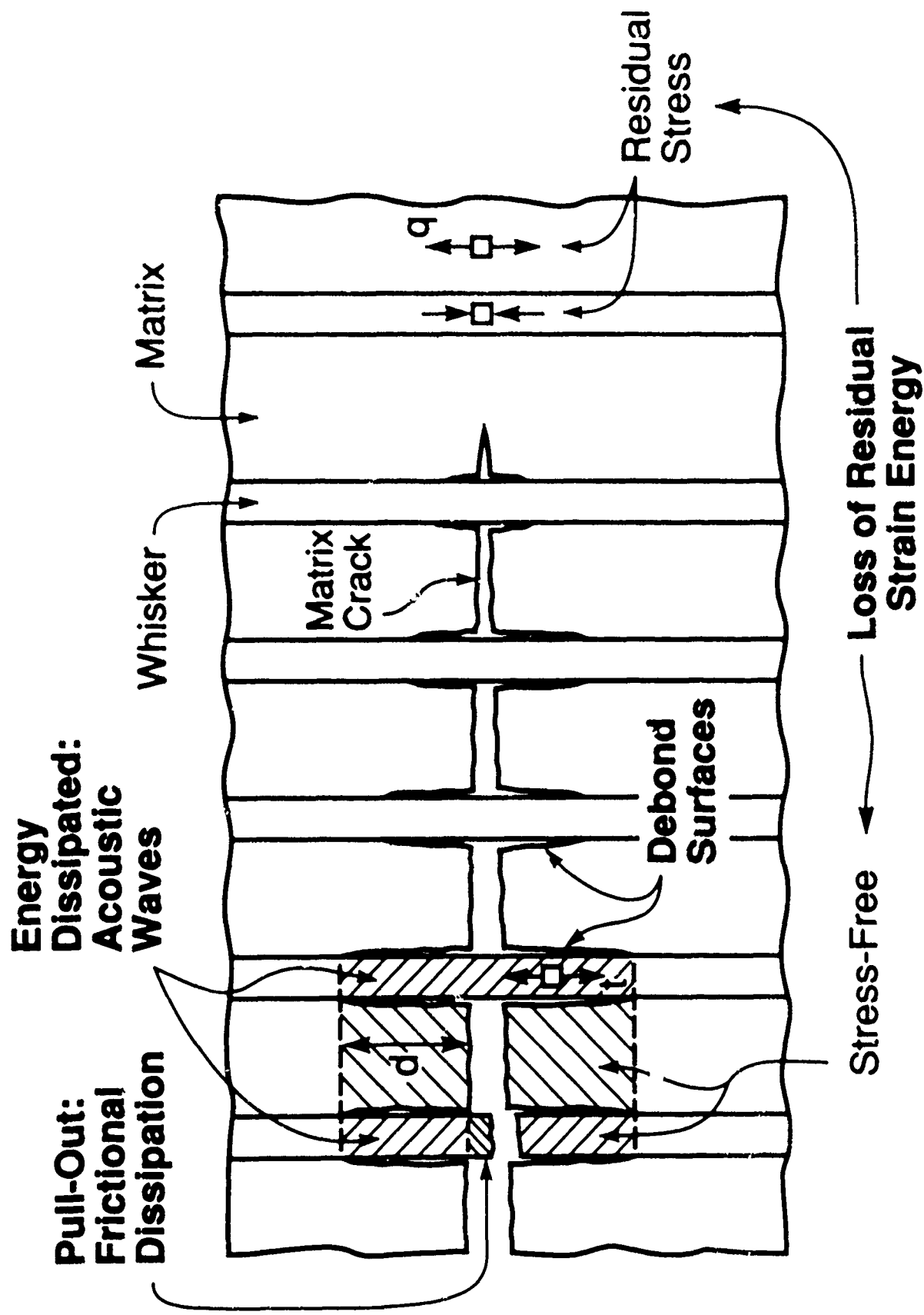


Figure 3

Sic Whisker

(i)

(ii)

(iii)

20 nm

Figure 4a

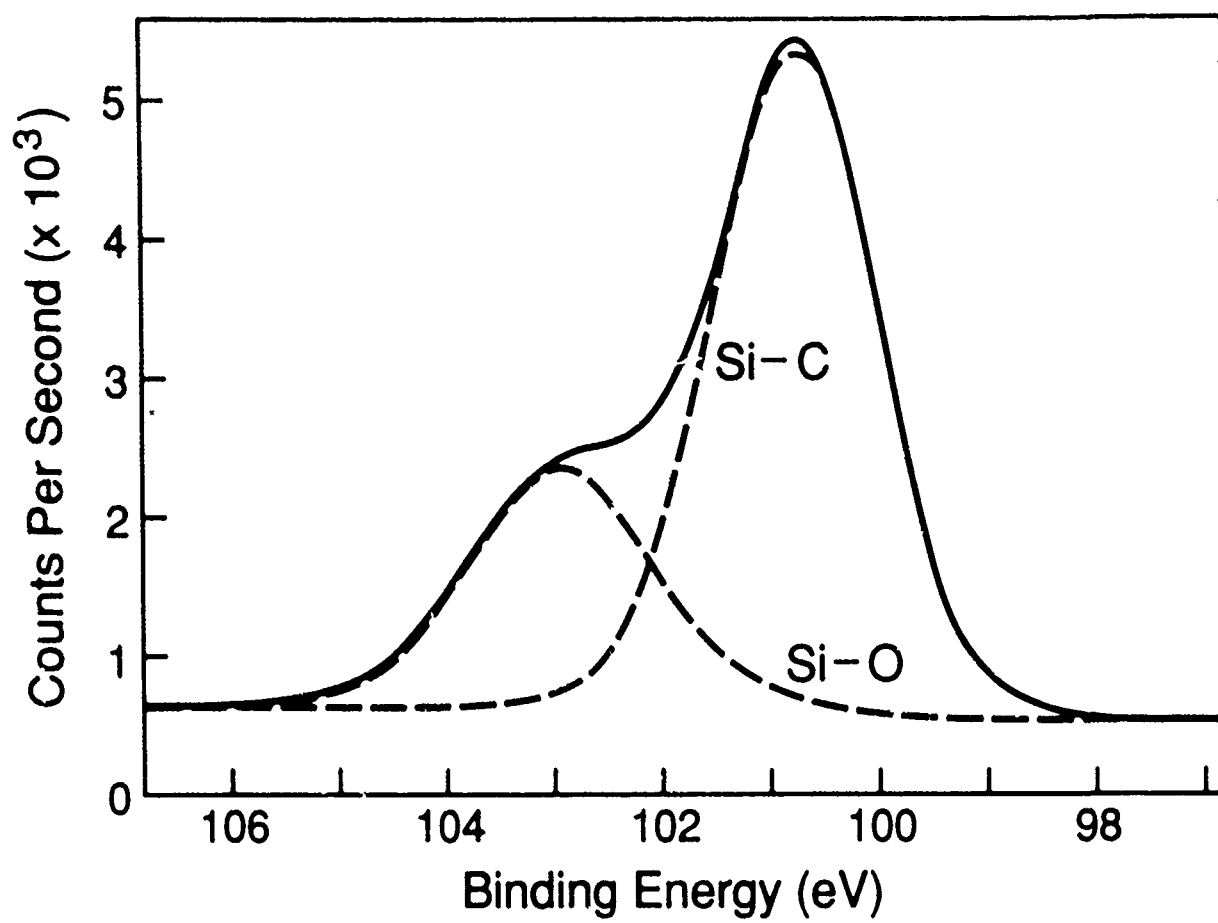


Figure 4b

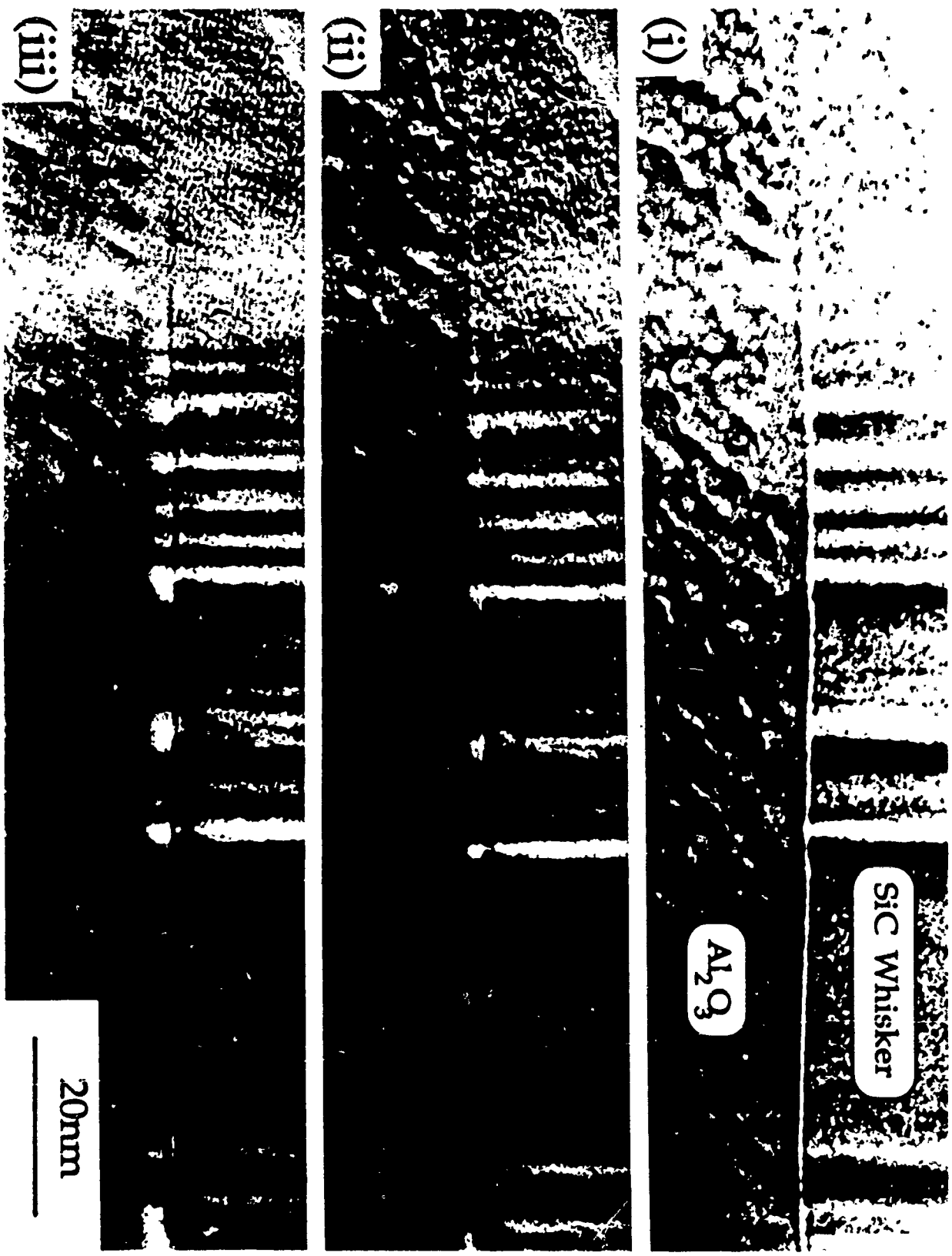


Figure 5

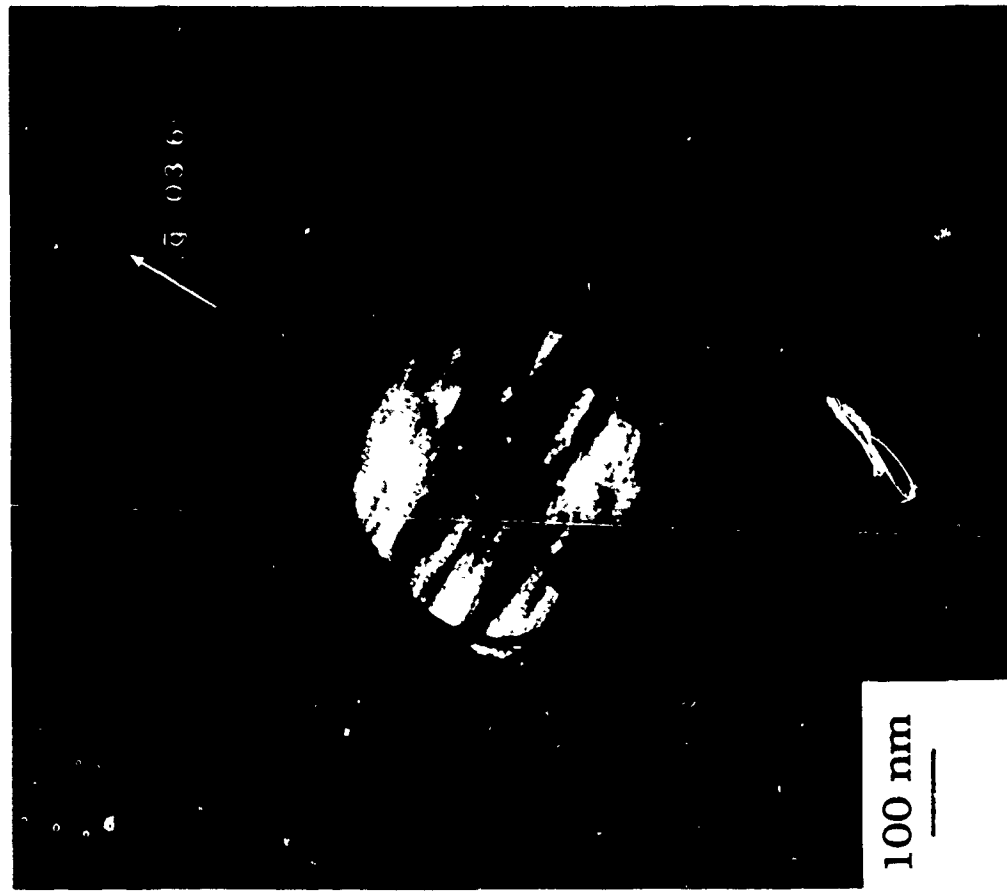


Figure 6a

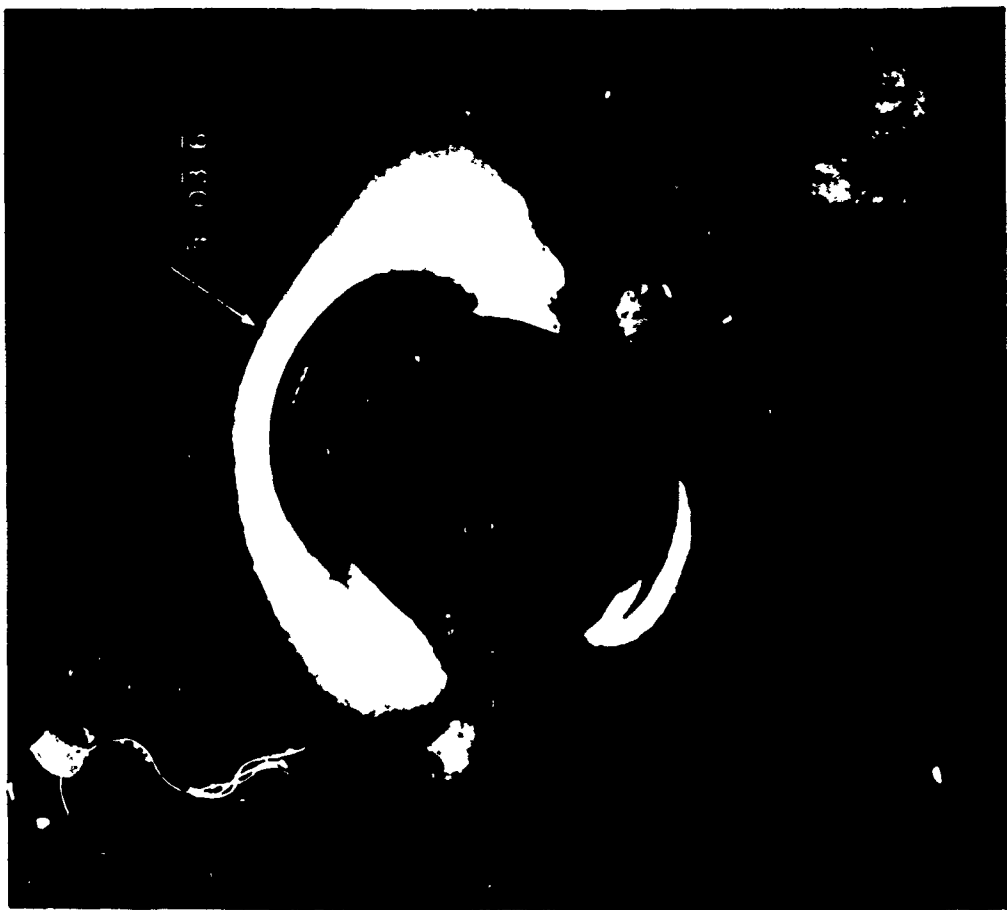


Figure 6b

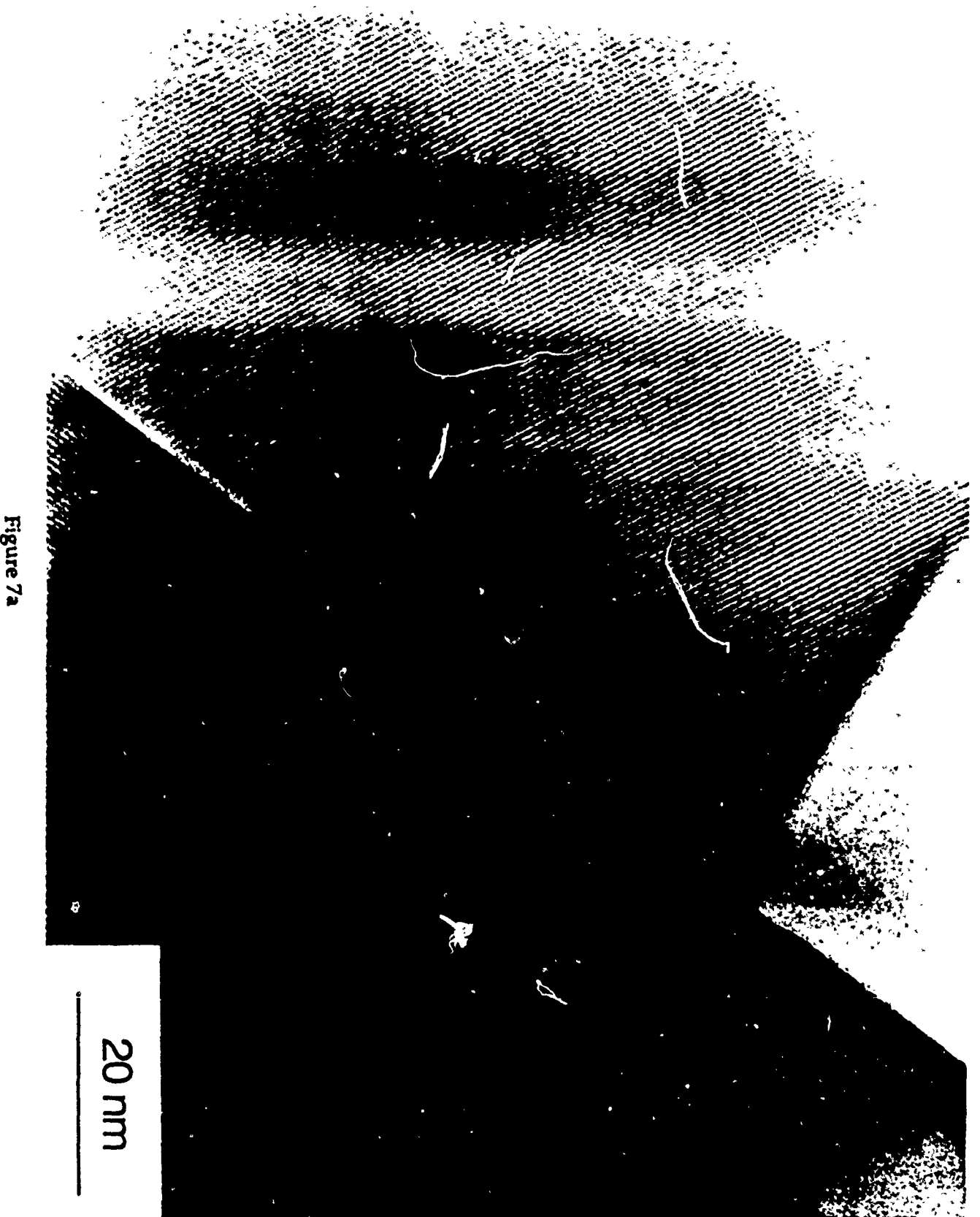


Figure 7a

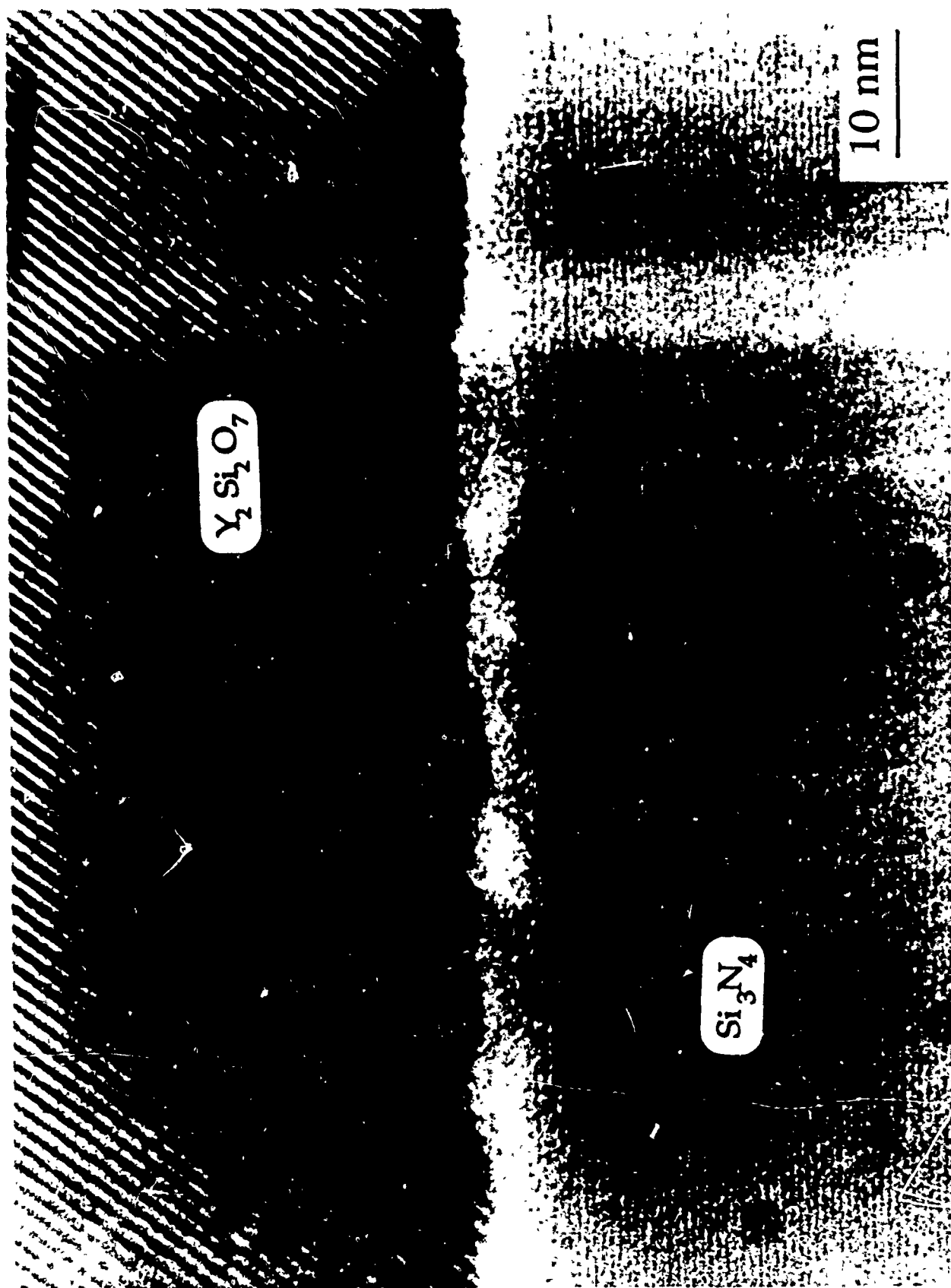


Figure 7b

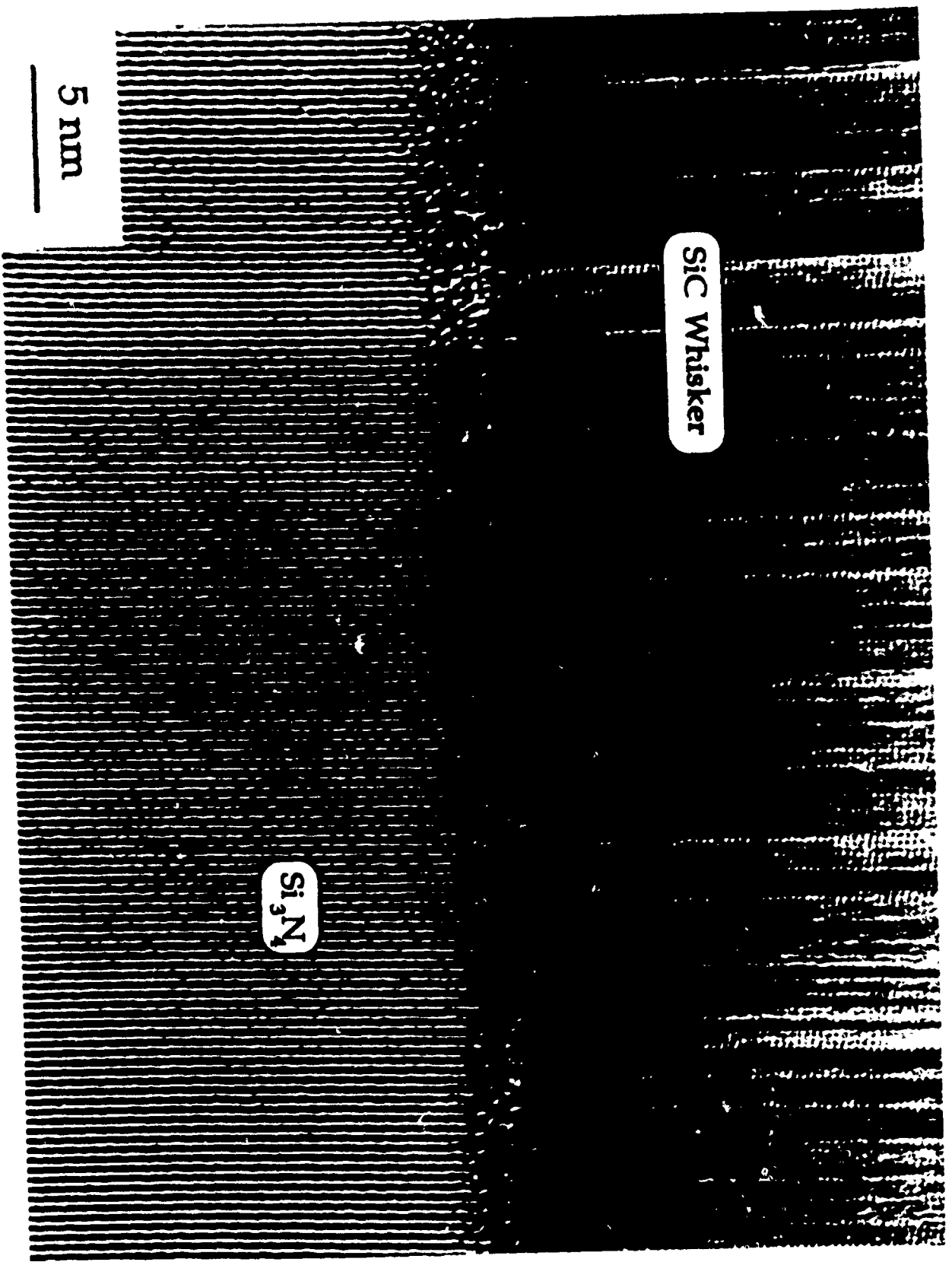
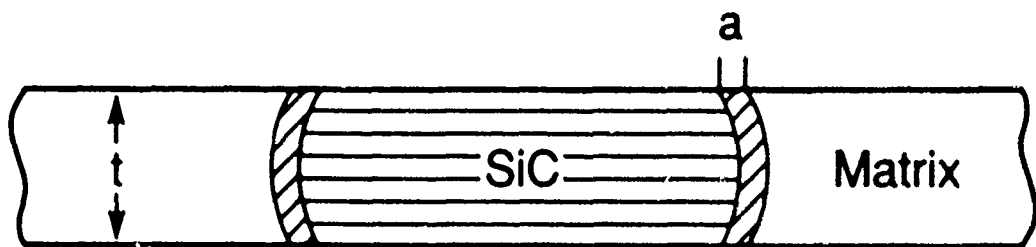


Figure 7c

TEM of Amorphous Grain Boundary Phase
(thickness a)



Maximum Foil Thickness $t \leq \sqrt{a \cdot D/2}$
(D = fiber diameter)

Figure 8



Figure 9a

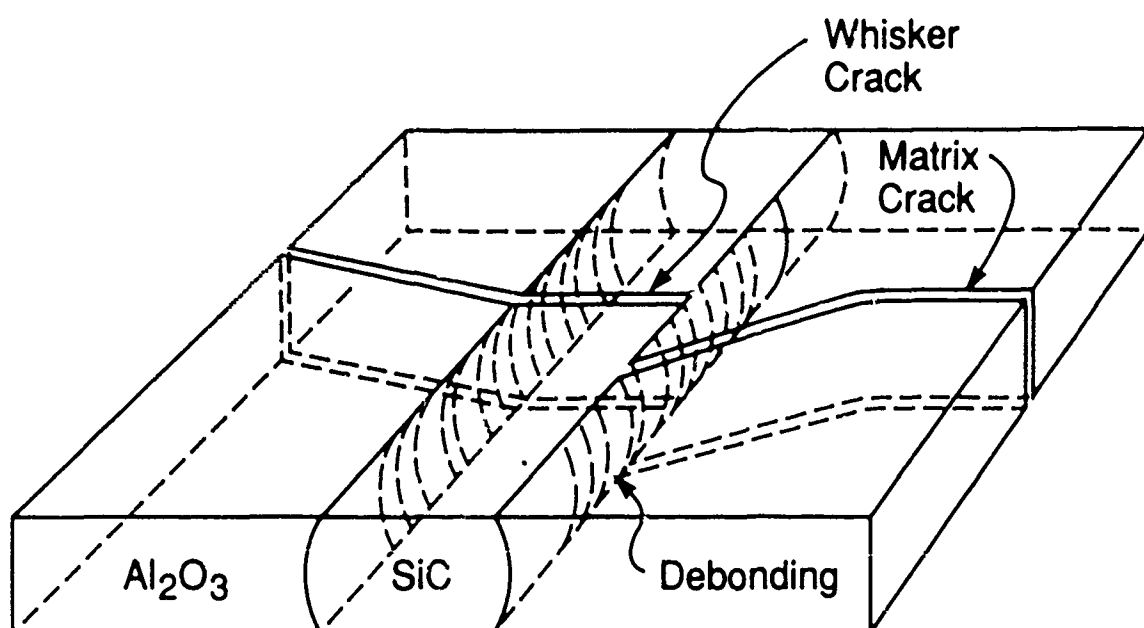


Figure 9b

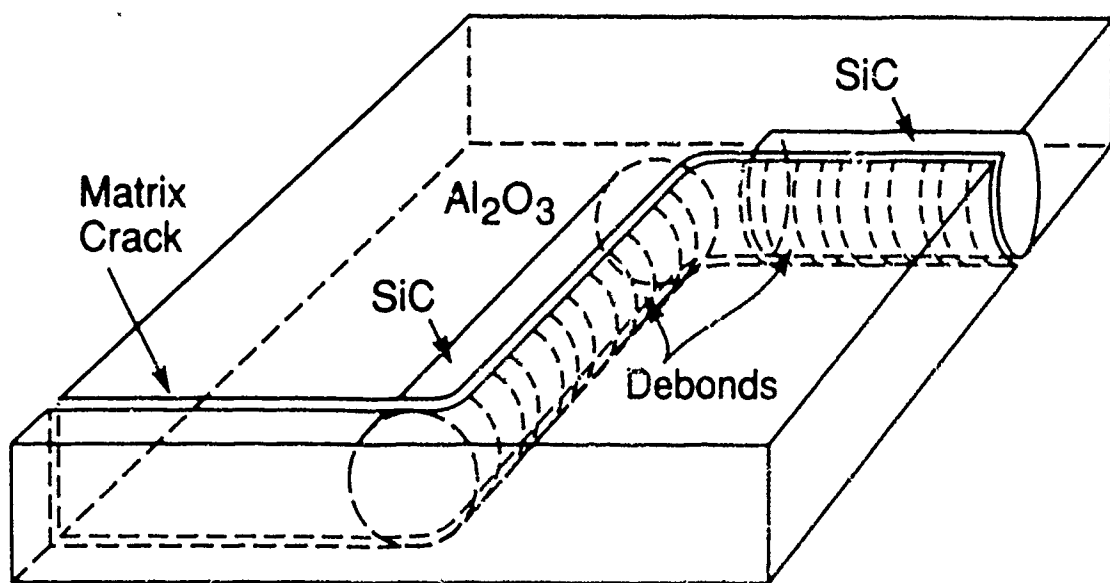


Figure 9c

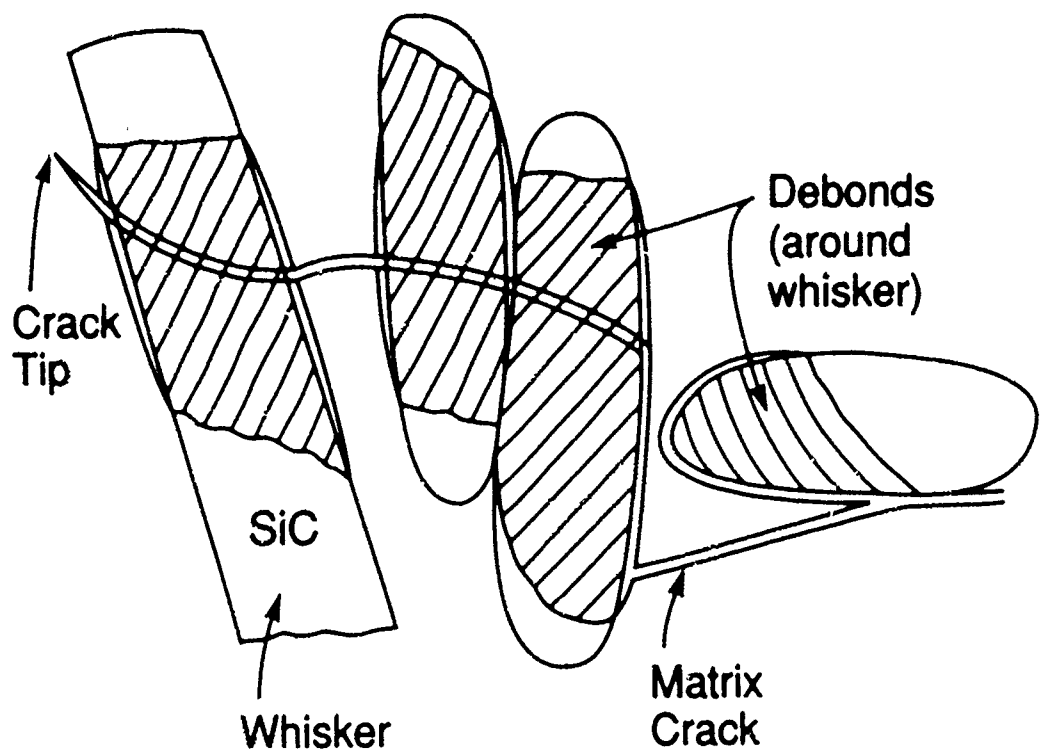


Figure 9d



Figure 10a

200 mm



Figure 10b



Figure 10c

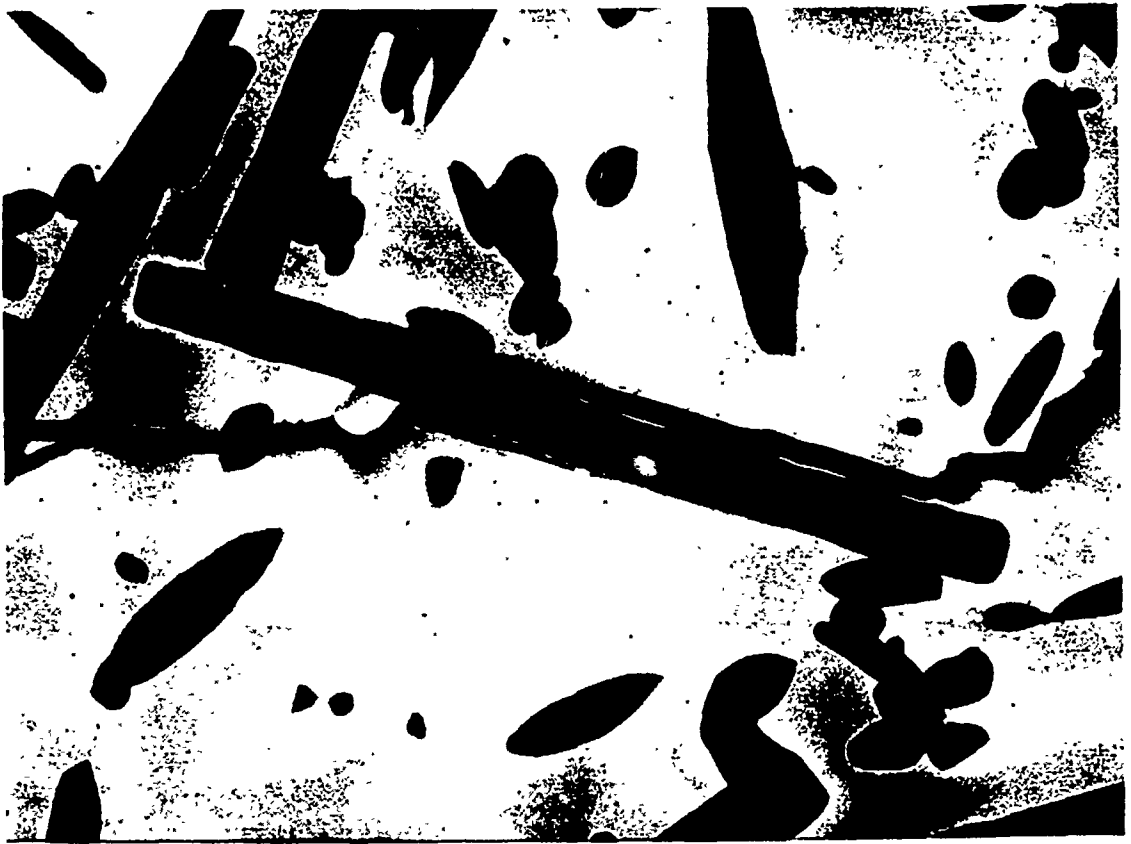


Figure 11a



Figure 11b

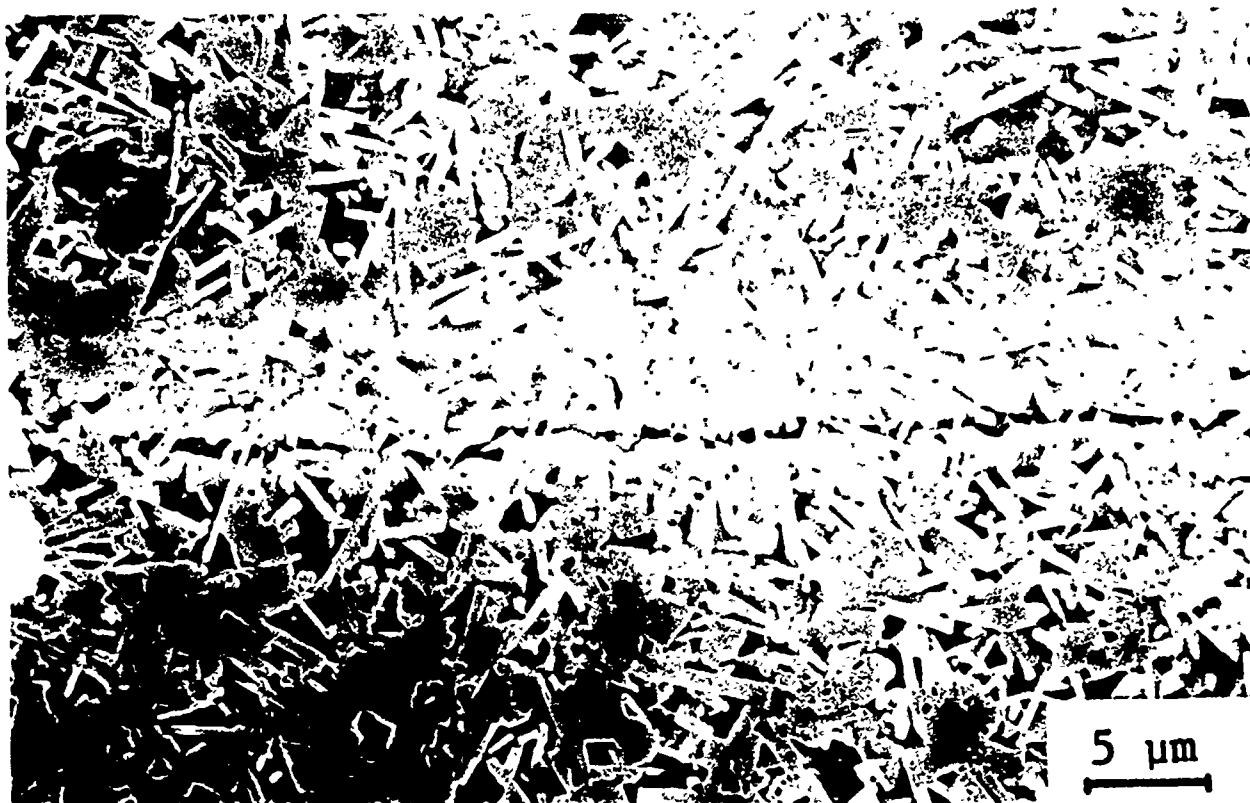


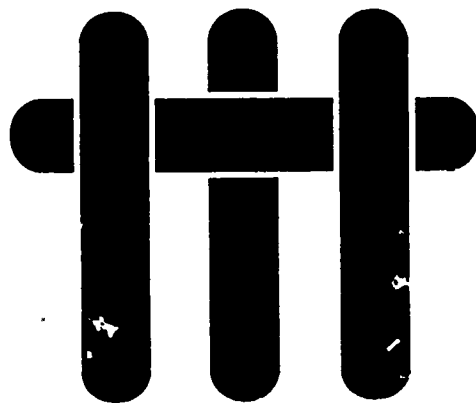
Figure 12a

Figure 12b



Figure 13

M A T E R I A L S



HIGH TOUGHNESS CERAMICS

A. G. Evans

Materials Department
College of Engineering
University of California, Santa Barbara
Santa Barbara, California 93106

High Toughness Ceramics*

A. G. EVANS

Materials Department, College of Engineering, University of California, Santa Barbara, CA 93106 (U.S.A.)

(Received November 10, 1987)

Abstract

The principal microstructural sources of toughening are reviewed, with emphasis on comparisons between theory and experiment. Process zone mechanisms, such as transformation and microcracking, as well as bridging mechanisms induced by either ductile phases or fibers and whiskers are afforded primary consideration. Microstructural variables which allow toughness optimization are discussed.

1. Introduction

The last decade has witnessed major advances in the development of ceramics having enhanced toughness. All the mechanisms which provide appreciable toughening have the common feature that material elements at, or near, the crack surfaces exhibit non-linear behavior, with hysteresis, as schematically illustrated in Fig. 1. Indeed, the toughening can be explicitly related to the hysteresis, as will be elaborated for each of the important mechanisms. Furthermore, in most cases, the mode of toughening results in resistance curve characteristics (Fig. 2), wherein the fracture resistance systematically increases with crack extension. The individual mechanisms that have been established include displacive transformations, microcracking, ductile phase and brittle fiber or whisker reinforcement. The general philosophy adopted in the modelling of the toughening includes the classical concept of homogenizing the properties of the material around the crack and formulating a constitutive law which then characterizes the material response. This approach fully describes the toughening behavior when the length of the non-

linear zone (Fig. 1) is appreciably larger than the spacing between the microstructural entities which dictate the non-linearity, as elaborated below. Otherwise, microstructural interactions must be treated discretely.

The known mechanisms can be conveniently considered to involve either a process zone or a bridging zone (Fig. 3). The former category exhibits a toughening fundamentally governed by a critical stress for the onset of non-linearity (σ_0 in Fig. 1) and by the permanent strain induced by the non-linear mechanism (ϵ_0 in Fig. 1). The hysteresis is dictated by the stress-strain behavior of composite elements within the process zone, such that integration over the zone gives

$$\Delta G_c \approx 2f\sigma_0 E h \quad (1)$$

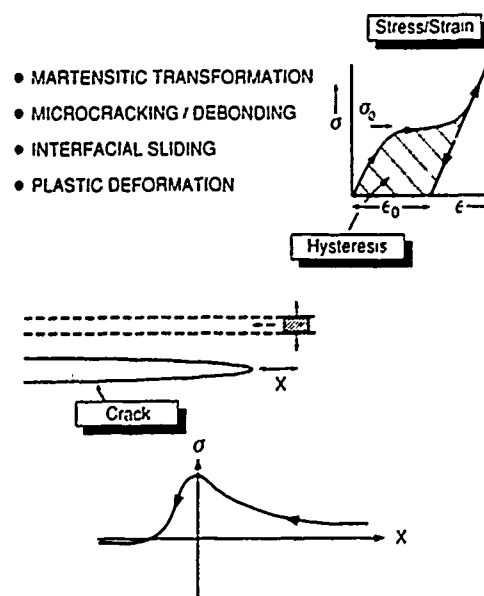


Fig. 1. A schematic diagram illustrating non-linear hysteretic elemental response and associations with enhanced toughness.

*Paper presented at the 3rd International Conference on the Science of Hard Materials, Nassau, The Bahamas, November 9-13, 1987.

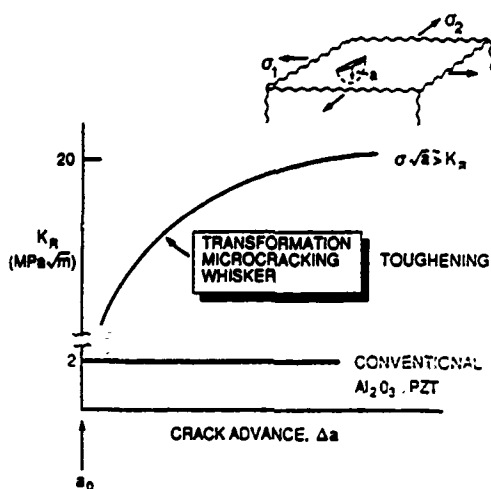


Fig. 2. Resistance curve behavior characteristically encountered in tough ceramics: K_R is the fracture resistance and Δa the crack advance.

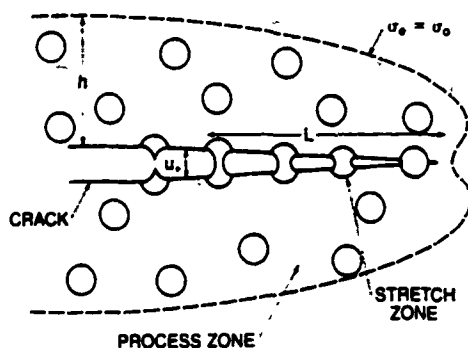


Fig. 3. A schematic diagram illustrating both process zone and bridging zone mechanisms of toughening.

where ΔG_c is the increase in critical strain energy release rate, f is the volume fraction of toughening agent and h is the width of the process zone (Fig. 3). Transformation and microcrack toughening are mechanisms of this type.

The latter category exhibits toughening governed by hysteresis along the crack surface:

$$\Delta G_c = f_A \int_0^{u_0} \sigma(u) du \quad (2)$$

where u is the crack opening, u_0 the opening at the edge of the bridging zone, σ the tractions on the crack surfaces exerted by the intact toughening agent (Fig. 3) and f_A is the area fraction of reinforcements along the crack plane. The rela-

tionship between f_A and the volume fraction f depends on reinforcement morphology, on the residual stress and on the elastic mismatch (through crack attraction-repulsion effects). Ductile dispersions, as well as whiskers and fibers, toughen by means of bridging tractions.

In the toughest materials, a steady state cracking phenomenon has been identified, wherein the crack extension stress becomes independent of crack length. For such materials, the toughness is usually non-unique and not, therefore, a useful material parameter. It is also noted that some of the composite systems of interest have anisotropic toughness, causing the properties to depend on the loading axis and the mode of loading. However, the central problem that must first be resolved in order to have a successful tough composite concerns the mode I (tensile) crack propagation resistance on planes normal to the reinforcement axis. This mode of crack propagation is thus emphasized in the present paper.

2. Steady state cracking

In certain composite ceramics, matrix cracking occurs at a constant stress [1-3]. This phenomenon is referred to as steady state cracking. Such behavior is most widely known in fiber-reinforced ceramics but is also possible in ductile-phase-reinforced ceramics. Steady state cracking in fiber-reinforced ceramics involves mode I cracks which extend normal to the fiber axis, resulting in a crack bridged by strong reinforcements (Fig. 4). An equilibrium crack opening then develops, with the load fully supported by the intact reinforcements. For such cases, the stress intensity associated with matrix cracking becomes independent of crack length. The steady state stress depends on the response of the interface and matrix to the load on the reinforcements between the crack surfaces. For fibers which resist opening by friction, the cracking stress is [1-3]

$$\sigma_s = \left\{ \frac{6\tau K_{II}^2 f^2 E_f E_m^2}{(1-f)E_m^3 R} \right\}^{1/3} + \frac{\sigma_R E}{E_m} \quad (3)$$

where τ is the shear resistance of the interface, K_{II} is the fracture resistance of the matrix, f is the volume fraction of fibers, E is Young's modulus, R is the fiber radius, σ_R is the residual stress in the matrix, and the subscripts f and m refer to the fiber and matrix respectively. This prediction



agrees well with various experimental results [2, 3] obtained on fiber-reinforced ceramics and glasses.

The equivalent result for partially debonded fibers without friction is [3]

$$\sigma_c = \frac{K_0 E}{E_m} \left[\frac{6f^2 E_l}{E(1-f)^2 R(1+\nu_m)} \right]^{1/4} \times \left[1 + \frac{4f\theta}{R(1-f)} \right]^{1/2} \left(1 + \frac{\rho l}{R} \right)^{-1} + \frac{\sigma_n E}{E_m} \quad (4)$$

where l is the debonded length, θ is the ratio of the debond to matrix toughness, ν is Poisson's ratio and $\rho = \{0.8/(1-f)\} \{6E/E_l(1+\nu_m)\}^{1/2}$.

Steady state crack growth conditions exist when the reinforcement strength \bar{S} satisfies the inequality $\bar{S} > \sigma_c/f$. Such materials have very desirable properties, by virtue of the associated damage tolerance and significant non-linearity before ultimate failure [4, 5]. The transition from matrix cracking to toughness-controlled fracture can sometimes be conveniently represented as a map. For example, when frictional sliding dominates the composite fracture process, imposing $\bar{S} = \sigma_c/f$ onto eqn. (3) gives a transition condition.

3. Transformation toughening

The stress-induced transformations which can cause significant toughening include martensitic [6, 7] and ferroelastic [8] transformations, as well as twinning. The former involves both dilatational and shear components of the transformation strain, while the latter typically have only a shear component. Martensitic transformation toughening in ZrO_2 has been most extensively investigated and will be given primary emphasis.

At the simplest level, transformation toughening can be regarded as a process dominated by the dilatational component of the stress-free strain, e_u^T , as expressed by the associated supercritical* stress-strain curve. Then, on the basis of the path independence of the J integral, initial crack growth occurs without toughening (Fig. 2). However, on crack extension, J becomes path dependent, and toughening develops. For steady state conditions, the supercritical toughening is readily derived as [6, 9-11]

$$\Delta G_c = 2hf \int \sigma d\epsilon \quad (5)$$

where the integral represents the hysteresis area depicted in Fig. 1, such that (cf. eqn. (1))

$$\Delta G_c = 2hf\sigma_n e_u^T \quad (6)$$

This steady state level is attained after crack extensions of about $5h$ [9]. A directly equivalent result for the increase ΔK_c in critical stress intensity factor can be derived by considering the residual stress field created by transformation, giving [9]

$$\Delta K_c = \frac{\lambda E e_u^T f h^{1/2}}{1-\nu} \quad (7)$$

where E is the composite modulus and $\lambda = 0.22$ is a coefficient.

Comparison with experimental data [6] (Fig. 5) has revealed that eqn. (6) consistently underestimates the toughness, because shear effects and zone widening have not been incorporated. One hypothesis regarding the shear strain which seemingly coincides with existing observations and measurements involves non-associated flow [6]. Specifically, it is presumed that the shear stress dominates the nucleation of the transformation, because of the large transformation shear strain

*Supercritical refers to the condition wherein all particles within the process zone fully transform.

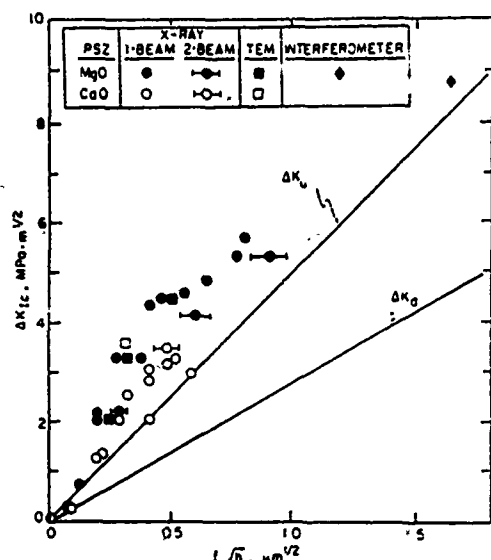


Fig. 5. A comparison between theory and experiment for various partially stabilized zirconia materials: ΔK_u refers to a zone shape dictated by the equivalent stress, whereas ΔK_m refers to a zone shape governed by the mean stress.

associated with the nucleus, but that the residual particle strain is predominantly dilatational, because extensive twinning eliminates long-range shear strains [12]. This premise results in the zone profile, in plane strain, which, by virtue of the absence of the transformed material ahead of the crack, predicts a toughening that exceeds eqn. (6) and furthermore agrees well with experimental data (Fig. 5). Such zone profiles are also consistent with available observations [13, 14]. While the above notions offer a self-consistent explanation of the transformation toughening in some cases, it is emphasized that alternative models of the influence of shear strains must be used to address other transformation problems, especially twin and ferroelastic toughening.

The zone size h represents the major microstructural influence on toughness. Clearly, h is governed by a nucleation law [15]. However, a fully validated law for nucleation does not yet exist, because the nucleation sequence has not been established. Consequently, connections between h and the microstructure still cannot be specified. Nevertheless, certain trends are apparent, based on the free energy of the fully transformed product [16, 17]. Specifically, h invariably decreases with increase in temperature and decrease in particle size. A temperature- and parti-

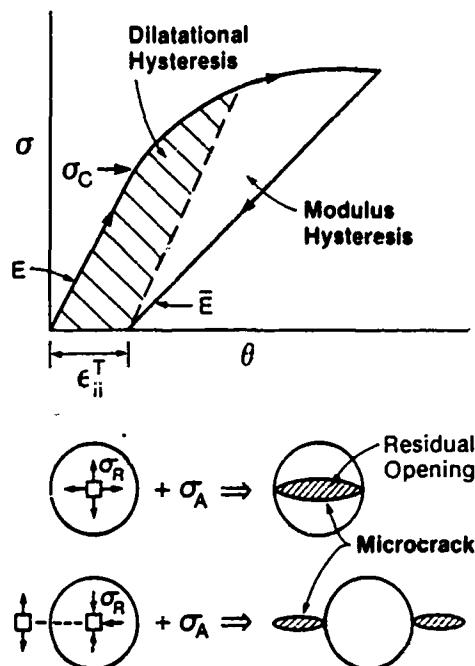


Fig. 6. The basic concepts of microcrack toughening.

cle-size-dependent toughness is thus inevitable for this mechanism.

Finally, it should be noted that h is not usually unique but varies with crack extension, especially during initial growth [9, 18, 19]. This behavior leads to resistance curves which increase over larger crack extension lengths than expected from the constant- h analysis [20]. The full simulation of this process has yet to be performed.

4. Microcrack toughening

The phenomenon of microcrack toughening has been postulated for over a decade [21–23] and, indeed, a range of materials exhibit trends in toughness with particle size, temperature, etc., qualitatively consistent with this mechanism. However, as yet there is only one fully validated example of this mechanism: Al_2O_3 toughened with monoclinic ZrO_2 [24]. The fundamental premise concerning the mechanism is depicted in Fig. 6. Microcracks occur within regions of local residual tension, caused by thermal expansion mismatch or by transformation [25, 26]. The microcracks locally relieve the residual tension and thus cause a dilatation governed by the volume

displaced by the microcrack. Furthermore, the microcracks reduce the elastic modulus within the microcrack process zone. Consequently, the elemental stress-strain curve for a microcracking solid has the form depicted in Fig. 6. The hysteresis dictated by this curve, when the microcracks are activated by the passage of a macrocrack, contributes to the change in toughness, as elaborated below. However, this contribution is partially counteracted by a degradation of the material ahead of the microcrack. The full extent of the degradation is at present unknown.

The crack shielding can be conveniently separated into dilatational and modulus contributions. The former depends on the process zone size and shape, while the latter depends only on the zone shape. The dilatational contribution ΔK_d has essentially the same form as eqn. (7). Notably for steady state supercritical conditions [24, 26],

$$\Delta K_d = -\lambda E f \theta^T h^{1/2} \quad (8)$$

where θ^T is the volume strain, as governed by the microcrack shape and the prior residual tension. The steady state modulus contribution ΔK_m is [26]

$$\frac{(1-\nu)\Delta K_m}{K_c} = (k_1 - \frac{1}{2}) \left(\frac{\mu}{\bar{\mu} - 1} \right) + (k_2 + \frac{1}{2}) \left(\frac{\bar{\nu}\mu}{\bar{\mu} - \nu} \right) \quad (9)$$

where $k_1 \approx 0.017$, $k_2 \approx -0.043$, μ is the shear modulus, the bar refers to microcracked material and K_c is the composite toughness. The contributions ΔK_d and ΔK_m are additive unless both are large compared with K_c , whereupon interaction effects occur and numerical procedures are then needed to determine the change in toughness [27].

Comparison between theory and experiment has been made for the $\text{Al}_2\text{O}_3\text{-ZrO}_2$ system [24], based on the microcrack density measurements presented in Fig. 7 (obtained using electron microscopy), and the θ^T results for annular microcracks with interface opening. For this case, the contributions to toughening from the dilatation and the modulus are evaluated as approximately 2.5 and 5 $\text{MPa m}^{1/2}$ respectively, compared with a measured composite toughness of about 6 $\text{MPa m}^{1/2}$. While this comparison is reasonable and validates microcracking as the prevalent toughening mechanism, present understanding of micro-

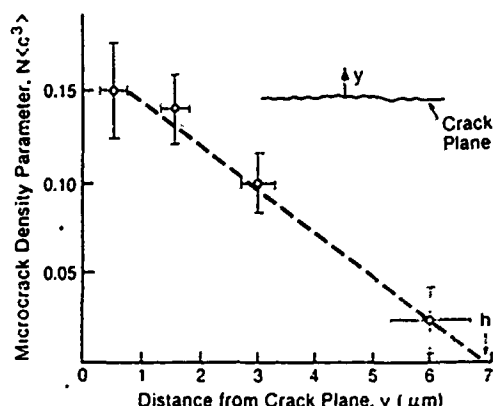


Fig. 7. Trends in microcrack density with distance from the crack surface for an $\text{Al}_2\text{O}_3\text{-ZrO}_2$ material with predominantly monoclinic ZrO_2 .

crack toughening is nevertheless incomplete. In particular, interaction effects between the modulus and dilatational contribution, as well as near-tip degradation effects require further investigation.

Because of the experimental difficulty involved in detecting microcracks*, there are no other validated examples of microcrack toughening. However, it is noted that several particulate-reinforced systems exist wherein enhanced toughness only develops when the particulates exceed a critical size. Microcracking is a likely contribution to the toughening in several of these systems.

One potentially detrimental feature of microcrack toughening is the incidence of thermal microcracks at the largest particles in the distribution [24]. Such cracks can be strength limiting, resulting in material which is relatively tough but has only moderate strength [28]. Avoidance of such strength-limiting cracks requires stringent control of the size distribution of the reinforcing particles, just beneath the critical size for thermal microcracking.

Finally, it is noted that the dilatational contribution to microcrack toughening would usually be temperature dependent because of the reduction in residual stress with increase in temperature. However, the modulus contribution is temperature invariant, at least at temperatures below which the process zone size is relatively large compared with the microcrack spacing. Microcrack toughening is, typically, less potent than transformation toughening.

*Typical residual crack openings are less than 2 nm.

5. Ductile phase toughening

Practical ceramic systems toughened by ductile phases typically have interpenetrating networks of the brittle and ductile phases. For such systems, cracks in the brittle ceramic phase are required to intercept the ductile phase such that the area fraction of reinforcing phase on the crack plane is of the same order as the volume fraction. In these materials, two sources of toughening occur, as governed by plasticity in the ductile phase. Segments intercepted by the crack exhibit plastic stretching in the crack wake [29] (Fig. 3) and contribute to the toughness by inhibiting crack opening. Simultaneously, plastic straining of segments in a process zone causes crack shielding (Fig. 3). The former mechanism has the general characteristics that high toughness is encouraged by a large value of the product of the work of rupture and particle size [29]. By contrast, the crack shielding process tends to become larger for ductile sections having a small size and low yield strength. An estimate of the shielding has been derived by considering the residual strain in the crack wake caused by plastic distortion of ductile enclaves in an elastic matrix. This estimate indicates that, to achieve an appreciable shielding contribution to the toughness, the yield strength Y must be less than about 10 MPa and the ductile phase sections less than about $1\text{ }\mu\text{m}$ in diameter.

The contribution to the toughness from stretching between crack surfaces is explicitly governed by the stress-opening curve (eqn. (2)), as depicted in Fig. 8, such that [29, 30]

$$\Delta G_c = \chi f Y a \quad (10)$$

where a is the radius of the ductile enclave and χ is a parameter which depends on the work-hardening rate n , the ductility of the ductile phase and the bonding between the ductile and brittle phases. Calculations conducted for fully bonded, fully ductile phases which neck to a point predict χ values of between 0.5 and 3 [29] (Fig. 9). However, larger values of χ are possible when limited debonding occurs [30]. The maximum χ observed by experiment is about 6. Based on this maximum value, experimental toughness data obtained for the $\text{Al}_2\text{O}_3\text{-Al}$ system (Fig. 10) conform well with the values predicted by eqn. (10). However, the incidence of debonding in this system has not been established. Further understanding of this mode of toughening is thus predicated on a rigorous assessment of interface debonding.

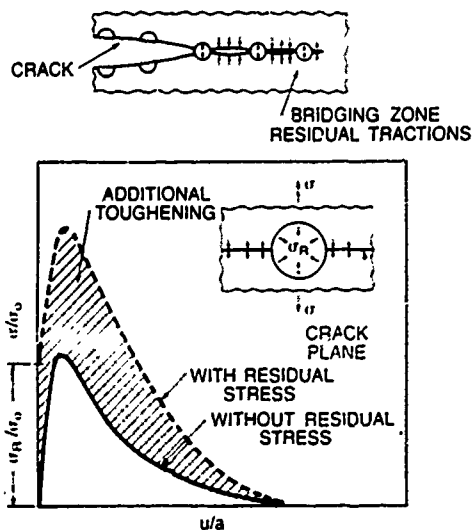


Fig. 8. Stress-crack opening relation for a crack bridged by a ductile particle.

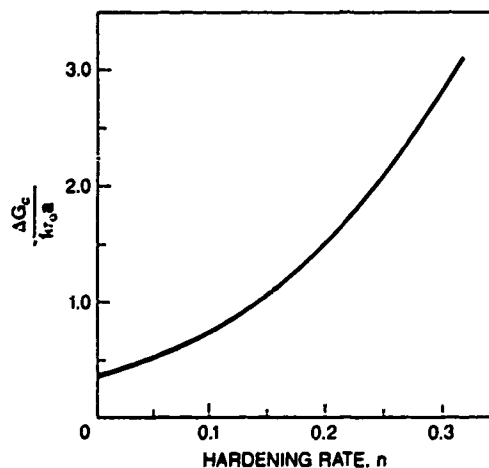


Fig. 9. Trends in toughness with hardening rate with $\Delta G_c / f Y a$ being equivalent to χ in eqn. (10).

Finally, it is noted that ductile particle toughening should be temperature sensitive, because of the temperature dependence of the yield strength.

6. Fiber and whisker toughening

The toughening of ceramics by brittle fibers and/or whiskers occurs subject to debonding at the interface. In the absence of debonding, because the fiber and matrix typically have comparable toughnesses, the composite is brittle and



Fig. 10. Ductile rupture in $\text{Al}_2\text{O}_3\text{-Al}$ revealing that the aluminum fails by necking.

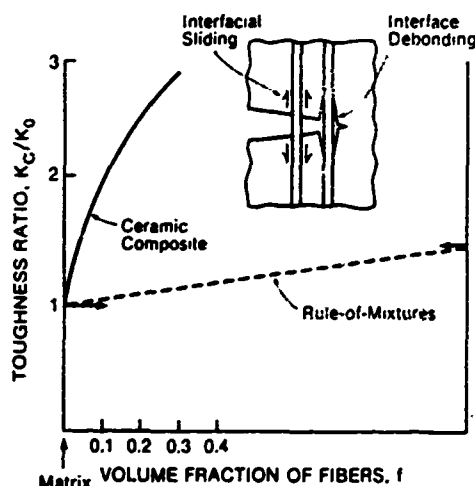


Fig. 11. The role of debonding in toughening.

satisfies a rule of mixtures (Fig. 11). Debonding reduces the amplitude of the stress concentration at the fiber along the matrix crack front and, when sufficiently extensive, allows the crack to circumvent the fiber, leaving the fiber intact in the crack wake. The intact fiber inhibits crack opening and allows a composite toughness exceeding that of either constituent (Fig. 11). The overwhelmingly important issue in fiber or whisker toughening thus concerns the extent of debond-

ing, its dependence on interface properties, and its effect on crack opening and fiber failure.

The full debonding and fiber fracture problem has several different aspects which eventually require resolution. These include the characteristics of interface fracture properties and associated requirements for the initiation and extent of debonding at the matrix crack tip, as well as the influence of debond length on the crack-opening force and the relationship between debond length and the fiber fracture force. While some progress has been made toward an understanding of these problems, several important questions remain. The present status is briefly reviewed.

The central issue to be addressed in this article concerns the mode I propagation resistance for matrix cracks on a plane normal to the fiber axis. Once this problem has been confronted and resolved in terms of interface debonding etc., mixed-mode and delamination cracking effects require resolution, in order to describe the overall fracture behavior of the composite.

6.1. Initial debonding

Even though debonding at the matrix crack tip is a prerequisite to fiber toughening, there is minimal quantitative understanding of the phenomenon. Two mechanics solutions have relevance: one for forked or kinked cracks [31] and the other for debonding ahead of a crack tip [3]. The solution to the former clearly indicates that debonding is a mixed-mode problem (Fig. 12). Furthermore, debonding initiates when the interface fracture resistance is about quarter that of the fibers. However, further debonding becomes increasingly difficult. The extent of the difficulty is estimated from the latter solution, which reveals that, in order to achieve extensive debonding, the interface fracture resistance should be about an order of magnitude less than that of the matrix (Fig. 13). Further experimental and theoretical study of this important phenomenon would greatly facilitate the design of interfaces that allow optimal debonding.

6.2. Crack opening

Preliminary results have been obtained for the crack-opening forces associated with intact fibers normal to the crack plane. For the extreme condition of extensive debonding, with opening inhibited by friction, a shear lag analysis [2, 3] indicates that the initial segment is linear and represents behavior wherein the interfacial shear stress is

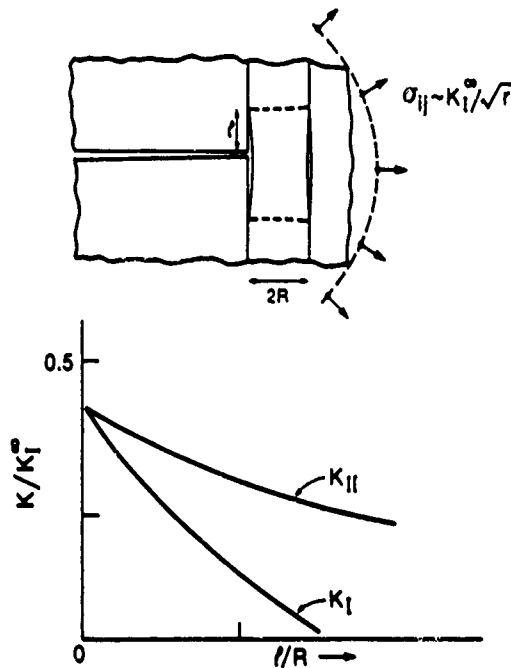


Fig. 12. A schematic diagram illustrating trends in local K with debond length.

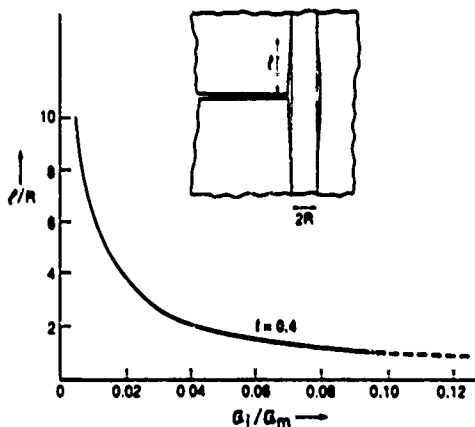


Fig. 13. Trends in debond length with relative interface fracture resistance.

less than the sliding stress τ such that the stress on the fiber end is

$$\sigma = \frac{l/E_f(1+\xi)}{R} u \quad (11)$$

where $\xi = E_f f / (1-f) E_m$. At larger stresses ($\sigma > 2\tau E_f(1+\xi)/l$), the behavior is dominated by

sliding and is given by

$$\sigma = 2f(1+\xi) \left(\frac{E_f \tau}{R} \right)^{1/2} \left(u - \frac{\tau R}{E_f} \right)^{1/2} \quad (12)$$

For debonds without friction, it is noted that a steady state condition exists when the debond length $l > 2R$, wherein the stress intensities and strain energy release rate for the debond become independent of l [32]. When the matrix has the same elastic properties, the steady state quantities are

$$\begin{aligned} \frac{K_I}{E \Delta \alpha \Delta T R^{1/2}} &= 0.28 + \frac{0.11l}{E \Delta \alpha \Delta T} \\ \frac{K_{II}}{E \Delta \alpha \Delta T R^{1/2}} &= -0.51 + \frac{0.45l}{E \Delta \alpha \Delta T} \\ \frac{G}{ER(\Delta \alpha \Delta T)^2} &= 0.31 - \frac{0.37l}{E \Delta \alpha \Delta T} \\ &\quad + 0.20 \left(\frac{l}{E \Delta \alpha \Delta T} \right)^2 \end{aligned} \quad (13)$$

where l is the stress on the fiber between the crack surfaces, $\Delta \alpha$ is the thermal expansion mismatch (fiber minus matrix) and ΔT is the cooling range. Steady state debonding behavior dictates that the crack opening u varies linearly with debond length, such that [32, 33]

$$u = \frac{l}{E} \beta(f, \Sigma) + u_0(\Delta \alpha \Delta T, f) \quad (14)$$

where β is a function of the volume fraction f of fibers and the modulus ratio Σ and u_0 is an offset at zero stress.

When fibers fail, the above functions are clearly modified and the further opening of the crack often occurs subject to a declining stress, as elaborated below.

6.3. Fiber failure

The process of fiber failure is not yet understood in detail. Available analyses have focused on the problem of fracture behind the matrix crack front, neglecting fractures which might occur in the crack tip field. When fibers fail in the wake, large debond lengths encourage a statistical mode of fracture within the debond zone, as governed by the flaw size distribution in the fiber.

The statistical mode of fiber failure leads to a fiber failure probability which increases with

increase in distance behind the crack tip [34], while the most probable fiber failure location displaces further from the crack surface. The associated stress-displacement curves have sliding and pull-out contributions which can be derived in terms of the fracture properties of the fibers and the shear resistance of the interface. For fibers normal to the crack having a flaw strength distribution,

$$\int g(S) dS = \left(\frac{S}{S_0} \right)^m \quad (15)$$

where S_0 is a scale parameter and m a shape parameter; weakest-link statistics give the crack-opening stresses, plotted in Fig. 14, in terms of the non-dimensional quantities σ/Σ and u/v where, in this case, Σ and v are defined by

$$\Sigma = \left[\frac{S_0^m \Gamma(m+1)}{2\pi R^2} \right]^{1/(m+1)} \quad (16)$$

$$v = \frac{\Sigma^2 R}{4E_f \Gamma(1 + \frac{1}{m})}$$

When the fibers or whiskers are inclined to the crack plane, additional effects occur. Clearly, the inclination angle affects the debond length and the stress at fiber fracture. However, following such fracture, crack-opening interference may persist, because of the trajectory of the associated fiber crack. An enhanced declining segment of the $\sigma(u)$ function may then obtain.

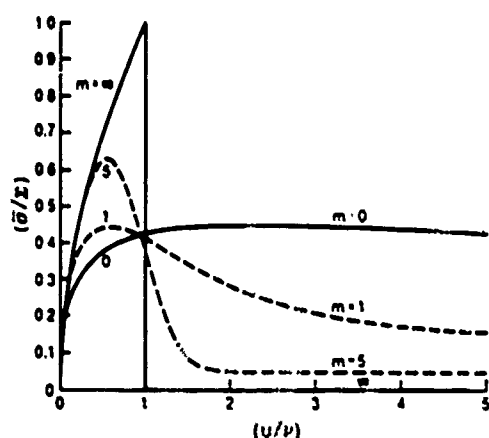


Fig. 14. Stress-crack-opening functions for statistical fiber failure with friction.

6.4. The toughening

Trends in toughening can be deduced from the $\sigma(u)$ function, using eqn. (2). However, resistance curve and steady state cracking effects must be considered as important related effects. Perhaps the most straightforward case involves the whisker-reinforced systems, Al_2O_3 -SiC and Si_3N_4 -SiC. For these materials, limited debonding along an amorphous interphase, without friction, seems to contribute to the toughness. Consequently, for aligned whiskers normal to the crack plane, eqns. (2) and (14) predict a toughening that varies linearly with debond length. The fiber fracture condition, as well as the initial crack-opening force, is also influenced by the residual field. Analysis of this problem has not yet been conducted and, hence, trends in toughness with residual stress are at present unknown. Furthermore, satisfactory solutions for toughness in the presence of non-aligned whiskers, which fail in the crack wake by bending plus tension, have yet to be developed.

Composites which exhibit extensive debonding and frictional sliding typically have pull-out contributions to the toughness [34, 35]. The associated $\sigma(u)$ functions (Fig. 14) may simply be integrated to predict the asymptotic toughness, using eqn. (2). Frequently, however, the mean pull-out length exceeds the crack mouth opening (except for very long cracks), indicating that asymptotic behavior does not occur and, instead, fracture is governed by a rising resistance curve. Simulation of trends in toughness with crack extension has yet to be conducted.

One important feature of fiber and whisker toughening is the absence of an obvious temperature-dependent parameter, except for possible temperature effects on the debond resistance. This toughening approach thus seems to have the greatest potential for toughness at elevated temperature.

7. Other mechanisms

A number of ceramic materials have a contribution to toughness from intact grains along the crack surface [36]. The phenomenon is evident in several large-grained polycrystals, most notably Al_2O_3 , and in certain glass ceramics. The contribution of these intact grains to toughness is formally similar to whisker toughening. However, the corresponding $\sigma(u)$ law and the analogous criteria which govern grain intactness are not yet

well understood. Nevertheless, by direct analogy to whisker toughening, grain boundaries weakened by additives have been demonstrated [37] to encourage bridging effects and thus to enhance toughness. The ability of certain grains to remain intact probably involves residual stresses, with associated grain size effects [38], perhaps coupled with statistical variability of the grain boundary fracture resistance.

8. Synergism

When bridging and process zone mechanisms occur in conjunction, synergistic toughening becomes possible [39, 40]. The basic concept is illustrated in Fig. 3. Specifically, the tractions exerted on the crack surface by the intact particles can locally widen the process zone. This zone widening, in turn, enhances the tip shielding above the level expected in the absence of bridging. The net effect of both processes on toughness is larger than the sum of the individual mechanisms. Indeed, cases exist wherein the toughening is multiplicative. This intriguing topic is expected to be the subject of appreciable future research.

9. Concluding remarks

A number of substantial issues remain to be addressed, particularly for fiber- and whisker-toughened materials. Present evidence suggests that coatings are needed on the fibers having a low debond resistance and a small subsequent sliding resistance along the debond. The coatings must also be thermodynamically and microstructurally stable. Coatings such as BN, SiO₂ and carbon have been widely used, but all have major limitations, especially at elevated temperatures. Other interphases are needed and primary attention is now being focused on the identification of appropriate materials and fiber coating approaches. Interesting approaches include refractory metal and intermetallic coatings as well as porous coatings.

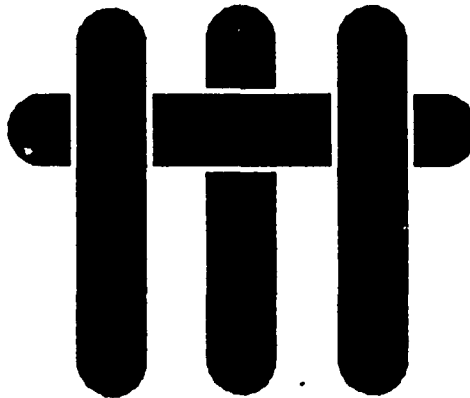
References

- 1 J. Aveston, G. A. Cooper and A. Kelly, *National Physical Laboratory Conf. on the Properties of Fiber Composites*, IPC, Guildford, 1971, p. 15.
- 2 D. B. Marshall, B. N. Cox and A. G. Evans, *Acta Metall.*, **33**(1985) 2013.
- 3 B. Budiansky, J. W. Hutchinson and A. G. Evans, *J. Mech. Phys. Solids*, **2**(1986) 167.
- 4 K. Prewé and J. J. Brennan, *J. Mater. Sci.*, **15**(1980) 463.
- 5 D. B. Marshall and A. G. Evans, *J. Am. Ceram. Soc.*, **68**(1985) 225.
- 6 A. G. Evans and R. M. Cannon, *Acta Metall.*, **34**(1986) 761.
- 7 N. Claussen, M. Rühle and A. H. Heuer (eds.), *Advances in Ceramics*, Vol. 12, American Ceramic Society, Columbus, OH, 1985.
- 8 A. Virkar and R. Matsumoto, *J. Am. Ceram. Soc.*, **69**(1986) C224.
- 9 R. McMeeking and A. G. Evans, *J. Am. Ceram. Soc.*, **65**(1982) 242.
- 10 D. B. Marshall, M. D. Drory and A. G. Evans, in R. C. Bradt, A. G. Evans, D. P. H. Hasselman and F. F. Lange (eds.), *Fracture Mechanics of Ceramics*, Vol. 5, Plenum, New York, 1983, p. 289.
- 11 B. Budiansky, J. W. Hutchinson and J. Lambropoulos, *Int. J. Solid Struct.*, **19**(1983) 337.
- 12 M. Rühle and W. M. Kriven, in H. Aaronson, D. Laughlin, R. F. Sekerka and C. M. Wayman (eds.), *Solid-Solid Phase Transformations*, AIME, New York, 1982, p. 97.
- 13 M. V. Swain and L. R. F. Rose, *J. Am. Ceram. Soc.*, **69**(1986) 511.
- 14 M. Rühle, B. Kraus, A. Strecker and D. Waidelich, in N. Claussen, M. Rühle and A. H. Heuer (eds.), *Advances in Ceramics*, Vol. 12, Plenum, New York, 1985, p. 256.
- 15 M. Rühle and A. H. Heuer, in N. Claussen, M. Rühle and A. H. Heuer (eds.), *Advances in Ceramics*, Vol. 12, Plenum, New York, 1985, p. 14.
- 16 A. G. Evans, M. D. Drory, N. Burlingame and W. Kriven, *Acta Metall.*, **29**(1981) 447.
- 17 F. F. Lange, *J. Mater. Sci.*, **17**(1982) 225.
- 18 D. B. Marshall, *J. Am. Ceram. Soc.*, **69**(1986) 173.
- 19 A. H. Heuer, *J. Am. Ceram. Soc.*, **70**(1987) 689.
- 20 M. V. Swain and R. J. H. Hannink, in N. Claussen, M. Rühle and A. H. Heuer (eds.), *Advances in Ceramics*, Vol. 12, Plenum, New York, 1985, p. 225.
- 21 R. G. Hoagland, J. D. Embury and D. J. Green, *Scr. Metall.*, **9**(1975) 907.
- 22 N. Claussen, J. Streeb and R. F. Pabst, *Am. Ceram. Soc. Bull.*, **56**(1977) 559.
- 23 R. G. Hoagland and J. D. Embury, *J. Am. Ceram. Soc.*, **63**(1980) 404.
- 24 M. Rühle, A. G. Evans, P. G. Charalambides, R. M. McMeeking and J. W. Hutchinson, *Acta Metall.*, **35**(1987) 2701.
- 25 A. G. Evans and K. T. Faber, *J. Am. Ceram. Soc.*, **67**(1984) 255.
- 26 J. W. Hutchinson, *Acta Metall.*, to be published.
- 27 P. G. Charalambides and R. M. McMeeking, *Mech. Mater.*, **6**(1987) 71.
- 28 M. Rühle, N. Claussen and A. H. Heuer, *J. Am. Ceram. Soc.*, **69**(1986) 195.
- 29 L. Sigl, P. Mataga, B. J. Dalgleish, R. M. McMeeking and A. G. Evans, *Acta Metall.*, **36**(1988) 945.
- 30 M. F. Ashby, to be published.
- 31 B. Cotterell and J. R. Rice, *Int. J. Fract.*, **16**(1980) 155.
- 32 P. G. Charalambides and A. G. Evans, *J. Am. Ceram. Soc.*, to be published.
- 33 M. Rühle, B. J. Dalgleish and A. G. Evans, *Scr. Metall.*, **21**(1987) 681.
- 34 M. D. Thouless and A. G. Evans, *Acta Metall.*, **36**(1988) 517.
- 35 D. C. Phillips, *J. Mater. Sci.*, **7**(1972) 1175.

- 36 P. L. Swanson, C. J. Fairbanks, B. R. Lawn, Y. W. Mai and B. J. Hockey, *J. Am. Ceram. Soc.*, **70**(1987) 289.
- 37 R. F. Cook, C. J. Fairbanks, B. R. Lawn and Y. M. Mai, *J. Mater. Res.*, **2**(1987) 345.
- 38 Y. Fu and A. G. Evans, *Acta Metall.*, **30**(1982) 1619.
- 39 B. Budiansky, in J. P. Lamb (ed.), *Micromechanics II, Proc. 10th U.S. Congr. of Applied Mechanics, Austin, TX, 1986*, p. 25.
- 40 A. G. Evans, P. W. R. Beaumont, Z. Ahmad and D. G. Gilbert, *Acta Metall.*, **34**(1986) 79.

To appear in the International Journal for Numerical Methods in Engineering

M A T E R I A L S



SOME RECENT DEVELOPMENTS IN NUMERICAL MODELLING OF FRACTURE TOUGHNESS IN BRITTLE MATRIX COMPOSITES

C. L. HOM, P. A. MATAGA AND R. M. MCMEEKING
DEPARTMENT OF MATERIALS AND DEPARTMENT OF MECHANICAL
ENGINEERING
UNIVERSITY OF CALIFORNIA
SANTA BARBARA, CA 93106

May 1989

ABSTRACT

Finite element analysis was used to study the fracture toughening of a ceramic by a stress induced dilatant transformation of second phase particles. The finite element method was based on a continuum theory which modelled the composite as subcritical material. Transient crack growth was simulated in the finite element mesh by a nodal release technique. The crack's remote tensile opening load was adjusted to maintain the near tip energy release rate at the level necessary for crack advance. The transformation zone surrounding the crack developed as the crack propagated through the composite. Resistance curves were computed from the analysis; and the results show that during crack advance maximum toughness is achieved before steady-state is reached.

The toughening effect of a crack-bridging ductile phase in a brittle material may be predicted if ligament deformation is characterized. A plastically deforming ligament constrained by surrounding elastic matrix material is modelled using finite elements and the relevant toughness enhancement information extracted. Comparison is made to model experiments as well as to toughnesses measured for technologically important materials. The results suggest that debonding along the interface between the ligament and the matrix may enhance the toughening effect of a ductile phase.

INTRODUCTION

There is a critical need for light weight high strength materials, especially for high temperature applications. Candidates for development are ceramics and intermetallics which both have the disadvantage of brittleness with little elongation at failure. As a substitute in such materials, it is desirable to improve the fracture toughness so that notch and flaw sensitivity becomes less of a problem. A common strategy for improving fracture toughness is to make a composite material by putting whiskers, fibers or particles into the brittle matrix. The design of optimal composite microstructures must be based on accurate models of the mechanism of toughening arising from the reinforcements. This paper reviews two such model calculations for transformation toughened and ductile particle toughened materials.

TRANSFORMATION TOUGHENING

The fracture toughness of ceramic materials can be greatly enhanced by the presence of particles which undergo a stress induced martensitic transformation (Evans and Heuer [1]; Evans and Cannon [2]) such as takes place in systems containing stabilized zirconia (ZrO_2) particles. At sufficiently high stress, the particles of such systems undergo a transformation from the tetragonal to monoclinic phase which is accompanied by a volume increase of 4% for the particles. This dilatation strain is the mechanism which increases the effective fracture toughness of the composite material. Since the transformation is stress induced, a zone of material containing transformed particles will surround the crack tip. The volume expansion of the particles in this zone will cause eigenstresses which will tend to close the crack and

lower the stress intensity factor at the tip. This shielding mechanism means that a higher applied load than otherwise, and therefore, an apparently higher stress intensity factor, is required to propagate the crack.

Transformation toughening was first modelled by McMeeking and Evans [3] and Budiansky, Hutchinson and Lambropoulos [4]. The effect of phase transformation was represented by the hydrostatic stress versus dilatation strain shown in Fig. 1. At the critical stress σ_m^* phase transformation commences. If the slope \bar{B} of the stress-strain curve during transformation is below $-4G/3$, where G is the shear modulus, then the transformation continues spontaneously to completion [4]. This situation has been termed supercritical. In the model of McMeeking and Evans, the phase transformation was supercritical and the volume increase due to transformation was small. They obtained estimates of the R-curve, the toughness value which rises as the crack grows. Eventually, a steady state toughness value develops after an amount of crack growth which is about 3 transformation zone widths. Budiansky et al. [4] considered supercritical and also subcritical materials in steady-state crack advance only. In the subcritical case, with $\bar{B} > -4G/3$, the phase change occurs gradually and the material can remain stably in a state in which the particles are only partially transformed. Budiansky et al. also accounted accurately for the perturbation of the transformation zone size and shape due to the stresses induced by the transformation itself. Using finite element analysis, they calculated steady state fracture toughnesses including cases where the volume increase from the transformation was quite large.

Stump and Budiansky [5] have recently provided a more accurate estimate of the R-curve for a crack advancing in supercritically transforming

material. The transformation zone evolves as the crack advances and remote load was adjusted to maintain the stress intensity factor at the critical value at the crack tip. Their numerical analysis shows that maximum fracture toughness occurs after a finite amount of crack advance, and that this maximum can be significantly higher than the steady-state fracture toughness which develops later. This indicates that the amount of toughening is underestimated by the steady state value. The steady state estimate generally underpredicts experimental data [2] so the new predictions bring the theory into better agreement.

The purpose of the calculations performed for this paper is to examine the transient behavior of a crack advancing in a material which transforms subcritically. Experimental evidence indicates that the transformation zones surrounding a crack tip tend to be diffuse or partially transformed indicating a subcritical transformation. Finite element analysis is used to solve the problem of a semi-infinite crack growing in a transforming material under Mode I loading and plane strain conditions. Crack growth in the finite element mesh is modelled using a nodal release technique; the transformation zone develops as the crack advances. Resistance curves are computed for different dilatant transformation strains and the results are compared with the steady-state analysis of Budiansky et al. [4]. A near critical case equivalent to one done by Stump and Budiansky [5] was also analyzed for comparison.

Constitutive Relations

In this section we describe the constitutive relations used to model transformation toughened composites. Developed by Budiansky et al. [4], the

model assumes the transformation zone contains many particles so that an incremental continuum description of the composite can be formulated. The composite material is isotropic and consists of a linear elastic matrix containing particles which undergo an irreversible dilatant transformation. The particles are otherwise isotropic and linear elastic and have a volume fraction of c .

Since the transformation is purely dilatant, the macroscopic shear response is entirely linear elastic with modulus G , which will depend on the composite properties of the material. Thus the deviatoric stress-strain relationship for the composite is

$$\sigma'_i = 2G \epsilon'_i \quad (1)$$

where σ' is the deviatoric part of the macroscopic stress and ϵ' is the deviatoric part of the macroscopic strain.

The dilatant behavior of the composite is depicted in Fig. 1, and can be represented by

$$\epsilon_{kk} = \frac{\sigma_m}{B} + \theta \quad (2)$$

where ϵ_{kk} denotes the total dilatation; σ_m is the hydrostatic part of the stress equal to $\sigma_{kk}/3$; B is the bulk modulus for the material; and θ is the current dilatation due to particle transformation in a macroscopic element of the composite material. (Einstein summation is used on repeated indices throughout.)

When the strain $\epsilon_{kk}^c = \sigma_m^c / B$ is exceeded, particles at the material point change phase to some extent, and an individual particle experiences a

dilatation θ_p^T when it transforms completely. When all of the particles at a material point transform, the macroscopic dilatation θ is equal to $\bar{c}\theta_p^T$. In a material in which the elastic moduli of the particles are identical with those of the matrix $\bar{c} = c$ [4]. However, McMeeking [6] has shown that in binary elastic composites, \bar{c} differs from c by a factor which depends on the ratios of elastic moduli. When the material is partially transformed in subcritical materials, the incremental dilatation during loading ($e_{kk} > 0$) and due to transformation is [4]

$$\dot{\theta} = (1 - \bar{B} / B) \dot{e}_{kk} \quad (3)$$

when $\sigma_m^c / B + \theta (1 - \bar{B} / B) \leq e_{kk} \leq \sigma_m^c / B + \bar{c}\theta_p^T (1 - \bar{B} / B)$. Since the phase transformation is irreversible, θ remains constant during unloading ($e_{kk} < 0$) in all cases. In the critical and supercritical case, eq. (3) is replaced by

$$d\theta / d\varepsilon_{kk} = \bar{c} \theta_p^T \delta_D (\varepsilon_{kk} - \sigma_m^c / B) \quad (4)$$

where δ_D is a Dirac delta function.

For critical and supercritical behavior, a region of partially transformed material does not exist, and θ is discontinuous at the edge of the transformation zone. In this situation, the governing equations are no longer completely elliptic as they are for subcritical materials [4].

Boundary Value Problem

A boundary-layer formulation, as described by Rice [7], was used to solve the problem of a semi-infinite crack growing in plane strain with a small scale zone of phase transforming particles (see Fig. 2). In this formulation it is assumed the outer boundary of the problem domain is large compared with the transformation zone surrounding the crack tip.

Displacement boundary conditions corresponding to a Mode I linear elastic plane strain field are applied remote to the crack tip. This displacement field is given by the singular part of the near tip field

$$u_a(r, \theta) = \frac{K^{APP}}{2G} \sqrt{\frac{r}{2\pi}} \bar{u}_a(\theta, \nu) \quad (5)$$

where K^{APP} is the Mode I elastic stress intensity factor applied remote from the crack tip, u is the displacement field, ν is Poisson's ratio and \bar{u} are universal functions for mode I which can be found in any fracture mechanics text. The coordinate system is chosen so that the origin lies at the crack tip. The x_1 and x_2 axes are parallel and perpendicular to the crack respectively and r and θ are polar coordinates as shown in Fig. 2. The external load applied to the plane strain region is then characterized by the stress intensity factor K^{APP} .

The material behavior described in the previous section was used to model the transforming strain region. As shown in Fig. 2, material near the tip transforms due to the stress concentration generated by the crack. A zone of material which has completely transformed ($\theta = \bar{c} \theta_r^T$) surrounds the crack tip. This core region is incrementally linear elastic with a permanent residual strain. Consequently, the stress field at the crack tip has a $r^{-1/2}$ singularity and is characterized by a stress intensity factor K^{TIP} . For the subcritical case, the region of purely transformed material is surrounded by a zone of material which is partially transformed ($\theta < \bar{c} \theta_r^T$).

For a stationary crack with monotonically increasing K^{APP} , no unloading occurs and the J-integral of Rice [7] is path independent[4]. The value of J on a contour taken entirely within the fully transformed zone near the tip is

$$J = \frac{1-\nu^2}{E} (K^{TIP})^2 \quad (6)$$

On a contour completely outside the transformed zone,

$$J = \frac{1-\nu^2}{E} (K^{APP})^2 \quad (7)$$

where E is the composite Young's modulus. Since J is path independent for a stationary crack, then $K^{APP} = K^{TIP}$. Thus, prior to any crack growth, there is no shielding [3,4]. The crack will commence growing when $K^{APP} = K^c$ the fracture toughness of the composite.

As the crack propagates and a wake of transformed material develops, K^{TIP} decreases due to shielding. To maintain crack growth, K^{APP} must be continually adjusted so that K^{TIP} equals K^c . K^{APP} is the effective fracture toughness of the composite material and the R-curve is its graph versus the amount of crack growth Δa .

Finally, all length scales in the moving crack tip problem were normalized by L , where L is defined by

$$L = \frac{2}{9\pi} \left[\frac{K^c(1+\nu)}{\sigma_m^c} \right] \quad (8)$$

Physically, L is the horizontal length of the nominal transformation zone for the stationary crack with $K^{APP} = K^c$. By normalizing all lengths with respect to L a self similar solution in terms of K^c is obtained. The solution depends on the strength of the transformation which is characterized by the nondimensional parameter ω , where

$$\omega = \frac{E_c \theta^T}{\sigma_m^c} \left[\frac{1+\nu}{1-\nu} \right] \quad (9)$$

In the calculation subcritical materials were considered for different values of α .

Finite Element Formulation

For plane strain ($\dot{\epsilon}_{13} = \dot{\epsilon}_{23} = \dot{\epsilon}_{33} = 0$) and in the absence of body forces, the principle of virtual velocities is ($\alpha = 1, 2$)

$$\int_A \dot{\sigma}_{\alpha\beta} \delta \dot{\epsilon}_{\alpha\beta} dA = \int_{S_T} t_\alpha \delta \dot{u}_\alpha dS \quad (10)$$

where A is the area domain of the plane strain problem and S_T is its surface where tractions t are prescribed. $\delta \dot{u}$ is an arbitrary virtual velocity variation which disappears on the surface $S - S_T$ where displacements are prescribed. The incremental form of the constitutive relation given by equations (1) and (2) is

$$\dot{\sigma}_{\alpha\beta} = 2G \dot{\epsilon}_{\alpha\beta} + [(B - 2G/3) \dot{\epsilon}_{\mu\mu} - B\theta] \delta_{\alpha\beta} \quad (11)$$

for plane strain where δ is the Kronecker delta.

The principle (10) can be used to formulate a finite element method. For this purpose, we define an of the appropriate velocity field as

$$\{\dot{u}_x, \dot{u}_y\}^T = \{\dot{u}\} = [N] \{\dot{u}^N\}, \{\dot{\epsilon}\} = [B] \{\dot{u}^N\} \quad (12)$$

where $\{\dot{u}^N\}$ are the nodal velocities, $[N]$ and $[B]$ are the shape functions and $\{\dot{\epsilon}\} = \{\dot{\epsilon}_{xx}, \dot{\epsilon}_{yy}, \dot{\epsilon}_{xy}\}^T$. Substituting (12) into the virtual work principle (10) and using the constitutive relation (11) gives the finite element equations

$$\int_A [B]^T [C] [B] dA \{\dot{u}^N\} = \int_{S_T} \{t\} [N] dS + \int_A [B]^T [C] \{\dot{\epsilon}^T\} dA \quad (13)$$

where $(\dot{\epsilon}^T)$ are the strain rates due to transformation and $[C]$ is the linear elasticity matrix such that $(\dot{\sigma}) = [C](\dot{\epsilon})$ when $\dot{\theta} = 0$ $((\dot{\sigma}) = (\dot{\sigma}_x \dot{\sigma}_y \dot{\sigma}_{xy})^T)$. For plane strain $(\dot{\epsilon}^T)$ conforms to

$$\dot{\epsilon}_{xy}^T = \frac{(1+\nu)}{3} \dot{\theta} \delta_{xy} \quad (14)$$

The material's non-linear behavior is reflected completely in the second term on the right hand side of equation (13). This term is the contribution to the load vector due to $\dot{\theta}$. The parameter $\dot{\theta}$ itself depends on the velocity field. Therefore, (\dot{u}^N) and $\dot{\theta}$ must be found iteratively. A successive approximations approach is used. Given an estimate of $\dot{\theta}$ then (\dot{u}^N) can be computed from (13). Use of this estimate for the velocity field provides a new estimate for $\dot{\theta}$ computed from equation (3) or (4) if it is non zero. This process is repeated until adequate convergence is achieved. The converged velocity field (\dot{u}^N) is then used to provide an increment of nodal displacements. The iteration procedure was started by an initial guess of $\dot{\theta} = 0$. In the case of the critical and supercritical materials, eq. (13) should be interpreted as representing a finite increment.

In the finite element analysis, 4-noded quadrilateral elements with four stations for the integration of the stiffness were used (Zienkiewicz [8]). The domain containing the crack was modelled with 2720 elements and 2860 nodes as shown in Fig. 3. Since Mode I loading is symmetric, only the upper half of the region was considered. Symmetry conditions were applied directly ahead of the crack tip ($u_2=0$ on $x_2=0$), while traction free conditions exist at the crack surface. Initially, the tip of the crack was located two elements to the right of the left hand side of the finite element mesh in Fig. 3c. Displacement boundary conditions given by (5) were applied to the outer boundary of the

mesh (Fig. 3a). The dimensions of the mesh were chosen so that the outer radius was at least 100 times the transformation zone height, h , thus ensuring small scale transformation. The refined mesh core was designed so the crack could grow a distance of $10h$ entirely in the fine mesh.

The nodal release technique was used to simulate crack growth in the finite element mesh. This method has been used successfully by Sham [9], Hawk and Bassani [10], and Charalambides and McMeeking [11]. The stationary crack solution was first obtained for $K^{APP} = K^{TIP} = K^C$. Crack growth was simulated by relaxing the nodal reaction force at the current crack tip node in five increments. After the node was released, K^{TIP} was obtained by calculating the I -integral close to the new crack tip. This computation was done using the stress derivative method of Parks [12, 13]. Then K^{APP} was adjusted in five increments to return K^{TIP} to the critical value. The procedure was repeated to release the new crack tip node. As the crack grows, the crack tip moves from node to node towards the right side of the mesh (Fig. 3c). The boundary conditions were also adjusted to maintain the singular field origin at the moving crack tip.

The rate of convergence for the iterative procedure depends strongly on the type of material modelled. Subcritical material converges quite rapidly. For the case $\bar{B} = 0$ the stationary crack solution only required eleven iterations for the convergence of the displacement norm (the sum of $u_i u_i$ over all the nodes) to five significant figures. On the other hand, the critical and supercritical cases did not converge at all. In that case the material behavior is represented by equation (4) and the transformation zone for the stationary crack increases steadily in size with each iteration. To overcome this problem, the transformation behavior was modelled with equation (3) as for a

subcritical material but with \bar{B} slightly above the critical value. This method involves a stable transformation. The value of B can be chosen so that the transition zone of partial transformation is confined to a layer of material of thickness less than the distance between integration stations. Although the transformation that occurs is not exactly critical, the results should be almost the same. The reason is that the discreteness of the mesh would spread the discontinuity which characterizes the zone boundary in the critical and supercritical case. Even when the critical case was modelled by just subcritical conditions with $\bar{B}/G = -1.3$, the stationary crack solution required fifty-three iterations for the convergence of the displacement norm to five significant figures.

The computations were done on a Convex C1-XP2 at the University of California, Santa Barbara. A typical finite element run with $\bar{B} = 0$ required 4000 minutes of computer time to propagate the crack through 90 elements.

Results for a Growing Crack

Using finite element analysis, the problem of a moving crack was solved for various material parameters. These characteristic parameters are the transformation strength ω , Poisson's ratio ν , and \bar{B}/G . Three sets of finite element computations were done with $\omega = 5, 10$ and 15 . In each set of calculations, cases were run for $\bar{B}/G = 0, -0.5$, and -1.0 with $\nu = 0.3$. A calculation with $\omega = 5$ and $\bar{B}/G = -1.3$ was also done to compare a near critical result with the calculations of Stump and Budiansky [5]. The two cases where $\omega = 10$ and 15 with $\bar{B}/G = -1.3$ were not done because of the large amount of computer time required; indeed the stationary crack solutions needed more than 200 iterations to converge. In all the finite element cases the crack was

propagated a distance of approximately $9L$. In this paper, the near critical solution and one of the others is described. The complete set of results are presented elsewhere [14].

Transformation Zones

The transformation zone for the near critical case ($\bar{B}/G=-1.3$) with $\omega=5$ and $\Delta a = 11.4L$ is shown in Fig. 4. In this case, the layer of partially transformed material is very thin. Apart from this thin layer, the material inside the zone has transformed completely. It is clear from the zone shape, that as the crack grew, the zone first widened. After reaching a maximum width, the zone narrowed sharply with growth and then appears to settle into a steady state.

In this case, the maximum zone height is $1.06L$ and occurs after the crack has grown a distance $3.7L$. The finite element results show that the zone reaches a steady-state height of $0.88L$. The transient behavior of a crack growing in a supercritical material has also been considered by Stump and Budiansky [5]. For $\omega=5$, their results show that the maximum zone height is $1.03L$ and occurs when $\Delta a=2.4L$. Their computation also predicts a steady-state zone height of $0.89L$.

Fig. 5 shows the transformation zone when $\bar{B}/G=0$ and $\omega=5$ after the crack has propagated a distance $8.6L$. The zone is depicted as contour plots of the transformation dilatation θ . The dilatation is normalized by $\bar{c} \theta_r^T$. As expected the crack tip is surrounded by a region of fully transformed material which in turn is surrounded by a region of partially transformed material. In this case h reaches a maximum of $0.87L$ after the crack has propagated a

distance $1.4L$. The steady-state zone height predicted by the finite element calculations is $0.81L$.

Resistance Curves

As mentioned earlier, the remote applied stress intensity factor was varied during crack advance to maintain K^C at the crack tip. The parameter K^{APP} is a measure of the effective fracture toughness in a transformation toughened composite and the R-curves (K^{APP} versus Δa) for the case when $\omega=5$ are shown in Fig. 6. As expected, in each case the transformation zone shields the crack tip and toughening is observed. The R-curves rise to a peak level associated with the widest part of the zone. Thereafter, the R-curve falls as the zone narrows. The relative amount of toughening is higher for the lower values of \bar{B} because there is relatively more fully transformed material in the wake zone. In addition, the peak toughening is more pronounced when \bar{B} is more negative.

After the crack has propagated a sufficient distance, the R-curve reaches an asymptotic value. This steady-state value of K^{APP} corresponds to the steady-state region in the transformation zone. For comparison, the dashed lines in Fig. 6 denote the toughnesses predicted by the steady-state finite element analysis of Budiansky et al. [4]. The subcritical steady-state values of K^{APP} predicted by our transient finite element analysis are higher than those of [4]. For example when $\bar{B}=0$, the steady-state toughness predicted by the finite element analysis is $1.19K^C$ while the analysis of Budiansky et al [4] predicts $1.17K^C$. This means that our prediction of the zone contribution is about 10% higher. The difference is unresolved.

The toughness for the near critical material $\bar{B}/G=-1.3$ predicted by our finite element calculation agrees well with the steady-state analysis for critical and supercritical materials which is exact. This latter result gives us a degree of confidence in our numerical solutions. For the near critical case ($\bar{B}=-1.3$) with $\omega=5$, the finite element analysis predicts a maximum and steady-state K^{APP} of $1.30K^C$ and $1.27K^C$ respectively. The peak in K^{APP} occurs when the crack has grown a distance $5.6L$. For the supercritical material, Stump and Budiansky [5] predict values of $1.29K^C$ and $1.26K^C$ for $\omega=5$. In their analysis, they found that maximum K^{APP} occurred when $\Delta a=5.5L$.

For the subcritical material, the difference in the peak and steady-state toughnesses are much smaller than the supercritical case. For $\bar{B}=0$ the finite element analysis shows that both the peak and steady-state K^{APP} are indistinguishable at $1.19K^C$. Even for $\bar{B}=-1.0$, the peak K^{APP} is only $1.27K^C$ compared to a steady-state value of $1.26K^C$.

Discussion

The finite element results presented in this paper indicate agreement between our near critical solution and the accepted steady state toughening estimate of previous work [3, 4, 5]. In addition, the peak toughness predicted here by finite elements agrees with the value obtained by Stump and Budiansky [5] by another method. This gives us confidence in our numerical results even though some of our other calculations disagree with the established solutions [4]. It is worth noting that we have achieved agreement with other results in the case in which we found convergence most difficult to obtain.

As with the work of Stump and Budiansky [5], the importance of the transient numerical results over the previous steady state solutions is that the predicted peaks in the R-curves are higher. Since the peak values of toughening will determine the potential toughness of the composite material, these higher values are significant. Since theory has so far underpredicted the potency of the transformation toughening mechanism [2], the new results offer the prospect of bringing theory into better agreement.

DUCTILE PHASE TOUGHENING

The addition of a dispersed ductile phase to a brittle material can lead to significant increases in fracture resistance compared to the untoughened matrix material. Examples of current or potential technological significance which have been studied are tungsten carbide reinforced with cobalt [15], alumina reinforced with aluminum [16, 17] and a brittle titanium-aluminum alloy reinforced with niobium [18]. The first two systems are interconnecting networks, while in the third the niobium phase is in the form of oriented thin disks. Successful toughening has also been observed in a model system consisting of large aluminum particles in glass [19]. The primary mechanism responsible for the enhanced toughnesses appears to be bridging by intact ligaments of the ductile phase behind the advancing crack tip (Fig. 7), although other effects such as crack deflection and crack trapping by the ductile phase also contribute. One of the aims of the modeling presented here is to determine the extent to which bridging effects due to deformation of ligaments can account for the observed toughness increases.

The contribution to fracture energy from bridging has been modeled in various contexts: examples are ligaments due to ledge formation in quasi-cleavage of steels [20, 21] and fiber reinforcements of various kinds [22, 23, 24]. Recently, bridging models based on distributions of nonlinear springs have been considered in some detail [25, 26]. In general, the enhancement of steady-state (i.e. resistance curve plateau) fracture toughness of a brittle material due to crack bridging effects may be estimated [27] if a relationship is established between the distance of separation of the faces of a crack in the composite and the average stress supported across the crack faces by the bridging ligaments at that separation. Given this framework, the problem of estimating the toughness enhancement due to the presence of a bridging ductile phase (particulate or network) may be reduced to that of determining the load-separation relation for a "typical" bridging ligament, whence the fracture energy increase may be written as

$$\Delta G = G - G_m = f \int_0^{u^*} \sigma du - f G_m \quad (15)$$

where G is the fracture energy of the composite, G_m is the matrix fracture energy, σ is the nominal stress supported across a bridging ligament at stretch u (σ falling to zero at $u = u^*$), and f is the volume fraction of ductile phase (assumed to be the same as the area fraction intercepted by the crack). The final term on the right hand side is introduced [26] to account for the fact that the area of matrix fractured is reduced by the presence of a significant area fraction of bridging phase.

This relationship may be written in a form scaled by the properties of the bridging ligament as

$$G = f \sigma_0 a_0 w + (1-f) G_m \quad (16)$$

where a_0 is the radius of the ligament, σ_0 is the initial yield stress of the ductile phase and w is a number defined by

$$w = \int_0^{\frac{u}{a_0}} \frac{\sigma}{\sigma_0} d\left(\frac{u}{a_0}\right) \quad (17)$$

The scalar w may be interpreted as containing information about the geometric constraint experienced during the deformation of the ligament, about strain-hardening and about the failure of the ligament. The problem thus becomes that of determining w by obtaining the (σ/σ_0) versus (u/a_0) relation for some representative configuration and computing the area under the curve (Fig. 8).

The preceding formulation is well-established. However, there is a lack of detailed modeling of the σ - u relation (and hence of the bridging contribution to toughening). Measurements of composite fracture toughness may be employed to infer values of w via the inverted relationship

$$w = \frac{1}{f \sigma_0 a_0} \left\{ \frac{(1-\nu^2)K^2}{E} - \frac{(1-f)(1-\nu_m^2)K_m^2}{E_m} \right\} \quad (18)$$

where the energy release rates have been expressed in term of plane strain fracture toughness and elastic properties for the matrix (K_m, E_m, ν_m) and composite (K, E, ν). Values of w inferred in this way for several systems of

interest are displayed in Table 1.* The wide variation in w for the various systems remains to be explained.

Some recent model experiments on lead fibers surrounded by glass [28] provide direct measurements of σ - u relations for constrained ligaments, as distinct from comparison to values of w inferred from toughness measurements. The insights gained from these tests will be discussed below.

Alternatively, experimental observations of bridging zone length L have been compared to the predictions of a cohesive zone model with an assumed shape of the σ - u relation and used to infer the peak load supported by the ligament [26]. In one limit of this model, the bridging zone is a constant stress (Dugdale) zone. The $(\sigma_{cohesive}/\sigma_0)$ level then required to explain the observed toughnesses are shown in Table 2. These levels are anomalously high in both the WC/Co and Al_2O_3/Al materials. The predicted failure stretches conjugate to these stress levels are shown in Table 2, and are seen to be quite small.

Objectives and Idealized Problem

The work described in the present article is an initial attempt to model numerically the behavior of a single ductile bridging particle suitably constrained by a stiffer, elastic matrix, and to determine whether the contribution to toughness thereby predicted via the bridging model is

* The two entries for the TiAl/Nb material represent different orientations of the reinforcements, which in this case are disks of niobium (a_0 corresponding to half the thickness of the disks)

sufficient to explain experimental observations. The problems to be considered concern the response of a single elastic/plastic particle surrounded by a cylinder of an elastic material with a considerably higher modulus. The cylinder is fully cracked in the equatorial plane of the particle perpendicular to the axis of the cylinder (Fig. 9) as needed to model circumstances in which the matrix crack has left the intact particle in its wake. The numerical study consists of deforming the ensemble axially (with boundary conditions appropriate to an array of such particles) and determining the $\sigma-u$ characteristics. The constraint experienced by the particle is also expected to be similar to that experienced by a ligament which is part of a fibrous network of ductile material, since only the region near the crack faces can deform plastically.

The idealized model considered here closely corresponds to the model experiments [28], a few of the results of which are schematically shown in Fig. 10. The first set of results (a) involve circumstances in which there was no debonding of the lead from the glass. The second set of results (b) involve substantial matrix cracking near the lead-glass interface adjacent to the crack tip. Significant differences are apparent between the two sets of results. In particular, the results of type (a) indicate an average w of about 1.6, while those of type (b) indicate a range of values with an average of about 4.5 and an extreme of around 6.

Regimes of Ligament Behavior

Fractographic examination of toughened composites and the model experiments show that several distinct types of behavior may be expected for the constrained bridging particle. Indeed, analysis of the deformation history

may be distilled into the circumstances wherein the transitions between regimes take place. Under very low loads, the particle should be largely elastic, with plasticity confined to a region close to the tip of the crack, which has a blunted tip in the particle (Fig. 11a). The detailed stress fields will not be classical elastic/plastic small-scale yielding fields, due to the material inhomogeneity around the tip, but should have many of the same features. When the entire particle has yielded, one possibility is that constraint levels remain high enough to produce a deformation field resembling a perfectly-plastic plane strain slip-line solution [27] (Fig. 11b and Fig. 12). Under these circumstances, the stress distribution within the particle would be expected to be very sensitive to events at the blunt tip and would tend to involve relatively high levels of hydrostatic stress. The load supported by the particle would be correspondingly high (note that no effect of strain-hardening has been included in Fig. 12).

An alternative for the fully yielded particle is that the constraint of the stiffer surrounding matrix is relieved sufficiently by crack-tip deformation and/or interfacial debonding or sliding to allow the bridging ligament to begin to neck (Fig. 10c). The necking process involves lower stress levels within the particle; moreover, lower nominal stress levels σ arise because of the decreased load-bearing area. Constraint by the surrounding stiff matrix will have a significant effect on the load history since the rate at which necking takes place is strongly influenced. This regime must dominate the later stages of deformation when the ligament fails in a highly ductile manner.

In what follows the stress-strain behavior of the ligament material has been taken to be that of the bulk material, with incompressible, pressure-

insensitive plastic deformation assumed. The toughening effectiveness of a ductile phase will in general be enhanced by strain-hardening or an increased yield stress, unless an associated lack of ductility leads to failure at significantly decreased separation distance. Any increase in σ_0 will lead to a proportionate decrease in the inferred value of w (Table II) and in the constraint factors emerging from the analysis of Ref. [26] (Table III) which employed properties appropriate to pure bulk materials. For instance, microstructural studies of the Al phase in the $\text{Al}_2\text{O}_3/\text{Al}$ material [29] suggest that dispersion strengthening might significantly raise the yield stress of the ligaments, perhaps by as much as a factor of three, although no quantitative hardness data is available. (Note, though, that the yield stress used to compute w for the model experiments of Ref. [28] was measured from a batch of identical but unconstrained lead wires.)

It is initially assumed that the interfacial bond is strong enough that no debonding takes place. However, under circumstances where the particle remains highly constrained for a significant portion of its history, features near the crack tip may control stresses throughout the particle. Should this be the case, small scale events such as debonding of the interface near the tip affect the load history of the ligament in the early stages of deformation. In general, debonding will tend to lower constraint levels and hence lead to lower peak loads. However, the influence of debonding on the necking regime is also very strong, since the dimensions of the necking ligament are thereby determined. Debonds which are significant fractions of the ligament radius in extent are observed both in model experiments [28] and in detailed fractographic examination of the $\text{Al}_2\text{O}_3/\text{Al}$ material [29].

Interaction between bridging ligaments is likely to be an important effect when the volume fraction of ductile phase is significant. The cylinder model employed here incorporates this interaction to lowest order by having an outer radius to the matrix jacket which reflects the volume fraction, and appropriate "unit cell" boundary conditions: straight but unconstrained boundaries. Again, with a stiff matrix, these effects are small.

Numerical Modeling

The numerical modeling of this problem was implemented using the finite element package ABAQUS [30], again on a CONVEX C1-XP2. The unit cell of Fig. 9 was discretized and analyzed for both the axisymmetric geometry and the corresponding plane strain problem. The computations employed a finite strain formulation in order to account for geometry changes, with elastic behavior assumed for the matrix and J_2 -flow theory elastic/plastic behavior for the ductile phase. The upper boundary of the unit cell was extended gradually in order to generate σ - u curves for the ligament. Separation u is measured as the axial displacement of the matrix point at the tip of the crack, while σ is computed from the total force exerted on the upper boundary, normalized by the original ligament area.

Constrained Regime

The aim at the outset was to describe the initial σ - u and also the necking regime as far as possible. However, serious difficulty was encountered in extending the σ - u curves to large u . Indeed, the results never extend into a regime of clearly decreasing total load on the ligament. This failure is attributed to the characteristics of the deformation in the crack tip/interface region (inset in Fig. 9). This is discussed later on in this section.

To produce results relevant to larger stretches, a blunt tip of finite initial radius was included, and the results for different radii compared for consistency.

The majority of the results were obtained for material parameters characteristic of the (bulk) properties of Al_2O_3 and Al : the matrix Young's modulus is six times larger than that of the inclusion; the inclusion initial yield stress is 1/1000 of its Young's modulus and the material strain-hardens with an exponent of $n=0.2$ until the flow stress saturates at three times initial yield.

Typical $\sigma-u$ curves for these material parameters is shown in Fig. 13 . The small-scale yielding regime exists only for nominal stress levels of $(\sigma/\sigma_0) < 1$, corresponding to openings u which are extremely small. The growth of the plastic zone is rather more rapid than for a similar homogeneous small-scale yielding problem, due to the shear induced at the interface. The particle is fully plastic at $(\sigma/\sigma_0) = 4$. The constrained fully plastic regime appears to produce a peak stress level $(\sigma/\sigma_0) = 6$, by which time a macroscopic softening due to the onset of necking has begun, even though all of the material in the particle is still slowly strain-hardening. Fig. 13 also includes results in which no strain-hardening is incorporated. The constraint magnification factor is seen to be similar in either case.

However, a typical failure stretch, whether observed experimentally or predicted on the basis of necking calculations, corresponds to (u/a_0) on the order of 1 when failure occurs by necking to a point. The results displayed here thus cover only a tiny range of the expected total load-displacement relation for the ligament.

The solid curve in Fig. 13 was generated using an initial tip radius r such that $(r/a_0) = 0.05$. Even when this rather large initial radius is used, the computations fail at a small stretch. The results suggest that necking becomes important rather rapidly, although additional results obtained using smaller initial radii (dashed curves in Fig. 13) indicate that the characteristics described above may be sensitive to the choice of initial tip radius.

A comparison to some analogous plane strain results is displayed in Fig. 14. With the given normalization, the results are seen to be similar, as are the limiting stretches achievable by the computation.

In an effort to improve the solution, a number of variants of the computations were carried out. Differing degrees of strain-hardening and material descriptions were employed to investigate the possibility of flow localization. Differing degrees and natures of near-tip mesh refinement and focusing were also investigated. The numerical problems encountered, however, appear to be independent of the details of material behavior and of the extent and nature of near-tip/interface discretization. Currently, interest is focused on the near-tip fields themselves.

Near-Tip Deformation

The breakdown of the numerical solution is exacerbated by the intense and non-uniform deformation in the tip-interface region. A sample deformed mesh in that region (for a rather crude mesh) is shown in Fig. 15.

The reason for this deformation may be seen from the fact that the large-scale deformation of the ligament material is essentially volume-conserving. The behavior is exemplified by considering the volume

contained in that part of the stretched ligament which extends below its original midplane (Fig. 16). This volume must be accounted for by the "void space" contained in the blunting crack-tip. If a small amount of necking Δr has occurred, but large enough that elastic volume changes are not important, the volume to be accounted for is of order $\pi a_0^2 u$. The corresponding volume of the toroidal "void" is of order $\pi a_0 \Delta r \Delta h$. Volume conservation then requires that

$$\frac{\Delta h}{u} = \frac{a_0}{\Delta r} \quad (19)$$

That is, a small crack-tip "void" is driven in a direction normal to the crack plane more rapidly than the opening rate of the tip itself. Without debonding or sliding, the constraint of the stiff surrounding matrix produces intense shear deformation. When no debonding occurs, this pattern of deformation leads to a "hollowing out" of the ductile phase near the matrix crack tip. Such behavior is observed experimentally.

This type of constrained interfacial flow is encountered frequently in problems involving a composite of a brittle and a ductile material. As a prototype problem which may shed some light on the difficulties encountered here, consider plane strain deformation near the intersection of a free surface with an interface between an elastic material and a rigid/perfectly-plastic (Mises) material (Fig. 17). The asymptotic solutions are very similar to those encountered in homogeneous plastic crack and notch problems, as is sketched briefly below.

Searching for solutions with bounded stresses in the yielded plastic sector P means that asymptotically

$$\sigma = \sigma(\theta) \quad (20)$$

and the governing equations reduce to

$$\begin{aligned} \sigma'_{r\theta} &= \dot{\sigma}_{\theta\theta} - \sigma_{rr} \\ \sigma'_{\theta\theta} &= -2\sigma_{r\theta} \end{aligned} \quad (21)$$

where a prime denotes a derivative with respect to r .

The yield condition in P is

$$4\tau_y^2 = 4\sigma_{r\theta}^2 + (\sigma_{\theta\theta} - \sigma_{rr})^2 \quad (22)$$

where τ_y is the yield stress in shear of the plastic material. Differentiation of (22) with substitution from (21) yields

$$\sigma'_{r\theta} (\sigma'_{r\theta} + 4\sigma'_{\theta\theta}) = 0 \quad (23)$$

Solution and more substitution shows that the two types of solution to (23) are

$$\left. \begin{aligned} \sigma_{r\theta} &= \pm \tau_y \\ \sigma_{\theta\theta} - \sigma_{rr} &= \sigma_{\theta\theta}(\theta_0) \pm 2\tau_y(\theta_0 - \theta) \end{aligned} \right\} \text{(fan)} \quad (24a)$$

or

$$\left. \begin{aligned} \sigma_{rr} + \sigma_{\theta\theta} &= \text{constant} \\ \sigma_{rr} - \sigma_{\theta\theta} &= \pm 2\tau_y \sin 2(\theta - \theta') \end{aligned} \right\} \text{(constant state)} \quad (24b)$$

where θ_0 and θ' are arbitrary angles. These are the familiar singular fan and rigid constant state region, respectively, of slipline plasticity.

The asymptotic stresses in the elastic sector are determined by the traction stresses on the interface, since the homogeneous solutions are less singular than r^0 in a non-reentrant wedge [31].

The only way to arrange the plastic sectors in a fully yielded plastic quarter-space is in the sequence shown in Fig. 18, where the fan is possibly of vanishing extent. Traction continuity is then sufficient to calculate the stresses in the constant state region adjacent to the interface in terms of the fan extent θ_f . In particular, the traction stresses are

$$\left. \begin{aligned} \sigma_{xy} &= \tau_0 \sin 2\theta_f \\ \sigma_{yy} &= \tau_0 (1 + 2\theta_f + \cos 2\theta_f) \end{aligned} \right\} \text{(at interface)} \quad (25)$$

where a local tension has been assumed at the free surface.

Increasing load transfer to the near-surface interface thus correlates with a growing fan. One possibility for the numerical difficulties experienced in this and similar work is speculated to be the growth of the fan region as loading continues.

For instance, preliminary finite element results for a sample problem consisting of two slabs (one elastic, one plastic) bonded together and in tension perpendicular to the interface [32] suggest that the results may be improved by extreme mesh refinement in the tangential direction, apparently due to improved modeling of the fan growth. (Over the range that results can be extracted, agreement with the asymptotic results above is excellent.) To what extent this is a general feature of finite element solutions of such problems is being further investigated.

Necking Regime

Since the numerical approach described in the previous section was not successful in providing results extending into a clearly necking behavior, and since debonding of ligaments from the matrix appears to significantly affect

toughening, a different class of problem was next studied. The axial deformation of plastic bars was modeled, with the ends of the bars constrained from shrinking radially (Fig. 19). This is intended to model a ligament for which the constraint of the surrounding stiff matrix has been partially relaxed by debonding of the ligament near the crack tip. Finite element modeling was employed to discover how the initial bar height affects the subsequent load-displacement history. The stretch u is now measured as the extension of the bar.

A set of results (Fig. 20) with material properties appropriate to the $\text{Al}_2\text{O}_3/\text{Al}$ material for initial 'debonds' ranging from $(h_0/a_0)=0.1$ to $(h_0/a_0)=0.5$ indicate that two effects are important: (a) a small debond leads to higher constraint levels than a large one, but (b) the necking process is strongly accelerated by the constraint when the debond is short, so that the load decreases more rapidly with increasing ligament stretch than for the long bar.

Similar trends can be seen in the plane strain analogs of the above calculations, corresponding to slab-like reinforcements. The comparison in Fig. 21 shows that there is slightly more constraint for the plane strain case.

Approximate models of the necking process in constrained ligaments may be constructed [16, 33] which agree well with the finite element results. Using these over the whole range of ligament deformation or extrapolating the finite element results predicts a value for w of about 3 for the large debond case $(h_0/a_0)=0.5$.

Discussion

Comparison of the models described above to the experiments of [28] shows qualitative agreement, but convincing quantitative predictions are yet to be obtained. For the initial, constrained stages of deformation, the numerical results indicate constraint factors in the requisite range. A priority of future work will be to extend the constrained results into a clearly necking regime.

For debonded ligaments, the observed correlation between increased debond length and increased w [28] is predicted by the models, but the largest measured w values with debonding are not approached, apparently due to the accelerated necking predicted compared to the experiments.

The toughness enhancement due to bridging is dominated by the contribution from the necking regime, since the high stresses in the constrained plasticity regime persist only briefly. However, this conclusion does not exclude the early stages of deformation as irrelevant, since the initial stresses and near-tip deformation may control whether debonding occurs. Clearly the significance of such effects will depend strongly on the material and interfacial properties. In addition, the evolution of the necking ligament geometry may depend on the details of the initial deformation even when no debonding takes place. It is thus important to model the whole range of ligament deformation accurately. Achievement of the numerical modeling of the whole range of deformation, including if possible the evolution of debonding along the matrix-ligament interface, is a priority of ongoing work.

From the materials design viewpoint, perhaps the most interesting aspect of the results is the suggestion that the ductile phase need not be

completely bonded to the matrix during deformation to provide toughening. Limited debonding may well be beneficial in terms of toughness enhancement.

CLOSURE

The results presented in this paper indicate useful directions for optimizing the toughness of brittle matrix composite materials. Large scale numerical simulation of these problems has proved to provide insight and will be necessary for further progress in this area.

ACKNOWLEDGEMENT

This work was supported by the DARPA University Research Initiative under ONR contract N00014-86-K-0753. The finite element package ABAQUS was provided by Hibbitt, Karlsson and Sorensen, Inc.

REFERENCES

- [1] Evans, A. G., and Heuer, A. H., 1980, *J. Am. Ceram. Soc.* 63 [5-6], 241-248.
- [2] Evans, A. G., and Cannon, R. M., 1986, *Acta Metall.* 34 [5], 761-800.
- [3] McMeeking, R. M. and Evans, A. G., 1982, *J. Am. Ceram. Soc.* 65 [5], 242-246.

- [4] Budiansky, B., Hutchinson, J. W. and Lambropoulos, J. C., 1983, *Int. J. Solids Struct.* **19** [4], 337-355.
- [5] Stump, D. M. and Budiansky, B., "Crack Growth Resistance in Transformation-Toughened Ceramics", to be published.
- [6] McMeeking, R. M. "The Effective Transformation Strain of Binary Elastic Composites", 1986, *J. Amer. Ceram. Soc.* **69**, C301-302.
- [7] Rice, J. R., 1968, *Trans. ASME* **80**, Series E, *J. Appl. Mech.* **35**, 379-386.
- [8] Zienkiewicz, O. C., 1977, *The Finite Element Method*, 3rd Edition, McGraw-Hill, London.
- [9] Sham, T. L., 1983, "A Finite Element Study of the Asymptotic Near Tip Fields for Mode I Plane-Strain Cracks Growing in Elastic-Ideally Plastic Solids", *Elastic-Plastic Fracture: Second Symposium, Volume I-Inelastic Crack Analysis*, ASTM STP 803 (Eds: Shih, C. F., and Gudas, J. P.) 52-79.
- [10] Hawk, D. E. and Bassani, J. L., 1986, *J. Mech. Phys. Solids* **34** [3], 191-212.
- [11] Charalambides, P. G. and McMeeking, R. M., 1987, *Mechanics of Materials* **6**, 71-78.
- [12] Parks, D. M., 1974, *Int. J. Fract.* **10**, 487-502.
- [13] Parks, D. M., 1978, "The Virtual Crack Extension Method For Non-Linear Material Behavior", *Numerical Methods in Fracture Mechanics* (Eds: Luxmore, A.R. and Owen, D. R. J.) 464-478.
- [14] HoM, C. L. and McMeeking, R. M., 1989, "Numerical Results for Transformation Toughening in Ceramics", to be published.

- [15] L. S. Sigl and H. E. Exner, *Met. Trans. A* 18A, 1299 (1987)
- [16] L. S. Sigl, P. A. Mataga, B. J. Dalgleish, R. M. McMeeking and A. G. Evans, *Acta Met.* 36, 945 (1988)
- [17] B. J. Dalgleish and A. G. Evans, to appear
- [18] C. K. Elliot, G. R. Odette, G. E. Lucas and J. W. Sheckherd, Proceedings of M.R.S. Meeting, Reno (April 1988)
- [19] V. D. Krstic, *Phil. Mag. A* 48, 695 (1983)
- [20] R. G. Hoagland, A. P. Rosenfield and G. T. Hahn, *Met. Trans.* 3, 123 (1972)
- [21] W. W. Gerberich and E. Kurman, *Scripta Met.* 19, 295 (1985)
- [22] P. Hing and G. W. Groves, *J. Mater. Sci.* 1, 427 (1972)
- [23] G. A. Cooper and A. Kelly, *J. Mech. Phys. Solids* 15, 279 (1967)
- [24] W. W. Gerberich, *J. Mech. Phys. Solids* 19, 71 (1971)
- [25] L. R. F. Rose, *J. Mech. Phys. Solids* 35, 383 (1987)
- [26] B. Budiansky, J. Amazigo and A. G. Evans, *J. Mech. Phys. Solids* 36, 167 (1988)
- [27] A. G. Evans and R. M. McMeeking, *Acta Met.* 34, 2435 (1986)
- [28] M. F. Ashby, F. J. Blunt and M. Bannister, Cambridge University Engineering Department Technical Report (1988)
- [29] B. D. Flinn, M. Rühle and A. G. Evans, to appear

- [30] Hibbitt, Karlsson and Sorensen, Inc., Providence, R.I.
- [31] S. P. Timoshenko and J. N. Goodier, *Theory of Elasticity*, McGraw-Hill
(1959)
- [32] H. C. Cao, unpublished work
- [33] P. A. Mataga, to appear

FIGURE CAPTIONS

- Figure 1. The hydrostatic material behavior of a ceramic containing particles which undergo a stress induced phase transformation.
- Figure 2. The boundary value problem of a semi-infinite crack subject to a mode I tensile opening load.
- Figure 3. The finite element mesh used to examine a growing crack in a transformation toughened composite.
- Figure 4. Transformation zone for the case $\omega=5$ and $\bar{B}/G=-1.3$ when $\Delta a=11.4L$.
- Figure 5. Contour plot of $\theta/\bar{c}\bar{\theta}_p$ and transformation zone for the case $\omega=5$ and $\bar{B}/G=0$ when $\Delta a=8.9L$.
- Figure 6. R-curves for $\omega=5$. The steady-state results of Budiansky et al. [4] are shown with dashed lines.
- Figure 7. Schematic of crack-bridging behavior of ductile particles in a brittle matrix.
- Figure 8. Non-dimensional stress vs. stretch behavior of a typical ligament and associated area w .
- Figure 9. Idealized configuration for analysis of behavior of a single particle. Inset shows initial blunting of crack tip at particle equator.

- Figure 10. Sketch of results of model experiments of Ref [28].
 (a) without debonding between ligament and matrix
 (b) with debonding
- Figure 11. Regimes of ligament behavior.
 (a) small-scale yielding (b) constrained plasticity
 (c) plastic necking
- Figure 12. Plane strain slipline solution of Ref [27].
 (a) slipline geometry for $a_0/u=1150$ (b) $\sigma - u$ relation
- Figure 13. Initial stage finite element results for different choices of work-hardening exponent n and of initial root radius r_0 . (Bonded interface).
- Figure 14. Finite element plane strain vs. axisymmetric comparison for initial stages. (Bonded interface).
- Figure 15. Deformed mesh in tip/interface region.
- Figure 16. Geometry for initial deformation near crack tip in ductile phase.
- Figure 17. Prototype asymptotic problem near the intersection of a free surface and a brittle/ductile interface.
- Figure 18. Asymptotic sector arrangement for prototype problem.
- Figure 19. Constrained necking bar geometry designed to simulate the large deformation of a ligament with debonding.
- Figure 20. Constrained necking bar finite element results for various 'debond' lengths h_0 . Also shown for comparison are

corresponding uniform deformation (unconstrained ends) results.

Figure 21. Plane strain vs. axisymmetric comparison for constrained necking bars for various debond lengths h_0 .

TABLE CAPTIONS

- Table I.** Matrix, ligament and composite properties and inferred values of w for some materials of interest.
- Table II.** Values of cohesive stress in Dugdale model inferred in Ref. [26] from observed bridging zone lengths, and corresponding failure stretches.

System	K_m (MPa \sqrt{m})	E_m (GPa)	ν_m	f	σ_0 (MPa)	a_0 (μm)	E (GPa)	ν	K (MPa \sqrt{m})	w
glass/Al	0.8	70	0.20	0.2	70	55	70	0.23	6.5	0.73
Al ₂ O ₃ /Al	3	420	0.20	0.2	70	2	310	0.22	8.4	7.2
WC/Co	8	710	0.21	0.2	450	0.75	570	0.22	16	5.3
TiAl/Nb (L)	12.5	200	0.3	0.2	300	12.5	175	0.31	20	2.0
TiAl/Nb (H)	12.5	200	0.3	0.2	300	12.5	175	0.31	25	3.6

Table I

System	w	$\sigma_{cohesive}/\sigma_0$	u^*/a_0
glass/Al	0.73	3.6	0.20
Al ₂ O ₃ /Al	7.2	22	0.32
WC/Co	5.3	22	0.24

Table II

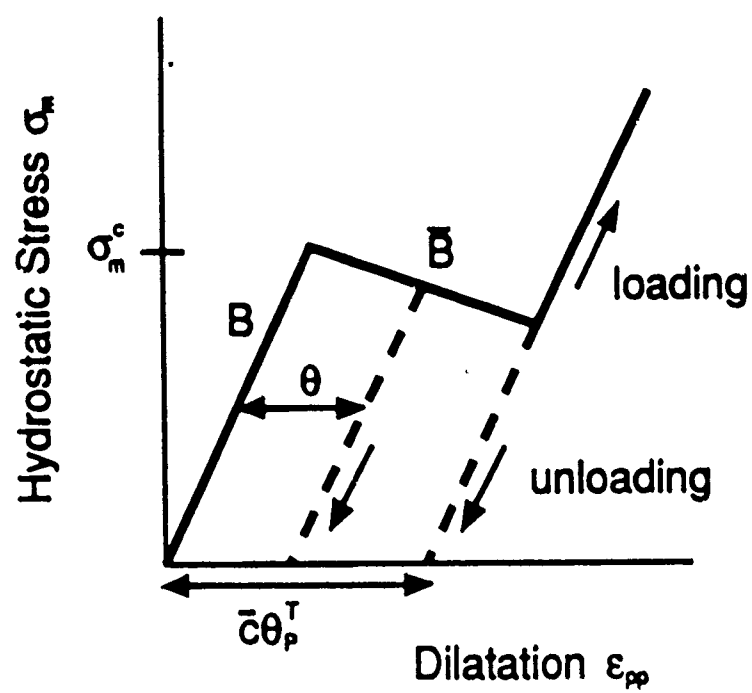


Fig 1.

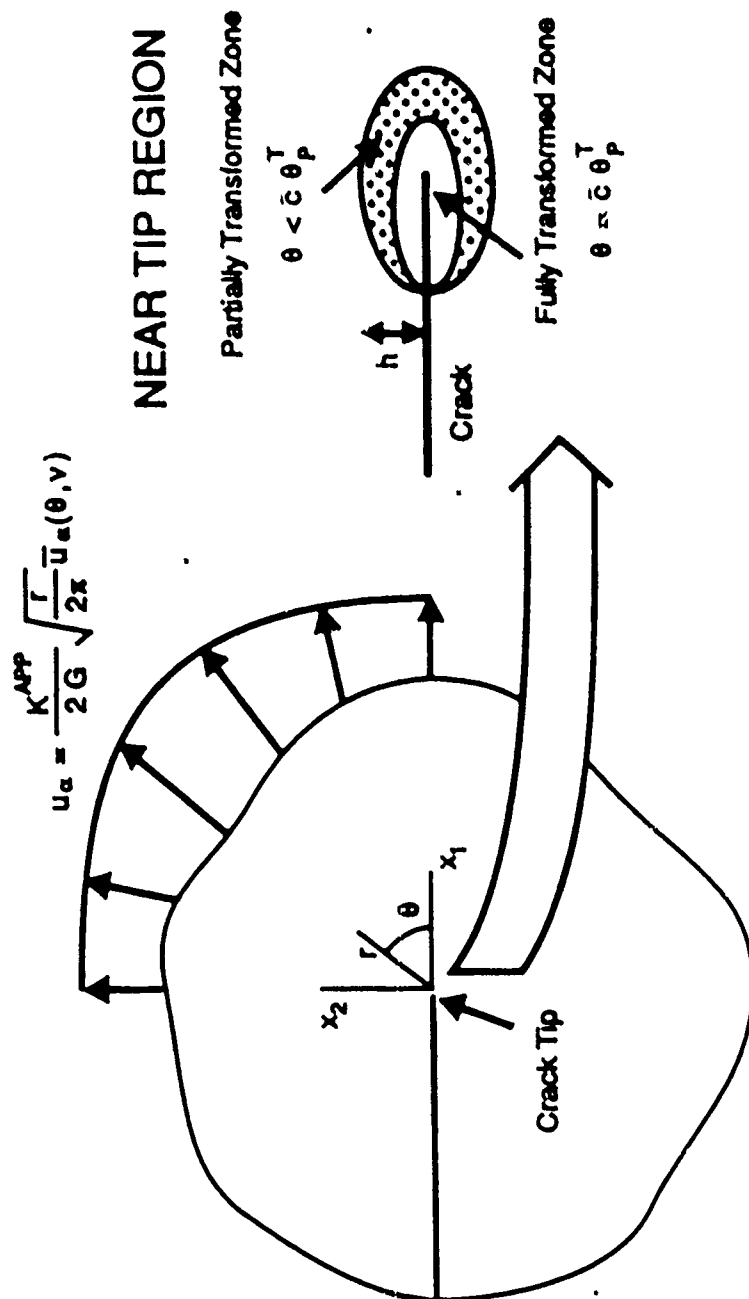
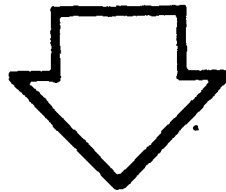
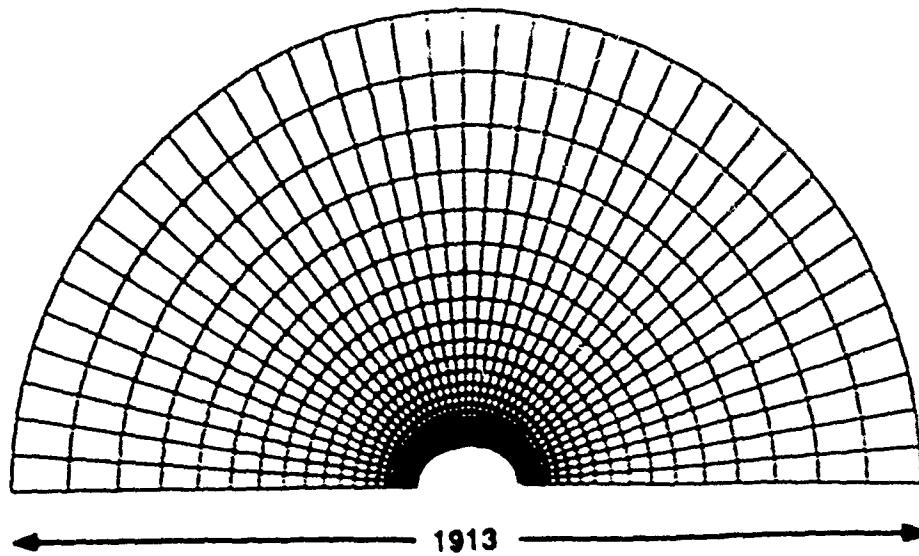
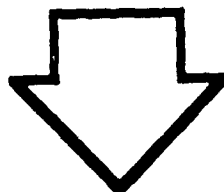
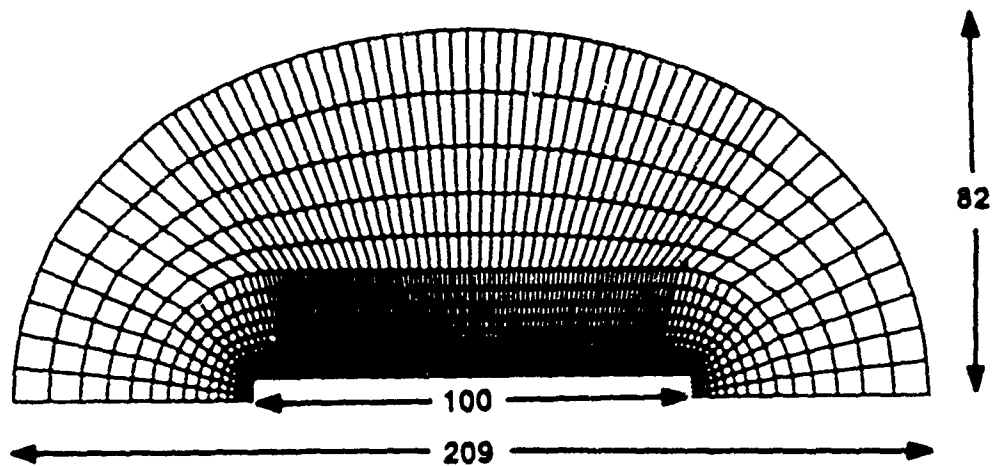


Fig 2.

(A)



(B)



(C)

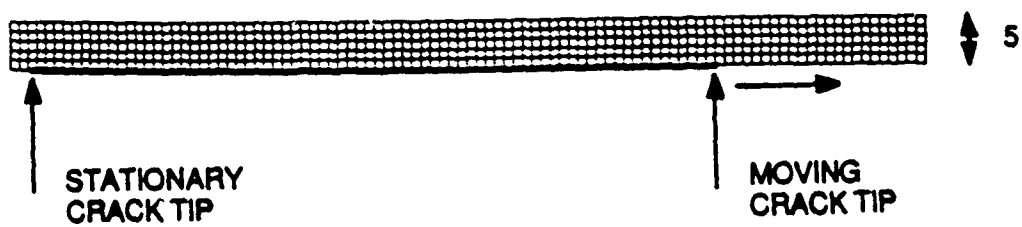


Fig 3.

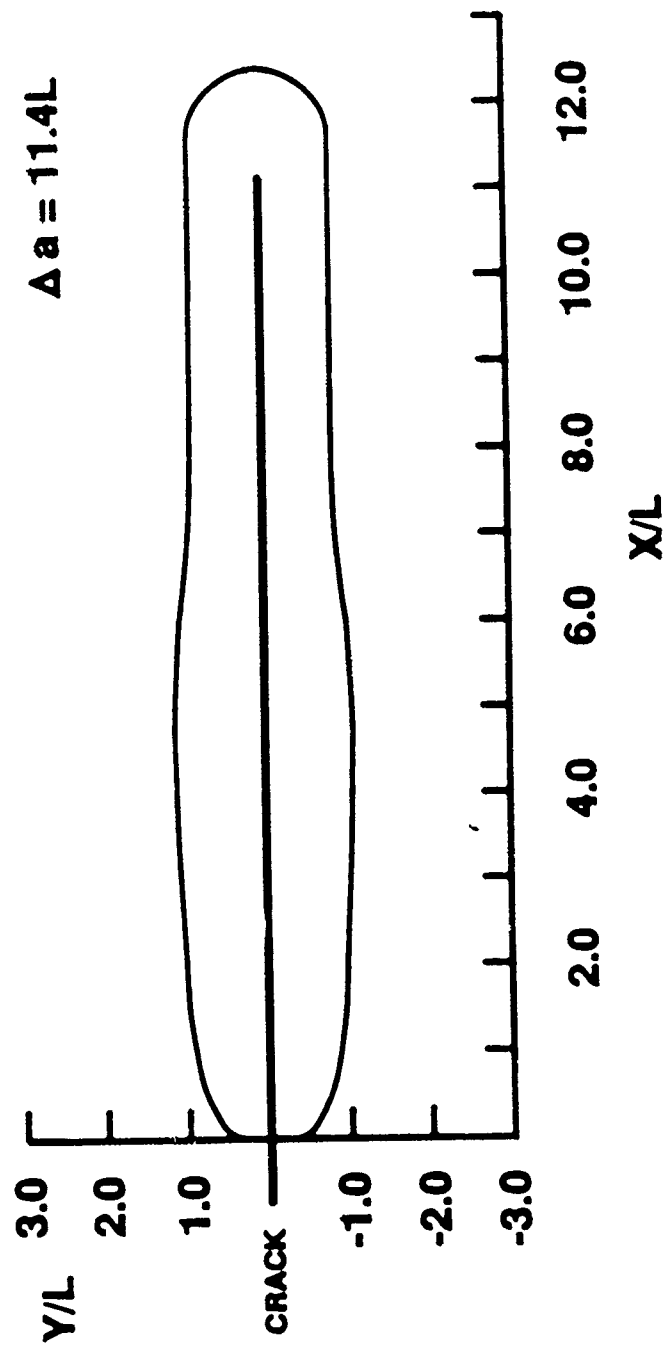


Fig. 4.

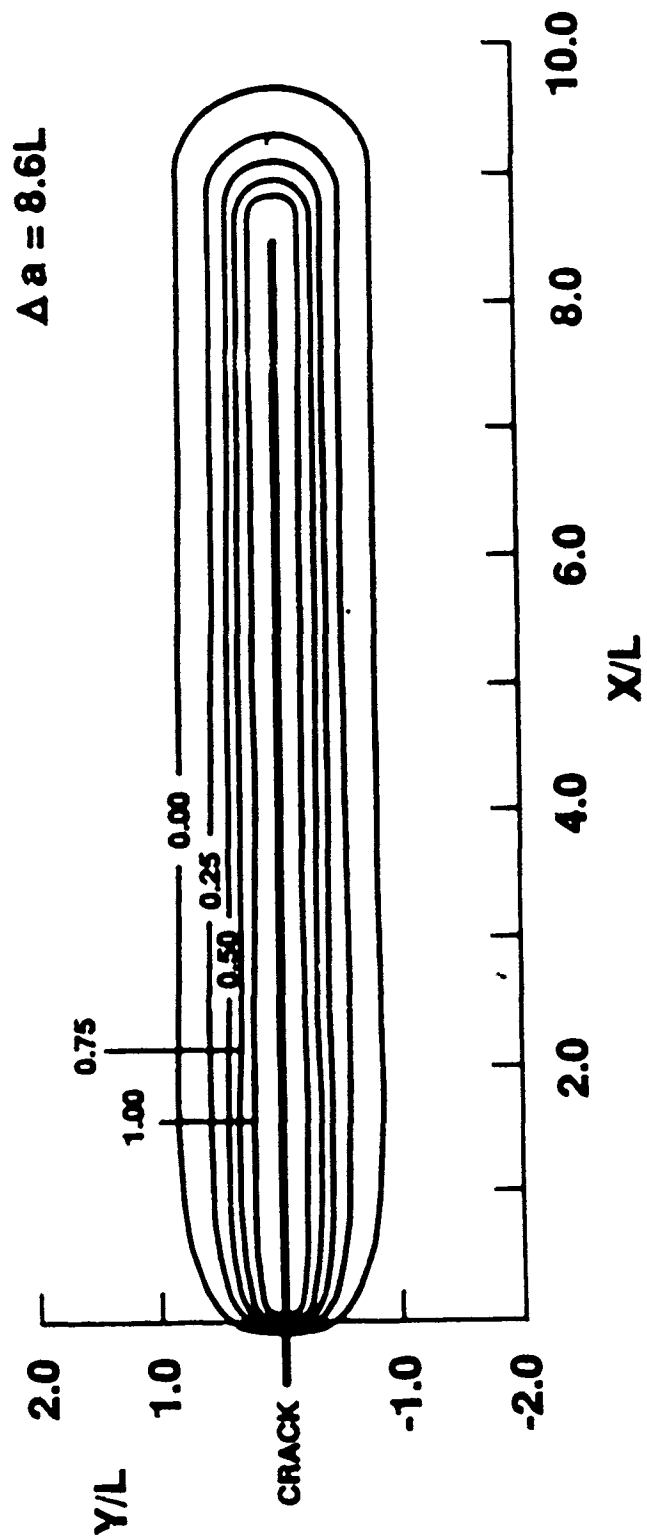


Fig 5

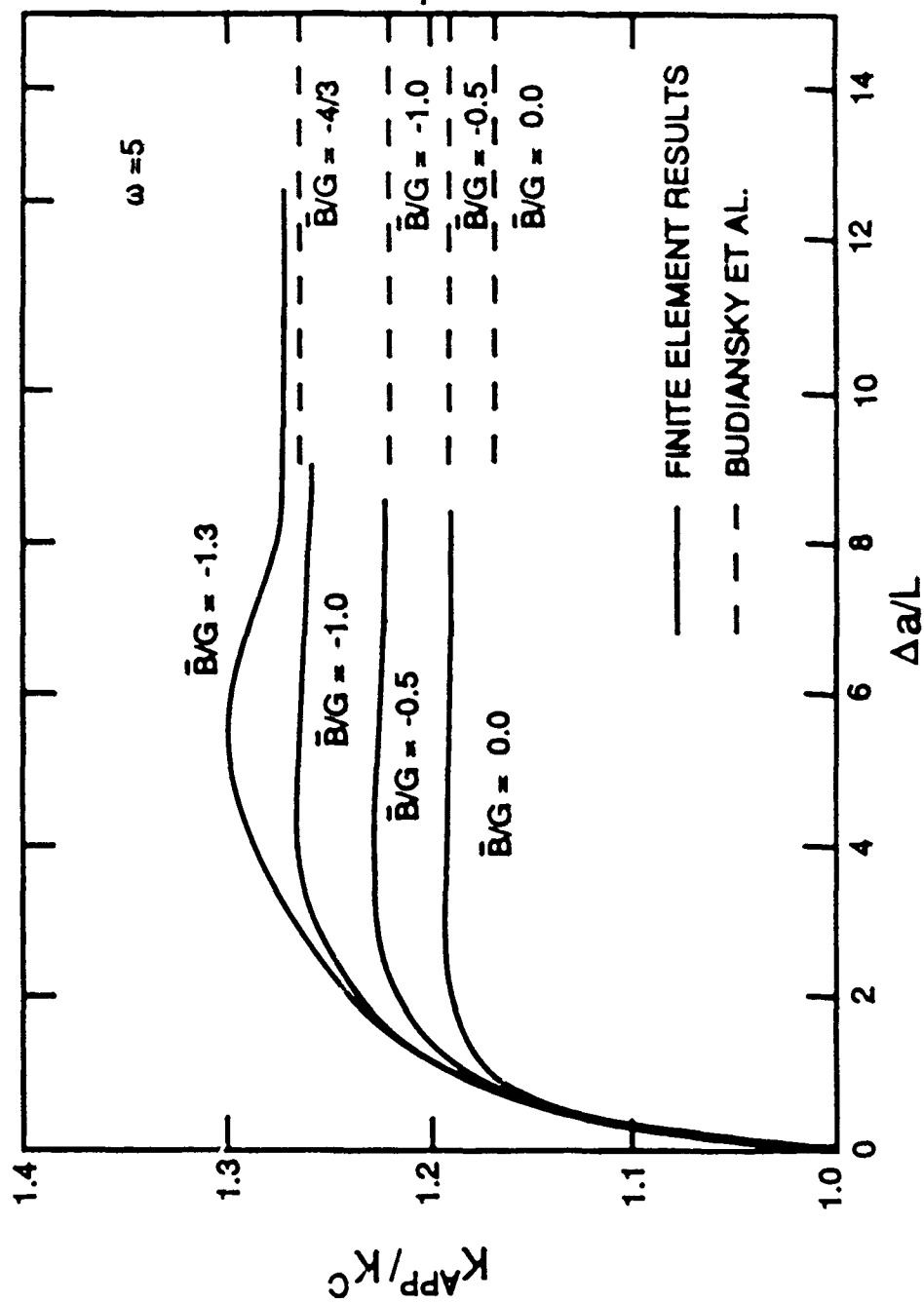


Fig. 6.

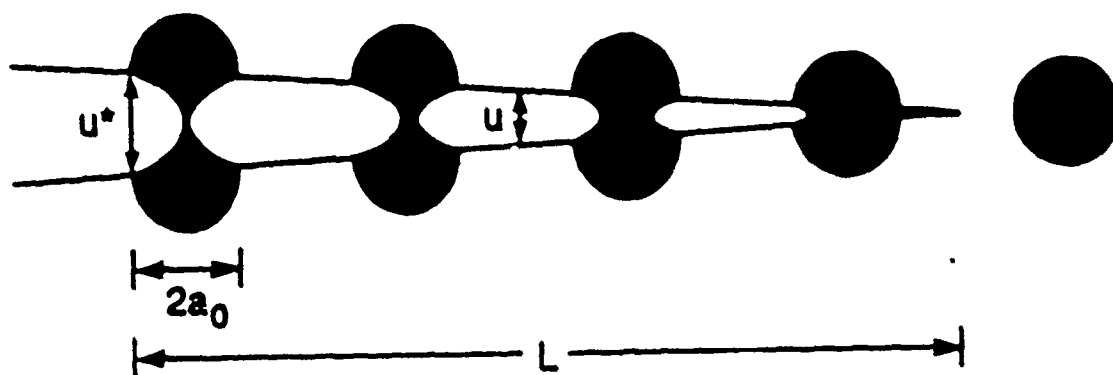


Fig. 7

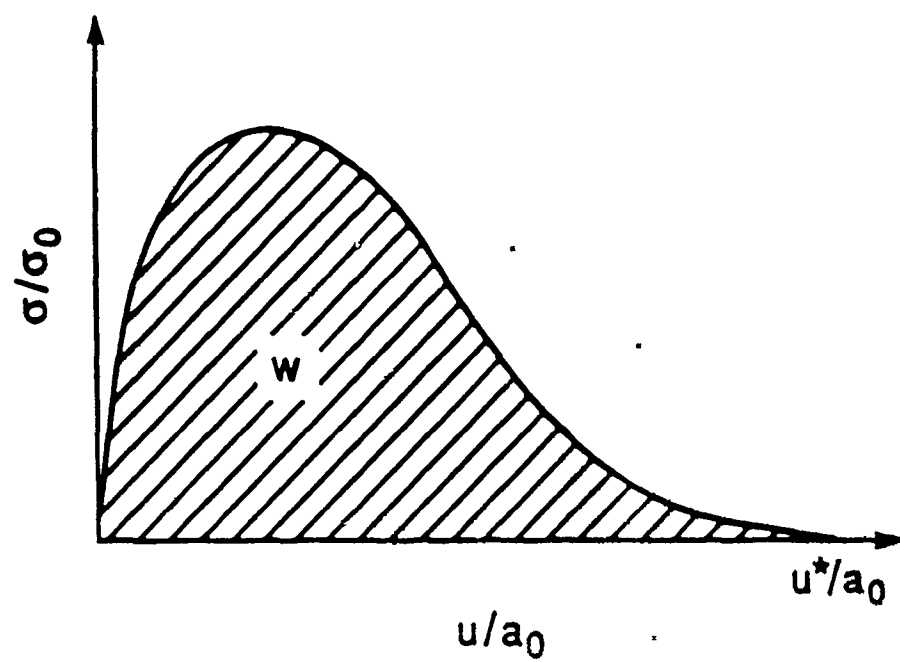


Fig 8.

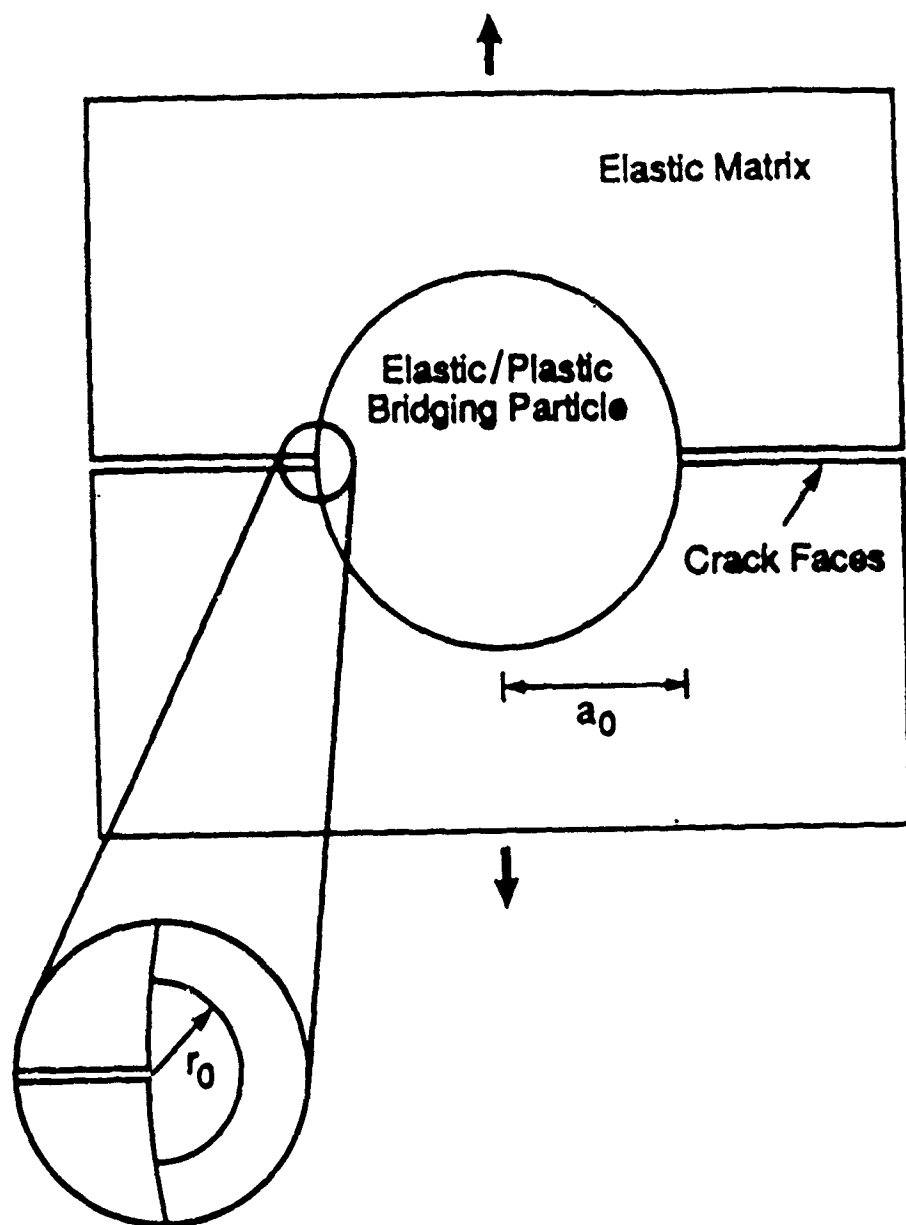


Fig 9.

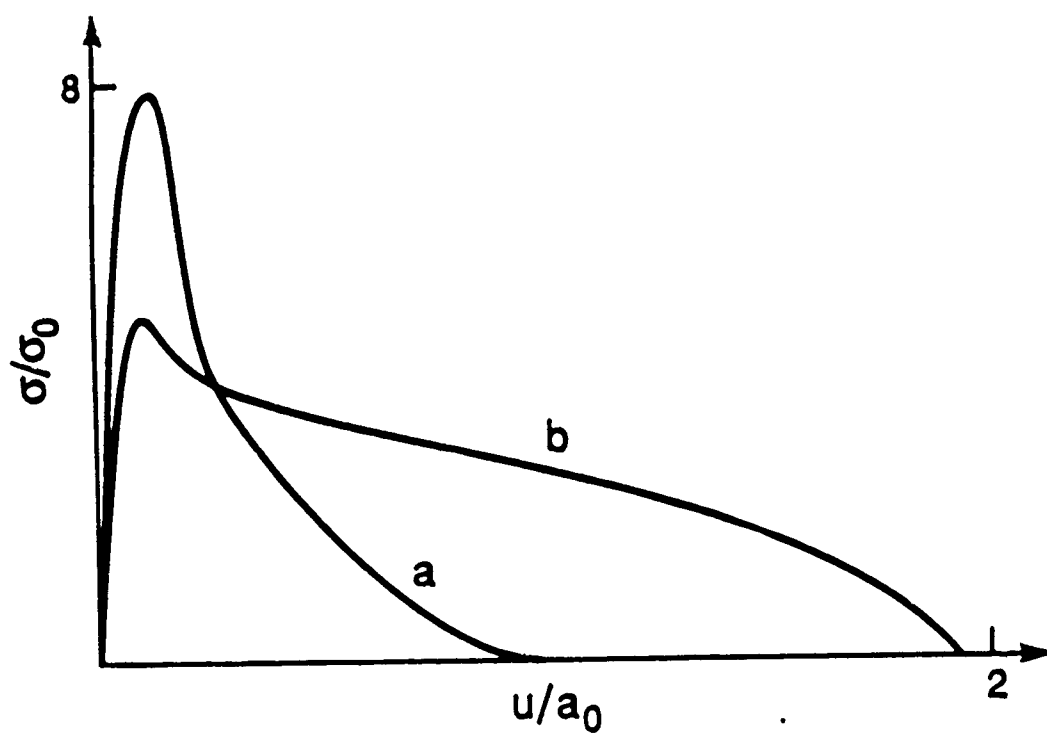


Fig 10.

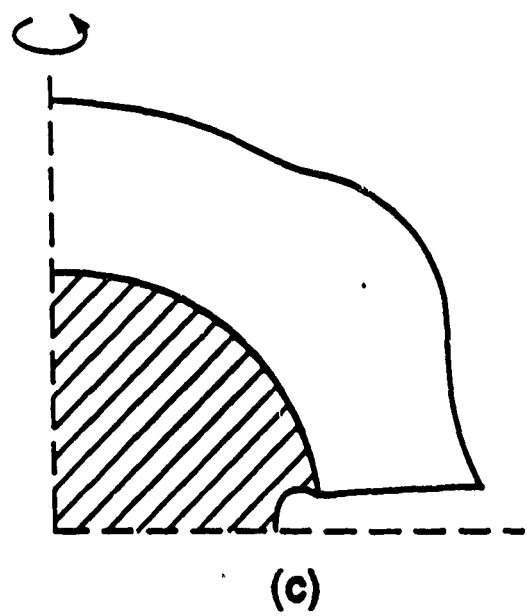
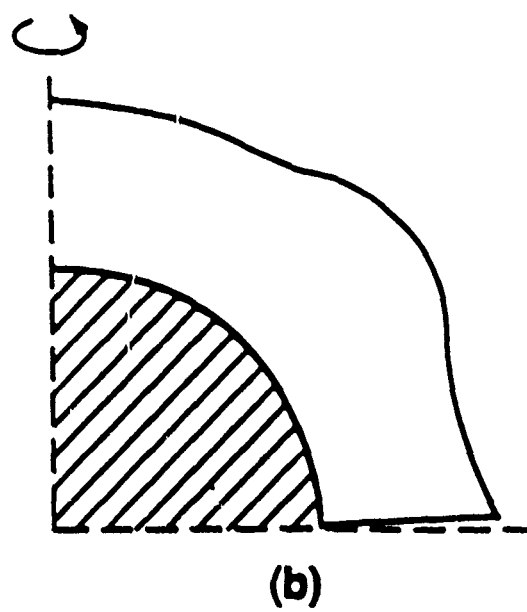
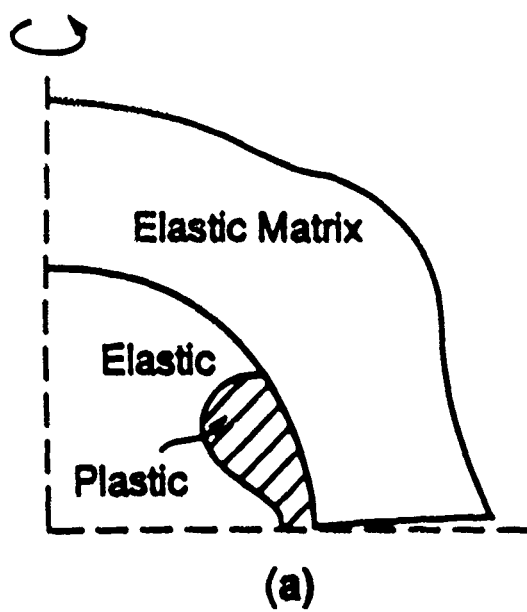


Fig 11.

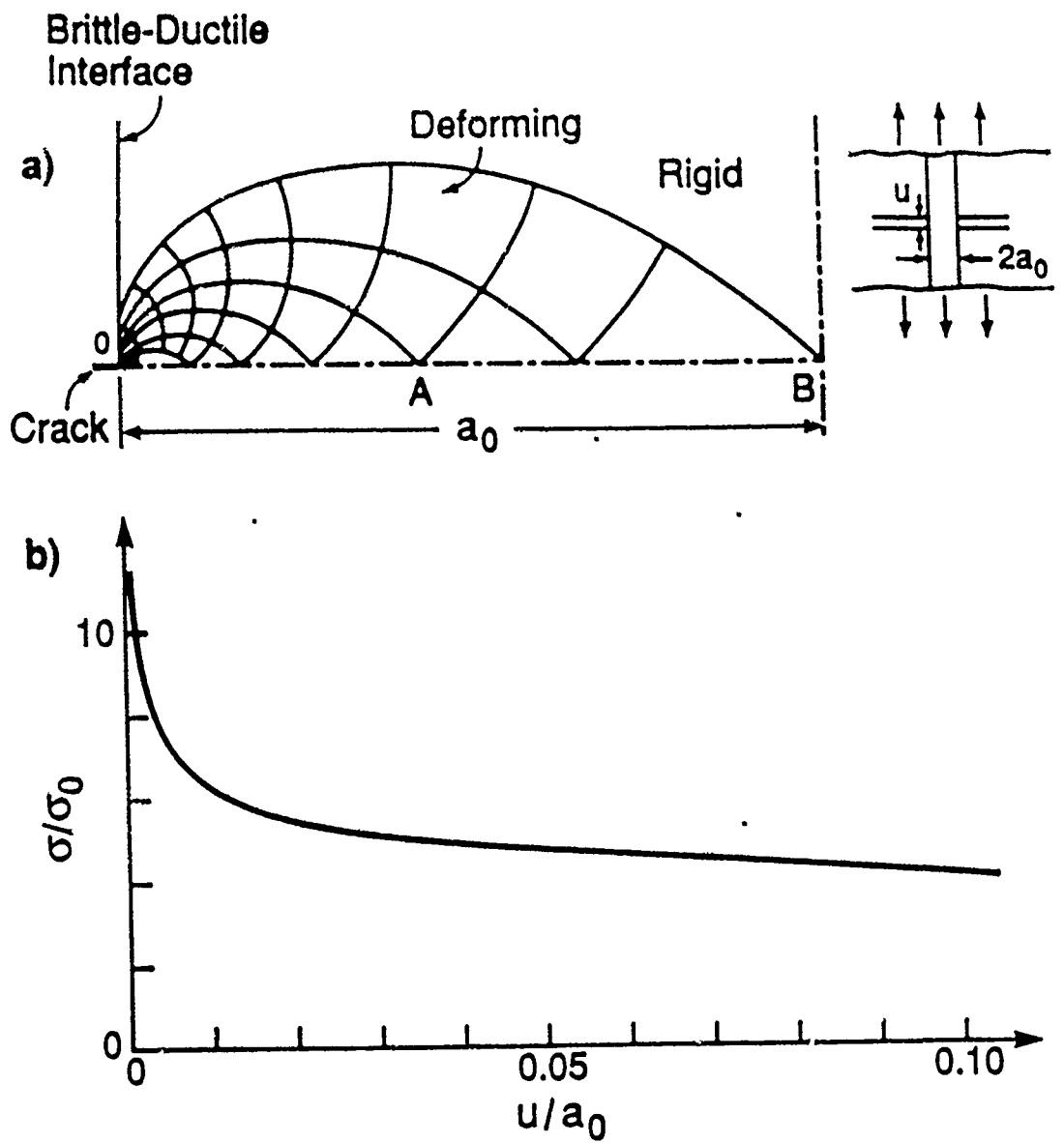


Fig 12.

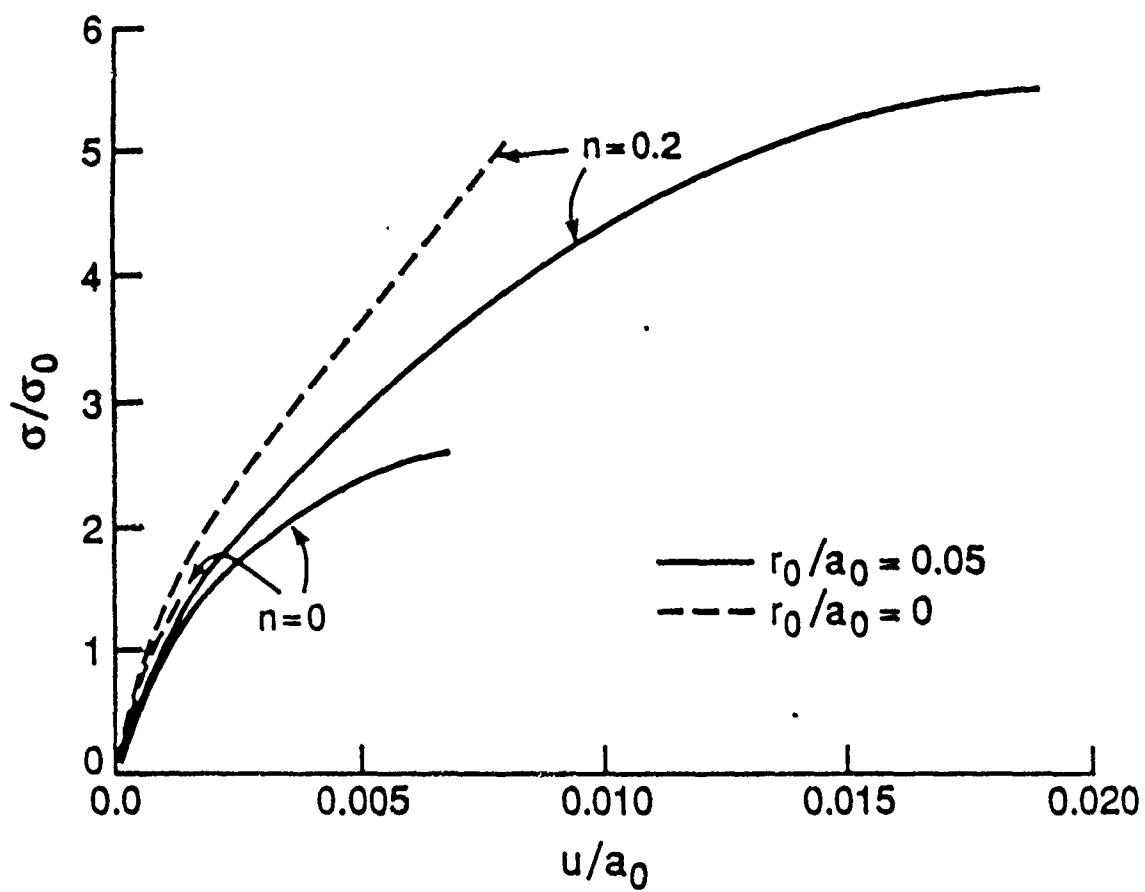


Fig 13.

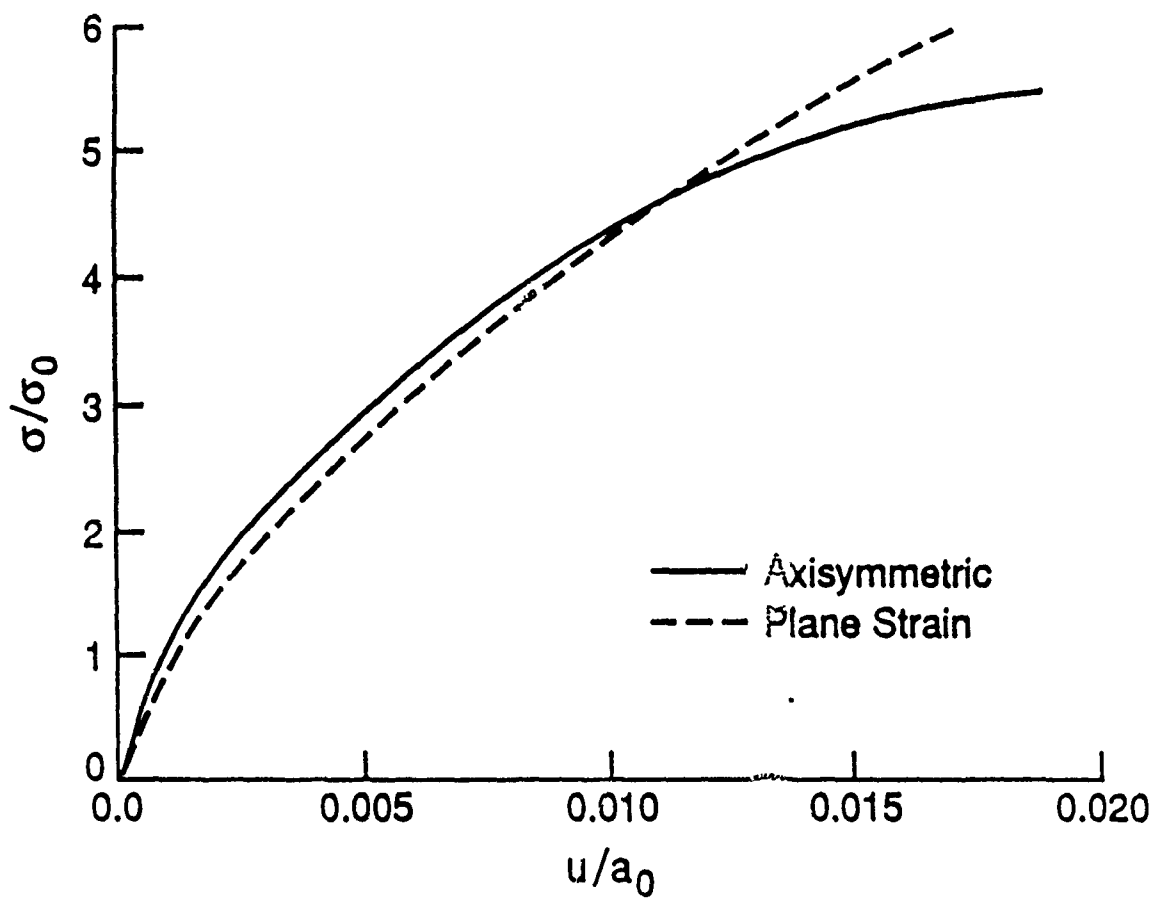


Fig 14.

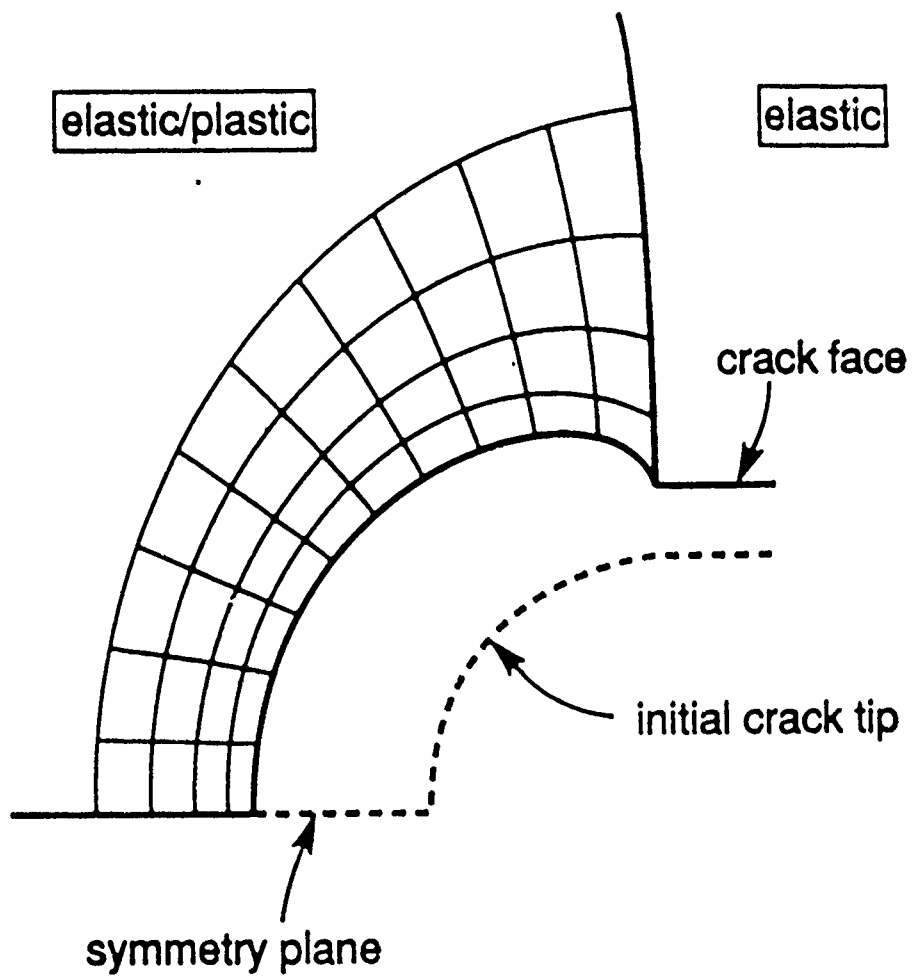


Fig 15.

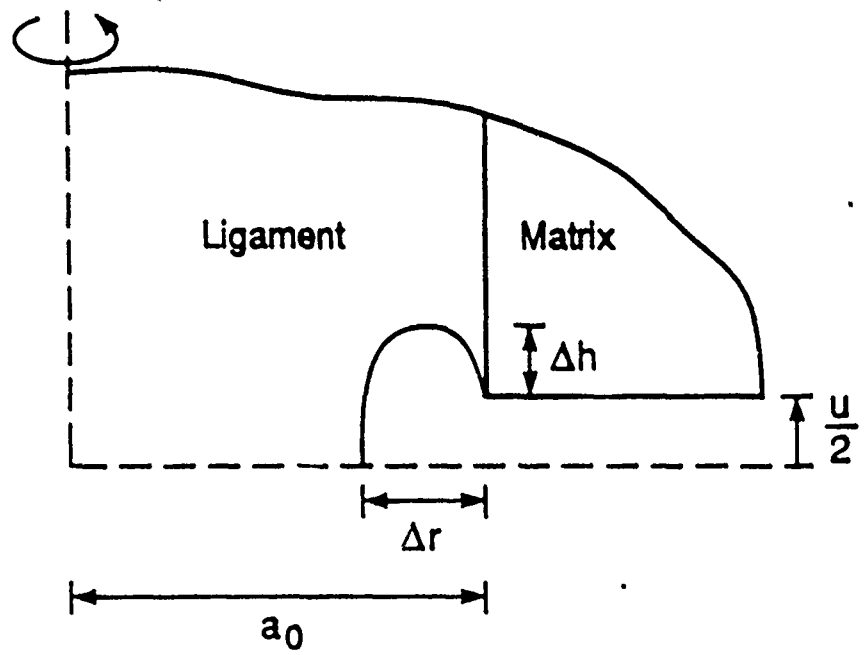


Fig 16.

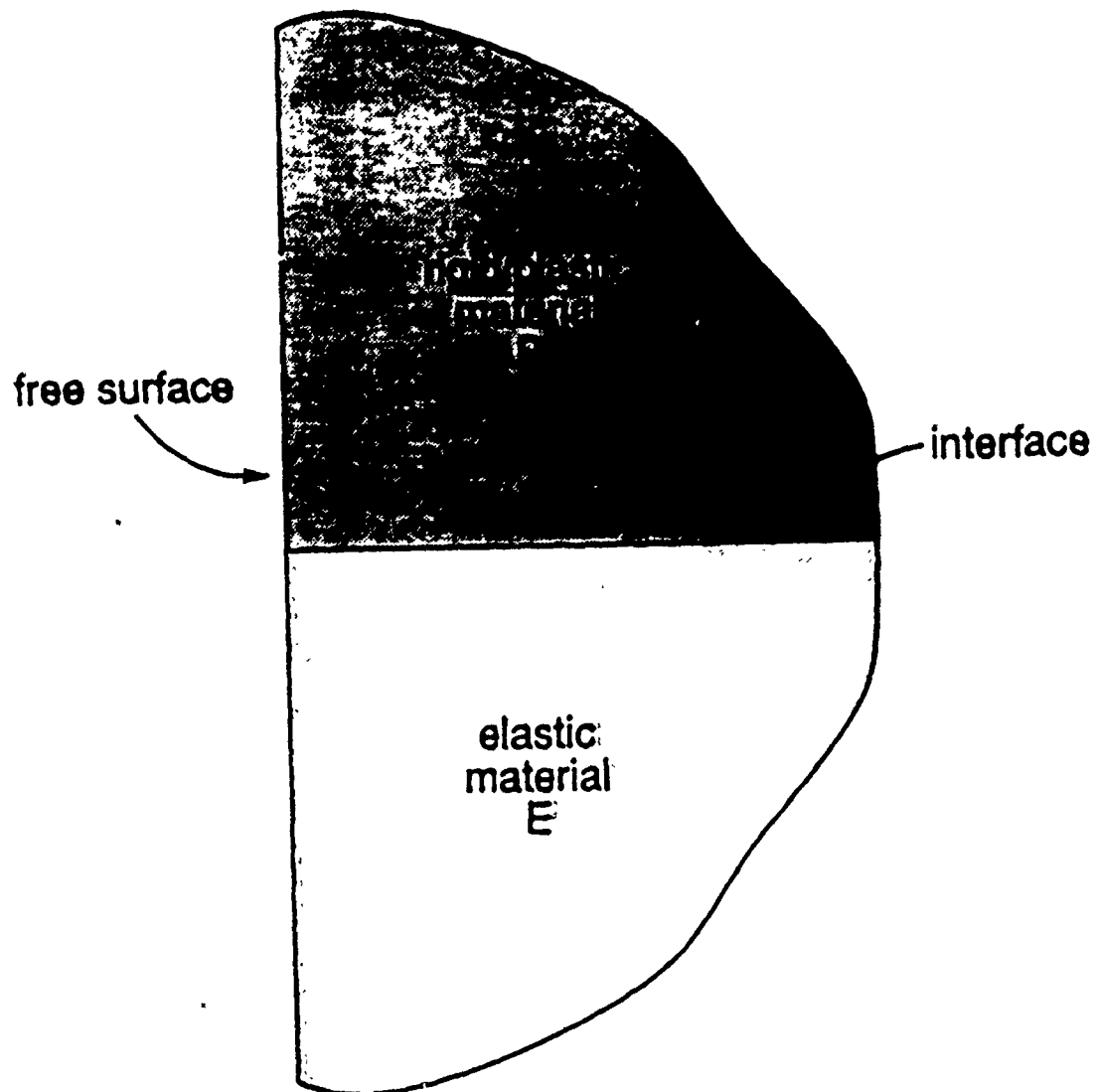


Fig 17.

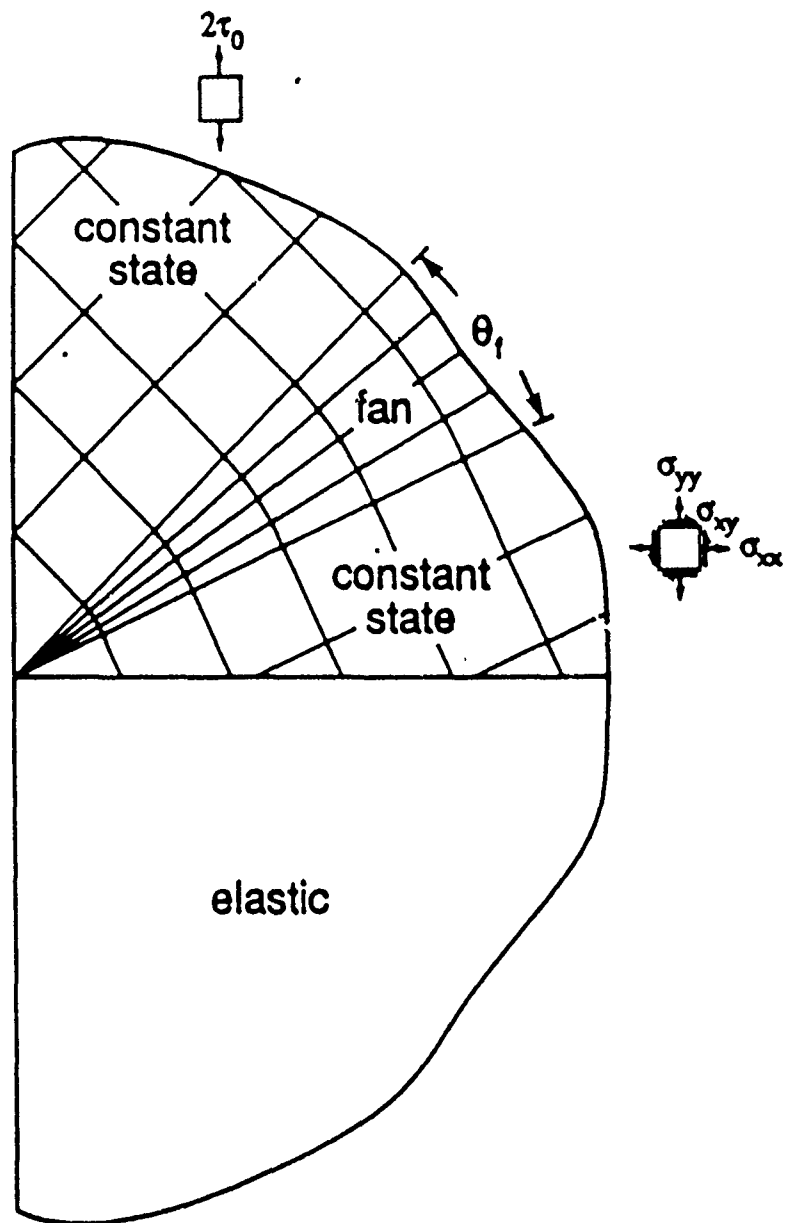


Fig 18.

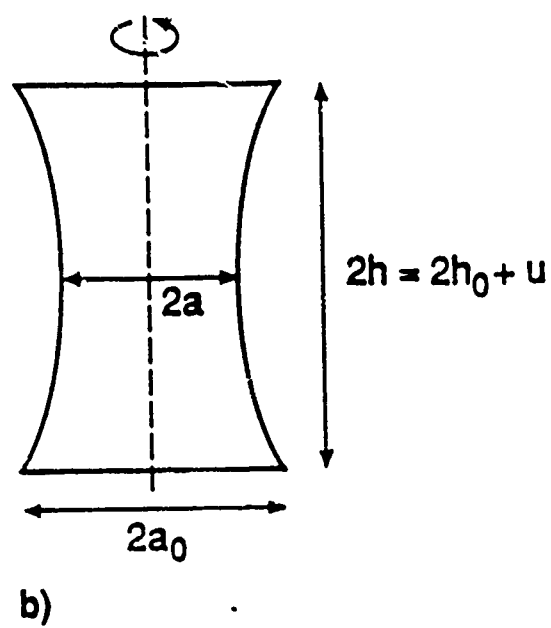
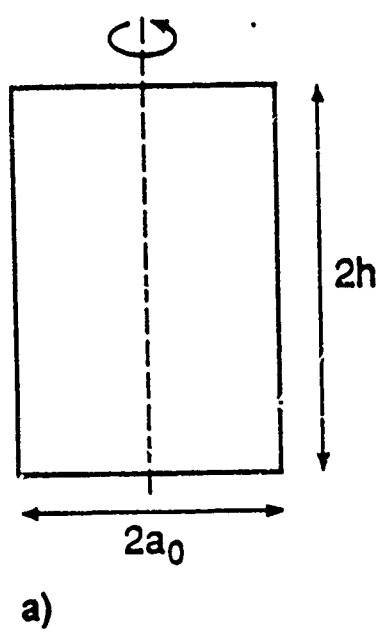


Fig 19.

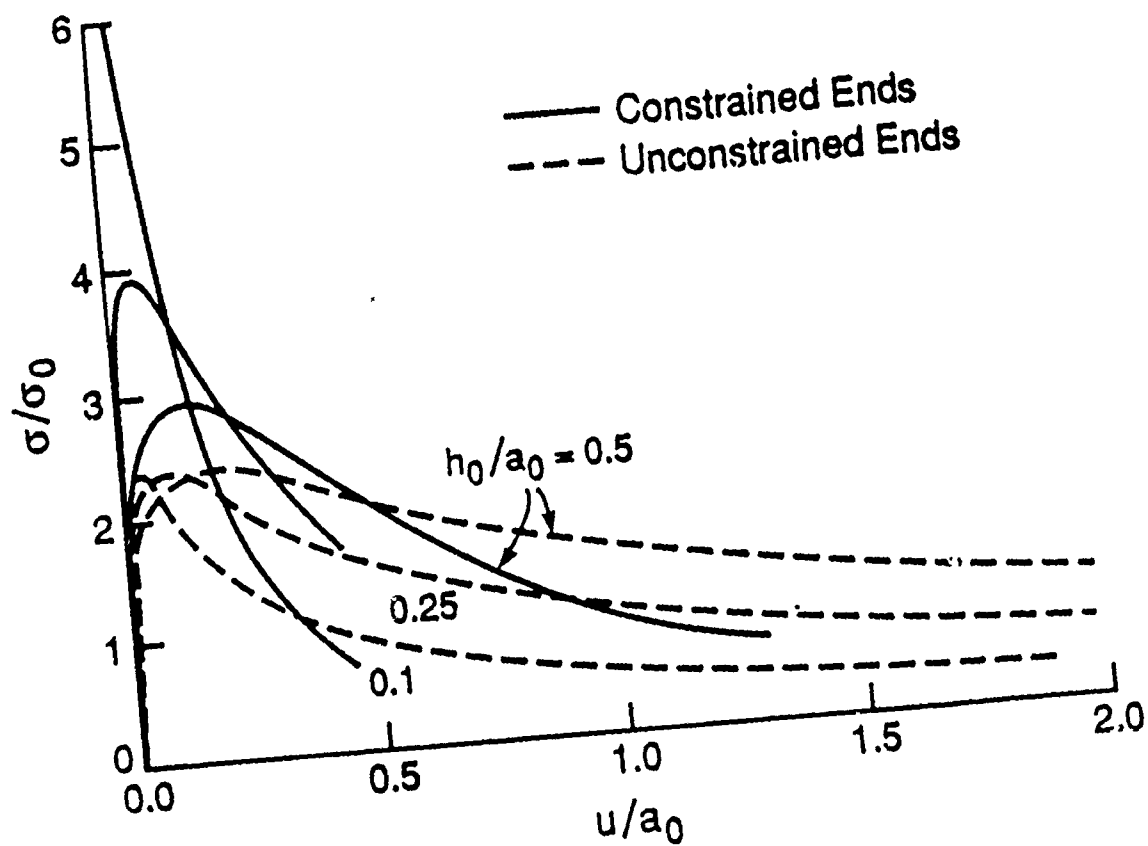


Fig 20.

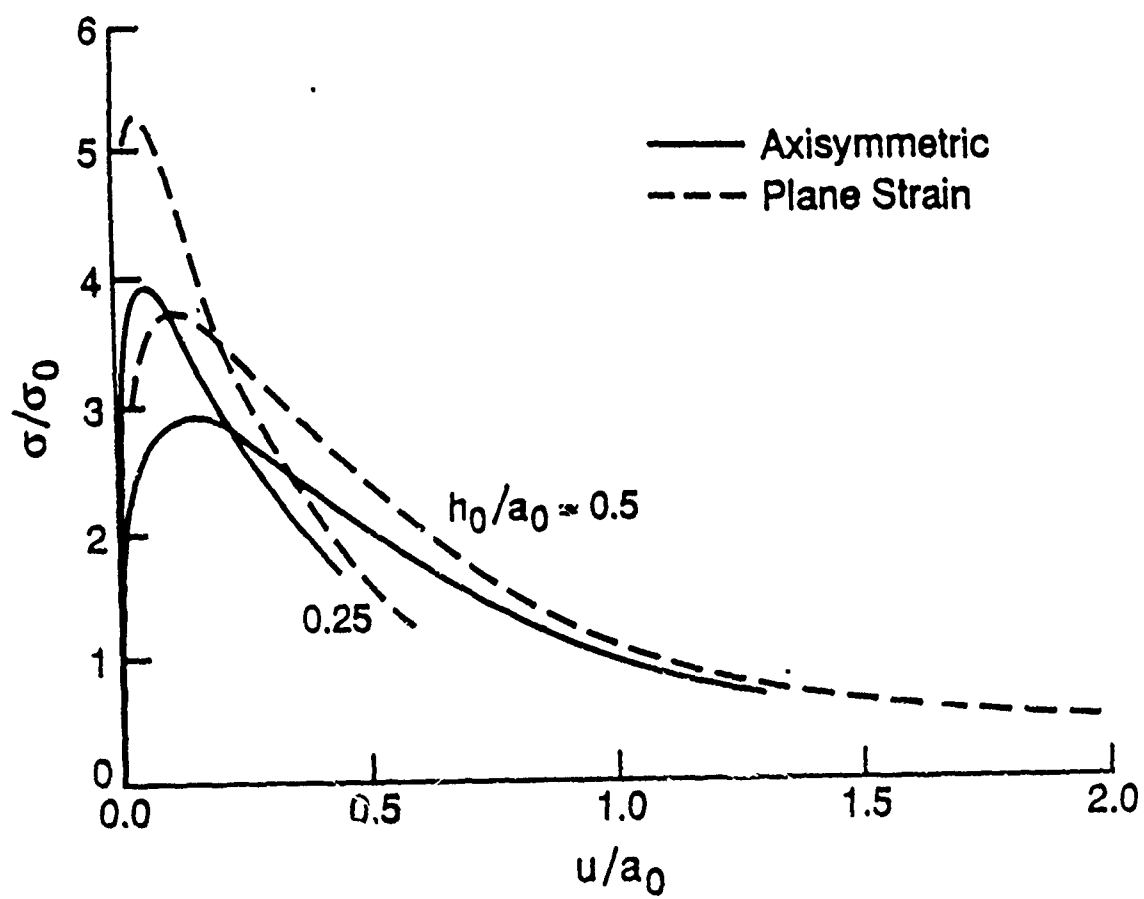
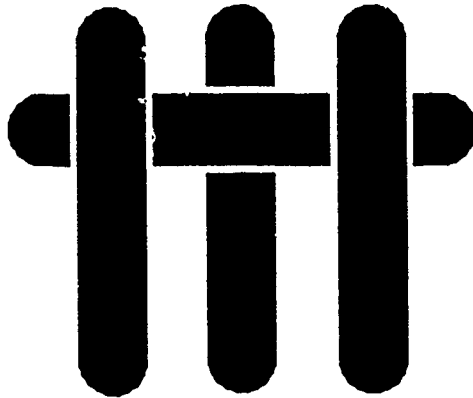


Fig 21.

M A T E R I A L S



**NUMERICAL RESULTS FOR TRANSFORMATION
TOUGHENING IN CERAMICS**

C. L. HOM AND R. M. MCMEEKING
DEPARTMENT OF MATERIALS AND DEPARTMENT OF MECHANICAL
ENGINEERING
UNIVERSITY OF CALIFORNIA
SANTA BARBARA, CA 93106

June 1989

To appear in the International Journal of Solids and Structures

ABSTRACT

Finite element analysis was used to study the fracture toughening of a ceramic by a stress induced dilatant transformation of second phase particles. The finite element method was based on a continuum theory which modelled the composite as a subcritical material. Transient crack growth was simulated in the finite element mesh by a nodal release technique. The crack's remote tensile opening load was adjusted to maintain the near tip energy release rate at the level necessary for crack advance. The transformation zone surrounding the crack developed as the crack propagated through the composite. Resistance curves were computed from the analysis; the results confirm that during crack advance maximum toughness is achieved before steady-state is reached. Diagrams of each transformation zone and R-curve are provided to expedite comparison with experimental data.

Introduction

The fracture toughness of certain ceramics can be greatly enhanced by the presence of particles which undergo a stress induced martensitic transformation (Evans and Heuer (1980); Evans and Cannon (1986); Green, Hannink and Swain (1989) such as takes place in systems containing stabilized zirconia (ZrO_2) particles. Examples include partially stabilized zirconia (PSZ) and zirconia toughened alumina (ZTA). At sufficiently high stress, the particles of such systems undergo a transformation from the tetragonal to the monoclinic phase which is accompanied by a volume increase of 4%. Since the transformation is stress induced, a zone of material containing transformed particles surrounds the crack tip after it has been stressed. The

volume expansion of the particles in this zone will cause eigenstresses which will tend to close the crack and lower the stress intensity factor at the tip. This shielding mechanism means that a higher applied load than otherwise, and therefore an apparently higher stress intensity factor, is required to propagate the crack.

Transformation toughening was first modelled by McMeeking and Evans (1982) and Budiansky, Hutchinson and Lambropoulos (1983). The phenomenology of phase transformation was represented by the macroscopic hydrostatic stress versus dilatation strain behavior shown in fig. 1. At the critical stress σ_m^c , phase transformation commences. If the slope \bar{B} of the stress-strain curve during transformation is below $-4G/3$, where G is the shear modulus, then the transformation continues spontaneously and immediately to completion (Budiansky et al. (1983)). In fact, points on the stress strain curve between 1 & 2 are excluded as unstable and the state jumps on transformation from 1 to the segment between 4 and 3. This situation has been termed supercritical. In the model of McMeeking and Evans, the phase transformation was supercritical and the volume increase due to transformation was asymptotically small. The transformation zones were also asymptotically small. By calculating the amount of crack tip shielding, they obtained estimates of the effective composite R-curve, the toughness value which rises as the crack grows. Eventually, a maximal steady state toughness value develops after an amount of crack growth which is about 3 transformation zone widths.

Budiansky et al. (1983) considered supercritical and also subcritical materials in steady-state crack advance only. In the subcritical case, with $\bar{B} >$

$-4G/3$, the phase change occurs gradually and the material can remain stably in a state in which the particles are only partially transformed. As a result, points in fig. 1 between 1 & 2 are stable and the material moves gradually from 1 to 2 as strain increases. If the strain decreases (unloading) while the material is between 1 and 2, the state follows the line with slope B through the current location as shown in fig. 1. In addition, Budiansky et al. also accounted accurately for the perturbation of the transformation zone size and shape due to the stresses induced by the transformation itself. Using finite element analysis, they calculated steady state fracture toughnesses including cases where the volume increase from the transformation was quite large. Rose (1986) and Amazigo and Budiansky (1988) have provided additional analyses of steady state toughening for dilatant transformations.

Stump and Budiansky (1989) have recently provided a more accurate estimate of the R-curve for a crack advancing in supercritically transforming material. The problems were solved numerically by means of an integral equation. The transformation zones evolved as the crack advanced and the remote load was adjusted to maintain the stress intensity factor at the critical constant value at the crack tip. Their solutions show that the maximum fracture toughness occurs after a finite amount of crack advance, and that this maximum can be significantly higher than the steady-state fracture toughness which develops later. The peak fracture toughness is associated with a transiently wider transformation zone. The result indicates that the amount of effective toughening is underestimated by the later steady state value since the system must be forced to grow through the peak toughness state. The steady state estimate generally underpredicts experimental data (Evans and Cannon (1986)) so the new predictions tend to bring the theory into better

agreement. Furthermore, R-curves with peaks in the toughness have been reported by Swain (1983) and Swain and Hannink (1984).

The purpose of the calculations performed for this paper is to consider the transient behavior of a crack advancing in a material which transforms subcritically. Experimental evidence indicates that the transformation zones surrounding a crack tip tend to be diffuse or partially transformed, indicating a subcritical transformation. Finite element analysis is used to solve the problem of a semi-infinite crack growing in a transforming material under Mode I loading and plane strain conditions. Crack growth in the finite element mesh is modelled using a nodal release technique; the transformation zone develops as the crack advances. Resistance curves are computed for different purely dilatant transformation strains and the results are compared with the steady-state analysis of Budiansky et al. (1983). A near critical case almost equivalent to the supercritical analysis done by Stump and Budiansky (1989) was also analyzed for comparison. Extensive documentation of each solution is provided so that comparisons with experimental data can be made more easily.

Constitutive Relations

In this section we describe the constitutive relations used to model transformation toughened composites. Developed by Budiansky et al. (1983), the model assumes that the transformation zone contains many particles and thus a continuum description of the composite can be formulated. The composite material is isotropic and consists of a linear elastic isotropic matrix containing linear elastic isotropic particles which undergo an irreversible dilatant transformation.

Since the transformation is purely dilatant, the macroscopic shear response is entirely linear elastic with modulus G , which will depend on the composite properties of the material. Thus the deviatoric stress-strain relationship for the composite is

$$\sigma'_{ij} = 2G \epsilon'_{ij} \quad (1)$$

where σ' is the deviatoric part of the macroscopic stress and ϵ' is the deviatoric part of the macroscopic strain.

The dilatant behavior of the composite is depicted in Fig. 1, and can be represented by

$$\epsilon_{kk} = \frac{\sigma_m}{B} + \theta \quad (2)$$

where ϵ_{kk} denotes the total dilatation; σ_m is the hydrostatic part of the stress equal to $\sigma_{kk}/3$; B is the bulk modulus for the material; and θ is the current dilatation due to particle transformation in a macroscopic element of the composite material. (Einstein summation is used on repeated indices throughout.)

When the strain $\epsilon_{kk}^c = \sigma_m^c / B$ is exceeded, locally particles change phase to some extent. When all of the particles have transformed locally, the macroscopic dilatation θ is equal to θ^T . In a material in which the elastic moduli of the particles are identical with those of the matrix $\theta^T = c\theta_p^T$ where c is the volume fraction of particles and θ_p^T is the free dilatation of an individual particle (4% in the case of zirconia) (Budiansky et al. (1983)). However, McMeeking (1986) has shown that in binary elastic composites,

$\theta^T = Fc\theta_p^T$. Where F is a factor which depends on the ratios of elastic moduli.

When the material is partially transformed in subcritical materials, the incremental dilatation during loading ($\epsilon_{kk} > 0$) and due to transformation is (Budiansky et al. (1983))

$$\dot{\theta} = (1 - \bar{B} / B) \dot{\epsilon}_{kk} \quad (3)$$

when $\sigma_m^c / B + \theta (1 - \bar{B} / B) \leq \epsilon_{kk} \leq \sigma_m^c / B + \theta^T (1 - \bar{B} / B)$.

Since the phase transformation is assumed irreversible, θ remains constant during unloading ($\epsilon_{kk} < 0$) in all cases. In the critical and supercritical case, eq. (3) is replaced by

$$d\theta / d\epsilon_{kk} = \theta^T \delta_D (\epsilon_{kk} - \sigma_m^c / B) \quad (4)$$

where δ_D is a Dirac delta function.

Boundary Value Problem

The problem of a very long crack growing in plane strain with a very small zone of phase transforming particles (see fig. 2) was solved using the finite element method. Displacement boundary conditions corresponding to a Mode I linear elastic plane strain field were applied around the outer perimeter of the domain. The magnitude of the applied load is characterized by K^{APP} , the Mode I elastic stress intensity factor. As shown in fig. 2, material near the tip transforms due to the stress intensification generated by the crack. A zone of material which has completely transformed ($\theta = \theta^T$) surrounds the crack tip. This core region is incrementally linear elastic with a permanent residual strain. Consequently, the stress field at the crack tip has a

$r^{-1/2}$ singularity and is characterized by a stress intensity factor K^{TIP} . In the subcritical case, the region of purely transformed material is surrounded by a zone of material which is partially transformed ($\theta < \theta^T$). In the critical and supercritical cases, partially transformed material does not exist and θ jumps from zero to θ^T across the zone perimeter.

For a stationary crack with monotonically increasing K^{APP} no unloading occurs and the J-integral of Rice (1968) is path independent (Budiansky et al. (1983)). As a result, $K^{TIP} = K^{APP}$ and thus, prior to any crack growth, there is no shielding (McMeeking and Evans (1982), Budiansky et al. (1983)). The crack will commence growing when $K^{TIP} = K^C$, the fracture toughness of the composite in the crack tip state, i.e. with pretransformed particles. Equivalently, crack-growth commences when $K^{APP} = K^C$.

As the crack propagates and a wake of transformed material develops, K^{TIP} decreases compared to K^{APP} due to shielding. To maintain crack growth, K^{APP} must be continually adjusted so that K^{TIP} equals K^C . K^{APP} is the effective fracture toughness of the composite material and the R-curve is its graph versus the amount of crack growth Δa .

Finally, all length scales in the moving crack tip problem were normalized by L , where L is defined by

$$L = \frac{2}{9\pi} \left[\frac{K^C(1 + \nu)}{\sigma_m^C} \right]^2 \quad (5)$$

Physically, L is the distance on the X_1 -axis from the tip ahead to the boundary of the nominal transformation zone for the stationary crack with $K^{APP} = K^C$.

The solutions depend on the strength of the transformation which is characterized by the nondimensional parameter ω , where

$$\omega = \frac{E \theta^T}{\sigma_m^c} \left[\frac{1 + \nu}{1 - \nu} \right] \quad (6)$$

Finite Element Solutions

The finite element method used to solve these problems has been described by Hom, Mataga and McMeeking (1989). The method was incremental with the load, K^{APP} , adjusted in steps as necessary to tend to maintain K^{TIP} equal to K^C . After each adjustment of the load, a successive approximation iteration was carried out until satisfactory convergence of the solution was achieved. When K^{TIP} equaled K^C , the crack tip node was released incrementally to advance the crack, with iterations carried out as necessary. Thereafter, K^{APP} was again adjusted in steps to return K^{TIP} to K^C and so on. The virtual crack extension method of Parks (1974, 1978) was used to calculate K^{TIP} when necessary. The finite element mesh in fig. 3 was used for the calculations. The crack was grown from the point marked "STATIONARY CRACK TIP" in that figure to near the point marked "MOVING CRACK TIP".

Attempts were made to compute results for the precisely critical case ($\bar{B} = -4G / 3$). However, it was found that the iterative procedure failed to converge. Without any change to the load or geometry, the transformation zone simply expanded with each iteration. Thus, no stable transformation zone size was ever established even for stationary cracks. No way was found by us to avoid this in the algorithm directly. Instead, subcritical materials were analyzed. Satisfactory convergence to a rather strict criterion was then

achieved. Few iterations were required when \bar{B} equaled zero but considerably more were necessary when \bar{B} was smaller.

The subcritical results we obtained involved partially transformed material within the zone. However, as \bar{B} approached $-4G/3$, the regions of partially transformed material formed a narrow band around the outer perimeter of the zone. For a sufficiently small value of \bar{B} and with appropriate choices of other parameters, this band was made narrower than the distance between 2 neighboring integration stations in the finite element mesh. Thus, at one integration station the material is untransformed and at the neighboring integration station across the partially transformed band, the material is completely transformed. This situation is as good as can be achieved anyway for the exactly critical material given the discreteness of the mesh. The near critical case so calculated is numerically equivalent to the exactly critical case for the given mesh. This equivalence was actually achieved for $\omega = 5$ with $\bar{B} = -1.3G$ in the mesh shown in fig. 3. This solution was slow to converge (~50 iterations per step compared to 5 for $\bar{B} = 0$) and the amount of computer time precluded us from carrying out other near critical solutions.

The parameters of the problems were chosen so that at least 10 elements spanned the transformation zone in the X_2 direction. To check if the mesh layout was fine enough, σ_m^* was made smaller to enlarge the zone, making L larger, equivalent to refining the mesh. The combination $E\theta^T$ was reduced also to keep ω fixed. The results of calculations then carried out were identical to those performed in the effectively coarser mesh, confirming that the mesh and calculation strategy were satisfactory.

Results for a Growing Crack

The problem of a crack in untransformed material growing and creating a transformation zone was solved for various material parameters. These characteristic parameters are the transformation strength ω , Poisson's ratio ν , (taken to be 0.3 throughout) and \bar{B}/G . Three sets of finite element computations were done with $\omega=5, 10$ and 15 . In each set of calculations, cases were run for $\bar{B}/G=0, -0.5$, and -1.0 . The calculation with $\omega=5$ and $\bar{B}/G=-1.3$ was also done for comparison with the calculations of Stump and Budiansky (1989). In all cases the crack was propagated a distance of at least $8L$.

Transformation Zones

The transformation zone for the near critical case ($\bar{B}/G=-1.3$) with $\omega=5$ and $\Delta a = 11.4L$ is shown in fig. 4. In this case, the layer of partially transformed material is very thin and has not been shown in the figure. It is thinner than the distance between neighboring integration stations in the finite element mesh - about 10% of the peak zone height above the crack, h shown in fig. 4. Apart from this thin layer, the material inside the zone has transformed completely. It is clear from the zone shape, that as the crack grew, the zone first widened sharply and then gradually. After reaching a maximum width, the zone narrowed sharply with growth and then appears to settle into a steady state.

In this case, the maximum zone height is $h_m = 1.06L$ and occurs after the crack has grown a distance $3.7L$. The finite element results show that the zone reaches a steady-state height of $0.88L$. The transient behavior of a crack

growing in a supercritical material has also been considered by Stump and Budiansky (1989). For $\omega=5$, their results show that the maximum zone height is $1.03L$ and occurs when $\Delta a=2.4L$. Their computation also predicts a steady state zone height of $0.89L$. Overall, the zones have very similar shapes. It should be noted that between $\Delta a=2.4L$ and $3.7L$, the zone height is almost steady, and the discrepancy in the position of the zone width peak should be considered in that context.

The development of the transformation zone for the case $\bar{B} / G = 0$ and $\omega = 10$ as the crack tip moves to the right is shown in fig. 5. The zone is shown for different crack lengths, where Δa is the amount of growth which has taken place. The zones are depicted as contour plots of the transformation dilatation θ . As expected the crack tip is surrounded by a region of fully transformed material which in turn is surrounded by a region of partially transformed material. As the crack grows, the zone expands in height. The height of the zone h reaches a maximum at $1.02L$ after the crack has propagated a distance $1.7L$. Thereafter, the zone narrows and when the crack reaches a steady state at around $\Delta a=8L$, the zone height in the steady state region is smaller at $0.88L$. The steady-state zone height predicted by Budiansky et al. (1983) for subcritical material with $\bar{B} / G = 0$ and $\omega = 10$ is $h=0.84L$.

Fig. 6(a) shows the transformation zone when $\bar{B} / G = 0$ and $\omega = 5$ after the crack has propagated a distance of $8.6L$. The fully transformed region in this case is larger than the fully transformed region for $\omega = 10$ case. However, the whole transformation region observed for $\omega = 5$ is smaller than for $\omega = 10$, and the peak height is not as large. In this case h reaches a

maximum of $0.87L$ after the crack has propagated a distance $1.4L$. The steady state zone height predicted by the finite element calculations is $0.81L$. The computations of Budiansky et al. (1983) predicted the steady-state zone height as $0.89L$. The transformation zone after the crack has propagated a distance $8.6L$ for $\omega = 5$ with $\bar{B}/G = -0.5$ and -1.0 are shown in figs. 6(b) and 6(c) respectively. It can be seen clearly that for the smaller values of \bar{B} there is a larger fully transformed zone compared to the total zone size. The next figure in this series for $\omega = 5$ is that in fig. 4 for $\bar{B}/G = -1.3$ discussed already where there is no partially transformed zone.

Figs. 7(a) and (b) are plots of the transformation zone after the crack has propagated a distance $8.6L$ for $\omega = 10$ when $\bar{B}/G = -0.5$ and -1.0 respectively. Comparison of figs. 7 with 6 show that a larger relative dilatation ω produces a larger final zone size even though they start growing from nearly the same initial zone size. Finally, figs. 8(a,b&c) show the transformation zones after the crack has propagated a distance $12.9L$ for the cases when $\omega = 15$.

Table I shows the peak and steady state zone heights and $\Delta\epsilon$ when the peak occurs for each case calculated. The finite element results show that for a given L , the peak height and the steady-state zone height are larger for stronger transformation strengths ω . Also, the crack must propagate further to reach both the maximum zone height and the steady state zone height for larger ω . Similarly, the closer \bar{B} is to the critical value of $-4G/3$, the larger is the peak zone height and the steady height. The latter comment applies except for the near critical case $\bar{B}/G = -1.3$ where the trend seems to reverse. But when the material is near critical, the distance the crack must

propagate to achieve both the maximum zone height and the steady-state is greater. Included in Table I for completeness are results taken from Stump and Budiansky (1989) for the supercritical material.

Resistance Curves

As mentioned earlier, the remote applied stress intensity factor was varied during crack advance to maintain $K^{TP} = K^C$ at the crack tip. The R-curves (K^{APP} versus Δa) for the case when $\omega=5$ are shown in fig. 9. As expected, in each case the transformation zone shields the crack tip and toughening is observed. The R-curves rise to a peak level associated with the widest part of the zone. Thereafter, the R-curve falls as the zone narrows. The curves then tend to settle down to a steady state. The relative amount of toughening is higher for the lower values of \bar{B} because there is relatively more fully transformed material in the wake zone. In addition, the peak toughening relative to the later steady state value is more pronounced when \bar{B} is more negative.

After the crack has propagated a sufficient distance, the R-curve approaches an asymptotic value. This steady-state value of K^{APP} corresponds to the steady state region in the transformation zone. For comparison, the dashed lines in fig. 9 denote the toughnesses predicted by the steady-state finite element analyses of Budiansky et al. (1983). The steady state toughness for the near critical material $\bar{B} / G = -1.3$ predicted by our finite element calculation agrees well with the steady-state analysis for critical and supercritical materials which is exact. Furthermore, the peak toughness

agrees well with the result of Stump and Budiansky (1989). These results give us confidence in our numerical solutions. For the near critical case ($\bar{B} / G = -1.3$) with $\omega=5$, our finite element analysis predicts a maximum and steady-state K^{APP} of $1.30 K^C$ and $1.27 K^C$ respectively. The peak in K^{APP} occurs when the crack has grown a distance $5.6L$. For the supercritical material, Stump and Budiansky (1989) predict a toughness value of $1.29 K^C$ for the peak and the steady state value is $1.26 K^C$ (Budiansky et al. (1983)). Therefore, the zone contributions to toughness agree to within a few percent. Maximum K^{APP} in the results of Stump and Budiansky (1989) occurred when $\Delta a = 5.5L$.

The subcritical steady-state values of K^{APP} predicted by our transient finite element analysis are higher than the steady state values of (Budiansky et al. (1983)). For example when $\bar{B} = 0$, the steady-state toughness predicted by the finite element analysis is $1.19 K^C$ while the analysis of Budiansky et al (1983). predicts $1.17 K^C$. This means that our prediction of the zone contribution is about 10% higher. The difference is unresolved.

For the subcritical material, the difference in the peak and steady state toughnesses are much smaller than the supercritical case. For $\bar{B} = 0$ the finite element analysis shows that both the peak and steady-state K^{APP} are indistinguishable at $1.19 K^C$. Even for $\bar{B} / G = -1.0$, the peak K^{APP} is only $1.27 K^C$ compared to a steady-state value of $1.26 K^C$.

Fig. 10 shows the R-curves for the case when $\omega = 10$. Because the strength of the transformation is greater, the toughnesses computed in these cases are higher than those for $\omega = 5$. Also, the peak value for K^{APP} is more pronounced compared to the steady-state value of K^{APP} . For $\bar{B} / G = -1.0$,

the computation was only done until $\Delta a = 8.6L$ and a steady state was not developed. However, a peak value of K^{APP} of $1.65 K^C$ was calculated. The dashed lines in fig. 10 indicate the results of Budiansky et al. (1983). As in the case of $\omega = 5$, the steady state toughness predicted by our finite element analyses for $\omega = 10$ are higher than those of the previous steady state analysis. The R-curves for $\omega = 15$ are shown in fig. 11. The higher toughnesses reflect the greater strength of the transformation. Again, the steady state toughnesses were higher than those predicted by Budiansky et al. (1983).

In addition to zone shape information, Table I shows the peak and steady state toughnesses and Δa to reach peak toughness predicted by our finite element analysis for all cases examined in this study. The numerical computations show that larger peak and steady toughnesses are achieved when ω is greater and \bar{B} is closer to critical, i.e. a stronger transformation with more material fully transforming. Also, with increasing ω and \bar{B} closer to critical, the crack must grow a greater distance in terms of L to reach both the peak toughness and the steady-state.

Discussion

The finite element results presented in this paper indicate agreement between our near critical solution and the accepted steady state toughening estimate of previous work (McMeeking and Evans (1982), Budiansky et al. (1983), Stump and Budiansky (1989)). In addition, the peak toughness predicted here for the near critical case by finite elements agrees with the value obtained by Stump and Budiansky (1989) by another method. This gives us confidence in our numerical results. It is worth noting that we have

achieved agreement with other results in the case in which we found convergence most difficult to obtain, i.e. the near critical situation.

In contrast, it is found that our predictions for steady state behavior of subcritical materials disagree with the established results of Budiansky et al. (1983). We have checked to see if lack of mesh refinement is the source of our problem, but that is not so. The discrepancy remains unresolved.

Our calculations confirm the novel R-curve behavior found by Stump and Budiansky (1989) in their calculations, namely that there is a peak in toughness prior to steady state. Since the peak of the R-curve will determine the potential toughness of the material, these new higher theoretical values are significant. The actual toughness measured in an experiment will depend on the compliance of the system (McMeeking and Evans (1982)) and this must be taken into account. However, it is interesting that theory has so far underpredicted experiments on transformation toughening (Evans and Cannon (1986)) and so the new results offer the prospect of the theory being brought into better agreement with the data.

It has also been observed that the original very approximate prediction of an R-curve by McMeeking and Evans (1982) has proved to be too stiff compared to the data (Heuer (1987)). It is likely that the R-curves now predicted by Stump and Budiansky (1989) and us will tend to rectify this situation. Compared to the original R-curve predicted by McMeeking and Evans (1982), those calculated in this case for $\omega = 5$ as well as that of Stump and Budiansky (1989) are more compliant. For higher values of ω , the new calculated R-curves are even more compliant so that the difference from the old curve of McMeeking and Evans (1982) will be greater.

A note of caution is called for, however. The ratio of Δa for peak K_{APP} / K_C divided by peak h is typically in the range 3 to 5 (see Table I). Thus, the amount of crack growth to reach peak toughness is only about 3 to 5 times the observed fully developed zone height. This range is not very different from the original prediction (McMeeking and Evans (1982)) that the R-curve would peak at about 3 zone heights.

It should be noted also that all the results obtained so far are for transformation zones which are very small compared to specimen dimensions. No allowance has been made for large scale transformation.

ACKNOWLEDGEMENT

The authors would like to thank A. G. Evans for many helpful discussions and comments on this paper. This work was supported by the DARPA University Research Initiative under ONR contract N00014-86-K-0753. The calculations were carried out on a Convex C1-XP2 computer.

REFERENCES

- Amazigo, J. C. and Budiansky, B., (1988) Steady-state crack growth in supercritically transforming materials, *Int. J. Solids Struct.* 24, 751-755
- Budiansky, B., Hutchinson, J. W. and Lambropoulos, J. C., (1983) Continuum theory of dilatant transformation toughening in ceramics, *Int. J. Solids Struct.* 19, 337-355.

Evans, A. G., and Cannon, R. M., (1986) Toughening of brittle solids by martensitic transformations, *Acta Metall.* 34, 761-800.

Evans, A. G., and Heuer, A. H., (1980) Review - Transformation toughening in ceramics: martensitic transformations in crack tip stress fields, *J. Am. Ceram. Soc.* 63, 241-248.

Green, D. J., Hannink, R. H. J. and Swain, M. V., (1989) Transformation Toughening of Ceramics, CRC Press.

Heuer, A. H., (1987) Transformation toughening in ZrO_2 - containing ceramics, *J. Am. Ceram. Soc.* 70, 689-698.

Hom, C. L., Mataga, P. A. and McMeeking, R. M., (1989) Some Recent Developments in Numerical Modelling of Fracture Toughness in Brittle Matrix Composites, *Int. J. Num. Methods Engg.*, to appear.

McMeeking, R. M., (1986) The effective transformation strain in binary elastic composites, *J. Am. Ceram. Soc.* 69, C301-302.

McMeeking, R. M. and Evans, A. G., (1982) Mechanics of transformation toughening in brittle materials, *J. Am. Ceram. Soc.* 65, 242-246.

Parks, D. M., (1974) A stiffness derivative finite element technique for determination of crack tip stress intensity factors, *Int. J. Fract.* 10, 487-502.

Parks, D. M., (1978), Numerical Methods in Fracture Mechanics (Eds: Luxmore, A.R. and Owen, D. R. J.) 464-478.

Rice, J. R., (1968) A path independent integral and the approximate analysis of strain concentrations by notches and cracks, *Trans. ASME 80, Series E, J. Appl. Mech.* 35, 379-386.

Rose, L. R. F., (1986) The size of the transformed zone during steady-state cracking in transformation-toughened materials, *J. Am. Ceram. Soc.* 34, 208-211.

Stump, D. M. and Budiansky, B., (1989) Crack growth resistance in transformation-toughened ceramics, *Int. J. Solids Struct.*, 25, 635-646.

Swain, M. V., 1983, Fracture Mechanics of Ceramics (Eds. R. C. Bradt et al.) Vol 6, pp. 355-370, Plenum.

Swain, M. V. and Hannink, R. H. J., 1984, Fracture Mechanics of Ceramics (Ed. N. Claussen) Vol 12, pp. 225-239, Plenum.

FIGURE CAPTIONS

Figure 1. The hydrostatic material behavior of a ceramic containing particles which undergo a stress induced phase transformation.

Figure 2. The boundary value problem of a semi-infinite crack subject to a mode I tensile opening load.

Figure 3. The finite element mesh used to examine a growing crack in a transformation toughened composite.

Figure 4. Transformation zone for the case $\omega=5$ and $\bar{B}/G=-1.3$ when $\Delta a=11.4L$.

Figure 5. Development of the transformation zone for the case $\omega = 10$ and $\bar{B}/G = 0$ as the crack grows; Δa is the amount of crack growth. Contour levels are for θ / θ^T .

Figure 6. Transformation zone contour plots of θ / θ^T for the case of $\omega = 5$ when $\Delta a = 8.6L$. (a) $\bar{B}/G = 0$ (b) $\bar{B}/G = -0.5$
(c) $\bar{B}/G = -1.0$

Figure 7. Transformation zone contour plots of θ / θ^T for the case of $\omega = 10$ when $\Delta a = 8.6L$. (a) $\bar{B}/G = -0.5$ (b) $\bar{B}/G = -1.0$

Figure 8. Transformation zone contour plots of θ / θ^T for the case of $\omega = 15$ when $\Delta a = 12.9L$. (a) $\bar{B}/G = 0$ (b) $\bar{B}/G = -0.5$
(c) $\bar{B}/G = -1.0$

Figure 9. Resistance curves for the cases of $\omega = 5$. The steady-state results of Budiansky et al. [5] are shown with dashed lines.

Figure 10. Resistance curves for the cases of $\omega = 10$. The steady-state results of Budiansky et al. [5] are shown with dashed lines.

Figure 11. Resistance curves for the cases when $\omega = 15$. The steady-state results of Budiansky et al. [5] are shown with dashed lines.

4:A4/mef-9/14/89

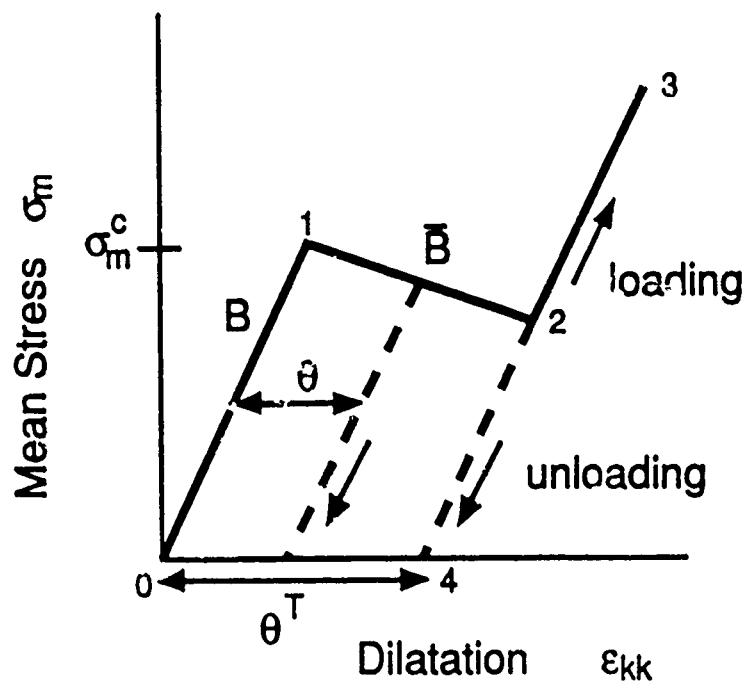


Figure 1

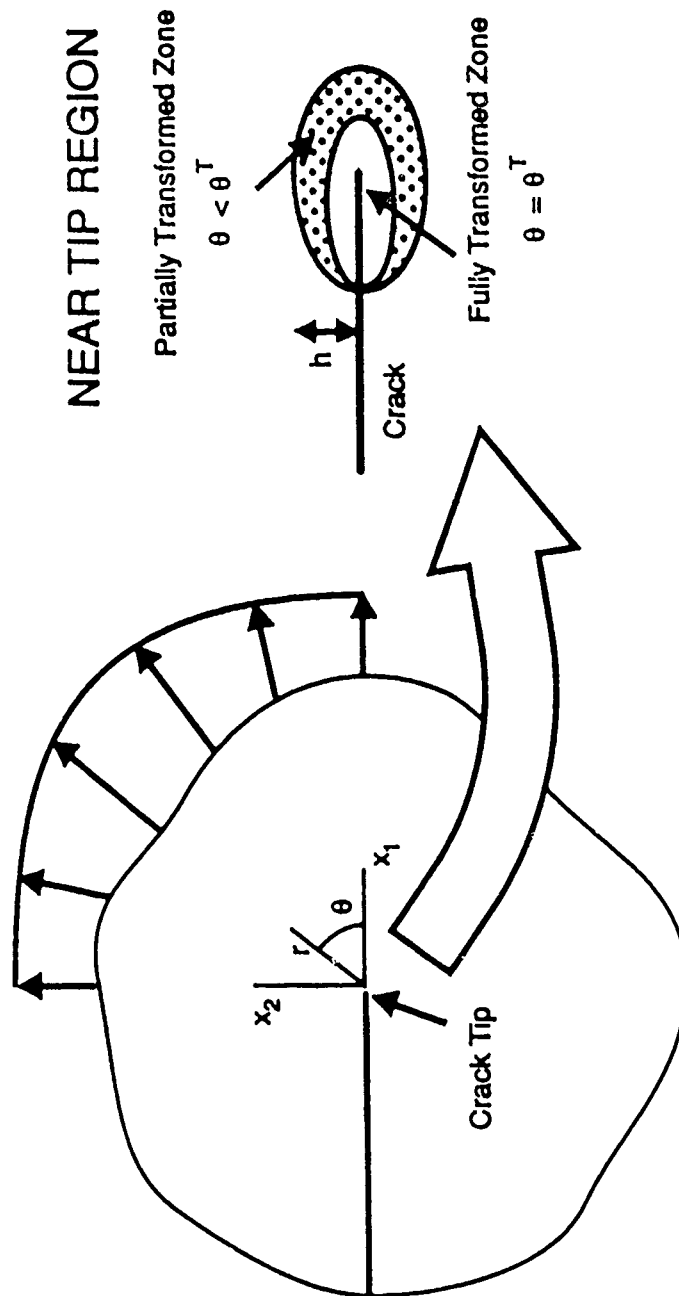


Figure 2

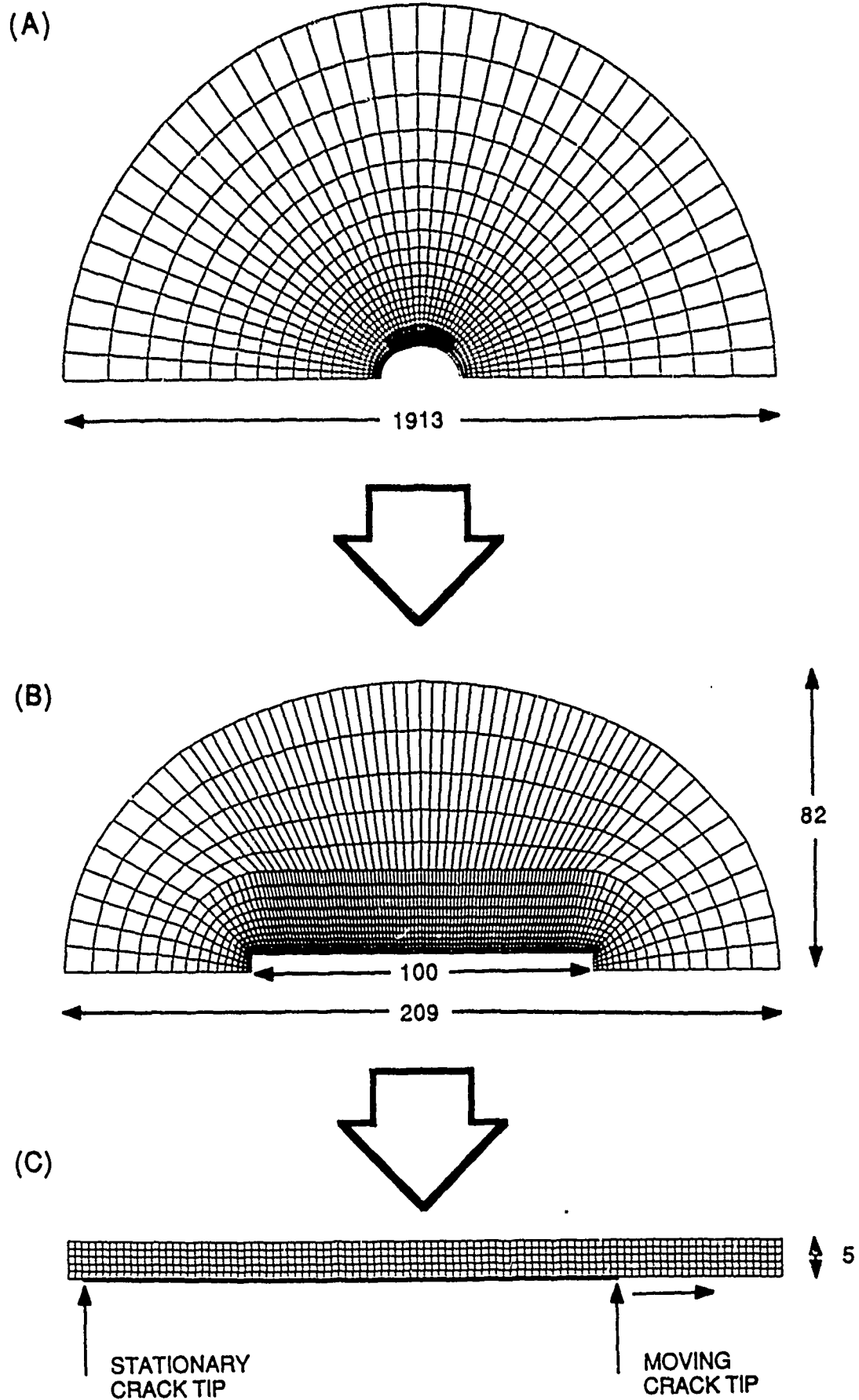


Figure 3

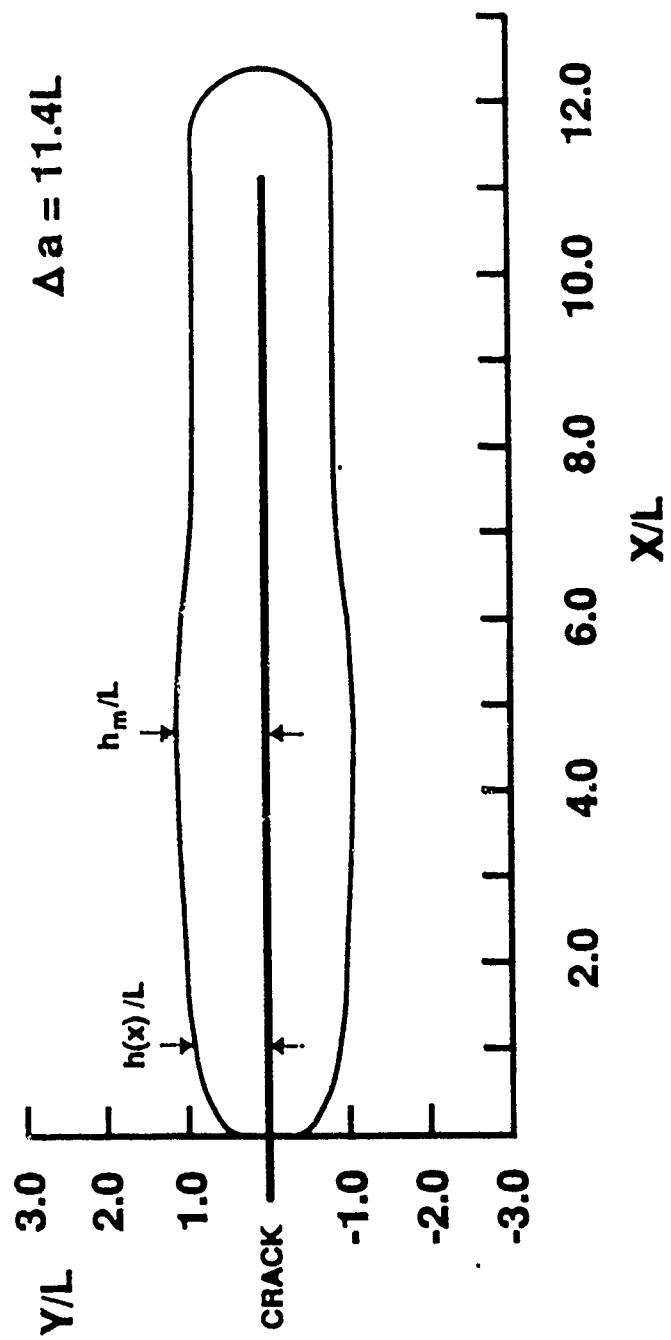


Figure 4

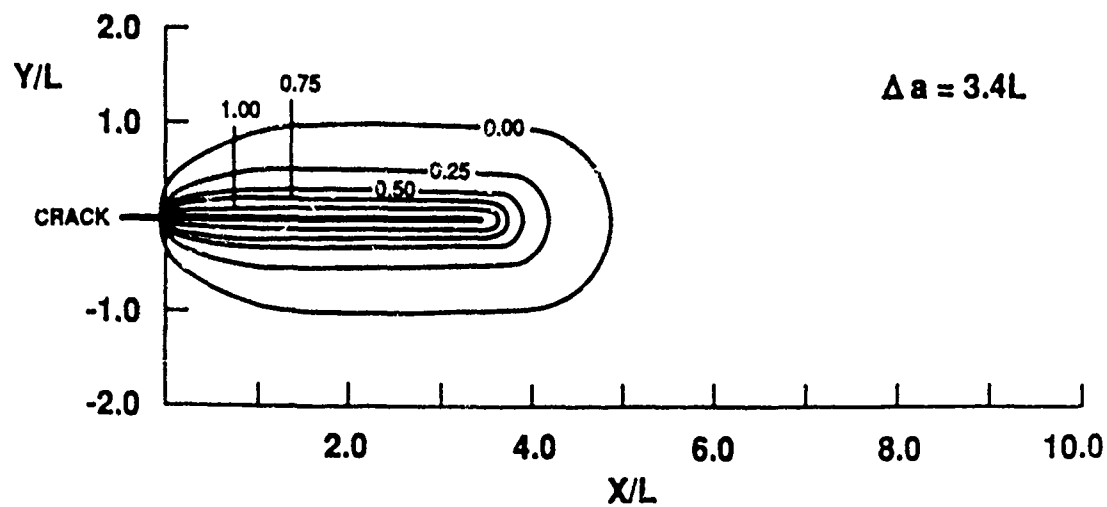
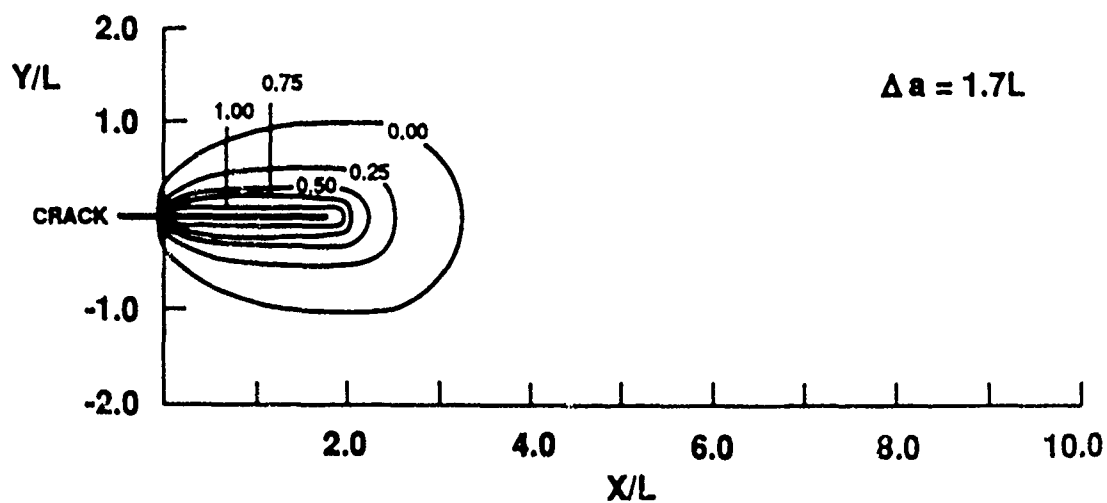
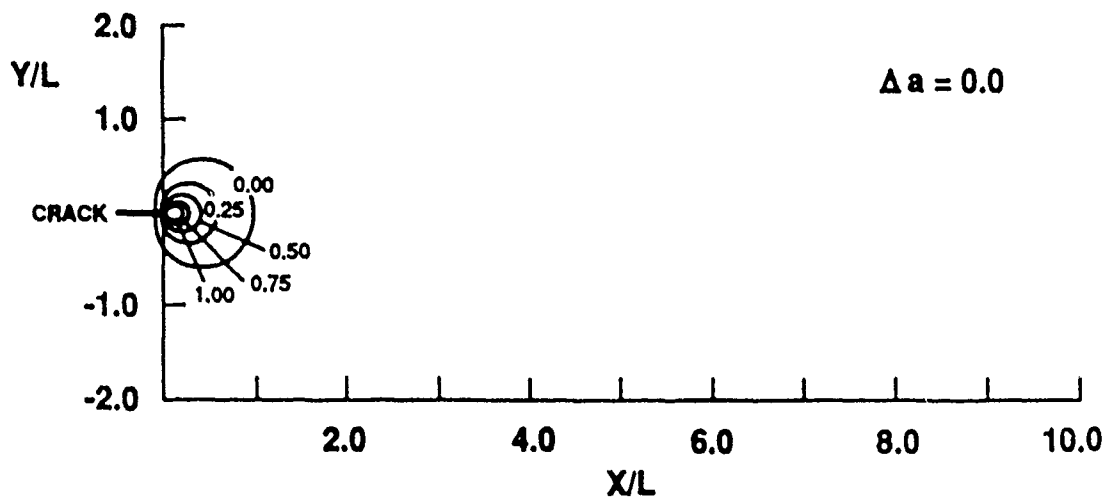


Figure 5

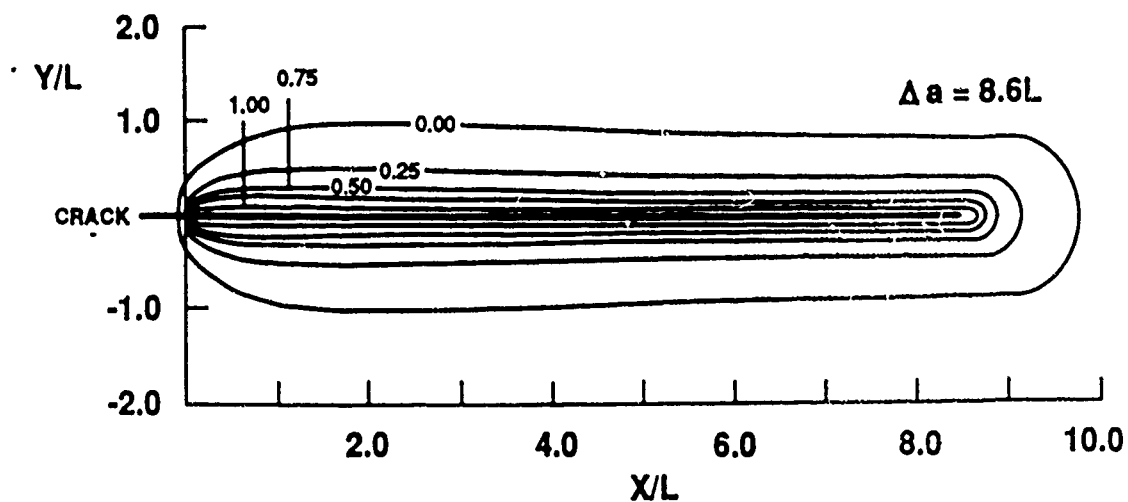
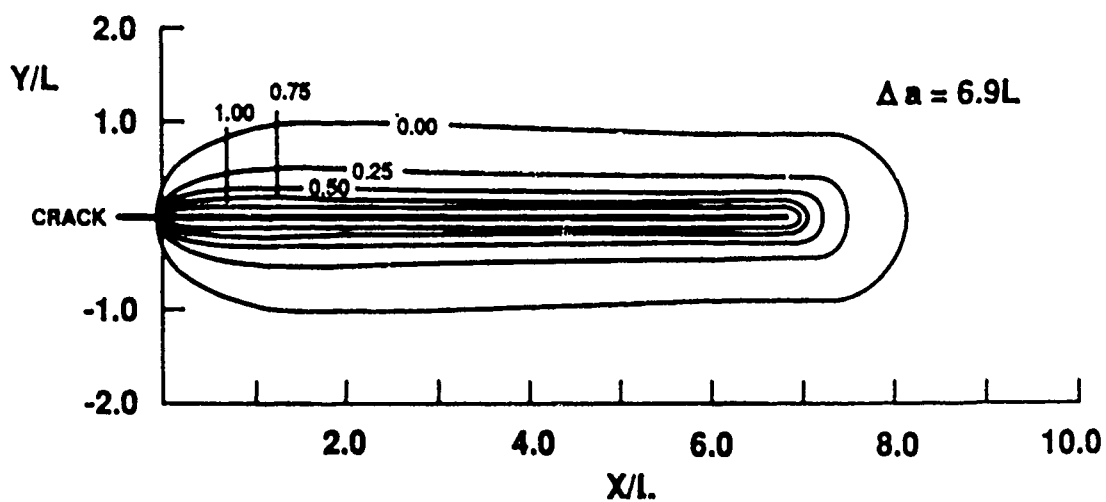
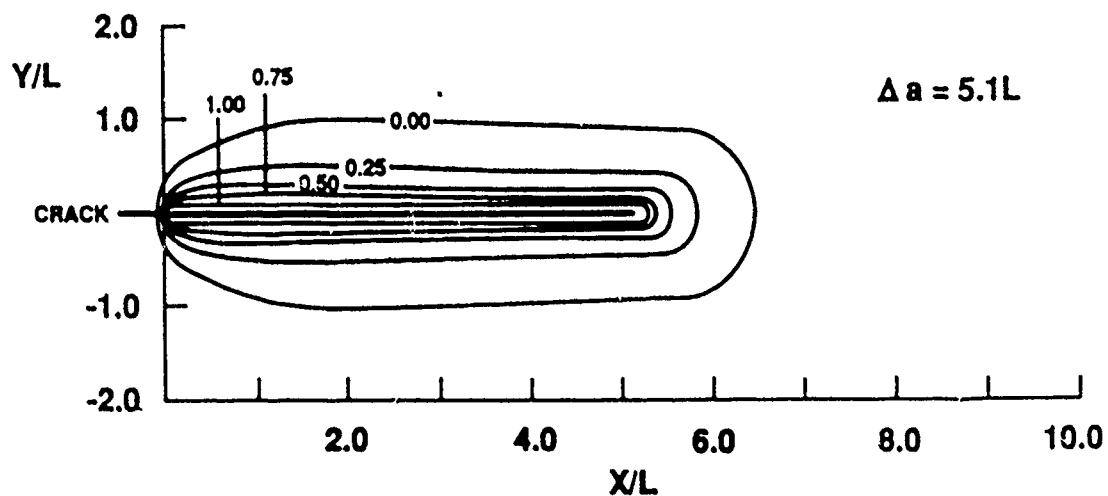


Figure 5 (cont.)

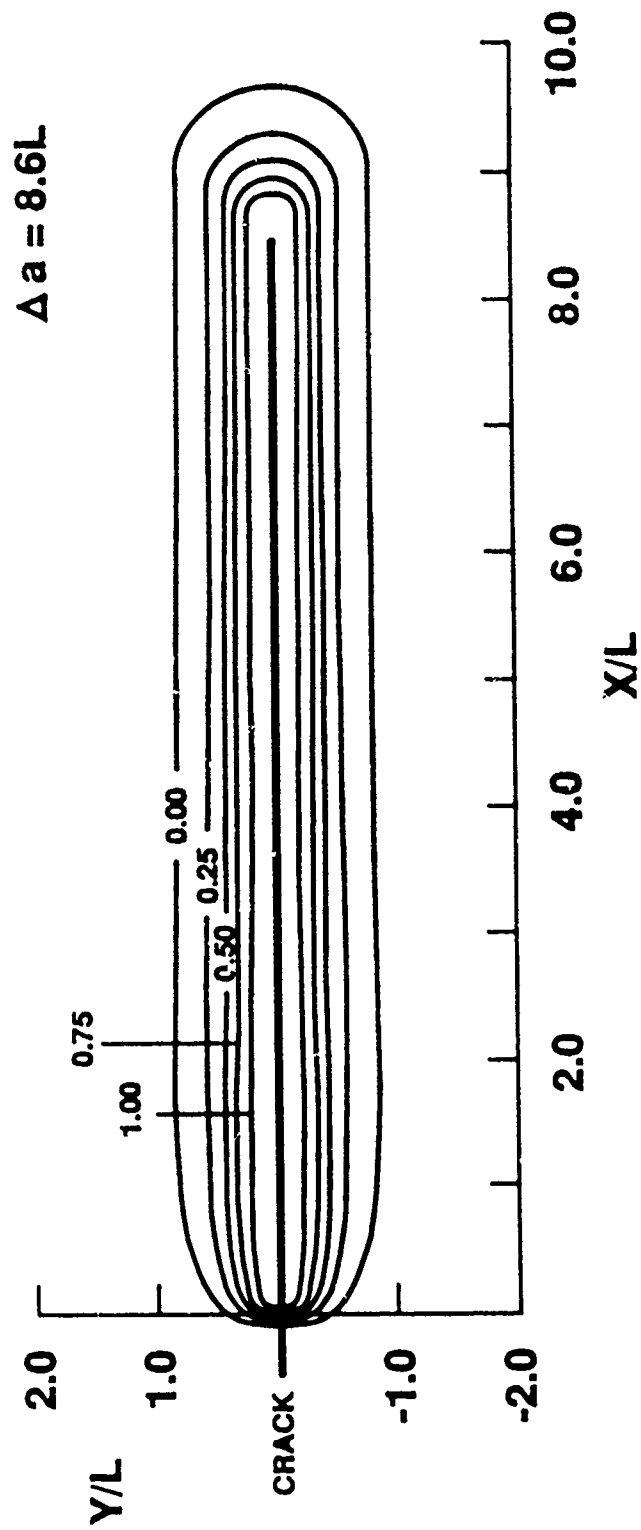


Figure 6 (a)

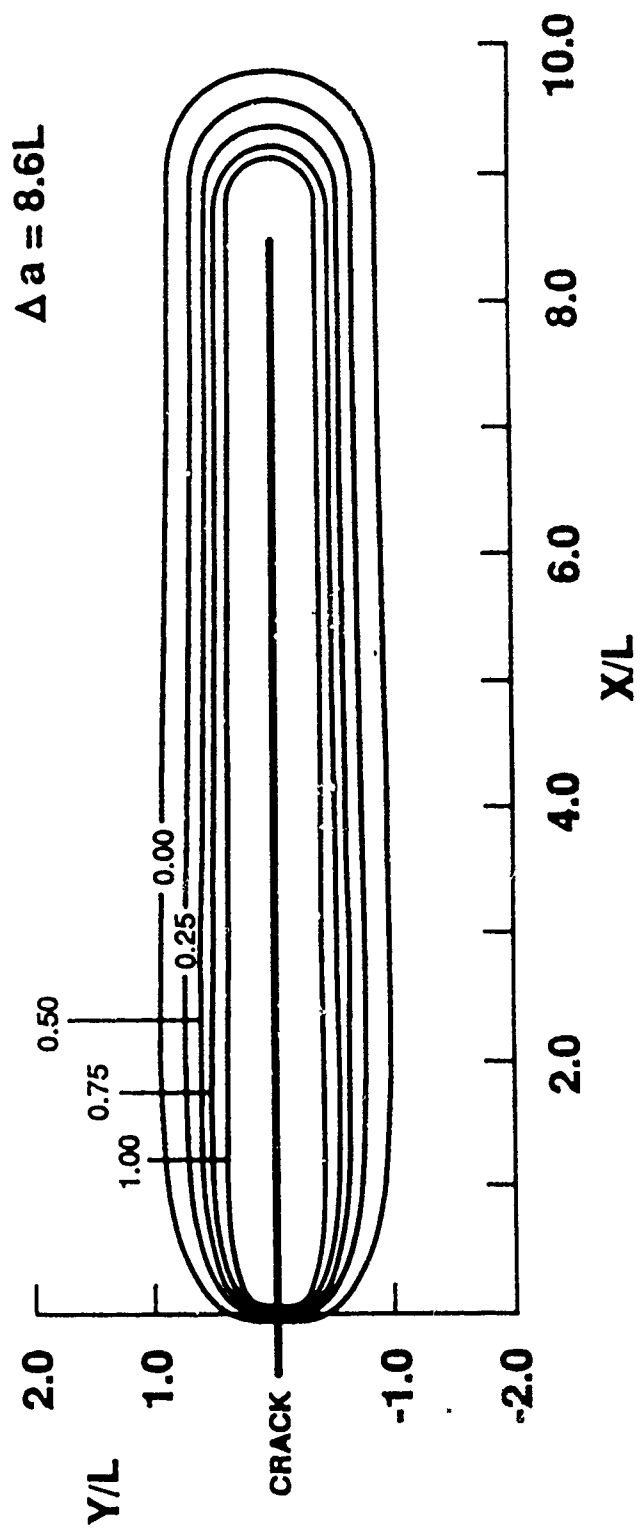


Figure 6 (b)

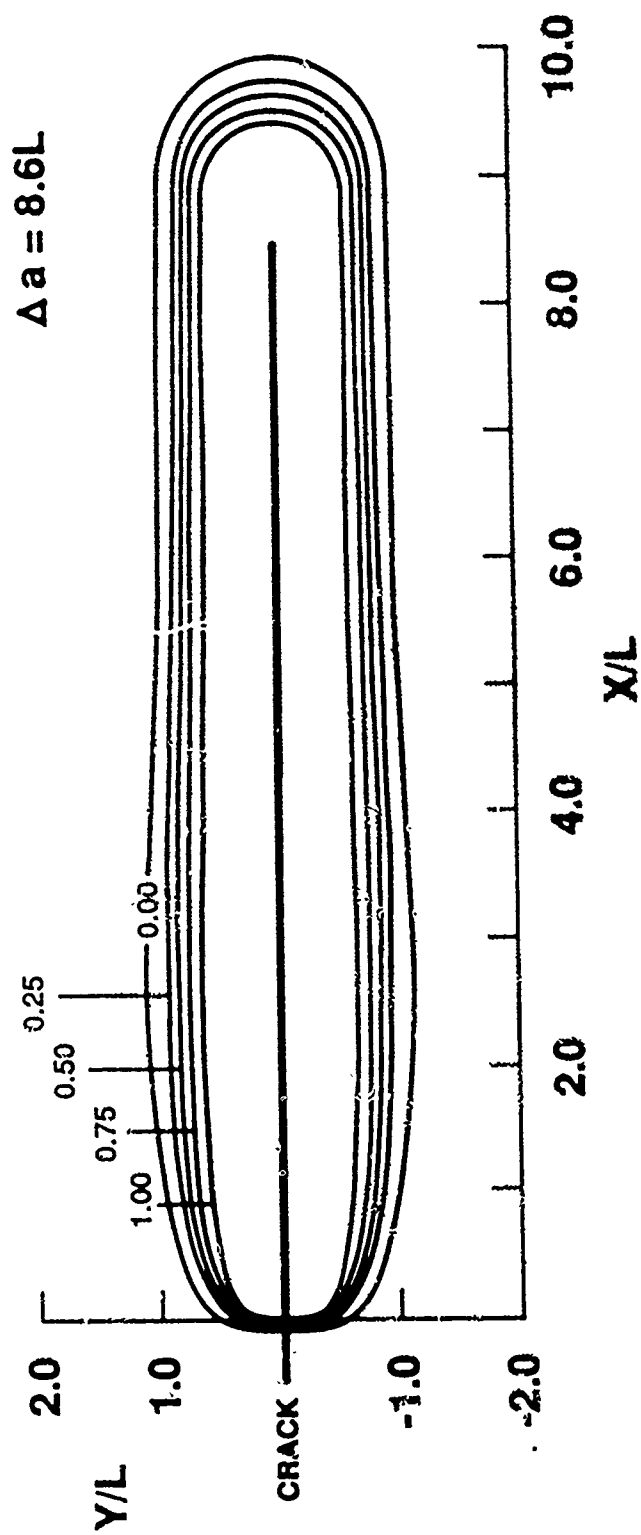


Figure 6 (c)

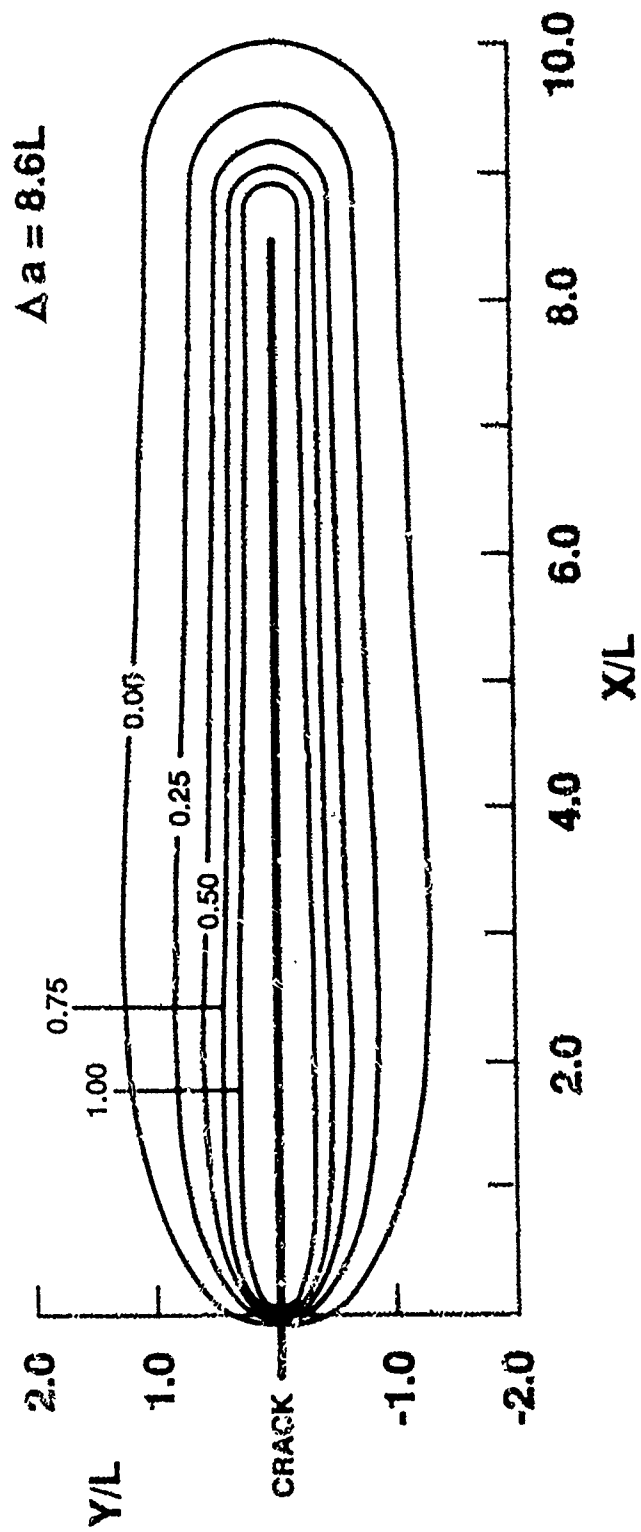


Figure 7 (a)

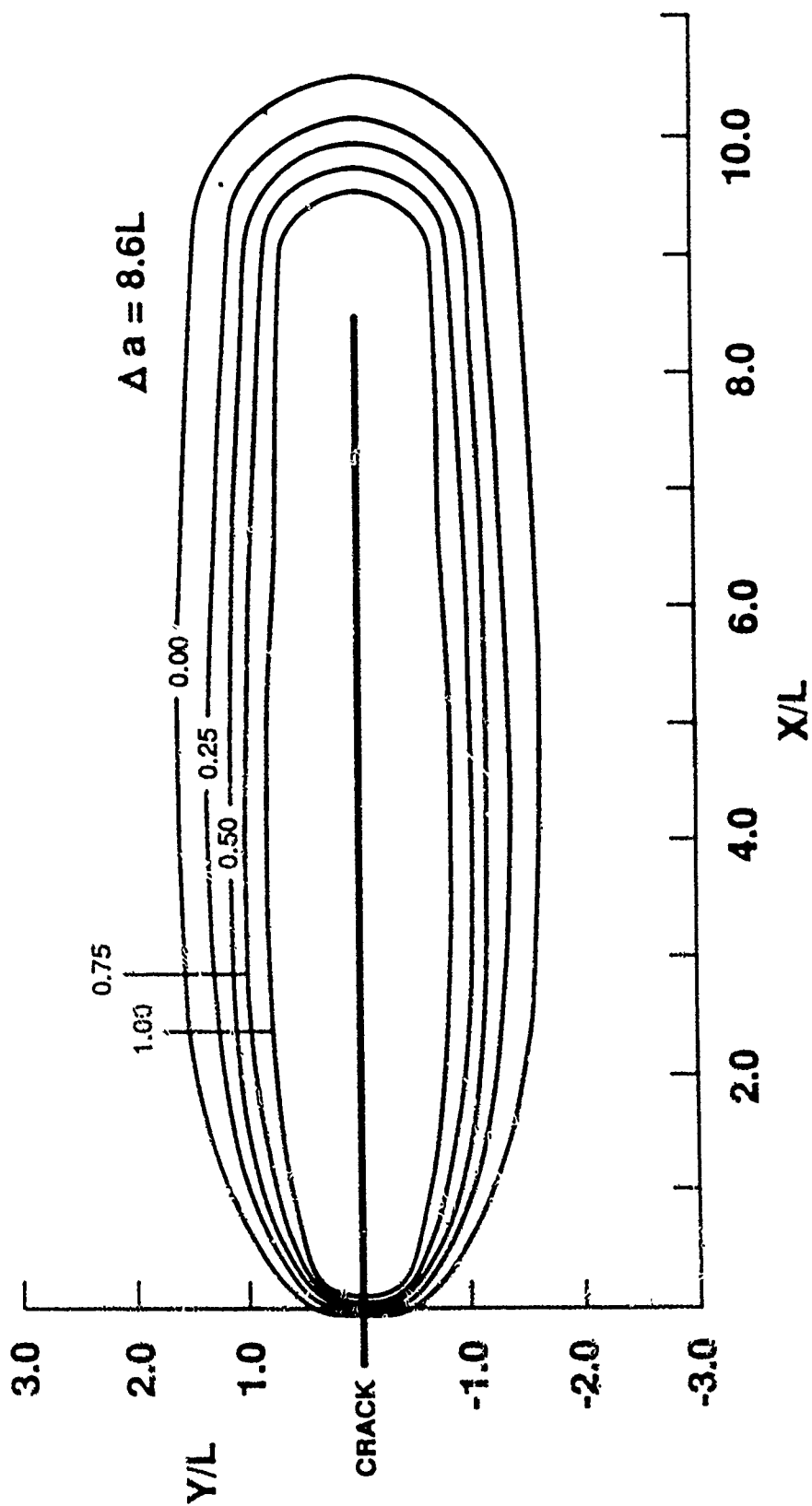


Figure 7 (b)

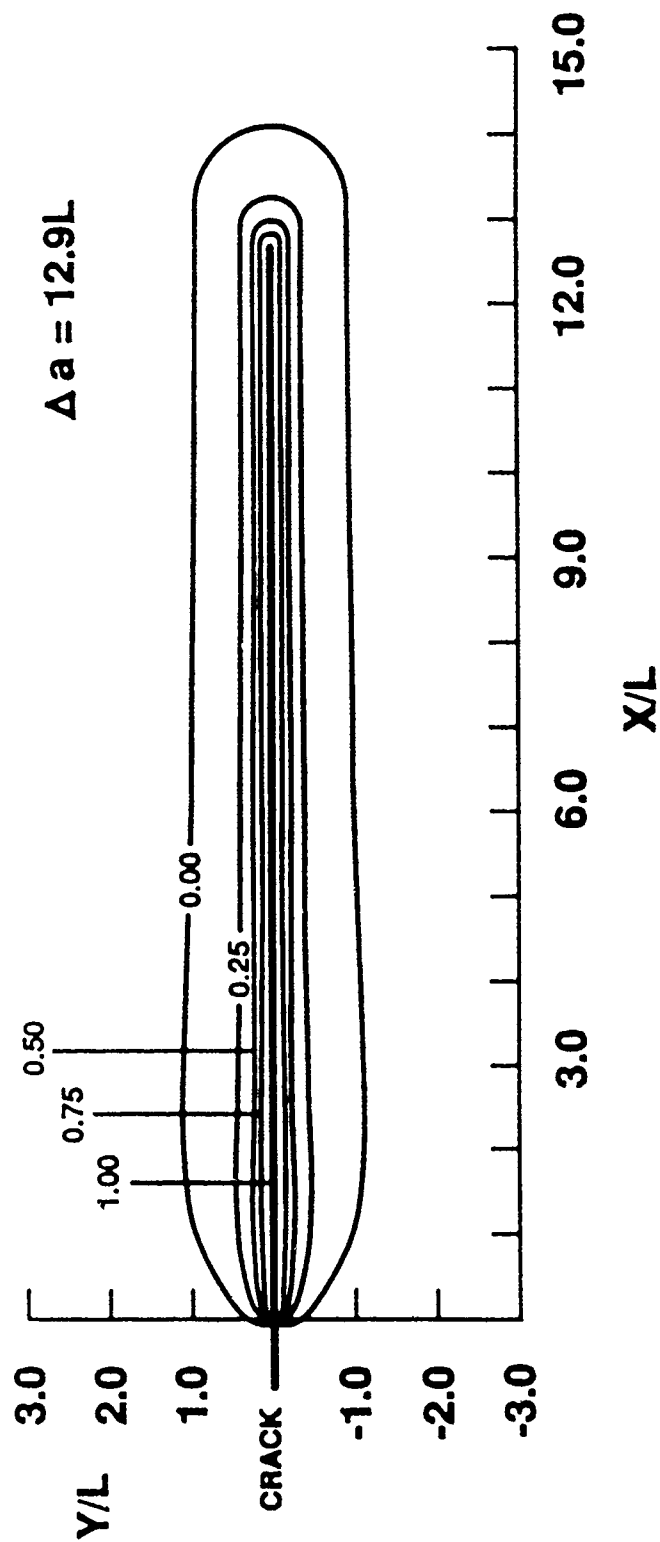


Figure 8 (a)

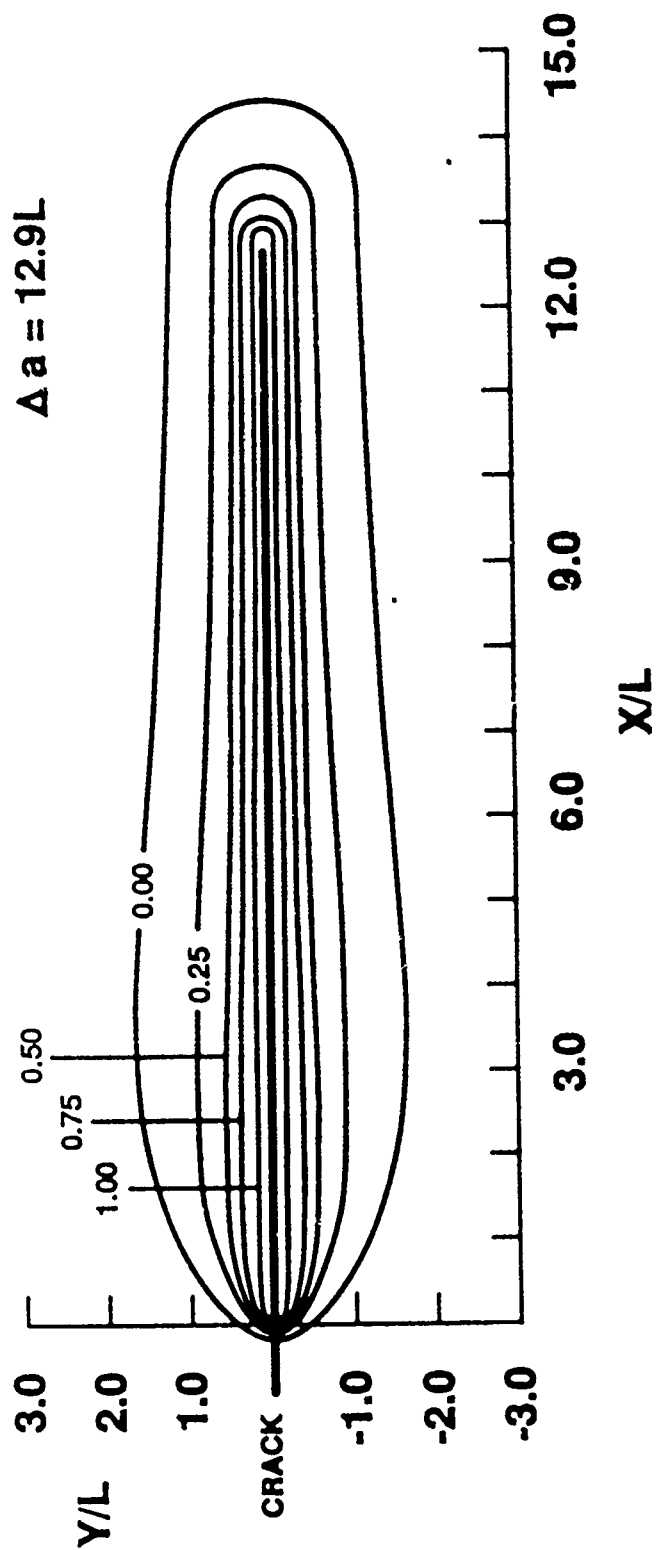


Figure 8 (b)

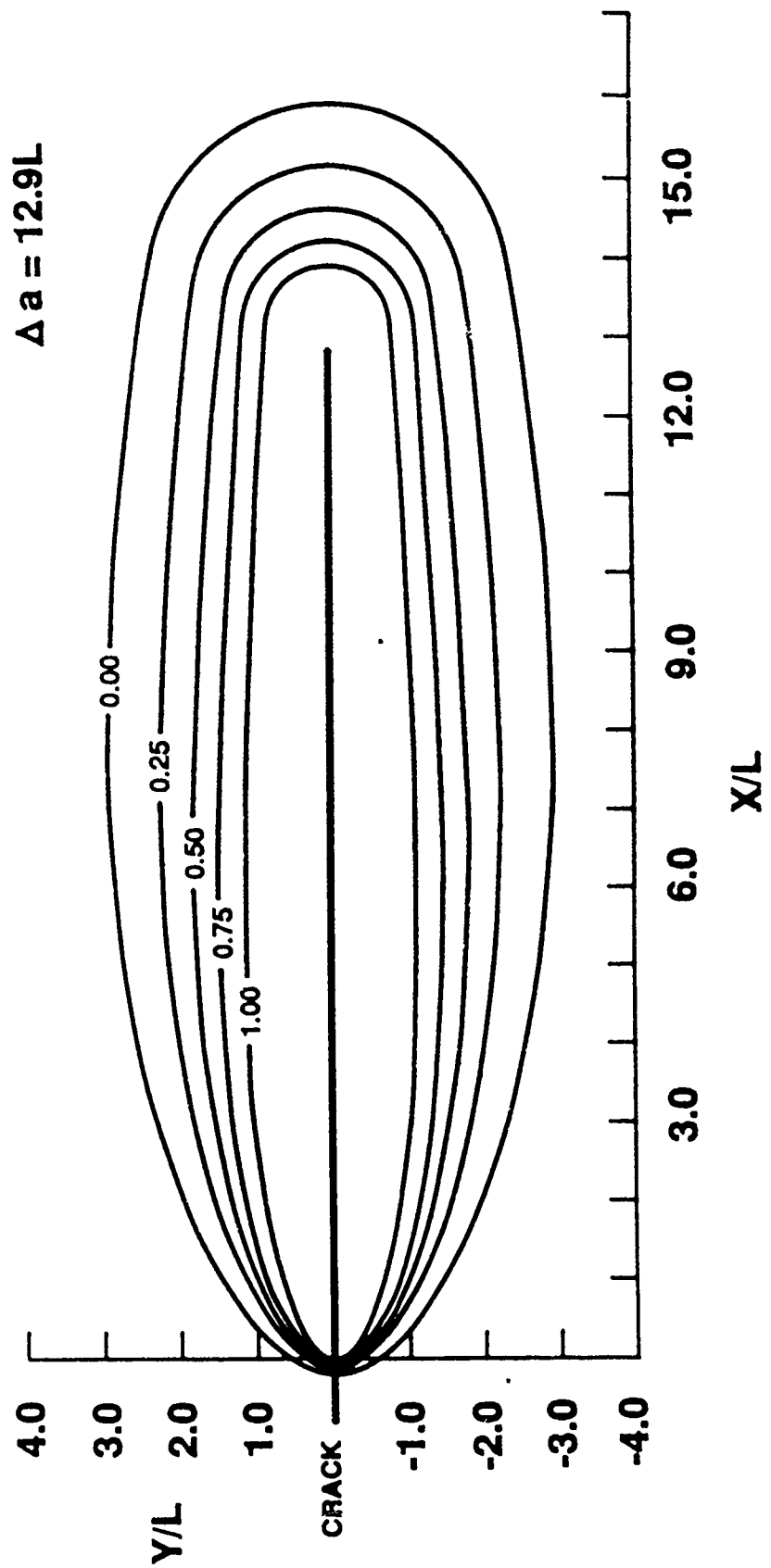


Figure 8 (c)

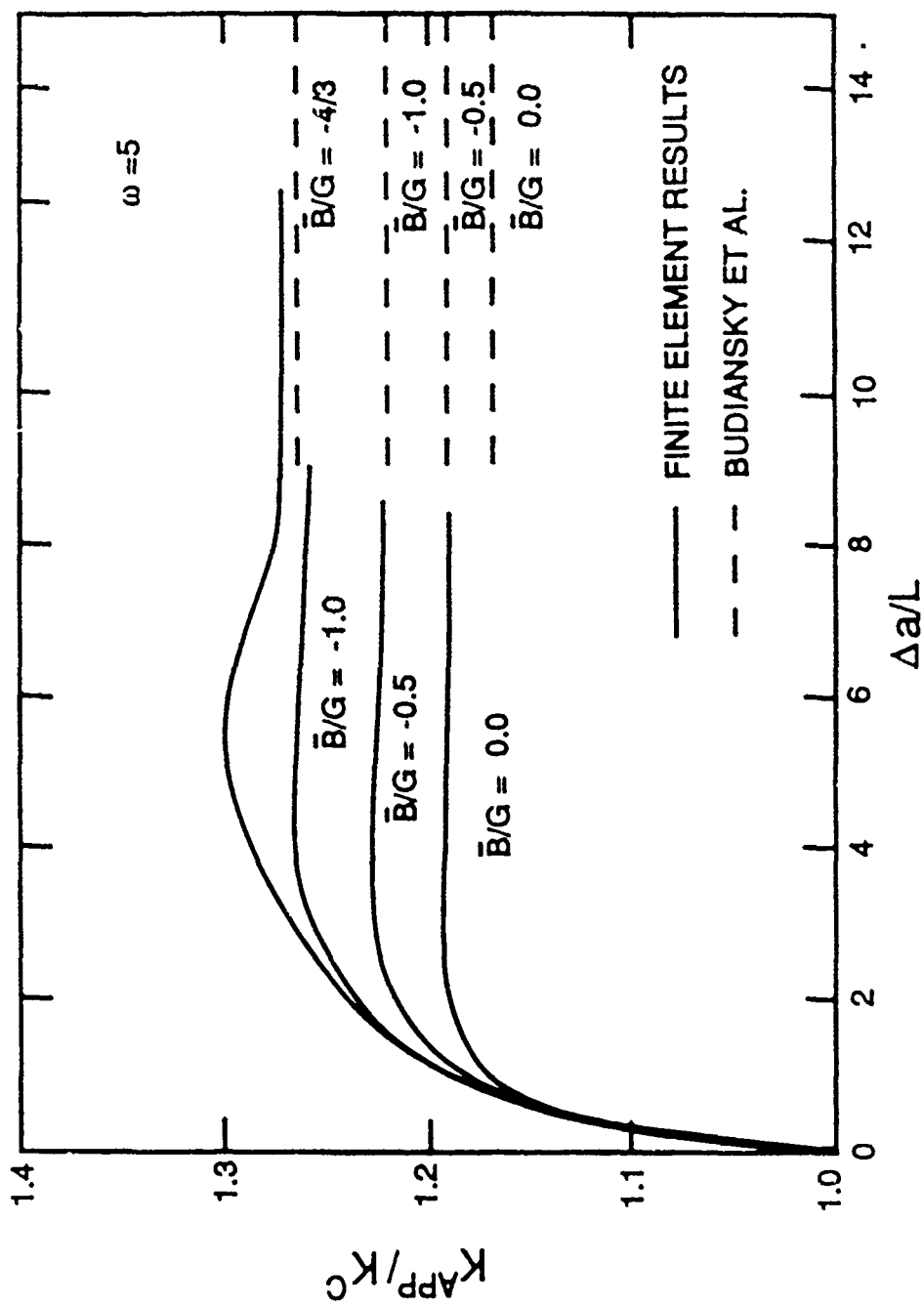


Figure 9

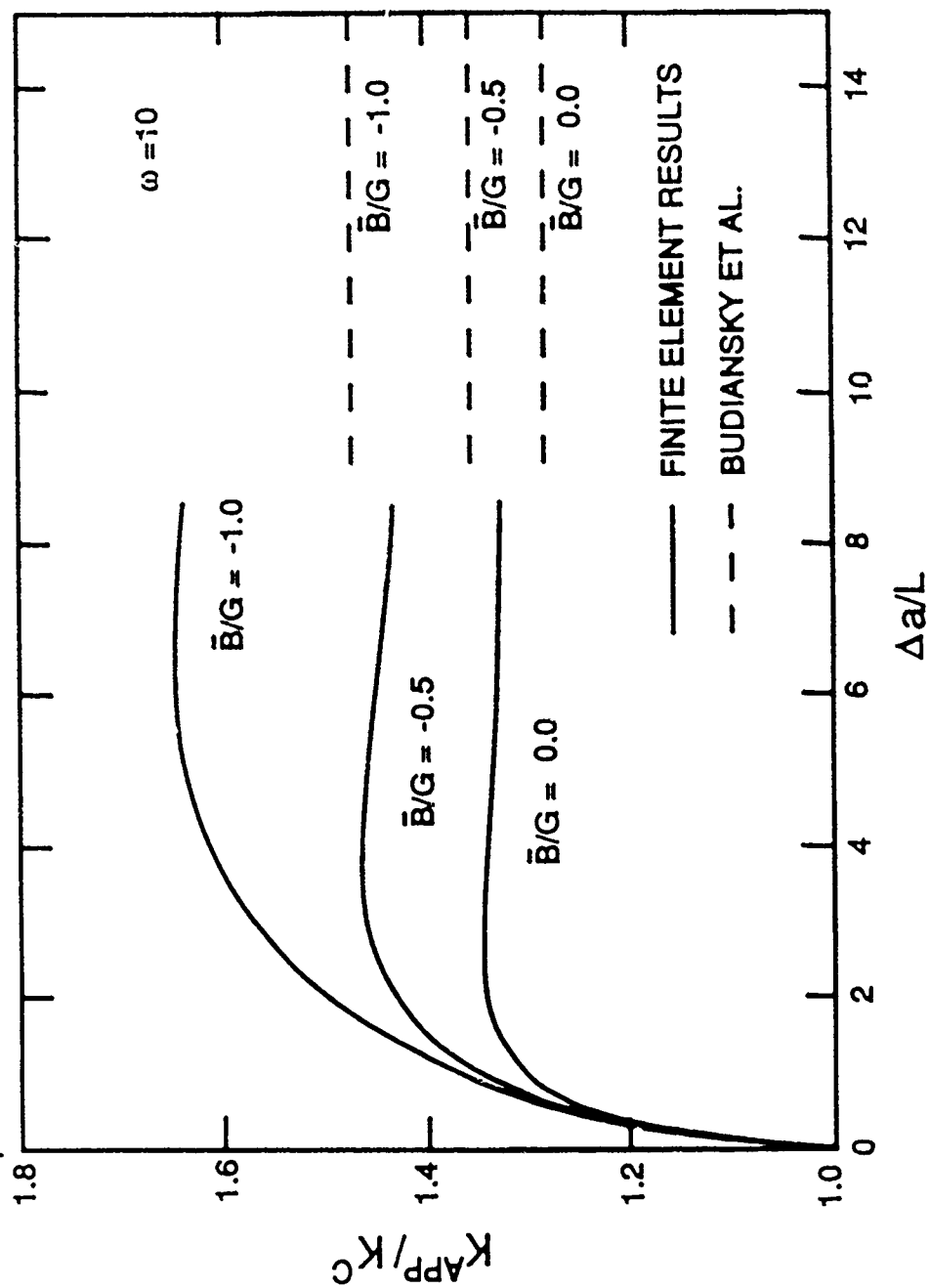


Figure 10

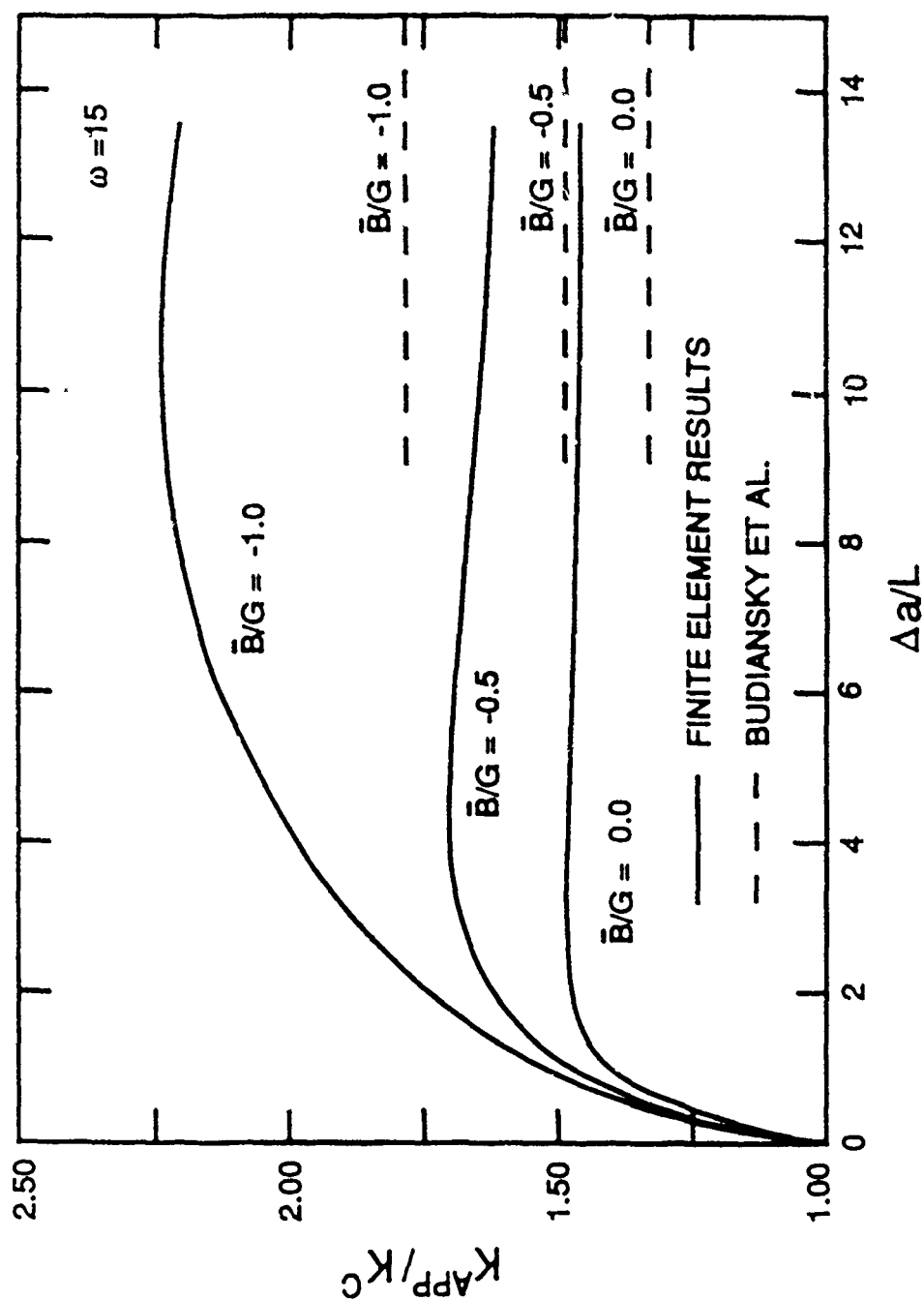


Figure 11



MECH-147

CRACK GROWTH RESISTANCE IN TRANSFORMATION-TOUGHENED
AND DUCTILE-PARTICLE REINFORCED CERAMIC

David M. Stump

Division of Applied Sciences
HARVARD UNIVERSITY
Cambridge, Massachusetts 02138

July 1989

CRACK GROWTH RESISTANCE IN TRANSFORMATION-TOUGHENED AND DUCTILE-PARTICLE REINFORCED CERAMIC

David M. Stump

Divison of Applied Sciences
Harvard University
Cambridge MA 02138

ABSTRACT

Transient crack growth resistance is studied in ceramics reinforced with both dilatant transforming particles and very ductile crack-bridging particles. The overall material toughness of a growing precut crack is found by modeling the evolution of the surrounding transformed region and the formation of a bridging particle strip behind the advancing crack tip. The maximum toughness occurs for finite amounts of crack growth and exceeds the corresponding steady-state level.

INTRODUCTION

Brittle ceramics have been toughened by a number of methods including reinforcement with partially-stabilized zirconia (PSZ) particles or dispersions of ductile metal particles [1,2]. Small PSZ particles which undergo a phase transformation near an advancing crack tip are responsible for transformation toughening. Ductile particles that bridge the faces of a growing crack cause particulate toughening.

A recent theoretical study [3] of steady-state crack growth in the combined material reinforced with both PSZ and very ductile particles has revealed that the component mechanisms can interact synergistically. This study contemplates the theoretical toughening during the growth of a semi-infinite precut (i.e. initially unbridged) combined-material crack. The analysis is motivated by a study [4] of crack growth resistance in PSZ materials, where it was discovered that for finite amounts of growth, the transient toughening ratio $\lambda_T = K/K_m$ (K is the "applied" stress intensity

factor; K_m is the critical crack-tip stress-intensity factor for fracture) reached a maximum λ_T^{\max} exceeding the corresponding steady-state value λ_T^{ss} [5]. We begin with a review of results for particulate and PSZ reinforcement.

PARTICULATE REINFORCEMENT

The semi-infinite precut crack is shown from above and the side in Figure 1a. The crack front is interrupted by a random dispersion of small ductile particles. The particles behind the front have been severed across the crack plane. As crack growth occurs, see Figure 1b, the crack front advances through the matrix leaving behind bridging particles that exert restraining forces as the crack-faces are drawn apart. We analyze crack growth by averaging the effects of the particles through the thickness of the body, and adopt a 2-dimensional model of a crack-tip bridged by a strip of deforming particles. This study uses a simplified "Dugdale-like" particle model that considers the bridging zone to be a uniform strip of particles obeying the crack-face deformation rule of Figure 2. The critical crack-opening displacement (COD) at the end of the strip is $2v_f$.

The enhanced toughness is expressed in terms of the *modified* toughness ratio

$$\Lambda_p = \frac{K}{K_m \sqrt{1-c}} \quad (1)$$

where K is the "applied" stress intensity factor, K_m is the critical crack-tip stress intensity factor for fracture in the *matrix*, and c is the concentration of ductile particles. The square-root term accounts for the decrease in crack front due to the presence of the particles. The toughness ratio for plane-strain steady-state crack growth, Λ_p^{ss} , is given by the J-Integral result [6]

$$\Lambda_p^{ss} = \left[1 + \frac{2v_f c S E}{(1-c)(1-v^2)K_m^2} \right]^{1/2} \quad (2)$$

where E and v are Young's modulus and Poisson's ratio of the matrix. The steady-state bridging length l_p , see Figure 1b, is given

$$\Lambda_p^{ss} = 1 + \frac{cS}{K_m} \sqrt{\frac{8l_p}{\pi(1-c)}} \quad (3)$$

During steady-state growth l_p remains constant with rupture of the particles at the end of the strip occurring simultaneously with crack growth.

The dependence of the transient toughening ratio Λ_p on the growth of the precut crack is found by replacing l_p in (3) with the tip advance Δa for an initial stage of growth when all the bridging particles remain intact. When Δa reaches the value l_p , steady-state growth commences with Λ_p remaining fixed at Λ_p^{ss} . Recent *in-situ* measurements of v_f and plausible estimates of S in the $\text{Al}_2\text{O}_3/\text{Al}$ system [7] reveal that (2) provides a reasonable approximation. Experimental confirmation of (3) is still lacking, but might be attributed to the fact that so far measurements of l_p have been made on the surface of specimens [7]. Nevertheless, we accept the validity of both relations for the subsequent combined material analysis.

PSZ REINFORCEMENT

Transformation toughening has been analyzed with the "supercritical" transformation model introduced in [8]. The transformed material is assumed to undergo a uniform stress-free transformation-dilatation of strength $c_t \theta_p^T$, where c_t is the PSZ volume fraction and θ_p^T is the unconstrained dilatation (typically 0.04). The transformation occurs supercritically (i.e. completely) when the mean stress $\sigma_m = \sigma_{kk}/3$ reaches the critical value σ_m^c . An important transformation strength parameter [8-10] is

$$\omega = \frac{E c_t \theta_p^T}{\sigma_m^c} \left(\frac{1+\nu}{1-\nu} \right) \quad (4)$$

A plane-strain characteristic length is given by

$$L = \frac{2}{9\pi} \left[\frac{K_m(1+\nu)}{\sigma_m^c} \right]^2 \quad (5)$$

STEADY-STATE CRACK GROWTH

Steady-state crack growth, wherein the faces of the growing crack are bordered by small-scale transformed wakes of height H_T is shown in Figure 3. Calculation of the steady-state

toughness ratio λ_T^{ss} and the nondimensional wake height H_T/L was accomplished by requiring the "applied" K and the transformation itself to keep σ_m at σ_m^c along the leading edge of the transformed boundary, while maintaining the crack-tip stress-intensity factor K_{tip} at the critical value K_m . Results for λ_T^{ss} are given by the outer curve of Figure 4, a plot of $(\lambda_T^{ss})^{-1}$ versus the parameter ω [5,6]. "Lock-up" of the steady-state crack occurs for $\omega = \omega_c = 29.99$ [9].

For weak transformations (i.e. $\omega \approx 0$), the fractional increase in toughness $\Delta K^{ss}/K_m$, where $\Delta K^{ss} = K - K_m$, is related to the zone height H_T by the approximate formula (8)

$$\frac{\Delta K^{ss}}{K_m} = \frac{E c_i \theta_p^T}{2(1-\nu)K_m} \left[\frac{H_T}{\pi\sqrt{3}} \right]^{1/2} \quad (6)$$

The relation (6) along with the finite-strength transformation results of [5] are plotted in Figure 5. When compared with experimental data, the steady-state results of Figure 5 are typically low by a factor of two [2]. Indications are that the shear stress also plays a role in triggering the transformation, which may account for this discrepancy [3].

R-CURVES

The dependence of the transient toughness ratio λ_T on the growth of an initially stationary semi-infinite crack was considered in [4]. Crack growth initiation occurs when $K_{tip} = K = K_m$ [7]. At this instant, the tip is surrounded by a transformed region along the exterior of which the mean stress equals σ_m^c . As crack growth occurs, the transformed region continues to surround the tip as the leading edge of the boundary advances, transforming "fresh" material and depositing "old" material in wake regions. The instantaneous toughness ratio λ_T was found by enforcing the σ_m^c criterion along the advancing portion of the boundary, while maintaining K_{tip} at K_m . R-curves, plots of λ_T versus the nondimensional crack extension $\Delta a/L$ such as Figure 6, were generated for various values of the parameter ω . The corresponding value of λ_T^{ss} is given by the dotted line. The nondimensional zone height H/L and the toughness ratio λ_T reached the maximum values H_T^{max}/L and λ_T^{max} for finite (but not the same!) amounts of crack growth. The dependence of $(\lambda_T^{max})^{-1}$ on ω is given by the inner curve of Figure 4. "Lock-up" of transient cracks occurs for

$$\omega \approx 20.2 [4].$$

COMBINED PSZ AND DUCTILE-PARTICLE REINFORCEMENT

We now study semi-infinite crack growth in the combined material by using the supercritical transformation model together with the very-ductile bridging-particle model. The component transformation toughening ratios λ_T^{max} and λ_T^{ss} , and the modified particulate toughness ratio Λ_p^{ss} are considered to be prescribed material parameters. We begin with a review of steady-state crack growth before studying the transient toughening of a growing precut crack.

STEADY-STATE CRACK GROWTH

Steady-state crack growth in the combined material is shown in Figure 7. The effects of the "applied" K , the bridging segment, and the transformation keep σ_m at σ_m^c along the exterior of the leading edge of the transformed region, while maintaining K_{up} at the critical value $K_m \sqrt{1-c}$ and keeping the COD at the end of the strip l , fixed at $2v_f$. The "natural" coupling parameter

$$\rho = \frac{cS(1+v)}{\sigma_m^c} \quad (7)$$

emerged from the analysis [3]. The steady-state *modified* toughness ratio Λ^{ss} , given by the form of (1), was found for various prescribed values of the toughness ratios λ_T^{ss} , Λ_p^{ss} , and the parameter ρ . In the limits $\rho = (0, \infty)$, the formulas

$$\Lambda^{ss} = \lambda_T^{ss} \Lambda_p^{ss} \quad \rho \rightarrow \infty \quad (8)$$

$$\Lambda^{ss} = \left[(\lambda_T^{ss})^2 + (\Lambda_p^{ss})^2 - 1 \right]^{1/2} \quad \rho \rightarrow 0 \quad (9)$$

were found to apply. An alternative coupling parameter was given by

$$\eta = \frac{H_T(1-c)}{l_p} \quad (10)$$

where H_T and l_p are the transformed wake height and bridge length of the uncoupled systems. Large values of η correspond to large values of ρ so that the formulas (8) and (9) continue to apply

for the limits $\eta = (0, \infty)$. Values as small as $\eta = .1$ gave toughness ratios almost as high as those of (8).

TRANSIENT CRACKS

The stationary precut crack at the instant of crack growth initiation is shown in Figure 8. The crack front is blocked by nondeformed particles while surrounded by a transformed region. Since particles ahead of the tip offer no resistance, crack growth initiation depends only on the applied K and the transformation, whose combined effects maintain σ_m at σ_m^c along the exterior of the transformed region while holding K_{tip} at the critical value $K_m \sqrt{1-c}$. As discussed in [9], the transformed region does not affect the near-tip stress intensity factor of a stationary crack, so that crack growth initiation occurs when $K_{tip} = K = K_m \sqrt{1-c}$. The shapes of the surrounding boundaries are found by rescaling the results of [4] with the modified length $L(1-c)$, as has been done in Figure 9 for various values of the transformation-strength parameter ω (λ_T^{ss} or λ_T^{max} via Figure 4).

The *upper* half of a crack that has grown by the amount Δa is shown in Figure 10. The growth process is divided into two distinct phases. During the initial stage of growth, all the bridging particles left behind by the advancing tip remain intact so that the length of the strip l is given by $\Delta l = \Delta a$. Throughout this phase, the *incremental* change in length of the strip l equals the *incremental* crack growth Δa . When Δa reaches the special value l_c , the critical COD $2v_f$ is achieved at the tip, the strip and particle rupture commences. Throughout the remainder of growth l varies continuously as the COD condition is enforced. However, in order to prevent the rehealing of ruptured particles, the restriction $l \leq \Delta a$ applies.

The boundary of the transformed region surrounding the growing crack is modeled by three pieces; the active, passive and residual, see Figure 10. The active piece, MN, is the leading edge of the transformed boundary along which material has just transformed according to the σ_m^c criterion. The residual piece, OP, is that portion of the boundary surrounding the stationary crack that is left behind with the first increment of crack growth. The passive segment is a growth

dependent piece connecting O, the end of the residual segment, with N, the end of the current active piece. For a crack that advances by a series of small finite increments δa , the passive segment is sequentially extended with a series of straight-line segments while always providing a smooth connection to the current active piece. Thus as the crack advances, a straight-line approximation to the actual passive segment is constructed. Points on the current active segment are given in terms of translating crack-tip coordinates by the complex variable $z = x+iy$ where

$$z(\theta) = R(\theta)[\cos(\theta) + i \sin(\theta)] \quad 0 < |\theta| < \alpha \quad (11)$$

The unknown angle α marks the end of the current active segment.

Calculations of the overall transient toughness ratio Λ along with the nondimensional active boundary radius $R(\theta)/L(1-c)$ and bridge length $l/L(1-c)$ for each of a series of growth increments δa is detailed in Appendix A for prescribed values of ω , Λ_p^{ss} , and p . Typical R-curves, plots of Λ versus the nondimensional crack advance $\Delta a/L(1-c)$ are shown in Figure 11 for the values $\omega = 10$ ($\lambda_T^{max} = 1.8$), $\Lambda_p^{ss} = 2$, and a variety of p . The reason for the peak in the toughness ratio is explained below. The dependence of some corresponding normalized bridge lengths $l/L(1-c)$ on $\Delta a/L(1-c)$ are shown in Figure 12. The critical values $l_c/L(1-c)$ occur when the curves depart from the line $l/L(1-c) = \Delta a/L(1-c)$.

Throughout crack growth, the "applied" K must overcome the combined resistances of the transformation and bridging particle mechanisms. As was previously discussed, the transformation contribution reaches a peak value for finite amounts of crack advance depending on the transformation-strength parameter ω . The particulate contribution increases steadily during initial growth as the bridging strip continually extends and then levels off near its "full" value as the length of the strip does not vary much once rupture commences, see Figure 12. The particulate toughness ratio due to the inherent tip resistance plus that provided by a strip of instantaneous length l is found by introducing (4), (5) and (7) into (3) to give

$$\Lambda_p = 1 + \frac{4p}{3\pi} \sqrt{\frac{l}{L(1-c)}} \quad (12)$$

The *interaction* of the bridging strip and the transformed wake regions during crack growth determines the peak in the transient toughness ratios of Figure 11. If the particulate component, given by (12), comes close to its "full" value Λ_p^{ss} prior to the peak in the transformation effect, the mechanisms reinforce each other to provide a maximum transient-toughness ratio Λ^{max} that can substantially exceed the corresponding steady-state value Λ^{ss} . On the other hand, if the particulate component approaches its "full" value well after the transformation peak has occurred, appreciable interaction takes place only when each mechanism has come close to its steady-state level so that Λ^{max} just slightly exceeds Λ^{ss} . We now consider transient toughening behavior for the limiting values $\rho = (0, \infty)$.

For "weak" particles (i.e. $\rho = 0$), the particulate contribution only becomes important after the crack has grown much further than the peak in the transformation contribution. Thus, for $\rho=0$, the transient toughness ratio is determined by just the applied K and the transformation, so that the rescaled growing crack results of [4] apply. Only in the limit of steady-state crack growth do the particulate and transformation component interact to provide the overall toughness ratio Λ^{ss} . For "extremely strong" particles (i.e. $\rho \rightarrow \infty$), the particulate effect reaches its "full" value just after the onset of growth and prior to the peak transformation contribution. In the limit $\rho = \infty$, the particulate contribution reaches its maximum value at the instant of crack growth initiation and acts to reinforce the transformation effects throughout growth. The special analysis for crack growth initiation and transient cracks in the limit $\rho \rightarrow \infty$, $\sqrt{l/L(1-c)} \rightarrow 0$ is detailed in Appendix B.

Finally, we present Figures 13-15, plots of the maximum overall toughness Λ^{max} versus the maximum transformation component λ_T^{max} for various values of ρ and $\Lambda_p^{ss} = 2, 3$, and 4. In the limits $\rho = (0, \infty)$, the maximum overall toughness Λ^{max} is given by the approximate and exact formulas

$$\Lambda^{max} \approx \lambda_T^{max} \Lambda_p^{ss} \quad \rho \rightarrow \infty \quad (13)$$

$$\Lambda^{max} = [(\lambda_T^{ss})^2 + (\Lambda_p^{ss})^2 - 1]^{1/2} \quad \rho \rightarrow 0 \quad (14)$$

Some corresponding values of the alternative parameter η have been included in Figures 13 - 15.

Small values of η are sufficient to provide a substantial transient synergism. It is noteworthy that slight changes in η can greatly influence the maximum toughness ratio.

DISCUSSION

The transient toughness ratios of ceramics reinforced with PSZ and ductile crack-bridging particles reach maximum values for finite amounts of crack growth. However, for the maximum toughness ratio to substantially exceed the corresponding steady-state value, the component toughening phenomena must occur on approximately the same size scale. Based on realistic estimates of the transformation-strength parameter $\omega \leq 15$, we conclude that for synergistic interactions transient cracks can experience a maximum toughness of up to 30% above the steady-state value.

ACKNOWLEDGEMENTS

The author wishes to thank Professor B. Budiansky for his insights and editorial help. This work was supported in part by the DARPA University Research Initiative (Subagreement P.O. #VB38639-0 with the University of California, Santa Barbara, ONR Prime Contract N00014-86-K-0753), the Office of Naval Research (Contract N00014-84-K-0510), and the Division of Applied Sciences, Harvard University. The support of the National Science Foundation through the Graduate Fellowship program is also acknowledged.

REFERENCES

1. B. Budiansky, *Micromechanics II*, Proc. 10th U.S. Nat. Cong. of Appl. Mech., Austin, Texas, June 1986.
2. A.G. Evans and R.M. Cannon, *Toughening of brittle solids by martensitic transformations*, Acta Met. 34, pp. 761-800, 1986.
3. J.C. Amazigo and B. Budiansky, *Interaction of particulate and transformation*

- toughening*, J. Mech. Phys. Solids 36, pp. 581-595, 1988.
4. D.M. Stump and B. Budiansky, *Crack growth resistance in transformation toughened ceramics*, Int. J. Solids Structures 25, pp. 635-646, 1989.
 5. J.C. Amazigo and B. Budiansky, *Steady-state crack growth in supercritically transforming materials*, Int. J. Solids Structures 24, pp. 751-756, 1987.
 6. B. Budiansky, J.C. Amazigo and A.G. Evans, *Small-scale crack bridging and the fracture toughness of particulate reinforced ceramics*, J. Mech. Phys. Solids 36, pp. 167-188, 1988.
 7. D. Flinn, M.H. Rühle, and A.G. Evans, Univ. Cal. Santa Barbara, 1989.
 8. R.M. McMeeking and A.G. Evans, *Mechanics of transformation toughening in brittle materials*, J. Am. Cer. Soc. 65, pp. 242-246, 1982.
 9. B. Budiansky, J.W. Hutchinson and J.C. Lambropoulos, *Continuum theory of dilatant transformation toughening materials*, Int. J. Solids Structures 19, pp. 337-356, 1983.
 10. L.R.F. Rose, *The size of the transformed zone during steady-state cracking in transformation toughened materials*, J. Mech Phys Solids 34, pp. 609-616, 1986.

APPENDIX A

TRANSIENT CRACKS

The equations governing the growing crack are formulated by enforcing the σ_m^c criterion along with $K_{tip} = K_m \sqrt{1-c}$ and when necessary the critical COD condition $2v_f$. Small-scale plane-strain conditions are assumed throughout the analysis. The effects of the applied K , the transformation, and the bridging zone are given respectively by the complex potentials

$$\phi_K(z) = K \sqrt{\frac{z}{2\pi}} \quad (A1)$$

$$\phi_T(z) = -\frac{Ec_t \theta_p^T}{6\pi(1-\nu)} \oint \log(\sqrt{z} + \sqrt{z_0}) dy_0 \quad (A2)$$

$$\phi_p(z) = -\frac{cS\sqrt{lz}}{\pi} + \frac{icS}{2\pi}(z+l) \log\left(\frac{\sqrt{z}-i\sqrt{l}}{\sqrt{z}+i\sqrt{l}}\right) \quad (A3)$$

where all coordinates are measured from the current crack-tip and the branch cuts lie along the crack. The integral of (A2) is carried out in the counter-clockwise direction over the points z_0 on the boundary of the transformed region.

The mean stress exterior to the transformed region, the *upper* crack-face opening at the end of the bridging segment, and K_{tip} are given by the relations

$$\sigma_m = \frac{4(1+\nu)}{3} \operatorname{Re}\left[\frac{\partial\phi}{\partial z}\right] \quad (A4)$$

$$v^+(-l) = \frac{2(1-\nu^2)}{iE} [\phi(-l)]_+^+ \quad (A5)$$

$$K_{tip} = \lim_{x \rightarrow 0} 2\sqrt{2\pi x} \left[\frac{\partial\phi(x)}{\partial x} \right] \quad (A6)$$

where $\phi = \phi_K + \phi_T + \phi_P$, the brackets indicate the jump in ϕ across the crack faces, and Re denotes the real part of a complex quantity. After substituting the combination of (A1)-(A3) into (A4)-(A6), we obtain

$$\sigma_m = \frac{K(1+\nu)}{3} \sqrt{\frac{2}{\pi}} \text{Re} \frac{1}{\sqrt{z}} - \frac{2cS(1+\nu)}{3\pi} \left\{ 2 \text{Re} \sqrt{\frac{l}{z}} + \text{Im} \log \left(\frac{\sqrt{z_0} - i\sqrt{l}}{\sqrt{z_0} + i\sqrt{l}} \right) \right\} - \frac{E c_i \theta_p^T}{9\pi} \left(\frac{1+\nu}{1-\nu} \right) \oint \text{Re} \frac{1}{\sqrt{z}(\sqrt{z} + \sqrt{z_0})} dy_0 \quad (\text{A7})$$

$$\nu^*(-l) = \frac{4(1-\nu^2)}{E} \left\{ K \sqrt{\frac{l}{2\pi}} - \frac{cS}{\pi} \right\} - \frac{c_i \theta_p^T (1+\nu)}{3\pi} \oint \text{Im} \log \left(\frac{\sqrt{z_0} + i\sqrt{l}}{\sqrt{z_0} - i\sqrt{l}} \right) dy_0 \quad (\text{A8})$$

and

$$K_m \sqrt{1-c} = K - cS \sqrt{\frac{8l}{\pi}} - \frac{E c_i \theta_p^T}{6(1-\nu)} \sqrt{\frac{2}{\pi}} \oint \text{Re} \frac{1}{\sqrt{z_0}} dy_0 \quad (\text{A9})$$

where Im denotes the imaginary part of a complex quantity. The governing equations are formulated by allowing z to approach $z(\theta)$ given by (12) while setting $\sigma_m = \sigma_m^c$, $K_{tip} = K_m \sqrt{1-c}$, and $\nu^*(-l) = \nu_f$. With the introduction of the parameters (4) and (7), along with the toughness ratio Λ given by the form of (1) and the nondimensional coordinates $Z = z/L(1-c)$, $l = l/L(1-c)$, we derive

$$1 = \Lambda \text{Re} \frac{1}{\sqrt{Z(\theta)}} - \frac{2\rho}{3\pi} \left\{ 2 \text{Re} \sqrt{\frac{l}{Z(\theta)}} + \text{Im} \log \left(\frac{1 - i\sqrt{l/Z(\theta)}}{1 + i\sqrt{l/Z(\theta)}} \right) \right\} - \frac{\omega}{9\pi} \int_{-\pi}^{\pi} \text{Re} \frac{1}{\sqrt{Z(\theta)}(\sqrt{Z(\theta)} + \sqrt{Z(\theta')})} dY(\theta') \quad |\theta| \leq \alpha \quad (\text{A10})$$

$$w_f = \Lambda \sqrt{l} - \frac{2\rho l}{3\pi} - \frac{\omega}{18\pi} \int_{-\pi}^{\pi} \text{Im} \log \left(\frac{1 + i\sqrt{l/Z(\theta)}}{1 - i\sqrt{l/Z(\theta)}} \right) dY(\theta) \quad (\text{A11})$$

and

$$l = \Lambda - \frac{4\rho \sqrt{l}}{3\pi} - \frac{\omega}{9\pi} \int_{-\pi}^{\pi} \text{Re} \frac{1}{\sqrt{Z(\theta)}} dY(\theta) \quad (\text{A12})$$

where

$$w_f = \frac{E v_f}{6L(1-c)(1-\nu)\sigma_m^c} \quad (\text{A13})$$

and

$$dY(\theta) = \frac{d}{d\theta} \left[\frac{R(\theta) \sin(\theta)}{L(1-c)} \right] \quad (\text{A14})$$

For $\alpha < |\theta| < \pi$, the boundary radius vector $R(\theta)$ describes the passive and residual segments with respect to the current crack-tip position. For specified levels of the particulate toughness ratio, the combination of (2), (5), (7) and (A13) provides the additional relation

$$(\Lambda_p^{ss})^2 = 1 + \frac{8\rho w_f}{3\pi} \quad (\text{A15})$$

that is used to fix the left side of (A11). The tangency condition between current active piece and the passive-segment extension is given by

$$\left. \frac{dY(\alpha)}{dX} \right|_{\text{ACTIVE}} = \left. \frac{dY}{dX} \right|_{\text{EXTENSION}} \quad (\text{A16})$$

The solution of (A10) - (A12) for $R(\theta)/L(1-c)$, l , Λ and α given specified values of Λ_p^{ss} , ω and ρ is described for the general crack increment Δa when $\Delta a > l_c$. The active boundary segment was expanded in the series

$$\frac{R(\theta)}{L(1-c)} = \sum_{n=0}^N a_n T_{2n}(\theta/\alpha) \quad 0 < |\theta| < \alpha \quad (\text{A17})$$

where the T 's are the Chebyshev polynomials of the first kind. The substitution of (A17) into (A10) - (A12) and (A16) resulted in a nonlinear integral equation and three constraints in the $N+4$

unknowns ($a_0, \dots, a_N, \alpha, \Lambda, \lambda$). A system of $N+4$ equations was generated by collocating (A10) at the $N+1$ points $\theta_j = j\alpha/N$ ($j = 0, \dots, N$) and asserting (A11), (A12), and (A16). Solution was accomplished by a Newton-Raphson iterative technique with convergence specified by a relative change of less than 0.1% in each of the unknowns between iterations. All integrals were evaluated by Gauss quadrature.

The initial stage of growth was handled by setting $\lambda = \Delta a/L(1-c)$ and relaxing the constraint (A11). When the right side of (A11) reached the critical value w_f , λ was allowed to vary and (A11) was turned on for subsequent growth increments. The restriction $\lambda \leq \delta a/L(1-c)$ was enforced to prevent ruptured particles from rehealing.

For the very first growth increment, the passive-residual juncture was located by augmenting the above system with the unknown angle β marking the end of the residual segment and the tangency constraint

$$\left. \frac{dY(\beta)}{dX} \right|_{\text{RESIDUAL}} = \left. \frac{dY}{dX} \right|_{\text{EXTENSION}} \quad (\text{A18})$$

Typically initial growth increments needed to be small but could be increased in size as growth proceeded. As a check on the accuracy, the calculations of select runs were repeated with the increment sizes halved. Only slight changes in results were observed.

APPENDIX B

EXTREMELY STRONG PARTICLES

We consider crack growth in the limit of "extremely strong" particles. In order to maintain a prescribed value of Λ_p^{ss} , we let $\rho \rightarrow \infty$, $\sqrt{l} = \sqrt{l/L(1-c)} \rightarrow 0$ in such a way that the product $\rho \sqrt{l}$ remains bounded. We derive the equations for the growing crack and then specialize the results to handle crack growth initiation. A portion of the boundary surrounding the stationary crack then serves as the residual segment for the transient crack.

The governing equations are derived by adapting (A10)-(A12). We proceed by noting that in the limit $\sqrt{l} \rightarrow 0$, the asymptotic form

$$\lim_{l \rightarrow 0} \text{Im} \log \left(\frac{1 - i\sqrt{l/Z(\theta)}}{1 + i\sqrt{l/Z(\theta)}} \right) = -2 \text{Re} \sqrt{\frac{l}{Z(\theta)}} \quad (\text{B1})$$

applies. After introducing (B1) into (A10)-(A12), the governing equations become

$$1 = \Lambda \text{Re} \frac{1}{\sqrt{Z(\theta)}} - \frac{\omega}{9\pi} \int_{-\pi}^{\pi} \text{Re} \frac{1}{\sqrt{Z(\theta)} (\sqrt{Z(\theta)} + \sqrt{Z(\theta')})} dY(\theta') \quad |\theta| \leq \alpha \quad (\text{B2})$$

$$\frac{3\pi}{8} ((\Lambda_p^{ss})^2 - 1) = \Lambda \rho \sqrt{l} - \frac{2(\rho \sqrt{l})^2}{3\pi} - \frac{\omega \rho \sqrt{l}}{9\pi} \int_{-\pi}^{\pi} \text{Re} \frac{1}{\sqrt{Z(\theta)}} dY(\theta) \quad (\text{B3})$$

and

$$1 = \Lambda - \frac{4\rho \sqrt{l}}{3\pi} - \frac{\omega}{9\pi} \int_{-\pi}^{\pi} \text{Re} \frac{1}{\sqrt{Z(\theta)}} dY(\theta) \quad (\text{B4})$$

where (A16) has been used to fix the left side of (B3) and $dY(\theta)$ is given by (A14). By eliminating the transformation contributions of (B3) and (B4), we derive the quadratic equation

$$(\rho \sqrt{l})^2 + \frac{3\pi}{2} \rho \sqrt{l} - \frac{9\pi^2}{16} ((\Lambda_p^{ss})^2 - 1) = 0 \quad (\text{B5})$$

for the product $\rho \sqrt{l}$. The positive root of (B5) yields the relation

$$\rho\sqrt{I} = \frac{3\pi}{4}(\Lambda_p^{ss} - 1) \quad (B6)$$

which remains constant for the stationary and growing crack. The introduction of (B6) into (B5) and the elimination of (B4) reduces the governing equations to (B3) and

$$\Lambda = \Lambda_p^{ss} + \frac{\omega}{9\pi} \int_{-\pi}^{\pi} \operatorname{Re} \frac{1}{\sqrt{Z(\theta)}} dY(\theta) \quad (B7)$$

For the stationary crack, (B7) was further simplified by noting that the integral is identically zero so that crack growth is initiated when $\Lambda = \Lambda_p^{ss}$. The surrounding boundary given by

$$z(\theta) = R(\theta)[\cos(\theta) + i \sin(\theta)] \quad 0 < |\theta| < \pi \quad (B8)$$

was found by setting $\Lambda = \Lambda_p^{ss}$ in (B2) and expanding $R(\theta)/L(1-c)$ in the series

$$\frac{R(\theta)}{L(1-c)} = \sum_{n=0}^N a_n \cos(n\theta) \quad (B9)$$

After substituting (B9) into (B2) and fixing Λ_p^{ss} and ω , a system of $N+1$ equations in the $N+1$ unknowns (a_0, \dots, a_N) was generated by collocating (B2) at the points $\theta_j = j\pi/N$ ($j = 0, \dots, N$). The Newton-Raphson procedure detailed in Appendix A was used to solve for the unknown coefficients. Typically, ten terms were sufficient to obtain a solution.

The solution of (B2) and (B7) for the growing crack paralleled the method of Appendix A. Equation (A17) was used to describe the active boundary segment and was substituted into (A16), (B2) and (B7) to yield a nonlinear integral equation and two constraints in the $N+3$ unknowns $(a_0, \dots, a_N, \alpha, \Lambda)$. A system of $N+3$ equations was then generated by collocating (B2) at the points $\theta_j = j\alpha/N$ ($j = 0, \dots, N$) and asserting (B7), and (A16). The Newton-Raphson procedure previously described was then to obtain a solution. The initial increment was handled by augmenting the system with the unknown β and equation (A18).

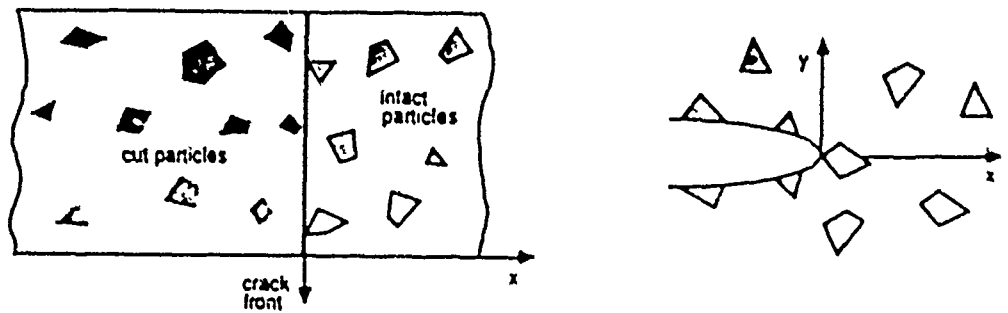


Fig. 1a Precut crack in the particulate reinforced material

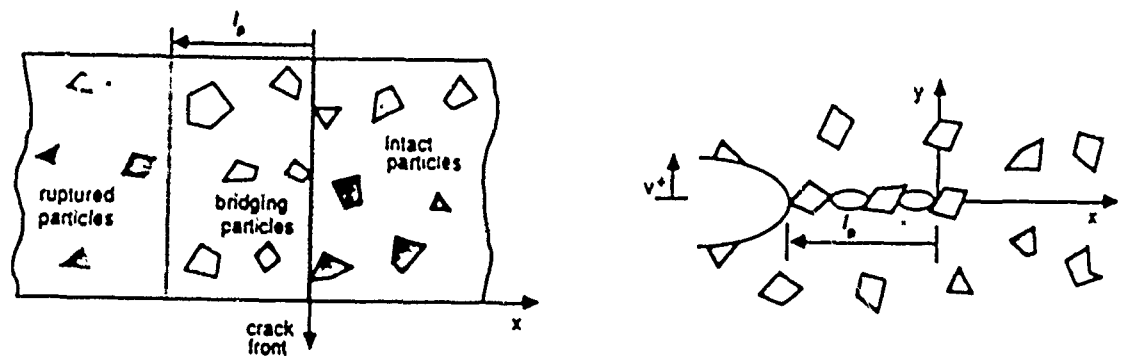


Fig. 1b Steady-state crack in the particulate reinforced material

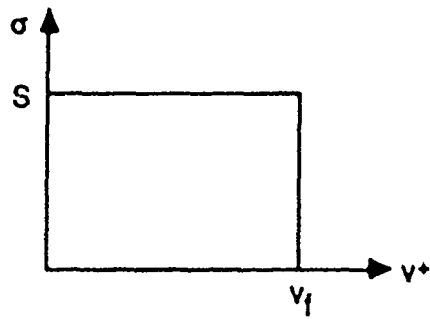


Fig 2 Bridging particle traction versus the *upper* crack-face displacement

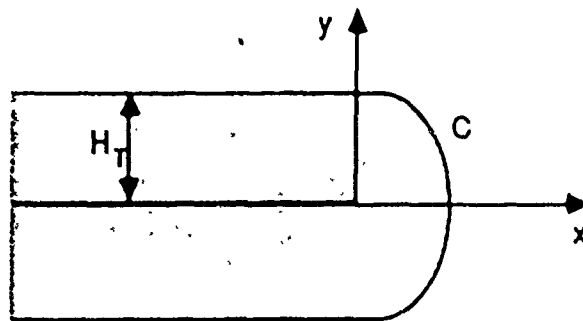


Fig 3 Steady-state crack growth in the PSZ reinforced material

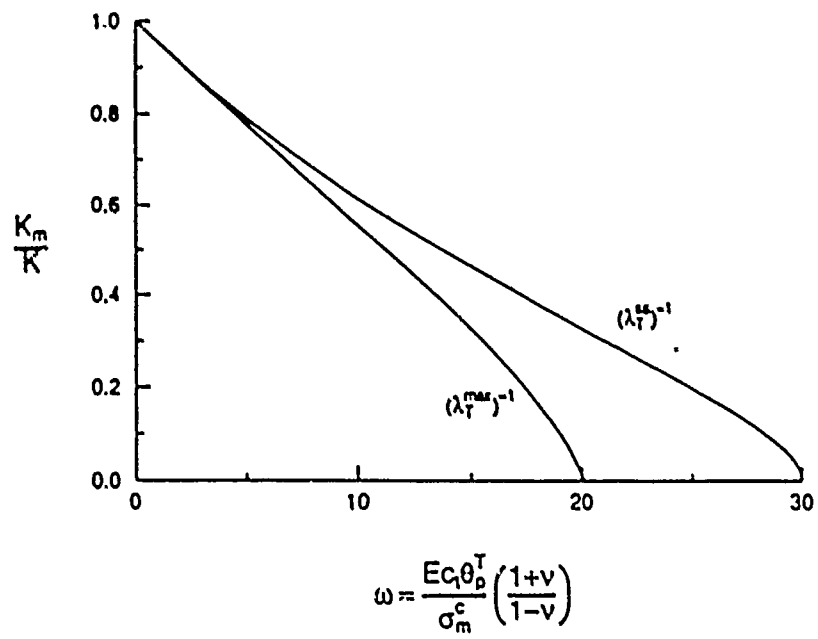


Fig. 3 Steady-state crack growth in the PSZ reinforced material

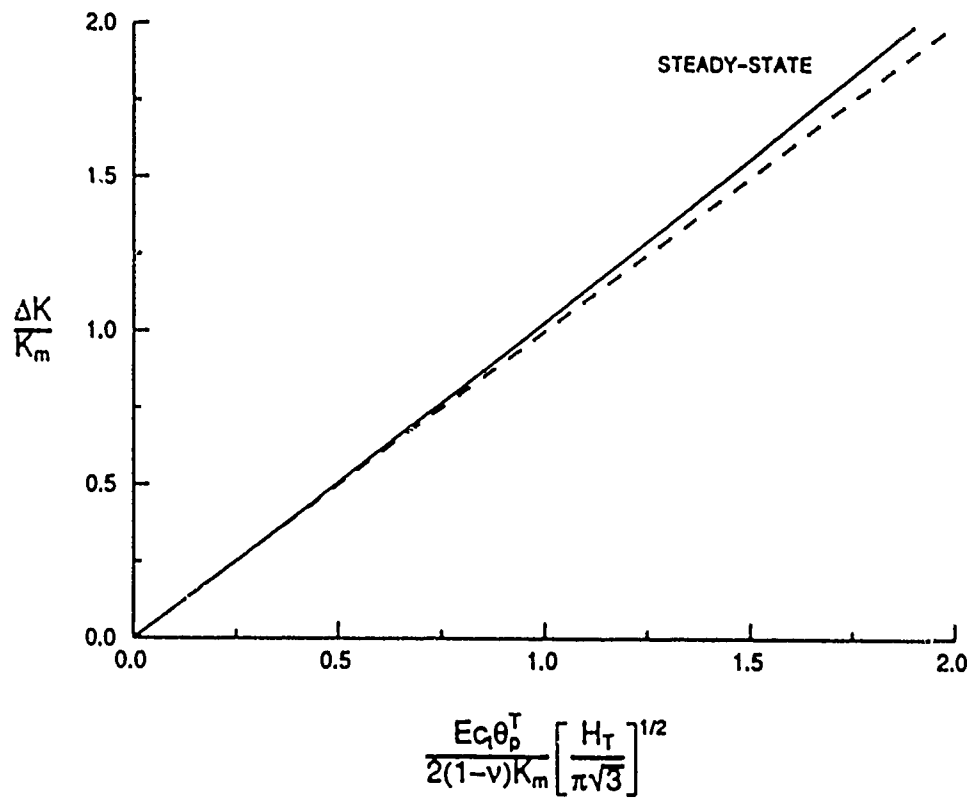


Fig 5 Fractional toughness increase versus the parameter given by the right side of (6).

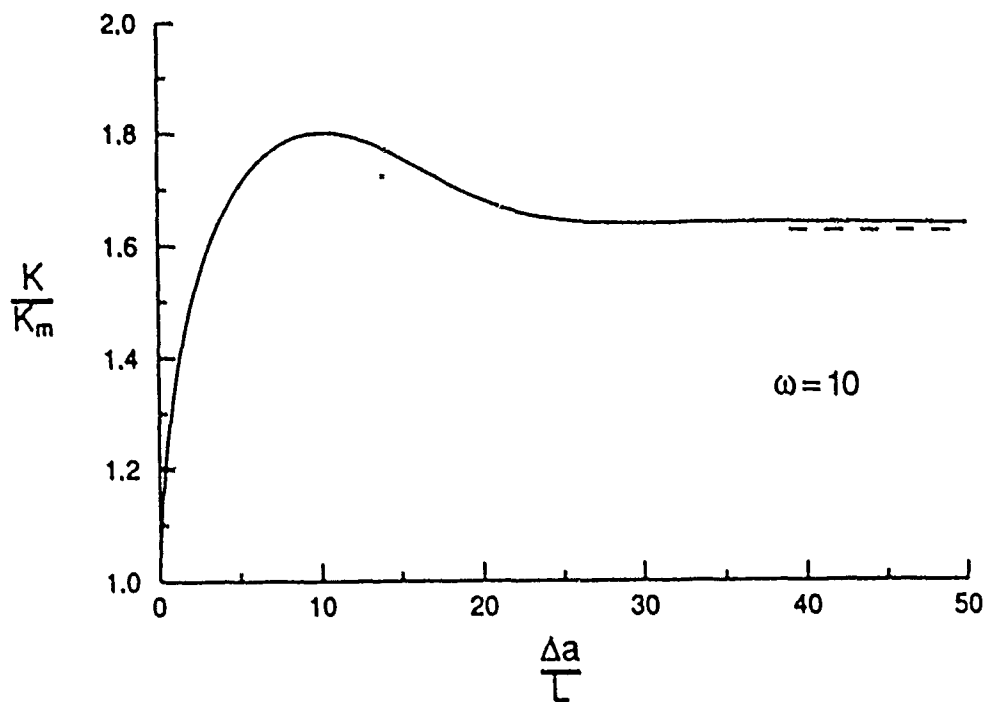


Fig. 6 Transient toughness ratio versus $\Delta a/L$; $\omega = 10$

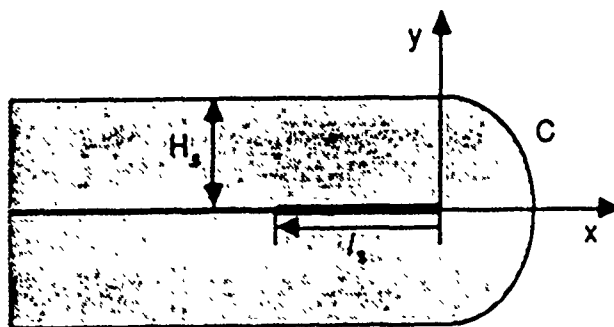


Fig. 7 Steady-state crack growth in the combined material.

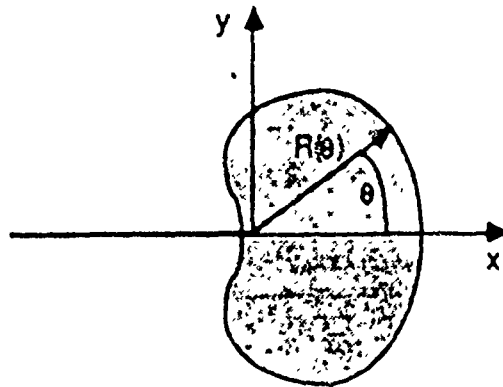


Fig 8 Stationary precut crack in the combined material.

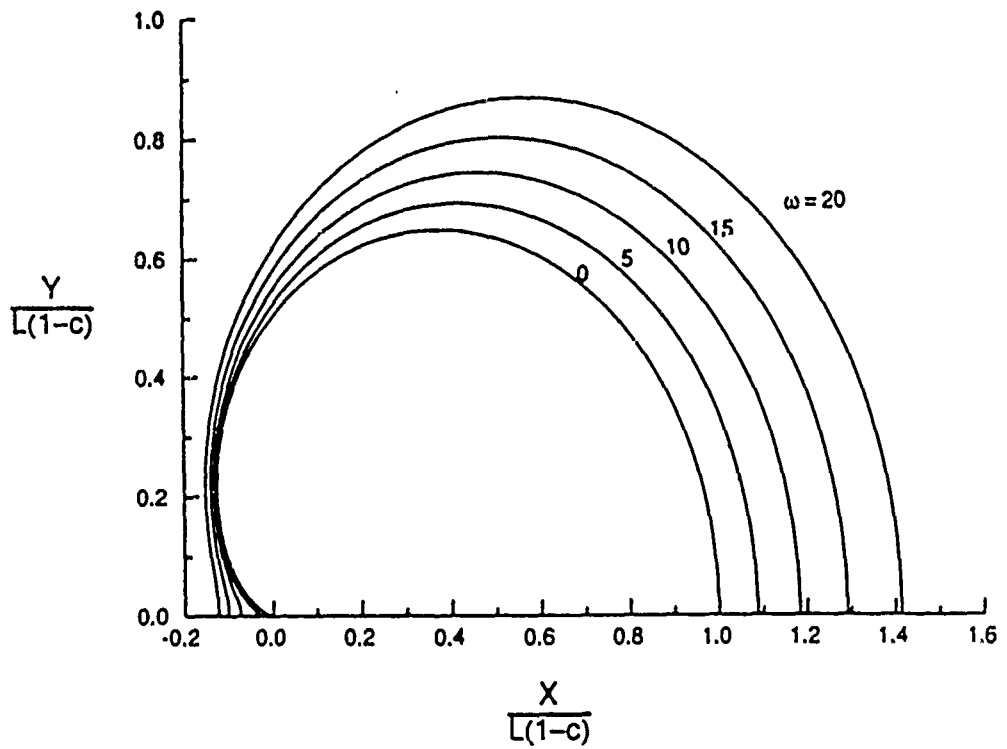


Fig 9 Normalized transformed regions just before crack growth initiation

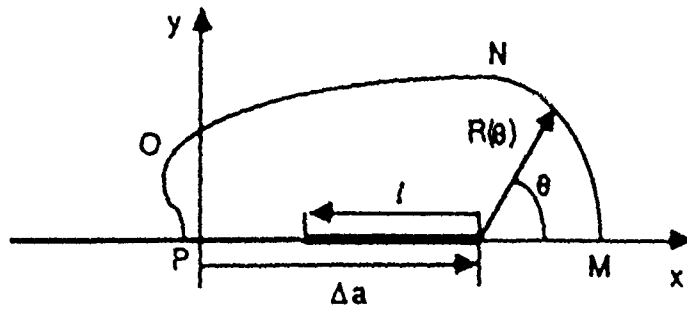


Fig. 10 Transient crack in the combined material

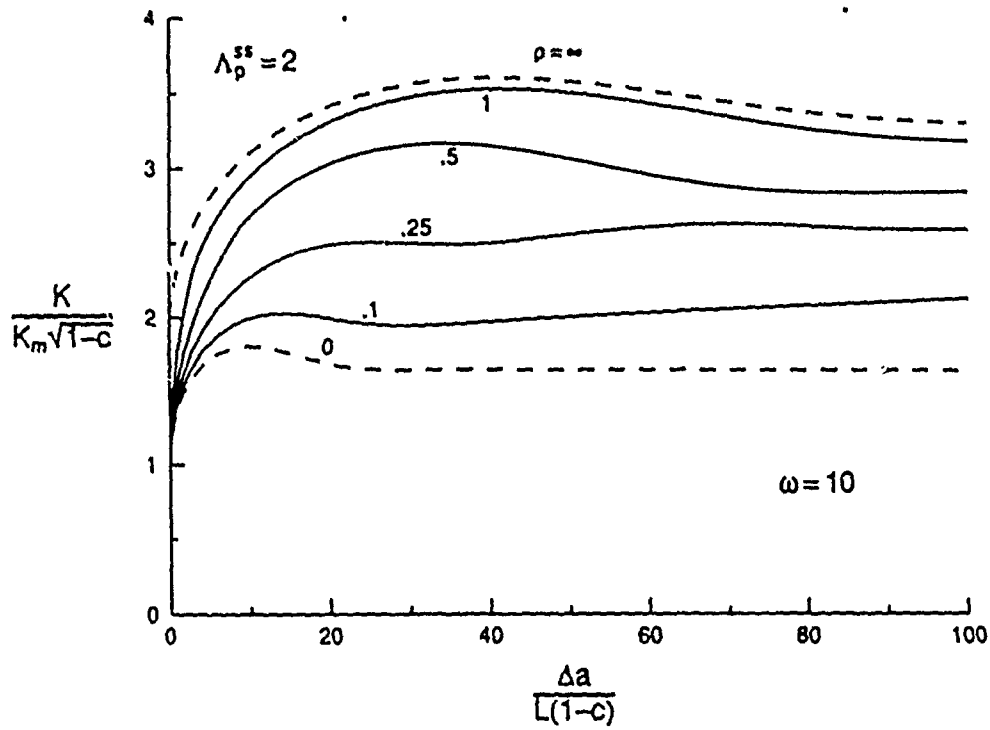


Fig. 11 Transient *modified* toughness ratio Λ versus $\Delta a/L(1-c)$ for various ρ ; $\omega = 10$, $\Lambda_p^{ss} = 2$

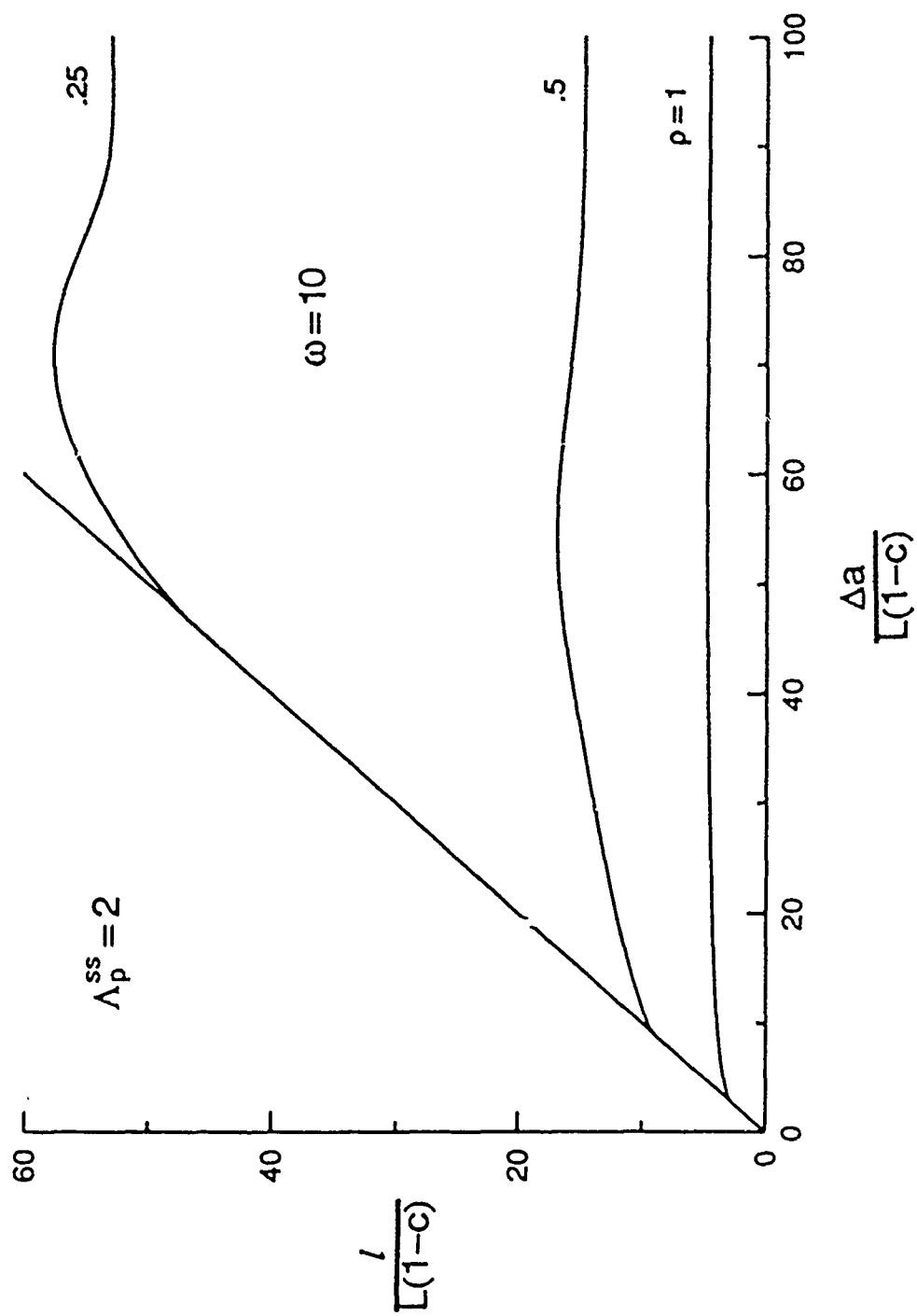


Fig. 12 Bridge length $l/L(1-c)$ versus $\Delta a/L(1-c)$ for various ρ ; $\omega = 10$, $\Lambda_p^{ss} = 2$

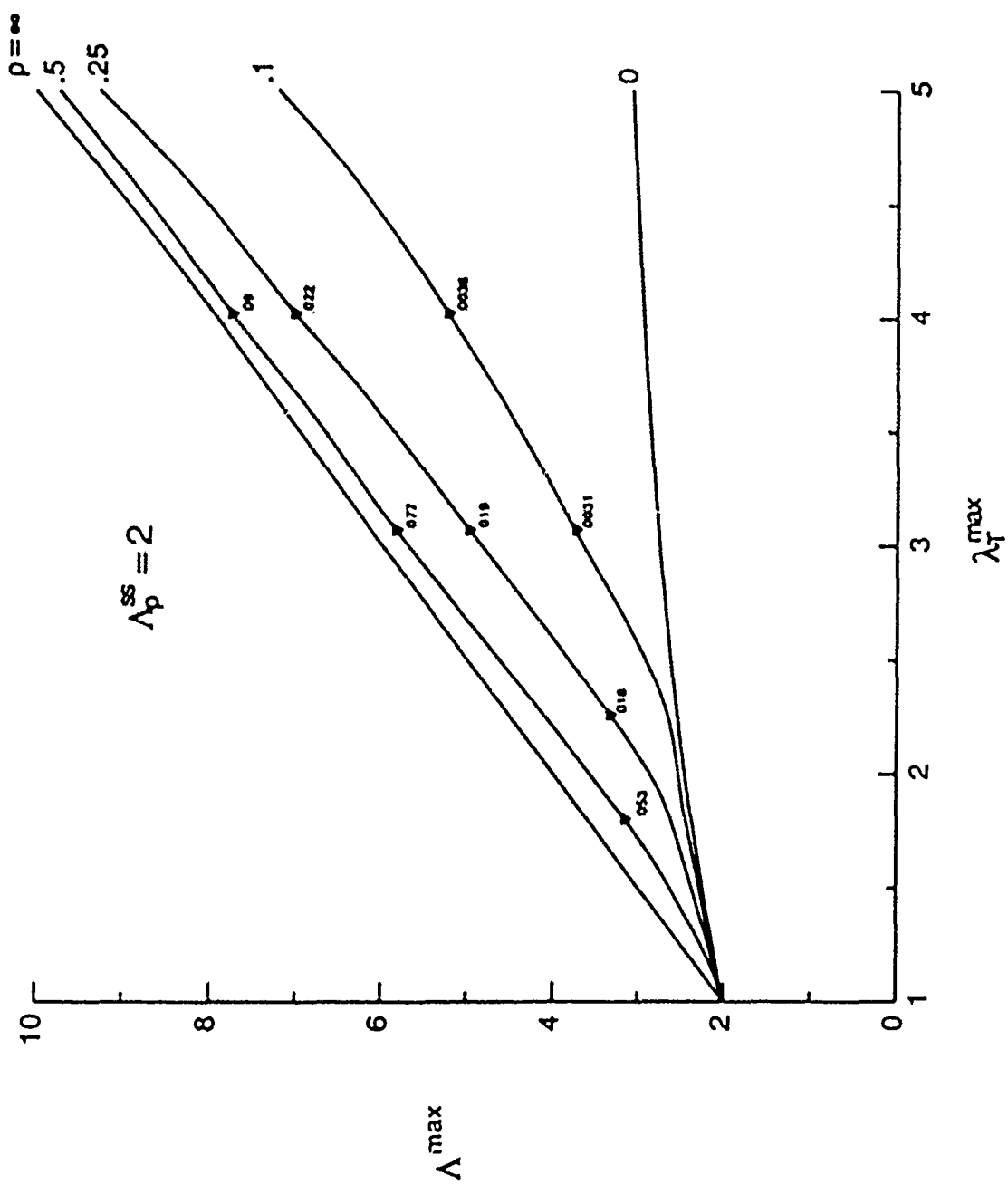


Fig. 13 Maximum overall toughness ratio Λ^{\max} versus λ_T^{\max} for various ρ ; $\Lambda_p^{ss} = 2$

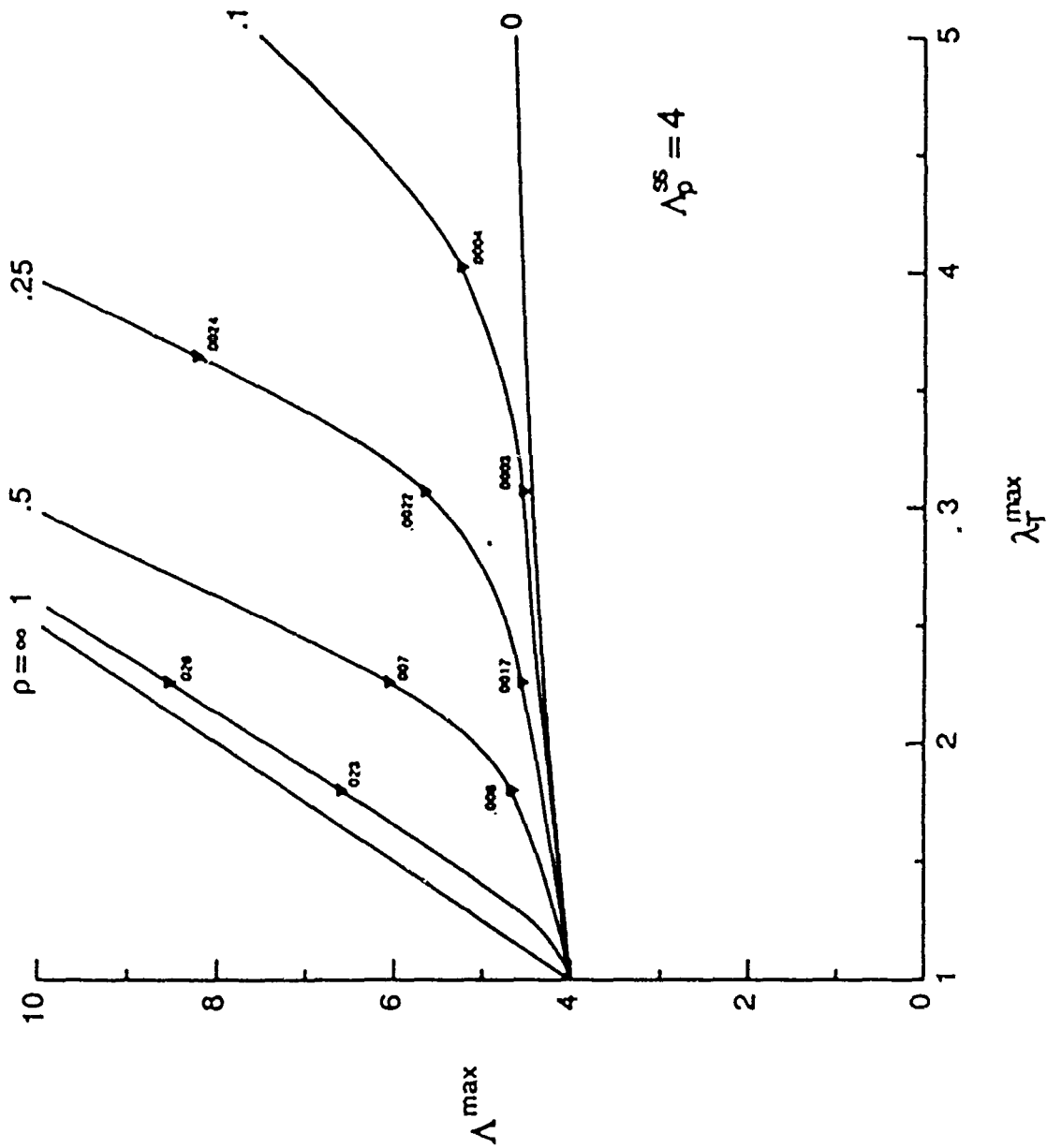


Fig. 14 Maximum overall toughness ratio Λ^{max} versus λ_T^{max} for various ρ ; $\Lambda_p^{ss} = 3$

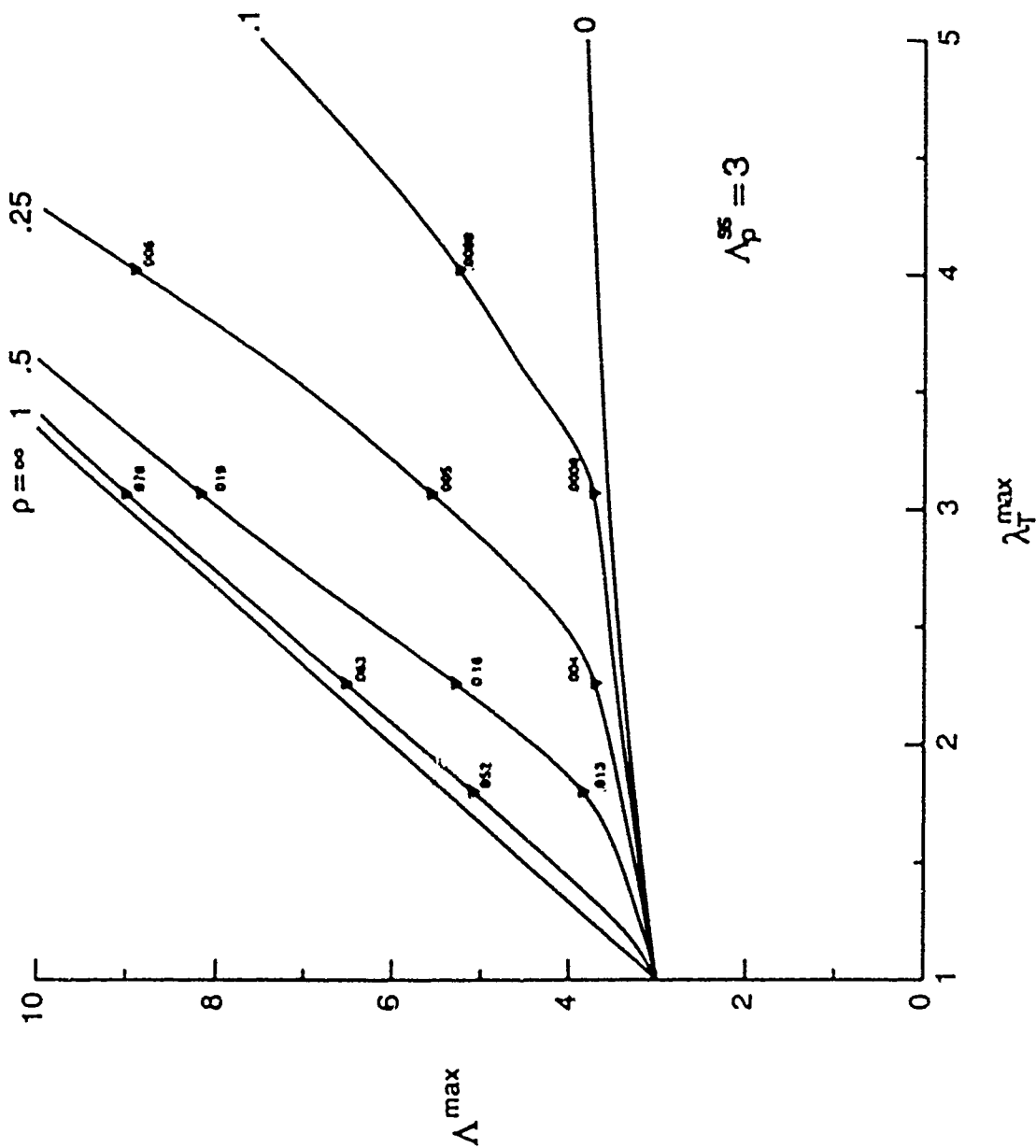


Fig. 15 Maximum overall toughness ratio Λ^{\max} versus λ_T^{\max} for various ρ ; $\Lambda_p^{ss} = 4$



MECH - 122

**A FIRST ORDER PERTURBATION ANALYSIS ON CRACK
TRAPPING BY ARRAYS OF OBSTACLES**

by

Huajian Gao

**Division of Applied Mechanics
Stanford University
Stanford, CA 94305**

and

James R. Rice

**Division of Applied Sciences
Harvard University
Cambridge, MA 02138**

November, 1988

Abstract

A first order perturbation analysis is presented for the configuration of an initially straight crack front which is trapped against forward advance by contact with an array of obstacles (i.e., regions of higher fracture toughness than their surroundings). The problem is important to the micromechanics of crack advance in brittle, locally heterogeneous solids. The formulation is based on a linear perturbation result for the stress intensity factor distribution along the front of a half-plane crack when the location of that front differs moderately from a straight line. The trapping solutions for a periodic array of blocking rectangular obstacles are given using an analogy to the plane stress Dugdale/BCS elastic-plastic crack model. The effects of the shape of the blocking obstacles on the limit load at which the crack breaks through the obstacles are discussed within the range of validity of the linear perturbation theory. We also formulate a numerical procedure using the FFT technique and adopting a "visco-plastic" crack growth model which, in an appropriate limit, simulates crack growth at a critical stress intensity factor. This is applied to show how a crack front begins to surround and penetrate into various arrays of round obstacles (with a toughness ratio of 2) as the applied load is gradually increased. The limitations of the first order analysis restrict its validity to

obstacles only slightly tougher than the surrounding elastic medium. Recently Fares (1988) analyzed the crack trapping problem by a Boundary Element Method (BEM) with results indicating that the first order linear analysis is acceptable when the fracture toughness of the obstacles differs by a moderate amount from that of their surroundings (e.g., the toughness ratio can be as large as 2 for circular obstacles spaced by 2 diameters). However, the first order theory is not only quantitatively inaccurate, but can make qualitatively wrong predictions when applied to very tough obstacles.

Introduction

The micromechanics of crack advance through brittle, locally heterogeneous materials is of fundamental interest. Generally speaking, the problems involved are of three dimensional (3D) character and often lack a theoretical treatment due to mathematical difficulties. Solution procedures based on finite element and boundary element analyses can be devised (see Fares, 1988) and they involve rather heavy numerical computations. This paper gives a simplified analysis, of limited validity, based on linear perturbation theory for the configuration of an initially straight crack front which is trapped against forward advance by contact with arrays of obstacles. The obstacles are modeled as having the same elastic properties as the rest of the elastic medium, but with slightly higher fracture toughness, so that the material considered here is treated as elastically homogeneous. We assume that the crack grows whenever the local stress intensity factor reaches the local fracture toughness at some point along the crack front. As the applied load increases, the crack front penetrates between and partially into the blocking obstacles and reaches new equilibrium states in which the intensity factor equals the fracture toughness value along the penetrating portions of the crack front. The distribution of stress intensity factors is calculated based on the linear perturbation result, developed earlier in Rice (1985a, 1988), for a half-plane tensile crack with a slightly curved front. The half-plane crack result models finite sized cracks assuming the lengths of the cracks are large compared to other parameters such as obstacle spacing along the crack front.

The trapping solutions for a periodic array of rectangular blocking obstacles are obtained using an analogy, following Rice (1988), to the two dimensional (2D) plane

stress Dugdale/BCS (for Bilby-Cottrell-Swinden) type of elastic-plastic crack model. The effects of the shape and size of the blocking obstacles on the limit load at which the crack breaks through the obstacles are discussed within the range of validity of the linear perturbation theory, although those concepts can be extended to a broader context.

The limitations of the linear perturbation theory are emphasized here, in that it is accurate only to the first order in crack front perturbations. This restricts the validity of the present first order analysis to obstacles only slightly tougher than their elastic surroundings, i.e. the fracture toughness ratio (of the obstacles to surroundings) must be near unity. It will be discussed in the text that when applied to very tough obstacles, the first order theory is not only quantitatively inaccurate, but can also be qualitatively wrong. Fares (1988) recently performed a BEM (Boundary Element Method) analysis on crack trapping configurations, based on a fundamental solution developed by Rice (1985b), for a prismatic opening dislocation source ahead of a half-plane crack with a straight front. By comparing the BEM results with those obtained by the first order theory, Fares showed that, for simple cosine wave form perturbations of the crack front, the first order theory gives quantitatively acceptable results for the stress intensity factor distribution (within 7% error) when the wave amplitude is within roughly 0.1 times the wavelength. For the case of periodically emplaced circular obstacles spaced by 2 diameters (figure 7a), which is analyzed both by Fares (1988) and the present authors, the first order theory can be applied to obstacles that are up to approximately twice as tough as the surrounding material.

Based on the linear perturbation theory, we formulate a numerical procedure for

crack penetration of a periodic array of blocking obstacles by using the Fast Fourier Transform (FFT) technique and adopting a "visco-plastic" crack growth model. In that model, once the stress intensity factor exceeds the local fracture toughness, the rate of the crack growth is linearly increased with the difference between them at the same location along the crack front. The crack then continues to grow until the new equilibrium state is reached. By controlling the rate term in such a visco-plastic formulation, the procedure may be made to simulate crack growth with the intensity factor equal, effectively, to the local fracture toughness. We give several examples of applications of the numerical model to show how a crack begins to surround and penetrate into arrays of round obstacles as the applied load is gradually increased.

Formulation of Crack Trapping and Penetration

Following Rice (1988) in formulating the crack trapping problem, we consider a half-plane crack in a linear, isotropic elastic solid. Assume that the crack lies on the plane $y = 0$ with a straight tip along $x = a_0$ parallel to the z axis (fig. 1a), and is subjected to fixed applied tensile loadings which induce mode I tensile stress intensity factor

$$K = K^0[z; a_0] \quad (1)$$

along the crack front. The following linear perturbation result was developed by Rice (1985a) to calculate the distribution of stress intensity factor K along a slightly perturbed crack front, along the arc $x = a(z)$ in the plane $y = 0$ (figure 1b)

$$K(z) = K^0[z; a(z)] + (1/2\pi)PV \int_{-\infty}^{+\infty} \frac{K^0[z'; a(z)][a(z') - a(z)]}{(z' - z)^2} dz' \quad (2)$$

to the first order accuracy in the deviation of $a(z')$ from constancy; PV denotes principal value. In writing the above equation for any chosen z , we have chosen a reference straight crack with tip along $x = a(z)$.

We will use the above half-plane crack results to model the trapping problems of a finite sized crack, a_0 now being the crack length in the x dimension (e.g., half of the length of a tunnel crack). We assume that the real intensity factor distribution along the reference straight crack front varies negligibly with z and also that the representative perturbation wavelength of the actual crack front is much smaller than the overall crack length. Thus the above half-plane crack result can be used with K^0 regarded as uniform along the crack front and independent of the crack length over the small perturbations to be considered. Note that the representative wavelength of the perturbation of the crack front must be consistent with that of the variation of the non-uniform fracture toughness along the crack front. Using an integration by part in eq. (2), one can show that

$$\frac{K(z) - K^0}{K^0} = (1/2\pi) PV \int_{-\infty}^{+\infty} \frac{da(z')/dz'}{z' - z} dz' \quad (3)$$

Let K_c and \hat{K}_c denote the fracture toughness, or the critical K 's, for the obstacle-free material and the obstacles respectively. Now imagine a crack front that is trapped by obstacles of some given distribution. The crack penetrates between and partially into the obstacles so that we may assume that $K = K_c$ on the portions of the front between the obstacles and $K = \hat{K}_c$ on the portions where the obstacles are being partially penetrated. However, the penetration depth $a(z)$ is unknown in those penetrated zones. Yet $a(z)$ is known but $K(z)$ is unknown where the crack front just contacts the obstacles.

One then needs to solve the singular integral equation (3) for $a(z)$ and $K(z)$ with the values of either $a(z)$ or $K(z)$ given along complementary portions of the z axis. The special solution to eq. (3) with $K(z) = K^0 = K_c$ and $a(z) = a_0 = \text{const}$, corresponds to the initial state when crack penetration is imminent.

Clearly, eq. (3) is strictly valid only if $|da(z)/dz| \ll 1$ over the whole crack front ($-\infty < z < \infty$). This is equivalent to $[K(z) - K^0]/K^0 \ll 1$. Crack penetration into the obstacles starts when the applied K^0 is increased from K_c . Hence during a penetration process one always have $[K(z) - K^0]/K^0 \leq [\dot{K}_c - K_c]/K_c$ so that the condition $|da(z)/dz| \ll 1$ can be guaranteed by having $[\dot{K}_c - K_c]/K_c \ll 1$. In practical terms, it appears that our results are still approximately valid when $[\dot{K}_c - K_c]/K_c$ is near unity.

Analogy to Elastic-Plastic Plane Stress Crack Model

Let us consider the two dimensional plane stress problem in the y, z plane, with an array of cracks along the z axis on $y = 0$ which can be represented by a continuous distribution of prismatic opening (edge) dislocations. A remotely applied uniform stress $\sigma_{yy} = \sigma^0$ generates an opening gap $\delta = \delta(z)$ (i.e., net y direction displacement) between $y = 0^+$ and $y = 0^-$. The stress σ_{yy} along the z axis, denoted by $\sigma(z)$, is the sum of σ^0 and the effect of a continuous distribution of edge dislocations representing the opening gap between the crack faces. Hence we write the following,

$$\frac{2[\sigma(z) - \sigma^0]}{E} = \frac{1}{2\pi} PV \int_{-\infty}^{+\infty} \frac{d\delta(z')/dz'}{z' - z} dz' \quad (4)$$

Equation (4) may be rearranged to coincide exactly with (3) provided that one makes the identifications (Rice, 1988)

$$\begin{aligned} 2 [\sigma(z) - \sigma^0]/E &\rightarrow [K(z) - K^0]/K^0; \\ \delta(z) &\rightarrow a(z) \end{aligned} \quad (5)$$

Thus the 3D linearized perturbation problem of a crack trapped by, penetrating between and partially into, an array of blocking obstacles has the following 2D plane stress analog: The z axis is divided into the following two parts, L_{trap} and L_{pen} , analogous to the contact and penetration regions along the crack front (see fig. 2b). Along L_{trap} the plane-stress opening gap is prescribed, i.e., as a given distribution of prismatic opening dislocation corresponding to $\delta(z) = a(z)$. Along the portions of L_{pen} between the obstacles, conditions correspond to an array of plane stress cracks with the stress sustained along the crack faces prescribed as $\sigma(z) = \sigma^0 + E(K_c - K^0)/2K^0$. The regions denoted as R in fig. 2b, as a part of L_{pen} , is analogous to a Dugdale/BCS line plastic zone in plane stress, along which $\sigma(z) = \sigma^0 + E(K_c - K^0)/2K^0$. The region L_{trap} reduces, and R increases, with increase of the "applied" stress intensity K^0 , as the crack front gradually penetrates into the obstacles. The size of the zones R must be determined as part of the solution by imposing the condition that $K(z)$ be finite (equal to K_c) as the border between L_{trap} and R is approached from within L_{trap} . A special case when $K_c \rightarrow \infty$, corresponding to impenetrable obstacles, has the analogy of purely elastic plane stress cracks without plastic regions.

The plastic flow in the above analogous 2D plane stress problem, of an array of cracks in an elastic-plastic sheet, is confined to line plastic zones along the z axis. Thus $\sigma(z) = \hat{\sigma}_c (> \sigma^0)$ along the plastic zones R , where the Dugdale/BCS tensile yield strength $\hat{\sigma}_c$ is

identified as $\sigma^0 + E(\dot{K}_c - K^0)/2K^0$. The portions of L_{pen} complementary to R correspond to loaded crack faces on which $\sigma(z) = \sigma_c (< \sigma^0)$ ($\sigma_c = \sigma^0 + E(K_c - K^0)/2K^0$).

Hence the solutions for the 3D problem of crack trapping by obstacles can be simply extracted from the known 2D Dugdale/BCS plane stress crack model solutions, or from new solutions that can be generated by solving the integral equation or, perhaps, by solving an alternative numerical model of the 2D plane stress problem.

Gradual Penetration of a Periodic Array of Obstacles

Figure 2 shows a periodic array of obstacles with center-to-center spacing of $2L$ and a gap $2H$ between them. The obstacles have flat edges, parallel to the z axis, and are aligned so that the crack front encounters them simultaneously. Thus they could represent aligned rectangular shaped obstacles of sufficiently large (see below) extent d in the z direction. As remarked, the trapping solution may be developed directly from the analogy to the 2D solution of plane stress Dugdale/BCS model. The Dugdale/BCS model for a periodic crack array has been solved by Bilby and Swinden (1965) and Smith (1966). In particular, the parameters R and a_{min} , characterizing spread of the crack into the obstacles as defined in fig. 2b, are given by:

$$R = H \{ (1/\epsilon) \arcsin[\sin \epsilon / \sin \mu] - 1 \}$$

$$a_{min} = \frac{2H \omega \sin \alpha}{\pi \epsilon} \int_{\mu}^{\pi/2} \frac{\cos \phi}{(1 - \sin^2 \alpha \sin^2 \phi)^{1/2}} \ln \left[\frac{\sin(\phi + \mu)}{\sin(\phi - \mu)} \right] d\phi \quad (6)$$

where

$$\mu = \pi(\dot{K}_c - K^0)/2(\dot{K}_c - K_c), \quad \omega = (\dot{K}_c - K_c)/K^0, \\ \epsilon = \pi H/2L, \quad \alpha = \pi(H + R)/2L \quad (7)$$

The above results are meaningful for the range

$$K_c \leq K^0 \leq K_c + f(\dot{K}_c - K_c) \quad (8)$$

where $f = (L - H)/L$ is the line fraction of contact zones. The crack front is predicted, within the linear perturbation formulation, to completely penetrate the obstacles (i.e., L_{trap} shrinks to zero in fig. 2b) at the upper limit. Of course, the linear perturbation procedures themselves are rigorously valid only for K^0 slightly greater than the lower limit K_c . Note that $\mu = \pi/2$ corresponds to the lower limit and $\mu = \epsilon$ to the upper limit.

The upper limit in (8) gives the limit load at which the crack front just breaks through the array of obstacles,

$$K^0 = K_c + f(\dot{K}_c - K_c) \quad (9)$$

This predicts the maximum load that the crack-obstacle system can sustain within the range of validity of the linear perturbation theory.

However, the limit load K^0 can be calculated exactly (Rice, 1988) if $K(z)$ is known everywhere along the crack front when the final failure of the crack-obstacle system occurs. This would be true if there is no instability prior to final breakthrough, so that the local $K(z)$ is everywhere equal to the local toughness. Since it is assumed here that

the straight-crack-front value K^0 of eq. (1) can be regarded as constant, it is necessary that

$$(K^0)^2 = \langle [K(z)]^2 \rangle \quad (10)$$

be satisfied for any crack front configuration $a(z)$ in fig. 1b. Here the brackets denote an average along the entire z axis. Equation (10) can be proved by considering the energy release in a unit translation of the crack front in the x direction without any change of the crack front shape. If no instabilities occurs, $K(z)$ is known everywhere at final breakthrough, i.e., $K(z) = K_c$ on regions between the obstacles and $K(z) = \tilde{K}_c$ within the obstacles. Hence eq. (10) gives the exact value of the limit load K^0 as

$$K^0 = \{K_c^2 + f(\tilde{K}_c^2 - K_c^2)\}^{1/2} \quad (11)$$

This agrees with eq. (9) to first order in $(\tilde{K}_c - K_c)$ and a table comparing the results over a range of parameters is given by Rice (1988).

However, a given crack-obstacle system can also fail by mechanisms that involve instabilities, in which cases eq. (11) does not apply. The BEM analysis of Fares (1986) showed that for a crack trapped by sufficiently tough obstacles, there is a maximum local $K(z) = W K_c$ which can be generated at the crack front prior to final instability. When the obstacle toughness \tilde{K}_c is more than $W K_c$, the penetrating crack front segments coalesce with one another and the crack front bypasses the still-intact obstacles. This mechanism of the final instability is completely different from anything explainable within the first order theory. In fact, the first order theory predicts that failure always occurs by having the crack front break through the obstacles, and the K^0 at breakthrough increases linearly with the obstacle toughness. The first order theory also

implies that an arbitrarily large local $K(z)$ can be developed where a crack is blocked by a sufficiently tough array of obstacles. Therefore, the first order theory can be even qualitatively, as well as quantitatively, wrong when applied to tough obstacles.

Hence W is defined as a critical parameter which sets the upper limit of the obstacle toughness value $\hat{K}_c = W K_c$ for having a breakthrough mechanism as predicted by the first order theory. In other words W sets the boundary between the breakthrough mechanism in which case the first order theory is at least qualitatively correct and the bypass mechanism (coalescence of penetrating crack front segments beyond an unbroken particle) which is completely beyond the scope of the first order theory. This W can only be determined through more accurate formulations such as the BEM analysis of Fares (1988). It can be justified that W depends only on the shape and size of the blocking obstacles and it increases with the obstacle size, d , in the x -direction. As a limiting case, W approaches infinity when $d \rightarrow \infty$, corresponding to straight-edge obstacles with semi-infinite extent in the x direction. The toughness ratio \hat{K}_c/K_c should be significantly smaller than W to get a quantitatively acceptable results from linear analysis.

Even if the breakthrough mechanism is guaranteed by having $\hat{K}_c/K_c < W$, there exists another type of instability which can lead to final breakthrough before the state of full penetration of the obstacle is attained. In these cases $K(z)$ is not known everywhere at breakthrough (unknown along the unpenetrated portion of the obstacle). In the next section we explore the critical parameters associated with this mechanism of instability within the first order theory. It will be shown that for rectangular obstacles as shown in figure 2, a critical length d^L can be defined so that the penetration process is stable

if $d > d^L$ and unstable if $d < d^L$.

Therefore, the failure processes of a crack trapped by blocking obstacles fall into three categories. Taking rectangular obstacles as a demonstration, there are two critical parameters W, d^L . If the toughness ratio $\dot{K}_c/K_c > W$, the crack will bypass the obstacles without breaking them (category 1). When $\dot{K}_c/K_c < W$, the crack will break the obstacles by penetration. The penetration process will be unstable (category 2) if $d < d^L$ and stable (category 3) if $d > d^L$. The first category involves the instability mechanism of crack bypassing the unbroken obstacles, which is completely beyond the scope of the first order theory. We will restrict our attention to the latter two categories (2 and 3) of breakthrough mechanism. For convenience, we will refer to processes in the second category that involve instability prior to full penetration of obstacles as "irregular" processes while others in the third category for which $K(z)$ is known everywhere at breakthrough as "regular" processes.

For regular processes all instabilities can be excluded so that the obstacles are gradually penetrated by the crack until final breakthrough. The argument leading to equation (11) for rectangular obstacles can be readily extended to arbitrarily shaped, but symmetric (about the x -direction), blocking obstacles in a periodic array. Let us define $f(x_0)$ as the line fraction of the obstacles on a straight line located at $x = x_0$ parallel to the original crack front. (For rectangular obstacles of fig. 2, the line fraction $f(x_0)$ is a constant which takes the value of $(L - H)/L$). Equation (11) then gives the exact value of the limit load K^0 , provided that f now represents the maximum line fraction, i.e., $f = \max_{x_0} f(x_0)$. This also gives an upper bound for the limit failure load in case of

instabilities. For general, possibly asymmetric, blocking obstacles, the limit load for regular processes can still be calculated from (11), but the line fraction f now depends on the crack front profile at final breakthrough. Again considering the energy release in a unit rigid translation of the crack front in the x -direction at the final breakthrough, one easily concludes that $f = S/2L$ where S represents the projection in the x -direction of all the crack front segments within the obstacles in one period. This is even true for multi-row systems of periodic arrays of obstacles (see later examples), in which case the bowing-out crack front will encounter obstacles in different rows.

Assuming $[\dot{K}_c - K_c]/K_c$ is sufficiently small, both regular and irregular crack penetration processes can be studied by first order perturbation theory. In particular, the instability in irregular processes deserves special attention. We next report a quantitative study on the role of the shape and size of the obstacles in crack penetration processes and discuss the limit load for irregular processes. The case discussed previously, for crack trapping by a periodic array of rectangular obstacles with large x -dimension shown in fig. 2, is important in the following discussions. For convenience we will refer to it as the "model" case.

Instability in Crack Penetration of an Array of Obstacles: Irregular Processes

The problem is addressed on the assumption that $[\dot{K}_c - K_c]/K_c$ is within a range suitable for linear perturbation theory. Referring to the model case shown in fig. 2, we denote the value of a_{\min} at the complete penetration of the obstacles (i.e., $R = L - H$) by a^L , and define the area between the line $x = a^L$ and the crack front within an obstacle

by A^L (fig. 3a). Taking the upper limit $\mu = \epsilon = (1 - f)\pi/2$ in eqs. (6), one obtains

$$\frac{a^L}{L} = \frac{4}{\pi^2} \frac{\dot{K}_c - K_c}{K_c + f(\dot{K}_c - K_c)} \int_0^{f\pi/2} \ln \left[\frac{\sin(f\pi/2 + \phi)}{\sin(f\pi/2 - \phi)} \right] d\phi \quad (12)$$

Hence a^L/L is expressed as a function of the line fraction f of the obstacles and the toughness ratio \dot{K}_c/K_c . Now imagine an array of arbitrarily shaped, but symmetric (about the x -direction), obstacles spaced by $2L$ with a minimum gap of $2H$ in the z direction. We choose a model case with parameters H, L for reference. If an obstacle can fully contain the area A^L associated with the chosen reference (fig. 3b), then at breakthrough the crack is undergoing exactly the same state as the reference model case. Therefore the penetration process is a regular one so that eq. (9) applies to give the limit load based on the maximum line fraction f of the obstacles in the z direction. For example, it can be proved that $a^L < L - H$ (the proof can be achieved by choosing a variable $u = (L - H)/L$, then forming a function $g(u) = a^L/L - u$ and proving that $g(u)$ is monotonously decreasing from zero over the interval $[0, 1]$). Therefore the crack penetration of an array of round obstacles with radius equal to $L - H$ is a regular process (figure 3d), in which case the limit load is predicted by eq. (9) for maximum line fraction $f = (L - H)/L$.

However, if the shape of the obstacle can not fully envelop the area A^L of the reference state, but rather is contained (below its maximum width line) fully within A^L (figure 3c), the full penetration of the obstacle will not be possible at the moment of final breakthrough. That is, an instability will lead to breakthrough prior to the full penetration and the penetration is irregular. Therefore the area A^L is the critical parameter that distinguishes between the regular and irregular processes. The actual

breakthrough loads for irregular processes are smaller than those predicted by eq. (9) using the maximum line fraction f .

Usually the calculation of limit loads for irregular processes requires numerical search for the occurrence of instability. However, there are some cases for which direct analysis suffices. For example, consider a periodic array of obstacles with shape shown in fig. 4a. Apparently the penetration would be a regular one if the height d of the base portion of the obstacles is greater than a^L , i.e., $d > a^L$. When $d < a^L$, the process is an irregular one if the angle $\psi < \pi/2$. Let us look at a moment at which the crack has penetrated into the obstacle an amount characterized by the parameter p shown in fig. 4a. It can be argued that the shown state, if in equilibrium with the imposed load, is the same as another model case with parameter H' defined by $H' = H + p$. It follows from eqs. (6) that

$$d + p \tan \psi = \frac{4L}{\pi^2} \omega \sin \epsilon \int_{\mu}^{\pi/2} \frac{\cos \phi}{(\sin^2 \mu - \sin^2 \epsilon \sin^2 \phi)^{1/2}} \ln \left[\frac{\sin(\phi + \mu)}{\sin(\phi - \mu)} \right] d\phi \quad (13)$$

where $\epsilon = \pi H'/2L$ and μ, ω are as defined in eqs. (7). If we take the derivative of both sides of eq. (13) with respect to p keeping other parameters constant, we can solve for the quantity dK^0/dp for any p . If $dK^0/dp > 0$ the current state is a stable one, in the sense that the load K^0 needs to be increased to increase the penetration p . Instability occurs when $dK^0/dp \leq 0$ with the critical point reached when the equal sign is taken. An important case is $dK^0/dp|_{p=0} = 0$, which determine a critical angle ψ_c below which the instability occurs instantly when $p = 0$. After some algebraic manipulations, it can

be shown that

$$\tan \psi_c = \frac{2}{\pi} \omega \int_{\mu}^{\pi/2} \frac{\cos \epsilon \cos \phi \sin^2 \mu}{(\sin^2 \mu - \sin^2 \epsilon \sin^2 \phi)^{3/2}} \ln \left[\frac{\sin(\phi + \mu)}{\sin(\phi - \mu)} \right] d\phi. \quad (14)$$

where $\epsilon = \pi H/2L$ at $p = 0$ and ω, μ are determined further by solving (13) for K_0 using $p = 0$. That is

$$d = \frac{4L}{\pi^2} \omega \sin \epsilon \int_{\mu}^{\pi/2} \frac{\cos \phi}{(\sin^2 \mu - \sin^2 \epsilon \sin^2 \phi)^{1/2}} \ln \left[\frac{\sin(\phi + \mu)}{\sin(\phi - \mu)} \right] d\phi \quad (15)$$

When the geometrical angle ψ is less than ψ_c , the limit load K^0 at which the crack breaks the obstacles is then determined directly by eq. (15). We observe that $\psi_c = \pi/2$ for $\mu = \epsilon$, corresponding to the upper limit in (8), so that at that limit the crack breaks through the obstacles with any ψ , up to $\psi = 90^\circ$ (corresponding to the model case). As $d \rightarrow 0$, as for a very thin obstacle, $\mu \rightarrow \pi/2$ and $\psi_c \rightarrow 0$. Usually $0 < \psi_c < \pi/2$. The value of ψ_c is plotted in figure 5 against d/a^L , the height of the obstacle non-dimensionalized by a^L , for $H/L = 0.5$ and $K_c/K_e = 2$. It is shown that ψ_c is nearly linear with d/a^L until $d/a^L \simeq 0.9$, after which a sharp increase toward 90° is then observed. A rectangular obstacle with $\psi = 0$ and $d < a^L$ can then be always categorized as $\psi < \psi_c$ (fig. 4b), and the limit load at which a crack breaks through an array of rectangular shaped obstacles is determined by the eq. (15) when $d < a^L$. Hence one can define a critical length $d^L (= a^L)$ for rectangular obstacles so that the crack penetration process is stable if $d > d^L$ and unstable if $d < d^L$.

Finally if $\psi > \psi_c$, instability will occur at some $p > 0$ and a similar critical location can be determined by the condition $dK^0/dp = 0$. We do not present the details of the analysis.

Numerical Formulation of Crack Penetration of Periodic Arrays of Obstacles

Within the range of validity of the linear perturbation theory, we have discussed the problem of crack trapping by arrays of obstacles based on an analogy to the 2D Dugdale/BCS plane stress crack model. The solutions are given for characteristic quantities such as the penetration depths and the limiting K value at which the final breakthrough occurs. In the following we formulate the trapping problem by an alternative, yet more powerful numerical procedure. The results are compared to those previously derived as well as applied to other cases for which analytical solutions are not known.

General Numerical Formulation

For the general formulation consider the fracture toughness varies in space so that on the crack plane, $K_c = K_c(x, z)$. The crack will grow at the positions along the crack front where the stress intensity factor exceeds the fracture toughness K_c . We adopt the following "visco-plastic" model for the crack growth

$$\frac{\partial a(z, t)}{\partial t} = \begin{cases} \rho [K(z, t) - K_c(a(z, t), z)] & K > K_c \\ 0 & \text{otherwise} \end{cases} \quad (16)$$

where t is a time parameter in this model, ρ is a coefficient that represents the "viscosity" of the system. By making ρ sufficiently large, or else (as we do) by waiting a sufficiently long time for a new equilibrium configuration of the crack front to be approached after each small increase of load K^0 in a "staircase" load vs. time history, we can make (stable) growth occur arbitrarily close to the condition that $K = K_c$ during growth.

Note that in eq. (16) $K = K(z, t)$ is related to $a(z, t)$ by eq. (3) at a time t . In

principle one can solve the coupled equations (3) and (16) for $K(z, t)$ and $a(z, t)$. Apparently $a(z) = a(z, \infty)$, after step increase to the K^0 of interest, is the final equilibrium crack profile, corresponding to the sort of solution for crack penetration discussed in the previous sections. While it is often impossible to solve the coupled equations analytically, numerical procedures can be designed by discretizing the equation (16) into small time steps, and for each step updating $a(z, t)$ and $K(z, t)$ according to (3). The time step Δt for any given value of ρ can be adjusted to speed up the convergence of the solution. We will apply this procedure to the periodic array of blocking obstacles in the following.

Tunnel Cracks With Periodic Arrays of Obstacles

Consider a tunnel crack lying in a homogeneous, isotropic elastic solid, having length $2a$ along the x axis, and subjected to a remote tensile stress σ that induces

$$K^0 = K^0[a] = \sigma\sqrt{\pi a} \quad (17)$$

along the crack front. The crack advance is blocked by an array of obstacles. Assuming the half-size of the tunnel crack is initially equal to a_1 , crack growth will be imminent once the load σ reaches a point that condition $K^0 = \sigma\sqrt{\pi a_1} = K_c$ is satisfied, where here K_c is the minimum fracture toughness of the elastic medium along $x = a_1$. With further increase of the load the crack will grow into a new equilibrium state having a slightly curved front. Now expand $a(z, t)$ and $K(z, t)$ in Fourier series,

$$a(z, t) = \sum_{n=-\infty}^{\infty} A_n e^{in\pi z/L}, \quad K(z, t) = \sum_{n=-\infty}^{\infty} K_n e^{in\pi z/L}. \quad (18)$$

where recall that $2L$ is the obstacle spacing. Here $A_n = A_{-n}$, $K_n = K_{-n}$ are necessary for $a(z, t)$, $K'(z, t)$ to be real valued. Substituting eqs. (18) into eq. (3) and carrying out the principal value integrations, one finds (Rice, 1985a),

$$K_0 = K^0[A_0] = \sigma\sqrt{\pi A_0} \quad \text{and, for } n \neq 0, \quad (19)$$

$$K_n = \left\{ \frac{dK^0[A_0]}{dA_0} - \frac{n\pi}{2L} K^0[A_0] \right\} A_n = \frac{K_0}{2} \left\{ \frac{1}{A_0} - \frac{n\pi}{L} \right\} A_n$$

The above equations (19) replace eq. (3) in the case of periodic array of obstacles. Since eq. (3) is for a half-plane crack and valid only to the first order in da/dz (or $\partial a(z, t)/\partial z$), the above equations are only valid when $L/A_0, |A_n|/A_0 \ll 1$.

For a single cosine wave perturbation, assuming that $A_n = 0$ for $|n| > 1$ so that $a(z) = A_0 + 2A_1 \cos(\pi z/L)$. In this case, it follows from (19) that

$$K'(z) = K_0 \left[1 + \left(1 - \frac{\pi A_0}{L} \right) \frac{A_1}{A_0} \cos(\pi z/L) \right] \quad (20)$$

Fares (1988) has shown that the error of (20), when $A_1/A_0 \ll 1$, is within seven percent for $A_1 = 0.1L$ and can be as large as 20 percent for $A_1 = 0.2L$. It is seen from (20) that $K'(z)$ is predicted to be linear with A_1 , and when A_1/L exceeds $1/\pi$, $K'(z)$ is predicted to be negative at the most protruding parts of the crack front, e.g., $z = 0$. This is why the first order theory can be qualitatively wrong when applied to tough obstacles in which case large crack front perturbations might occur. By contrast, the BEM results of Fares (1988) show that $K'(z)$ attains the smallest, but always positive, value at the most protruding parts along the crack front.

The fast Fourier transform (FFT) method is used to carry out the expansion and inversion of the Fourier series in eqs. (18). The numerical procedure of solving for

the equilibrium profile $a(z)$ at a given load σ is then formulated as follows: The initial shape function $a(z, 0)$ (e.g., a constant at the start of the procedure) is expanded into a Fourier series by the FFT method, and the coefficients K_n in the second of eqs. (18) are calculated by eqs. (19). A FFT inversion (or summation) by eq. (18) gives the distribution of $h'(z, 0)$. Equation (16) is then used, for a chosen small time interval Δt and constant (arbitrary) ρ , to calculate the amount of growth $\Delta a(z, 0)$ for one period $0 < z < 2L$, therefore updating $a(z, \Delta t)$ as $a(z, 0) + \Delta a(z, 0)$. The above procedure is repeated to calculate the subsequent growth until the final equilibrium state is achieved in which $a(z, t)$ no longer increases by any substantial amount, indicating that conditions $K(z) = K_c$, $h'(z) = h'_c$ are satisfied to the accuracy required along the corresponding portions of penetration. Then the applied stress may be increased by another step and the same sequence of steps followed. We have found that the above procedure is a rapidly convergent process for properly chosen time steps (scaling inversely with the constant ρ).

In order to compare the numerical solution to the previously derived results, we consider again the model case of crack penetration into a periodic array of semi-infinite obstacles spaced at gaps of $2L$ as shown in fig. 2. Figure 6a depicts the obstacles in one period $-1 < z/L < 1$. The initial crack length a_i is assumed to be 10 times L (the results for the case when a_i is 100 times L show no significant difference from this case) and the obstacle size is also L (i.e., $H = 0.5L$). The load σ_i for penetration to start and the initial crack length a_i are related by

$$\sigma_i \sqrt{\pi a_i} = K_c \quad (21)$$

We define a non-dimensional load parameter as $\bar{\sigma} = \sigma/\sigma_i$. The fracture toughness \hat{K}_c of the obstacles is taken as twice the value of K_c . The crack front trapping configurations are shown in fig. 6b. The full penetration, which is also the final breakthrough in this special case, occurs when $\bar{\sigma}$ reaches 1.5, as predicted in eq. (9). Also shown in fig. 6b in dashed lines are the corresponding curves when $a_i = 100L$, in which case the half-plane crack is better approximated. We see that the curves at $a_i = 10L$ is very close to those at $a_i = 100L$. The penetration curves also match closely the previously derived a_{mir} and R of eqs. (6).

Before concluding this section, we further consider a crack penetrating an array of round, circular shaped obstacles spaced by 2 diameters (figure 7a). To examine the validity range of the first order theory, let us first assume a toughness ratio (\hat{K}_c/K_c) of 4. The trapping configurations are shown in figure 7b and the final breakthrough occurs at $\bar{\sigma} = 2.5$. Fares (1988) calculated the stress intensity factor distribution corresponding to these first-order-accurate trapping configuration. His results show that only the first profile, corresponding to $\bar{\sigma} = 1.3$, gives the correct $K(z)$ distribution, i.e., $K(z) = K_c$ along the penetrating portion of the crack front. As shown in figure 7b, the maximum perturbation for the first trapping profile is slightly greater than $0.4L$, which is somewhat consistent with the BEM results on the single cosine wave perturbation shown before. Fares (1988) also pointed out that in this case the maximum local $K(z)$ which can be generated along the crack front is only $3.52K_c$, i.e., $W = 3.52$. The final failure occurs at $\bar{\sigma} = 2.35$, by having the crack front bypass the still-intact obstacles. The first-order-accurate trapping configurations at the higher $\bar{\sigma}$ values in figure 7b are hence

even qualitatively wrong.

The above indicates that it is necessary to reduce the toughness ratio substantially in order to apply the first order theory. The maximum perturbation of the crack front should be kept within a reasonable range. Figure 8a depicts the trapping profiles when the toughness ratio is reduced to 2. In this case the maximum perturbation is below 0.6l, and the linear perturbation theory can be regarded as an acceptable approximation. In fig. 8b a more detailed picture of the crack penetrating the round obstacles is shown as the applied load is gradually increased from 1.4 to 1.5 with a step increment of 0.01. The complete breakthrough of the whole array of obstacles occurs when $\bar{\sigma} = 1.5$. This confirms the previous conclusion that the penetration of round obstacles is a regular process when the toughness ratio is low enough for analysis within the first order theory. The penetration of the obstacle starts at a load level lower than but close to the final breakthrough load (in our case $\bar{\sigma}_{pen} = 1.44$). One may see in fig. 8a,b that the crack initially grows by following closely the outer curvature of the obstacles and starts penetrating the obstacle when $\bar{\sigma} = 1.44$. Shortly after the start of penetration the final breakthrough occurs. The reason for this is that the circular boundary of the obstacles is close to the bounding curve of A^L . A limiting case is when the shape of the blocking obstacles exactly coincides with the contour of A^L . In that case no partial penetration of the obstacles will occur before the final breakthrough.

Some Further Case Studies

Here we give several examples of using the developed "visco-plastic"/FFT numerical model to show how a crack starts to penetrate and surround round obstacles, emplaced in the form of multi-row periodic arrays, as the applied load is gradually increased. A toughness ratio of two is assumed for each crack-obstacle system.

Case 1. Figure 9a shows a two-row periodic array of round obstacles in one period $-1 < z/L < 1$. The radius of the obstacles is taken as $0.3L$. As can be observed from the resulting crack front trapping configurations depicted in figure 9b, the crack penetration starts by following the circular boundary of the round obstacles in the first row. When load $\bar{\sigma}$ is increased to 1.2, the central part of the penetrating crack front touches the second row of obstacles and at $\bar{\sigma} = 1.4$ the first row of the obstacles is fully penetrated. The final breakthrough occurs at $\bar{\sigma} = 1.55$.

Case 2. We consider in the second case two rows of round obstacles, still with radius $0.3L$, but with one more obstacle in the second row as shown in figure 10a. The trapping profiles display more complicated feature when the applied load $\bar{\sigma}$ is increased by step increments of 0.1. Figure 10b shows that the first row gets penetrated at $\bar{\sigma} = 1.3$ and the final breakthrough occurs at $\bar{\sigma} = 1.71$.

Case 3. In figure 11 three rows of blocking round obstacles are shown, each with radius equal to $L/2\sqrt{3}$. The final breakthrough occurs at $\bar{\sigma} = 1.87$. This obstacle arrangement is interesting, in that a toughening ratio (K^0/K_c) of 1.87 is achieved with the area fraction of the obstacles less than 0.5. This is due to the fact that at final breakthrough a large portion of the crack front lies within the obstacle region. Hence

this type of obstacle arrangement is quite efficient in toughening the elastic matrix material. This suggests an interesting problem to find the optimum arrangement for the obstacles at a given volume fraction such that the maximum toughening can be achieved. We leave it as future work to address such issue.

Case 4. Finally, we give a simulation of a crack penetrating smaller particles (with radius taken as $0.1L$) as shown in figure 12. Again three rows of blocking round obstacles are shown, each row contains one more obstacles such that it is harder to break than the previous row. As the obstacles in the first row have a large spacing, part of the crack front contacts the second row and the interaction effect results in stronger resistance to crack penetration. Such interaction becomes smaller between the second and third row and the final breakthrough occurs at $\bar{\sigma} = 1.30$.

The above case studies clearly show that significant toughening of a brittle matrix can be achieved through crack trapping by obstacles (e.g., second phase particles, inclusions, etc.) by having the obstacles emplaced in a "good arrangement" such that the bowing out crack front encounters the maximum number of obstacles at final breakthrough. In these discussions we have excluded the possibility of crack bypassing of tough obstacles (see previous discussions in the text). That mechanism gives rise to unbroken ligaments behind the crack front, which cause an additional toughening effect, referred to as the "bridging effect" in the literature, by reducing the effective crack front stress intensity factor. One expects that in reality these mechanisms will have a combined toughening effect on a brittle matrix containing tough second phase inhomogeneities.

While our considerations here are for tensile (mode I) cracks, the corresponding equations of the first order perturbation theory are of closely similar form for those loaded in mode II or mode III shear (Gao and Rice, 1986). Thus, to the extent that a shear crack adequately models a tectonic fault, the present considerations may be of interest for faulting in regions of heterogeneous shear toughness.

Acknowledgements

The work reported was supported by subagreement POAVB38639-O with Harvard University from the University of California at Santa Barbara, based on ONR contract N00014 - 86 - K - 0753, and by the U. S. Geological Survey under grant 14-08-0001-G1367 to Harvard. We are grateful to Dr. Nabil Fares for valuable discussions.

References

- Bilby, B. A. and Swinden, K. H., 1965, "Representation of Plasticity at Notches by Linear Dislocation Arrays," *Proc. Roy. Soc.*, vol. A285, pp. 23-33.
- Fares, N., 1988, "Crack Front Trapped by Arrays of Obstacles: Numerical Solutions Based on Surface Integral Representations," to be submitted for publication.
- Gao, H. and Rice, J. R., 1986, "Shear Stress Intensity Factors for a Planar Crack With Slightly Curved Front," *Journal of Applied Mechanics*, Vol. 53, pp. 774-778.
- Rice, J. R., 1988, "Crack Fronts Trapped by Arrays of Obstacles: Solutions Based on Linear Perturbation Theory," in *Proceedings of Symposium on Analytical, Numerical and Experimental Aspects of Three Dimensional Fracture Processes*, ASME AMD Volume 91 (ASME Book G00427), eds. A. Rosakis, K. RaviChandar and Y. Rajapakse, pp. 175-184.
- Rice, J. R., 1985a, "First Order Variations in Elastic Fields Due to Variation in Location of a Planar Crack Front," *Journal of Applied Mechanics*, Vol 52, pp. 571-579.

Rice, J. R., 1985b, "Three Dimensional Elastic Crack Tip Interactions with Transformation Strains and Dislocations", *International Journal of Solids and Structures*, Vol. 21, pp. 781-791.

Smith, E., 1966, *Proceedings of the 1st International conference on Fracture*, eds. T. Yokobori et al., vol. 1, pp. 133-152. Japanese Society for Strength and Fracture of Materials, Tokyo.

List of Figure Captions

Fig. 1: A half-plane crack in homogeneous, isotropic elastic medium with a (a) straight crack front; (b) slightly curved crack front.

Fig. 2: (a) A Crack front trapped by a periodic array of rectangular obstacles. (b) Regions L_{trap} , L_{pen} and R along the trapped crack front.

Fig. 3: (a) Area A^L distinguishing between regular and irregular penetration processes. Shapes of obstacles that cause (b) regular and (c) irregular processes. (d) Round obstacles.

Fig. 4: (a) A special shape of the blocking obstacles; parameter p describing the crack penetration into the obstacles. (b) An example of an irregular penetration process caused by rectangular obstacles.

Fig. 5: Critical angle ψ_c for the obstacle shape shown in figure 4.

Fig. 6: (a) Configuration of a periodic array of straight-edged obstacles aligned in front of a crack. (b) Crack penetration profiles with toughness ratio $\dot{K}_c/K_c = 2$. For solid line curves $a_i = 10L$ and for dashed line curves $a_i = 100L$.

Fig. 7: (a) An array of round obstacles spaced by 2 diameters and (b) the crack trapping profiles when toughness ratio $\dot{K}_c/K_c = 4$ (note that the first order theory gives qualitatively wrong predictions at the higher $\bar{\sigma}$ values in this case; see text).

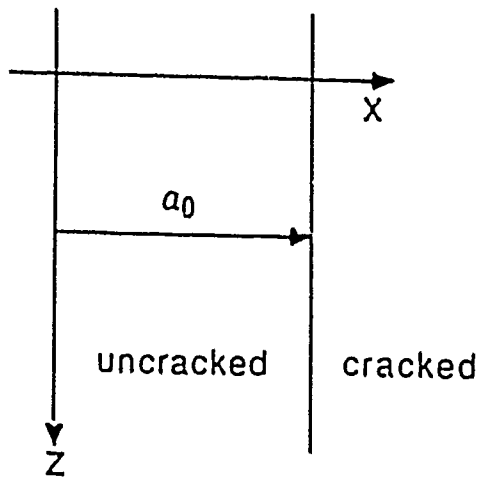
Fig. 8: Crack trapping profiles for round obstacles in figure 7a with toughness ratio $\dot{K}_c/K_c = 2$, when the load $\bar{\sigma}$ is increased (a) from 1.1 to 1.5 with a step increment of 0.1 and (b) from 1.4 to 1.5 with a step increment of 0.01.

Fig. 9: (a) Two rows of periodic arrays of round obstacles with diameter equal to 0.3 times the obstacle spacing. (b) The corresponding crack trapping profiles.

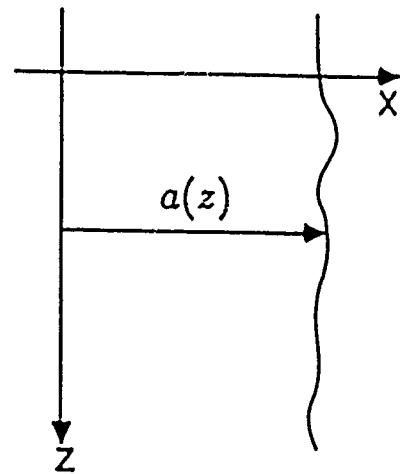
Fig. 10: (a) Two rows of periodic arrays of round obstacles with diameter equal to 0.3 times the obstacle spacing and (b) the corresponding crack trapping profiles.

Fig. 11: (a) Three rows of periodic arrays of round obstacles with diameter equal to $1/2\sqrt{3}$ times the obstacle spacing and (b) the corresponding crack trapping profiles.

Fig. 12: (a) Three rows of periodic arrays of round obstacles with diameter equal to 0.1 times the obstacle spacing and (b) the corresponding crack trapping profiles.

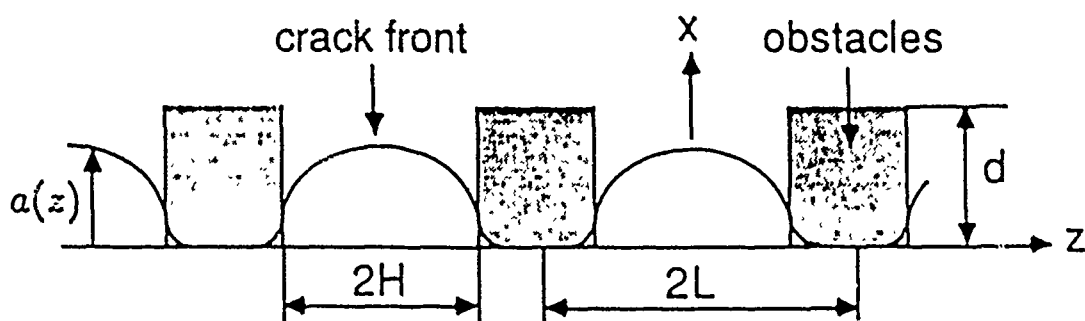


(a)

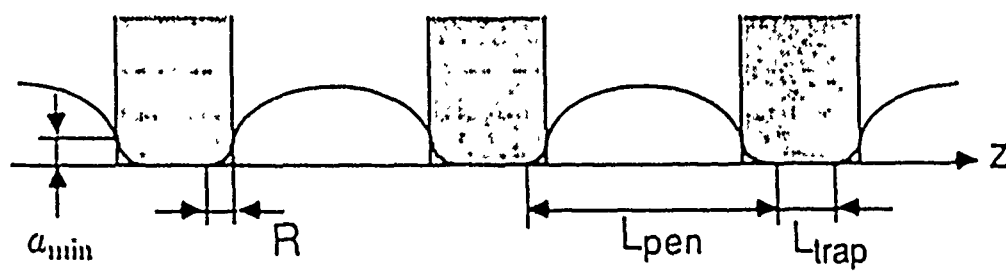


(b)

Figure 1

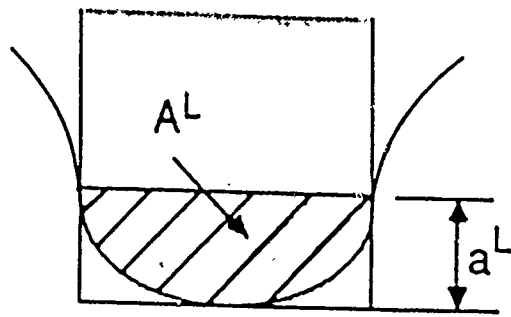


(a)

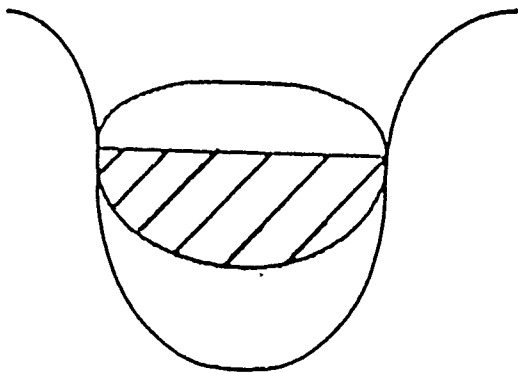


(b)

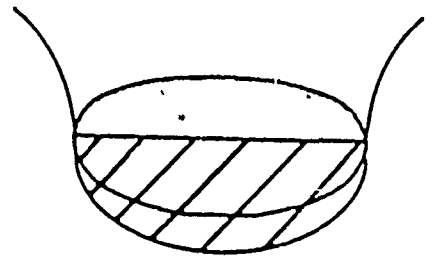
Figure 2



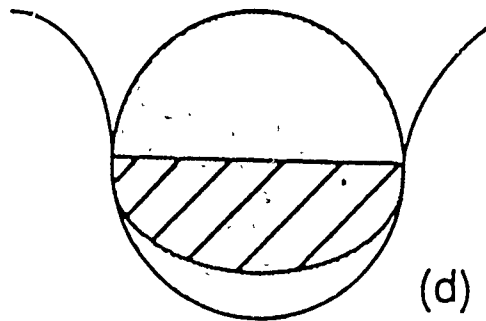
(a)



(b)

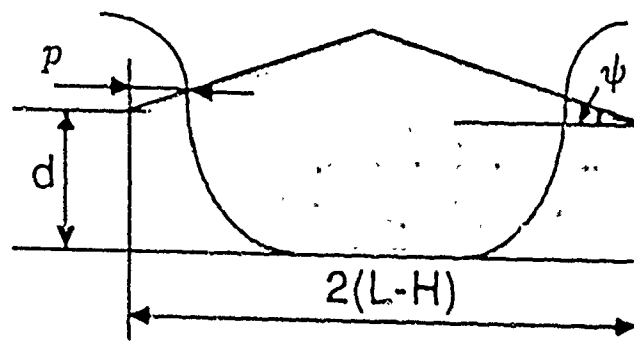


(c)

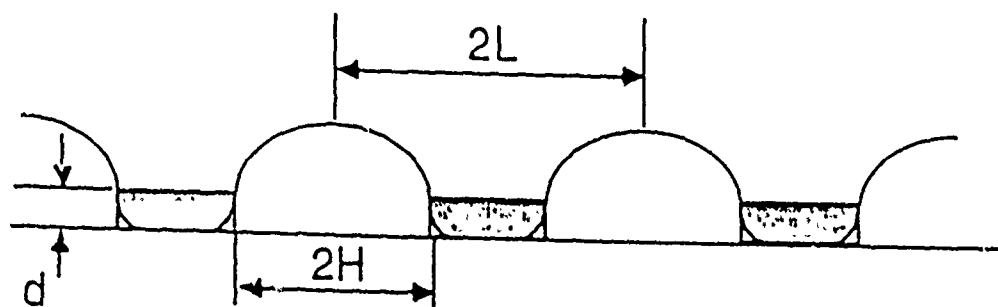


(d)

Figure 3



(a)



(b)

Figure 4

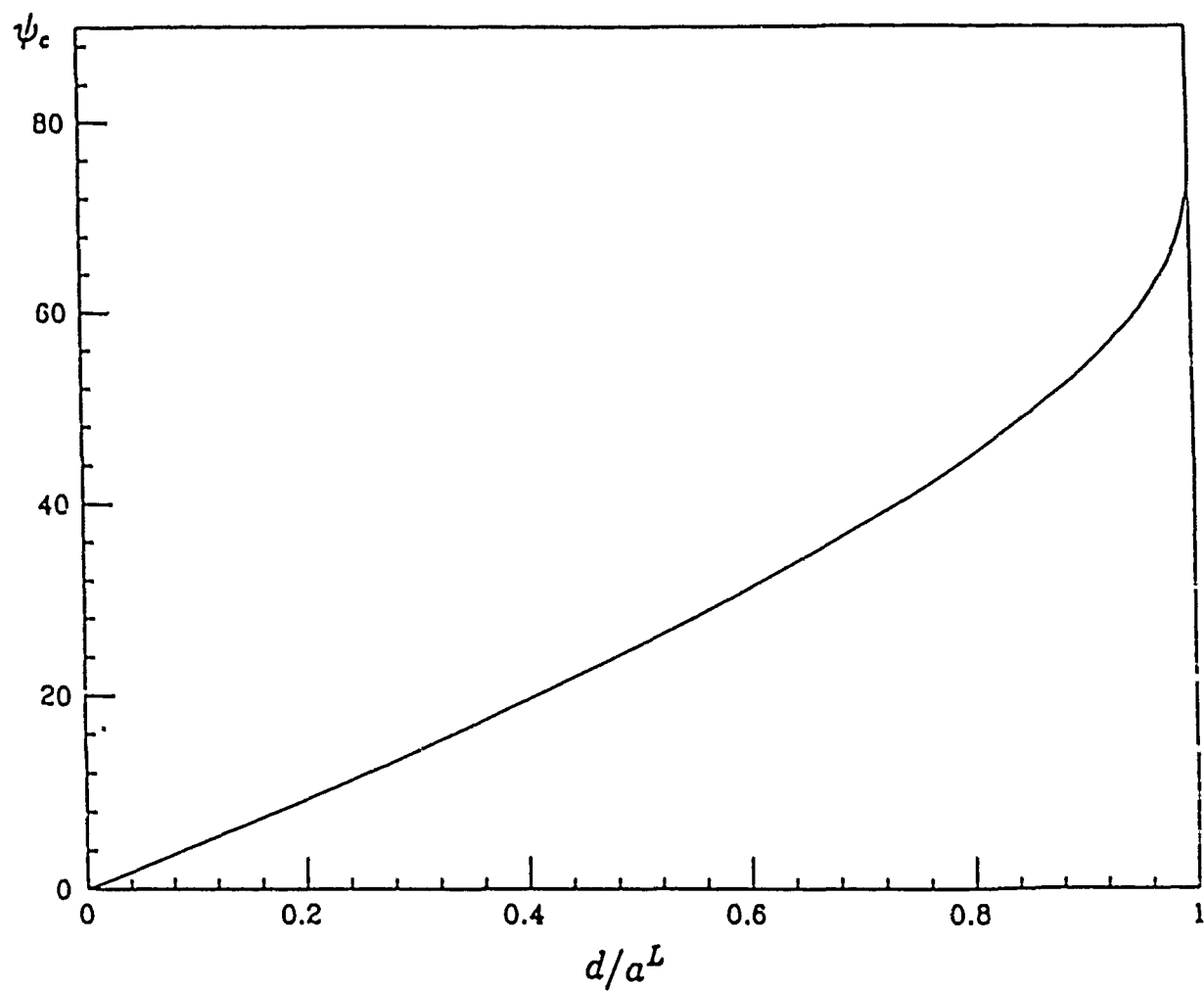


Figure 5

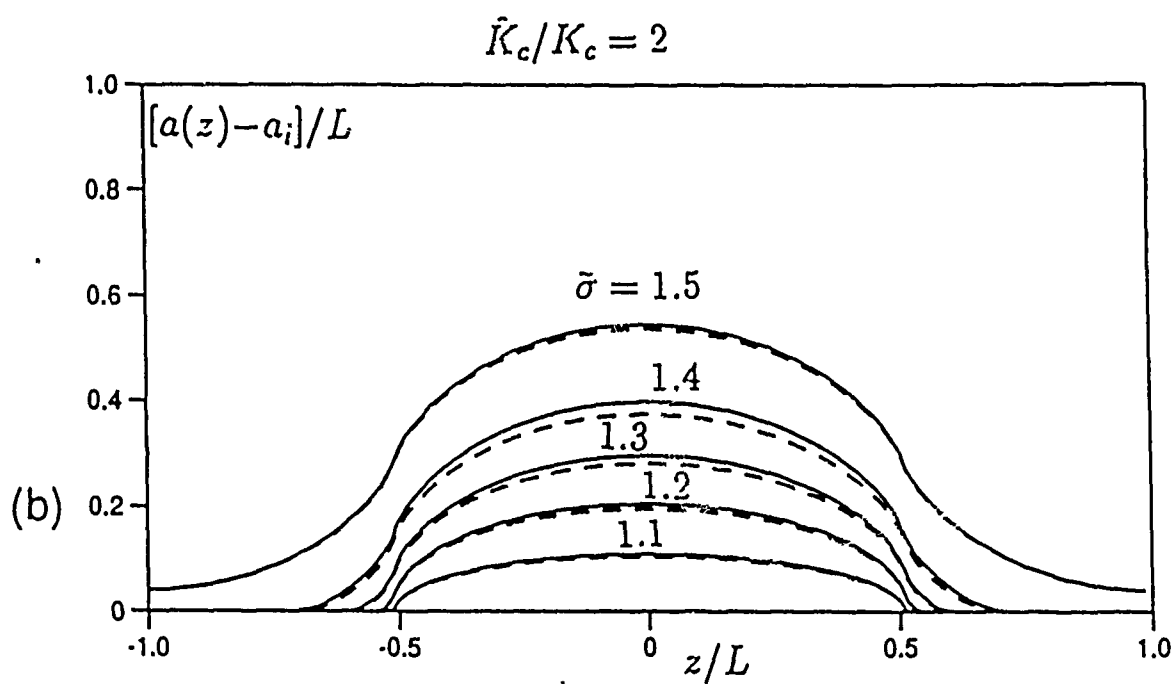
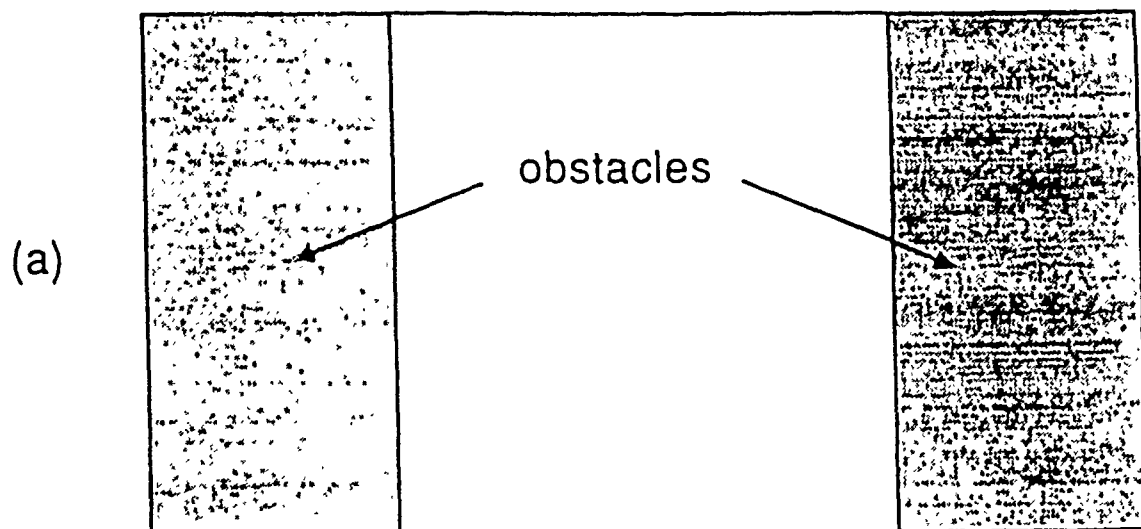


Figure 6

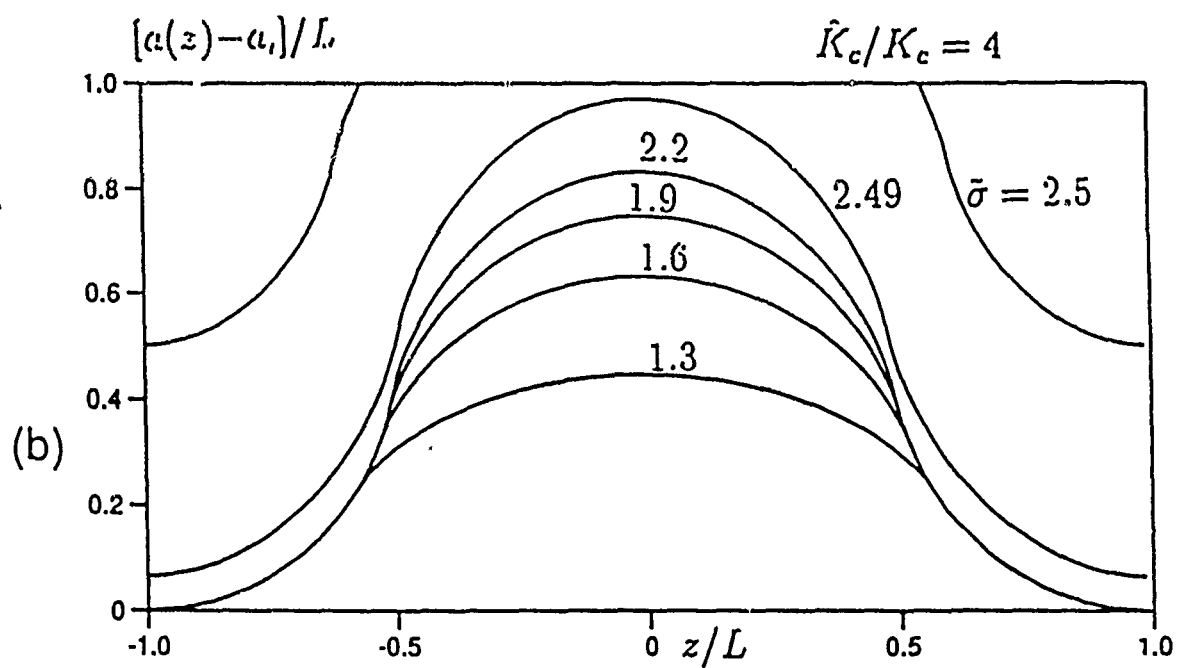
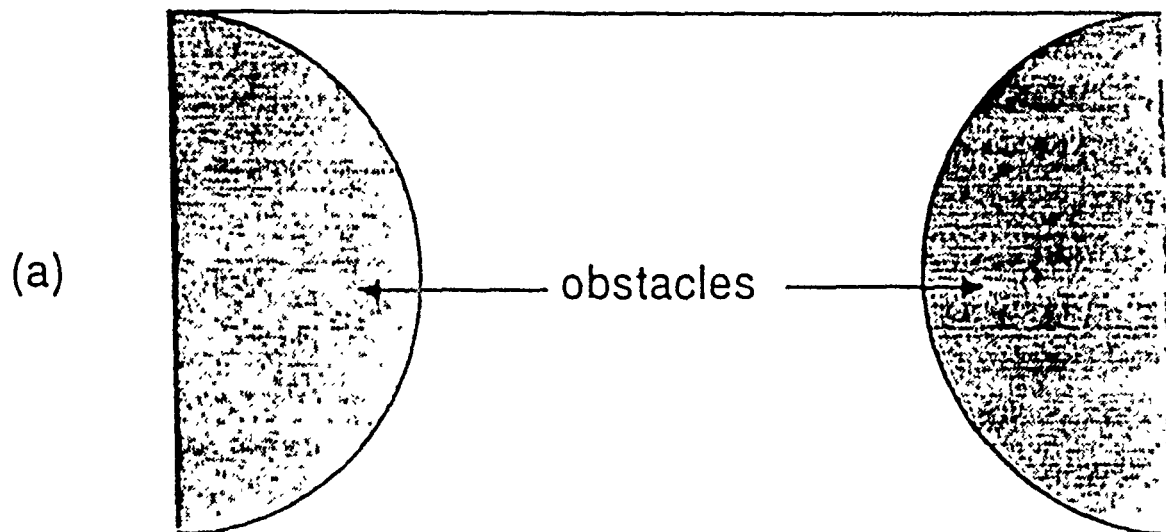


Figure 7

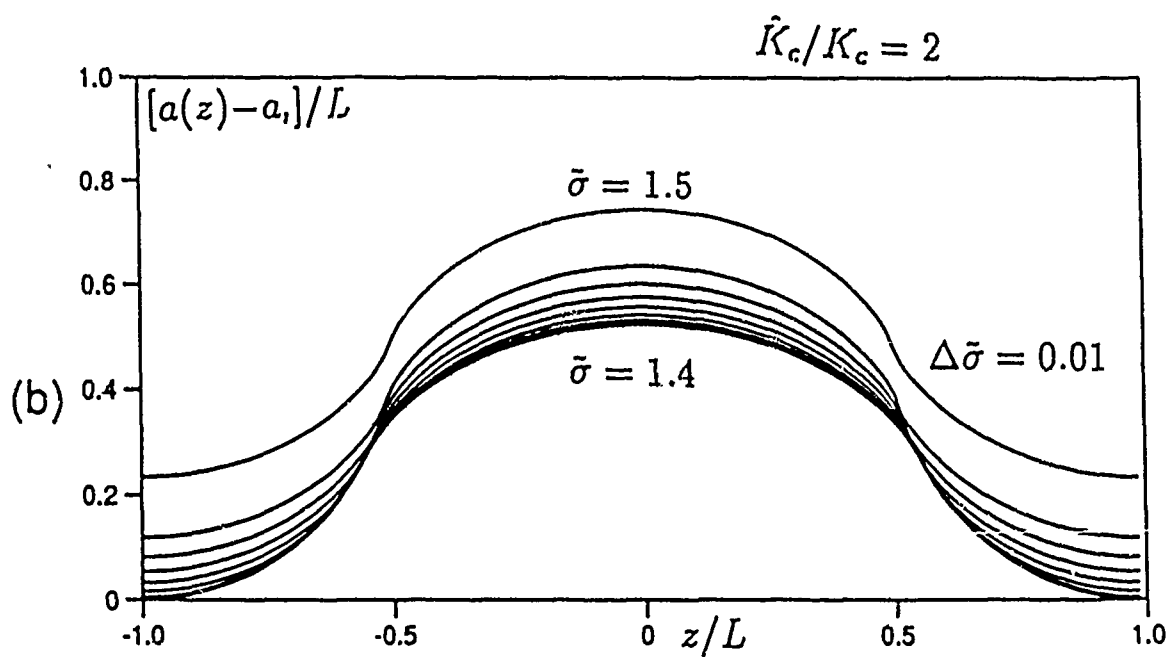
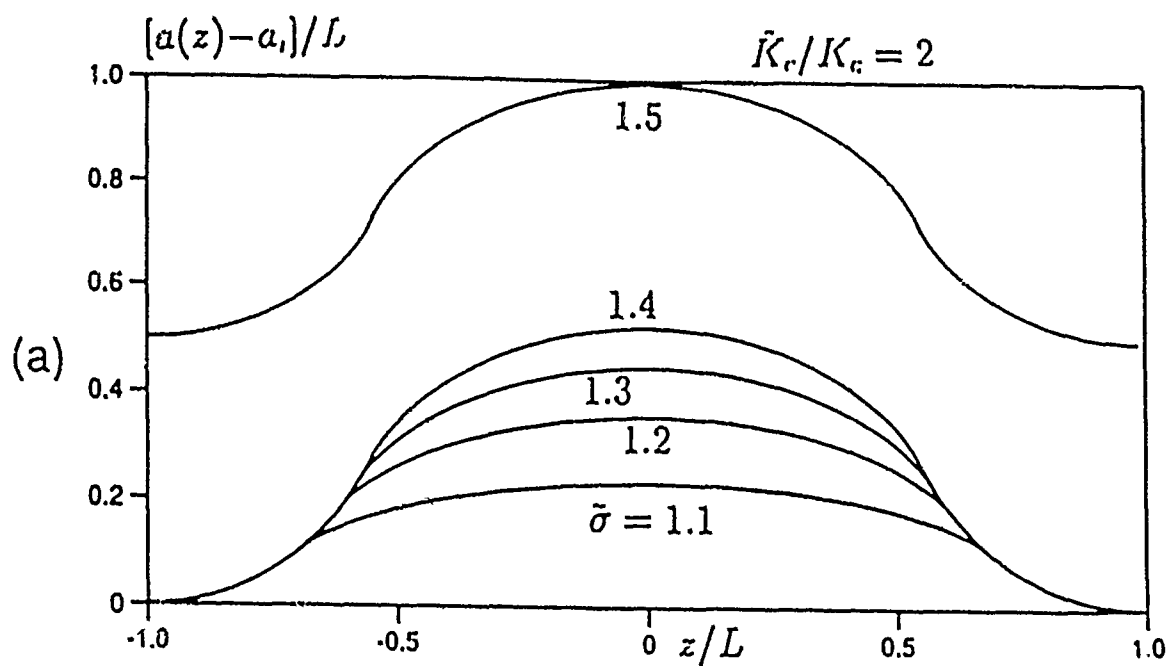


Figure 8

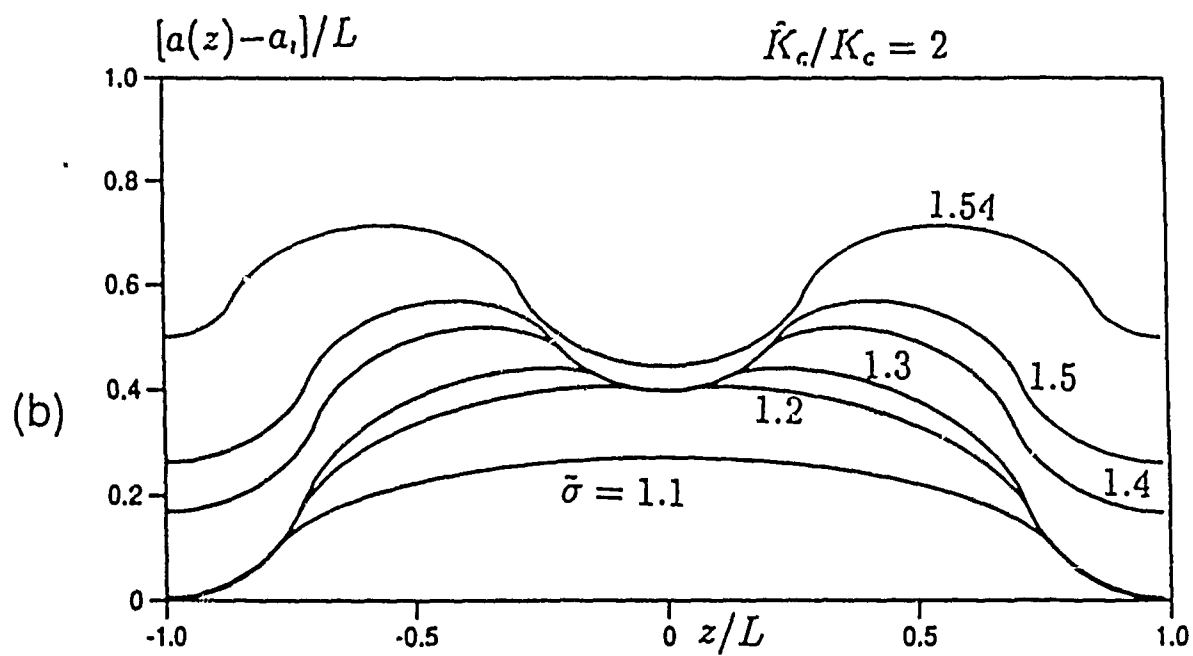
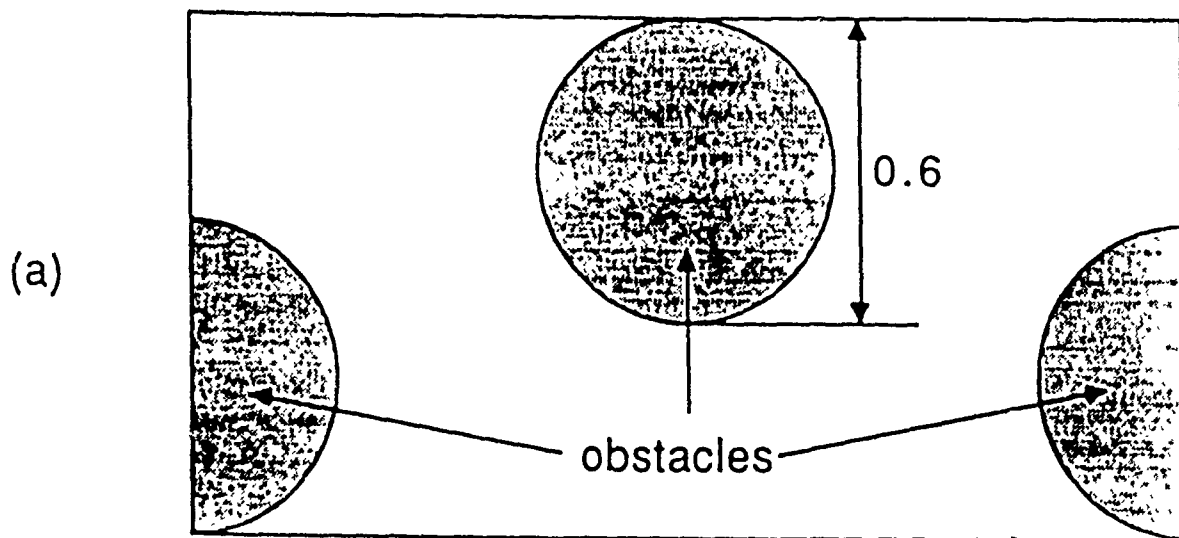


Figure 9

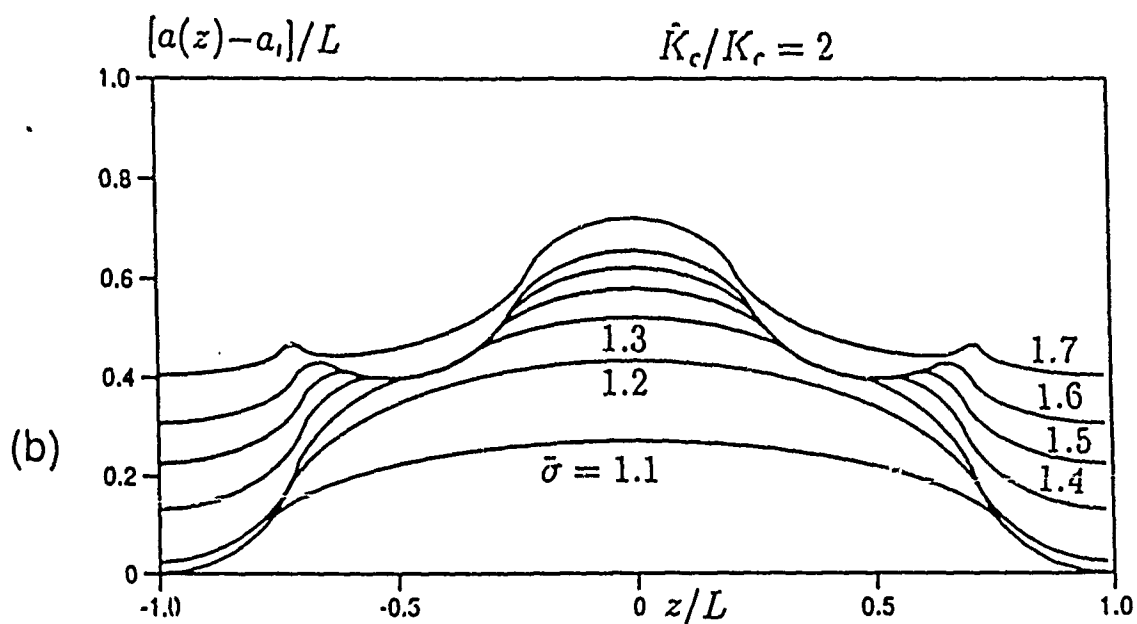
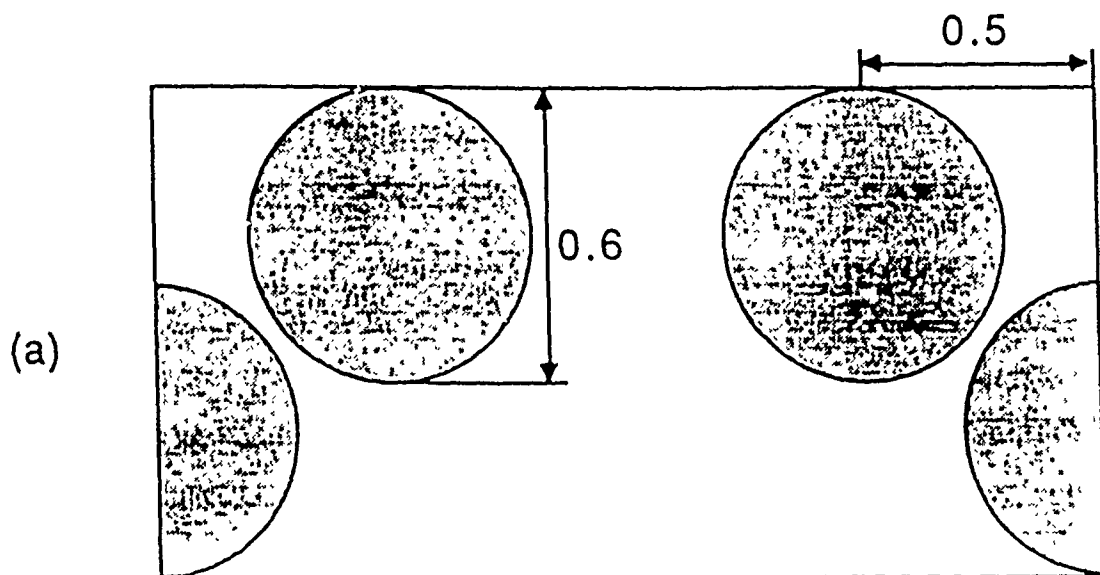


Figure 10

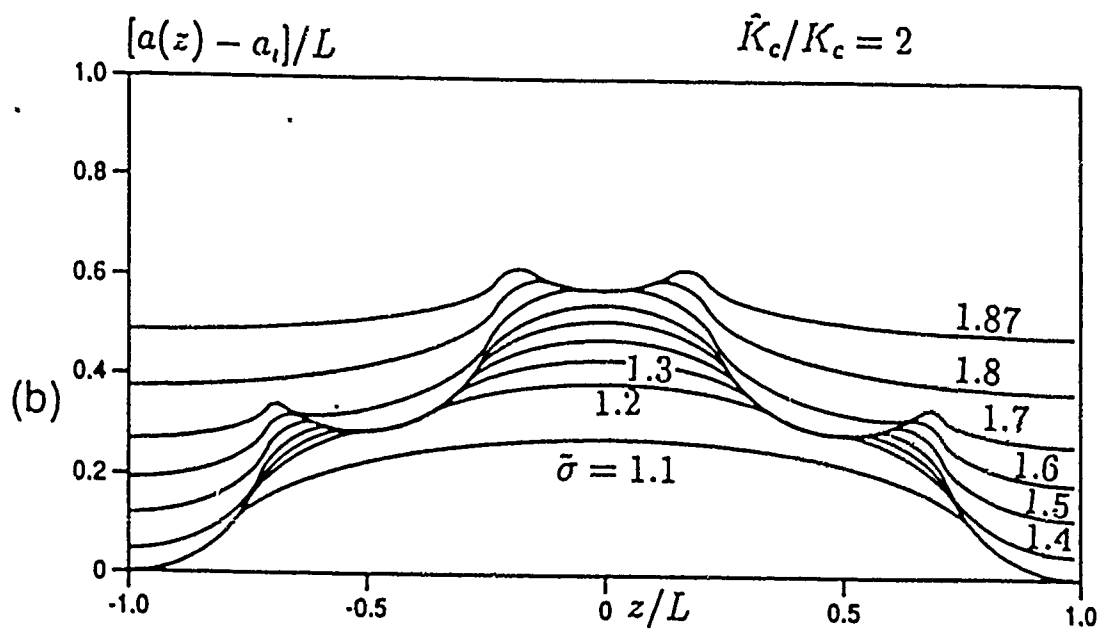
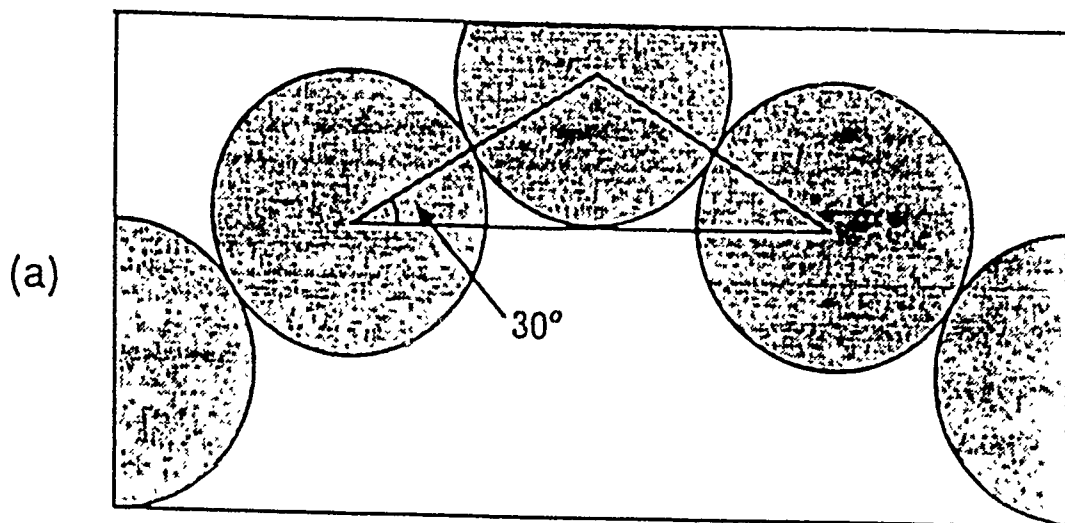


Figure 11

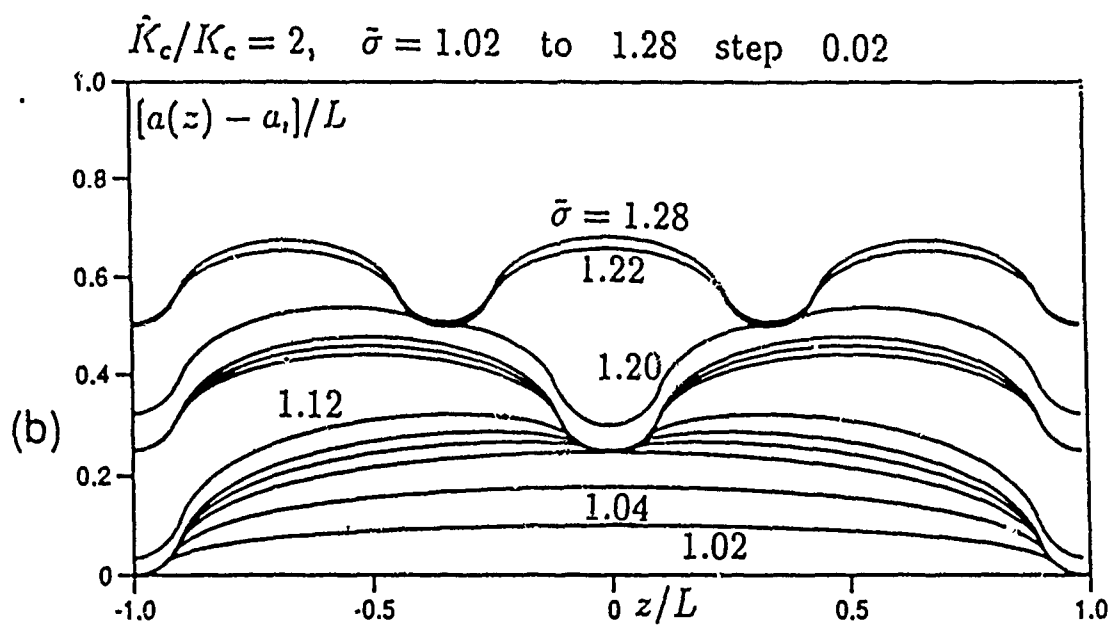
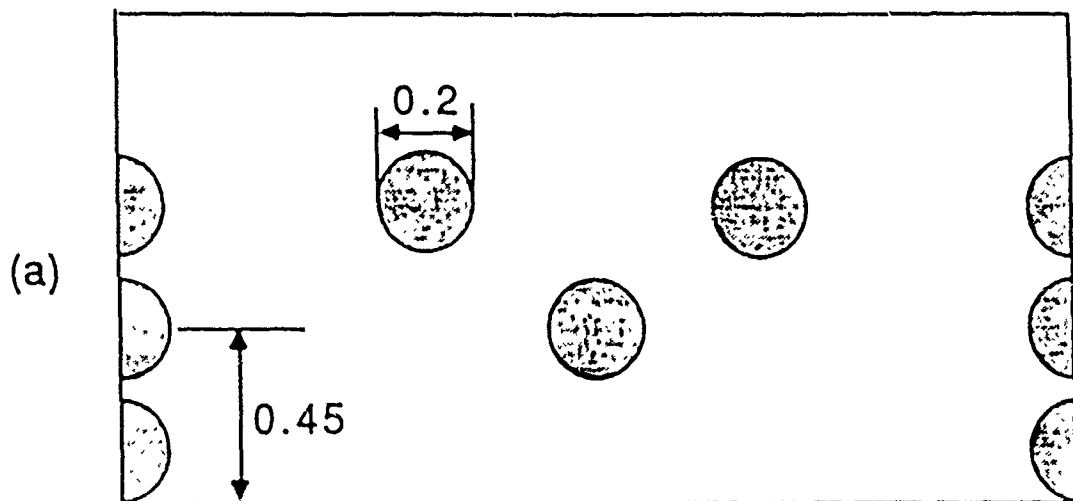


Figure 12



MECH - 192

**Crack Fronts Trapped by Arrays of Obstacles:
Numerical Solutions Based on
Surface Integral Representation**

by

Nabil Fares*

**Civil Engineering
Rensselaer Polytechnic Institute
Troy, NY 12181**

November 1988

* Formerly in the Division of Applied Sciences, Harvard University

Abstract

This paper addresses the trapping of the front of a planar crack as it impinges upon a row of periodically emplaced tough obstacles. The initial penetration of the crack between obstacles, under increasing load, as well as the ultimate unstable joining of penetrating segments so as to surround and by-pass the obstacles, are analyzed. The formulation used for the associated 3-D elasticity problems of half-plane cracks with non-uniform, curved fronts is a Boundary Element Method (BEM). This incorporates a specialized fundamental solution for an opening (prismatic) dislocation source ahead of a half-plane crack with a straight front (Rice, 1985a). The implementation of this BEM and associated mesh moving with the front is first discussed after which a series of case studies are carried out. The first two case studies evaluate the accuracy of previously obtained linear perturbation results (Rice (1985b), Gao and Rice (1988)). The last study is a crack growth simulation around a periodic array of circular obstacles with a particle size to spacing ratio of 0.5. The simulation shows in that case that crack trapping achieves a toughening ratio of 2.35 when the particle to matrix toughness ratio (K_{cp}/K_c) is greater than 3.52. The simulation also gives lower bounds on the net toughening when $K_{cp}/K_c < 3.52$.

Introduction

The object of this paper is to study crack trapping. Crack trapping is a specific micro-mechanism of toughening in a brittle matrix containing second-phase inclusions (Lange (1970)). Two related toughening micro-mechanisms of crackfront interaction with second-phase inclusions have been recognized in the literature. These are the bridging and the trapping effect. Unbroken ligaments surrounding second-phase inclusions or fibers can sometimes lag behind a main crackfront. These ligaments would then serve as bridges forming a process zone and reducing the effective crackfront stress intensity factor. This mechanism of toughening is referred to as the bridging effect and has been extensively studied (e.g. Krstic (1983), Rose (1987a), Budiansky et al. (1988)). On the other hand, crack trapping addresses the process by which tough second-phase inclusions get surrounded or cracked by an advancing crackfront. The crack trapping effect was first studied by Lange (1970, 1971) who (based on experimental observations) suggested an analogous mechanism in crackfront movement to that of dislocations bowing between obstacles. Lange attempted to quantify this possible source of toughening on the basis of a line tension associated with the crackfront. Evans (1972) further considered this idea and noted that toughening cannot be simply related to the increase in length of a crackfront due to bowing. Evans also noted that toughening should depend on the ratio of inclusion size to spacing and not solely on the spacing as was predicted by Lange's line tension model. Finally, Rose (1987b) developed a model which assumed the two effects identified here as crack trapping and crack bridging to be multiplicatively reinforcing. However, Rose circumvented the trapping studies by assuming a simple rule of mixtures as the crack trapping toughening effect.

In contrast to the bridging effect, the trapping effect requires explicit 3-D modelling in order to be effectively discussed. That is because the Stress Intensity Factor (SIF) variations along the crackfront have to be accounted for explicitly in crack trapping studies whereas smearing of the "bridges" along the direction parallel to the macrocrack in order to obtain a 2-D mechanical model plausibly retains the essence of the bridging effect. A means of effectively studying SIF variations along a crackfront occurred with the development of 3-D weight function theory (Rice (1985a,b)). In particular, the theory of first order variation of SIF due to variation in location of a planar crackfront (Rice 1985b) made the preliminary analysis of the crack trapping problem possible. In a first study (Rice (1985b)) a methodology of obtaining the configuration of the front of a planar crack which is stopped against forward advance by contact with an array of obstacles was presented. The method was then used to obtain an analytic solution to a periodic array of long rectangular obstacles. Gao and Rice (1988) further developed the first order perturbation crack trapping analysis and included discussions concerning the effect of obstacle shape. Gao and Rice also implemented a numerical procedure (based on the linear perturbation theory) having a "visco-plastic" crack growth model which, in the limit they considered, simulates growth with the intensity factor equal to the local fracture toughness. They simulated the evolution of a crackfront encountering an array of round obstacles as the applied load was quasi-statically increased. The present study evaluates the accuracy of the first order perturbation studies and performs an analogous crack growth simulation without the linearization assumptions. It analyzes the finite penetration of crack segments between obstacles and the ultimate joining of segments so as to by-pass particles. These problems are well beyond the scope of the linear perturbation theory.

Model description and limitations

In order to study the trapping effect, a specific mechanical model has to be considered. Following Gao and Rice (1988), the present model is a half-plane tensile crack with an arbitrarily shaped but symmetric and periodic crackfront in an elastic medium. The non-straightness of a crackfront could be ascribed to the trapping effect of periodic second-phase inclusions. Thus, by having the capability to evaluate the SIF values along a non-straight crackfront, investigation of the accuracy of the first order perturbation results as well as crack growth simulations could be performed. However, there are several limitations to the present model. For example, the half-plane crack idealization applies to finite-sized cracks only when the cracks are long compared to the micro-mechanical length parameters (such as second-phase size and spacing). The model also assumes that the elastic moduli of the inclusions are identical to those of the matrix. Some of the limitations in this study (such as periodicity of the crackfront) are due to a specific implementation of the weight function theory while others (such as homogeneity of elastic properties) require much more extensive numerical and/or theoretical developments to be overcome.

Mathematical formulation

In order to effectively model non-uniform 3-D crack growth of an initially straight-edged semi-infinite planar crack, its elastic interaction with opening dislocation distributions ahead of the initial crackfront is required. That is because by analytically accounting for the interaction of the initial crack surface with such dislocations, the half-

infinite initial crack surface can be excluded from the discretization requirements in a surface integral formulation of the problem. Fortunately, the interaction of a semi-infinite planar crack with arbitrary opening dislocations has been obtained by Rice (1985a). Consequently, the mathematical formulation of the present model of a semi-infinite crack with a wavy crackfront and the associated numerical method rely on equation (54) of Rice (1985a) with an additional term (the applied load) added. Specifically, referring to the coordinate system shown in figure 1, where $y=0$ is the plane of the crack, and σ_{yy} and Δu_y are the tensile stress and crack opening in the y -direction respectively, we have:

$$\sigma_{yy}(x,0,z) = \sigma_{yy}^0(x,0,z) + \frac{K^0}{\sqrt{2\pi x}} + \frac{\mu}{2\pi^2(1-\nu)} \int_0^\infty \int_{-\infty}^\infty \frac{1}{D^3} \left[\frac{D}{2\sqrt{xx'}} - \arctan \frac{D}{2\sqrt{xx'}} \right] \cdot \Delta u_y(x',z') \cdot dx' dz' \quad (1)$$

$$D = \sqrt{(x-x')^2 + (z-z')^2} \quad (2)$$

where μ , ν are the shear modulus and Poisson's ratio respectively. The expression σ_{yy}^0 is for the stress which a dislocation on $x>0$ with the same opening Δu_y induces in an infinite uncracked body, while K^0 is the amplitude of a macro-level applied cracktip stress field. By assuming that the crackfront is symmetric (with respect to the x -axis) and periodic (with a period $2L$ in the z -direction) and noting that Δu_y is non-zero only on the crack surface, the integration region in equation (1) can be further reduced to a representative sector. An example of a representative sector is shown shaded in figure 1. Denoting by $G(x,z;x',z')$ the kernel of the integrand in equation (1) the integral appearing in the equation can be rewritten as:

$$\int_S G^*(x,z;x',z') \cdot \Delta u_y(x',z') \cdot dx' dz' \quad (3)$$

$$G^*(x,z;x',z') = \sum_{n=-\infty}^{\infty} [G(x,z;x',z'+nL) + G(x,z;x',-z'+nL)] \quad (4)$$

In the above equations "2L" (see figure 1) is the period of the crackfront and "S" is a representative sector. The kernel in the integral representation of the expression for σ_{yy}^0 (e.g. equation (57) of Rice (1985a)) is similarly treated to account for periodicity and symmetry. Now, the crack surface is assumed to be traction free and hence $\sigma_{yy}=0$ on the representative sector. The previous condition leads to the following singular integral equation in $\Delta u_y(x,z)$:

$$\sigma_{yy}^0(x,0,z) + \frac{\mu}{2\pi^2(1-\nu)} \int_S G^*(x,z;x',z') \cdot \Delta u_y(x',z') \cdot dx' dz' + \frac{K^0}{\sqrt{2\pi x}} = 0 \quad \{\text{on } S\} \quad (5)$$

Once Δu_y is determined on "S", the SIF at any point along the crackfront can be determined using plane strain asymptotic relations involving the opening Δu_y . In general, equation (5) has to be numerically solved for each specific crackfront configuration. The numerical method used to solve equation (5) will next be described.

Numerical Formulation

In order to solve (5) numerically, a representation of Δu_y on "S" has to be chosen. Since the geometry of a representative sector can widely vary, a piecewise description of Δu_y would be most suitable. The surface "S" (defined in (5)) is first divided into straight-

edged triangular subregions forming a mesh. For example, figure 2 is a mesh of a representative sector. A local coordinate system is then associated with each triangle and functional variations in terms of the local coordinates are chosen and are multiplied by parameters to be determined by approximately satisfying the governing equation (5). Following Boundary Element terminology, specific functional variations with the corresponding parameters when associated with a particular triangular region will be called an element. Two types of elements have been used in the case studies to follow, and will be referred to as normal and crackfront elements. The normal elements have a linear variation of opening. Consequently, each normal element used contributes three unknown parameters to the representation of Δu_y over "S". The crackfront elements have a linear multiplied by a square-root opening variation and are used whenever an element has an edge or vertex lying along a crackfront. The use of crackfront elements incorporate the asymptotic functional variation of crack-opening near a crackfront. Again, each crackfront element used contributes three unknown parameters to the representation of Δu_y over "S". It is to be noted that the representation chosen allows Δu_y to be discontinuous along the edges of triangles. The elements in such a representation are described in Finite and Boundary element analysis as being incompatible. However, incompatible elements have been extensively and successfully used in Boundary Element analysis (e.g. Brebbia (1984)).

Once a discrete representation of Δu_y has been specified, the parameters corresponding to the amplitudes of the functional variation within each element have to be determined. In order to approximately satisfy the governing equation (5), the equality is enforced (apart from numerical errors) at Gaussian integration points of order 3 within each triangle

(Specifically those points in a triangle having area coordinates a permutation of $(1/6, 1/6, 2/3)$). This method of approximation is called a collocation procedure. Moreover, the method of representation and approximation described above could be classified as a Boundary Element method with a highly specialized fundamental solution. Thus the current method will be referred to as a Boundary Element Method (BEM). Some of the difficulties involved lie in the implementation of this BEM are in evaluating the infinite sum in (4) and in evaluating the singular integrals required in equation (5) and will next be discussed.

A closed form of the summation of (4) is difficult to obtain. The direct alternative of summing a large number of terms would be highly inefficient since the evaluation of $G^*(x, z; x', z')$ is repeatedly needed to obtain the integrals in (5) numerically. The first few terms in an asymptotic expansion of the error in evaluating (4) from $-N$ to N can be shown to be expressible as a power series in $"1/N"$. This makes the use of Richardson's extrapolation appropriate (e.g. see Bender and Orszag (1978)). The accuracy of implementing Richardson's extrapolation to obtain G^* in (4) is numerically verified by comparing with the direct alternative method of obtaining G^* (i.e. summing a large number of terms in (4)). The next difficulty to be addressed is the evaluation of singular integrals.

Two types of singular integrals are involved in (5). The first becomes evident once an integral representation for σ^0_{yy} is chosen. The other is present in $G^*(x, z; x', z')$ and occurs in the kernel of equation (1), namely:

$$\frac{1}{D^3} \left[\frac{D}{2\sqrt{xx'}} - \arctan \frac{D}{2\sqrt{xx'}} \right] \quad (6)$$

The expression (6) can be shown to be bounded as $(x, y) \rightarrow (x', y')$, and that the only

singularity is along $x=0$ with $\sqrt{x'}$ type behavior. The numerical evaluation of an integral representation of σ_{yy}^0 follows that given by Fares and Li (1988). The numerical evaluation of integrals with singular kernels of the type given in (6) can be alleviated by using the transformations:

$$t = (z' - z) / (x' + x) \quad (7a)$$

$$r = \sqrt{x'/x} \quad (7b)$$

The transformation of coordinates (7) (with the implied Jacobean) removes the singularity and smoothes the integrand for a wide range of functional variations of Δu_y . After using (7), integrals with kernels of type (6) can be numerically evaluated using quadrature formulas (assuming $x \neq 0$).

Once this BEM is implemented, it is numerically verified that a uniform translation of the crackfront gives SIF along the shifted crackfront equal (within a small tolerance) to the applied SIF. This is the only verification case problem in which the exact SIF variation is known. However, approximate crackfront SIF of a wavy crackfront are available which are obtained from a first order theory (Rice (1985b)). Comparisons with the first order results as well as other SIF solutions of non-straight crackfronts will next be presented.

Case Studies

Three case studies will be discussed. The first is a comparison of first order theory (Rice (1985b)) with BEM results of SIF along a sinusoidal crackfront. The second is an evaluation of SIF along crackfronts obtained from crack growth simulations based on the linear perturbation theory. The last is a crack growth simulation using the BEM.

i) sinusoidal crackfront

Referring to figure 1, consider a crackfront where:

$$a(z) = A \cdot [1 + \cos(\pi z/L)] + a_0 \quad (8)$$

The SIF variation along such a crackfront due to an applied macro-level cracktip stress field of amplitude K^0 which is correct to first order in $(A/2L)$ is given as (Rice (1985b)):

$$K_I/K^0 = 1 - (\pi A/2L) \cdot \cos(\pi z/L) \quad (9)$$

The discretization of a representative sector of a crackfront of form (8) where $(A/2L)=1.0$ is shown in figure 2. The number of straight-line segments (edges of triangular elements) discretizing the crackfront are chosen as a fixed fraction of the local radius of curvature. The parameters controlling the accuracy of the numerical integrations and infinite sums extrapolation are chosen so that the errors in SIF along a straight crackfront are less than 0.01%. In the other case studies, this tolerance value is increased to 0.1%. In addition, extra care in the meshing procedure was taken with the sinusoidal crackfronts in order to gain experience in the use of the method. Specifically the SIF results of a given mesh are considered acceptable only when the maximum discontinuity in SIF values at coincident edges of adjacent triangles lying along the crackfront is less than 1%. Otherwise a finer mesh is chosen. A comparison of BEM with the first order results for sinusoidal crackfronts will next be discussed.

A comparison of $\Delta K_I/K^0 = (K_I - K^0)/K^0$ versus $A/2L$ at the leading ($z=0$) and lagging ($z=L$) edges of the crackfront are shown in figures 3a and 3b respectively. At small values of $A/2L$ ($A/2L < 0.1$), the first order and BEM results agree closely (errors at the leading and lagging edges when $A/2L=0.1$ are around 7% and 5% respectively). This agreement could

be considered as further verification of the BEM. The comparisons in figure 3a and 3b also show that the errors in the first order results are tolerable up to $A/2L=0.2$ where the errors at the leading and lagging edges are around 21% and 19% respectively. Note that (unlike the first order results) the BEM predicts that the SIF at the leading edge never goes negative ($\Delta K_I/K^0 > -1$) as is intuitively expected of a crack loaded in tension. A further comparison of K_I/K^0 versus z/L (position along the crackfront) is shown in figure 4 at $A/2L=0.2, 0.5$ and 1.0 . It is interesting to note the qualitative change in the variation of SIF along the crackfront at successively larger values of $A/2L$. It appears that the part of the crackfront at which the SIF goes beyond K^0 localizes at a successively narrower region near the lagging edge of the crackfront.

ii) First order crack growth profiles

In the next two cases, crack growth simulations through or around a periodic array of circular obstacles (figure 5) are studied. The ratio H/L in figure 5 equals 0.5 in both of the next two case studies. Defining the matrix and particle toughness by K_C and K_{CP} respectively, a particular linear perturbation simulation (Gao and Rice (1988)) assumed $K_{CP}/K_C=4$. They use the "visco-plastic" crack growth model:

$$\frac{\partial a(z,t)}{\partial t} = \begin{cases} \rho(K_I - K_C) & K_I > K_C \text{ (or } K_{CP} \text{ when the crack is in the particle)} \\ 0 & \text{otherwise} \end{cases} \quad (10)$$

where "t" is a time parameter, ρ is a "viscosity" coefficient of the system and K_I is the SIF value at points along the crackfront. The details of the numerical implementation of the

crack growth studies using the linear perturbation theory are discussed in Gao and Rice (1988). Essentially, by making p large enough, they simulate growth at $K_I = K_C$. Crack growth profiles at various K^0/K_C values from Gao and Rice's simulations are shown in figure 6. These crackfront configurations are then discretized and the SIF along the crackfronts are determined using the BEM. A typical mesh used in these discretizations is shown in figure 7 and corresponds to the curve with $K^0/K_C = 2.4$ in figure 6.

The SIF along the crackfronts shown in figure 6 as determined by the BEM are shown in figure 8. In order to more easily discuss the results of figure 8, the crackfront will be divided into two parts. The part which touches the particle will be called CF_{trap} and that which doesn't will be called CF_{pen} . The linear perturbation results would predict that $K_I/K_C = 1$ along CF_{pen} and that when $K^0/K_C = 2.5$ then $K_I/K_C = 4$ along CF_{trap} . The BEM results show that the linear perturbation predictions are correct only for the first profile ($K^0/K_C = 1.3$). At subsequent profiles, the linear perturbation theory underestimates K_I/K_C along CF_{pen} . In addition, when $K^0/K_C = 2.5$, the linear perturbation results overestimate K_I/K_C along CF_{trap} . Both the previous observations would imply that crack growth would have to proceed deeper into the matrix before particle rupture occurs. This observation is borne out in the next simulation.

ii) Crack Growth Simulation using BEM

The last case study performs a crack growth simulation using the BEM. In these simulations, the "visco-plastic" crack growth model (equation (10)) will again be used but with the following modifications. First, $da(z,t)$ will be replaced by $da^*(s,t)$ where "s" is the arc length along the crackfront and da^* is an increment of crack advance measured in the

direction normal to the crackfront. This modification is necessary since $a(z,t)$ would be multi-valued when the crackfront wraps around the obstacles. Finally, in order to force the crackfront to wrap around instead of breaking the obstacles, K_{CP}/K_C will be allowed to be as large as necessary. Fortunately, the simulations show that the obstacle toughness K_{CP} needs only to satisfy $K_{CP} \geq 3.52K_C$ for the obstacles to remain unpenetrated as the protruding crack fronts begin to unstably grow towards one another and surround the obstacles. Some of the implementation details of the crack growth simulation will next be described.

The crack growth simulations require forming a new mesh (re-meshing) whenever the crack advances. The procedure for crack growth is therefore as follows. The SIF along the current crackfront is obtained using the BEM. Based on the SIF values a new crackfront is calculated. Re-meshing is performed with the new crackfront which is consequently considered as being the current one. Thereupon, the cycle of BEM analysis and crack growth is repeated. The time step taken in equation (10) while growing the crack is periodically readjusted to satisfy the following constraint. The maximum deviation of K_I/K_C from 1 along CF_{pen} should not exceed $\pm 6\%$. When the constraint is violated, the time step increment is decreased. When the constraint is again satisfied, larger time steps are again taken. Sample crackfront profiles from the crack growth simulations which satisfy the above-mentioned constraint are shown in figure 10. Further remarks on crack trapping and the deductions that can be made from figure 10 will next be discussed.

The toughening effect of crack trapping will be defined as the maximum of K^0/K_C that is to be applied in order to move the crackfront ahead of the first array of obstacles

(particles) lying parallel to the crackfront. The crackfront can move in such a way as to either break the obstacles or circumvent them by surrounding them.

When the particles break, then the value of K^0/K_C at breakthrough is the net toughening achieved by introducing the particles or second phase inclusions. The simulation shown in figure 10 gives lower bounds (since the particles' toughness is not fully mobilized) on the net toughening when $K_{CP}/K_C < 3.52$ with $H/L=0.5$. An upper bound is obtained from the rule of mixtures (Rose (1987b)), and the exact level depends on the shape of the particles as discussed in Gao and Rice (1988). For example, based on the first curve values of K^0/K_C and K_{max}/K_C (the maximum SIF acting on the particle), an upper and lower bound for the net toughness when $K_{CP}/K_C=1.77$ is 1.44 and 1.30 respectively.

When the obstacles are circumvented, the particles form bridges and lead to the bridging effect discussed in the introduction. The net toughening achieved in this case is due to both the bridging and the crack trapping effect. Accordingly, figure 10 suggests that at least the first array of obstacles might be circumvented when $K_{CP}/K_C \geq 3.52$ (with $H/L=0.5$) and that the crack trapping toughening contribution is then $K^0/K_C=2.35$. The actual K_{CP}/K_C value required to circumvent the first array of obstacles with a realistic loading situation depends on the location of the next array of obstacles. That is because with a realistic loading situation, there would be no way to suddenly reduce K^0/K_C from 2.35 after the penetrating crack segments began to join unstably with one another. For example, if the crack front is considered retrapped at the most advanced configuration shown in figure 10, and K^0/K_C remains at 2.35, then a lower bound on the K_{CP}/K_C required to circumvent the first array of obstacles is 3.64 (i.e. $2.35 \times 3.02/1.95$). In any

case, the crack trapping toughening contribution is independent of K_{CP}/K_C when $K_{CP}/K_C \geq 3.52$ (i.e. irrespective of whether the first array of obstacles are circumvented). However, the toughening contribution of crack trapping would depend on H/L and in a more general situation on obstacle elastic moduli, shape and configuration within the brittle matrix. Further case studies have to be performed in order to determine the dependence of the crack trapping toughening contribution on H/L ($(1-H/L)$ is the ratio of particle size to particle spacing).

Conclusion

A BEM was formulated and implemented for the case of a semi-infinite crack having a wavy crackfront. Using the BEM, the linear perturbation theory of wavy crackfronts was evaluated in two case studies. In general, the linear perturbation theory underestimates the SIF along the lagging part of a crackfront and overestimates them along the leading part. In the case of a sinusoidal crackfront, the linear perturbation theory gives acceptable agreement with the BEM when the amplitude to wavelength ratio is less than around 0.2. A crack growth simulation around obstacles using the BEM yields lower bounds on the toughness of the matrix-particles system when a crackfront breaks through the particles. The simulation also gives the toughening contribution of crack trapping when the particle to matrix toughness is above a critical ratio allowing the crackfront to circumvent the obstacles by surrounding them. Further studies have to be carried out in order to quantify the effect of particle size to spacing on crack trapping.

Acknowledgements

The work reported was supported by subagreement POA VB38639-0 with Harvard University from the University of California based on ONR contract N00014-86-K-0753. I am grateful to Professor J.R. Rice for having supervised this work. I am also grateful for discussions with Dr. Huajian Gao.

References

- Bender C.M. and Orszag S.A., (1978), "Advanced Mathematical Methods for Scientists and Engineers.", McGraw-Hill Book Company.
- Brebbia C.A., (1984), "Boundary Element Techniques: Theory and Applications in Engineering.", Springer-Verlag, New York.
- Budiansky B., Amazigo J.C. and Evans A.G., (1988), "Small-scale Crack Bridging and the Fracture Toughness of Particulate Reinforced Ceramics.", J. Mech. Phys. Solids, in Press.
- Evans A.G., (1972), "The Strength of Brittle Materials Containing Second Phase Dispersions.", Phil. Mag. A, 26, pp 1327-1344.
- Fares N., (1988), "Green's Functions for Plane-Layered Elastostatic and Viscoelastic Regions with Application to 3-D Crack Analysis.", Ph.D. thesis, Massachusetts Institute of Technology, 1987.
- Fares N. and Li V.C., (1988), "Boundary Element Method for 3-D Cracks in a Plate.", in Proceedings of Symposium in Analytical, Numerical and Experimental Aspects of Three-Dimensional Fracture Processes, ASME AMD volume 91 (ASME Book No. G00427), eds. A. Rosakis, K. Ravi-Chandar and Y. Rajapakse, pp. 113-124.
- Gao H. and Rice J.R., (1988), "A First Order Perturbation Analysis on Crack-Trapping by Arrays of Obstacles.", to be submitted for publication.
- Krstic V.D., (1983), "On the Fracture of Brittle-matrix/Ductile-particle Composites.", Phil. Mag. A, vol. 48, no. 5, pp 695-708.
- Lange F.F., (1970), "The Interaction of a Crack Front with a Second-phase Dispersion.", Phil. Mag., 22, pp 983-992.
- Lange F.F., (1971), "Fracture Energy and Strength Behavior of a Sodium Borosilicate Glass- Al_2O_3 Composite System.", J. Ceramic Soc. Amer., Vol 54, no 12, pp 614-620.

- Rice J.R., (1985a), "Three-dimensional Elastic Crack Tip Interactions with Transformation Strains and Dislocations.", *Int. J. Solids Struct.*, Vol.21, no 7, pp 781-791.
- Rice J.R., (1985b), "First Order Variations in Elastic Fields Due to Variation in Location of a Planar Crack Front.", *J. Appl. Mech.*, vol 52, pp 571-579.
- Rice J.R., (1988), "Crack Front Trapped by Arrays of Obstacles: Solutions Based on Linear Perturbation Theory.", in *Proceedings of Symposium in Analytical, Numerical and Experimental Aspects of Three-Dimensional Fracture Processes*, ASME AMD volume 91 (ASME Book No. G00427), eds. A. Rosakis, K. Ravi-Chandar and Y. Rajapakse, pp. 175-184.
- Rose L.R.F., (1987a), "Crack Reinforcement by Distributed Springs.", *J. Mech. Phys. Solids*, vol 35, no 4, pp 383-405.
- Rose L.R.F., (1987b), "Toughening Due to Crack-front Interaction with a Second-phase Dispersion.", *Mech. of Mat.*, 6, pp 11-15.

Figure Captions

Figure 1 shows a wavy crackfront of the type analyzed using the BEM. Only a representative sector (shown shaded) needs to be discretized.

Figure 2 shows a mesh of a representative sector whose crackfront shape is sinusoidal with the amplitude to wavelength ratio being 1.0.

Figure 3a,b: $\Delta K_I/K^0$ (the normalized difference between the actual and the macro Stress Intensity Factor) versus $A/2L$ (half the crackfront amplitude divided by crackfront wavelength) as determined by both the linear perturbation theory and the present Boundary Element Method. a) and b) show these comparisons at the leading and lagging tips of the crackfront respectively.

Figure 4: The normalized Stress Intensity Factor versus the location along the crackfront as determined by both the linear perturbation theory and the present Boundary Element Method at various amplitude to wavelength ratios.

Figure 5: An advancing crackfront encountering an array of obstacles is trapped thus causing the crackfront to have a wavy shape.

Figure 6: The crack growth profiles based on the linear perturbation theory are shown with the corresponding macro normalized stress intensity factor (K^0/K_c) required to reach that profile.

Figure 7: A typical mesh used to discretize the crack growth profiles based on the linear perturbation theory shown in figure 6.

Figure 8: The Stress Intensity Factor along the crack growth profiles shown in figure 6 as determined by the Boundary Element Method discussed in the text.

Figure 9: A typical mesh used to discretize the crack growth profiles based on a full numerical simulation using the Boundary Element Method discussed in the text.

Figure 10: Crack growth profiles based on a full numerical simulation are shown with the corresponding macro normalized stress intensity factor (K^0/K_C) required to reach that profile as well as the associated normalized maximum stress intensity factor (K_{max}/K_C) along the particle.

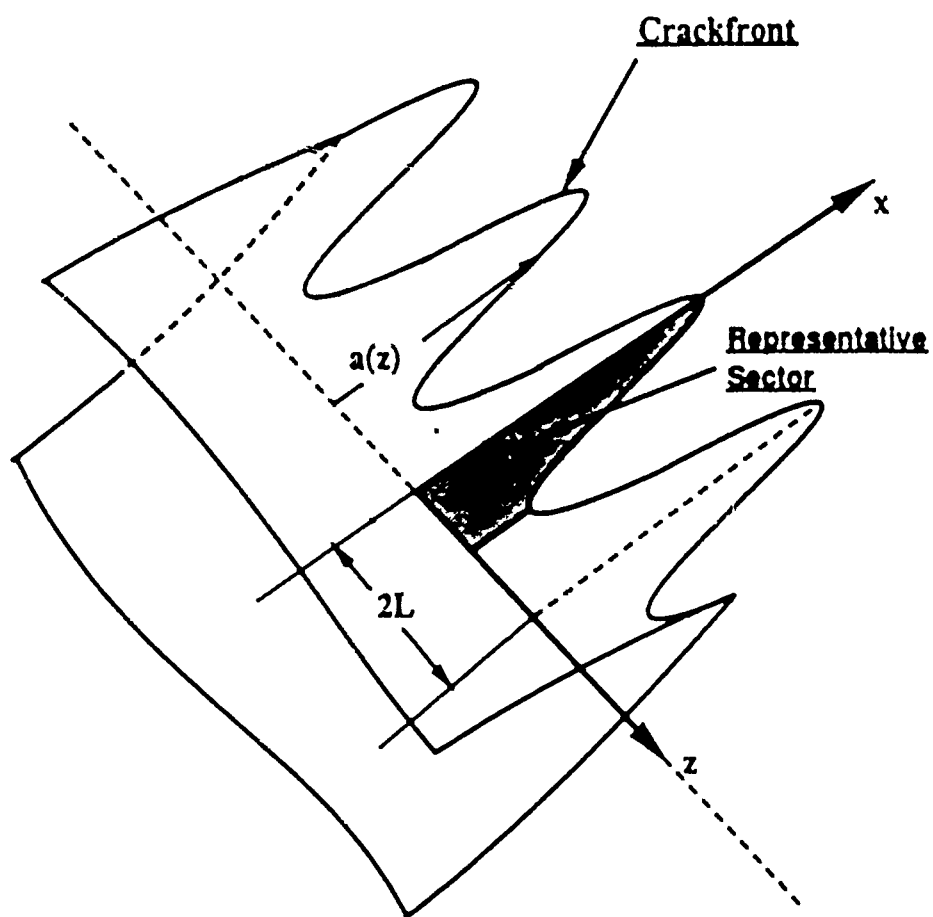
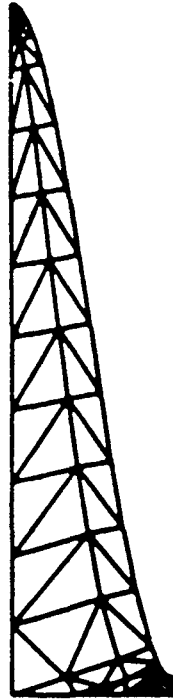
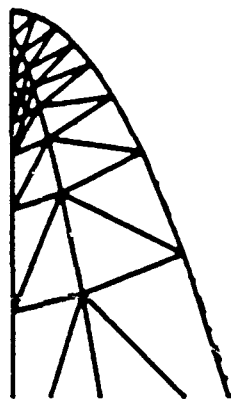


Figure 1



$a(z) = 0.1 + 2 \cdot [1 + \cos(\pi z/L)]$
 Representative sector mesh
 Sinusoidal crackfront

Focus on
 Leading part of crackfront



Focus on
 Lagging part of crackfront

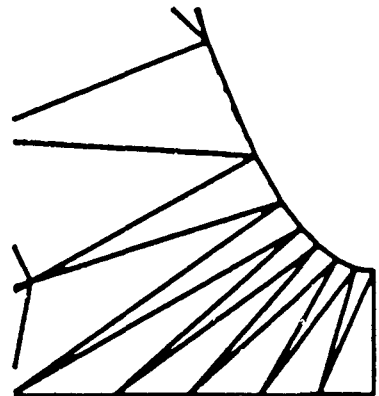


Figure 2

$\Delta K_I / K^0$ vs $A / (2 L)$ ($z/L=0.0$)

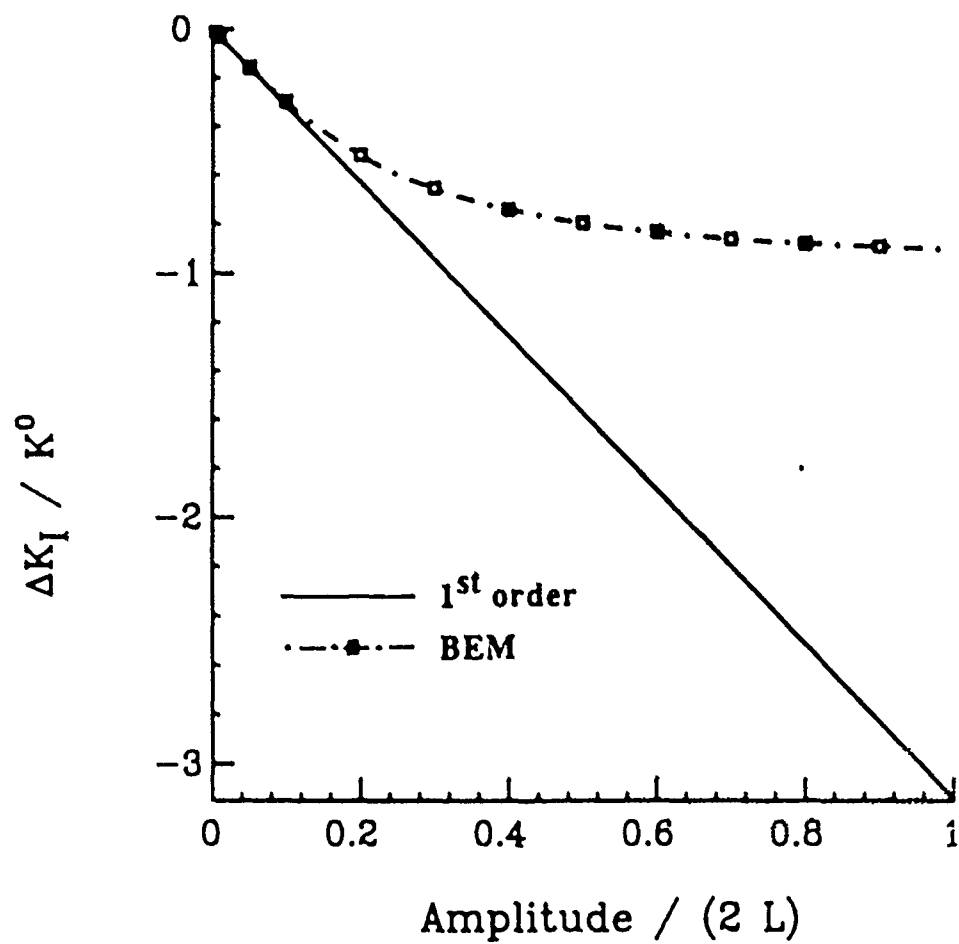


Figure 3a

$\Delta K_I / K^0$ vs $A / (2 L)$ ($z/L=1.0$)

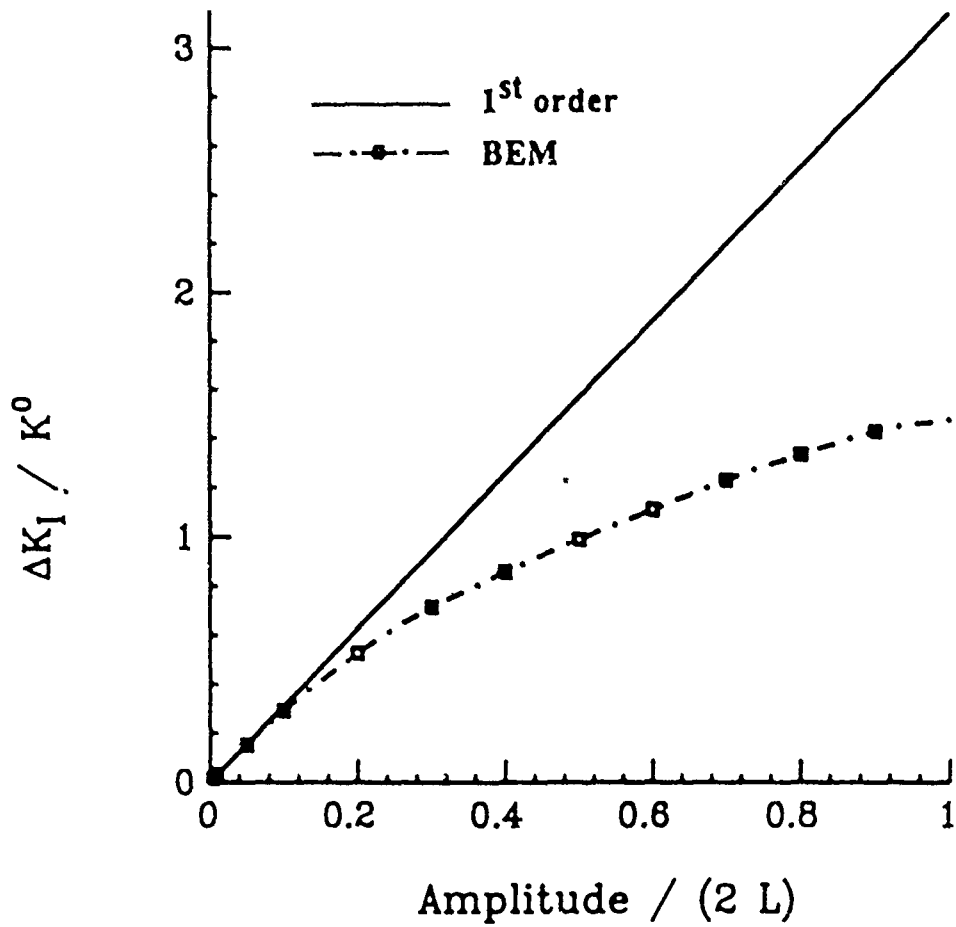


Figure 3b

(K_I / K^0) vs (z / L)

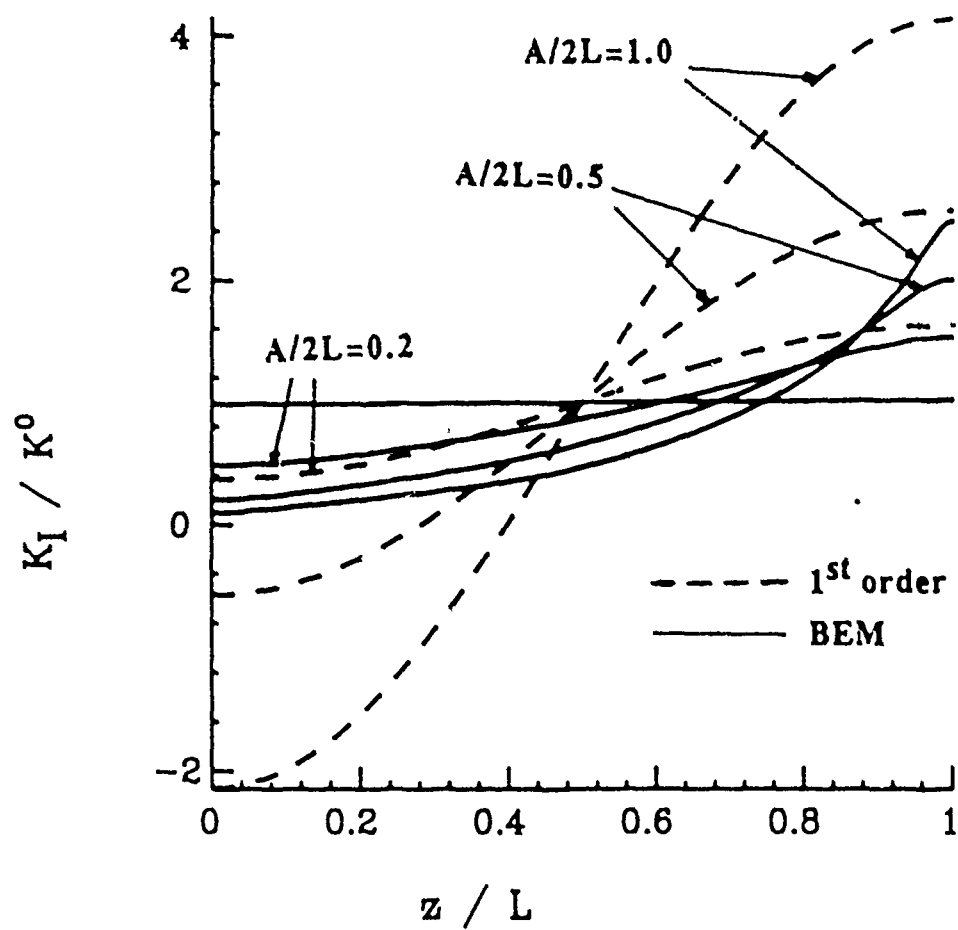


Figure 4

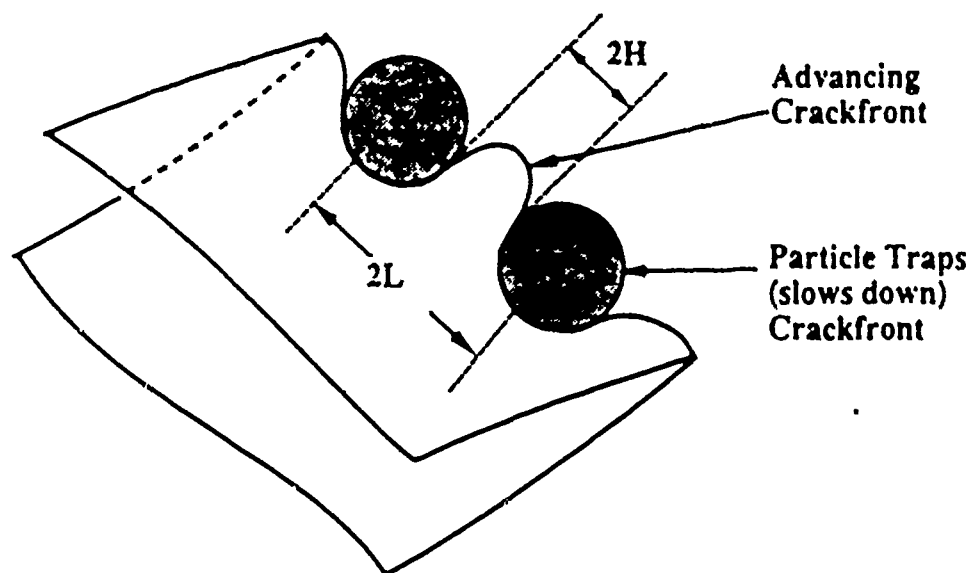


Figure 5

Linear Perturbation Crack Growth Profiles

$H/L=0.5$; $K_{cp}/K_c=4$

Reference Gao and Rice (1988)

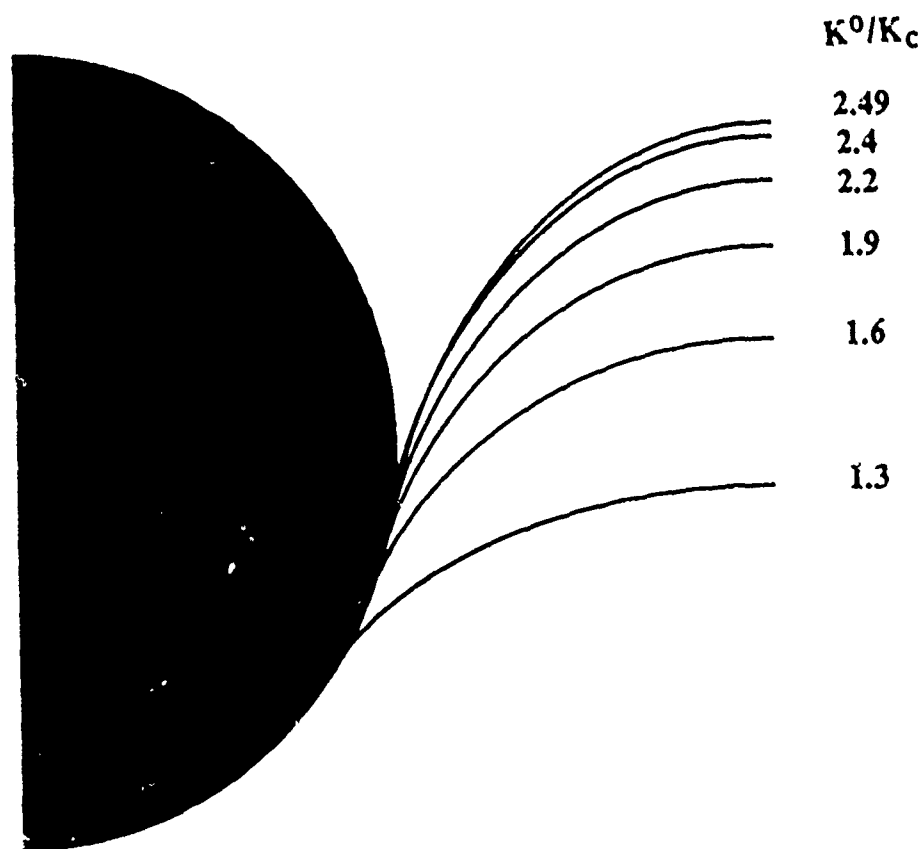


Figure 6

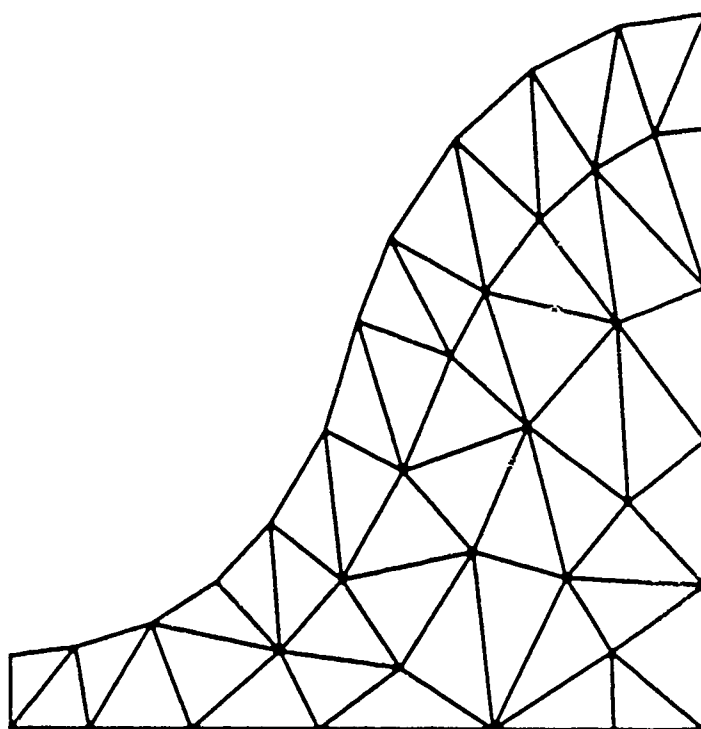


Figure 7

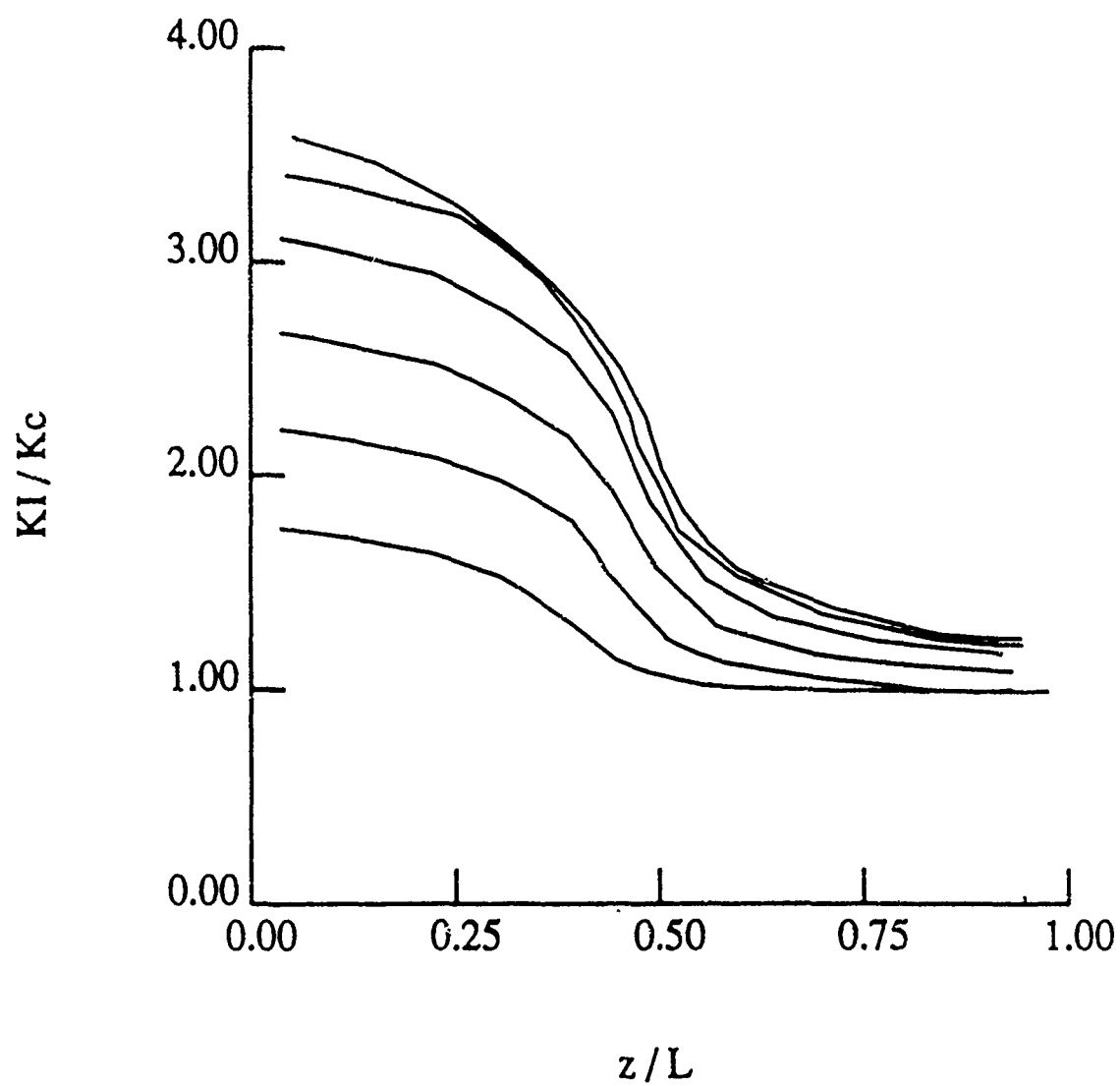


Figure 8

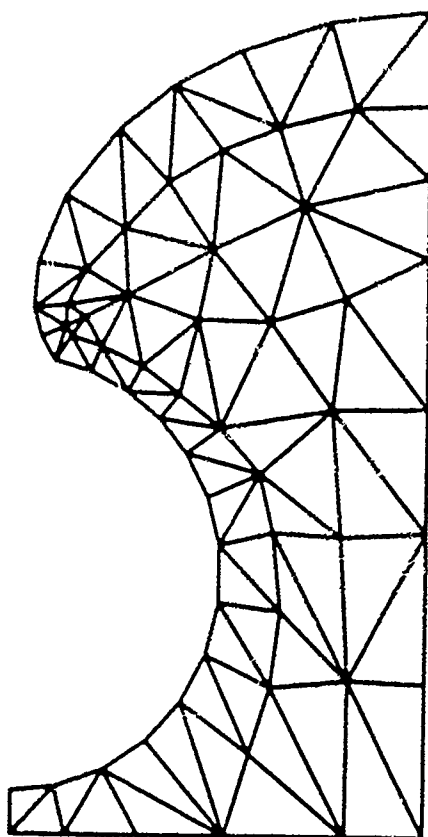


Figure 9

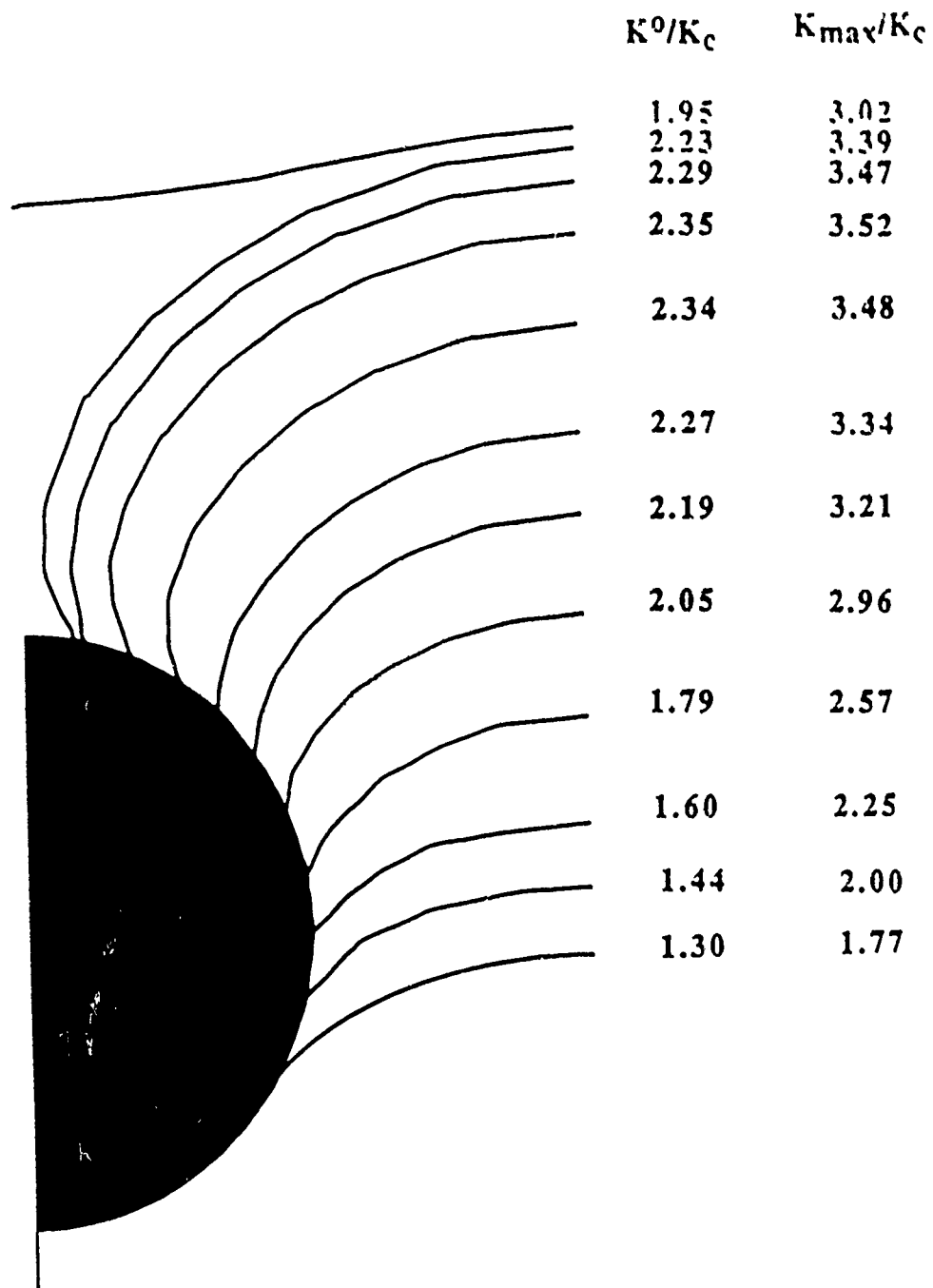


Figure 10

OVERVIEW NO. 80

ON THE ENGINEERING PROPERTIES OF MATERIALS

M. F. ASHBY

Cambridge University Engineering Department, Trumpington Street, Cambridge CB2 1PZ, England

(Received 8 October 1988)

Abstract—The basic mechanical and thermal properties of engineering materials are surveyed and inter-related. The survey reveals the range of each property, and the sub-range associated with each material class. These and the relationships between properties are displayed on Material Property Charts, of which 10 are presented here. The diagrams have numerous applications which range from the identification of fundamental relationships between material properties to the selection of materials for engineering design.

Résumé—Nous passons en revue et nous relient entre elles les propriétés mécaniques et thermiques fondamentales des matériaux technologiques. Cette revue met en évidence le domaine des valeurs possibles de chaque propriété, et le sous-domaine associé à chaque classe de matériaux. Nous représentons ces domaines et les relations entre propriétés sur des cartes de propriétés des matériaux (dix d'entre elles sont présentées dans cet article). Ces diagrammes ont de nombreuses applications qui vont de l'identification d'une relation fondamentale entre les propriétés du matériau au choix des matériaux à vocation technologique.

Zusammenfassung—Die grundlegenden mechanischen und thermischen Eigenschaften von Konstruktionswerkstoffen werden zusammengestellt und miteinander verknüpft. Diese Zusammenstellung beschreibt die Spanne einer jeden Eigenschaft und die für jede Materialklasse typische (kleinere) Spanne. Diese Spannen und die Zusammenhänge zwischen den Eigenschaften werden in "Karten der Materialeigenschaften" dargestellt; 10 davon werden hier vorgelegt. Die Diagramme finden vielfältige Anwendung von der Identifizierung fundamentaler Beziehungen zwischen Materialeigenschaften bis zu der Auswahl von Werkstoffen für Konstruktionen.

SYMBOLS, DEFINITIONS AND UNITS

α	thermal diffusivity (m^2/s)
a_c	crack half-length (m)
A, B, C	dimensionless constants (—)
v	velocity (m/s)
c_p	electronic specific heat (J/kg K)
c_p	at constant pressure (J/kg K)
c_v	at constant volume (J/kg K)
E	modulus (GPa)
E_A	activation energy (GPa)
E_T	threshold energy (GPa)
F	force (GPa)
G	shear modulus (GPa)
G_A	apparent fracture surface energy (J/m^2)
h	heat transfer coefficient ($\text{J/m}^2 \text{K}$)
k	Boltzmann's constant (J/K)
K	bulk modulus (GPa)
K_{IC}	fracture toughness ($\text{MPa m}^{1/2}$)
l	mean free path (m)
r_a	atom size (m)
R	radius of pressure vessel (m)
S	bond stiffness (N/m)
t	thickness of section (m)
T	temperature (K)
T_m	melting point (K)
v	elastic wave velocity (m/s)
α	linear expansion coefficient (K^{-1})
η	damping coefficient (—)
γ	surface energy (J/m^2)
γ_G	Grüneisen's constant (—)
λ	thermal conductivity (W/mK)
ρ	density (Mg/m^3)

σ	stress (MPa)
σ_c	yield/crushing/tear strength (MPa)
σ_t	tensile yield/fracture strength (MPa)
ν	Poisson's ratio (—)

1. INTRODUCTION: MATERIAL PROPERTY CHARTS

Each property of an engineering material has a characteristic range of values. The range is enormous: of the ten properties considered here—properties such as modulus, toughness, thermal conductivity—all but one ranges through roughly 5 decades, reflecting the diversity in the atomic mechanisms which determine the value of the property.

It is conventional to classify the solids themselves into the six broad classes shown in Fig. 1—metals, polymers, elastomers, ceramics, glasses and composites. Within a class the range of properties is narrower, and the underlying mechanisms fewer. But classifications of this sort have their dangers, notably those of narrowing vision and of obscuring relationships. Here we aim at a broad review of engineering materials, examining the relationships between the properties of all six classes.

One way of doing this is by constructing *Material Property Charts*. The idea is illustrated by Fig. 2. One property (the modulus, E , in this case) is plotted

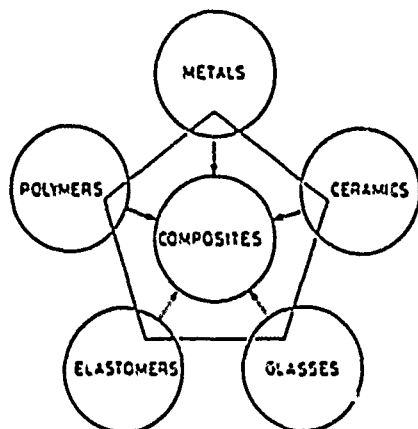


Fig. 1. The menu of engineering materials. Each class has properties which occupy a particular part (or "field") of the Materials Property Charts, which are the central feature of this paper

against another (the density, ρ) on logarithmic scales. The range of the axes is chosen to include all materials, from the lightest, flimsiest foams to the stiffest, heaviest metals. It is found that data for a given class of materials (polymers, for example) cluster together on the chart; the *subrange* associated with one material class is, in all cases, much smaller than the *full* range of that property. Data for one class can be enclosed in a property-envelope, as shown in Fig. 2. The envelope is constructed to enclose all members of the class.

All this is simple enough—no more than a way of displaying properties in a helpful way. But by choosing the axes and scales appropriately, more can be

added. The speed of sound in a solid depends on the modulus, E , and the density, ρ ; the longitudinal wave speed v , for instance, is

$$v = \left[\frac{E}{\rho} \right]^{1/2} \quad (1a)$$

or (taking logs)

$$\log E = \log \rho + 2 \log v \quad (1b)$$

For a fixed value of v , this equation plots as a straight line of slope 1 on Fig. 2. This allows us to add contours of *constant sound velocity* to the chart: they are the family of parallel diagonal lines, linking materials in which sound travels with the same velocity. All the charts allow additional fundamental relationships of this sort to be displayed

At the more applied end of the spectrum, the charts help in materials selection in engineering design. The performance, in an engineering sense, of load-bearing components is seldom limited by a single property but by one or more combinations of them. The lightest tie rod which will carry a given tensile load without exceeding a given deflection is that with the greatest value of E/ρ . The lightest column which will support a given compressive load without buckling is that with the greatest value of $E^{1/2}/\rho$. The lightest panel which will support a given pressure with minimum deflection is that with the greatest value of $E^{1/3}/\rho$. Figure 3 shows how the chart can be used to select materials which maximise any one of these combinations (1). The condition

$$\frac{E}{\rho} = C \quad (2a)$$

or, taking logs

$$\log E = \log \rho + \log C \quad (2b)$$

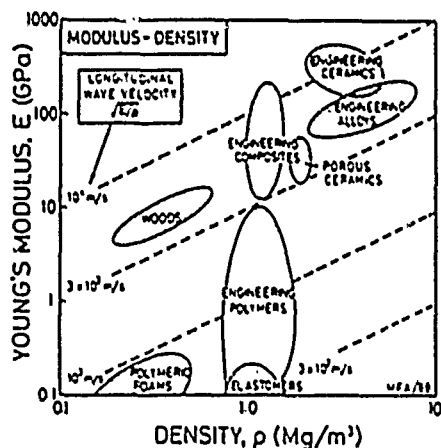


Fig. 2. The idea of a Materials Property Chart: Young's modulus, E , is plotted against the density, ρ , on log scales. Each class of material occupies a characteristic part of the chart. The log scales allow the longitudinal elastic wave velocity $v = (E/\rho)^{1/2}$ to be plotted as a set of parallel contours

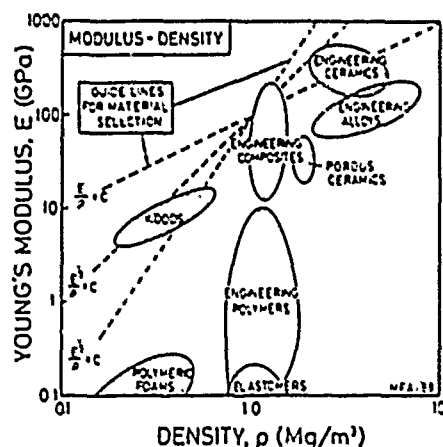


Fig. 3. The same diagram as Fig. 2 but showing guide lines for selecting materials for minimum weight design. Because of the log scales the lines are straight even though they describe non-linear relationships between the properties

is a family of straight lines of slope 1, one line for each value of the constant C . The condition

$$E^{1/2} p = C \quad (3)$$

gives a family with slope 2; and

$$\frac{E^{1/2}}{p} = C \quad (4)$$

gives another set with slope 3. One member of each family is shown on Fig. 3, labelled "Guide Lines for Material Selection". The others are found by translating the appropriate guide line sideways.

It is now easy to read off the subset of materials which are optimal for each loading geometry. If a straight-edge is laid parallel to the $E^{1/2} p = C$ line, all the materials which lie on the line will perform equally well as a light column loaded in compression; those above the line are better (they can withstand greater loads), those below, worse. If the straight-edge is translated towards the top left corner of the diagram while retaining the same slope, the choice narrows. At any given position of the edge, two materials which lie on it are equally good, and only those which remain above are better. The same procedure, applied to the line (E/p) or plate in bending $(E^{1/2}/p)$, lead to different equivalences and optimal subsets of materials. There are numerous such criteria for optimal materials selection, some of which are summarised in Fig. 4. All of these appear on one or another of the charts described below.

Among the mechanical and thermal properties, there are 10 which are of primary importance, both in characterising the material, and in engineering design. They are listed in Table 1: they include density, modulus, strength, toughness, thermal conductivity, diffusivity and expansion. The charts display data for these properties for the 9 classes of materials listed in Table 2. The class-list is expanded from the original 6 by distinguishing *engineering composites* from *foams* and from *woods* though all, in the most general sense, are composites; and by distinguishing the high-strength *engineering ceramics* (like silicon carbide) from the low strength, *porous ceramics* (like brick). Within each class, data are plotted for a representative set of materials, chosen both to span the full range of behaviour for the class, and to include the most common and most widely used members of it. In this way the envelope for a class encloses data not only for the materials listed in Table 2, but for virtually all other members of the class as well.

2. DATA AND DATA SOURCES

The data plotted on the charts shown below have been assembled over several years from a wide variety of sources. As far as possible, the data have been *calculated*: cross-checked by comparing values from more than one source, and they have been examined for consistency with physical rules. The charts show

a range of values for each property of each material. Sometimes the range is narrow: the modulus of a metal, for instance, varies by only a few percent about its mean value. Sometimes it is wide: the strength of a ceramic can vary by a factor of 100 or more. The reasons for the range of values vary: heat treatment and mechanical working have a profound effect on yield strength, damping and toughness of metals. Crystallinity and degree of cross-linking greatly influence the modulus of polymers. Grain size and porosity change considerably the fracture strength of ceramics. And so on. These *structure-sensitive* properties appear as elongated balloons within the envelopes on the charts. A balloon encloses a typical range for the value of the property for a single material. Envelopes (heavier lines) enclose the balloons for a class.

The framework of this study is one of maximum breadth at relatively low precision. In this context, a number of approximations are possible: that the shear modulus is roughly $1/3 E$, that the hardness is roughly 3σ , (where σ , is the yield strength), that the two specific heats C_p and C_v are (for solids) equal, and so forth. This allows us to deal with one modulus (Young's), one wave velocity (the longitudinal), and so on; the others are proportional to the one discussed here, and relationships, ranges and physical origins are the same.

Now to the data sources themselves. First, there are the standard handbooks: *The American Institute of Physics Handbook* [2]; the *Handbook of Physics and Chemistry* [3]; the *Landolt-Bornstein Tables* [4]; the *Materials Engineering "Materials Selector"* [5] and the *Fulmer Materials Optimiser* [6]. More specialised data can be found in the compilations by Simmons and Wang [7] for moduli, Lazan [8] for damping, Frost and Ashby [9] and the *Atlas of Creep and Stress Rupture Curves* [10] for strength at temperature, and in the major reference texts on specific materials such as the *ASM Metals Handbooks* [11] and Smithells [12] for metals, the *Handbook of Glass Properties* by Bansal and Doremus [13] for glasses, the *Handbook of Plastics and Elastomers* [14], the *International Plastics Selector* [15], the *Plastics Technology Handbook* of Chanda and Roy [16], and the *Handbook of Elastomers* of Bhowmick and Stephens, [17] for polymers, the *Handbook of Physical Constants* [18] for rocks and minerals, Creyke *et al.* [19] and Morrell [20] for ceramics, *Composites* [21] and the *Engineering Guide to Composite Materials* [22] for composites, Dinwoodie [23] for wood and wood products and Gibson and Ashby [24] for foams. Much of the data (particularly those for moduli, strength, toughness and thermal conductivity) are derived from scientific journals and conference proceedings, and from manufacturers data sheets for their products.

We now introduce charts which display the 10 properties and allow useful relationships between them to be explored.

MODE OF LOADING		MINIMISE WEIGHT FOR GIVEN			CHARTS 1, 2 AND 3		
		STIFFNESS	DUCTILE STRENGTH	BRITTLE STRENGTH			
TIE F, L SPECIFIED r FREE		E/a	σ/a	K/a			
TORSION BAR T, L SPECIFIED r FREE		G/a	σ/a	K/a			
TORSION TUBE T, L, r SPECIFIED i FREE		G/a	σ/a	K/a			
BENDING OF RODS AND TUBES F, L, r SPECIFIED i OR i FREE		E/a	σ/a	K/a			
BENDING OF COLUMN OR TUBE F, L, r SPECIFIED i OR i FREE		E/a	σ/a	K/a			
BENDING OF PLATE F, L, r SPECIFIED i FREE		E/a	σ/a	K/a			
BUCKLING OF PLATE F, L, r SPECIFIED i FREE		E/a	σ/a	K/a			
CYLINDER WITH INTERNAL PRESSURE P, L SPECIFIED r FREE		E/a	σ/a	K/a			
ROTATING CYLINDER M, L, r SPECIFIED i FREE		E/a	σ/a	K/a			
SPHERE WITH INTERNAL PRESSURE P, r SPECIFIED i FREE		E/a	σ/a	K/a			

Fig. 4 Some of the property-combinations which determine performance in design

ELASTIC DESIGN		OUTLET	
	SPRING OF MIN VOLUME	MAX σ_1/ϵ	ϵ
	SPRING OF MIN WEIGHT	MAX $\sigma_1/\rho\epsilon$	ϵ, ρ
	LINKAGE WITH NO EQUAL LOAD	MAX σ_1/ϵ	ϵ
	LINKAGE WITH JUNE LOAD	MAX σ_1/ϵ	ϵ
	KNIFE EDGES PIVOTS	MAX $\sigma_1/\epsilon, \rho$ AND ϵ	ϵ
	'POINT' OR 'LINE' CONTACT WITH MIN FRICTION LOSS		
PLASTIC AND FRACTURE-SAFE DESIGN			
	LOAD-CONTROLLED DESIGN	MAX K_1 AND σ_1	ϵ
	DISPLACEMENT CONTROLLED DESIGN	MAX K_1/ϵ AND σ_1/ϵ	ϵ, ρ
	YIELD BEFORE BREAK	MAX $K_1/\rho\epsilon$	ϵ
	LEAK BEFORE BREAK	MAX $K_1/\rho\epsilon$	ϵ
THERMAL DESIGN			
	THERMAL FLUX	MIN ΔT	ϵ
	MIN HEAT FLUX AT STEADY STATE	MIN $\Delta T/\epsilon$	ϵ
	THERMAL STRESS	MIN ΔT	ϵ
	MIN THERMAL STRESS	MIN $\Delta T/\epsilon$	ϵ

Table 1. Basic subset of material properties

Property	Units
Density, ρ	(Mg m^{-3})
Young's modulus, E	(GPa)
Strength, σ_s	(MPa)
Fracture toughness, K_{Ic}	($\text{MPa m}^{1/2}$)
Toughness, G_u	(J m^{-2})
Damping coefficient, η	(—)
Thermal conductivity, k	(W m K^{-1})
Thermal diffusivity, α	($\text{m}^2 \text{s}^{-1}$)
Volume specific heat, $C_p \rho$	($\text{J m}^{-3} \text{K}^{-1}$)
Thermal expansion coefficient, α	($1/\text{K}$)

3. THE MATERIAL-PROPERTY DIAGRAMS

3.1. The modulus–density chart (Chart 1, Fig. 5)

Modulus and density are among the most self-evident of material properties. Steel is used for stiff beams; rubber for compliant cushions. The density of lead makes it good for sinkers; that of cork makes it good for floats. Figure 5 shows the full range of Young's modulus, E , and density, ρ , for engineering materials.

Table 2. Material classes and members of each class

<i>Engineering alloys</i> (The metals and alloys of engineering)	Aluminium alloys Lead alloys Magnesium alloys Nickel alloys Steels Tin alloys Titanium alloys Zinc alloys	Al alloys Lead alloys Mg alloys Ni alloys Steels Tin alloys Ti alloys Zn alloys
<i>Engineering polymers</i> (The thermoplastics and thermosets of engineering)	Epoxies Melamines Polycarbonate Polyesters Polyethylene, high density Polyethylene, low density Polyformaldehyde Polymethylmethacrylate Polypropylene Polytetrafluorethylene Polyvinylchloride	EP MEL PC PEST HDPE LDPE PF PMMA PP PTFE PVC
<i>Engineering ceramics</i> (Fine ceramics capable of load-bearing application)	Alumina Diamond Sialons Silicon carbide Silicon nitride Zirconia	Al_2O_3 C Sialons SiC Si_3N_4 ZrO_2
<i>Engineering composites</i> (The composites of engineering practice. A distinction is drawn between the properties of a ply—"Uniply"—and of a laminate—"Laminates")	Carbon fibre reinforced polymer Glass fibre reinforced polymer Kevlar fibre reinforced polymer	CFRP GFRP KFRP
<i>Porous ceramics</i> (Traditional ceramics, cements, rocks and minerals)	Brick Cement Common rocks Concrete Porcelain Pottery	Brick Cement Rocks Concrete Pcln Pot
<i>Glasses</i> (Ordinary silicate glass)	Borosilicate glass Soda glass Silica	B-glass Na-glass SiO_2
<i>Woods</i> (Separate envelopes describe properties parallel to the grain and normal to it, and wood products)	Ash Balsa Fir Oak Pine Wood products (ply, etc)	Ash Balsa Fir Oak Pine Wood products
<i>Elastomers</i> (Natural and artificial rubbers)	Natural rubber Hard butyl rubber Polyurethanes Silicone rubber Soft butyl rubber	Rubber Hard butyl PU Silicone Soft butyl
<i>Polymer foams</i> (Foamed polymers of engineering)	These include: Cork Polyester Polystyrene Polyurethane	Cork PEST PS PU

characterised by a spring constant, S (units: N/m). Young's modulus, E , is roughly

$$E \approx \frac{S}{r_a} \quad (1)$$

where r_a is the atom size (r_a^3 is the (mean) atomic or ionic volume). The wide range of moduli is largely caused by the range of value of S . The covalent bond is stiff ($S = 20\text{--}200$ N/m); the metallic and the ionic a little less so ($S = 15\text{--}100$ N/m). Diamond has a very high modulus because the carbon atom is small (giving a high bond density) and its atoms are linked by very strong bonds ($S = 200$ N/m). Metals have high moduli because close-packing gives a high bond density and the bonds are strong. Polymers contain both strong covalent bonds and weak hydrogen or Van-der-Waals bonds ($S = 0.5\text{--}2$ N/m); it is the weak bonds which stretch when the polymer is deformed, giving low moduli.

But even large atoms ($r_a = 3 \times 10^{-10}$ m) bonded with weak bonds ($S = 0.5$ N/m) have a modulus of roughly

$$E \approx \frac{0.5}{3 \times 10^{-10}} \approx 1 \text{ GPa}. \quad (2)$$

This is the *lower limit* for true solids. The chart shows that many materials have moduli that are lower than this: they are either elastomers, or foams—materials made up of cells with a large fraction of pore space. Elastomers have a low E because the weak secondary bonds have melted (their glass temperature is below room temperature) leaving only the very weak "entropic" restoring force associated with tangled, long-chain molecules; and foams have low moduli because the cell walls bend (allowing large displacements) when the material is loaded.

The chart shows that the modulus of engineering materials spans 5 decades,† from 0.01 GPa (low density foams) to 1000 GPa (diamond); the density spans a factor of 2000, from less than 0.1 to 20 Mg/m³. At the level of approximation of interest here (that required to reveal the relationship between the properties of materials classes) we may approximate the shear modulus, G , by $3E/8$ and the bulk modulus, K , by E , for all materials except elastomers (for which $G = E/3$ and $K \gg E$).

The log-scales allow more information to be displayed. The velocity of elastic waves in a material, and the natural vibration frequencies of a component made of it, are proportional to $(E/\rho)^{1/2}$; the quantity $(E/\rho)^{1/2}$ itself is the velocity of longitudinal waves in a thin rod of the material. Contours of constant $(E/\rho)^{1/2}$ are plotted on the Chart, labelled with the longitudinal wave speed: it varies from less than

50 m/s (soft elastomers) to a little more than 10⁴ m/s (fine ceramics). We note that aluminium and glass, because of their low densities, transmit waves quickly despite their low moduli. One might have expected the sound velocity in foams to be low because of the low modulus, but the low density almost compensates. That in wood, across the grain, is low, but along the grain, it is high—roughly the same as steel—a fact made use of in the design of musical instruments.

The diagram helps in the common problem of material selection for applications in which weight must be minimised. Guide lines corresponding to three common geometries of loading are drawn on the diagram. They are used in the way described in Section 1 to select materials for elastic design at minimum weight.

3.2. The strength-density chart (Chart 2, Fig. 6)

The modulus of a solid is a well-defined quantity with a sharp value. The strength is not.

The word "strength" needs definition. For metals and polymers it is the *yield strength*, but since the range of materials includes those which have been worked, the range spans initial yield to ultimate strength; for most practical purposes it is the same in tension and compression. For brittle ceramics, it is the *crushing strength in compression*, not that in tension which is about 15 times smaller; the envelopes for brittle materials are shown as broken lines as a reminder of this. For elastomers, strength means the *tear strength*. For composites, it is the *tensile failure strength* (the compressive strength can be less, because of fibre buckling).

Figure 6 shows these strengths, for which we will use the symbol σ , (despite the different failure mechanisms involved), plotted against density, ρ . The considerable vertical extension of the strength-balloon for an individual material reflects its wide range, caused by degree of alloying, work hardening, grain size, porosity and so forth. As before, members of a class group together and can be enclosed in an envelope (heavy line). Each occupies a characteristic area of the chart, and, broadly speaking, encompasses not only the materials listed in Table 2, but most other members of the class also.

The range of strength for engineering materials, like that of the modulus, spans about 5 decades, from less than 0.1 MPa (foams, used in packaging and energy-absorbing systems) to 10⁴ MPa (the strength of diamond, exploited in the diamond-anvil press). The single most important concept in understanding this wide range is that of the *lattice resistance* or *Peterls stress*: the intrinsic resistance of the structure to plastic shear. Metals are soft and ceramics hard because the non-localised metallic bond does little to prevent dislocation motion, whereas the more localised covalent and ionic bonds of the ceramic (which must be broken and reformed when the structure is sheared) lock the dislocations in place. In

†Very low density foams and gels (which can be thought of as molecular-scale fluid filled foams) can have moduli far lower than this. As an example, gelatin (as in Jello) has a modulus of about 5×10^{-4} GPa. Their strengths and fracture toughness too, can be below the lower limit of the charts.

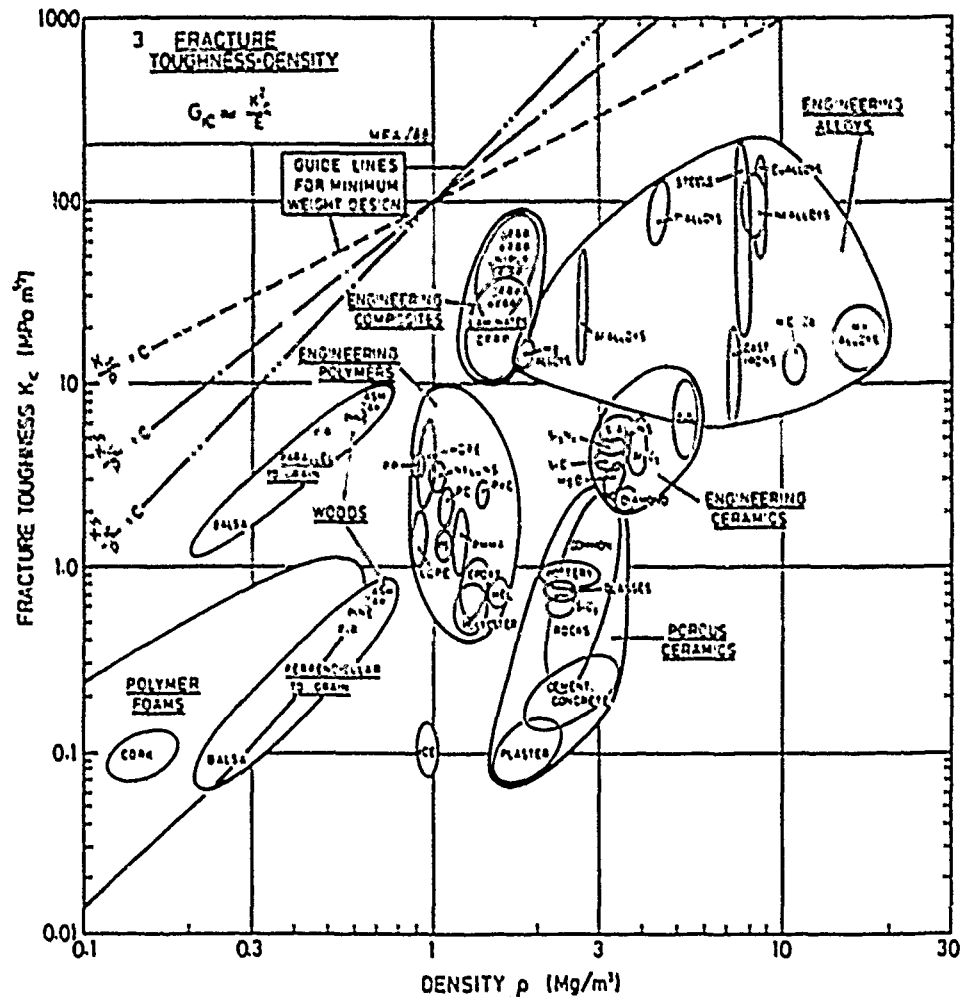


Fig. 7. Chart 3: Fracture toughness, K_{Ic} , plotted against density, ρ . The guide lines of constant K_{Ic}/ρ , $K_{Ic}^{2/3}/\rho$ and $K_{Ic}^{1/2}/\rho$ help in minimum weight, fracture-limited, design

fail by fast fracture. The resistance to the propagation of a crack is measured by the *fracture toughness*, K_{Ic} . It is plotted against density in Fig. 7. The range is large: from 0.01 to over 100 MPa m^{1/2}. At the lower end of this range are brittle materials which, when loaded, remain elastic until they fracture. For these, linear-elastic fracture mechanics works well, and the fracture toughness itself is a well-defined property. At the upper end lie the super-tough materials, most of which show substantial plasticity before they break. For these the values of K_{Ic} are approximate, derived from critical J -integral (J_c) and critical crack-opening displacement (δ_c) measurements [by writing $K_{Ic} = (EJ_c)^{1/2}$, for instance]. They are helpful in providing a ranking of materials. The figure shows one reason for the dominance of metals in engineering: they almost all have values of K_{Ic} above 20 MPa m^{1/2}, a value often quoted as a minimum for conventional design.

There are a number of fundamental points to be made about the fracture toughness, but they are best demonstrated with Charts 5 and 6, coming later. Here we simply note that minimum-weight design, when the design criterion is that of preventing brittle fracture from a flaw of given size, requires that K_{Ic}/ρ , $K_{Ic}^{2/3}/\rho$ or $K_{Ic}^{1/2}/\rho$ (depending on loading geometry) be maximised (see Fig. 4). Guide-lines corresponding to constant values of these parameters are plotted on the diagram. They are used as described in Section 1.

3.4. The modulus-strength chart (Chart 4, Fig. 8)

High-tensile steel makes good springs. But so does rubber. How is it that two such different materials are both suited for the same task? This and other questions are answered by Fig. 8, the most useful of all the charts.

It shows Young's modulus, E , plotted against strength, σ_y . The qualifications on "strength" are

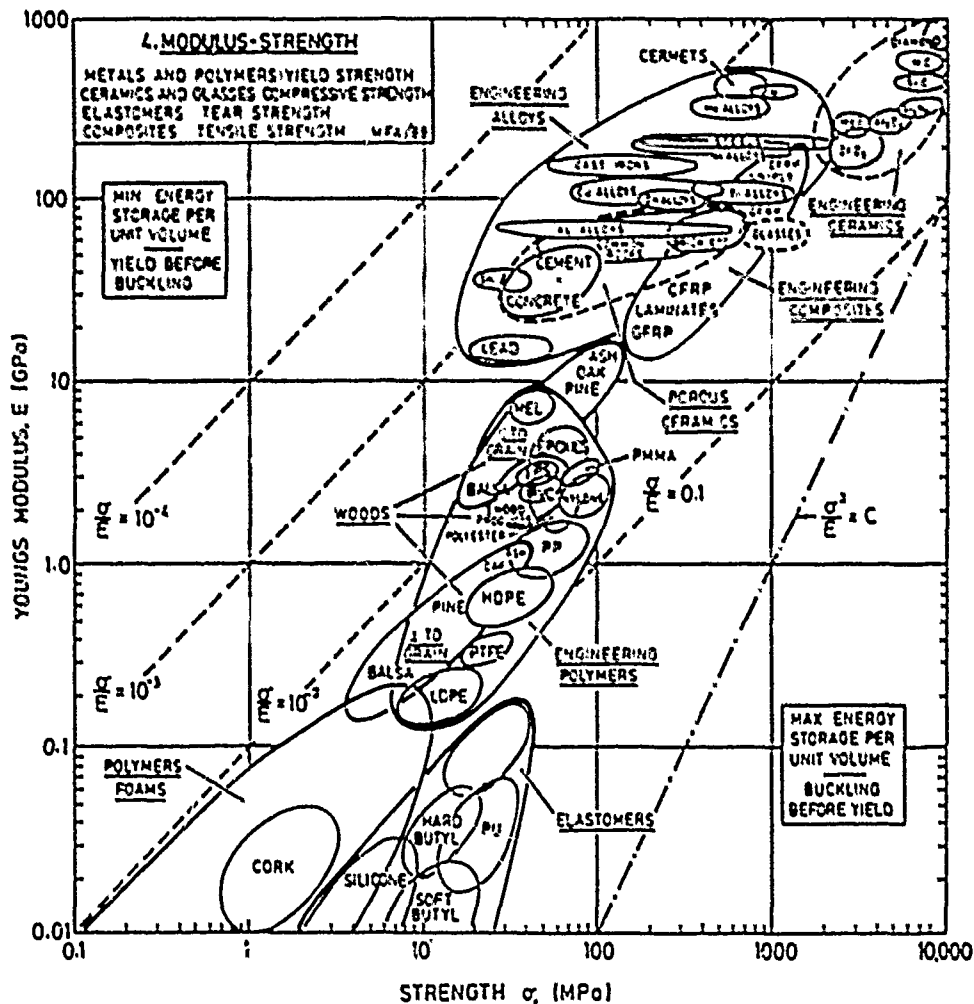


Fig. 8. Chart 4: Young's modulus, E , plotted against strength σ . The guide line of constant σ/E helps with the selection of materials for springs, pivots and knife-edges; those of constant σ, E with choosing materials for elastic hinges.

the same as before: it means yield strength for metals and polymers, compressive crushing strength for ceramics, tear strength for elastomers and tensile strength for composites and woods; the symbol σ , is used for them all. The ranges of the variables, too, are the same. Contours of *normalised strength*, σ/E , appear as a family of straight parallel lines.

Examine these first. Engineering polymers have normalised strengths between 0.01 and 0.1. In this sense they are remarkably strong: the value for metals are at least a factor of 10 smaller. Even ceramics, in compression, are not as strong, and in tension they are weaker (by a further factor of 15 or so). Composites and woods lie on the 0.01 contour, as good as the best metals. Elastomers, because of their exceptionally low moduli, have values of σ/E larger than any other class of material: 0.1 to 10.

The *ideal strength* of a solid is set by the range of interatomic forces. It is small—a bond is broken if it is stretched by more than 10% or so. So the force needed to break a bond is roughly

$$F = \frac{S r_0}{10}$$

where S is the bond stiffness (Section 3.1). If shear *breaks* bonds, the strength of a solid should be roughly

$$\sigma_s \approx \frac{F}{r_0^2} = \frac{S}{10 r_0} = \frac{E}{10} \quad (4)$$

The chart shows that, for some polymers, it is. Most solids are weaker, for two reasons.

First, non-localised bonds (those in which the cohesive energy derives from the interaction of one atom with large number of others, not just with its

nearest neighbours) are not broken when the structure is sheared. The metallic bond, and the ionic bond for certain directions of shear, are like this, very pure metals, for example, yield at stresses as low as $E/10,000$, and strengthening mechanisms (Section 3.2) are needed to raise the strength. The covalent bond is localised; and covalent solids do, for this reason, have yield strength which, at low temperatures, are as high as $E/10$. It is hard to measure them (though it can sometimes be done by indentation) because of the second reason for weakness: they generally contain defects—concentrators of stress—from which shear or fracture can propagate, often at stresses well below the "ideal" $E/10$. Elastomers are anomalous (they have strengths of about E) because the modulus does not derive from bond-stretching, but from the change in entropy of the tangled molecular chains when the material is deformed.

In the design of columns and beams, the ratio σ_y/E often appears. Structures which have a high value of σ_y/E will deflect or buckle before they yield; those with low σ_y/E do the opposite. The best materials for an elastic hinge (a thin web or ligament that bends elastically, forming the hinge of a box or container, for example) are those with the maximum value of σ_y/E : the diagram immediately identifies them as elastomers and certain polymers (the polyethylenes, for example).

Finally, to return to springs. The best material for a spring is that with the greatest value of σ_y^2/E (because it stores the most elastic energy per unit volume, $\frac{1}{2}\sigma^2/E$, before it yields). A guide-line corresponding to the condition

$$\frac{\sigma_y^2}{E} = C$$

is plotted on the diagram; it, or any line parallel to it, links materials that are equally good by this criterion. If such a line is drawn through the middle of the elastomers, it just touches spring steel. Ceramics must be rejected because they are weaker, by the factor of 15, in tension, but glass, which can be made defect-free, makes good springs. Slightly further to the right lie CFRP and GFRP. All are good for springs.

3.5. The fracture toughness-modulus chart (Chart 5, Fig. 9)

The fracture toughnesses of most polymers are less than those of most ceramics. Yet polymers are widely used in engineering structures, ceramics, because they are "brittle", are treated with much more caution. Figure 9 helps resolve this apparent anomaly. It shows the fracture toughness, K_{Ic} , plotted against Young's modulus, E . The restrictions described in Section 3.3 apply to the values of K_{Ic} , when small, they are well defined, when large, they are useful only as a ranking for material selection.

Consider first the question of the necessary condition for fracture. It is that sufficient external work be done, or elastic energy released, to supply the true surface energy (2 γ per unit area) of the two new surfaces which are created. We write this as

$$G \geq 2\gamma \quad (5)$$

where G is the energy release-rate. Using the standard relation $K \approx (\pi EG)^{1/2}$ between G and stress intensity K , we find

$$K \geq (2E\gamma)^{1/2} \quad (6)$$

Now the surface energies, γ , of solid materials scale as their moduli, to an adequate approximation $\gamma = E\epsilon_0/20$, where ϵ_0 is the atom size, giving

$$K \geq E \left[\frac{\epsilon_0}{20} \right]^{1/2} \quad (7)$$

We identify the right-hand side of this equation with a lower-limiting value of K_{Ic} , when, taking ϵ_0 as 2×10^{-10} m,

$$\frac{K_{Ic}}{E} \min \approx \left[\frac{\epsilon_0}{20} \right]^{1/2} \approx 3 \times 10^{-6} \text{ m}^{1/2}$$

This criterion is plotted on the chart as a shaded, diagonal band near the lower right corner (the width of the band reflects a realistic range of ϵ_0 and of the constant C in $\gamma = E\epsilon_0 C$). It defines a lower limit on values of K_{Ic} ; it cannot be less than this unless some other source of energy (such as a chemical reaction, or the release of elastic energy stored in the special dislocation structures caused by fatigue loading) is available, when it is given a new symbol such as $(K_{Ic})_{\text{eff}}$. We note that the most brittle ceramics lie close to the threshold: when they fracture, the energy absorbed is only slightly more than the surface energy. With metals and polymers the energy absorbed by fracture is vastly greater, almost always because of *plasticity* associated with crack propagation. We come to this in a moment, with the next chart.

Plotted on Fig. 9 are contours of toughness, G_{Ic} , a measure of the apparent fracture surface-energy ($G_{Ic} \approx K_{Ic}^2/E$). The true surface energies, γ , of solids lie in the range 10^{-4} to 10^{-3} kJ/m². The diagram shows that the values of the toughness start at 10^{-3} kJ/m² and range through almost six decades to 10^3 kJ/m². On this scale, ceramics are low (10^{-1} – 10^1 kJ/m²), much lower than polymers (10^{-1} – 10^3 kJ/m²)—and this is part of the reason that design with polymers is easier than with ceramics. This is not to say that engineering design relies purely on G_{Ic} ; it is more complicated than that. When the modulus is high, deflections are small. Then designers are concerned about the loads the structure can support. In load-limited design, the fracture toughness, K_{Ic} , is what matters. It determines, for a given crack length, the stress the structure can support. Experience shows that a value of K_{Ic} above about

requires that the structure will yield before it breaks. If the minimum detectable crack size is $2a_c$, then this condition can be expressed as

$$\frac{K_{Ic}}{\sigma_y} \geq \sqrt{\pi a_c} \quad (12)$$

The safest material is the one with the greatest value of K_{Ic}/σ_y ; it will tolerate the longest crack. But, though safe, it may not be efficient. The section required to carry the load decreases as σ_y increases. We want high K_{Ic} , σ_y , and high σ_y . The reader may wish to plot two lines onto the figure, isolating the material which best satisfies both criteria at once: it is steel. It is this which gives steel its pre-eminence as the material for highly stressed structures when weight is not important.

One such structure is the pressure vessel. Here safe design requires that the vessel leaks before it breaks; leakage is not catastrophic, fast fracture is. To ensure this, the vessel must tolerate a crack of length, $2a_c$, equal to the wall thickness t , and this leads to a different criterion for materials selection. From the last equation, the leak-before-break criterion is

$$\frac{K_{Ic}^2}{\sigma_y} \geq \pi t.$$

But the pressure, p , that the vessel can support is limited by yield, so that, for a thin walled cylindrical vessel of radius R ,

$$\frac{pR}{t} \leq \sigma_y.$$

Substituting for t gives

$$p \leq \frac{1}{\pi R} \left[\frac{K_{Ic}^2}{\sigma_y} \right].$$

The greatest pressure is earned by the vessel with the largest value of K_{Ic}^2/σ_y . A guide line of K_{Ic}^2/σ_y is shown on the chart. It, and the yield-before-break line, are used in the way described in Section 1. Again, steel and copper are optimal.

3.7. The loss coefficient—modulus chart (Chart 7, Fig. 11)

Bells, traditionally, are made of bronze. They can be (and sometimes are) made of glass; and they could (if you could afford it) be made of silicon carbide. Metals, glasses and ceramics all, under the right circumstances, have low intrinsic damping, or "internal friction", an important material property when structures vibrate. We measure intrinsic damping by the loss coefficient, η , which is plotted in Fig. 11. Other measures include the specific damping capacity D/U (the energy D dissipated per cycle of vibrational energy U), the log decrement, Δ (the log of the ratio of successive amplitudes), the phase lag, δ , between stress and strain and the resonance factor, Q . When the damping is small ($\eta < 0.01$) these measures are related by

$$\eta = \frac{D}{2\pi U} = \frac{\Delta}{\pi} = \tan \delta = \frac{1}{Q} \quad (13)$$

but when the damping is large, the definitions are no longer equivalent. Large η 's are best measured by recording a symmetric load cycle and dividing the area of the stress-strain loop by 2π times the peak energy stored.

There are many mechanisms of intrinsic damping and hysteresis. Some (the "damping" mechanisms) are associated with a process that has a specific time constant, then the energy loss is centred about a characteristic frequency. Others (the "hysteresis" mechanisms) are associated with time-independent mechanisms, and absorb energy at all frequencies.

One damping mechanism, common to all materials, is a thermoelastic effect. A suddenly-applied tensile stress causes a true solid to cool slightly as it expands (elastomers are not true solids, and show the opposite effect). As it warms back to its initial temperature it expands further, giving additional strain that lags behind the stress. The anisotropy of moduli means that a polycrystal, even when uniformly loaded, shows a thermoelastic damping because neighbouring grains distort—and thus cool—by differing amounts. The damping is proportional to the difference between the adiabatic modulus, E_A , and that measured at constant temperature, E_T . A thermodynamic analysis (e.g. [24]) shows that

$$\eta = C \frac{E_A - E_T}{E_T} = \frac{CT\alpha^2 E_T}{\rho C_p} \quad (14)$$

where α is the coefficient of linear thermal expansion, C_p the specific heat, T the temperature and C a constant. This leads to the shaded line on the Chart marked "thermal damping". Single crystals and glasses lie below the line, because, when loaded uniformly, no temperature gradients exist.

The loss coefficient of most materials is far higher than this. In metals a large part of the loss is hysteretic, caused by dislocation movement: it is high in soft metals like lead and aluminium, but heavily alloyed metals like bronze, and high-carbon steels have low loss because the solute pins the dislocations. Exceptionally high loss is found in the Mn-Cu alloys, because of a strain-induced martensite transformation, and in magnesium, perhaps because of reversible twinning. The elongated balloons for metals span the large range accessible by alloying and working. Engineering ceramics have low damping because the enormous lattice resistance (Section 3.2) pins dislocations in place at room temperature. Porous ceramics, on the other hand, are filled with cracks, the surfaces of which rub, dissipating energy, when the material is loaded, the high damping of some cast irons has a similar origin. In polymers, chain segments slide against each other when loaded, the relative motion lowers the compliance and dissipates energy. The ease with which they slide depends on the ratio of the temperature (in this case, room

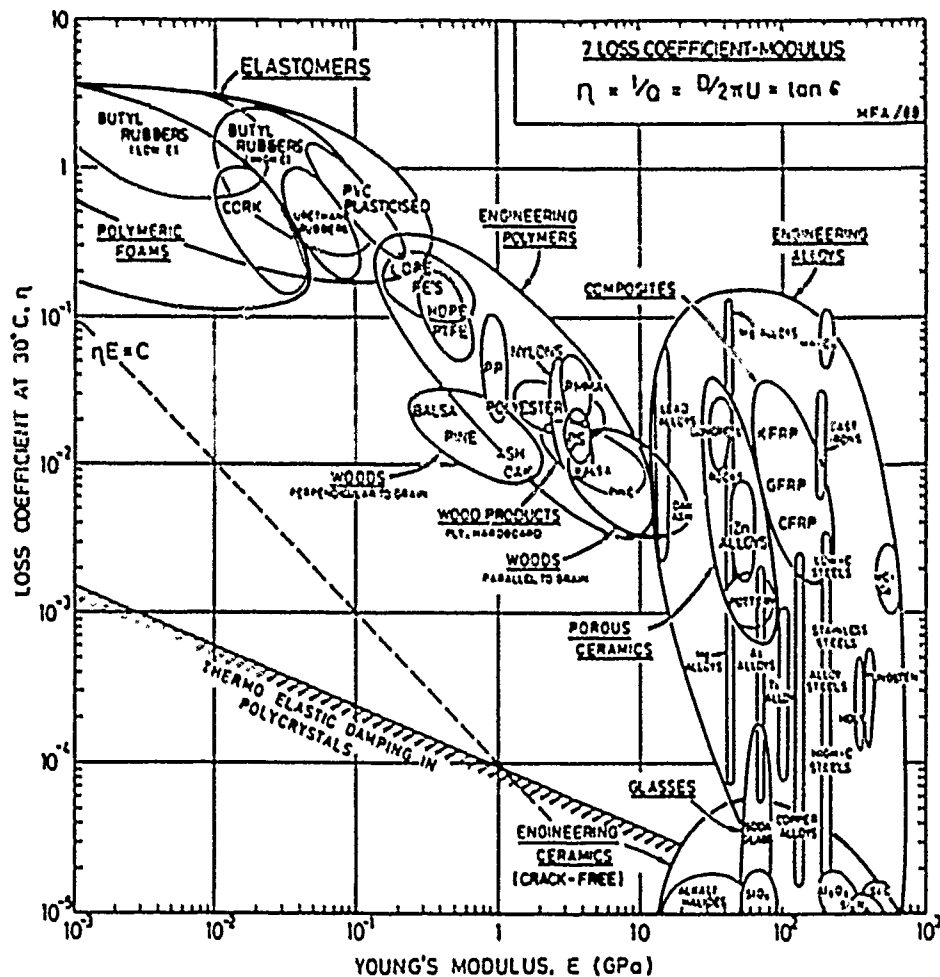


Fig. 11. Chart 7. The loss coefficient, η , plotted against Young's modulus, E , the guide-line corresponds to the condition $\eta = C/E$.

temperature) to the glass temperature, T_g , of the polymer. When $T/T_g < 1$, the secondary bonds are "frozen", the modulus is high and the damping is relatively low. When $T/T_g > 1$, the secondary bonds have melted, allowing easy chain slippage: the modulus is low and the damping is high. This accounts for the obvious inverse dependence of η on E for polymers in Fig. 11; indeed, to a first approximation

$$\eta = \frac{4 \times 10^{-2}}{E} \quad (15)$$

with E in GPa.

3.8. The thermal conductivity-thermal diffusivity chart (Chart 8, Fig. 12)

The material property governing the flow of heat through a material at steady state is the *thermal conductivity*, λ (units: J/mK); that governing transient heat flow is the *thermal diffusivity*, a (units: m²/s). They are related by

$$a \approx \frac{\lambda}{\rho C_p} \quad (16)$$

where ρ is the density and C_p the specific heat, measured in J/kg·K; the quantity ρC_p is the *volumetric specific heat*. Figure 12 relates conductivity, diffusivity and volumetric specific heat, at room temperature.

The data span almost 5 decades in λ and a . Solid materials are strung out along the line

$$\rho C_p \approx 3 \times 10^6 \text{ J/m}^3 \text{ K} \quad (17)$$

This can be understood by noting that a solid containing N atoms has $3N$ vibrational modes. Each (in the classical approximation) absorbs thermal energy kT at the absolute temperature T , and the vibrational specific heat is $C_p \approx C_v = 3Nk$ (J/K) where k is Boltzmann's constant. The volume per atom, Ω , for almost all solids lies within a factor of two of $2 \times 10^{-29} \text{ m}^3$, so the volume of N atoms is

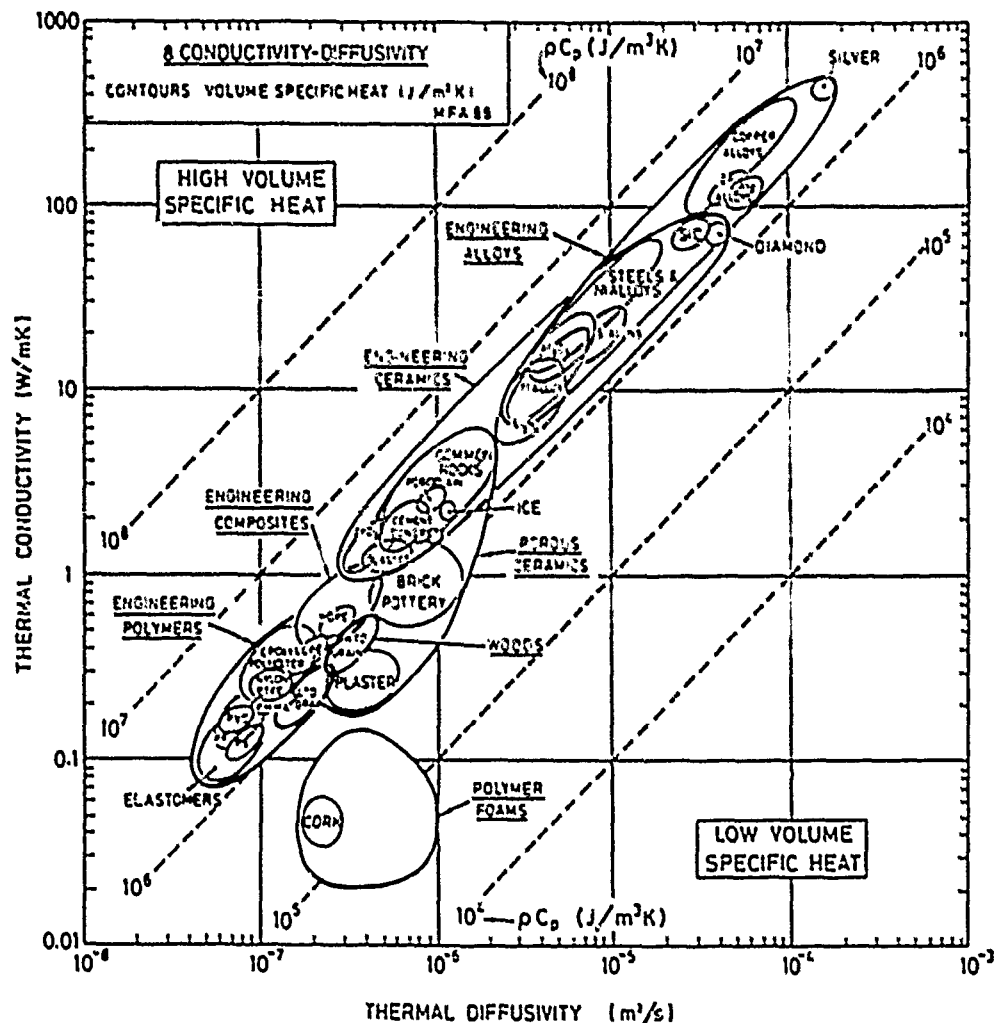


Fig. 12. Chart 5: Thermal conductivity, λ , plotted against thermal diffusivity, α ; the contours show the volume specific heat, ρC_p . All three properties vary with temperature; the data here are for room temperature.

2×10^{-23} N. The volume specific heat is then (as the Chart shows)

$$\rho C_p = 3Nk/N\Omega = 3k/\Omega = 3 \times 10^4 \text{ J/m}^3 \text{ K}. \quad (18)$$

For solids, C_p and C_v differ very little; at the level of approximation of this paper we assume them to be equal. As a general rule, then

$$\lambda = 3 \times 10^4 \alpha$$

(λ in J/mK and α in m^2/s). Some materials deviate from this rule: they have lower-than-average volumetric specific heat. A few, like diamond, are low because their Debye temperatures lie well above room temperature; then heat absorption is not classical, some modes do not absorb kT and the specific heat is less than $3Nk$. The largest deviations are shown by porous solids: foams, low density firebrick, woods and so on. Their low density means that they contain

fewer atoms per unit volume and, averaged over the volume of the structure, ρC_p is low. The result is that, although foams have low conductivities (and are widely used for insulation because of this) their thermal diffusivities are not low: they may not transmit much heat, but they reach a steady state quickly.

The range of λ and of α reflect the mechanisms of heat transfer in each class of solid. Electrons conduct the heat in pure metals such as copper, silver and aluminium (top right of chart). The conductivity is described by

$$\lambda = \frac{1}{3} C_v \bar{v} l \quad (19)$$

where C_v is the electron specific heat per unit volume, \bar{v} is the electron velocity (2×10^6 m/s) and l the electron mean free path, typically 10^{-7} m in pure metals. In solid solution (steels, nickel-based and titanium alloys) the foreign atoms scatter electrons,

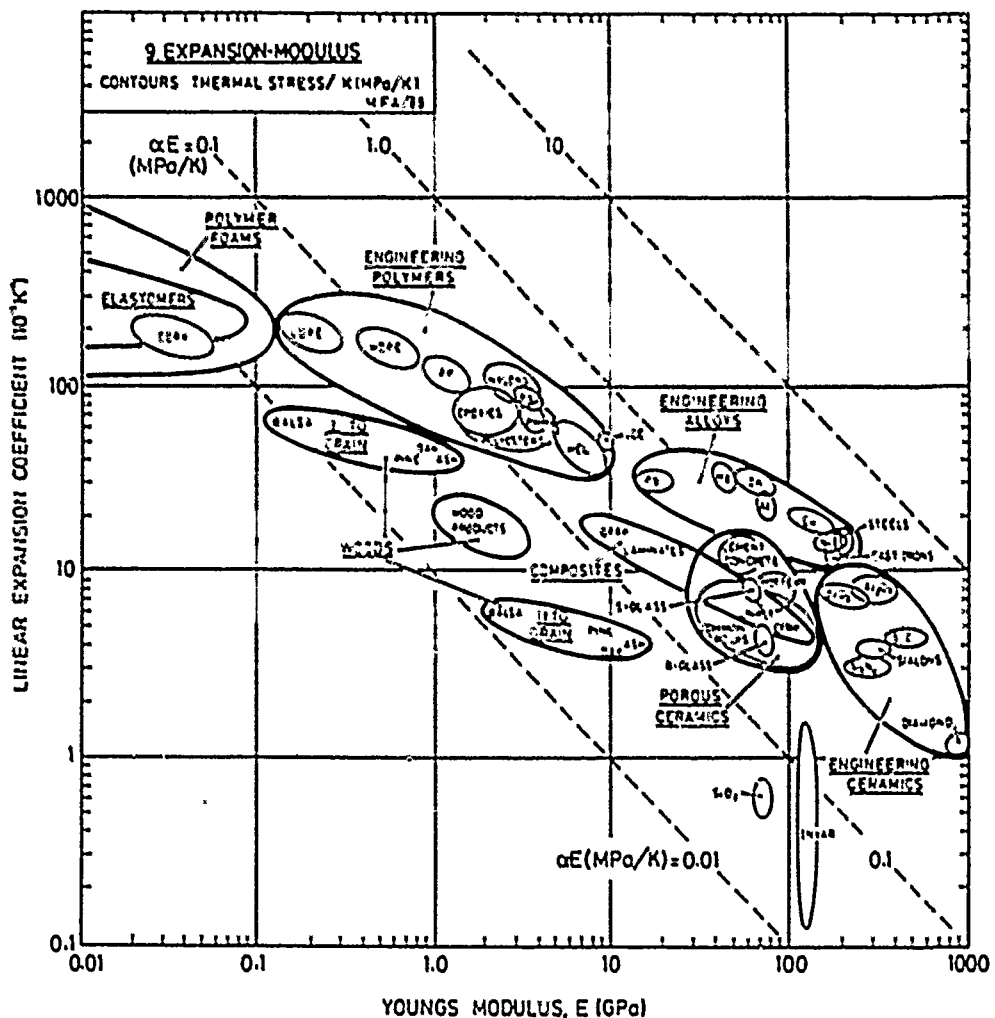


Fig. 13. Chart 9: The linear expansion coefficient, α , plotted against Young's modulus, E . The contours show the thermal stress created by a temperature change of 1°C if the sample is axially constrained. A correction factor C is applied for biaxial or triaxial constraint (see text)

reducing the mean free path to atomic dimensions ($\approx 10^{-10}$ m), much reducing λ and α .

Electrons do not contribute to conduction in ceramics and polymers. Heat is carried by phonons—lattice vibrations of short wavelength. They are scattered by each other (through an anharmonic interaction) and by impurities, lattice defects and surfaces; it is these which determine the phonon mean free path, l . The conductivity is still given by equation (19) which we write as

$$\lambda = \frac{1}{3} \rho C_p \bar{c} l \quad (20)$$

but now \bar{c} is the elastic wave speed (around 10^4 m/s—see Chart 1) and ρC_p is the volumetric specific heat. If the crystal is particularly perfect, and the temperature is well below the Debye temperature, as in diamond at room temperature, the phonon conductivity is high: it is for this reason that single crystal

diamond, silicon carbide, and even alumina have conductivities almost as high as copper. The low conductivity of glass is caused by its irregular amorphous structure: the characteristic length of the molecular linkages (about 10^{-8} m) determines the mean free path. Polymers have low conductivities because the elastic wave speed \bar{c} is low (Chart 1), and the mean free path in the disordered structure is small.

The best insulators are highly porous materials like firebrick, cork and foams. Their conductivity is limited by that of the gas in their cells, and (in very low density polymer foams) by heat transfer by radiation through the transparent cell walls.

3.9. The thermal expansion-modulus chart (Chart 9, Fig. 13)

Almost all solids expand on heating. The bond between a pair of atoms behaves like a linear-elastic

spring when the relative displacement of the atoms is small; but when it is large, the spring is non-linear. Most bonds become stiffer when the atoms are pushed together, and less stiff when they are pulled apart. The thermal vibration of atoms, even at room temperature, involves large displacements; as the temperature is raised, the non-linear spring constant of the bond pushes the atoms apart, increasing their mean spacing. The effect is measured by the *linear expansion coefficient*

$$\alpha = \frac{1}{l} \frac{dl}{dT} \quad (21)$$

where l is a linear dimension of the body. A quantitative development of this theory leads to the relation

$$\alpha = \frac{\gamma_0 \rho C}{3E} \quad (22)$$

where γ_0 is Grüneisen's constant, its value ranges between about 0.4 and 4, but for most solids it is near 1. Since ρC is almost constant [equation (18)], the equation tells us that α is proportional to $1/E$. Figure 13 shows that this is so. Diamond, with the highest modulus, has one of the lowest coefficients of expansion; elastomers with the lowest moduli expand the most. Some materials with a low coordination number (silica, and some diamond-cubic or zinc-blende structured materials) can absorb energy preferentially in transverse modes, leading to a very small (even a negative) value of γ_0 and a low expansion coefficient—that is why SiO_2 is exceptional. Others, like Invar, contract as they lose their ferromagnetism when heated through the Curie temperature and, over a narrow range of temperature, show near-zero expansion, useful in precision equipment and in glass-metal seals.

One more useful fact: the moduli of materials scale approximately with their melting point, T_m (see, for example, Ref. [9])

$$E \approx \frac{100 k T_m}{\Omega} \quad (23)$$

where k is Boltzmann's constant and Ω the volume-per-atom in the structure. Substituting this and equation (18) for ρC , into equation (22) for α gives

$$\alpha = \frac{\gamma_0}{100 T_m} \quad (24)$$

—the expansion coefficient varies inversely with the melting point, or (equivalently stated), for all solids the thermal strain, just before they melt, is the same. The result is useful for estimating and checking expansion coefficients.

Whenever the thermal expansion or contraction of a body is prevented, thermal stresses appear; if large enough, they cause yielding, fracture, or elastic collapse (buckling). It is common to distinguish between thermal stress caused by external constraint (a rod, rigidly clamped at both ends, for example) and that which appears without external constraint because of

temperature gradients in the body. All scale as the quantity αE , shown as a set of diagonal contours on Fig. 13. More precisely, the stress $\Delta\sigma$ produced by a temperature change of 1°C in a constrained system, or the stress per $^\circ\text{C}$ caused by a sudden change of surface temperature in one which is not constrained, is given by

$$C\Delta\sigma = \alpha E \quad (25)$$

where $C = 1$ for axial constraint ($1 - \nu$), for biaxial constraint or normal quenching, and $(1 - 2\nu)$ for triaxial constraint, where ν is Poisson's ratio. These stresses are large: typically 1 MPa/°C. They can cause a material to yield, or crack, or spall, or buckle, when it is suddenly heated or cooled. The resistance of materials to such damage is the subject of the next section.

3.10. The normalised strength—thermal expansion chart (Chart 10, Fig. 14)

When a cold ice-cube is dropped into a glass of gin, it cracks audibly. The ice is failing by thermal shock. The ability of a material to withstand such stresses is measured by its *thermal shock resistance*. It depends on its thermal expansion coefficient, α , and its normalised strength, σ_c/E . They are the axes of Fig. 14, on which contours of constant $\sigma_c/\alpha E$ are plotted. The tensile strength, σ_c , requires definition, just as σ , did. For brittle solids, it is the tensile fracture strength (roughly equal to the modulus of rupture, or MOR). For ductile metals and polymers, it is the tensile yield strength; and for composites it is the stress which first causes permanent damage in the form of delamination, matrix cracking or fibre debonding.

To use the chart, we note that a temperature change of ΔT , applied to a constrained body—or a sudden change ΔT of the surface temperature of a body which is unconstrained—induces a stress

$$\sigma = \frac{E\alpha\Delta T}{C} \quad (26)$$

where C was defined in the last section. If this stress exceeds the local strength σ_c of the material, yielding or cracking results. Even if it does not cause the component to fail, it weakens it. Then a measure of the thermal shock resistance is given by

$$\frac{\Delta T}{C} = \frac{\sigma_c}{\alpha E} \quad (27)$$

This is not quite the whole story. When the constraint is internal, the thermal conductivity of the material becomes important. Instant cooling requires an infinite heat transfer coefficient, h , when the body is quenched. Water quenching gives a high h , and then the values of ΔT calculated from equation (27) give an approximate ranking of thermal shock resistance. But when heat transfer at the surface is poor and the thermal conductivity of the solid is high (thereby reducing thermal gradients) the thermal stress is less than that given by equation (26) by a

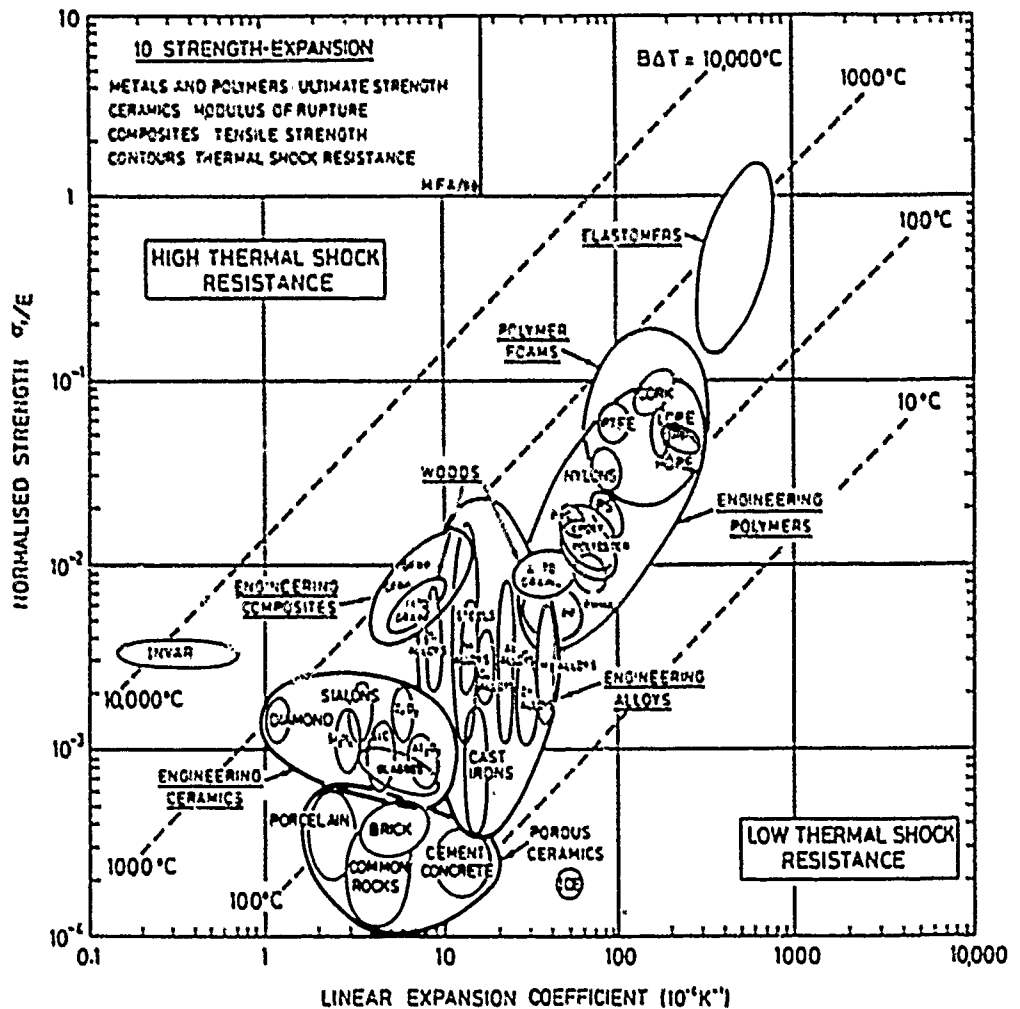


Fig. 14. Chart 10: The normalised tensile strength, σ/E , plotted against linear coefficient of expansion, α . The contours show a measure of the thermal shock resistance, ΔT . Corrections must be applied for constraint, and to allow for thermal conduction during quenching.

factor A which, to an adequate approximation, is given by

$$A = \frac{th/\lambda}{1 + th/\lambda} \quad (28)$$

where t is a typical dimension of the sample in the direction of heat flow, the quantity th/λ is usually

called the Biot modulus. Table 3 gives typical values of A , for each class, using a section size of 10 mm.

The equation defining the thermal shock resistance, ΔT , now becomes

$$\Delta T = \frac{\sigma_t}{\alpha E} \quad (29)$$

Table 3 Values of the factor A (Section $t = 10$ mm)

Conditions	Foams	Polymers	Ceramics	Metals
Air flow, slow ($h = 10 \text{ W/m}^2 \text{ K}$)	0.75	0.5	3×10^{-2}	3×10^{-3}
Black body radiation 500 to 0°C ($h = 40 \text{ W/m}^2 \text{ K}$)	0.93	0.6	0.12	1.3×10^{-2}
Air flow, fast ($h = 10^3 \text{ W/m}^2 \text{ K}$)	1	0.75	0.25	3×10^{-2}
Water quench, slow ($h = 10^4 \text{ W/m}^2 \text{ K}$)	1	1	0.75	0.23
Water quench, fast ($h = 10^5 \text{ W/m}^2 \text{ K}$)	1	1	1	0.1-0.9

where $B = C/A$. The contours on the diagram are of $B \Delta T$. The table shows that, for rapid quenching, A is unity for all materials except the high conductivity metals; then the thermal shock resistance is simply read from the contours, with appropriate correction for the constraint (the factor C). For slower quenches, ΔT is larger by the factor $1/A$, read from the table.

4. CONCLUSIONS AND APPLICATIONS

Most research on materials concerns itself, quite properly, with precision and detail. But it is occasionally helpful to stand back and view, as it were, the general lie of the land; to seek a framework into which the parts can be fitted; and when they do not fit, to examine the interesting exceptions. These charts are an attempt to do this for the mechanical and thermal properties of materials. There is nothing new in them except the mode of presentation, which summarises information in a compact, accessible way. The logarithmic scales are wide—wide enough to include materials as diverse as polymer foams and high performance ceramics—allowing a comparison between the properties of all classes of solid. And by choosing the axes in a sensible way, more information can be displayed: a chart of modulus E against density ρ reveals the longitudinal wave velocity $(E/\rho)^{1/2}$; a plot of fracture toughness K_{IC} against modulus E shows the fracture surface energy G_{IC} ; a diagram of thermal conductivity λ against diffusivity, α , also gives the volume specific heat ρC_v ; expansion, α , against normalised strength, σ_1/E , gives thermal shock resistance ΔT .

The most striking feature of the charts is the way in which members of a material class cluster together. Despite the wide range of modulus and density associated with metals (as an example), they occupy a field which is distinct from that of polymers, or that of ceramics, or that of composites. The same is true of strength, toughness, thermal conductivity and the rest: the fields sometimes overlap, but they always have a characteristic place within the whole picture. The position of the fields and their relationship can be understood in simple physical terms: the nature of the bonding, the packing density, the lattice resistance and the vibrational modes of the structure (themselves a function of bonding and packing), and so forth. It may seem odd that so little mention has been made of microstructure in determining properties. But the charts clearly show that the first-order difference between the properties of materials has its origins in the mass of the atoms, the nature of the interatomic forces and the geometry of packing. Alloying, heat treatment and mechanical working all influence microstructure, and through this, properties, giving the elongated balloons shown on many of the charts; but the magnitude of their effect is less, by factors of 10, than that of bonding and structure.

The charts have other applications. One is the checking of data. Computers consume data; their

output is no better than their input; garbage in (it is often said), garbage out. That creates a need for *data validation*, ways of checking that the value assigned to a material property is reasonable, that it lies within the expected field of values. The charts define the limits of the fields. A value, if it lies within the field, is reasonable; if it lies outside it may not be wrong, but it is exceptional and should, perhaps, be questioned.

Another concerns the nature of data. The charts (this is not meant to sound profound) are a section through a multi-dimensional property-space. Each material occupies a small volume in this space; classes of material occupy a somewhat larger volume. If data for a material (a new polymer, for instance) lie outside its characteristic volume, then the material is, in some sense, novel. The physical basis of the property deserves investigation and explanation.

There is another facet to this, that of "the new material looking for an application". Established materials have applications; they are known. The first-order approach to identifying applications for a new material is to plot its position on charts and examine its environment, is it lighter, or stiffer, or stronger than its neighbours? Does it have a better value of a design-limiting combination like σ_1/E than they? Then it may compete in the applications they currently enjoy.

Finally, the charts help in problems of materials selection. In the early stages of the design of a component or structure, *all* materials should be considered; failure to do so may mean a missed opportunity for innovation or improvement. The number of materials available to the engineer is enormous (estimates range from 30,000 to 80,000). But any design is limited by certain material properties—by stiffness E or strength σ_1 , for instance, or by combinations such as $E^{1/2}/\rho$ or K_{IC}/σ_1 . These *design-limiting properties* are precisely those used as the axes of the charts, or the "guide lines" plotted on them. By following the procedures of Section 1, a subset of materials is isolated which best satisfies the primary demands made by the design; secondary constraints then narrow the choice to one or a few possibilities (examples in Refs [1] and [24]).

A final word. Every effort has been made to include in the charts a truly representative range of materials; to find reliable data for them; and to draw the envelopes to enclose all reasonably common members of a class to which they belong (not just those specifically listed). I am aware that the charts must still be imperfect, and hope that anyone with better information will extend them.

Acknowledgements—Many colleagues have been generous with experience, suggestions and advice. I particularly wish to thank Dr L. M. Brown and Dr J. Woodhouse of Cambridge University. I also wish to acknowledge the influence of Professor A. H. Cottrell, whose book *Mechanical Properties of Matter* (Wiley, 1964), though not referenced here, has been the driving force behind this paper.

REFERENCES

1. M. F. Ashby, Materials Selection in Mechanical Design In *Materials Engineering and Design, Proc Conf "Materials '88"*, Institute of Metals, London (1988)
2. American Institute of Physics Handbook, 3rd edn McGraw-Hill, New York (1972)
3. *Handbook of Chemistry and Physics*, 52nd edn Chemical Rubber, Cleveland, Ohio (1971)
4. *Landolt-Bornstein Tables* Springer, Berlin (1966)
5. *Materials Engineering Materials Selection*, Pantan, Cleveland, Ohio (1987)
6. *Fulmer Materials Optimiser* Fulmer Research Institute, Stoke Poges, Bucks, U.K. (1974)
7. G. Simmons and H. Wang, *Single Crystal Elastic Constants and Calculated Aggregate Properties* MIT Press, Cambridge, Mass. (1971)
8. B. J. Lazan, *Damping in Materials and Members in Structural Mechanics* Pergamon Press, Oxford (1968)
9. H. J. Frost and M. F. Ashby, *Deformation Mechanism Maps*, Pergamon Press, Oxford (1982)
10. H. E. Boyer, *Atlas of Creep and Stress-Rupture Curves* ASM International, Columbus, Ohio (1983)
11. *ASM (1973) Metals Handbook*, 8th edn Am Soc Metals, Columbus, Ohio (1973)
12. C. J. Smithells, *Metals Reference Book*, 6th edn Butterworths, London (1984)
13. N. P. Bansal and R. H. Doremus, *Handbook of Glass Properties* Academic Press, New York (1986)
14. *Handbook of Plastics and Elastomers* (edited by C. A. Harper) McGraw-Hill, New York (1973)
15. *International Plastics Selector, Plastics*, 9th edn Int Plastics Selector, San Diego, Calif (1987)
16. A. K. Ilavnick and H. L. Stephens, *Handbook of Elastomers* Marcel Dekker, New York (1983)
17. S. P. Clark Jr (Editor) *Handbook of Physical Constants*, Memoir 97 Geol Soc. Am., New York (1966)
18. W. E. C. Creyke, I. E. J. Sainsbury and R. Morrell, *Design with Non Ductile Materials* (1982) Appl Sci., London (1982)
19. R. Morrell, *Handbook of Properties of Technical and Engineering Ceramics*, Parts I and II Natl Physical Lab., HMSO, London
20. *Composites, Engineered Materials*, Vol. I ASM Int., Columbus, Ohio (1987)
21. *Engineering Guide to Composite Materials*, ASM Int., Columbus, Ohio (1987)
22. J. M. Dinwoodie, *Timber, Its Nature and Behaviour* Van Nostrand-Reinhold, Wokingham, U.K. (1981)
23. L. J. Gibson and M. F. Ashby, *Cellular Solids, Structure and Properties* Pergamon Press, Oxford (1988)
24. M. F. Ashby, *Materials Selection in Design* To be published
25. C. E. Pearson, *Theoretical Elasticity* Harvard Univ Press, Cambridge, Mass (1959)

Overview

Materials selection in conceptual design

M. F. Ashby

Information on material properties is essential to engineering design. The breadth and precision of the data that the designer requires depend on the stage the design has reached: at the start (the 'conceptual' stage), low level data for all materials; at the finish (the 'detailed design' stage), data at a high level of precision for one or a few materials. In this paper, a procedure for materials selection in mechanical design is described which allows the identification, from among the full range of materials available to the engineer, the subset most likely to perform best in a given application.

MST 1064

© 1989 The Institute of Metals. The author is in the Engineering Department University of Cambridge. This paper was presented at the Materials '88 conference 'Materials and Engineering Design', held in London on 9-13 May 1988 and organised by The Institute of Metals.

Introduction

It is said that there are more than 50 000 materials available to the engineer. Materials enter all aspects of engineering design, from the most integrated of microelectronics to the most massive of civil engineering structures. The cost of materials in microelectronics is a small fraction (2-3%) of the cost of the product. By contrast, in mechanical and civil engineering, material costs often exceed 50% of the product cost and the volume of material used is very large. Thus, this overview is restricted to the materials of mechanical and civil engineering. It is here that the competition between materials is greatest and opportunities for innovation are most marked. It is convenient to catalogue these materials into six broad classes (see Fig. 1): metals, polymers, elastomers, ceramics, glasses, and composites. Within each class, there is some commonality in properties, processing, and use pattern, e.g. ceramics have high moduli, polymers have low moduli; metals can be shaped by casting and forging, composites require lay-up or special moulding techniques. However, this compartmentalisation has its dangers: it can lead to specialisation (the metallurgist who knows nothing of polymers) and to conservative thinking ('we use steel, because we have always used steel').

There was a time when metals so dominated mechanical design that ignorance of the potential of other materials was hardly a handicap, but that has changed dramatically. The range of materials available to the engineer is larger, and is growing faster, than ever before (see also Ref. 1). New materials create opportunities for innovation, for new products, and for the evolutionary advance of existing products to give greater performance at lower cost. Markets are captured by the innovative use of new materials and lost by the failure to perceive the opportunities they present: but how is one to find one's way through the enormous catalogue, narrowing it down to a single, sensible choice? Can one devise a rational procedure for material selection? To answer that the design process must first be discussed briefly.

Materials data in design process

In the central column of the flowchart of Fig. 2, the stages of the design process^{2,3} are shown much simplified. A market need is identified. A concept for a product which meets that need is devised. If approximate calculations (left-hand columns) show that, in principle, the concept will work, the design proceeds to the embodiment stage: a more detailed analysis, leading to a set of working drawings giving the size and layout of each component of the product, estimates of its performance, cost, etc. If the

outcome is successful, the designer proceeds to the detailed design stage: full analysis using computer methods (if necessary) of critical components, preparation of detailed production drawings, specification of tolerance, precision, joining methods, finishing, etc.

Materials selection^{4,5} enters at every stage of the design process, but the nature of the data for the material properties required at each stage differs greatly in its level of precision and breadth (Fig. 2, right-hand column). At the conceptual design stage, the designer requires approximate data for the widest possible range of materials. All options are open: a polymer may be the best choice for one concept, a metal for another, even though the function is the same. Those types of data are found in low precision tables such as those of the Fulmer Materials Optimiser,⁶ the Materials Selector,⁷ or in materials selection charts of the type shown below. The low level of precision is not a problem; it is perfectly adequate for this task. The problem is access: how can the data be presented to give the designer the greatest freedom in considering alternatives? The charts help here and examples are given below.

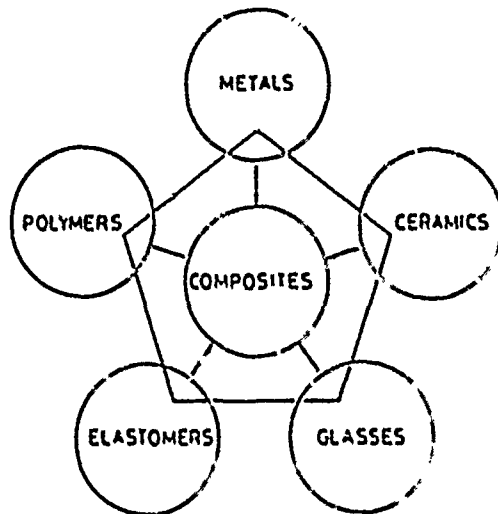
Embodiment design requires data at the second level of precision and detail. The more detailed calculations involved in deciding on the scale and lay-out of the design require the use of more detailed compilations, multivolume handbooks such as Refs. 8-12 or computer databases that contain the same information. These list, plot and compare properties of a single class of materials and allow choice at a level of detail not possible from the broader compilations which include all materials.

The final stage of detailed design requires a still higher level of precision and detail. This is best found in the datasheets issued by the material producers. A given material (e.g. low density polyethylene) has a range of properties, which derive from differences in the methods of manufacture of the various producers. At the detailed design stage, a supplier should be identified and the properties of his product used in the design calculation, but sometimes even this is not good enough. If the component is a critical one (meaning that its failure could, in some sense or another, be disastrous), then it may be prudent to conduct in-house tests, measuring the critical property on a sample of the batch of material that will be used to make the actual product.

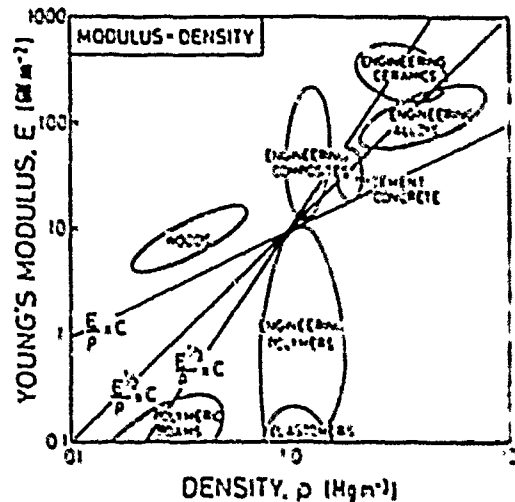
This overview is concerned with the first level of data: the broad, low precision compilation - and methods of presentation to simplify the task of selection.

Materials selection in conceptual design

It is important, as is stated above, to start the design process with the full menu of materials in mind; failure to



1 'Menu' of engineering materials: each class has properties which occupy particular part (or field) of each of materials selection charts (e.g. see Figs. 3, 5, 7, 9, 11)



3 Schematic of materials selection chart - Young's modulus E is plotted against density ρ on log scales so performance criteria (e.g. E/ρ or $E^{1/2}/\rho$) can be examined easily - each class of material (see Fig. 1) occupies characteristic part of chart

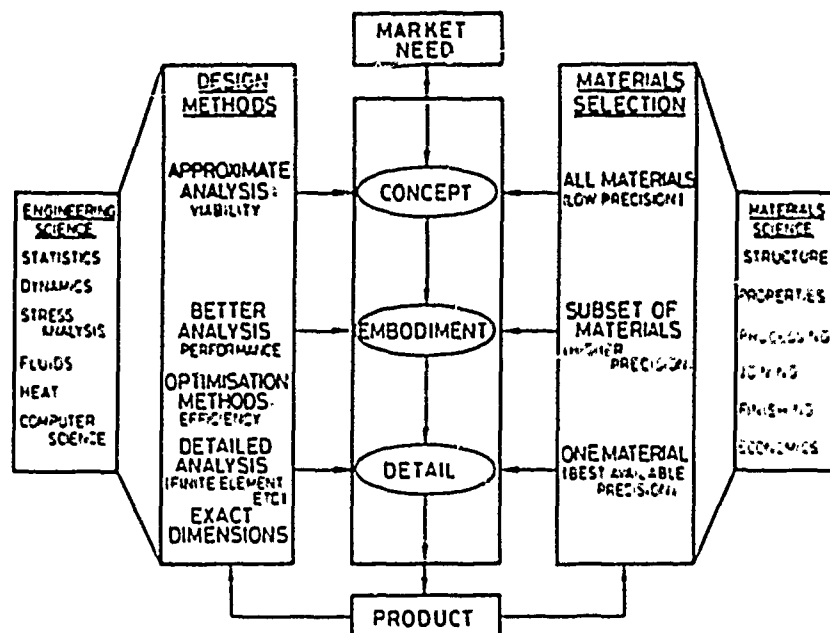
do so may mean a missed opportunity. The immensely wide choice is narrowed, first, by primary constraints dictated by the design, then by seeking the subset of materials which maximise the performance of the component. One way of doing this quickly and effectively is by using materials selection charts.

The idea behind the charts is illustrated by Fig. 3. One material property (the modulus in this instance) is plotted against another (the density) on logarithmic scales. When this is done, it is found that data for a given class of materials (e.g. engineering polymers) cluster together; they can be enclosed in a single 'balloon'. The balloon is constructed to enclose all materials in the class - even those not explicitly listed on the chart. As a result, data for E and

ρ for all materials, are displayed in a conveniently accessible way.

Primary constraints in materials selection are imposed by those characteristics of the design of a component that are non-negotiable: the temperature and environment to which it is exposed, its weight, its cost, etc. If these are specified, all but the subset of materials which satisfy these constraints can be eliminated. A primary constraint corresponds to a horizontal or vertical line on the diagram: all materials to one side of the line can be rejected.

Further narrowing is achieved by seeking that combination of properties which maximises the performance of the component. For most common load bearing components, performance is limited, not by a single property, but by a



2 Design process, much simplified (central column), showing how engineering science and materials science interface with each stage: breadth and precision of materials data required at each stage differ greatly

combination of properties. The lightest tie rod which will carry a given axial load is that with the greatest value of σ_y/ρ , where σ_y is the yield strength and ρ is the density of the material. The lightest column which will support a given compressive load without buckling is that with the greatest value of $E^{1/2}/\rho$ where E is Young's modulus. The best material for a spring, regardless of its shape or the way it is loaded, is that with the greatest value of σ_y/E . Ceramics with the best thermal shock resistance are those with the largest value of $\sigma_f/\alpha E$, where σ_f is the fracture stress and α is


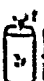

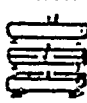






the thermal coefficient of expansion. There are numerous such combinations, depending on the application and those for some simple loading geometries are given in Table 1. The charts can be used to select materials which maximise any one of these combinations. Referring again to Fig. 1 the condition

$$E/\rho = C$$

or, taking logs,

$$\log E = \log \rho + \log C$$

Table 1 Property combinations which determine performance in minimum weight design (for minimum cost design, ρ is replaced by $C_0\rho$, where C_0 is relative cost per unit weight of material)

Mode of loading		Minimum weight for given		
		Stiffness	Ductile strength	Brittle strength
Tie rod F, L specified r free		E/ρ	σ_y/ρ	K_{IC}/ρ
Tension bar F, L specified r free		$G^{1/2}/\rho$	$\sigma_y^{1/2}/\rho$	$K_{IC}^{1/2}/\rho$
Tension tube F, L, r specified t free		$G^{1/2}/\rho$	$\sigma_y^{1/2}/\rho$	$K_{IC}^{1/2}/\rho$
Bending of rods and tubes F, L specified r or t free		$E^{1/3}/\rho$	$\sigma_y^{2/3}/\rho$	$K_{IC}^{2/3}/\rho$
Buckling of slender column or tube F, L specified r or t free		$E^{1/2}/\rho$		
Bending of plate F, L, w specified t free		$E^{1/3}/\rho$	$\sigma_y^{2/3}/\rho$	$K_{IC}^{2/3}/\rho$
Buckling of plate F, L, w specified t free		$E^{1/2}/\rho$		
Cylinder with internal pressure p, r specified t free		E/ρ	σ_y/ρ	K_{IC}/ρ
Rotating cylinder w, r specified t free		E/ρ	σ_y/ρ	K_{IC}/ρ
Sphere with internal pressure p, r specified t free		$E/(1-\nu)/\rho$	σ_y/ρ	K_{IC}/ρ

K_{IC} is fracture toughness, G is bulk modulus.

Table 2 Basic subset of material properties

Relative cost, C_r
Density ρ , Mg m^{-3}
Young's modulus E , GN m^{-2}
Strength σ , MN m^{-2}
Damping coefficient (1/m)
Thermal conductivity k , $\text{W m}^{-1} \text{K}^{-1}$
Thermal diffusivity α , $\text{m}^2 \text{s}^{-1}$
Thermal expansion β , K^{-1}
Strength at temperature σ_t , MN m^{-2}
Wear rate WTA
Corrosion resistance

is a family of straight parallel lines of unit slope: one line for each value of the constant C .

The condition

$$E^{1/2}/\rho = C$$

gives another set, in this instance having a slope of 2.

A third condition

$$E^{1/3}/\rho = C$$

gives yet another set of slope 3.

It is now easy to read off the materials which are optimal for each loading geometry—assuming, of course, that no other factors (e.g. corrosion resistance) need be considered. If a straight edge is laid parallel to the line $E^{1/2}/\rho = C$, all the materials which lie on the line will perform equally well as a light column loaded in compression; those above the line are better, those below, worse. If the straight edge is translated towards the top left corner of the diagram, the choice narrows. At any given position of the edge, two materials which lie on its edge are equally good and only the subsets which remain above are better. The same procedure, applied to the tie rod (E/ρ) or plate in bending ($E^{3/2}/\rho$), lead to different equivalences and optimal subsets of material.

In mechanical design, there are 12 properties which, singly or in combination, usually limit performance and these are given in Table 2. There are charts for all these properties in the combinations which occur most frequently.¹² Four of the charts are discussed below using brief examples of how each chart allows materials to be selected for a particular application.

Materials selection charts and their uses

MATERIALS FOR TABLE LEGS

Luigi Tavolino, furniture designer, conceives of a light-weight table of daring simplicity: a flat sheet of toughened glass supported on slender, unbraced, cylindrical legs (Fig. 4). The legs must be solid (to make them thin) and as light as possible (to make the table easier to move). They must support the load imposed on them by the table top and whatever is placed upon it, without buckling. What materials could one recommend?

Slenderness imposes a primary constraint: slender columns must be stiff, that is, they must be made of a material having a high modulus E . Lightness, while still supporting the design load, puts a further restriction on the material choice: reference to Table 1 (and the discussion of the previous section) suggests that the choice should focus on materials having high values of $E^{1/2}/\rho$. The appropriate chart is shown in Fig. 5a, on which Young's modulus E is plotted against density ρ ; it is the chart of which Fig. 3 is a schematic. Materials of a given class cluster together: metals in the top right, composites near the middle, polymers near the bottom, etc. In Fig. 5b, the selection procedure is shown. A line of slope 3 is drawn on the

diagram; this line links materials having equal values of $E^{1/2}/\rho$. Materials above the line are better choices for this application than materials on the line; materials below are worse. The line is displaced upwards until a reasonably small selection of materials remains above it. These are identified on Fig. 5b: woods, composites (particularly CFRP) and certain special engineering ceramics. Metals are not suitable: they are far too heavy; so also are polymers, because they are not nearly stiff enough. The choice is further narrowed by the primary constraint that, for slenderness, E must be large. A horizontal line on the diagram links materials having equal values of E ; those above are stiffer. It can be seen from Fig. 5b that this now eliminates woods. The best choice is CFRP—using which legs of the same weight as, but thinner than, wooden ones can be made. At this stage, other aspects of the design must be examined: strength, cost, etc., for which there are other charts, but discussion is limited to those presented here.

MATERIALS FOR FORKS OF RACING BICYCLES

The first consideration in bicycle design (Fig. 6) is strength. Stiffness is a factor, of course; but the initial design criterion is that the frame and forks should not yield or fracture in normal use. The loading on the frame is not obvious; in practice, it is a combination of axial loading and bending. That on the forks is simpler: it is predominantly bending. If the bicycle is for racing, then the weight is a primary consideration: the forks should be as light as possible in a material having the greatest value of $\sigma^{2/3}/\rho$, should be chosen (see Table 1).

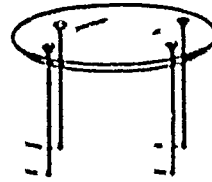
The appropriate chart is shown in Fig. 7a: strength (yield strength for ductile materials, crushing strength for brittle) plotted against density. As in the previous example, materials of the same class cluster together in one area of the chart: metals near the top right, polymers in the middle, structural foams in the bottom left. In Fig. 7b the selection procedure is shown. A line of slope 3 is drawn on the chart. It links materials having the same value of $\sigma^{2/3}/\rho$, i.e. materials which (as far as strength is concerned) are equally good for making the forks of a racing bicycle. All materials above the line are better; those below are worse.

Four materials are singled out: high strength aluminium (7075, T6) and titanium alloys are equally good. Reynolds 531 (a high strength steel popular for bicycle frames) is a little less good; CFRP is definitely better. At this stage, it is necessary to examine other aspects of the material choice: stiffness, resistance to fracture, etc. (there are charts to assist with this), and to examine the cost of fabrication (though, to the committed racing cyclist, cost is irrelevant). Again, CFRP emerges from such an analysis as an attractive, though expensive, choice; and, of course, it is used in exactly this application.

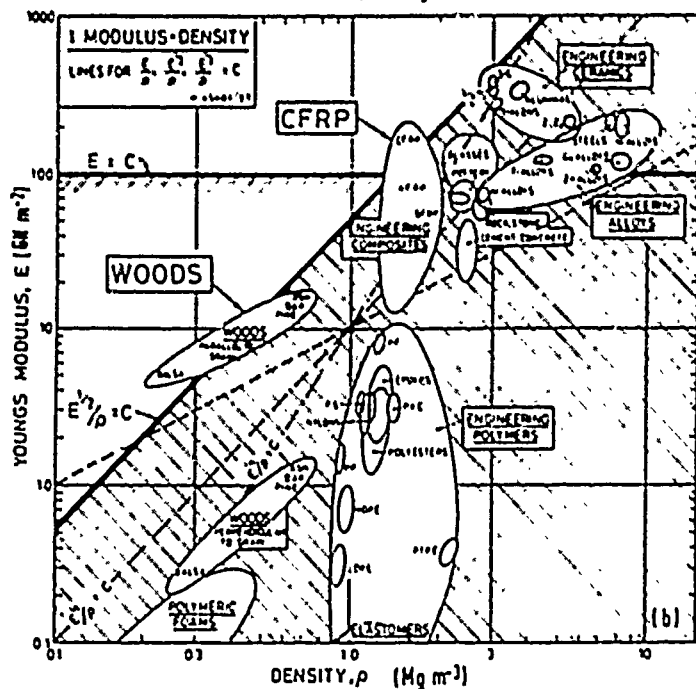
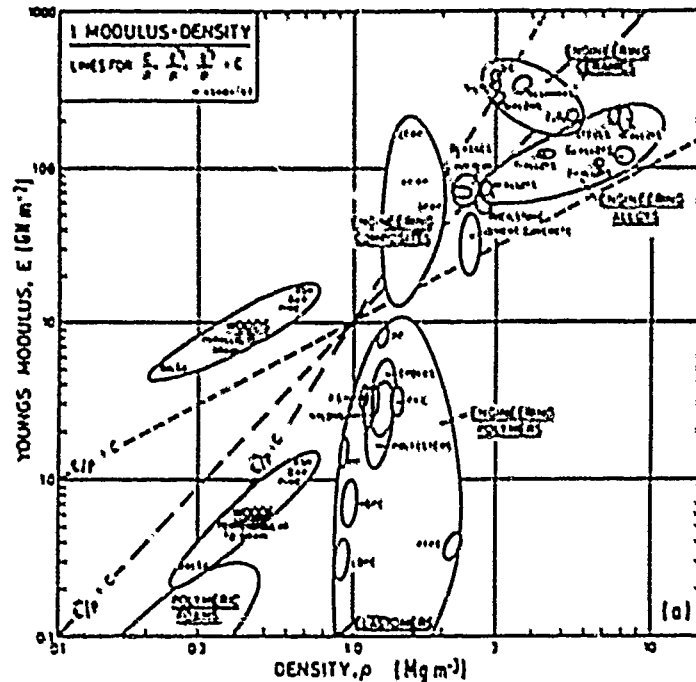
MATERIALS FOR SPRINGS

Springs can be of many shapes (Fig. 8) and have many purposes. Regardless of their shape or use, the best material for a spring of minimum volume (e.g. for a watch) is that having the greatest value of σ^2/E . The reasons for this are not discussed here, but the result is used to introduce the chart shown in Fig. 9a: modulus E plotted against strength σ . As usual, materials cluster together by class although there is some overlap. This diagram has many uses: one is the identification of good materials for springs.

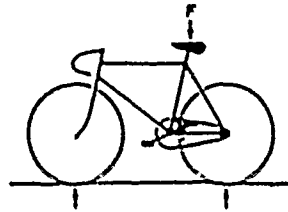
The selection procedure is shown in Fig. 9b. A line of slope 1 links materials having the same value of σ^2/E . As the line is moved to the right (to increasing values of σ^2/E) a smaller selection of materials remains. The result is shown in the figure, where candidate materials are identified. The best choices are a high strength steel (spring steel, in fact) and at the other end of the line, rubber. Certain other



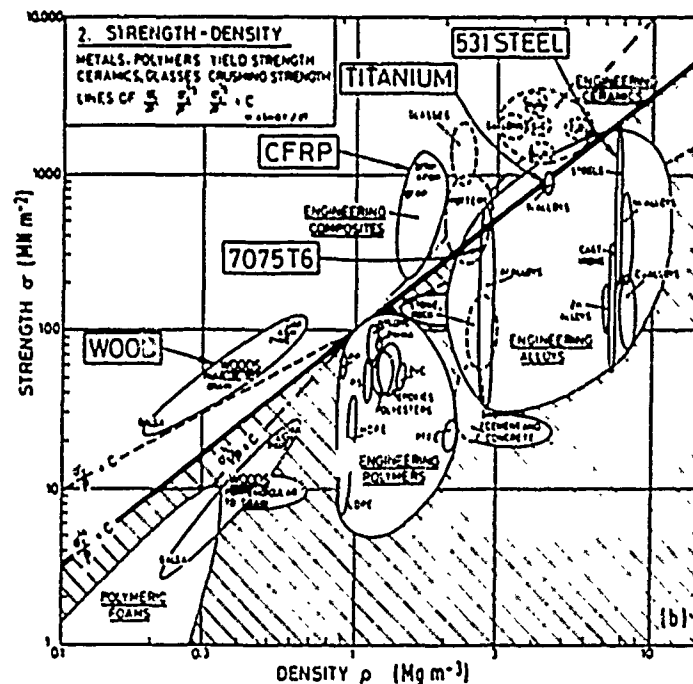
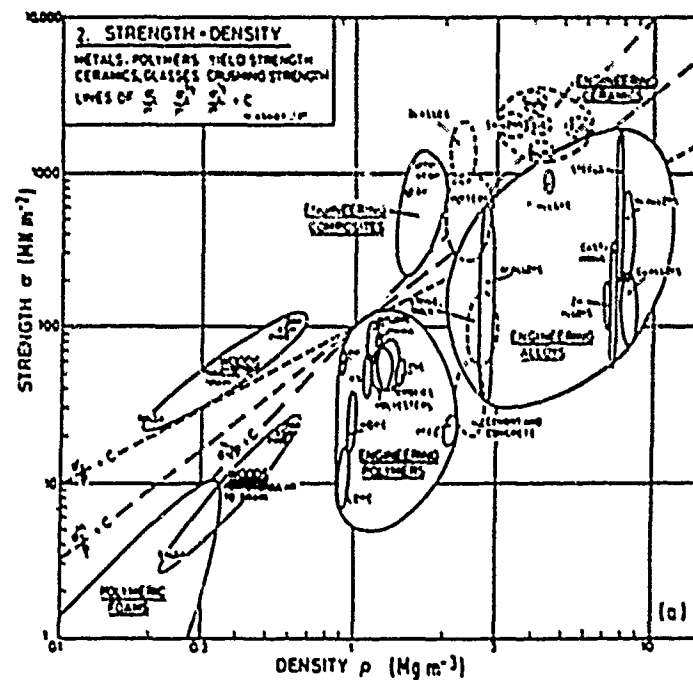
- 4 Lightweight table with cylindrical legs which are required to be slender, but which must not buckle elastically when table is loaded; material having high values of E and $E^{1/3}/\rho$ is therefore required



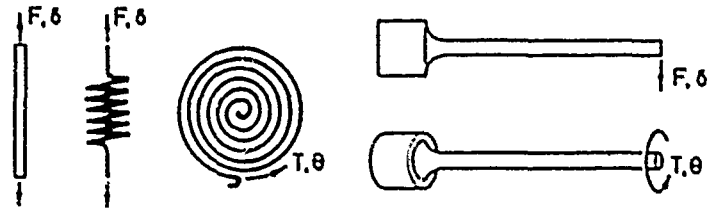
- 5 a Materials selection chart 1: Young's modulus against density (balloons enclose data for given class of material);
b materials for light, slender column: wood is good choice, so is composite such as carbon fibre reinforced plastic (CFRP), which (having higher modulus) gives column that is both light and slender



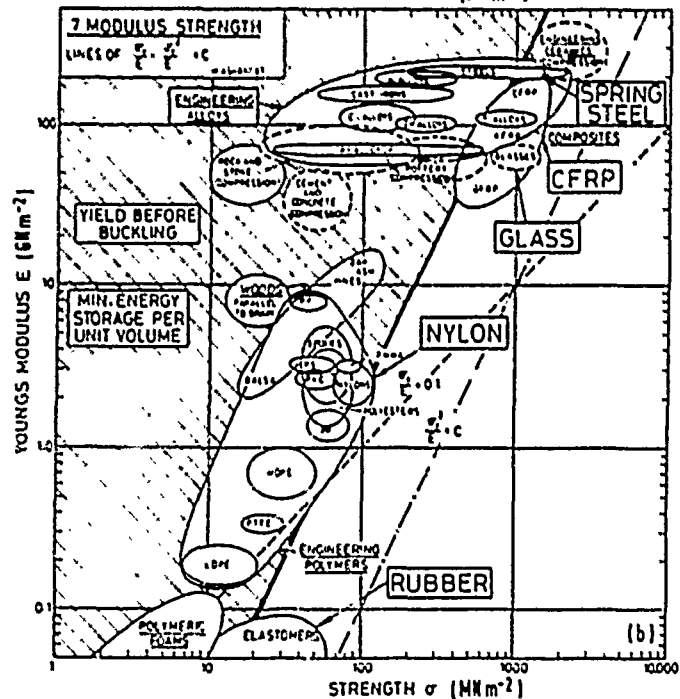
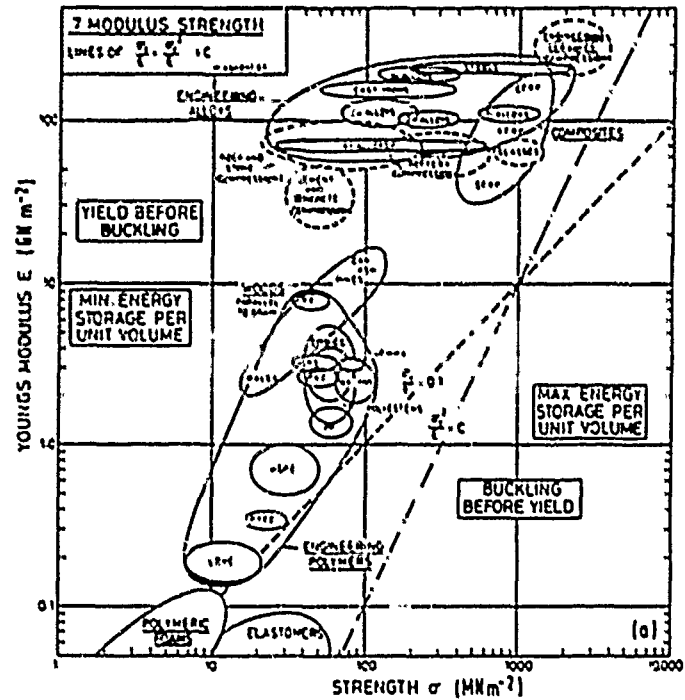
- 6 Racing bicycle having forks that are loaded in bending: lightest forks which will not collapse plastically are made with material having greatest value of $\sigma_y^{2/3}/\rho$



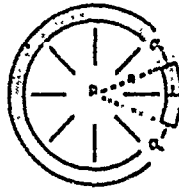
- 7 a Materials selection chart 2: strength (yield strength σ_y for ductile materials, compressive crushing strength for brittle solids) plotted against density ρ ; b materials for forks of racing bicycle: Ti alloy or 7075 Al alloy perform better than steel. CFRP better still, but other aspects of design (stiffness, resistance to fracture, fabrication costs, etc.) must be examined before final choice is made



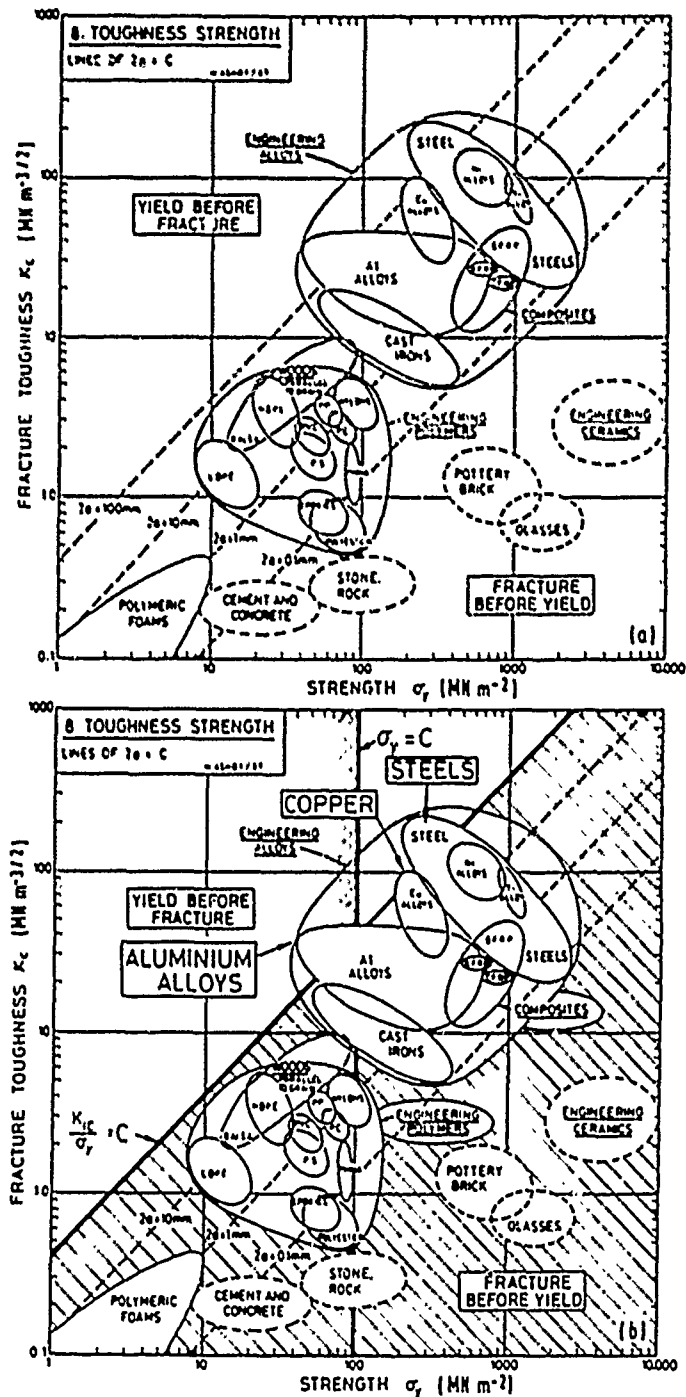
- 8 Springs: best material for any spring, regardless of its shape or way in which it is loaded, is that having highest value of σ_y^2/E



- 9 a Materials selection chart 7: Young's modulus E against strength (yield strength σ_y for ductile materials, compressive crushing strength for brittle solids); b materials for springs: rubber, of course, is good, high strength ('spring') steel is good, but both glass and CFRP under correct conditions, also make excellent springs



- 10 Pressure vessel containing a flaw: safe design requires that pressure vessels should leak before they break and therefore best material is that having greatest value of K_{IC}/σ_y



- 11 a Materials selection chart 8: fracture toughness K_{IC} against strength σ_y ; b materials for pressure vessels: steel, Cu alloys, and Al alloys best satisfy 'yield before break' criterion and high yield strength allows high working pressure – materials in remaining triangle are best choice

materials are also suggested: CFRP (now used for truck springs), titanium alloys (good but expensive), glass (used in galvanometers), and nylon (children's toys often have nylon springs). Note how the procedure has identified the best candidates from almost every class: metals, glasses, polymers, and composites.

SAFE PRESSURE VESSELS

Pressure vessels, from the simplest aerosol can to the biggest boiler, are designed, for safety, to yield before they break. The details of this design method vary. Small pressure vessels are usually designed to allow general yield at a pressure still too low to propagate any crack the vessel may contain ('yield before break'); then materials having the largest possible value of K_{Ic}/σ_y are the best choice - they will tolerate the biggest flaw. With large pressure vessels this may not be possible; instead, safe design is achieved by ensuring that the smallest crack that will propagate unstably has a length greater than the thickness of the vessel wall ('leak before break', Fig. 10), and the best choice of material is one having a large value of K_{Ic}^2/σ_y . That covers safety; the actual pressure that the vessel can hold is proportional to σ_y , so the designer also seeks to maximise that property.

These selection criteria are most easily applied by using the chart shown in Fig. 11a on which the fracture toughness K_{Ic} is plotted against strength σ_y . Strong, tough, materials lie towards the top right; hard, brittle materials in the bottom right, etc. The three criteria appear as lines of slopes 1 and 1 and as lines that are vertical. Taking yield before break as an example (Fig. 11b): a diagonal line corresponding to $K_{Ic}/\sigma_y = C$ links materials of equal performance; those above the line are better. The line shown on Fig. 11b excludes everything but the toughest steels, copper, and aluminium alloys, although some polymers are only just excluded (pressurised lemonade and beer containers are made of these polymers).

The pressure which the vessel can hold depends also on the magnitude of σ_y . The vertical line excludes all materials of yield strength $< 100 \text{ MN m}^{-2}$, leaving only tough steels and copper alloys. Large pressure vessels are always made of steel. Those for models (e.g. model steam traction engine) are of copper which is favoured in the small scale application, because of its greater resistance to corrosion.

Conclusions

Materials are being evolved faster than ever before. New and improved materials create opportunities for innovation. The opportunities can be missed unless a rational procedure for material selection is followed.

At the conceptual stage, while the design is still 'fluid', the designer must consider the full menu of materials: metals, polymers, elastomers, ceramics, glasses, and numerous composites. Material data for a single class or subgroup of materials (suitable for the embodiment stage) are available in handbooks and computerised databases; and the precise, full data for a single material (required at the detailed design stage) are available from the supplier of the material,

or can be generated by in-house tests.

The difficult step is the first: choosing from the vast range of engineering materials an initial subset on which design calculations can be based. One approach to this problem is described in this paper. Data for the mechanical and thermal properties of all materials are presented as a set of materials selection charts. The axes are chosen to display the common performance limiting properties: modulus, strength, toughness, density, thermal conductivity, wear rate, etc. The logarithmic scales allow performance limiting combinations of properties (such as $E^{1/2} \rho$ or σ_y^2/E) to be examined and compared.

The examples given in the text show how the charts give a broad overview of material performance in a given application and allow a subset of materials (often drawn from several classes) to be identified quickly and easily. The uses are much wider than those shown here; charts exist which help with problems of dynamics, heat transfer, thermal stress, wear, and cost. They help, too, in finding a niche for new materials: plotted on the charts, the applications in which the new material offers superior performance become apparent.

At present, the charts exist as hand drawn diagrams such as those shown here, but it is an attractive (and attainable) goal to store the data from which they are constructed in a database coupled to an appropriate graphics display to allow charts with any combination of axes to be presented, and to construct on them lines which isolate materials with attractive values of performance limiting properties (just as in the examples) leading to a printout of candidate materials with their properties. A microcomputer based system of this type is at present under development in the Engineering Department at the University of Cambridge.

References

1. J. A. CHARLES: *Mater. Sci. Technol.*, this issue, S09-S16.
2. G. PAHL and W. BEITZ: in 'Engineering design', 1984, The Design Council (London) Springer (Berlin).
3. M. J. FRENCH: in 'Conceptual design for engineers', 1985, The Design Council (London) Springer (Berlin).
4. G. E. DIETZ: in 'Engineering design: A materials and processing approach', 1983, New York/London, McGraw-Hill.
5. F. A. A. CRANE and J. A. CHARLES: in 'Selection and use of engineering materials', 1984, London, Butterworths.
6. 'Fulmer materials optimiser', Fulmer Research Institute, Stoke Poges, Bucks, 1974.
7. 'Materials selector': *Mater. Eng.* (special issue), Reinhold, Stamford, CT, 1976.
8. 'ASM metals handbook', 8 edn; 1973, Metals Park, OH, ASM.
9. C. J. SMITHIELLS (ed.): 'Metals reference book', 6 edn, 1984, London, Butterworths.
10. C. A. HARPER (ed.): 'Handbook of plastics and elastomers', 1975, New York, McGraw-Hill.
11. R. MORRELL: 'Handbook of properties of technical and engineering ceramics', Part 1, 1985, London, HMSO.
12. R. MORRELL: 'Handbook of properties of technical and engineering ceramics', Part 2, 1987, London, HMSO.
13. M. F. ASHBY: 'Materials selection in design', Internal Report, University of Cambridge, 1987 (to be published).

Part 2 of Section 2
continues in
Book 3